UNIVERSITÉ DE LORRAINE | BIBLIOTHÈQUES UNIVERSITAIRES

AVERTISSEMENT

Ce document est le fruit d'un long travail approuvé par le jury de soutenance et mis à disposition de l'ensemble de la communauté universitaire élargie.

Il est soumis à la propriété intellectuelle de l'auteur. Ceci implique une obligation de citation et de référencement lors de l'utilisation de ce document.

D'autre part, toute contrefaçon, plagiat, reproduction illicite encourt une poursuite pénale.

Contact bibliothèque : ddoc-theses-contact@univ-lorraine.fr
*(Cette adresse ne permet pas de contacter les auteurs)*

LIENS

Code de la Propriété Intellectuelle. articles L 122. 4
Code de la Propriété Intellectuelle. articles L 335.2- L 335.10
http://www.cfcopies.com/V2/leg/leg_droi.php
http://www.culture.gouv.fr/culture/infos-pratiques/droits/protection.htm

Thèse

Présentée et soutenue publiquement pour l'obtention du titre de

# DOCTEUR DE l'UNIVERSITE DE LORRAINE

Mention : GÉOSCIENCES

par Marius Lothar HUBER

Sous la direction de Jérôme LAVÉ et Luc SCHOLTÈS

# Dynamique des grands glissements de terrain rocheux, modélisation numérique et études de cas en Himalaya

soutenue le 26 juin 2024

Membres du jury :

| | | |
|---|---|---|
| Président de jury : | M. David AMITRANO | Professeur d'université, Université Grenoble Alpes, Laboratoire ISTerre, Grenoble |
| Rapporteurs : | M. Federico AGLIARDI | Professeur associé, Università degli Studi di Milano-Bicocca, Milan, Italie |
| | M. Pascal LACROIX | Chargé de recherche IRD, Université Grenoble Alpes, Laboratoire ISTerre, Grenoble |
| Examinatrice : | Mme Marin CLARK | Professeure, Université du Michigan, Ann Arbor, les États-Unis d'Amérique |
| Membre invitée : | Mme Monique FORT | Professeure émérite, Université Paris Cité (Paris Diderot), Paris |
| Directeurs de thèse: | M. Jérôme LAVÉ | Directeur de recherche, CRPG – CNRS et Université de Lorraine, Nancy, France |
| | M. Luc SCHOLTÈS | Maître de conférence, CNRS, IRD, OPGC, LMV, Clermont-Ferrand, France |

**TITRE :**

**Dynamique des grands glissements de terrain rocheux, modélisation numérique et études de cas en Himalaya**

**RÉSUMÉ :**

Les glissements de terrain sont un phénomène courant à la surface de la Terre. Ils représentent à la fois un risque naturel majeur pour les populations et les infrastructures, et un processus dominant dans l'érosion des pentes montagneuses et dans l'évolution des surfaces continentales. Les facteurs qui conditionnent et préparent les pentes avant de les conduire à s'effondrer sont multiples et comprennent, entre autre, les caractéristiques du matériau constitutif du versant ainsi que des facteurs externes tels que le climat et la sismicité. L'étude de ces facteurs est fondamentale pour pouvoir comprendre l'apparition des mouvements gravitaires et leur dynamique. Cela inclut notamment la compréhension des déformations de grande ampleur, qui bien que se produisant rarement ou avec un faible taux d'activité, ont un fort impact en termes d'aléas naturels et de développement des reliefs.

Cette thèse de doctorat se concentre sur les glissements de terrain profonds qui se produisent au sein du substrat rocheux des versants. La première partie de cette thèse s'intéresse à deux phénomènes gravitaires majeurs se produisant dans le massif de l'Annapurna en Himalaya (Népal central) : les écroulements rocheux géants (volume de débris > 0,1 $km^3$) et les déformations gravitaires non-catastrophiques de versants (DSGSD en anglais). Des mesures d'âge d'exposition basées sur les nucléides cosmogéniques (isotopes $^{10}Be$ et $^{36}Cl$) et d'âge d'enfouissement ($^{14}C$) nous ont permis de dater l'âge de 3 écroulements géants en flanc nord des Annapurnas, et de reconstruire la paléo-activité d'un grand DSGSD en flanc sud. Combinés avec la reconstruction des volumes, nos résultats indiquent que les écroulements géants se sont produits pendant l'optimum climatique de l'Holocène (EHCO) et l'optimum climatique médiéval, c'est-à-dire principalement à la fin de périodes plus chaudes et plus humides qu'ait connu la Terre. Ce synchronisme suggère un forçage climatique sur le déclenchement des effondrements géants. Nous identifions également une plus grande activité du DSGSD à la fin de l'EHCO, soulignant de même le rôle du forçage climatique sur la déstabilisation des versants himalayens.

Dans la deuxième partie de la thèse, un modèle numérique aux éléments discrets est utilisé pour étudier comment l'anisotropie mécanique de la roche affecte la rupture d'un versant de pente uniforme. Après avoir défini un matériau à isotropie transverse et aux caractéristiques mécaniques proches de celles d'un gneiss, nous explorons de manière systématique et en deux dimensions (0 - 180°), l'influence sur la rupture de l'orientation relative du plan d'isotropie par rapport à celle du versant. Nos résultats indiquent que si le plan d'isotropie est légèrement moins incliné que la pente topographique (configuration cataclinale), la stabilité de la pente n'est assurée qu'avec une résistance du substrat beaucoup plus élevée que dans une configuration où le plan d'isotropie est perpendiculaire à la pente (configuration anaclinale). De plus, comme constaté sur le terrain en Himalaya, les modes d'effondrement des versants dépendent fortement de l'orientation du plan d'isotropie. Nous observons : pour les pentes cataclinales, un glissement parallèle au plan d'isotropie ou sinon un flambage, si le versant est plus ou respectivement moins raide que le plan d'isotropie ; pour les pentes anaclinales, un basculement/fléchissement ou l'éboulement par blocs, suivant que le plan d'isotropie est à fort ou à faible pendage.

Contredisant, pour les montagnes actives, la vision simplifiée de versants aux pentes uniformes et proches de l'angle de frottement interne des roches, notre travail met en évidence une diversité de pentes critiques et de processus de glissement de terrain qui dépendent à la fois de facteurs internes (e.g. l'anisotropie) et de facteurs externes (contexte tectono-climatique).

ce qui suit est rédigé en anglais

**TITLE:**

**Dynamics of large bedrock landslides, numerical modelling and Himalayan case studies**

**ABSTRACT:**

Landslides are a common phenomenon on the Earth's surface. They come in many forms as a wide range of environmental conditions determine the characteristics of slope failure. They are a threat to human society and play an important role in the denudation of hillslopes and thus in the evolution of the Earth's surface. Factors that precondition and prepare slopes to failure are diverse and include the characteristics of the failure material as well as external factors such as climate and seismicity. A conceptually coherent understanding of these factors is required to better assess landslides, especially their large representatives which occur with low frequency and activity rates, but are however critical in terms of natural hazards and development of reliefs.

This PhD-thesis is focused on bedrock landslides, which are slope failures that occur in rock masses. In the first part of the thesis, two subtypes of bedrock landslides located in the Annapurna Massif of central Nepal are investigated: Giant rock avalanches (> 0,1 $km^3$ failure volume) and non-catastrophic Deep-Seated Gravitational Slope Deformations (DSGSDs). Absolute dating techniques, including cosmogenic nuclide exposure measurements ($^{10}Be$ and $^{36}Cl$ isotopes) and $^{14}C$ carbon burial dating were used to determine the age and volumes of 3 giant rock avalanches and reconstruct the paleo-activity of a DSGSD. Our results indicate that the giant rock avalanches occurred predominantly at the end of Holocene periods with warmer and wetter climatic conditions, i.e. during the Early Holocene Climatic Optimum (EHCO) and the Medieval Warm Period (MWP). This highlights the role of climatic forcing on slope failure. We also identified a higher activity of the DSGSD at the end of the EHCO, further emphasizing the role of climatic forcing on slope destabilization. Besides their implications for natural hazards, our results offer new perspectives on mountain-scale erosion fluxes and landscape denudation in the region.

In the second part of the thesis, a discrete element model is used to investigate how rock strength anisotropy affects the failure of a 1 000 m high slope with constant slope angle. After setting up the transverse isotropic material with the mechanical characteristics of a gneiss, the whole range of possible isotropy plane

orientations with respect to the slope face is systematically explored in two dimensions (0 – 180°). Our results indicate that if the isotropy plane is slightly less inclined than the topographic slope (i.e. cataclinal overdip configuration), slope stability requires a material strength one order of magnitude higher than in a configuration where the isotropy plane is perpendicular to the slope (i.e. anaclinal configuration). Moreover, as expected from field observations, slope failure modes are directly constrained by the isotropy plane orientation: sliding is observed for cataclinal overdip slopes, buckling for cataclinal underdip slopes, toppling for anaclinal slopes with steeply dipping isotropy planes, and crumbling for anaclinal slopes with less steeply dipping isotropy planes. By analysing the south-facing slopes of the Annapurna Massif (Nepal), we were able to evidence the role of material anisotropy in landscape shaping in the area. The relative orientation of the anisotropy with respect to the topography is an important precondition of slope failure, controlling both the stability and the failure mode. The systematic investigation performed in this thesis contributes to slope stability analysis in general as well as to a better understanding of landscape shaping by slope failure.

Our work highlights a diversity of critical slopes and landslide processes that depend on both internal factors (in this case, anisotropy) and external factors (tectono-climatic context).

*I would rather have questions that can't be answered*
*than answers that can't be questioned.*

*Richard Feynman (no source)*

**Acknowledgements:**

First, I would like to thank the two Rapporteurs Federico Agliardi and Pascal Lacroix for reviewing my PhD-manuscript and the other jury members Marin Clark, David Amitrano, and Monique Fort for joining the thesis defence. I hope you have discovered some interesting science that made it worthwhile to read this mémoire and participate in the jury.

My thanks also go to the members of the Comité de Suivi Individuel, Frédéric Donzé and Thomas Lebourg, for the time they have devoted to our annual meetings. They gave me useful feedback and advice and motivated me to continue with the PhD-project.

You don't write a thesis alone. Several people have contributed to the scientific content of this thesis and helped me on the long journey of completing this doctorate. My deepest thanks go to all these people, not only for supporting me in my PhD-project but also for helping me set up my life here in France.

My thanks go to Maarten Lupker, who conducted an additional sampling campaign in the upper Marsyangdi Valley in autumn 2020, when the outbreak of a pandemic complicated travelling internationally.
To Valéry Guillou I would like to express my thanks for his contribution to the processing and handling of the 36Cl-samples at Cerege. Although we never met, things went smoothly and the results are fantastic.
My special thanks go to Mustapha Zakari, who helped me with many computer issues, especially setting up the numerical modelling environment. With his tireless support, straightforward help and ability to deal with my frustration when things did not work as they should, he has contributed greatly to the success of this thesis.
Thanks to Apolline Mariotti, who helped me to become acquainted with the CRPG mineral separation and 10Be sample preparation procedures during the Covid crisis, when the laboratory was officially closed.
Studying landforms with a high resolution DSM, going down from 30 to 2 metres, is a whole different game. It was only with the help of Simon Daout, Florian Leder and Sylvain Breton that I was able to use a properly processed DSM from the Pléiades images. Thanks guys!
I would like to thank the two Master's students Aboubacar Demba Diarra and Maëlle Groult for their work on the volume reconstructions of the Pisang Bowl and Latamrang rock avalanche deposits.
Abdellah Zitouni is to be thanked for powdering many of our SARM samples when time was short.
Thanks also to Etienne Large and Catherine Zimmermann for managing and organising the laboratory spaces dedicated to 10Be sample preparation, and for allowing me to be the first to prepare samples when time was running out towards the end of my PhD.
Thanks to all the technicians and staff at the CRPG and the staff at the Georessources Lab for their support.
My thanks go to the guys who helped me the most, besides my thesis supervisors, with the preparation of the defence presentation: Aswin Pradeep Tachambalath, Emmanouil Diakos, Alexis Derycke, and Qasid Ahmad.
I would like to thank my office colleagues Aswin, Julien, Maxime, Gabriel, Yafet, Blandine, and Mme Françoise Chalot-Prat for a pleasant time. And, I would like to mention all the people who made my time in the lab, at lunch, or elsewhere worthwhile: Marine, Julien, Guillaume, Apolline, Gabriel, Olivier, Claire, Belén, Simon, Etienne, Sumith, Nicolas, Qasid, Julie, Baptiste, Hugo, Mara, and everybody I forgot here. Thanks to all of you!

My family and friends always support me in my endeavours. Thank you so much, you are great! Here at Nancy I have made some lifelong friends and many good memories that will stay with me for my future life.

Last but not least, I would like to thank my two supervisors, Jérôme Lavé and Luc Scholtès. They took me on this journey and always supported me despite obstacles and delays. We have done some great science and I have learned a lot from you.

This PhD-thesis was funded by both the Région Grand Est (50%) and the CRPG (50%).

# Table of Contents


| | | page |
|---|---|---|
| | **Title and Abstract in French** | **I** |
| | **Title and Abstract in English** | **V** |
| | **Acknowledgements** | **IX** |
| | **Table of Contents** | **XI** |
| | **Table of Figures** | **XVII** |
| | **Table of Tables** | **XIX** |
| | **Extended summary of doctoral thesis in French** | **1** |
| | **Extended summary of doctoral thesis in English** | **13** |

| **CHAPTER 1** | **INTRODUCTION** | *page* |
|---|---|---|
| **1.1** | **What are bedrock landslides?** | **23** |
| 1.1.1 | Landslides | 23 |
| 1.1.2 | Bedrock landslides | 23 |
| **1.2** | **Some landslide theory** | **26** |
| 1.2.1 | The Factor of Safety | 26 |
| 1.2.2 | Causes and Triggers of landslides | 26 |
| 1.2.3 | The progressive failure of rock slopes | 28 |
| **1.3** | **Catastrophic rock slope failures** | **30** |
| 1.3.1 | Terms and differentiation | 30 |
| 1.3.2 | Short-lived nature of catastrophic bedrock landslides and scarcity of large events | 31 |
| 1.3.3 | Causes and chronology of large catastrophic rock slope failures | 32 |
| 1.3.4 | Morphological and sedimentological consequences | 34 |
| 1.3.5 | Deposit characteristics | 37 |
| 1.3.6 | Societal hazards and risks | 40 |

**1.4** **Non-catastrophic bedrock landslides** **42**

1.4.1 Terminology and characteristic features 42

1.4.2 Causes and temporal evolution 45

1.4.3 Consequences for society and remaining research questions 50

**1.5** **Numerical Modelling for the study of landslides** **53**

1.5.1 Numerical methods for slope stability problems 53

1.5.2 Causes and Triggers of bedrock landslides explored with numerical models 55

**1.6** **Research objectives** **61**

References 63

**CHAPTER 2** **BEDROCK LANDSLIDES IN THE ANNAPURNA MASSIF** *page*

**2.1** **Introduction** **69**

**2.2** **Study area** **71**

2.2.1 Geologic and tectonic setting of the central Himalayas 71

2.2.2 Climate in the central Himalayas 74

**2.3** **Landslides in the central Himalayas and in the Annapurna Massif** **77**

2.3.1 Hazards and risks from central Himalayan bedrock landslides 78

2.3.2 The role of bedrock landslides in mountain-scale erosion 79

2.3.3 Causes and Triggers of central Himalayan rock slope failures 80

2.3.4 Giant catastrophic bedrock landslides in the central Himalayas and the Annapurna Massif 81

2.3.5 Non-catastrophic bedrock landslides in the central Himalayas and the Annapurna Massif 83

**2.4** **Methods** **88**

2.4.1 Field study and mapping 89

*2.4.1.1* *Field surveys* *89*

*2.4.1.2* *Spatial data sets used* *92*

*2.4.1.3* *Dating giant rock slope failures* *93*

*2.4.1.4* *Reconstructing paleo-movement of non-catastrophic rock slope failures* *93*

2.4.2 Carbon burial dating (14C) 94

2.4.3 Cosmogenic nuclide dating 95

*2.4.3.1 Beryllium exposure dating (10Be) 95*

*2.4.3.2 Chlorine exposure dating (36Cl) 96*

*2.4.3.3 Corrections and exposure age calculation 97*

*2.4.3.4 Scarp movement reconstruction 100*

2.4.4 Volume reconstruction of valley deposits 103

**2.5 Results – Upper Marsyangdi 107**

2.5.1 Pisang Bowl 107

*2.5.1.1 Field observations and mapping – Pisang Bowl 107*

*2.5.1.2 Dating results – Pisang Bowl 111*

2.5.2 Deposits around Humde / Manang 118

*2.5.2.1 Field observations and outcrops – Humde / Manang 118*

*2.5.2.2 Mapping and volume reconstruction – Humde / Manang 123*

*2.5.2.3 Dating results – Humde / Manang 128*

2.5.3 Rock avalanche at Tilicho Lake 132

*2.5.3.1 Field observations and outcrops – Tilicho Lake 132*

*2.5.3.2 Mapping and volume reconstruction – Tilicho Lake 136*

*2.5.3.3 Dating results – Tilicho Lake 139*

**2.6 Discussion – Upper Marsyangdi *143***

2.6.1 Integration of our results into the central Himalayan giant rock avalanche record 143

2.6.2 Causes and Triggers of giant rock avalanches in the upper Marsyangdi Valley 148

*2.6.2.1 Precondition Factors 148*

*2.6.2.2 Internal Preparatory Factors 150*

*2.6.2.3 High relief 151*

*2.6.2.4 Climatic forcing 153*

*2.6.2.5 Potential Triggers 158*

**2.7 Results – Annapurna south-face 161**

2.7.1 Khudi Ridge and Phalo Danda site 161

2.7.2 Movement reconstruction on conjugate scarp at Phalo Danda 168

2.7.3 Main scarp movement reconstruction at Phalo Danda 175
*2.7.3.1 Exposure dating profiles 175*
*2.7.3.2 Trench 180*
2.7.4 DSGSD activity of the western Khudi ridge 185
2.7.5 Dating failed masses in Midhi and Khudi valleys 185
**2.8 Discussion – Annapurna south face 187**
2.8.1 Causes of the Phalo Danda DSGSD movement 187
2.8.2 Long-term evolution of the Phalo Danda DSGSD 192
2.8.3 Landscape evolution on the southern Annapurna slopes 195
**2.9 Discussion – Annapurna Massif 201**
2.9.1 Causes of bedrock landslides in the central Himalayas 201
*2.9.1.1 Precondition Factors 201*
*2.9.1.2 Preparatory and Movement Sustaining Factor of bedrock slope failures 203*
*2.9.1.3 Triggers 207*
2.9.2 Implications for natural hazards 210
2.9.3 Implications for erosion fluxes 212
**2.10 Conclusions 215**
References 217

**CHAPTER 3 NUMERICAL MODELLING EXPERIMENT** *page*

**3.0 Motivation 225**
Research article submitted for publication in Geomorphology: **227**
**Stability and failure modes of slopes with anisotropic strength: Insights from discrete element models**
**Abstract 229**
**3.1 Introduction 231**
**3.2 Methods 234**
3.2.1 The DEM model 234
3.2.2 Modelling anisotropic rock materials 234

3.2.3 Model set-up 236

*3.2.3.1 Geometry, boundary conditions and Preconditioning 236*

*3.2.3.2 Upscaled mechanical behaviour 239*

*3.2.3.3 Strength reduction method 240*

**3.3 Relevance of the discrete element approach for investigating slope stability 241**

**3.4 Results 244**

3.4.1 Slope stability over the 180° range 244

3.4.2 Stability extrema: overall kinetics 246

3.4.3 Stability extrema: failure behaviour 249

**3.5 Discussion 253**

3.5.1 Modes of failure 253

3.5.2 Mechanical interpretation 256

3.5.3 Comparison with natural settings 259

*3.5.3.1 How representative is our DEM approach? 259*

*3.5.3.2 Rock anisotropy and hillslope angle at erosional steady state 261*

**3.6 Conclusion 264**

References 265

**CHAPTER 4 SYNTHESIS** *page*

**4.1 Achievements of this PhD project 269**

**4.2 Outlook and perspectives 271**

4.2.1 Next steps for exploring Causes and Triggers of bedrock landslides in the central Himalayas 271

4.2.2 Further site specific investigations 274

4.2.3 Modelling study 277

References 279

**Annexes** *page*


**A.2 Bedrock landslides in the Annapurna Massif 281**

Supplementary Figures 281

Supplementary Tables 293

**A.3 Numerical modelling experiment 295**

Supplementary Text 295

*A3.1 Strength reduction method: criteria 295*

*A3.2 Parametrization sensitivity 296*

*A3.3 Results visualisations 296*

Supplementary Figures 297

Supplementary Tables 308

# Table of Figures

## Chapter 1


| *No.* | *Description* | *page* |
|---|---|---|
| 1.1 | Sketches illustrating landslide failure modes | *24* |
| 1.2 | Schematic progression of the FoS for a destabilising slope | *26* |
| 1.3 | Categorisation of bedrock landslides | *29* |
| 1.4 | Köfels rockslide volume reconstruction | *36* |
| 1.5 | Explanatory sketch of the stratigraphy of a “giant” rock avalanche deposit | *39* |
| 1.6 | DSGSD phenomena as known from the literature | *44* |
| 1.7 | DSGSD behaviour | *49* |
| 1.8 | Bedrock landslides explored with numerical models, examples from existing studies | *59* |


## Chapter 2


| *No.* | *Description* | *page* |
|---|---|---|
| 2.1 | Map of Annapurna study region including the two sub-areas for investigation | *70* |
| 2.2 | Schematic cartoon of the 2015 Gorkha earthquake rupture on the MHT | *72* |
| 2.3 | Geologic cross-section through the western Annapurna Massif | *73* |
| 2.4 | Precipitation contrast and paleo-glacial extend in the Annapurna Massif/upper Marsyangdi | *76* |
| 2.5 | Figures from studies investigating bedrock landslides in the Annapurna Massif | *87* |
| 2.6 | Studied objects, upper Marsyangdi Valley | *90* |
| 2.7 | Studied objects, upper Annapurna South Face | *91* |
| 2.8 | Theory sketch and graphs for scarp movement reconstruction with cosmogenic nuclides | *102* |
| 2.9 | Schematic cross-section for volume reconstruction of valley deposits | *106* |
| 2.10 | Map of upper Marsyangdi Valley with mapped deposits and glaciology | *108* |
| 2.11 | Pisang Bowl, overview | *110* |
| 2.12 | Pisang Bowl, outcrops | *113* |
| 2.13 | Pisang Bowl, mapping and dating results | *114* |
| 2.14 | Pisang Bowl, plot with cosmogenic nuclide exposure dating results | *117* |
| 2.15 | Humde / Manang, overview | *119* |
| 2.16 | Humde / Manang, outcrops | *122* |
| 2.17 | Humde / Manang, mapping and dating results | *125* |
| 2.18 | Humde / Manang, visualisations of volume reconstruction | *127* |
| 2.19 | Humde / Manang, plot with cosmogenic nuclide exposure dating results | *130* |
| 2.20 | Tilicho Lake, overview | *133* |
| 2.21 | Tilicho Lake, outcrops | *135* |
| 2.22 | Tilicho Lake, mapping and dating results | *137* |
| 2.23 | Tilicho Lake, visualisations of volume reconstruction | *138* |
| 2.24 | Tilicho Lake, plot with cosmogenic nuclide exposure dating results | *142* |
| 2.25 | Additional profiles showing tectonic structures in the upper Marsyangdi Valley | *149* |
| 2.26 | Sketch describing relief and giant rock slope failure formation | *152* |
| 2.27 | Giant rock avalanche timing in the Annapurna Massif plotted with climate and earthquakes | *156* |
| 2.28 | Map of the Khudi Ridge and Phalo Danda areas | *162* |
| 2.29 | Overview of Khudi Ridge and Phalo Danda site | *163* |
| 2.30 | Close-up maps of the investigated locations | *165* |
| 2.31 | Schematic profile of the Phalo Danda DSGSD | *167* |

| | | |
|---|---|---|
| 2.32 | Phalo Danda conjugate scarp, overview and movement reconstruction results | *169* |
| 2.33 | Phalo Danda main scarp, overview and movement reconstruction results | *176* |
| 2.34 | Cosmogenic nuclide profile UM-21-56 | *179* |
| 2.35 | Trench results | *181* |
| 2.36 | Boulders sampled for 10Be nuclide exposure dating upslope of retrogressive erosion scars | *186* |
| 2.37 | Additional profiles drawn for reconstruction of total offset | *194* |
| 2.38 | Saituti retrogressive erosion scarp and Schematic sketch of hillslope processes | *198* |
| 2.39 | Schematic sketches illustrating long-term hillslope evolution on the Annapurna south-face | *199* |


## Chapter 3


| *No.* | *Description* | *page* |
|---|---|---|
| 3.1 | Sketch illustrating anisotropy introduction and uniaxial testing | *235* |
| 3.2 | Slope model set-up and example of slope failure simulation by strength reduction | *238* |
| 3.3 | 60° slope angle DEM results compared with 2D analytical slope stability solution | *243* |
| 3.4 | Results plot, stability versus isotropy plane orientation (40° and 60°) | *245* |
| 3.5 | Failure characteristics of the four stability extrema observed for the 60° slope | *248* |
| 3.6 | Strain deviator maps and layer cake visualisations for the four stability extrema | *252* |
| 3.7 | Failure modes observed for the 60° slope models depending on the isotropy orientation | *255* |
| 3.8 | Stress distributions within the slope before failure for the four stability extrema | *258* |
| 3.9 | Raster analysis of aspect and slope angle on the Annapurna south-facing slopes | *263* |


## Annexes


| *No.* | *Description* | *page* |
|---|---|---|
| A2.1 | Sampling spots / surfaces / objects at Pisang Bowl site | *282* |
| A2.2 | Sampled boulders on top of Humde rock avalanche deposit from the years 2018 and 2020 | *283* |
| A2.3 | Sampled boulders on top of Humde rock avalanche deposit from the year 2021 | *284* |
| A2.4 | Samples boulders on top surface of Tilicho rock avalanche deposit, near Tilicho Lake | *285* |
| A2.5 | Visualisation of Master's students' volume reconstruction at Pisang Bowl | *286* |
| A2.6 | Visualisation of Master's students' volume reconstruction at Latamrang | *287* |
| A2.7 | OxCal output for 14C carbon burial samples at Pisang Bowl | *288* |
| A2.8 | Additional sampling surfaces at Phalo Danda site and on Khudi Ridge | *289* |
| A2.9 | Supplementary graphs from scarp movement reconstruction | *290* |
| A2.10 | Sensitivity analysis for some input parameters of the scarp movement reconstruction | *291* |
| A2.11 | OxCal output for 14C carbon burial samples collected in the trench at Phalo Danda site | *292* |
| A3.1 | Sketch illustrating the interparticle model used for the numerical simulations | *297* |
| A3.2 | Complete loading procedure of anisotropic slope models | *298* |
| A3.3 | Biaxial tests results (lab-scale), evolution of the emergent Mohr-Coulomb properties | *299* |
| A3.4 | Exploring the ratio between the model thickness T and the diameter D of the particles (T/D) | *300* |
| A3.5 | 40° slope angle DEM results compared with 2D analytical slope stability solution | *301* |
| A3.6 | Visualisation for cracks counting | *302* |
| A3.7 | Evolution of the marker particles' velocity, 60° slope angle, extreme stability configurations | *303* |
| A3.8 | Displacement of particles during failure and damage index for the four stability extrema | *304* |
| A3.9 | Result plots of additionally extracted model outputs | *305* |
| A3.10 | Strain deviator maps and layer cake visualisation for the isotropic case | *306* |
| A3.11 | Examples of rapid rock slope failures from the central Himalayas | *307* |

# Table of Tables


## Chapter 1

| *No.* | *Description* | *page* |
|---|---|---|
| 1.1 | List of some very voluminous and famous rapid rock slope failures | *31* |

## Chapter 2

| *No.* | *Description* | *page* |
|---|---|---|
| 2.1 | Pisang Bowl cosmogenic nuclide exposure dating results (10Be and 36Cl) | *116* |
| 2.2 | Pisang Bowl 14C carbon burial dating results | *117* |
| 2.3 | Humde cosmogenic nuclide exposure dating results (10Be and 36Cl) | *131* |
| 2.4 | Tilicho Lake cosmogenic nuclide exposure dating results (36Cl) | *141* |
| 2.5 | Volume estimates and age constraints for central Himalayan rock avalanches | *147* |
| 2.6 | Sample positions for scarp movement reconstruction | *170* |
| 2.7 | Annapurna south-face cosmogenic nuclide exposure dating results | *172* |
| 2.8 | Parameter input table for scarp movement reconstruction calculation | *174* |
| 2.9 | Trench at Phalo Danda main scarp, 14C carbon burial dating results | *182* |

## Chapter 3

| *No.* | *Description* | *page* |
|---|---|---|
| 3.1 | Inter-particle bond properties of the slope models before strength reduction is applied | *237* |
| 3.2 | Comparison of DEM results and analytical solution after Leshchinsky et al. (1985) | *242* |

## Annexes

| *No.* | *Description* | *page* |
|---|---|---|
| A2.1 | Snow cover shielding calculation for cosmogenic nuclide exposure samples | *293* |
| A2.2 | Additional chemical compositions of 36Cl cosmogenic nuclide exposure samples | *294* |
| A3.1 | Inter-particle bond properties of the DEM material | *308* |
| A3.2 | Inter-particle strength values at failure for the isotropic slope models | *308* |

## RÉSUMÉ ÉTENDU EN FRANÇAIS

*Voir les figures dans le texte principal*

Les glissements de terrain sont des mouvements en masse de matériaux solides, illustrant la façon dont les forces gravitationnelles façonnent activement la surface de la Terre. Ils peuvent varier considérablement en taille et se produire selon différentes modalités, en fonction du matériau impliqué et de son comportement pendant la rupture (e.g. Hungr et al., 2014). Ce travail de thèse se focalise plus spécificiquement sur les éboulements rocheux ou écroulements en masse de roches cohérentes, où la rupture s'enracine profondément dans la masse rocheuse des versants, connues également sous le nom de glissements profonds. Les versants montagneux se dégradent progressivement au fil du temps, et les écroulements rocheux peuvent se manifester sous la forme d'événements catastrophiques qui se déplacent rapidement, comme les avalanches granulaires, ou sous la forme de déformations non catastrophiques qui évoluent très lentement ou épisodiquement sur de longues périodes de temps (théorie de la rupture progressive des pentes, voir par exemple Eberhardt et al., 2004 ; Amitrano et Helmstetter, 2006 ; *voir figure 1.3, p. 29*). Les taux de déformation moyens pour les ruptures non catastrophiques peuvent parfois être inférieurs à quelques millimètres par an. De telles ruptures progressives peuvent néanmoins à terme s'accélérer et finalement conduire à des effondrements catastrophiques (par exemple, Pánek et Klimeš, 2016). Les conséquences morphologiques de l'effondrement à grande échelle et non catastrophique du substratum rocheux sont appelées déformations gravitationnelles profondes des pentes (DSGSD pour Depp Seated Gravitational Slope Deformation) dans la littérature (*voir figure 1.6, p. 44*).

Les glissements de terrain rocheux constituent un risque naturel pour l'homme, mettant en péril les bâtiments et les infrastructures dans les régions montagneuses. A ce titre leur étude revêt un intérêt sociétal majeur. Une autre motivation pour les étudier est de mieux comprendre comment ils façonnent les paysages à l'échelle des temps géologiques. Dans les deux cas, il est nécessaire d'étudier les causes de ces glissements, à la fois les facteurs qui préconditionnent un versant et favorisent la possibilité de sa rupture, les facteurs qui préparent le versant à la rupture en réduisant activement sa stabilité, et les facteurs déclenchants des glissements de terrain rocheux (voir, McColl, 2015).

Dans cette thèse de doctorat, nous avons étudié les causes et les facteurs déclenchants des glissements de terrain rocheux en utilisant une approche multidisciplinaire.

Tout d'abord, nous avons étudié la rupture des pentes rocheuses à grande échelle dans l'Himalaya central, principalement en proposant de nouvelles contraintes d'âge dérivées de la datation par nucléides cosmogéniques. Notre zone d'étude, le massif des Annapurna au Népal central, offre l'opportunité d'exploiter et d'étendre les études existantes, non seulement sur les avalanches rocheuses catastrophiques géantes (> 1 $km^3$), mais aussi de documenter de manière pionnière pour l'Himalaya des massifs fracturés en cours de déformation gravitaire. Ces déformations de pente long terme et non catastrophiques ont en effet été peu étudiées dans l'ensemble de la chaîne himalayenne. A contrario des Alpes, elles sont observées dans des reliefs et vallées qui n'ont pas connu d'englacement au cours de la dernière période glaciaire. Ces déformations sont de ce fait intéressantes car leur origine n'est pas liée au recul des glaciers comme souvent invoqué dans les Alpes. En déterminant la paléo-chronologie des grandes ruptures de pentes rocheuses dans le massif des Annapurna et en comparant nos résultats avec les enregistrements sismiques et paléo-climatiques existants, nous visons à mieux évaluer l'importance relative des facteurs préparatoires externes qui déstabilisent les pentes dans la région.

Deuxièmement, nous avons étudié de manière systématique un facteur de préconditionnement crucial des ruptures de pentes rocheuses, à savoir le rôle de l'orientation de l'anisotropie de résistance des roches du substrat par rapport à la pente topographique sur la stabilité des versants et son mode de rupture. Cette démarche a été menée par le biais de modélisations numériques basées sur la méthode des éléments discrets (DEM).

**Études de terrain au Népal :**

Les études de terrain que nous avons effectuées au Népal peuvent être divisées en deux parties : L'étude des avalanches rocheuses catastrophiques dans la haute vallée de Marsyangdi, et l'étude des déformations lentes, non catastrophiques, sur le flanc sud du massif.

<u>Les avalanches rocheuses catastrophiques géantes en flanc nord du massif des Annapurna</u>

Plusieurs avalanches de roche ont été identifiés dans le massif des Annapurna au cours des dernières décennies (par exemple, Weidinger, 2006 ; Fort, 2011 ; Lavé et al., 2023). Nous avons visité deux de ces sites dans la haute vallée de la rivière Marsyangdi, où les contraintes d'âge absolu sur ces événements font actuellement défaut : l'effondrement de Pisang Bowl et les dépôts autour de Humde et Manang (*voir figure*

*2.10, p. 108*).

Le Pisang Bowl est une surface de rupture spectaculaire de forme lisse et concave de plus de 1500 m de haut, avec un plan de détachement subparallèle à la foliation de la roche (*voir figure 2.11, p. 110*). Des dépôts d'avalanches rocheuses sont situés de l'autre côté de la vallée (*voir figure 2.12, p. 113*). Nous avons cartographié ces dépôts (*voir figure 2.13, p. 114*), effectué des datations par nucléides cosmogéniques (10Be et 36Cl) sur des blocs rocheux des dépôts et de la surface, et prélevé des fragments de bois ou de charbons ensevelis par les débris d'avalanche dater leur enfouissement par la méthode du carbone 14C. La surface des dépôts présente trois crêtes, avec des âges d'exposition des blocs de deux de ces crêtes relativement distincts (*voir figure 2.14, p. 117*). Les échantillons provenant de la surface d'arrachement et de la crête la plus proche de la rivière donnent un âge moyen de 0,50 ± 0,05 ka BP (avant 1950 AD). Les échantillons provenant de la crête principale et la plus éloignée de la surface d'effondrement donnent un âge moyen de 0,73 ± 0,13 ka BP, en bonne corrélation avec les résultats de la datation par enfouissement du carbone 14C, tandis que deux échantillons de blocs rocheux d'un chaos de blocs situ par-delà cette crête principale donnent un âge moyen beaucoup plus élevé de 7,0 ± 1,1 ka BP. Nos recherches dans la zone du Pisang Bowl révèlent une histoire de ruptures multiples avec au moins deux ruptures de pente indépendantes, voire trois.

Plus en amont, dans la haute vallée de la rivière Marsyangdi, de vastes dépôts d'avalanches rocheuses, aujourd'hui profondément érodés et disséqués, s'observent sur les flancs de la vallée autour des villages de Humde et de Manang (*voir les figures 2.10 et 2.15, pp. 108+119*). Nous avons cartographié ces dépôts et prélevé des blocs rocheux situés sur les sommets des dépôts autour de Humde pour la datation par exposition aux nucléides cosmogéniques (36Cl et accessoirement 10Be) (*voir figure 2.17, p. 125*). Les échantillons prélevés sur différentes surfaces reliques donnent tous un âge moyen de 0,64 ± 0,05 ka BP (*voir figure 2.19, p. 130),* qui indique un âge beaucoup plus jeune que ce qui avait été supposé précédemment (e.g. Fort, 2011). Nous avons également trouvé des indications suggérant que les dépôts d'avalanches rocheuses situés plus à l'ouest autour de Manang proviennent d'un événement distinct de celui de Humde (*voir les figures 2.16D et 2.17, pp. 122+125*). Cet événement est probablement plus ancien, comme l'indiquent les âges d'enfouissement du carbone 14C des horizons de formation du sol dans une moraine près de Manang par Röthlisberger et Geyh (1986). Les zones d'origine des avalanches rocheuses à Humde et à Manang n'ont néanmoins pas pu être clairement identifiées pour l'instant. Finalement, une reconstitution du volume des dépôts de Humde suggère un volume de 4,8 km³, dont environ 75 % ont été érodés jusqu'à aujourd'hui (*voir figure 2.18, p. 127*).

Plus en amont, dans la haute vallée de la rivière Marsyangdi, des dépôts d'avalanches rocheuses massifs ont pu être nouvellement identifiés : ils font barrage à la rivière Tilicho (affluent en rive droite de la Marsyandi supérieure) et un lac de haute altitude, le lac de Tilicho, s'est formé en aont (*voir les figures 2.20 et 2.21, pp.*

*133+135*). Nous avons cartographié les vastes dépôts autour du lac Tilicho et échantillonné, sur une surface relique vallonnée, des blocs rocheux pour les dater par âge d'exposition avec le nucléide cosmogénique 36Cl (*voir figure 2.22, p. 137*). Les résultats montrent une large gamme d'âges allant de 5,0 à 12,5 ka BP. Nous attribuons l'existence d'âges « rajeunis » à une importante érosion de surface des blocs due à des processus de cryo-fracturation efficaces dans cet environnement froid de haute altitude (*voir figure 2.24, p. 142*). L'avalanche géante responsable des dépôts du lac Tilicho s'est produite au début de l'Holocène ou à la fin du Pléistocène. Une reconstitution du volume des dépôts montre un volume original de ~21 km³, dont environ 52 % ont été érodés à ce jour. La zone d'origine la plus probable de cette gigantesque rupture de pente rocheuse est la crête abrupte orientée est-ouest près du sommet de l'Annapurna I (8091 m.a.s.l.) (*voir figure 2.23 en bas, p. 138*). Cette avalanche rocheuse géante, qui n'avait pas encore été reconnue et documentée, représente un apport majeur au catalogue existant des avalanches de roches dans l'Himalaya central.

Notre catalogue désormais plus étoffé des avalanches rocheuses géantes dans le massif des Annapurna (six événements datés au total) permet de comparer les âges des événements avec les reconstructions paléoclimatologiques pour la région. Les avalanches rocheuses géantes dans le massif des Annapurna se sont produites pendant ou peu après des périodes de conditions climatiques plus humides et plus chaudes, en particulier l'optimum climatique de l'Holocène précoce (EHCO, ~5,5 à ~11,0 ka BP) et la période chaude médiévale (MWP, ~950 à ~1450 AD) (*voir figure 2.27, p. 156*). Cet alignement temporel suggère fortement un forçage climatique des avalanches rocheuses géantes dans le massif des Annapurna.

Les facteurs préparatoires et déclencheurs de ces événements sont très probablement liés à l'augmentation des précipitations et à l'augmentation des températures au cours de ces périodes climatiques, qui, selon la littérature, entraînent une plus grande activité des glissements de terrain (par exemple, Pánek, 2019 et citations dans ce document). L'augmentation des précipitations a fait monter les niveau piézométriques dans les versants, ce qui a entraîné une augmentation de la pression interstitielle qui a rendu les pentes plus instables. Les précipitations extrêmes, éventuellement combinées à la fonte des neiges, et le débit moyen plus élevé des rivières ont accru l'incision des rivières, c'est-à-dire l'érosion à la base des versants, les déstabilisant encore davantage. Le réchauffement des températures de l'air peut également avoir provoqué des ruptures de pente dues à la dégradation du pergélisol et au recul des glaciers (débâcle glaciaire). L'observation selon laquelle les avalanches de roches géantes se produisent pendant les périodes climatiques plus humides et plus chaudes est cohérente avec d'autres études sur les avalanches de roches géantes dans d'autres régions de l'Himalaya (Bookhagen et al., 2005 ; Dortch et al., 2009).

Une déstabilisation progressive accrue par des facteurs préparatoires internes, tels que la présence d'eaux souterraines ou des processus d'altération en profondeur (Viles, 2013), pourrait expliquer pourquoi la plupart des ruptures se sont produites au milieu ou vers la fin des phases climatiques humides et chaudes.

Les déformations lentes de type DSGSD en flanc sud du massif des Annapurna

Sur la face sud du massif des Annapurna, nos recherches sur les effondrements rocheux non catastrophiques se sont concentrées sur une zone allant d'environ 4 200 m d'altitude à environ 2 000 m d'altitude, juste en dessous de la zone de pergélisol (*voir les figures 2.28 et 2.29, pp. 162+163*). Le site de Phalo Danda, une crête présentant d'abondantes structures morphologiques de type escarpement de fracture indiquant un DSGSD, a été sélectionné pour des reconstructions de paléomouvements à l'aide de nucléides cosmogéniques (10Be). Des profils ont été réalisés à la fois sur l'escarpement principal et sur un escarpement secondaire conjugué, et une tranchée a été creusée au travers de l'escarpement principal (*voir les figures 2.30a et 2.31, pp. 165+167*).

Pour reconstruire des paléomouvements sur un escarpement à l'aide de nucléides cosmogéniques, nous avons prélevé des échantillons de la surface d'escarpement à intervalles réguliers (*voir les figures 2.32 et 2.33, pp. 169+176*). Les concentrations en nucléides y reflètent une histoire d'exposition en plusieurs étapes, influencée à la fois par la géométrie de l'escarpement au cours du temps et par une production atténuée au travers du talus en pied d'escarpement et de l'épaule supérieure de l'escarpement. Une approche bayesienne utilisant un modèle direct de production des nucléides cosmogéniques nous a alors permis d'explorer les scénarios de rupture (en âge et amplitude de glissement) compatibles avec les concentrations mesurées modulo les erreurs analytiques et les incertitudes du modèle de production.

Le comportement des paléo-mouvements du DSGSD de Phalo Danda peut être caractérisé comme suit : des étapes discrètes de mouvement à l'échelle décimètrique (observées dans la tranchée, *voir la figure 2.35, p. 181*), certainement une activité de mouvement pré-Holocène du DSGSD, et une phase d'augmentation des taux de mouvement entre 4,5 et 7,3 ka BP. Cette phase active est évidente à la fois sur l'escarpement principale et sur l'escarpement conjugué d'après les profils de nucléides cosmogéniques, l'escarpement conjugué semblant se rompre moins fréquemment que l'escarpement principal (*voir les figures 2.32 et 2.33, pp. 169+176*). Nos données ne nous permettent pas de déterminer si la phase la plus active du DSGSD est due à des ruptures plus fréquentes ou à des déplacements plus importants produits par des ruptures individuelles.

Les archives paléoclimatiques de la région centrale de l'Himalaya montrent que l'activité accrue des DSGSD coïncide avec la fin de l'EHCO, une période pendant laquelle les conditions climatiques étaient plus chaudes et nettement plus humides. Cette activité de mouvement accrue peut être attribuée au forçage climatique, en particulier à une nappe phréatique plus élevée au cours de cette période, qui a augmenté la pression de pore dans la zone de décollement du glissement, rendant les DSGSD plus sensibles aux facteurs déclenchants du glissement, tels que séismes ou cumul en quelques jours de fortes précipitations. Le changement des conditions hydrologiques, induit par une augmentation de la percolation de l'eau dans la subsurface, et ses

conséquences sur les mouvements de DSGSD sont bien documentés dans les études de surveillance ou de suivi des glissements lents actifs (voir les analyses de Pánek et Klimeš, 2016 ; Agliardi et Crippa, 2022).

Cependant, pourquoi l'activité de mouvement n'a-t-elle augmenté qu'à la fin de l'EHCO et pas plus tôt, alors que le climat était déjà plus chaud et plus humide ? Une explication possible est une déstabilisation progressive accrue dans la zone de décollement du glissement, induite par la présence d'eaux souterraines et de processus d'altération en profondeur (Viles, 2013), induisant un déphasage de la réponse au changement de climat. Une autre explication est que l'évolution mécanique de la rupture, spécifique au site, influence largement le modèle de mouvement du DSGSD. Si le forçage climatique peut affecter cette évolution mécanique, il peut également faire en sorte que l'activité du DSGSD ne corresponde pas directement aux périodes climatiques. Par ailleurs, des déclencheurs sismiques sont certainement concevables (par exemple, Jibson et al., 2004 ; Lacroix et al., 2022), mais leur importance pour le DSGSD de Phalo Danda ne peut être évaluée en raison de l'enregistrement limité des paléoséismes et de la résolution limitée de la chronologie des ruptures à partir des contraintes de datation de l'enfouissement du carbone 14C dans la tranchée.

Dans notre zone d'étude en flanc sud du massif des Annapurna, certains versants présentent sur plusieurs dizaine de mètres d'épaisseur du matériel rocheux très fracturé voire désintégré dans leur partie inférieure et moyenne, avec des surfaces légèrement basculées vers le bas (*voir les figures 2.28 ; 2.30, b + c ; 2.36 ; et 2.38 ; pp. 162, 165, 186 et 198*). Nous interprétons ce matériau fracturé comme résultant de « masses effondrées » produites par une déformation des pentes remontant loin dans le Pléistocène. Quelques datation par âge d'exposition (10Be) indiquent que les surface de ces masses glissées peuvent avoir plusieurs dizaines voire une centaine de milliers d'années, c'est-à-dire qu'elles sont relativement stables sur le long terme. Plusieurs de ces masses rocheuses fracturées présentent néanmoins une érosion épisodique au niveau de ravines d'érosion rétrogrades se propageant rapidement vers l'amont. L'érosion induite par ces ravines domine fortement la production de sédiments à l'échelle de l'ensemble des bassins versants associés (Gallo et Lavé, 2014 ; Lavé et al., 2019) et contribue à remobiliser sur le long terme le matériel de ces versants glissés. A partir de nos observations préliminaires en flanc sud du massif des Annapurna, nous faisons l'hypothèse qu'il existe une relation génétique entre l'activité initiale des versants sous forme de DSGSD et le glissement psotérieur de ces masses effondrées (*voir figure 2.39, p. 199*). L'activité des DSGSDs contrôlerait ainsi la déformation des versants, l'érosion et la dénudation des montagnes dans le contexte himalayen.

Les résultats de l'étude de terrain sont pour certains préliminaires et mériteraient d'être approfondis. Ils ouvrent cependant de nouvelles perspectives de recherche dans la région de l'Himalaya. En ce qui concerne les avalanches rocheuses géantes, des travaux de terrain futurs pourraient viser à fournir davantage de preuves d'un effondrement dans la zone de Manang antérieur à celui de Humde, et à dater ces dépôts.

L'identification des zones d'origine des ruptures de Humde et de Manang serait également un objectif prioritaire. En vue de constituer un catalogue complet des grands effondrements et de quantifier leur rôle dans l'évolution des reliefs himalayens, la reconnaissance d'autres avalanches rocheuses géantes est également un effort qui doit se poursuivre.

Pour les glissements de terrain rocheux en général, et les DSGSD en particulier, un inventaire par le biais d'une cartographie des structures de déformation et des dépôts à partir de données de télédétection permettrait une analyse plus systématique de l'importance et de la pertinence des facteurs préalables et préparatoires possibles, y compris la lithologie du substratum rocheux, les structures et les facteurs climatiques. La mise en œuvre d'études de surveillance pour suivre la déformation contemporaine des pentes et vérifier les étapes discrètes du mouvement après les tremblements de terre, en combinaison avec des reconstitutions supplémentaires des paléomouvements, faciliterait une meilleure évaluation des mécanismes de forçage et des facteurs déclenchants possibles de la déformation progressive des versants.

D'autres aspects devraient être étudiés pour le massif des Annapurna, notamment le rôle des processus d'altération en profondeur dans la déstabilisation progressive des pentes et le rôle des DSGSD dans la dénudation globale des montagnes.

**Étude de modélisation numérique :**

Les propriétés mécaniques (rigidité et résistance) de la plupart des matériaux rocheux sont anisotropes en raison du litage, de la foliation ou de la schistosité. Les roches sédimentaires et métamorphiques, en particulier, présentent une isotropie transversale. Cette anisotropie influence considérablement la stabilité et le mode de rupture dominant, faisant de l'anisotropie des roches un facteur de conditionnement préalable important pour les glissements de terrain sur substratum rocheux. Ceci est particulièrement pertinent dans le massif des Annapurna, qui est principalement composé de roches sédimentaires et métasédimentaires, fortement anisotropes. En outre, on sait que l'anisotropie façonne les paysages, en créant des pentes fortement et faiblement inclinées respectivement sur les versants anaclinaux et cataclinaux (terminologie de Cruden et Hu, 1996).

Bien qu'elle soit souvent décrite de manière qualitative, la manière dont l'orientation de l'anisotropie affecte la stabilité et le mode de rupture des pentes rocheuses, ainsi que ses implications pour le modelage du paysage, n'est pas encore comprise de manière systématique. Dans le cadre de cette thèse de doctorat, une étude de modélisation numérique a été menée pour étudier l'ensemble des orientations possibles de l'anisotropie par rapport à la pente (180° d'isotropie transversale) et leurs effets sur la stabilité des pentes et leur mode de rupture. Les résultats de cette étude de modélisation numérique ont été publiés récemment

dans la revue Geomorphology (Huber et al., 2024).

Pour nos expériences numériques, nous avons utilisé la méthode des éléments discrets (DEM) mise en œuvre dans le logiciel libre Yade Open DEM (Šmilauer et al., 2021). Le matériau rocheux a été simulé à l'aide de particules sphériques liées entre elles par des lois d'interaction frictionnelle élastique-cohésive basées sur le critère de Mohr-Coulomb modifié (voir Scholtès et Donzé, 2013 et *figure A3.1, p. 297*). Ces liaisons peuvent se rompre, créant des « fissures » sans cohésion au sein du matériau. Les propriétés mécaniques attribuées aux liaisons interparticulaires (par exemple, la résistance, la rigidité, l'angle de frottement) doivent être calibrées via des essais numériques spécifiques afin d'obtenir des propriétés émergentes similaires à celles du matériau simulé.

Pour évaluer les performances de notre approche DEM, nous avons comparé le comportement à la rupture, de pentes modèles de matériaux homogènes et isotropes dans une configuration en tranches 2D (*voir figure 3.2, a+b ; p. 238*) avec une solution analytique dérivée de Leshchinsky et al. (1985). Notre vaste série d'essais a montré une bonne concordance entre les modèles numériques et les résultats analytiques (*voir figure 3.3, p. 243*).

L'anisotropie de la roche a été introduite dans nos modèles en suivant la méthode de Dinç et Scholtès (2018). Nous avons d'abord identifié les liaisons orientées subparallèlement à un plan de « faiblesse » souhaité (le plan d'isotropie) dans une plage d'angles prédéfinie. Ces liaisons ont ensuite été réorientées le long du plan de faiblesse, et de nouvelles propriétés interparticulaires ont été attribuées à ces « liaisons faibles » (faible rigidité, faible résistance). Nous avons calibré les propriétés émergentes du matériau DEM anisotrope pour nous assurer qu'elles correspondaient étroitement aux essais mécaniques en laboratoire sur des échantillons de roches réelles (Saroglou et al., 2004) (*voir figure 3.1, b+c ; p. 235*). Le passage de l'échelle du laboratoire à l'échelle de la pente a été réalisé en utilisant l'indice de résistance géologique (GSI) comme référence (Hoek et Diederichs, 2006) et en réduisant le degré d'imbrication des particules.

Dans les expériences de rupture de pente, les tranches 2D ont d'abord été soumises à une charge gravitationnelle, puis la pente a été découpée pour simuler une évolution naturelle de la topographie (*voir figure A3.2, p. 298).* La stabilité de la pente a été évaluée à l'aide d'une approche de réduction de la résistance : tant que l'énergie cinétique de l'ensemble des particules reste inférieure à certains seuils et qu'aucune fissure n'est apparue, la pente est considérée comme stable et la résistance interparticulaire continue à être progressivement réduite. En cas de début de rupture, les valeurs de résistance sont maintenues constantes et l'on suit ensuite l'évolution du système pour cette résistance interparticulaire fixée.

Nos simulations de réduction de la résistance, ont été réalisées en considérant deux modèles de pente avec des angles de pente de 40° et 60° respectivement, et ont révélé des variations significatives dans la résistance à la rupture et, par conséquent, dans la stabilité de la pente selon l'inclinaison de l'anisotropie (*voir figure*

*3.4, p. 245*). L'exploration des inclinaisons sur 180° nous a permis d'identifier quatre modes de rupture distincts, chacun différant par l'initiation, la localisation, le type et la progression de la déformation (*voir les figures 3.5, 3.6, 3.7 et A3.8 ; pp. 248, 252, 255 et 304*) :

- **Rupture par glissement :** Survenant dans les pentes cataclinales en surplomb (Cruden et Hu, 1996), ces ruptures s'initient dans la moitié inférieure de la pente, formant une zone de rupture localisée subparallèle au plan de faiblesse. La rupture progresse ensuite vers le haut de la pente, aboutissant à un bloc cohérent qui va s'effondrer suivant une rupture translationnelle. Pour une pente donnée, cette configuration est la moins stable de toutes et opère pour des valeurs de cohésion élevées.

- **Rupture par flambage :** Elles se produisent dans les pentes cataclinales avec un plan de faiblesse à fort pendage (i.e. plus élevé que celui de la pente topographique). La rupture commence à la base de la pente où le matériau se bombe vers la surface avant de progresser vers le haut, conduisant finalement à la désintégration complète du matériau par un mouvement de rotation. Les configurations qui se rompent en mode flambage sont plus stables que celles qui se rompent en mode glissement.

- **Rupture (ou écroulement) par basculement (ou fauchage) :** Survenant dans les pentes anaclinales avec un plan de faiblesse à fort pendage, ces ruptures commencent à la base de la pente, où une grande partie du matériau pivote vers le pied de la pente en raison d'un cisaillement parallèle au plan de faiblesse. La rupture se déplace ensuite vers le haut de la pente, entraînant la désintégration du matériau. Les configurations qui s'effondrent en mode basculement sont plus stables que les configurations qui s'effondrent en mode glissement, mais moins stables que les configurations qui s'effondrent en mode flambage.

- **Rupture (ou écroulement) en mode d'écroulement :** Elle se produit dans les pentes anaclinales avec un plan d'anisotropie à faible inclinaison. Bien qu'aucune déformation importante ne soit observée, les ruptures en mode écroulement présentent le plus grand nombre de fissures. Le matériau s'effrite de la face du talus vers l'intérieur du talus, la plupart des configurations n'entraînant la rupture que d'une couche superficielle de particules. Les configurations d'effritement sont les plus stables de toutes les configurations, souvent plus stables que le cas isotrope. Cette stabilité est due au fait que les contraintes induisent un état de blocage, provoquant le durcissement du matériau et augmentant sa résistance au cisaillement (*voir figure 3.8, p. 258*).

Il est évident que les modèles simplifiés de pentes utilisés dans cette étude numérique ne peuvent pas rendre compte de la complexité des pentes naturelles. Dans l'environnement naturel, les pentes présentent souvent de nombreuses hétérogénéités, y compris des structures discrètes (par exemple, des joints), des conditions rocheuses variables et une résistance qui peut varier vers la surface. En outre, la dégradation de la résistance

des pentes naturelles, par exemple par l'altération progressive du substratum rocheux, se produit de manière très variable, contrairement à l'altération homogène supposée dans nos simulations. La dégradation a tendance à être localisée dans les zones mécaniquement affaiblies ou sous la surface, et l'influence des eaux souterraines, c'est-à-dire l'augmentation de la pression interstitielle, est un facteur important que nos modèles ne prennent pas en compte. Malgré ces limites, nos simulations numériques reproduisent avec succès les modes de rupture couramment observés dans les environnements naturels caractérisés par une anisotropie du substratum rocheux (p. ex. Chigira, 2000 ; Cruden, 2003 ; Cui et al., 2022). Plus précisément, notre mode d'effondrement sur des pentes anaclinales avec des plans de faiblesse à faible pendage ressemble aux chutes de pierres observées dans les environnements naturels.

Ainsi, nous pouvons établir un lien entre les modes de rupture observés dans nos simulations numériques et ceux observés sur les versant montagneux. Sur la base de notre modélisation, nous pourrions prévoir que les pentes cataclinales s'effondrent à des angles plus faibles que les pentes anaclinales, les angles des pentes s'adaptant à l'orientation du substrat rocheux anisotrope et façonnant activement le paysage. Le flanc sud du massif des Annapurna, caractérisé par des gneiss présentent une foliation avec une orientation relativement uniforme (pendage à ~20° vers le nord), constitue un bon cas d'école. Les données topographiques révèlent que les pentes orientées vers le sud sont jusqu'à 9° plus raides que les pentes orientées vers le nord (*voir figure 3.9, p. 263*). Cette asymétrie dans les angles de pente correspond qualitativement aux prévisions de nos résultats de modélisation.

Notre étude de modélisation a, pour la première fois, analysé systématiquement la relation entre l'orientation de l'anisotropie des roches par rapport à la pente et les modes de rupture et la stabilité qui en résultent. Cela a des implications significatives pour l'analyse de la stabilité des pentes et notre compréhension de l'évolution du paysage. Les études futures basées sur cette configuration de modélisation pourraient être étendues de plusieurs manières : en examinant comment l'effet des eaux souterraines (c.-à-d. la pression interstitielle) influence les résultats, en explorant comment l'incorporation de lois d'évolution basées sur des processus physiques pourrait permettre une dégradation de la résistance plus localisée et hétérogène, ou en simulant l'érosion à la base de la pente en introduisant un enlèvement des particules. Ces modifications pourraient améliorer la représentation de l'évolution naturelle des pentes dans le temps, en fournissant une représentation plus réaliste des processus dépendant du temps dans les simulations.

Les deux composantes de cette thèse de doctorat, le travail de terrain dans l'Himalaya et l'étude de numérique de la stabilité des pentes anisotropes, améliorent notre compréhension des causes et des facteurs déclenchants des glissements de terrain sur substratum rocheux. Elles ont des implications importantes pour l'évaluation des dangers et des risques, offrent un aperçu de l'évolution du paysage et proposent des pistes de recherche pour l'avenir.

# Références :


Agliardi, F., Crippa, C., 2022. Deep-Seated Gravitational Slope Deformations, in: Treatise on Geomorphology. Elsevier, pp. 183–199. https://doi.org/10.1016/B978-0-12-818234-5.00182-6

Amitrano, D., Helmstetter, A., 2006. Brittle creep, damage, and time to failure in rocks. Journal of Geophysical Research: Solid Earth 111. https://doi.org/10.1029/2005JB004252

Bookhagen, B., Thiede, R.C., Strecker, M.R., 2005. Late Quaternary intensified monsoon phases control landscape evolution in the northwest Himalaya. Geology 33, 149–152. https://doi.org/10.1130/G20982.1

Chigira, M., 2000. Geological structures of large landslides in Japan. Journal of Nepal Geological Society 22, 497–504. https://doi.org/10.3126/jngs.v22i0.32423

Cruden, D., Hu, X.Q., 1996. Hazardous Modes of Rock Slope Movement in the Canadian Rockies. Environmental and Engineering Geoscience 2, 507–516. https://doi.org/10.2113/gseegeosci.II.4.507

Cruden, D.M., 2003. The shapes of cold, high mountains in sedimentary rocks. Geomorphology 55, 249–261. https://doi.org/10.1016/S0169-555X(03)00143-0

Cui, S., Wu, H., Pei, X., Yang, Q., Huang, R., Guo, B., 2022. Characterizing the spatial distribution, frequency, geomorphological and geological controls on landslides triggered by the 1933 Mw 7.3 Diexi Earthquake, Sichuan, China. Geomorphology 403, 108177. https://doi.org/10.1016/j.geomorph.2022.108177

Dinç, Ö., Scholtès, L., 2018. Discrete Analysis of Damage and Shear Banding in Argillaceous Rocks. Rock Mech Rock Eng 51, 1521–1538. https://doi.org/10.1007/s00603-017-1397-6

Dortch, J.M., Owen, L.A., Haneberg, W.C., Caffee, M.W., Dietsch, C., Kamp, U., 2009. Nature and timing of large landslides in the Himalaya and Transhimalaya of northern India. Quaternary Science Reviews 28, 1037–1054. https://doi.org/10.1016/j.quascirev.2008.05.002

Eberhardt, E., Stead, D., Coggan, J.S., 2004. Numerical analysis of initiation and progressive failure in natural rock slopes—the 1991 Randa rockslide. International Journal of Rock Mechanics and Mining Sciences 41, 69–87. https://doi.org/10.1016/S1365-1609(03)00076-5

Fort, M., 2011. Two large late Quaternary rock slope failures and their geomorphic significance, Annapurna Himalayas (Nepal). Geografia Fisica e Dinamica Quaternaria 34, 5–14.

Gallo, F., Lavé, J., 2014. Evolution of a large landslide in the High Himalaya of central Nepal during the last half-century. Geomorphology 223, 20–32. https://doi.org/10.1016/j.geomorph.2014.06.021

Hoek, E., Diederichs, M.S., 2006. Empirical estimation of rock mass modulus. International Journal of Rock Mechanics and Mining Sciences 43, 203–215. https://doi.org/10.1016/j.ijrmms.2005.06.005

Huber, M.L., Scholtès, L., Lavé, J., 2022. How does anisotropy control rock slope deformation? A discrete element modelling investigation (No. EGU22-2954). Presented at the EGU22, Copernicus Meetings. https://doi.org/10.5194/egusphere-egu22-2954

Hungr, O., Leroueil, S., Picarelli, L., 2014. The Varnes classification of landslide types, an update. Landslides 11, 167–194. https://doi.org/10.1007/s10346-013-0436-y

Jibson, R.W., Harp, E.L., Schulz, W., Keefer, D.K., 2004. Landslides Triggered by the 2002 Denali Fault, Alaska, Earthquake and the Inferred Nature of the Strong Shaking. Earthquake Spectra 20, 669–691. https://doi.org/10.1193/1.1778173

Lacroix, P., Gavillon, T., Bouchant, C., Lavé, J., Mugnier, J.-L., Dhungel, S., Vernier, F., 2022. SAR and optical images correlation illuminates post-seismic landslide motion after the Mw 7.8 Gorkha earthquake (Nepal). Sci Rep 12, 6266. https://doi.org/10.1038/s41598-022-10016-2

Lavé, J., Gallo, F., Lanord, C.F., Morin, G., Gajurel, A., 2019. Landslide dynamics and debris export in the central Himalaya, as documented by a multi-methods approach. Presented at the Geophysical Research Abstracts.

Lavé, J., Guérin, C., Valla, P.G., Guillou, V., Rigaudier, T., Benedetti, L., France-Lanord, C., Gajurel, A.P., Morin, G., Dumoulin, J.P., Moreau, C., Galy, V., 2023. Medieval demise of a Himalayan giant summit induced by mega-landslide. Nature 619, 94–101. https://doi.org/10.1038/s41586-023-06040-5

Leshchinsky, D., Baker, R., Silver, M.L., 1985. Three dimensional analysis of slope stability. Int. J. Numer. Anal. Methods Geomech. 9, 199–223. https://doi.org/10.1002/nag.1610090302

McColl, S.T., 2015. Landslide Causes and Triggers, in: Landslide Hazards, Risks, and Disasters. Elsevier, pp. 17–42. https://doi.org/10.1016/B978-0-12-396452-6.00002-1

Pánek, T., 2019. Landslides and Quaternary climate changes—The state of the art. Earth-Science Reviews 196, 102871. https://doi.org/10.1016/j.earscirev.2019.05.015

Pánek, T., Klimeš, J., 2016. Temporal behavior of deep-seated gravitational slope deformations: A review. Earth-Science Reviews 156, 14–38. https://doi.org/10.1016/j.earscirev.2016.02.007

Röthlisberger, F., Geyh, M.A., 1986. 10000 Jahre Gletschergeschichte der Erde. Sauerländer, Aarau.

Saroglou, H., Marinos, P., Tsiambaos, G., 2004. The anisotropic nature of selected metamorphic rocks from Greece. Journal of the Southern African Institute of Mining and Metallurgy 104, 217–222. https://doi.org/10.10520/AJA0038223X_2825

Scholtès, L., Donzé, F.-V., 2013. A DEM model for soft and hard rocks: Role of grain interlocking on strength. Journal of the Mechanics and Physics of Solids 61, 352–369. https://doi.org/10.1016/j.jmps.2012.10.005

Šmilauer, V., Angelidakis, V., Catalano, E., Caulk, R., Chareyre, B., Chèvremont, W., Dorofeenko, S., Duriez, J., Dyck, N., Elias, J., Er, B., Eulitz, A., Gladky, A., Guo, N., Jakob, C., Kneib, F., Kozicki, J., Marzougui, D., Maurin, R., Modenese, C., Pekmezi, G., Scholtès, L., Sibille, L., Stransky, J., Sweijen, T., Thoeni, K., Yuan, C., 2021. Yade documentation. The Yade Project. https://doi.org/10.5281/zenodo.5705394

Viles, H.A., 2013. Linking weathering and rock slope instability: non-linear perspectives: Linking weathering and rock slope instability. Earth Surf. Process. Landforms 38, 62–70. https://doi.org/10.1002/esp.3294

Weidinger, J.T., 2006. Predesign, failure and displacement mechanisms of large rockslides in the Annapurna Himalayas, Nepal. Engineering Geology 83, 201–216. https://doi.org/10.1016/j.enggeo.2005.06.032

## EXTENDED SUMMARY

*Refer to figures in main text*

Landslides are mass movements of solid material, illustrating how gravitational forces actively shape the Earth's surface. They can vary greatly in size and occur through different configurations, depending on the material involved and its behaviour during failure (e.g., Hungr et al., 2014). This thesis focuses on landslides originating from rock material, where the failure extends deep into the affected slopes, known as deep-seated rock slope failures. Bedrock slope failure can manifest as either catastrophic events that move rapidly, like rock avalanches, or as non-catastrophic deformations that move slowly or episodically over long periods of time (progressive slope failure theory, see e.g., Eberhardt et al., 2004; Amitrano and Helmstetter, 2006; *see Figure 1.3, p. 29*). The average deformation rates for non-catastrophic failures are sometimes below millimetres per year and can eventually lead to catastrophic collapses (e.g., Pánek and Klimeš, 2016). The morphological consequences of large-scale, non-catastrophic bedrock failures are referred to as Deep-Seated Gravitational Slope Deformations (DSGSDs) in the literature (*see Figure 1.6, p. 44*).

For years, researchers and engineers have paid a lot of attention to bedrock landslides since they are a natural hazard for humans, putting buildings and infrastructure at risk. Besides the threat that bedrock landslides pose on human society, another motivation for studying them is to gain a better understanding of how they shape landscapes over geological time scales. Therefore, it is of particular interest to investigate their origin, including the factors that precondition a slope for failure and those that prepare a slope for failure by actively reducing its stability, and Triggers of rock slope failures (see, McColl, 2015).

In this PhD thesis, we investigated the causes and Triggers of bedrock landslides using a multidisciplinary approach:

First, we studied the failure of large-scale bedrock slopes in the central Himalayas, primarily by producing new age constraints derived from cosmogenic nuclide dating. Our study area, the Annapurna Massif in central Nepal, offers an opportunity to build on and extend existing studies, not only on giant catastrophic rock avalanches (> 1 $km^3$) but also in other fields of geology. In contrast, non-catastrophic DSGSD failures remain largely unresearched across the entire Himalayan range, highlighting a significant knowledge gap for

DSGSDs in low-latitude mountain ranges that lacked extensive valley glaciation during the last Ice Age. By determining the paleo-timing of large bedrock slope failures in the Annapurna Massif and by comparing our findings with existing earthquake and paleo-climate records, we aim to better assess the relative importance of external Preparatory or Triggering factors that destabilize slopes in the region.

Second, we systematically investigated a crucial Precondition Factor of rock slope failures, that is to say the role of the rock strength anisotropy orientation with respect to slope on hillslope stability and failure mode. To document this role, we consider a numerical modeling approach using the Discrete Element Method (DEM).

**Nepal field studies:**

The Nepal field studies can be divided primarily into two parts: The study of catastrophic giant rock avalanches in the upper Marsyangdi Valley and the study of non-catastrophic DSGSDs on the south face of the Massif.

The giant rock avalanches along the northern Annapurna region

Several deposits of giant rock avalanches have been identified in the Annapurna Massif in recent decades (e.g., Weidinger, 2006; Fort, 2011; Lavé et al., 2023). We revisited two of these sites in the upper Marsyangdi Valley, where absolute age constraints on these events are currently lacking: the Pisang Bowl failure and the deposits around Humde and Manang (*see Figure 2.10, p. 108*).

The Pisang Bowl is a spectacular bowl-shaped failure scarp over 1500 m high, with a detachment plane sub-parallel to the rock foliation (*see Figure 2.11, p. 110*). Rock avalanche deposits are located on the opposite side of the valley (*see Figure 2.12, p. 113*). We mapped these deposits (*see Figure 2.13, p. 114*), performed cosmogenic nuclide dating (10Be and 36Cl) on boulders on the deposit and the failure scarp, and sampled soil buried by avalanche debris for 14C carbon burial dating. The deposit surface features three ridges, with exposure ages from different sampling locations grouping together (*see Figure 2.14, p. 117*). Samples from the failure scarp and a ridge closest to the river yield a mean age of 0,50 ± 0,05 ka BP (before 1950 AD). Samples from a ridge further from the failure scarp yield a mean age of 0,73 ± 0,13 ka BP, correlating well with the 14C carbon burial dating results, while two boulder samples at an even greater distance yield a much older mean age of 7,0 ± 1,1 ka BP. Our investigations at the Pisang Bowl locality reveal a multi-failure history with at least two individual slope failure events, possibly three.

Further upstream in the upper Marsyangdi Valley, vast rock avalanche deposits are eroding on the valley flanks around the villages of Humde and Manang (*see Figures 2.10 and 2.15, pp. 108 & 119*). We mapped these deposits and sampled boulders situated on deposit tops around Humde for cosmogenic nuclide exposure dating (10Be and 36Cl) (see Figure 2.17, p. 125). Samples from different locations yield a mean age of 0,64 ± 0,05 ka BP (*see Figure 2.19, p. 130*). These results indicate a much younger age for a rock avalanche around Humde than previously assumed (e.g., Fort, 2011). We also found evidence that the rock avalanche deposits around Manang originate from a separate event (*see Figures 2.16D and 2.17, pp. 122 & 125*). This event is presumably older, as indicated by 14C carbon burial ages from soil formation horizons within a moraine near Manang by Röthlisberger and Geyh (1986). However, more field investigations are necessary to validate the existence of a separate event at Manang. The source areas of the rock avalanches at Humde and Manang have yet to be identified. A volume reconstruction for the dated deposits around Humde suggests a volume of 4,8 km³, of which about 75% has been eroded to the present day (*see Figure 2.18, p. 127*).

Further upstream in the upper Marsyangdi Valley, rock avalanche deposits outcrop and impound a high-altitude lake, Tilicho Lake (*see Figures 2.20 and 2.21, pp. 133 & 135*). We mapped the extensive deposits around Tilicho Lake and sampled boulders for 36Cl cosmogenic nuclide exposure dating situated on a plain close to the lake (*see Figure 2.22, p. 137*). The results show a wide range of ages from 5,0 to 12,5 ka BP, which we attribute to significant surface erosion by frost cracking over a long period of time (*see Figure 2.24, p. 142*). The giant rock avalanche event responsible for the deposits at Tilicho Lake occurred sometime in the Early Holocene or Late Pleistocene, adding a new entry to the rock avalanche record of the Annapurna Massif. A volume reconstruction of the deposits shows an original volume of ~21 km³, of which approximately 52% has eroded to date. The most probable source area of this gigantic rock slope failure is the steep east-west oriented ridge near the Annapurna I peak (8091 m.a.s.l.) (*see Figure 2.23 bottom, p. 138*).

With a much more complete record of giant rock avalanches in the Annapurna Massif (six dated events in total), we can now compare the event ages with paleo-climatological reconstructions for the region. The giant rock avalanches in the Annapurna Massif occurred during or shortly after periods of wetter and warmer climatic conditions, specifically the Early Holocene Climatic Optimum (EHCO, ~5,5 to ~11,0 ka BP) and the Medieval Warm Period (MWP, ~950 to ~1450 AD) (*see Figure 2.27, p. 156*). This temporal alignment provides substantial evidence for climatic forcing of the giant rock avalanche events in the Annapurna Massif.

The Preparatory Factors and Triggers of these events are most likely linked to increased precipitation and warmer temperatures during these climatic periods, which, according to the literature, lead to higher landslide activity (e.g., Pánek, 2019 and citations therein). Increased precipitation raised groundwater levels within slopes, resulting in higher pore pressure that rendered slopes more unstable and susceptible to

Triggers. The severity of extreme precipitation events, possibly combined with snowmelt, and higher average river discharge increased erosion at the base of slopes, further destabilizing them. Warmer air temperatures may have caused slope failures due to permafrost degradation and glacier retreat (glacial debuttressing) as well. The observation that giant rock avalanches occur during wetter and warmer climatic periods is consistent with other studies on giant rock avalanches in other regions of the Himalayas (Bookhagen et al., 2005; Dortch et al., 2009).

Enhanced progressive destabilization by internal Preparatory Factors, such as the presence of groundwater or deep weathering processes (Viles, 2013), could explain why most failures occurred in the middle or towards the end of wet and warm climatic phases.

The DSGSD activity along the southern Annapurna region

On the south face of the Annapurna Massif, investigations into non-catastrophic bedrock failures focused on an area ranging from approximately 4 200 m.a.s.l. to about 2 000 m.a.s.l., just below the permafrost zone (*see Figures 2.28 and 2.29, pp. 162 & 163*). The Phalo Danda site, a ridge with abundant morphological structures indicative of DSGSD, was selected for paleo-movement reconstructions using cosmogenic nuclides (10Be). Profiles were taken from both the main scarp and a secondary conjugate scarp, and a trench was excavated cross-cutting the main scarp (*see Figures 2.30a and 2.31, pp. 165 & 137*).

For the paleo-movement reconstruction with cosmogenic nuclides, samples were taken at regular intervals on the scarp surfaces (*see Figures 2.32 and 2.33, pp. 169 & 176*). The nuclide concentrations reflect a multi-stage exposure history, influenced both by the geometry of the scarp over time and by attenuated production by a colluvial wedge at the foot of the scarp and the hanging wall. A Bayesian approach using a direct cosmogenic nuclide production model then enabled us to explore rupture scenarios (various timing and ruptures with different offset) compatible with the concentrations measured taking the analytical errors and uncertainties of the production model into account.

The paleo-movement behavior of the Phalo Danda DSGSD can be characterized as follows: discrete dm-scale movement steps (observed in the trench, *see Figure 2.35, p. 181*), certainly a pre-Holocene movement activity of the DSGSD, and a phase of increased movement rates between 4,5 and 7,3 ka BP. This active phase is evident on both the main and conjugate scarp from the cosmogenic nuclide profiles, with the conjugate scarp appearing to rupture less frequently than the main scarp (*see Figures 2.32 and 2.33, pp. 169 & 176*). Our data does not allow us to determine whether the more active phase of the DSGSD is due to more frequent ruptures or larger offsets of individual ruptures.

The paleo-climatic record for the central Himalayan region shows that the higher activity on the DSGSD-scarps coincides with the end of the EHCO, a period of warmer and significantly wetter climatic conditions.

This increased movement activity can be attributed to climatic forcing, specifically a higher water table during this period, which increased pore pressure in weak zones, making the DSGSD scarps more susceptible to Triggers that initiate rupture. In addition to a widespread and persistent weakening of the slopes during this period, a wetter climate would possibly also have intensified climatic Triggers: more severe extreme precipitation events, possibly combined with snowmelt, could have caused more ruptures or greater offsets of individual ruptures during this period. The potential of changing hydrological conditions, induced by increased water percolation into the subsurface, to cause DSGSD movement is well-documented in contemporary monitoring studies (see reviews by Pánek and Klimeš, 2016; Agliardi and Crippa, 2022).

However, why did the movement activity increase only at the end of the EHCO and not earlier, when the climate was already warmer and wetter? One possible explanation is increased progressive destabilization within the weak zones, induced by the presence of groundwater or deep weathering processes (Viles, 2013), which may have delayed the response to climate. Another explanation is that the site-specific mechanical evolution of the failure largely influences the DSGSD movement pattern. While climatic forcing may affect this mechanical evolution, it might also cause the DSGSD activity to not directly correspond to climatic periods. Seismic Triggers are certainly conceivable (e.g., Jibson et al., 2004; Lacroix et al., 2022), but their importance for the Phalo Danda DSGSD cannot be assessed due to the limited paleo-earthquake record and the limited resolution of rupture timing from 14C carbon burial dating constraints from the trench.

Besides DSGSDs that deform hillslopes on the Annapurna south-face non-catastrophically, we observe numerous slopes consisting of highly fractured, disintegrated bedrock material in their lower to middle reaches, with gently sloping surfaces towards the top (*see Figures 2.28; 2.30, b + c; 2.36; and 2.38; pp. 162, 165, 186, & 198*). We interpret this fractured material as 'failed masses' resulting from slope deformation dating back far into the Pleistocene. Some of these failed masses exhibit pulse-like erosion by retrogressive erosion scars, which strongly dominate the erosional output within the associated drainage catchments (Gallo and Lavé, 2014; Lavé et al., 2019). We infer a genetic relation between DSGSD activity and these failed masses on the south face of the Annapurna Massif (*see Figure 2.39, p. 199*). DSGSD activity is a crucial control on slope deformation, erosion, and mountain denudation in this Himalayan setting, characterized by high orographic precipitation and a lack of valley glaciation during the Glacial period.

The achievements of the field studies suggest further investigations and open up new research perspectives in the Annapurna region. For the giant rock avalanches, further fieldwork should aim to provide more evidence for an independent Manang failure, including absolute dating of deposits. Identifying the source areas for the Humde and Manang failures remains essential. Additionally, there is a possibility of discovering other, as yet unrecognized, giant rock avalanche events that still have remnants in the Annapurna Massif.

For bedrock landslides in general, and DSGSDs in particular, an inventory through literature review and mapping of deformation structures and deposits from remote sensing data would enable a more systematic analysis of the importance and relevance of possible Precondition and Preparatory Factors, including bedrock lithology, structures, and climatic factors. Implementing monitoring studies to track contemporary slope deformation and verify discrete movement steps following earthquakes, in combination with additional paleo-movement reconstructions, would facilitate a better assessment of possible forcing mechanisms and Triggers of progressive slope deformation.

Other aspects that should be studied for the Annapurna Massif include the role of deep weathering processes in progressive slope destabilization and the role of DSGSDs in overall mountain denudation.

**Numerical modelling study:**

The mechanical properties (stiffness and strength) of most rock materials are direction-dependent due to bedding, schistosity, or regular jointing. Sedimentary and metamorphic rocks, in particular, exhibit transverse isotropy. This anisotropic rock strength significantly influences stability and the prevailing failure mode, making rock strength anisotropy an important Precondition Factor for bedrock landslides. This is especially relevant in the Annapurna Massif, which is primarily composed of sedimentary and metasedimentary rocks. Moreover, anisotropy in rocks is known to shape landscapes, creating escarpments and dip slopes on cataclinal and anaclinal slopes, respectively (terminology from Cruden and Hu, 1996).

Despite being often described qualitatively, there is a lack of systematic understanding of how anisotropy orientation affects the stability and failure mode of rock slopes and its implications for landscape shaping. Within the framework of this PhD thesis, a numerical modelling study was conducted to investigate the full range of possible orientations of rock strength anisotropy towards the slope (180° of transverse isotropy) and their effects on slope stability and failure mode on homogeneous model slopes. The results of this numerical modelling study were published recently in the journal Geomorphology (Huber et al., 2024).

For our numerical modeling experiments, we used the Discrete Element Method (DEM) implemented in the open-source software Yade Open DEM (Šmilauer et al., 2021). The rock material was simulated using spherical particles bonded together through elastic-cohesive frictional interaction laws based on the modified Mohr-Coulomb criterion (see Scholtès and Donzé, 2013 and *Figure A3.1, p. 297*). These bonds can break, creating cohesionless “cracks” within the material. The mechanical properties assigned to the interparticle bonds (e.g., strength, stiffness, friction angle) differ from those obtained from numerical lab-scale tests of the simulated rock mass, which are referred to as emergent properties in this study.

To evaluate the performance of our DEM approach, we compared the failure behavior, cohesion, friction angle at failure, and failure surface from model slopes of homogeneous, isotropic material in a 2D-slice

configuration (*see Figure 3.2, a+b; p. 238*) with an analytical solution derived by Leshchinsky et al. (1985). Our extensive test series showed good agreement between the numerical models and the analytical results (*see Figure 3.3, p. 243*).

Rock strength anisotropy was introduced into our slope models following the method of Dinç and Scholtès (2018). We first identified bonds oriented subparallel to a desired "weakness" plane (isotropy plane) within a predefined angle range. These bonds were then reoriented along the weakness plane, and new interparticle properties were assigned to these "weak bonds" (low stiffness, low strength). We calibrated the emergent properties of the anisotropic DEM material to ensure they closely matched rock-mechanical lab-scale tests on real rock samples (Saroglou et al., 2004) (*see Figure 3.1, b+c; p. 235*). Scaling from laboratory to slope scale was achieved by adjusting the interparticle Young's modulus using the Geological Strength Index (GSI) as a reference (Hoek and Diederichs, 2006) and by reducing the degree of particle interlocking.

In the slope failure experiments, the 2D slices were first subjected to gravitational loading, and then the slope was cut to simulate a natural evolution of topography (*see Figure A3.2, p. 298*). Slope stability was assessed using a strength reduction approach: The stability of the slope was monitored by tracking the model's kinetic energy and the occurrence of cracks near the slope. As long as the kinetic energy remained below certain thresholds and no cracks appeared, the slope was considered stable, and interparticle strength was gradually reduced. If failure was initiated, the strength values were kept constant.

Our strength reduction simulations, which covered a full range of possible weakness plane orientations towards the slope and were conducted for two different packings and slope angles of 40° and 60°, revealed significant variations in strength reduction at failure and, consequently, in slope stability (*see Figure 3.4, p. 245*). The full range of angles encompasses four distinct failure modes, each differing in the initiation, location, type, and progression of deformation (*see Figures 3.5, 3.6, 3.7, and A3.8; pp. 248, 252, 255, & 304*):

- **Sliding Mode Failures:** Occurring on cataclinal overdip slopes (Cruden and Hu, 1996), these failures begin in the lower half of the slope, forming a localized failure zone subparallel to the weakness plane. The failure then progresses upwards towards the top of the slope, resulting in a coherent block remaining after a translational failure. These configurations are the least stable.

- **Buckling Mode Failures:** These happen on cataclinal underdip slopes. Failure starts at the base where the material bulges towards the surface before progressing upwards, eventually leading to the complete disintegration of the material through rotational movement. Configurations failing in buckling mode are more stable than configurations failing in sliding mode.

- **Toppling (or Bending) Mode Failures:** Occurring on anaclinal slopes with a steeply dipping weakness plane, these failures initiate at the base of the slope, where a large portion of material rotates

towards the slope toe due to shearing parallel to the weakness plane. The failure then moves up the slope, causing the material to disintegrate. Configurations failing in toppling mode are more stable than configurations failing in sliding mode but less stable than configurations failing in buckling mode.

- **Crumbling Mode Failures:** These take place on anaclinal slopes with a shallow-dipping weakness plane. Although no large deformation is observed, crumbling mode failures exhibit the highest number of cracks. The material crumbles from the slope face into the slope, with most configurations resulting in only a surface layer of particles failing. Crumbling configurations are the most stable of all the configurations, often more stable than the isotropic case. This stability arises because the stress conditions induce a locking state, causing the material to harden and increasing its shear resistance (*see Figure 3.8, p. 258*).

The simplified model slopes used in this numerical investigation cannot fully capture the complexity of natural slopes. In the natural environment, slopes often feature numerous heterogeneities, including discrete structures (e.g., joints), variable rock conditions, and rock conditions and strength may vary towards the surface. Additionally, strength degradation in natural slopes, such as through progressive weathering of bedrock, occurs in a highly variable manner, unlike the continuous increments assumed in our simulations. Degradation tends to be localized in weak zones, and the influence of groundwater, i.e. pore pressure increase, is a significant factor that our models do not account for. Despite these limitations, our numerical simulations successfully reproduce the failure modes commonly observed in natural environments characterized by widespread bedrock strength anisotropy (e.g., Chigira, 2000; Cruden, 2003; Cui et al., 2022). Specifically, our crumbling mode on anaclinal slopes with shallow-dipping weakness planes resembles rockfalls observed in natural settings.

We can relate the variable slope stability observed in our numerical simulations to real-world slopes. Based on our modelling, we would anticipate that cataclinal slopes fail at lower angles compared to anaclinal slopes, with slope angles adapting to the orientation of the anisotropic bedrock and actively shaping the landscape. The south face of the Annapurna Massif in central Nepal, where gneisses dip consistently, offers a fitting test case. Topographic data reveals that south-facing slopes are up to 9° steeper than north-facing slopes (*see Figure 3.9, p. 263*). This asymmetry in slope angles aligns qualitatively with the predictions from our modelling results.

Our modelling study has, for the first time, systematically analysed the relationship between the orientation of rock strength anisotropy relative to the slope and the resulting failure modes and slope stabilities. This has significant implications for slope stability analysis and our understanding of landscape evolution. Future investigations based on this modelling setup could be expanded in several ways: examining how the inclusion of groundwater effects (i.e., pore pressure) impacts the results, exploring how incorporating evolution laws

based on physical processes might allow for more localized and heterogeneous strength degradation, or simulating erosion at the slope base by introducing particle removal laws. These modifications could enhance the representation of natural slope evolution over time, providing a more realistic depiction of time-dependent processes in the simulations.

The two components of this PhD thesis, the Himalayan fieldwork and the numerical modelling study, both enhance our understanding of the causes and Triggers of bedrock landslides. They have important implications for hazard and risk assessment, offer insights into landscape evolution, and propose avenues for further research.

# References:


Agliardi, F., Crippa, C., 2022. Deep-Seated Gravitational Slope Deformations, in: Treatise on Agliardi, F., Crippa, C., 2022. Deep-Seated Gravitational Slope Deformations, in: Treatise on Geomorphology. Elsevier, pp. 183–199. https://doi.org/10.1016/B978-0-12-818234-5.00182-6

Amitrano, D., Helmstetter, A., 2006. Brittle creep, damage, and time to failure in rocks. Journal of Geophysical Research: Solid Earth 111. https://doi.org/10.1029/2005JB004252

Bookhagen, B., Thiede, R.C., Strecker, M.R., 2005. Late Quaternary intensified monsoon phases control landscape evolution in the northwest Himalaya. Geology 33, 149–152. https://doi.org/10.1130/G20982.1

Chigira, M., 2000. Geological structures of large landslides in Japan. Journal of Nepal Geological Society 22, 497–504. https://doi.org/10.3126/jngs.v22i0.32423

Cruden, D., Hu, X.Q., 1996. Hazardous Modes of Rock Slope Movement in the Canadian Rockies. Environmental and Engineering Geoscience 2, 507–516. https://doi.org/10.2113/gseegeosci.II.4.507

Cruden, D.M., 2003. The shapes of cold, high mountains in sedimentary rocks. Geomorphology 55, 249–261. https://doi.org/10.1016/S0169-555X(03)00143-0

Cui, S., Wu, H., Pei, X., Yang, Q., Huang, R., Guo, B., 2022. Characterizing the spatial distribution, frequency, geomorphological and geological controls on landslides triggered by the 1933 Mw 7.3 Diexi Earthquake, Sichuan, China. Geomorphology 403, 108177. https://doi.org/10.1016/j.geomorph.2022.108177

Dinç, Ö., Scholtès, L., 2018. Discrete Analysis of Damage and Shear Banding in Argillaceous Rocks. Rock Mech Rock Eng 51, 1521–1538. https://doi.org/10.1007/s00603-017-1397-6

Dortch, J.M., Owen, L.A., Haneberg, W.C., Caffee, M.W., Dietsch, C., Kamp, U., 2009. Nature and timing of large landslides in the Himalaya and Transhimalaya of northern India. Quaternary Science Reviews 28, 1037–1054. https://doi.org/10.1016/j.quascirev.2008.05.002

Eberhardt, E., Stead, D., Coggan, J.S., 2004. Numerical analysis of initiation and progressive failure in natural rock slopes—the 1991 Randa rockslide. International Journal of Rock Mechanics and Mining Sciences 41, 69–87. https://doi.org/10.1016/S1365-1609(03)00076-5

Fort, M., 2011. Two large late Quaternary rock slope failures and their geomorphic significance, Annapurna Himalayas (Nepal). Geografia Fisica e Dinamica Quaternaria 34, 5–14.

Gallo, F., Lavé, J., 2014. Evolution of a large landslide in the High Himalaya of central Nepal during the last half-century. Geomorphology 223, 20–32. https://doi.org/10.1016/j.geomorph.2014.06.021

Hoek, E., Diederichs, M.S., 2006. Empirical estimation of rock mass modulus. International Journal of Rock Mechanics and Mining Sciences 43, 203–215. https://doi.org/10.1016/j.ijrmms.2005.06.005

Huber, M.L., Scholtès, L., Lavé, J., 2022. How does anisotropy control rock slope deformation? A discrete element modelling investigation (No. EGU22-2954). Presented at the EGU22, Copernicus Meetings. https://doi.org/10.5194/egusphere-egu22-2954

Hungr, O., Leroueil, S., Picarelli, L., 2014. The Varnes classification of landslide types, an update. Landslides 11, 167–194. https://doi.org/10.1007/s10346-013-0436-y

Jibson, R.W., Harp, E.L., Schulz, W., Keefer, D.K., 2004. Landslides Triggered by the 2002 Denali Fault, Alaska, Earthquake and the Inferred Nature of the Strong Shaking. Earthquake Spectra 20, 669–691. https://doi.org/10.1193/1.1778173

Lacroix, P., Gavillon, T., Bouchant, C., Lavé, J., Mugnier, J.-L., Dhungel, S., Vernier, F., 2022. SAR and optical images correlation illuminates post-seismic landslide motion after the Mw 7.8 Gorkha earthquake (Nepal). Sci Rep 12, 6266. https://doi.org/10.1038/s41598-022-10016-2

Lavé, J., Gallo, F., Lanord, C.F., Morin, G., Gajurel, A., 2019. Landslide dynamics and debris export in the central Himalaya, as documented by a multi-methods approach. Presented at the Geophysical Research Abstracts.

Lavé, J., Guérin, C., Valla, P.G., Guillou, V., Rigaudier, T., Benedetti, L., France-Lanord, C., Gajurel, A.P., Morin, G., Dumoulin, J.P., Moreau, C., Galy, V., 2023. Medieval demise of a Himalayan giant summit induced by mega-landslide. Nature 619, 94–101. https://doi.org/10.1038/s41586-023-06040-5

Leshchinsky, D., Baker, R., Silver, M.L., 1985. Three dimensional analysis of slope stability. Int. J. Numer. Anal. Methods Geomech. 9, 199–223. https://doi.org/10.1002/nag.1610090302

McColl, S.T., 2015. Landslide Causes and Triggers, in: Landslide Hazards, Risks, and Disasters. Elsevier, pp. 17–42. https://doi.org/10.1016/B978-0-12-396452-6.00002-1

Pánek, T., 2019. Landslides and Quaternary climate changes—The state of the art. Earth-Science Reviews 196, 102871. https://doi.org/10.1016/j.earscirev.2019.05.015

Pánek, T., Klimeš, J., 2016. Temporal behavior of deep-seated gravitational slope deformations: A review. Earth-Science Reviews 156, 14–38. https://doi.org/10.1016/j.earscirev.2016.02.007

Röthlisberger, F., Geyh, M.A., 1986. 10000 Jahre Gletschergeschichte der Erde. Sauerländer, Aarau.

Saroglou, H., Marinos, P., Tsiambaos, G., 2004. The anisotropic nature of selected metamorphic rocks from Greece. Journal of the Southern African Institute of Mining and Metallurgy 104, 217–222. https://doi.org/10.10520/AJA0038223X_2825

Scholtès, L., Donzé, F.-V., 2013. A DEM model for soft and hard rocks: Role of grain interlocking on strength. Journal of the Mechanics and Physics of Solids 61, 352–369. https://doi.org/10.1016/j.jmps.2012.10.005

Šmilauer, V., Angelidakis, V., Catalano, E., Caulk, R., Chareyre, B., Chèvremont, W., Dorofeenko, S., Duriez, J., Dyck, N., Elias, J., Er, B., Eulitz, A., Gladky, A., Guo, N., Jakob, C., Kneib, F., Kozicki, J., Marzougui, D., Maurin, R., Modenese, C., Pekmezi, G., Scholtès, L., Sibille, L., Stransky, J., Sweijen, T., Thoeni, K., Yuan, C., 2021. Yade documentation. The Yade Project. https://doi.org/10.5281/zenodo.5705394

Viles, H.A., 2013. Linking weathering and rock slope instability: non-linear perspectives: Linking weathering and rock slope instability. Earth Surf. Process. Landforms 38, 62–70. https://doi.org/10.1002/esp.3294

Weidinger, J.T., 2006. Predesign, failure and displacement mechanisms of large rockslides in the Annapurna Himalayas, Nepal. Engineering Geology 83, 201–216. https://doi.org/10.1016/j.enggeo.2005.06.032

# CHAPTER 1 – INTRODUCTION

## 1.1 What are bedrock landslides?

### 1.1.1 Landslides

The English term landslide refers to the downslope movement of rock or soil when shear stresses exceed shear strength under the influence of gravitational loading (Encyclopædia Britannica, 2023). "Landslide" is a general term that describes mass movements of solid material on the surface of the Earth. Landslides are also documented on other planetary bodies than Earth (e.g., Lucchitta 1979; Lucas et al., 2014; Duarte et al., 2019), proving therefore that such processes actively shape the surfaces of celestial bodies. Landslides appear abundantly on the Earth's surface because the latter is under constant renewal through the processes of plate tectonics and volcanism (e.g., Frisch et al., 2011). Indeed, these processes go along with gravitational adjustments which are accompanied by all sorts of landsliding (e.g., Clague and Stead, 2012). Natural landslides have always been part of people's lives, not only as they present a threat to life and our living environment, but also as they shape the landscapes we live in (e.g., von Poschinger, 2011; Normandeau et al., 2019). Besides the natural phenomenon, anthropogenic landscaping, e.g. the construction of open-pit mines and dams, and the ever-increasing need for safe and solid ground for buildings and infrastructures, created an interest in better understanding how slopes fail (Jaeger et al., 2007; Read and Stacey, 2009). Slope stability analysis has thus emerged as an engineering discipline used to prevent slope failure while reducing cost and preventing damage to man-made structures (e.g., Cheng and Lau, 2014).

### 1.1.2 Bedrock landslides

Landslide types and processes are manifold (Varnes 1978; Hungr et al. 2014, Figure 1.1): The work of researchers subdivide nowadays in an extensively growing body of literature in which slope failure is differentiated by their failure modes (defining falls, topples, and slides), the transport characteristics of the failing material (flows and spreads), or other imprecisely defined spatial and temporal constraints (like Slope Deformations in Figure 1.1). Another aspect that can be used to distinguish landslides is the material in which

they occur: For instance, whether they occur in rocks or unconsolidated sediments or soils (e.g., Hungr et al., 2014). Looking specifically at the source area, failures can extend to considerable depth below the surface and can reach far into the bedrock, affecting large volumes. Such failures are referred to in the literature as "deep-seated" failures (e.g., Petley and Allison, 1997; Roering et al., 2005; Dou et al. 2015). Bedrock landslides in general are very often deep-seated, as bedrock, usually covered by soil, is normally only found at greater depths below the surface. However, rockfalls occurring on steep slopes not covered by soil can also be considered as bedrock landslides, even if they are not deep-seated. In this PhD project's work we are not concerned with rockfalls but specifically focus on bedrock landslides which are deep-seated.

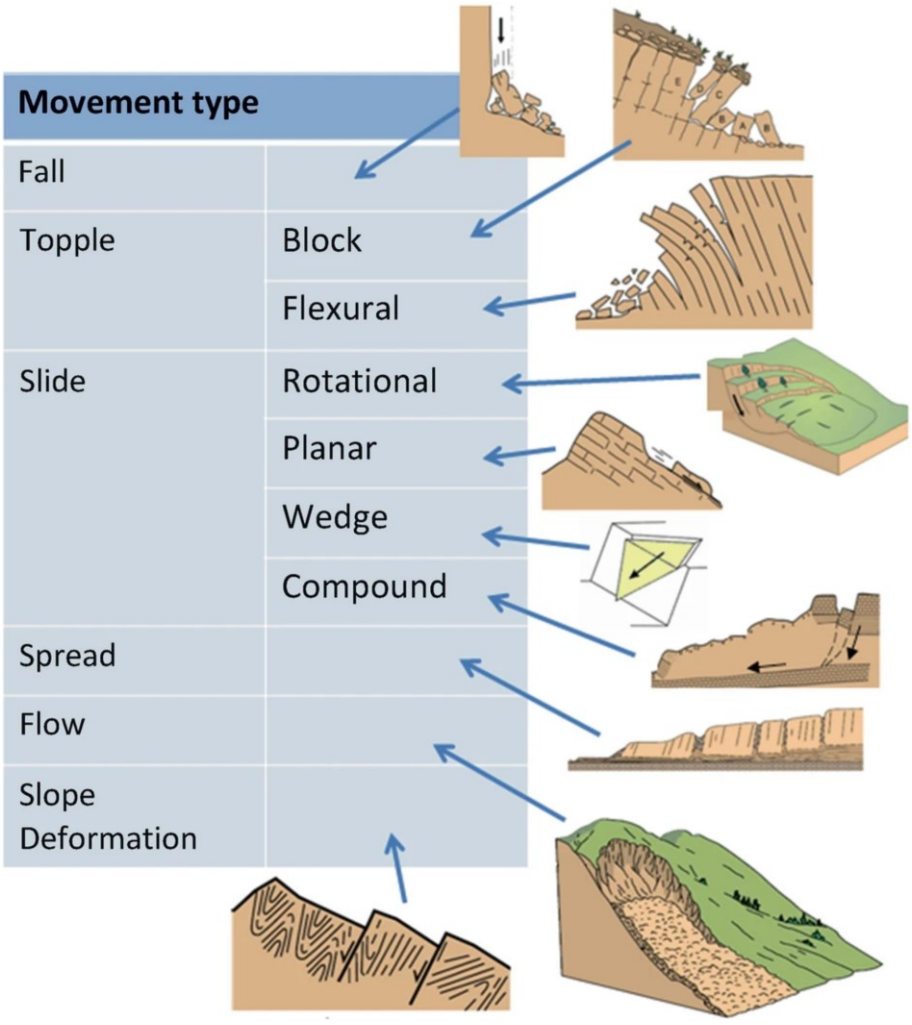


*Figure 1.1: Sketches illustrating landslide failure modes. Adopted from Bobrowski and Marker (2018), simplified after Hungr et al. (2014).*

## 1.2 Some landslide theory

### 1.2.1 The Factor of Safety

Geotechnical engineers are interested in assessing the stability and failure potential of natural and artificial slopes consisting of geomaterials. The need to estimate the resistance of a slope to failure has led to the discipline of slope stability analysis and one of its most conventional methods, the Limit Equilibrium Analysis (e.g., Cheng and Lau, 2014). A large variety of approaches for different failure geometries and mechanisms exists based on various assumptions and estimations of rock mechanical parameters, for both two-dimensional and three-dimensional problems (e.g., Duncan et al., 1996). All these approaches are based on force (and/or moment) balance considerations: the slope fails when the total shear stress along the failure surface is greater than the resisting shear strength along this surface (Kliche, 2018). The stability of the slope can be expressed by the ratio of these forces, the Factor of Safety,

$$FoS = \frac{resisting\ forces}{driving\ forces} \quad . \qquad (1.1)$$

If the Factor of Safety is less than 1 (FoS < 1.0), the slope is expected to fail. If the Factor of Safety is greater than 1 (FoS ≥ 1), the slope is considered to be stable. Softwares used by engineers for limit equilibrium slope stability analysis can account for complex slope configurations, groundwater conditions or can even consider probabilistic approaches (see, Eberhardt, 2003). But, they cannot provide a detailed insight into stress and deformation localisation within the slope or the kinematics of failure. These techniques are made for calculating a FoS for a given slope condition, or to provide shear strength parameters on the surface on which the slope is expected to fail. Although the FoS is a concept predominantly used in engineering, it is also commonly used by researchers studying landslides. It is a simple way to express whether a slope is considered stable or not.

### 1.2.2 Causes and Triggers of landslides

The stability of a slope is conditioned by its resistance against failure. Both intrinsic and extrinsic factors can affect the stability of a slope and reduce its resistance to failure, either short-term or permanent. It is important to introduce to the reader some of the terminology associated with these factors used in the literature and clarify which definitions we are settling on. Any factors responsible for the failure of slopes is sometimes referred to in the literature under the umbrella term "causes" (see, e.g., Varnes 1978; Popescu, 1994; McColl, 2015). We would like to differentiate further between different causes of landslides and adopt the classification by Glade and Grozier (2005):

- **Precondition Factors** are static, inherent factors that do not directly alter the stability of a slope, but which determine how other factors affecting slope stability act. They are predetermined and do not change over time scales relevant for slope failures. These are specific properties of the potential failing material, including properties relevant for fluid circulation (e.g., porosity), or the presence or orientation of geological structures (layering or schistosity). They can be seen as catalysts or inhibitors of slope failures.

- **Preparatory Factors** reduce the stability of the slope without initiating any deformation or movement that would ultimately lead to failure. Reduction in stability is often permanent. It can take action within a very short period of time or last a very long time. Processes that act as Preparatory Factors include: fluvial or glacial undercutting, weathering processes, or other factors related to long-term climate change (vegetation cover, permafrost, groundwater). Preparatory Factors are enabled or facilitated by Precondition Factors, they bring the slope from a stable state to a marginally stable state where a slope is susceptible to be triggered to failure.

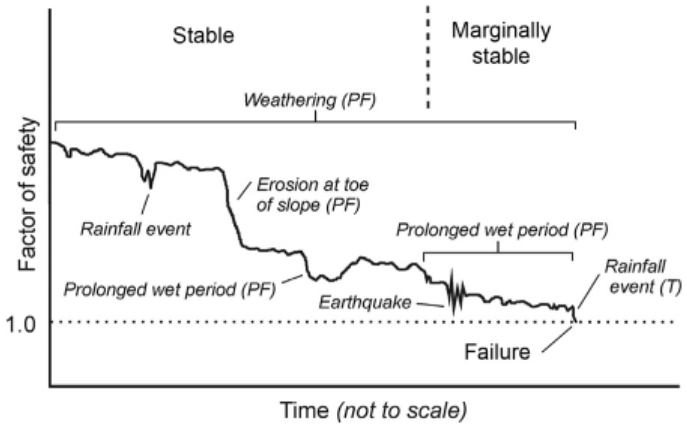


*Figure 1.2: Schematic progression of the FoS against time for a slope that is in the process of being destabilised by Preparatory Factors. Finally, the failure is triggered by a rainfall event. From McColl (2015), modified from Popescu (1994).*

- **Triggers** are directly responsible for transitioning a slope from a marginally stable state to an unstable state across the theoretical line of the FoS = 1 (Figure 1.2). A slope failure is always initiated by a Trigger which is a process that eventually provokes active deformation and relocation of slope material. Usually, Triggers are dynamic processes imposed on the slope externally. These processes

are normally active over a short period of time and their impact on the slope's stability is often reversable. Known Triggers are: short-term pore pressure increase by percolation of water into the subsurface due to heavy rainfall or the thawing of snow and ice, seismic loading by earthquakes or instantaneous removal of vegetation by wildfire. Sometimes, an obvious Trigger is not recognizable because no external forcing can be associated with the failure. In this case it is plausible that a stability threshold was eventually surpassed by processes reducing stability by acting intrinsically and progressively inside the slope. This could be, for example, advanced weathering or progressive rock fatigue (see Preparatory Factors above). However, due to the ambiguity in this case, it is better to state "no obvious Trigger" because we cannot relate the triggering to a process that was directly observable. This can prevent from confusion of obvious Triggers and Preparatory Factors. For instance, we don't want to define "climate" as a "Trigger" of a landslide.

The reader can refer to McColl (2015) for a more detailed example list of Precondition Factors, Preparatory Factors and Triggers and the processes involved.

Both Preparatory Factors and Triggers of landslides in the natural setting can be anthropogenic. Many examples are documented in literature where human activity is directly responsible for the failure of slopes, e.g., deforestation or the excavation at the slope base for mining or construction can bring a slope to a marginally stable state (see, e.g., Jaboyedoff et al., 2018; Lehmann et al., 2019; Figure 1.2).

### 1.2.3 The progressive failure of rock slopes

It is known from rock-mechanical experiments that, under certain conditions (i.e. stress state, microstructure, presence of water), rock material can deform plastically below the critical resistance for dynamic instantaneous failure, which is FoS = 1 (e.g. Atkinson and Meredith, 1987; Brantut et al., 2013; Voigtländer et al., 2018). Plastic deformation results from sub-critical crack growth (FoS > 1) and is described in the literature as brittle creep or static fatigue, or referred to as progressive failure (see e.g. Amitrano and Helmstetter (2006) and Brantut et al. (2013)). Strain rates in sub-critical conditions can vary by several orders of magnitude depending on the experimental conditions (e.g. applied differential stress, see Brantut et al. (2013)), making subcritical failures highly time-dependent.

The behaviour of rock material deforming sub-critically can be applied to slope stability analysis, providing a useful explanation for the very slow deformation rates (less than millimetres per year) and the long time-scales (up to $10^5$ years) observed in bedrock slope deformations (see reviews by Jaboyedoff et al., 2013; Pánek and Klimeš (2016); Discenza and Esposito (2021); Agliardi and Crippa (2022)). Slow deformation and resulting morpho-structures on hillslopes can be attributed to deep-seated weak zones affected by sub-critical deformation located sometimes deep within the slope (see Section 1.4.1 below). Progressive sub-critical rock failure is also taken into account for modelling the temporal evolution of rock slopes with numerical methods (e.g., Eberhardt et al., 2004; Brückl and Parotidis, 2005; Lacroix and Amitrano, 2013; Riva et al., 2018; see Section 1.5 below).

Within slopes, sub-critical strain rates can be constant (i.e. secondary creep), or episodic acceleration of brittle creep can happen due to a transient change in the mechanical conditions within the weak zone (e.g. by pore pressure increase, see Agliardi et al (2020) and Section 1.4.2 below). All rock slope failures that stay in the realm of sub-critical brittle creep (FoS > 1) can be referred to as non-catastrophic rock slope failures (Section 1.4), whereas failures that fail critically, involving dynamic ruptures with a high release in energy (FoS < 1; Section 1.3) can be referred to as catastrophic rock slope failures (see review by Agliardi and Crippa, 2022). Figure 1.3 illustrates the categorization of rock slope failures, which has been outlined to assist the reader of this thesis manuscript in understanding the terminology used. One can note that non-catastrophic subcritical deformation of a slope can transition to rapid catastrophic failure (by tertiary creep, runaway process), as we know from some studied slopes in the literature (see, for example, the review by Pánek and Klimeš (2016) or Ostermann and Sanders (2017), and Section 1.4.3).

For non-catastrophic bedrock landslides that are deforming sub-critically, the terminology for stability-depriving factors needs to be modified. When sub-critical, non-catastrophic failure is ongoing, Preparatory Factors should be redefined as Movement Sustaining Factors. Theoretically, these Movement Sustaining

Factors do not necessarily need to be the same as the Preparatory Factors that initially triggered the sub-critical deformation (McColl, 2015).

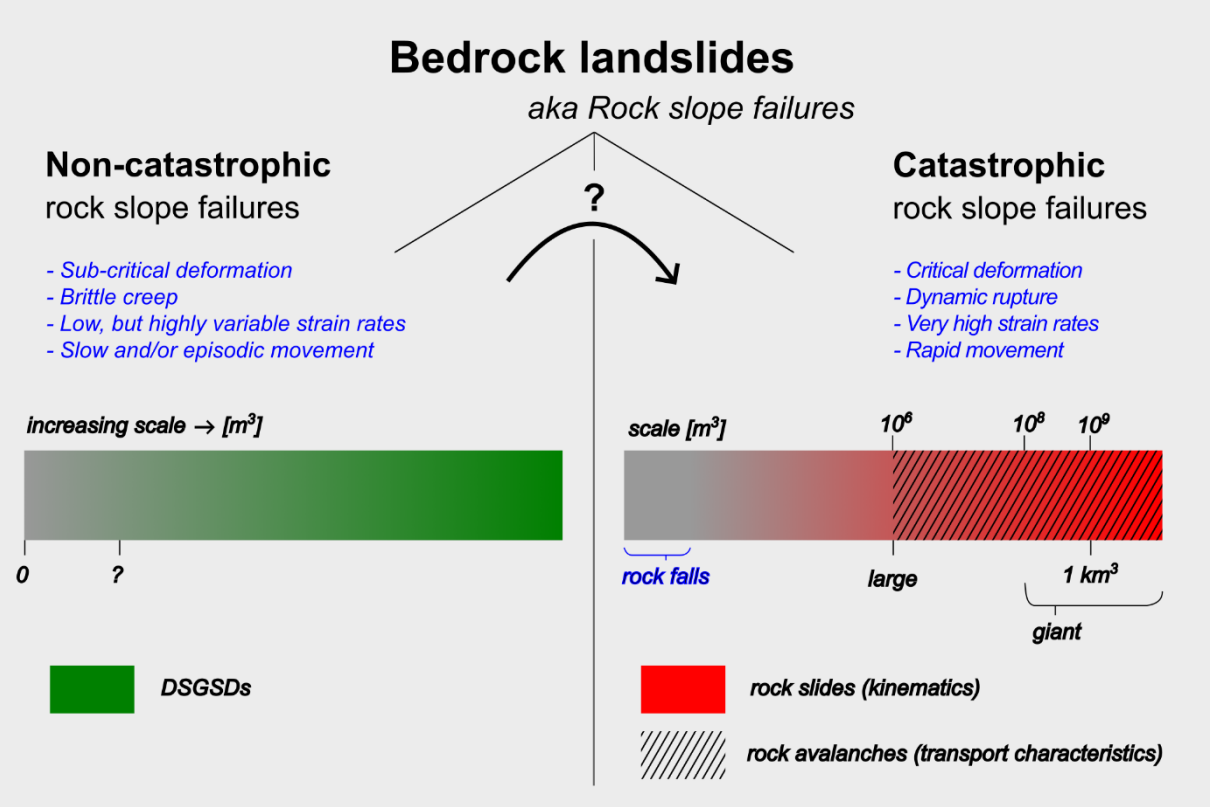


*Figure 1.3: Categorisation of bedrock landslides sketched out for the reader. This helps to better distinguish between different terms used in the PhD thesis.*

## 1.3 Catastrophic rock slope failures

### 1.3.1 Terms and differentiation

Catastrophic, critical rock slope failures, or alternatively referred to as catastrophic bedrock landslides, are characterised by a high and sudden release of gravitational energy, resulting from the dynamic rupture of the rock, and causing rapid movement of material at speeds in the order of metres per second (see Figure 1.3). Catastrophic rock slope failures preferentially originate from relatively freshly exposed, unweathered massive rock in high relief terrain, which is typically exposed in active, young mountain ranges along major plate boundaries (Hewitt et al., 2008; Korup et al., 2007). Catastrophic bedrock landslides either fail as rockfalls, rock topples or rockslides depending on the mode of failure from its source area (see Hungr et al., 2014). When significant volumes are involved, they are often simply referred to as "rockslides" by scientists, likely because they always exhibit some sort of basal shear failure plane (see, e.g., inventory of large rapid rock slides by Glastonbury and Fell (2010)). Many case studies of large-scale catastrophic rock slope failures (failure volume > $10^6$ $m^3$, Figure 1.3) exist around the world covering historic and prehistoric times (see, e.g., review by Hewitt et al., 2008; Pánek (2019) and Table 1.1). They are sometimes called “(rapid) rockslides”, and sometimes “rock avalanches”.

The term "rock avalanche" is derived from the specific transport characteristics that can arise from large-scale catastrophic rock slope failures. Not only presenting high volumes (>$10^6$ $m^3$), they are bedrock landslides with exceptionally fast transport velocities (100 - 250 km/h), short event durations (rapid runout), and their deposits consist of extensively fragmented (i.e. crushed, pulverised) and dry rock material (Eisbacher and Clague, 1984; Hungr et al., 2014). The ratio of the runout distance to fall height of rock slope failures described as rock avalanches are usually high, easily reaching 5, up to 10 (Hewitt et al., 2008). Not all large catastrophic rock slope failures are necessarily “rock avalanches”. Looking only at the failure in the source area, large rock slope failures referred to as 'rock slides' and those referred to as 'rock avalanches' are identical, two terms used for the same type of failure that appear regularly in the literature. Even if we admit it makes sense to distinguish some rockslides with special transport characteristics from others by calling them rock avalanches (see above, especially when looking at deposits), this can cause sometimes confusion. Also because these terms are not used stringently in the literature anyway. It is perhaps better to simply use the general terms “catastrophic rock slope failure” or “catastrophic bedrock landslide” if one does not want to emphasise avalanche transport characteristics (“rock avalanche”) or the sliding failure mode (“rockslide”) for the purpose of differentiation (Figure 1.3).

Table 1.1: List of some very voluminous and famous catastrophic rock slope failures not triggered by volcanic eruption

| Name | Location | Lat. ,Long. [°] | Volume [km³] | Age | Sources |
|---|---|---|---|---|---|
| *pre-historic events* | | | | [ka BP] | |
| **Flims** | Alps, Switzerland | 46.81, 9.31 | 7,5 ($V_F$) | 9,3 – 9,5 | Aaron et al., 2020; Nicolussi et al., 2015 |
| **Köfels** | Alps, Austria | 47.16, 10.93 | 3,1 ($V_F$) | 9,5 | Nicolussi et al., 2015; Zangerl et al., 2021; Figure 1.4 |
| **Green Lake** | Southern Alps, NZ | -45.78, 167.36 | ~ 27 ($V_D$) | 15,5 ± 0,7 | Eaves et al., 2023 |
| **Seymareh** | west Iran | 33.00, 47.62 | ~ 20 ($V_D$?) | unclear, ~10 | Petley, 2009 |
| **Bridge of the Goods** | Cascades, US | 45.66, -121.93 | not studied, ~ 1 ($V_D$) | 0,5 – 0,6 | Reynolds et al., 2022 |
| *historic events* | | | | [AD] | |
| **Usoi Dam** | Tajikistan | 38.26, 72,61 | ~ 2 ($V_D$?) | 1911 | Schuster & Alford, 2004 |
| **Mayunmarca** | Andes, Peru | -12.62, -74.66 | 1 – 1,6 ($V_F$ or $V_D$?) | 1974 | Schuster & Highland, 2001 |

*$V_F$ = volume of failed material, $V_D$ = volume of deposit*

### 1.3.2 Short-lived nature of catastrophic bedrock landslides and scarcity of large events

The actual duration of a catastrophic bedrock landslide, from the detachment of the main mass to the point the deposit comes to rest, takes place within only a few minutes. However, it has been documented from voluminous large-scale events in history that precursors due to progressive sub-critical rock failure occur in periods of hours and sometimes even years or decades before the catastrophic failure: cracking, visible slope deformations (i.e., slumping or buckling), rock falls or changes in the hydrological regime (e.g., Glastonbury and Fell, 2010; Lacroix et al., 2020). For example, analysis of optical imagery prior to the 2021 Ronti Peak rock slope failure in the Indian Garhwal Himalayas (about 450 km WNW of the Annapurna Massif) shows that the failure zone was already moving five years before the catastrophic detachment (Shugar et al., 2021). Catastrophic rock slope failures often occur in remote areas and the warning signs of such an event are usually not recognised by humans in time to react. Due to their unpredictable nature and short duration, catastrophic bedrock landslides are approached by researchers almost exclusively in retrospect, after the event happened and the debris is emplaced (e.g., Lacroix et al., 2020). In some slopes that showed signs of instability, the installation of scientific monitoring (geodetic methods) was successful to predict a catastrophic rock slope

failure some time before it happened, allowing timely evacuation of residents (Fan et al., 2019; Connolly, 2023).

From a human perspective and only in the context of a specific region, catastrophic bedrock landslides with a considerable fracture volume occur relatively rarely. With reference to the non-exhaustive Wikipedia List of landslides (2023), there has been approximately one catastrophic rock slope failure per decade worldwide in the historical past with a fracture volume > $10^8$ $m^3$ (see Figure 1.3), which corresponds to a cube with the dimensions 1km - 1km - 100m. But, smaller events are, of course, much more common. However, due to the increasing use of smartphones in recent years, videos of smaller events have emerged in which the failure was recorded directly: From the European Alps, for example, the Piz Cengalo event in Switzerland in 2017 (3 · $10^6$ $m^3$ fracture volume; see Supplementary by Walter et al. (2020)) and also the Fluchthorn landslide in Austria last summer (~1 · $10^6$ $m^3$ fracture volume; UnwetterChaseR, 2023) were recorded on video. Despite the poor quality of such recordings, which sometimes do not even capture the entire collapse from start to finish, they provide an interesting insight into the dynamics of catastrophic rock slope failures. There will be certainly more video recordings of even larger events in the near future.

### 1.3.3 Causes and chronology of large catastrophic rock slope failures

In order to study causes, temporal and spatial distribution, and other characteristics of large catastrophic bedrock landslides more objectively, researchers have made inventories from literature studies and remote sensing analyses: Their endeavours have leaded to regional (Hewitt et al., 2008; Wen et al., 2004) or global (e.g., Glastonbury and Fell, 2010; Korup et al., 2007) collections of large catastrophic rock slope failures in particular, and to their integration into general landslide inventories (e.g., Pánek (2019); Blondeau et al., 2021; Cui et al., 2022). Dating techniques, both relative and absolute, come into play to investigate the timing of events that were not recorded in historical documents. Among the absolute dating techniques, the most commonly used are carbon burial dating (14C), cosmogenic radio-nuclide dating (CRN, mainly 10Be and 36Cl) and luminescence dating applied mostly on the following objects: buried material, deposited boulders and exhumated rupture planes (see reviews by Pánek (2015, 2019) and references therein). The analytical resolution of most dating techniques results in error ranges from decades to centuries depending on the method. Climate related Preparatory Factors leading up to the failure can be inferred by comparison with paleoclimate proxy data (e.g., Pánek, 2019). Short lived Triggers, however, affecting a rock slope only for a very short moment in the past remain most often elusive. However, a correlation between historical records or other dated events in close proximity can provide clues to a possible Trigger. In general, conclusions about the timing and frequency of large, catastrophic rock slope failures lack credibility due to the incompleteness of their records (especially for certain regions of the world) and the precision of the dating techniques used

(see Pánek, 2019). The deposits of identified prehistoric events often lack any dating, and there is a typical preservation bias in favour of more recent events.

Precondition Factors for large catastrophic bedrock landslides are large-scale (folds, faults and joints) and small-scale (foliation, unconformities) structures, and other lithological characteristics. Catastrophic rock slope failures typically rupture on distinct failure planes: structures presenting a favourable orientation for slope failure have specifically the potential to act as rupture planes (see, e.g., Brideau and Roberts, 2015; Stead and Wolter, 2015). It is noteworthy that most of the catastrophic translational and compound rockslides studied by Glastonbury and Fell (2010) involved surfaces that had previously been sheared, for example by tectonic processes, including shearing on bedding surfaces during folding. It is conceivable that tectonic activity (incl. uplift) and regionally induced tectonic stresses may influence the abundance of large catastrophic rock slope failures and their prevalence over other landslide types: Blondeau et al. (2021), by comparing their extensive inventory of landslides in the Western European Alps with other datasets from other orogens, concluded that more tectonically and seismically active orogens in a compressional state, such as the Southern Alps of New Zealand (Allen et al., 2011) or the Himalayas (Hewitt et al., 2008), exhibit more large catastrophic bedrock landsliding than orogens of crustal extension and limited seismicity (like the Western European Alps).

Preparatory Factors that seem especially relevant for bringing a rock slope into a marginally stable state for large catastrophic failure are either directly related to the cryosphere (glacial de-buttressing, freeze–thaw cycles, snowmelt), fluvial or marine erosion (results in slope undercutting), precipitation, or recurring seismic activity (see, Glastonbury and Fell, 2010). Especially, very voluminous catastrophic rock slope failures appear in close proximity to major active tectonic faults where high magnitude earthquakes are frequent (e.g., Wen et al., 2004; Korup et al., 2007). Loss of permafrost leads directly to a reduction in the shear strength of the bedrock, a deepening of the active layer affected by freeze-thaw cycles, and can have a further destabilising effect on a rock slope deeper in the subsurface through higher pore pressures caused by increased hydrological connectivity and responsiveness to atmospheric conditions (e.g., Patton et al. (2019) and citations therein). The interregional timing of catastrophic bedrock landslides is in line with the global signal of landslides (see review by Pánek (2019)): There is evidence from the past that landslides (in general) occur more commonly during or after a climate change, possibly due to the amplification of Preparatory Factors (i.e., changes in temperature, precipitation, and the cryosphere). A particularly high number of landslides have been recorded in formerly glaciated regions where glacial erosion created steep slopes and high relief susceptible to slope failure (see studies mentioned by inventories above). A particular clustering can be recognized at the last glacial to interglacial transition (Pleistocene – Holocene boundary). The dating of the events, however, shows a considerable delay of several thousand years after the last major glacial retreat, possibly when progressive sub-critical rock slope deformation was active in conjunction with weathering

processes, which followed the glaciation and preceded many large catastrophic bedrock landslides dated in literature (Hewitt et al., 2008; Pánek, 2019). In non-glaciated regions, warming and wetting of the climate (e.g., Holocene climate optimum) leaded also to more mass-movements, including large catastrophic rock slope failures (Pánek, 2019).

When Triggers are known, they are listed in decreasing order of importance as follows: heavy rainfall events, earthquakes and, to a much lesser extent, snowmelt and gravitational loading (e.g., Glastonbury and Fell, 2010; Wen et al., 2004). Interestingly, Glastonbury and Fell (2010) found that for large catastrophic rockslides failing in translational mode, rainfall was most commonly cited as the triggering factor, whereas for compound landslides, it was earthquakes. The significance of climate-related Causes and Triggers for large catastrophic bedrock landslides depends on the climatic zone, and is less evident in arid environments (Korup et al., 2007; Hewitt et al., 2008).

### 1.3.4 Morphological and sedimentological consequences

Satellite imagery and remote sensing techniques allows the study of the Earth's surface topography with Digital Terrain Models (DTMs) and optical satellite imagery before and after an event. DTMs typically originate from spaceborne Synthetic Aperture Radar (SAR), spaceborne or airborne optical imagery, or airborne Lidar (see, e.g., Petley, 2012; Tarolli and Mudd, 2020). A difference analysis approach using DTMs is commonly utilized to precisely determine outline and volume of failed rock material, thickness and volume of deposits and to investigate other morphological consequences of contemporary events (see, e.g., Delaney and Evans, 2015; Walter et al., 2020; Shugar et al., 2021). The study of older large historic events and pre-historic events can also highly profit from modern DTMs and optical satellite imagery. Such data can support field surveys and estimates of deposit extend, volume and source area (refer, e.g., to case studies in Table 1.1 and Figure 1.4). It should be noted that failure will result in an increase in the volume of the material due to the increased pore space as the rock disintegrates. A distinction must be made between the volume of the failed material ($V_F$) and the deposit volume ($V_D$) (Hungr and Evans, 2004; Table 1.1 and Figure 1.4). In case studies found in the literature, reported values for the volume increase of large catastrophic rock slope failures commonly range between 15% and 35%.

General deposit geometry, slope angles, and morphological features at the top of large deposits may reveal some of the failure kinematics and can indicate a potential source area. Ridges and troughs can be formed when flowing debris interacts with topography, e.g. valley walls and junctions, or by multiple debris bodies moving at different speeds (Hewitt, 2002). After a large catastrophic rock slope failure event has happened, its deposit and surroundings are subject to further changes in morphology. The emplaced failed material

interacts with the fluvial system and/or glaciers which expresses itself in the form of various morphological consequences: damming upstream from the deposit, channel avulsion, sediment aggradation, formation of terrasses and moraines (see, Hewitt et al. (2008) and many case studies). Especially, the physical barriers of dams created by large catastrophic bedrock landslides highly impact sediment and water fluxes in the fluvial reach affected. A landslide dam can establish permanently, which can last for tens of thousands of years, or breach catastrophically (outburst event). It is known from reviewing historic events that most dams (~85%) breach within a year by overtopping (Costa and Schuster, 1988; Peng and Zhang, 2012). Nevertheless, we know from lacustrine sediments that many pre-historic voluminous failures have impounded lakes for considerable time in the past which gradually transformed into aggradation flats by infill of sediment (e.g., Hewitt et al., 2008; Pánek, 2021). River channel steepness is typically showing first a gradual decrease then a rapid increase when crossing over the sediment body left behind by the slope failure. Deposits of large catastrophic bedrock landslides typically form a stable knickpoint clearly visible in the extracted river profile (see, Korup, 2006; Korup et al., 2010; Ouimet et al., 2007). If the river erodes into bedrock when flowing alongside the sediment body, epigenetic bypass gorges can form (Korup et al., 2006). In some case studies, the volume of sediment exported from the area since the large catastrophic bedrock landslide was deposited was quantified by reconstructing the valley morphology before and immediately after the failure. (e.g., Aaron et al., 2020; Zangerl et al., 2021; Figure 1.4).

Along with general landsliding, the contribution of catastrophic bedrock landslides to erosion and denudation of mountains is known to be significant, if not dominant for some settings, especially in high relief terrain (Hovius et al., 1997; Korup et al., 2007; Marc et al., 2019). However, the quantification of landslide material originating exclusively from catastrophic rock slope failures suffers from the absence or poor reliability of volume estimations, and from an incomplete event record, particularly if the erosional budget is dominated by very rare and highly voluminous events (Hovius et al., 1997). We know for sure that large catastrophic rock slope failures chronically disturb the sediment flux in higher reaches of mountainous river catchments (see above). The lack of quantification of produced sediment volumes, the long timescales involved, and the overall complexity of the system, including intermontane sediment storage (fluvial, glacial processes intertangling with mass-movement events), prevent a better understanding of the impact of large catastrophic bedrock landslides on sediment budgets in high mountain ranges (e.g., Hewitt et al., 2008; Korup et al., 2007).

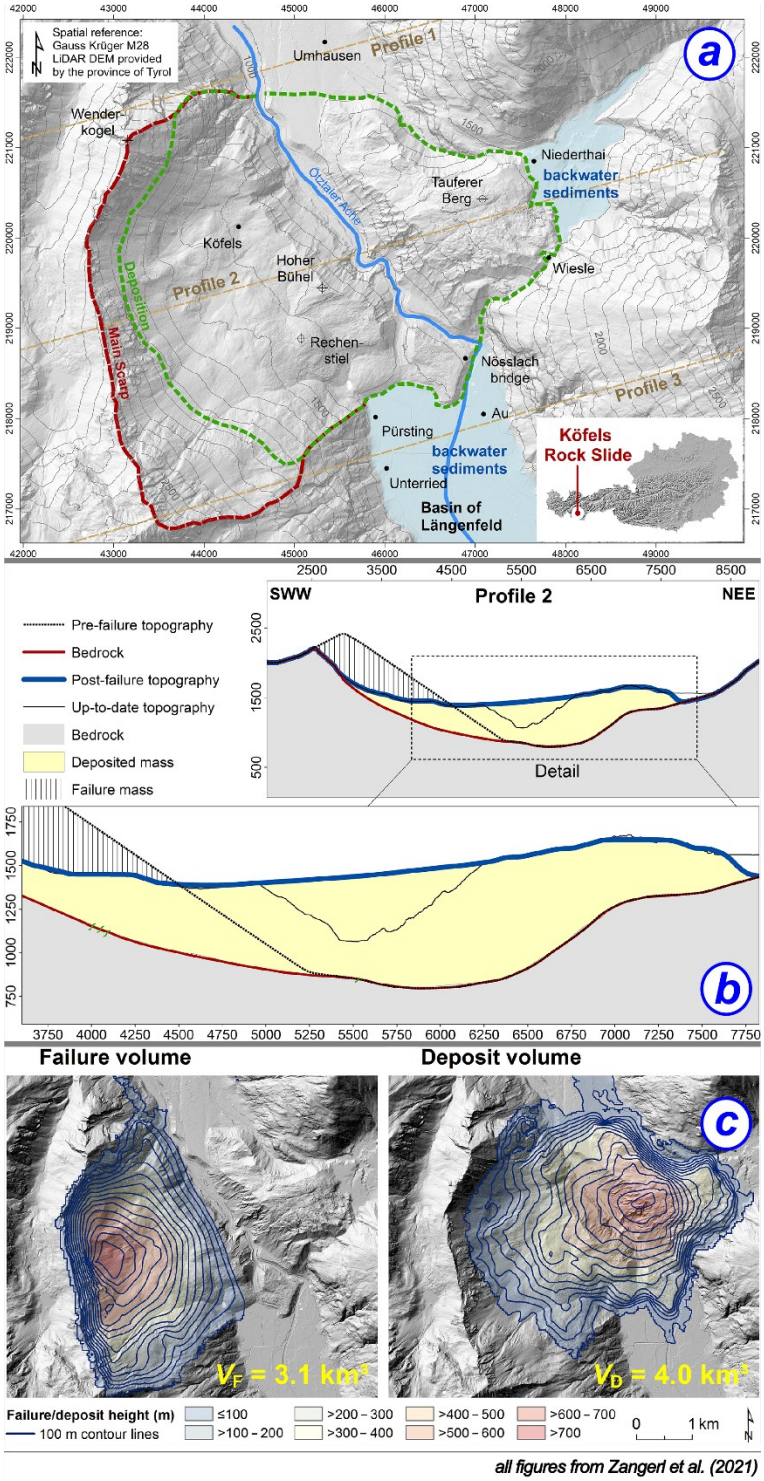


*Figure 1.4: Case study of the Köfels rockslide, European Alps (Austria). (a) Overview map showing failure scarp and deposition outline including consequences to the fluvial system after deposition (eroded channel, sediment aggradation upstream). (b) Profile through the central part the rockslide deposit with pre- and post-failure topographies. (c) Reconstruction of failure volume ($V_F$) and deposit volume ($V_D$). From Zangerl et al. (2021).*

### 1.3.5 Deposit characteristics

Lithological characterization of large catastrophic bedrock landslide deposits can help to distinguish them from other sedimentary bodies commonly abundant in mountainous terrain, like fluvial or glacial sediments. This can be of relevance if the existence of a large catastrophic rock slope failures is unclear, in case large parts have already been eroded or covered by other sediments (e.g., Weidinger and Korup, 2009). Further, study of the sedimentary facies of the bedrock landslide deposit can provide insight into the failure dynamics and conditions within the material during failure. As previously mentioned when explaining the terminology of catastrophic bedrock landslides (see above, Figure 1.3), two end members of bedrock landslide deposits can be identified by looking at the transport characteristics (see, Hewitt et al., 2008): a rapid streaming flow resulting in a thin and highly fragmented debris sheet usually referred to as "rock avalanche deposit" in case the failure is not or hardly retrained by topography, and, a rock slope failure detaching along a singular flat surface (translational rockslide) with little fragmentation and disintegration happening before coming to rest on its final position, usually an opposing valley flank. However, despite the possible differences in the transport path and source lithology between individual events, three sedimentary facies were identified as characteristic of large bedrock landslide deposits (>$10^6$ $m^3$) (Hewitt et al., 2008; Weidinger et al., 2014; Dufresne et al., 2016; see Figure 1.5):

- For many source lithologies, the surface of a deposit consists of an open network of several meters of large boulders forming a "**carapace**". It is the surface of a **top layer** consisting of a chaotic, blocky clasts (diamict-like) within a finer matrix and downward increasing fractionation.

- This top layer transitions into the **main body facies** of the landslide deposit with fragmented, shattered, diamict-like clasts (incl. jigsaw-fractured clasts and facies). Often lithological boundaries and structures from the source rock are highly disturbed from the fractionation but still easily recognizable. The proportion of matrix can be variable, which consists of more sand than silt, not so much clay. The sediment body features many shear zones or bands of different scales, sometimes discontinuous. Mixing within the deposit is commonly described as low but further down-ward increasing fragmentation is observed.

- The contact to the underlying pre-existing topography is the highly fractured, granulated **basal mixed facies** (mélange). Although often described as a sharp basal contact, the debris of the rock slope failure typically mixes with the underlying pre-existing substrate that can be soil cover or other sediments. The underlying substrate can be found intruded or entrained as rip-up clasts. This bottom layer is highly disturbed by the bedrock landslide movement: shear-bands and often folding are observed.

Near the base contact of some very voluminous bedrock landslide deposits, partial melting of rock mass was described, referred to as “frictionite” (Masch et al., 1985; Weidinger et al., 2014; see Figure 1.5): High release of frictional energy within shear bands consisting of thin, undulating micro-breccias resulted in high temperatures (1500 - 1700 °C) and consequently created short-lived melts forming a matrix with a different colour than the surrounding crushed material (sometimes pumice-like with gas bubbles). The clasts within a large catastrophic rock slope failure deposit are usually fairly compacted, but originally not cemented. However, cementation can occur after deposition due to meteoric water percolation and groundwater flow (see, Weidinger et al., 2014).

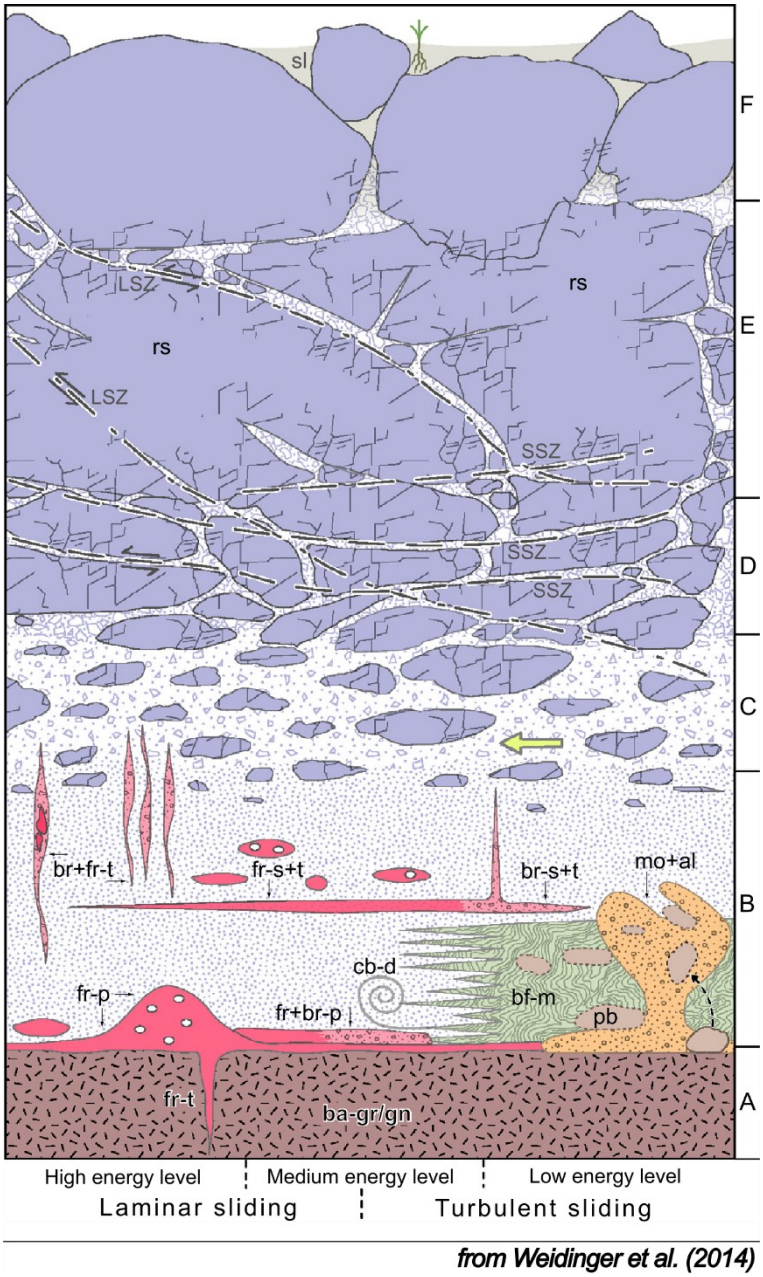


*Figure 1.5: Explanatory sketch of the stratigraphy of a "giant" bedrock landslide deposit, or rock-avalanche deposit, after Weidinger et al. (2014).Different layers not to scale, bold arrow shows direction of movement. Descriptions of features after Weidinger et al. (2014): "(A) Nearly undisturbed basement rock (ba-gr/gn) with occasional frictionite-filled joints (fr-t). (B) Shear planes in heavily shattered matrix of rockslide material: fr = frictionite with gas bubbles, br = micro-breccias; suffixes -p/-s/-t = primary, secondary, tertiary shear planes, respectively; mo + al = entrained alluvial or glacigenic sediments (pb = phantom blocks, dashed arrow = direction of entrainment) at the rockslide base; bf-m = base facies mélange with underlying sediments potentially containing phantom blocks; cb-d = convoluted bands of diamictic rockslide mass. (C–E) "En masse" rockslide deposit (rs); fragmented rock or diamict-like shattered rock blocks and boulders with downward increasing intensity of fragmentation to crushed rock, separated by shear zones: LSZ = listric shear zone (formed by partial deceleration of rockslide mass, e.g. due to impact on an obstacle), SSZ = sub-parallel shear zones (additionally to -p and -s shear planes; in analogy to a sheared deck). (F) Boulder carapace, optionally hosting soil (sl)".*

### 1.3.6 Societal hazards and risks

The main reason why human society is interested in the phenomenon of catastrophic rock slope failures is that it poses a potential threat to people, their belongings and infrastructures (e.g., Glade et al., 2005; Davies, 2015; Turner, 2018; Froude and Petley, 2018). Throughout history, many natural disasters have been associated with catastrophic bedrock landslides, causing loss of life and considerable damage to society (see, e.g., Wikipedia List of landslides, 2023). Logically, the hazard potential increases with the volumes concerned causing devastating effects on the surrounding areas. If the hazard is not directly caused by the impact of debris from a rapid bedrock landslide, the initial failure event can also cause immediate secondary hazards and risks, which in most cases are caused by the following:

- far reaching **debris flows** by interaction of debris from the slope failures with ice, water or other sediment immediately after the event or later (see Hewitt et al., 2008; Hungr et al., 2014),
- damming of a river by the bedrock landslide deposit and the potential subsequent breaching of the dam which then causes a **landslide lake outburst flood** (LLOF) (e.g., Evans et al., 2011),
- the generation of **tsunami waves** when rock masses fall in a lake or the sea (e.g., Bornhold and Thompson, 2012),
- or, the response of the fluvial system causing **sediment aggradation or channel avulsion** up and downstream of the deposit (e.g., Korup et al., 2004).

Famous examples of natural disasters related to large catastrophic bedrock landslides from the European Alps are:

- **Tauredunum event,** CH/FR (*AD 563*): a rock slope failure occurred somewhere where the Rhone river enters Lake Geneva and resulted in a tsunami wave that devasted towns and villages along the lake, including Geneva, causing many casualties (Kremer et al., 2012).
- **1219 Flood of Grenoble**, FR (*AD 1219*): a LLOF originating from a landslide deposit emplaced AD 1191 upstream from Grenoble in the Romanche Valley inundated Grenoble and led to severe destruction and a large number of deaths (Berlioz, 1997).
- **Mount Granier rockslide,** FR (*AD 1248*): a giant rock avalanche close to Chambery travelled more than 7.5 km and destroyed five villages (about 5000 casualties), Trigger unknown (Pachoud, 1991).
- **Goldau rockslide**, CH (*AD 1806*): after two preceding years of high precipitation and heavy rain a big rockslide fell on two villages burying houses below more than 30 m of material, causing 457 casualties (Heim, 1932).

More recent examples of large catastrophic bedrock landslides that have caused many victims worldwide are (only the last century, ones related to volcanic eruptions not included):

- **Diexi landslides**, CN (AD 1933): a Mw 7.3 earthquake triggered many voluminous rock and debris slope failures (Dai et al., 2021). Several landslide dammed lakes were formed, of which one breached 45 days later. Total death toll of more than 6800 people (Cui et al., 2022).
- **Khait rockslide**, TJ (AD 1949): ca. 800 people were directly killed by a rock avalanche that overrode two villages after a Mw 7.4 earthquake (Evans et al., 2009)
- **Vajont disaster**, IT (AD 1963): a rockslide fell into a dam reservoir and almost 2000 people were killed by a water wave that devasted the villages nearby (Genevois and Ghirotti, 2005).
- **Nevados Huascaran debris avalanche**, PE (AD 1970): subsequent to a major earthquake (Mw 7.9), a bedrock landslide fell on a glacier resulting in a "cataclysmic debris avalanche" which buried the town of Yungay. More than 18 000 people lost their lives directly (Schuster et al., 2002).

As for other natural hazards, the threat to human society by large catastrophic bedrock landslides will rise due to anthropogenic climate change and the ongoing growth of population in mountainous regions (IPCC, 2023; Ehrlich et al., 2021). Temperature rise, glacier retreat, and climate change towards more extreme weather patterns have a direct impact on the Preparatory Factors of catastrophic rock slope failures in general, and may increase the magnitude and frequency of potential climatic Triggers (e.g., Huggel et al., 2012; Gariano and Guzzetti, 2016; Patton et al., 2019). Research is needed to better understand the dynamics of catastrophic bedrock landslides, to better adapt to future events and to reduce the risks they pose (Gariano and Guzzetti, 2016).

## 1.4 Non-catastrophic bedrock landslides

### 1.4.1 Terminology and characteristic features

Alongside catastrophic bedrock landslides, non-catastrophic landslides originating from bedrock substrate are a common phenomenon on the Earth's surface (besides slow moving slope failures in debris or soil which are not considered in this PhD thesis, see e.g., Lacroix et al. (2020)). The movement rates of sub-critical brittle creep deforming slopes are so slow that they are imperceptible to the naked eye, ranging widely from meters per day to as little as millimetres per year (see reviews by Pánek and Klimeš, 2016; Lacroix et al., 2020). The categorisation and naming of non-catastrophic bedrock landslides is not clear at all in the literature and can be confusing when studying the research contributions of different authors. In the case a non-catastrophic rock slope failure involves considerable volume of bedrock, slope deformation occurs to greater depths (i.e., several tens of metres). The deep-seated deformation is diffuse and boundaries cannot always be clearly identified. Also, characteristic morphological features evolve for large-scale non catastrophic bedrock landslides, and researchers avoided the term "rockslide" and used a variety of different expressions such as "sackung" (e.g., Zischinsky, 1968), "deep-seated creep" (e.g., Mahr and Nemčok, 1977), "mass rock creep" (e.g., Chigira, 1992), "mountain/rock slope deformation" (Hungr et al., 2014), or "gravitational deformation" (Jaboyedoff et al., 2013). The term "Deep-seated gravitational slope deformation" (DSGSD) seems to be the most widely used in recent literature (e.g., Dramis and Sorriso-Valvo, 1994; Agliardi et al., 2001, 2012; Pánek and Klimeš, 2016; Discenza and Esposito, 2021).

Characteristic morphological features of so called DSGSDs are quite similar to tectonic features, but less continuous in the landscape. They are limited to individual ridge lines, often extend from the slope toe up to the crest or beyond, and commonly form arcuate shapes typical for gravitational slope failures of all kind (e.g., Agliardi et al., 2012; Jaboyedoff et al., 2013; Figure 1.6). Both brittle and ductile deformations in the subsurface are responsible for their formation (Chigira, 1992; Agliardi et al., 2001). Features described in many case studies all around the world are mentioned in reviews by Agliardi et al. (2012), Jaboyedoff et al. (2013), Pánek and Klimeš (2016) and Discenza and Esposito (2021): At the top and middle sections of the slopes, downhill or uphill facing scarps (counter slope scarps), trenches, tensional cracks or downthrown blocs appear, in some cases resulting in double-crested ridge lines (Figure 1.6). All these structures may converge underground towards a basal rupture plane or shear zone (see the many geometries compiled by Discenza and Esposito (2021), and Figure 1.6a), whose absence was actually once regarded as a characteristic feature to discriminate DSGSDs from non-catastrophic deep-seated "rockslides" (e.g., Mahr and Nemčok, 1977; Dramis and Sorriso-Valvo, 1994). But, according to contemporary research progress, a discrete rupture zone is strongly suspected in many DSGSDs or even directly proven by exposure or geophysical surveys; this is

especially the case when considerable displacement is involved (e.g., Brückl and Brückl, 2006; Barla et al., 2010; Strauhal et al., 2017). The shear zones in m-scale (sometimes up to a few tens of meters thick), are characterized by uncemented fault-breccia and localized fault gouge, including slickensides and limonitization (e.g., Barla et al., 2010; Strauhal et al., 2017; Wolter et al., 2020; Figi et al., 2022; Figure 1.6f). At the bottom section of the slope deformation, internal folding and shearing lead to bulging or buckling of the slope surface (see review papers mentioned above and Figure 1.6g). The overriding of fluvial sediments at the valley bottom is known from some case studies and is accompanied by a forced shift of the river channel away from the affected slope (i.e., interaction with the fluvial system) (e.g., Barla et al., 2010; Figi et al., 2022). Ongoing movement can evolve into nested secondary landsliding (i.e., rockfalls, rockslides) that can appear within DSGSDs in all sections of the slope (e.g., Agliardi et al., 2001; Helmstetter and Garambois, 2010; Pánek and Klimeš, 2016). At a given location where a DSGSD occurs, there may be several successive phases of activity, originating from different failure geometries (e.g., Agliardi et al., 2012).

Some researchers argue for a distinction between DSGSD phenomena and other non-catastrophic deep-seated rock slope failures (see reviews by Crosta et al. (2013), Agliardi et al. (2012), Pánek and Klimeš (2016) and Figure 1.6e): They note that DSGSDs have less distinct boundaries, less pronounced head scarps and a bigger width to length ratio. “Slow-moving rockslides” are expected to have only “limited lengths with respect to the slope dimension”, with rock material more internally deformed and disintegrated. In view of the latest scientific results, it is a legitimate question to ask whether a distinction between DSGSDs and other non-catastrophic deep-seated bedrock landslides referred to as “slow-moving rockslides” is really beneficial. Although some variability in morphological characteristics can be evidenced, we believe it is less confusing if DSGSDs are solely differentiated from other non-catastrophic rock slope failures by the volumes involved into the slope failure (Figure 1.3). Indeed, DSGSDs are large-scale non-catastrophic failures. When moving to larger spatial scales, the delimitation between purely gravitational slope processes and large-scale tectonic processes is not necessarily clear and depends on whether rock masses are influenced by purely gravitational stress fields or by tectonic stresses, or and whether more than just a mountain slope or a ridge line is affected (see review by Jaboyedoff et al. (2013)). In the following, we will address all non-catastrophic -moving processes of rock slope failure in a predominantly gravitational stress field on the scale of a mountain slope.

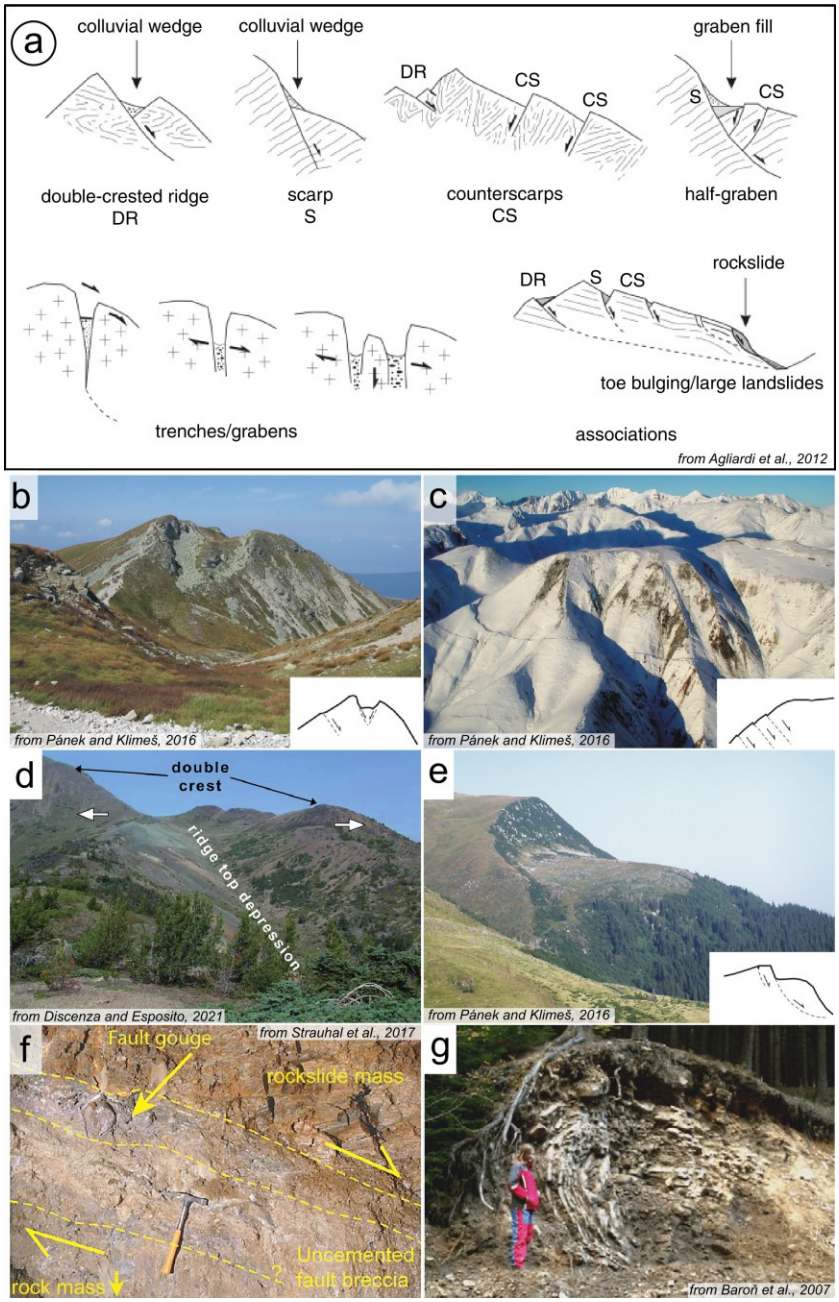


*Figure 1.6: (a) Morphological features characteristic of DSGSDs sketched by Agliardi et al. (2012). (b) Double-crested ridge at Salatín Mt., Tatra Mts., Slovakia (Pánek and Klimeš, 2016). (c) Counter slope scarps appeared after the 2002 Denali Fault earthquake, Gilette Pass, Alaska, USA (Pánek and Klimeš, 2016). (d) Double-crested ridge line at Mission Ridge, Pacific Coast Mountains, Canada (Discenza and Esposito, 2021). (e) "Slow-moving rock rockslide" at Pietrosh Mt., Eastern Carpathians, Ukraine (Pánek and Klimeš, 2016; not a DSGSD following the authors). (f) Exposed shear zone at Klasgarten rockslide, European Alps, Austria (Strauhal et al., 2017) (g) A fold resulting from brittle creep at the bottom of a slope affected by a DSGSD at Komarovsky potok, Western Carpathians, Czech Republic (Baroň et al., 2007).*

### 1.4.2 Causes and temporal evolution

Slopes that are affected by non-catastrophic rock slope failure are usually subjected to deformation over long periods of time, in the magnitudes of $10^4$ to $10^5$ years (e.g., Discenza and Esposito, 2021). This is a fundamental difference to the ephemeral nature of catastrophic bedrock landslides that fail catastrophically in a few minutes or hours. As for catastrophic rock slope failures, there are many case studies that describe the movement of non-catastrophic rock slope failure phenomena. In general, research can be divided into two main groups that use different methods: Studies that focus on current slope deformation, and studies that attempt to reconstruct past non-catastrophic bedrock landslide activity (e.g., Pánek and Klimeš, 2016). Typical methods used when researchers are concerned with the contemporary activity of non-catastrophic rock slope failures are geodetic measurements, extensometer readings, deformation tracking with GNSS (Global Navigation Satellite System) or space born Synthetic Aperture Radar (SAR), and the recording of other physical parameters associated with the landslide activity, including piezometer readings or ambient seismicity (see, e.g., review by Pánek and Klimeš, 2016 and citations therein; Le Breton et al., 2021). For reconstruction of past activity, absolute dating techniques commonly used for dating pre-historic landslide events find application: Most notably, surface exposure dating with $^{10}$Be and $^{36}$Cl cosmogenic nuclides is applied on exposed rupture surfaces ( see, e.g., Le Roux et al., 2009; Hermanns et al., 2013; Zerathe et al., 2014), and trenches are dug over detachment scarps covered by deformed sediments or soils (like paleo-seismic trenches), in combination with the use of $^{14}$C carbon burial or luminescence dating (see, e.g., McCalpin and Irvine, 1995; Tibaldi and Pasquarè, 2008; Livio et al., 2022).

From the investigation of the temporal evolution of active or formerly active non-catastrophic rock slope failures, some general, repeatedly observed characteristics of short- and long-term movement behaviour can be identified. Additionally, with the increasing availability of inventories, which include extensive mapping of non-catastrophic rock slope failures for entire mountain regions, certain attributes, like lithology or last glacial ice cover, can be correlated with the spatial distribution of non-catastrophic bedrock failures (see, Crosta et al., 2013; Jarman and Harrison, 2019; Pánek , 2019; Blondeau et al., 2021). The combination of different research approaches allow to define important Precondition, Preparatory, Movement Sustaining, and Triggering Factors of the non-catastrophic bedrock landslide phenomenon, as outlined in the following paragraphs.

The rock intrinsic Precondition Factors known to have an influence on the occurrence of non-catastrophic rock slope failures are, like for the catastrophic failures, mostly linked to lithology and structures. Non-catastrophic bedrock landslides are observed in all rock types but are more common in metamorphic and sedimentary rocks that feature rock strength anisotropy in the form of layering, schistosity or regular jointing (e.g., Chigira, 1992; Agliardi et al., 2012; Crosta et al., 2013). In addition to the ubiquitous structures, there

are also tectonically induced structures such as faults and folds, which are often associated with non-catastrophic bedrock landslides and can dictate the kinematics of the failures. (e.g., Jaboyedoff et al., 2013; Stead and Wolter, 2015; Discenza and Esposito, 2021; and citations therein). According to Blondeau et al. (2021), the supra-local stress regime appears to correlate with the occurrence of non-catastrophic rock slope failures in the European Alps. As a matter of fact, non-catastrophic bedrock landslides seem to be more frequent in extensional settings.

The Preparatory Factors for non-catastrophic bedrock landslides are the same as those identified for catastrophic bedrock failures (see above). In the European Alps, abundance of DSGSDs correlates with landscapes of intermediate exhumation rates that are not so deeply dissected by streams but have prominent glacial troughs from the Pleistocene (Agliardi et al., 2013). In formerly glaciated mountain ranges, glacial debuttressing is assumed to be one of the most important factors causing unstable slopes with DSGSDs. Actually, the exposed valley flanks of main glacial flow channels active during the Pleistocene seem particularly affected by them (e.g., Crosta et al., 2013; Pánek and Klimeš, 2016). Whether located in glacially sculpted orogens or not, fluvial erosion at the base of the slope produces steep terrain susceptible to DSGSD activity (e.g., Discenza and Esposito, 2021). Progressive sub-critical rock damage (Brantut et al., 2013) plays a role in destabilising slopes, as well as deep weathering processes that further destabilise the slopes (e.g., Viles, 2013) Progressive rock deformation in slopes is also controlled by hydrological conditions and topographic stresses (Li and Moon, 2021). Climatic factors, their frequency and intensity, become therefore relevant Preparatory Factors for non-catastrophic rock slope failures. DSGSDs are frequently encountered in tectonically and seismically active regions where repeated loading by earthquakes likely prepares slopes not only for catastrophic bedrock landsliding but also for non-catastrophic failures (e.g., Pánek and Klimeš, 2016; Discenza and Esposito, 2021).

We know from monitoring studies that movement rates measured on non-catastrophic bedrock landslides can be very variable and are often unsteady. The following three movement characteristics (all three can occur in one single landslide) are described: long-lasting steady deformation, cyclic behaviour (daily and yearly cycles with strong seasonal variations), and sudden impulsive accelerations of movement followed by a long dormant phase (see reviews by Pánek and Klimeš, 2016; Lacroix et al., 2020). By far the most important factor in modulating the movement of non-catastrophic bedrock landslides is groundwater (see reviews by Pánek and Klimeš, 2016; Lacroix et al., 2020). The rise of the groundwater table, accompanied by an increase in pore pressure, is usually induced by prolonged periods of rain, short-term extreme events (heavy rain), or snow melt, and may directly result in an acceleration of movement. The long-term monitoring of the Spriana rockslide in the Italian Alps as seen in Figure 1.7a is a good example of the influence of groundwater on landsliding activity (Agliardi et al., 2020).

Earthquake-induced gravitational loading is scarcely monitored but it is definitely a potential Trigger for a short-term increase in movement rates or the episodic reactivation of otherwise dormant landslides (e.g., Moro et al., 2007; Klimeš et al., 2012; Tolomei et al., 2013; Amato et al., 2018). Space-borne SAR Interferometry (InSAR) and GPS (Global Positioning System, a GNSS) measurements from the Apennines (Italy) have shown that movement along scarps of non-catastrophic bedrock landslides is strongly elevated or caused when earthquakes occur, described as instantaneous episodic reactivation (see Amato et al., 2018 and citations therein). Figure 1.6c shows up to 5 m high counter slope scarps on a mountain that were discovered after the 2002 7,9 magnitude Denali Fault earthquake (Pánek and Klimeš, 2016). The slope shows evidence of past movement activity along the same failure scarps which indicates reactivation only during strong earthquakes (Jibson et al., 2004).

Other Movement Sustaining Factors, sometimes anthropogenic, are: upslope loading from deposition of material, erosion at the slope toe, or change in waterbody height at the base of a slope (see, e.g., review by Lacroix et al., 2020; Booth et al., 2018).

By looking deeper into the slope, all these Movement Sustaining Factors destabilise the material in the shear zones, provoking elevated rates of brittle creep or sometimes enabling episodic movement steps for otherwise stable slopes (see reviews by Pánek and Klimeš, 2016; Lacroix et al., 2020). Shear zones are affected by deep weathering processes with further destabilising effect. Displacement in the shear zones leads to further deformation and displacement of the slope, accompanied with stress re-distribution. Climate actively modulates the Movement Sustaining Factors mentioned above. Except maybe earthquakes which are supposed to follow a seismic cycle governed by tectonic forces (e.g., Avouac, 2015). Figure 1.7b, adapted from Agliardi and Crippa (2022), graphically summarises the Precondition, Preparation and Movement Sustaining factors of non-catastrophic bedrock landslides, together with a conceptual evolution curve illustrating the strain that takes place in a shear zone.

Monitoring studies can only capture the movement of non-catastrophic rock slope failures on time scales of a few years or decades. Although paleo-movement reconstructions provide a much less precise and vague record of movement patterns, they offer an insight that goes far beyond the contemporary monitoring horizons. They often extend well into the recent geological past, i.e., Holocene and Late Pleistocene. As expected, the prevailing Movement Sustaining Factors and Triggers are identical to those known from the contemporary monitoring studies and very similar to the Preparatory Factors and Triggers of catastrophic bedrock landslides (see Section 1.3.3 above). What do studies into the recent geological past reveal about the temporal activity patterns of non-catastrophic bedrock landslides? Evidence of both continuous and episodic movement can be obtained from trenches dug across failure scarps (see, Pánek and Klimeš, 2016

and citations therein). Long-term movement rates (averaged over $>10^2$ years) either remain constant or change over time.

In the case of formerly glaciated areas, the different movement patterns that can be found are strongly influenced by glacial retreat (e.g., Pánek and Klimeš, 2016 and citations therein; Pánek, 2019 and citations therein): After the disappearance of the glaciers, non-catastrophic bedrock landslides either immediately emerged or appeared within a lag period of a few thousand years (Figure 1.7c). Movement rates may be higher after the onset of movement and then decrease significantly (e.g., Hermanns et al., 2013) or are increasing throughout the Holocene (e.g., Le Roux et al., 2009). Or, they may have stopped moving completely after an active period of a few thousand years and are now found in an inactive state (see, e.g., Hippolyte et al., 2009). For all the cases in glacially sculpted areas, no life spans beyond the Last Glacial Maximum (LGM) are expected. However, Tibaldi et al. (2004) found evidence that a non-catastrophic rock slope failure was already active in the previous Interglacial and has been reactivated in the Holocene.

In non-glacial areas, the life spans of non-catastrophic rock slope failures can extend far beyond the last LGM (e.g., Pánek and Klimeš, 2016 and citations therein). Some studies, both for lower and higher latitudes, indicate that the activity of non-catastrophic bedrock landslides correlates with humid periods in the Holocene (Sewell et al., 2015 and references therein; Livio et al., 2022). Non-catastrophic rock slope failures with episodic paleo-movements, known from absolute dating methods, are found in the close vicinity of active tectonic faults and suggest individual seismic Triggers for step-wise displacements on failure scarps (Thompson et al., 1997; Gutiérrez et al., 2008; Agliardi et al., 2009; Moro et al., 2012). Movement intervals could possibly coincide with the return period of major earthquakes (Pánek and Klimeš, 2016). As with the unique failure of the catastrophic rock slope failures, the attribution of an earthquake Trigger to a single episodic movement step is not certain due to the resolution of dating methods. Even if an earthquake correlating with a discrete rupture is found in the records for a given region at a given time, other Triggers cannot be completely excluded.

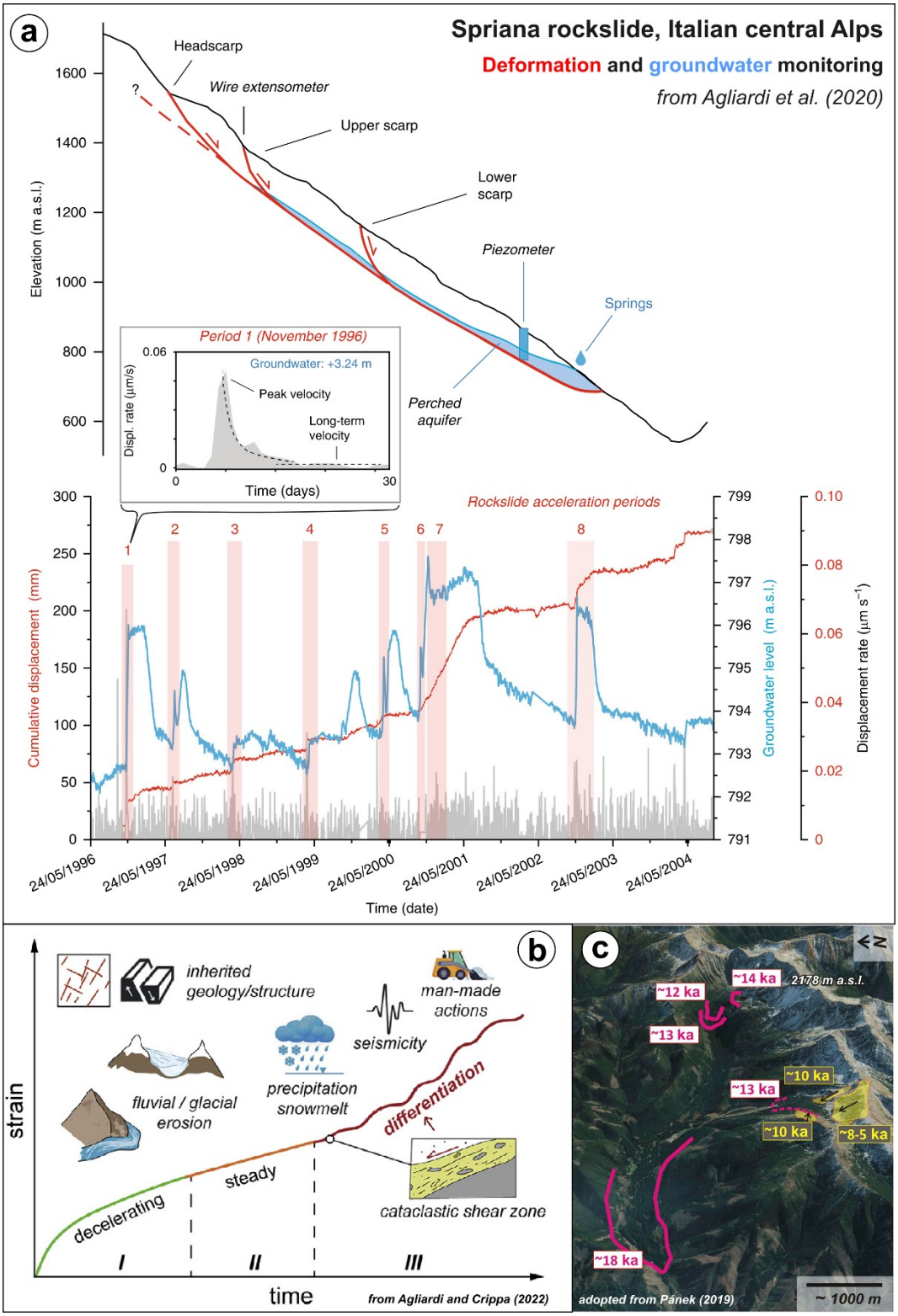


*Figure 1.7: (a) Schematic profile and monitoring data (displacement after wire extensometer and groundwater level) of Spriana rockslide, central Italian Alps. This example illustrates how pore pressure correlates with the movement of a non-catastrophic bedrock landslide (Agliardi et al., 2020). (b) Causes and Triggers of non-catastrophic rock slope failures illustrated together with a conceptual evolution curve of a deforming shear zone (Agliardi and Crippa, 2022). (c) Non-catastrophic bedrock landslides succeed glacier retreat with considerable lag time, Roháčská Valley, Western Tatra Mountains, Slovakia (Engel et al., 2017; Pánek et al., 2017; Pánek, 2019).*

### 1.4.3 Consequences for society and remaining research questions

Contrary to catastrophic bedrock landslides, the evolution of non-catastrophic bedrock landslides do not pose an immediate threat to human life and safety (enough time to run away). However, the slow deformations could have particularly negative consequences for infrastructures and land use: The literature contains numerous examples where non-catastrophic bedrock landslides threaten to cause or have already caused significant damage to roads, buildings, dams, entire settlements or agricultural lands, thus jeopardising considerable economic values (e.g., Záruba and Mencl, 1982; Ambrosi and Crosta, 2006; Barla et al., 2010; Mansour et al., 2011; Zangerl et al., 2010; Frattini et al., 2013; Nappo et al., 2019; Godone et al., 2023). Often, relevant hazards for society originate from the formation of secondary landslide phenomena within the realm of a DSGSD (e.g., Agliardi et al., 2001; El Bedoui et al., 2009; Pánek and Klimeš, 2016; Helmstetter and Garambois, 2010; Grippa et al., 2020), taking the shape of rockfalls and other fast-moving landslides (incl. debris-flows). The progressive deformation within the entire body of a DSGSD can lead to damage to the rock mass, tilting or steepening of parts of the slope which eventually provokes other fast-moving failures. So, DSGSD-deformation can be considered as a Preparatory Factor of catastrophic rock slope failures.

A few examples of non-catastrophic rock slope failures from the European Alps are listed below (including cases currently unfolding):

- **Spriana**, Central Alps, Italy: DSGSD within gneisses and shists with most prominent movement phases in the 1960s and 70s resulted in the abandonment of settlements and many site investigations due to the imminent concern of a LLOF (e.g., Agliardi and Crosta, 2014; Agliardi et al., 2020; Figure 1.7a).

- **La Clapière**, Western Alps, France: The front lobe of a large-scale DSGSD within gneissic and migmatitic rocks was subjected to a significant increase in movement rates (~10 cm/d max.) in the 1980s and 90s and therefore to extensive monitoring measures. As a result, a 2,5 km long diversion tunnel was constructed to redirect the adjacent river for the case a transition to catastrophic failure occurs. This was done to avoid an imminent risk of flooding from a landslide dam and a potential LLOF (e.g., El Bedoui et al., 2009; Palis et al., 2017).

- **Séchilienne**, Western Alps, France: The slope consisting of micaschists located in the Romanche valley has been producing rockfalls since historic times. It became the focus of attention in 1985 following a major rockfall event. Constant surveillance was established, a road was diverted and a settlement abandoned. There was concern about a large mass of rock sliding down, which would have had the potential to cause flooding and a LLOF (IRMA, 2023).

- **Brienz/Brinzauls**, Central Alps, Switzerland: A slope affected by a DSGSD, known to be active for centuries, has shown an increase in movement rates (up to 1,5 m/yr) and rock fall activity since

around 2018. A section from the top of the slope broke off in June 2023 as a catastrophic landslide and came to a halt just in front of the village. Extensive monitoring has been carried out and a costly system of drainage tunnels is currently being built to protect settlements, an important road, and a railway track from abandonment (Figi et al., 2022; Connolly, 2023).

- **Viella**, Central Pyrenees, France: The increased activity of an unstable slope above a village threatens its existence with rockfalls, debris flows and rockslides. Increased activity is known also from the late 19$^{th}$ century. The sedimentary body below the village is also in motion. Buildings have been damaged. Extensive investigations have been initiated (Le Petit Journal, 2018).

Other landslides, including superficial mass-wasting phenomena, are generally more common within slopes affected by DSGSDs (e.g., Pánek and Klimeš, 2016 and citations therein). This is well known to specialists since decades. More sediment from the hillslopes is eventually produced in areas affected by non-catastrophic bedrock landslides. This impacts fluvial systems and lets nearby fluvial channels aggrade (e.g., Sorriso-Valvo, 1999). DSGSDs have been and continue to be a threat to mountain communities and could become even more relevant as climate change progresses (Gariano and Guzzetti, 2016; IPCC, 2023), and population in mountain areas grows (Ehrlich et al., 2021).

Remaining research questions concerning non-catastrophic rock slope failures are largely relate to a better understanding of these phenomena and what controls their dynamics. Many Movement Sustaining Factors have been identified, but their relative importance in different settings is not always fully understood. This includes the triggering mechanisms of discrete movement steps or periods of enhanced activity. The role of climatic conditions on movement patterns and the expected effects of climate change require further research (Lacroix et al., 2020). The interplay between external influences and certain internal factors, such as lithology, structures, and groundwater, and its influence on the observed movement behaviour, needs to be better understood. The destabilising contribution of pore pressure and deep-seated weathering to the mechanical conditions in shear zones needs further research. In particular, the interaction of water and rock and the emergence of different movement characteristics (continuous brittle creep vs. discrete ruptures) should be the subject of ongoing investigation. Research on the Movement Sustaining Factors of non-catastrophic rock slope failures will eventually help engineering projects challenged by slow-moving slopes to mitigate and avoid damage to infrastructure, minimise costs, and to better understand the evolution of secondary landslide phenomena associated with non-catastrophic rock slope failures.

Since the early days of landslide research, people have been concerned with a potential catastrophic failure of DSGSDs from their basal rupture surface(s) (see reviews by Hewitt et al., 2008; Pánek and Klimeš, 2016; Lacroix et al., 2020; Discenza and Esposito, 2021). However, this seems to be the exception rather than the norm, given the widespread occurrence of DSGSDs in many mountains and the relative rare occurrence of very voluminous catastrophic rock slope failures. DSGSDs could be seen as a form of gradual self-adjustment of the slope enabled by a dynamic equilibrium maintained within the rupture zone by Movement Sustaining Factors and shear-strengthening conditions (Agliardi et al., 2020 and citations therein). However, some catastrophic bedrock landslides are known to have detached from basal fracture planes formed by non-catastrophic slope failure (no secondary landsliding): the Daguangbao rockslide in Sichuan, China (Chigira et al., 2010), many catastrophic rock slope failures in the Norwegian Fjordlands (Blikra et al., 2006), and the Hope rockslide in the Rocky Mountains, Canada (Hewitt, 2008). The infamous Vajont disaster in Italy (see above) is the result of anthropogenic impact on a non-catastrophic bedrock landslide that ultimately accelerated and had catastrophic consequences (e.g., Genevois and Ghirotti, 2005). The transition from continuous brittle creep to runaway acceleration of bedrock landslides is the subject of ongoing research primarily concerned with a rock-mechanical regime change in the deep-seated shear zones (see review by Lacroix et al. (2020), and e.g., Amitrano and Helmstetter (2006); Segall et al. (2010); Handwerger et al. (2016); Agliardi et al. (2020)). Monitoring deformation or endogenous seismicity of non-catastrophic slopes has promising potential to successfully forecast a transition into a catastrophic failure, but further research is needed (e.g., Carlà et al., 2019; Lacroix et al., 2020).

It is also important to better assess the relevance of factors that predispose a slope to non-catastrophic failure in the first place (i.e. Precondition and Preparatory Factors). Although many systematics have been studied in terms of topography, climate, lithology, and structures (e.g. Crosta et al., 2013), these systematics and their dependencies and interactions need to be further explored in order to better transfer them to individual field study sites in different settings. The long-term contribution of DSGSDs to mountain denudation and sediment fluxes is thought to be significant (Agliardi et al., 2013). However, it has not yet been quantitatively investigated. In particular, the role of glacial landscape shaping on the abundance, characteristics and activity of DSGSD phenomena can be further explored for a better understanding of landscape evolution.

To improve our understanding of non-catastrophic rock slope failures, it is important to combine knowledge from both monitoring studies and paleo-movement reconstructions (Pánek and Klimeš, 2016).

## 1.5 Numerical Modelling for the study of bedrock landslides

### 1.5.1 Numerical methods for slope stability problems

The reason for the interest in using numerical methods in analysing slope stability is that other conventional methods based on force (and/or moment) equilibrium approaches used previously, namely limit equilibrium methods (see section 1.2.1 above), have inherent limitations (see reviews by Eberhardt, 2003; Stead et al., 2006; Read and Stacey, 2009; Stead and Eberhardt, 2013; Stead and Wolter, 2015): The calculation of a FoS first of all determines whether a slope is stable or not. These calculations are based on assumptions about failure mechanisms (e.g., planar or rotational failure), the mechanical behaviour of the material (e.g., elasticity), and the homogeneity of the properties. But many of the slopes that need assessment have complex characteristics (geometry, structures, heterogeneities) that are difficult or impossible to manage using limit equilibrium methods. When applying these methods, a clear and sometimes important insight into the failure processes in terms of stress localisation, development of failure mechanisms, and especially failure kinematics cannot be obtained. For this reason, numerical modelling methods have become increasingly important to geotechnical engineers (e.g., Read and Stacey, 2009) and researchers (e.g., Stead and Eberhardt, 2013) in recent years. Moreover, they have become more applicable due to the significant increase in computing power of desktop computers and the continuous improvement of codes. In research, numerical modelling is often preferred to analogue modelling of rock slope failures, simply because analogue experiments are usually laborious to prepare and technically demanding to perform (see e.g., Fang et al., 2023). In numerical simulations, individual physical parameters can be easily changed in the programming code and calculations can be replicated more systematically, without additional cost. Many examples exist in the literature of studies that have successfully reproduced the failure behaviour of specific case studies of deep-seated rock slope failures with numerical models by calibrating them with field observations and monitoring data and varying the input parameters. This has provided valuable insights into failure localisation, kinematics and timing of these specific bedrock landslides (e.g., Eberhardt et al., 2004; Bouissou et al., 2012; Riva et al., 2018; Donati et al., 2020; Marmoni et al., 2023; Mreyen et al., 2023; and many more).

When it comes to the methods, numerical methods for slope stability analyses can be divided into three main groups, each of which has its advantages, limitations and disadvantages (e.g., Eberhardt, 2003; Stead et al., 2006):

- Continuum approaches:

  They are based on continuous meshes/grids (2D or 3D) and on constitutive equations which allow to model stresses and strains for various types of behaviours (elastic, elasto-plastic, etc.). Among others,

mainly Finite Element Method (FEM), Finite Difference Method (FDM), and Finite Volume Method (FVM) are used. They are computationally efficient but not suited to model large displacements and brittle failures. They are most appropriate for the analysis of weak and homogeneous rock slopes (i.e., heavily fractured).

- Discontinuum approaches:

  The most commonly used discontinuum method is the Discrete Element Method (DEM) (some scholars divide the DEM further into distinct element methods and particle flow codes). The DEM is designed to simulate failures characterised by discrete behaviours in space and time. Therefore, this approach is particularly suited to incorporate discrete structures (faults, joints and discontinuities), and to describe brittle failure and large displacements, which makes it especially attractive to assess the stability of structurally complex rock slopes and advanced failure modes in general. The medium is discretized into discrete elements (DEs) (squares, discs, polyhedral blocks or spherical particles) which interact one with each other through predefined contact laws. In a simulation, DEs follow movements dictated by the boundary conditions and loadings applied to the medium. The DEs responses are calculated iteratively through time integration of the equations of motion. The iterative calculations can be very computationally intensive, especially when it comes to 3D models with high resolution. The high computational cost comes mainly from the contact detection but improvements in the calculation procedure are possible (e.g., parallelisation).

- Hybrid finite-discrete element methods (FDEM):

  These are methods that combine finite-/distinct-element methods by performing remeshing steps during a simulation. The deformable mesh elements can detach from the initial mesh and interact one with another following the DEM principles. A deformable continuous medium can thus be discretized into discrete blocks as a result of fracturing (e.g., Eberhardt et al., 2004; Munjiza, 2004). Hybrid approaches are thus especially suitable for exploring brittle fracturing, including initiation and propagation of fractures. Their application is however hampered by complex calibrations and costly computations.

The application of numerical models for slope stability analysis should be undertaken prudently, thoroughly, and with an understanding of their limitations (see e.g., Eberhardt, 2003): Numerical models are always based on simplifications, assumptions, and estimations, and can never fully account for the complexities, heterogeneities, and contingencies encountered in natural slopes. For practitioners, the model setup should be well thought out, including the geometry, the boundary conditions, and the loading conditions, which

defines the slope in its pre-failure state by the initiation of gravitational (and possibly other) stresses. Eventually, the input parameters should be carefully chosen, if possible by verification with laboratory tests, field observations or field monitoring data (see e.g., Stead and Wolter, 2015). The rock mass mechanical properties require adequate scaling considerations when going from laboratory scale properties to slope scale properties (e.g., Brideau et al., 2009; Marinos and Carter, 2018) and the critical input parameters should be subjected to sensitivity analyses (preferably in multiple steps). Users of numerical approaches should be aware of what they want to analyse and how meaningful the results can be interpreted in comparison to real existing slopes.

### 1.5.2 Causes and Triggers of bedrock landslides explored with numerical models

Numerical approaches are particularly adapted to conducting parametric studies and investigating the role of various factors whose influence is otherwise difficult to grasp because it is hidden in the great complexity of a natural slope. Based on a literature review, here we list some Precondition and Preparatory Factors of deep-seated rock slope failures that have already been investigated using numerical modelling and mention how these factors have implications for the occurrence and behaviour of deep-seated rock slope failures. Studies considering specific sites of slope failures (i.e. case studies), which also explore Causes and Triggers within a specific setting were excluded from this short review.

- **Inherent rock-mechanical properties**:
  Katz et al. (2014) used DEM models consisting of spherical particles to investigate different material strengths (cohesion and internal friction angle) for different configurations of slope heights and slope angles. After the models were brought to failure, they analysed the post-failure geometry of the apron. Weaker material strength results in overall less stable slopes, greater disintegration of material, bigger failure volumes, and longer runout distances (see, Figure 1.8a). Post-failure geometry does not depend on initial slope angle and height.

- **Pervasive geological discontinuities (non-singular structures):**
  Scholtès and Donzé (2015) investigated the failure of fractured escarpments combining a DEM approach and Discrete Fracture Networks (DFNs). They considered configurations with uniform fracture orientations and with multiple joint sets. They could highlight the fact that the overall slope stability is governed by both the frictional properties of the discontinuities and the tensile strength of the rock bridges located in between those discontinuities which tend to concentrate stress.

Zheng et al. (2021) made use of a DEM model with joint representation to study flexural toppling in rock slopes. The stability of slopes with uniform, regular joints that slope steeply in the opposite direction to the slope angle depends on the joint angle, the joint spacing and the slope angle. However, the deformation and failure characteristics remain generally the same.

Sun et al. (2022) modelled the failure of regularly jointed rock slopes with a FDEM approach. The orientation of the joints within the slope has a critical effect on the stability of the slope and the failure mode: If the joints are inclined in the same direction as the slope, it becomes less stable and fails by sliding along the joints; if the joints are inclined in the opposite direction to the slope, it is more stable and fails in toppling mode (see Figure 1.8b).

- **Progressive damage by repeated seismic shaking:**

  Gischig et al. (2016) demonstrated in a conceptual study with a two-dimensional DEM model how recurrent seismic events can progressively weaken a robust rock slope by generating and extending fractures, ultimately leading to failure. The extent of damage and displacement caused by a specific earthquake is greatly influenced by the pre-existing damage within the rock mass. This influence is comparable in its significance to the maximum ground acceleration.

- **Progressive weakening by weathering front**

  Utili and Crosta (2011) used a two-dimensional DEM approach to model the intrusion of a weathering front into an escarpment, by reducing the rock strength according to space and time considerations. Where there is a sharp transition from intact to fully weathered rock, superficial failure occurs by detachment of individual particles from the slope. For a considerable distance between intact and fully damaged zones, larger blocks detach from the slope.

- **Progressive damage by creep:**

  Lacroix and Amitrano (2013) proposed a FEM model to assess the sensitivity of rockslide dynamics to the effect of deglaciation. More specifically, they applied a progressive damage model to simulate localization along shear bands associated with creep and were able to reproduce the different phases of deformation associated with morphologies typical of large rockslides. Also, they showed that the deglaciation velocity can affect the geometry of the failure.

- **Stress variations induced by topography**

  Bois et al. (2014), through the use of three-dimensional FEM models, found that the spacing and depth of side valleys have an influence on slope stability. If the side valleys are not deeply incised, an

increase in the lateral distance between the side valleys has no effect on failure localisation, but destabilises the slope. If the side valleys cut deeper into the valley flank, this will not affect the stability of the slope, but it will determine the failure location.

Moon et al. (2017) have investigated how tectonic stresses in the subsurface interact with the overlying topography, resulting in zones affected by higher stresses and hence suffering fracture induced damage. The stress field in the subsurface is most strongly influenced by topographic perturbations, with the strongest compressive stress orientated orthogonally to the longitudinal axis of elongated landforms such as ridges and valleys. Stress disturbances induced by topography are particularly strong under merging valley troughs and on ridge crests, where the curvatures are very pronounced. Furthermore, fracture abundance has implications for the localisation of groundwater flow and deep-seated weathering.

- **Stress variations induced by glacial history and topography**

  Spreafico et al. (2021) conducted a systematic analysis on how the timing and behaviour of slope failures are influenced by deglaciation characteristics such as initial ice thickness, deglaciation rate, rock-slope strength, and valley morphology. Using their two-dimensional FEM slope models to simulate progressive damage processes, they found that melting of thicker glaciers is associated with slope failures that occur at higher elevations on the slope and initiate failure shortly after deglaciation. Glacial morphology, i.e. U-shaped valleys, promote shallower and suspended failures (see Figure 1.8c), and weaker slope material and rapid deglaciation results in shorter lag time of failures after deglaciation.

To our knowledge, the effect of pore pressure on slope stability has not been systematically investigated. However, the effects of groundwater and pore pressure on the failure behaviour of specific case studies have been investigated. What distinguishes them from a systematic study, which would instead use a simplified example slope, is that they are modelled for the structural configuration of a given case study and make use of monitoring data collected at the site. We list some notable studies that can provide a more general insight into the impact of groundwater on slopes:

- Cappa et al. (2004) used a hydromechanically coupled DEM model to analyse surface velocity measurements from the La Clapière landslide (see Section 1.4.3). They investigated how the hydromechanical behaviour of the moving slope is affected by both the location and the volume of water percolation. Water percolation has the most destabilising effect on the middle section of the slope, where the impact of groundwater on deformation patterns in the subsurface is greatest.

- Cappa et al. (2014) modelled the non-catastrophic landslide of Séchilienne with a hydromechanically coupled FDM approach, and found that a significant proportion of the observed landslide movement is due to poro-elastic strain beneath the primarily moving landslide body, driven by fluctuations in groundwater levels.
- Preisig et al. (2016) proposed a link between seasonal groundwater fluctuations and acceleration phases of a non-catastrophic landslide by studying the Campo Vallemaggia site, a non-catastrophic rock slope failure in Switzerland. They utilized a hydromechanically coupled DEM to reproduce the progressive failure behaviour of the case study. Within the slope, displacement along pre-existing fractures and the breaking of rock bridges results in localised weakening of the rock mass. Areas that are already more severely damaged can be deformed to a greater extent by small seasonal fluctuations in groundwater level and hence pore pressure increase. The arrangement and interconnection of pre-existing permeable weak zones is of critical importance.
- Riva et al. (2018) were able to model the evolution of a non-catastrophic rock slope failure from deglaciation, through paraglacial to postglacial conditions, using geometry and calibration data from the Spriana slope failure (see Section 1.4.3). This was made possible by the use of a time-dependent FEM model, which takes into account hydromechanical effects, which in turn depend on the damage within the slope material. The model simulates a long period of progressive subcritical damage to the bedrock before slope failure initiates. During failure, the formation of a basal shear zone, which forms a hydraulic barrier, leads to perched groundwater conditions. Such slope evolution is consistent with the known behaviour of natural examples from glaciated mountain ranges and therefore reflects a long-term destabilisation of slopes following the Last Glacial Maximum. In addition, the study demonstrates the strong influence of deglaciation on posterior damage and landslide displacement localisation.

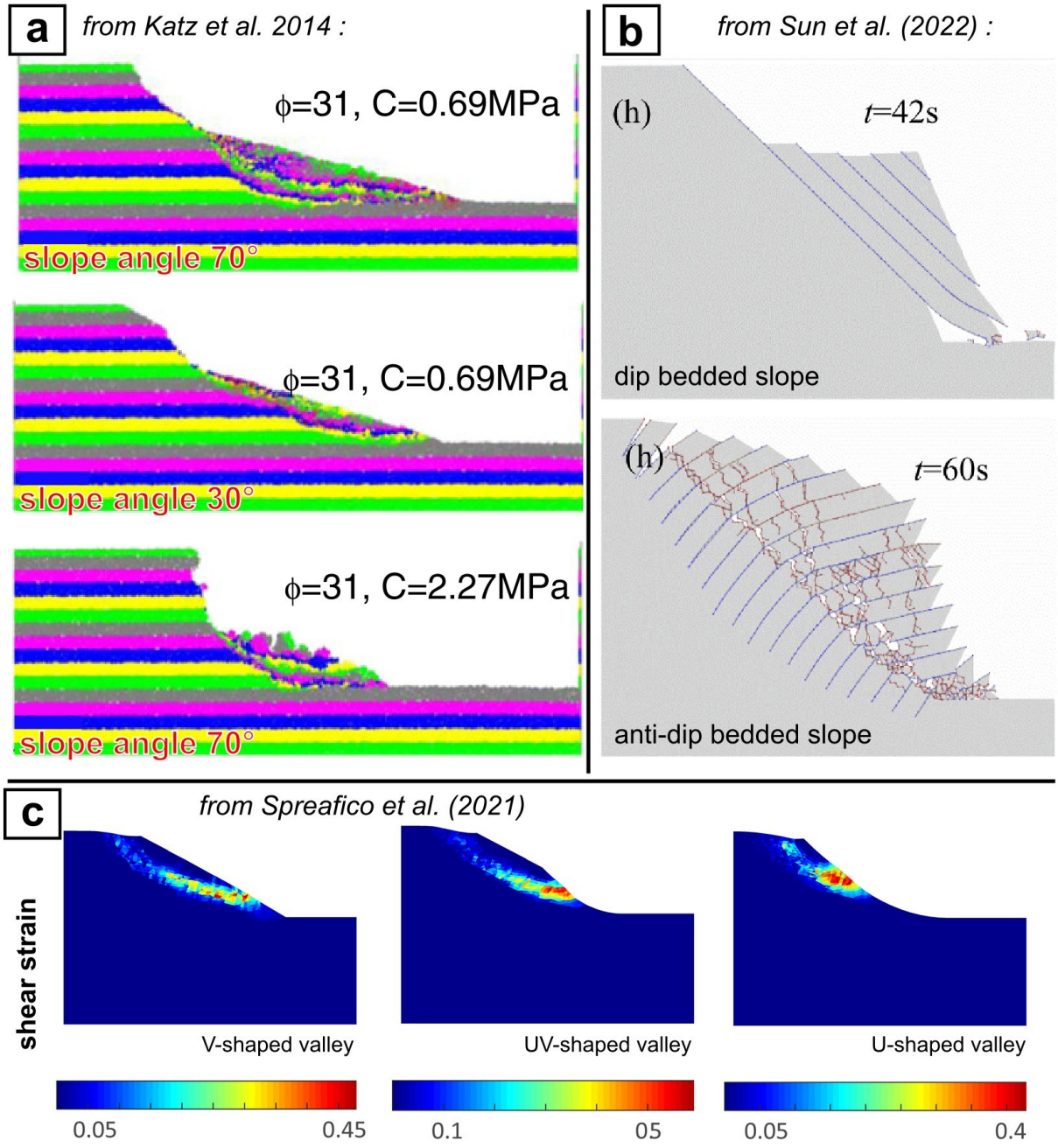


*Figure 1.8: (a) DEM simulations of slope failures of different material cohesion and slope angle. The simulation runs with weaker rock material (less cohesion) yield more particle disintegration and longer runout distances as the more cohesive run, and have similar failure geometries despite the initial slope angle was different (Katz et al., 2014). (b) FDEM simulations of dip bedded and anti-dip bedded slopes. Failure mode and severity of fracture formation differ significantly: dip-bedded slope fails as translational planar slide, anti-dip bedded slope as toppling failure (Sun et al., 2022). (c) Different valley topographies result in different shear strain localisations within the slope (Spreafico et al., 2021).*

### 1.6 Research objectives

Landscapes are affected by bedrock landslides, both catastrophic and non-catastrophic. The overarching questions that guide us in this PhD-thesis, before focusing on our specific research endeavours, are very general and fundamental to landslide research: What are the Causes and Triggers of terrestrial, non-volcanic, bedrock landslides and how do they influence abundance, characteristics and temporal behaviour of bedrock landslides? Within this broader context this PhD aims to particularly investigate the dynamics of rock slope failures, focusing on two main questions that are considered to be important gaps in current knowledge of rock slope failures in active tectonic settings: on the one hand, understanding the occurrence, characteristics, and timing of large bedrock landslides in the Himalayas, their age, causes and triggering factors; and, on the other hand, the role of rock anisotropy on failure modes, slope stability, and its impact on the steepness of mountain landscapes.

First, in Chapter 2, we will present case studies from the Annapurna Massif of the central Himalayas (Nepal). The Annapurna Massif is an extraordinary place: It features one of the most extreme reliefs on earth and high altitude terrain within an actively thrusting orogen. Thus, in this area, glaciation and high seismicity affect rock masses sculpted by strong tectonic forces. Particularly important for our research, the area is very much affected by bedrock landslides due to the steep slopes that occur almost everywhere. The Annapurna Massif is exposed to climatic conditions under the influence of the Indian summer monsoon, most notably heavy seasonal precipitation on the south face of the massif. The Annapurna area has been the focus of considerable research activity over recent decades, with studies conducted in the fields of geology, tectonics and geomorphology representative for the central Himalayan region (see, e.g., Hagen, 1969 Burbank et al., 2003; Pratt-Sitaula et al., 2011). This existing body of research will assist us in the interpretation of our new findings. Moreover, the field sites can be reached within a few days' journey of Kathmandu.

In this PhD-thesis we approach the bedrock landslides of the Annapurna Massif with a new survey focusing on the upper Marsyangdi Valley and the south-eastern slopes of the massif. Investigations are conducted with the help of remote sensing products and directly in the field with the first-time application of absolute dating techniques on some of the large bedrock landslides in these areas:

- To the north of the main ridge line (upper Marsyangdi Valley) deposits originating from giant (> 1 $km^3$) catastrophic rock slope failures are notified, but extend and failure processes are poorly identified (see, Weidinger, 2006; Fort, 2011). One objective of this PhD-thesis is to extend the existing record of these giant events by identifying source areas, quantifying volumes and constraining the timing of these giant catastrophic rock slope failures in the upper Marsyangdi Valley.

- Another objective of this PhD-thesis is to better constrain the spatial extent and temporal behaviour of individual DSGSD phenomena on the south-eastern slopes of the Annapurna Massif. Research on non-catastrophic rock slope failures is very sparse in this region, and falls far short of accounting for the many manifestations of these phenomena, which can be easily spotted on satellite images, especially at altitudes above 3,000 m, i.e. above forest-covered slopes. In the framework of this PhD-thesis we perform the first DSGSD paleo-movement reconstruction for the whole Himalayas, in a setting that did not experience extensive valley glaciation during Glacial periods. This contrasts with many previously studied DSGSD settings in mountain ranges such as the European Alps, the Carpathians or the Rocky Mountains. Consequently, studies of DSGSD in valleys that have not been shaped by glaciers are notably underrepresented in the existing literature (see, e.g., Pánek and Klimeš, 2016).

We study bedrock landslides in consideration of climatic, structural and lithological conditions, which will provide information on possible Causes and Triggers of rock slope failures in the Annapurna Massif, both catastrophic and non-catastrophic. These achievements are important contributions to the record of bedrock landslides in the Annapurna Massif and globally, and will be in the following available to other researchers.

Then, in Chapter 3, we will make use of a DEM modelling approach for a theoretical study of a Precondition Factor that was not explored systematically in greater detail so far: Rock strength anisotropy and its orientation towards the slope. This factor, in its ubiquitous form that fills the entire rock mass and is not induced by discrete structures, is investigated for the first time for the full range ( in 2D) of possible anisotropy orientations towards the slope. This form of rock strength anisotropy occurs in natural slopes due to the lithological characteristics of the bedrock, both layering in sedimentary rocks and schistosity in metamorphic rocks are responsible. It has long been known among slope stability analysts that rock strength anisotropy and its orientation towards the slope have very relevant consequences for rock slope failure (see, for example, the review by Stead and Wolter, 2015), as they influence the stress distribution in the slope, determine the failure localisation and failure mode (e.g. sliding, toppling), and thus control the overall stability of the slope. A systematic study of the orientation of rock strength anisotropy can contribute to a better understanding of the evolution of terrain with an underlying anisotropic substrate. In particular, this applies to areas of high relief in active orogens.

# References:


Aaron, J., Wolter, A., Loew, S., Volken, S., 2020. Understanding Failure and Runout Mechanisms of the Flims Rockslide/Rock Avalanche. Frontiers in Earth Science 8.

Abele, G., 1997. Rockslide movement supported by the mobilization of groundwater-saturated valley floor sediments. Zeitschrift für Geomorphologie 1–20.

Agliardi, F., Crippa, C., 2022. Deep-Seated Gravitational Slope Deformations, in: Treatise on Geomorphology. Elsevier, pp. 183–199. https://doi.org/10.1016/B978-0-12-818234-5.00182-6

Agliardi, F., Crosta, G., Zanchi, A., 2001. Structural constraints on deep-seated slope deformation kinematics. Engineering Geology 59, 83–102. https://doi.org/10.1016/S0013-7952(00)00066-1

Agliardi, F., Crosta, G.B., 2014. Long-and short-term controls on the Spriana rockslide (Central Alps, Italy). Presented at the Landslide Science for a Safer Geoenvironment: Volume 2: Methods of Landslide Studies, Springer, pp. 243–249.

Agliardi, F., Crosta, G.B., Frattini, P., 2012. Slow rock-slope deformation, in: Clague, J.J., Stead, D. (Eds.), Landslides. Cambridge University Press, Cambridge, pp. 207–221. https://doi.org/10.1017/CBO9780511740367.019

Agliardi, F., Crosta, G.B., Frattini, P., Malusà, M.G., 2013. Giant non-catastrophic landslides and the long-term exhumation of the European Alps. Earth and Planetary Science Letters 365, 263–274. https://doi.org/10.1016/j.epsl.2013.01.030

Agliardi, F., Crosta, G.B., Zanchi, A., Ravazzi, C., 2009. Onset and timing of deep-seated gravitational slope deformations in the eastern Alps, Italy. Geomorphology, Dating, triggering, modelling, and hazard assessment of large landslides 103, 113–129. https://doi.org/10.1016/j.geomorph.2007.09.015

Agliardi, F., Scuderi, M.M., Fusi, N., Collettini, C., 2020. Slow-to-fast transition of giant creeping rockslides modulated by undrained loading in basal shear zones. Nat Commun 11, 1352. https://doi.org/10.1038/s41467-020-15093-3

Allen, S.K., Cox, S.C., Owens, I.F., 2011. Rock avalanches and other landslides in the central Southern Alps of New Zealand: a regional study considering possible climate change impacts. Landslides 8, 33–48. https://doi.org/10.1007/s10346-010-0222-z

Amato, G., Devoti, R., Fubelli, G., Aringoli, D., Bignami, C., Galvani, A., Moro, M., Polcari, M., Saroli, M., Sepe, V., Stramondo, S., 2018. Step-like displacements of a deep seated gravitational slope deformation observed during the 2016–2017 seismic events in Central Italy. Engineering Geology 246, 337–348. https://doi.org/10.1016/j.enggeo.2018.10.014

Ambrosi, C., Crosta, G.B., 2006. Large sackung along major tectonic features in the Central Italian Alps. Engineering Geology 83, 183–200. https://doi.org/10.1016/j.enggeo.2005.06.031

Amitrano, D., Helmstetter, A., 2006. Brittle creep, damage, and time to failure in rocks. Journal of Geophysical Research: Solid Earth 111. https://doi.org/10.1029/2005JB004252

Atkinson, B.K., Meredith, P.G., 1987. The theory of subcritical crack growth with applications to minerals and rocks. Fracture mechanics of rock 2, 111–166.

Avouac, J.-P., 2015. From Geodetic Imaging of Seismic and Aseismic Fault Slip to Dynamic Modeling of the Seismic Cycle. Annu. Rev. Earth Planet. Sci. 43, 233–271. https://doi.org/10.1146/annurev-earth-060614-105302

Barla, G., Antolini, F., Barla, M., Mensi, E., Piovano, G., 2010. Monitoring of the Beauregard landslide (Aosta Valley, Italy) using advanced and conventional techniques. Engineering Geology 116, 218–235. https://doi.org/10.1016/j.enggeo.2010.09.004

Baroň, I., Janos, V., Klimes, J., Novotny, R., Hubatka, F., 2007. Holocenni vrasova deformace hornin godulskeho souvrstvi svahovymi pohyby. ZGV 2006, 46–49.

Berlioz, J., 2019. Une catastrophe en Dauphiné (septembre 1219). Témoignages contemporains, in: Morenzoni, F., Mornet, É. (Eds.), Milieux naturels, espaces sociaux : Études offertes à Robert Delort, Histoire ancienne et médiévale. Éditions de la Sorbonne, Paris, pp. 43–53. https://doi.org/10.4000/books.psorbonne.27536

Blikra, L.H., Longva, O., Braathen, A., Anda, E., Dehls, J.F., Stalsberg, K., 2006. Rock slope failures in Norwegian fjord areas: examples, spatial distribution and temporal pattern, in: Evans, S.G., Mugnozza, G.S., Strom, A., Hermanns, R.L. (Eds.), Landslides from Massive Rock Slope Failure, NATO Science Series. Springer Netherlands, Dordrecht, pp. 475–496. https://doi.org/10.1007/978-1-4020-4037-5_26

Blondeau, S., Gunnell, Y., Jarman, D., 2021. Rock slope failure in the Western Alps: A first comprehensive inventory and spatial analysis. Geomorphology 380, 107622. https://doi.org/10.1016/j.geomorph.2021.107622

Bobrowsky, P.T., Marker, B., 2018. Encyclopedia of engineering geology. Springer Berlin.

Bois, T., Tric, E., Lebourg, T., 2014. Influence of inherited topography on gravitational slope failure: three-dimensional numerical modelling of the La Clapière slope, Alpes-Maritimes, France. Terra Nova 26, 354–362. https://doi.org/10.1111/ter.12105

Booth, A.M., McCarley, J., Hinkle, J., Shaw, S., Ampuero, J., Lamb, M.P., 2018. Transient Reactivation of a Deep-Seated Landslide by Undrained Loading Captured With Repeat Airborne and Terrestrial Lidar. Geophysical Research Letters 45, 4841–4850. https://doi.org/10.1029/2018GL077812

Bornhold, B.D., Thomson, R.E., 2012. Tsunami hazard assessment related to slope failures in coastal waters, in: Clague, J.J., Stead, D. (Eds.), Landslides. Cambridge University Press, pp. 108–120. https://doi.org/10.1017/CBO9780511740367.011

Bouissou, S., Darnault, R., Chemenda, A., Rolland, Y., 2012. Evolution of gravity-driven rock slope failure and associated fracturing: Geological analysis and numerical modelling. Tectonophysics, Modelling in Geosciences 526–529, 157–166. https://doi.org/10.1016/j.tecto.2011.12.010

Brantut, N., Heap, M.J., Meredith, P.G., Baud, P., 2013. Time-dependent cracking and brittle creep in crustal rocks: A review. Journal of Structural Geology 52, 17–43. https://doi.org/10.1016/j.jsg.2013.03.007

Brideau, M.-A., Roberts, N.J., 2015. Mass Movement in Bedrock, in: Landslide Hazards, Risks, and Disasters. Elsevier, pp. 43–90. https://doi.org/10.1016/B978-0-12-396452-6.00003-3

Brideau, M.-A., Yan, M., Stead, D., 2009. The role of tectonic damage and brittle rock fracture in the development of large rock slope failures. Geomorphology 103, 30–49. https://doi.org/10.1016/j.geomorph.2008.04.010

Brückl, E., Brückl, J., 2006. Geophysical models of the Lesachriegel and Gradenbach deep-seated mass-movements (Schober range, Austria). Engineering Geology, Large Landslides: dating, triggering, modelling, and hazard assessment 83, 254–272. https://doi.org/10.1016/j.enggeo.2005.06.035

Brückl, E., Parotidis, M., 2005. Prediction of slope instabilities due to deep-seated gravitational creep. Natural Hazards and Earth System Sciences 5, 155–172. https://doi.org/10.5194/nhess-5-155-2005

Burbank, D.W., Blythe, A.E., Putkonen, J., Pratt-Sitaula, B., Gabet, E., Oskin, M., Barros, A., Ojha, T.P., 2003. Decoupling of erosion and precipitation in the Himalayas. Nature 426, 652–655. https://doi.org/10.1038/nature02187

Cappa, F., Guglielmi, Y., Soukatchoff, V.M., Mudry, J., Bertrand, C., Charmoille, A., 2004. Hydromechanical modeling of a large moving rock slope inferred from slope levelling coupled to spring long-term hydrochemical monitoring: example of the La Clapière landslide (Southern Alps, France). Journal of Hydrology 291, 67–90. https://doi.org/10.1016/j.jhydrol.2003.12.013

Cappa, F., Guglielmi, Y., Viseur, S., Garambois, S., 2014. Deep fluids can facilitate rupture of slow-moving giant landslides as a result of stress transfer and frictional weakening. Geophysical Research Letters 41, 61–66. https://doi.org/10.1002/2013GL058566

Carlà, T., Intrieri, E., Raspini, F., Bardi, F., Farina, P., Ferretti, A., Colombo, D., Novali, F., Casagli, N., 2019. Perspectives on the prediction of catastrophic slope failures from satellite InSAR. Sci Rep 9, 14137. https://doi.org/10.1038/s41598-019-50792-y

Cheng, Y.M., Lau, C.K., 2014. Slope stability analysis and stabilization: new methods and insight, Second edition. ed. CRC Press, Taylor & Francis Group, Boca Raton.

Chigira, M., 1992. Long-term gravitational deformation of rocks by mass rock creep. Engineering Geology 32, 157–184.

Chigira, M., Wu, X., Inokuchi, T., Wang, G., 2010. Landslides induced by the 2008 Wenchuan earthquake, Sichuan, China. Geomorphology 118, 225–238. https://doi.org/10.1016/j.geomorph.2010.01.003

Clague, J.J., Stead, D., 2012. Landslides: types, mechanisms and modeling. Cambridge University Press.

Connolly, K., 2023. Huge landslide misses Swiss mountain village of Brienz 'by a hair.' the Guardian.

Costa, J.E., Schuster, R.L., n.d. The formation and failure of natural dams.

Crippa, C., Franzosi, F., Zonca, M., Manconi, A., Crosta, G.B., Dei Cas, L., Agliardi, F., 2020. Unraveling Spatial and Temporal Heterogeneities of Very Slow Rock-Slope Deformations with Targeted DInSAR Analyses. Remote Sensing 12, 1329. https://doi.org/10.3390/rs12081329

Crosta, G.B., Frattini, P., Agliardi, F., 2013. Deep seated gravitational slope deformations in the European Alps. Tectonophysics 605, 13–33. https://doi.org/10.1016/j.tecto.2013.04.028

Cui, S., Wu, H., Pei, X., Yang, Q., Huang, R., Guo, B., 2022. Characterizing the spatial distribution, frequency, geomorphological and geological controls on landslides triggered by the 1933 Mw 7.3 Diexi Earthquake, Sichuan, China. Geomorphology 403, 108177. https://doi.org/10.1016/j.geomorph.2022.108177

Dai, L., Fan, X., Jansen, J.D., Xu, Q., 2021. Landslides and fluvial response to landsliding induced by the 1933 Diexi earthquake, Minjiang River, eastern Tibetan Plateau. Landslides 18, 3011–3025. https://doi.org/10.1007/s10346-021-01717-2

Davies, T., 2015. Landslide Hazards, Risks, and Disasters, in: Landslide Hazards, Risks, and Disasters. Elsevier, pp. 1–16. https://doi.org/10.1016/B978-0-12-396452-6.00001-X

Davies, T.R., McSaveney, M.J., 2009. The role of rock fragmentation in the motion of large landslides. Engineering Geology 109, 67–79. https://doi.org/10.1016/j.enggeo.2008.11.004

Delaney, K.B., Evans, S.G., 2015. The 2000 Yigong landslide (Tibetan Plateau), rockslide-dammed lake and outburst flood: Review, remote sensing analysis, and process modelling. Geomorphology 246, 377–393. https://doi.org/10.1016/j.geomorph.2015.06.020

Discenza, M.E., Esposito, C., 2021. State-of-art and remarks on some open questions about dsgsds: hints from a review of the scientific literature on related topics. Italian journal of engineering geology and environment 31–59. https://doi.org/10.4408/IJEGE.2021-01.O-03

Donati, D., Stead, D., Stewart, T.W., Marsh, J., 2020. Numerical modelling of slope damage in large, slowly moving rockslides: Insights from the Downie Slide, British Columbia, Canada. Engineering Geology 273, 105693. https://doi.org/10.1016/j.enggeo.2020.105693

Dou, J., Paudel, U., Oguchi, T., Uchiyama, S., Hayakawa, Y.S., 2015. Shallow and Deep-Seated Landslide Differentiation Using Support Vector Machines: A Case Study of the Chuetsu Area, Japan. Terr. Atmos. Ocean. Sci. 26, 227. https://doi.org/10.3319/TAO.2014.12.02.07(EOSI)

Dramis, F., Sorriso-Valvo, M., 1994. Deep-seated gravitational slope deformations, related landslides and tectonics. Engineering Geology, Deep-seated Landslides and Large-scale Rock Avalanches 38, 231–243. https://doi.org/10.1016/0013-7952(94)90040-X

Duarte, K.D., Schmidt, B.E., Chilton, H.T., Hughson, K.H.G., Sizemore, H.G., Ferrier, K.L., Buffo, J.J., Scully, J.E.C., Nathues, A., Platz, T., Landis, M., Byrne, S., Bland, M., Russell, C.T., Raymond, C.A., 2019. Landslides on Ceres: Diversity and Geologic Context. Journal of Geophysical Research: Planets 124, 3329–3343. https://doi.org/10.1029/2018JE005673

Dufresne, A., Bösmeier, A., Prager, C., 2016. Sedimentology of rock avalanche deposits – Case study and review. Earth-Science Reviews 163, 234–259. https://doi.org/10.1016/j.earscirev.2016.10.002

Duncan, J.M., 1996. State of the Art: Limit Equilibrium and Finite-Element Analysis of Slopes. J. Geotech. Engrg. 122, 577–596. https://doi.org/10.1061/(ASCE)0733-9410(1996)122:7(577)

Eaves, S.R., McColl, S.T., Tielidze, L.G., Norton, K.P., Hopkins, J.L., Hidy, A.J., 2023. The age and potential causes of the giant Green Lake Landslide, Fiordland, New Zealand. Landslides 20, 1883–1892. https://doi.org/10.1007/s10346-023-02075-x

Eberhardt, D.E., 2003. Rock Slope Stability Analysis – Utilization of Advanced Numerical Techniques, University of British Columbia teaching material.

Eberhardt, E., Stead, D., Coggan, J.S., 2004. Numerical analysis of initiation and progressive failure in natural rock slopes—the 1991 Randa rockslide. International Journal of Rock Mechanics and Mining Sciences 41, 69–87. https://doi.org/10.1016/S1365-1609(03)00076-5

Ehrlich, D., Melchiorri, M., Capitani, C., 2021. Population Trends and Urbanisation in Mountain Ranges of the World. Land 10, 255. https://doi.org/10.3390/land10030255

Eisbacher, G.H., Clague, J.J., 1984. Destructive mass movements in high mountains: hazard and management. Geological Survey of Canada.

El Bedoui, S., Guglielmi, Y., Lebourg, T., Pérez, J.-L., 2009. Deep-seated failure propagation in a fractured rock slope over 10,000 years: The La Clapière slope, the south-eastern French Alps. Geomorphology 105, 232–238. https://doi.org/10.1016/j.geomorph.2008.09.025

Encyclopædia Britannica, 2023. landslide. written by Meng, Xingmin, online version, Earth Science, Geologic Time & Fossils.

Engel, Z., Mentlík, P., Braucher, R., Křížek, M., Pluháčková, M., Arnold, M., Aumaître, G., Bourlès, D., Keddadouche, K., 2017. 10Be exposure age chronology of the last glaciation of the Roháčská Valley in the Western Tatra Mountains, central Europe. Geomorphology 293, 130–142. https://doi.org/10.1016/j.geomorph.2017.05.012

Evans, S.G., Hermanns, R.L., Strom, A., Scarascia-Mugnozza, G. (Eds.), 2011. Natural and Artificial Rockslide Dams, Lecture Notes in Earth Sciences. Springer Berlin Heidelberg, Berlin, Heidelberg. https://doi.org/10.1007/978-3-642-04764-0

Evans, S.G., Roberts, N.J., Ischuk, A., Delaney, K.B., Morozova, G.S., Tutubalina, O., 2009. Landslides triggered by the 1949 Khait earthquake, Tajikistan, and associated loss of life. Engineering Geology 109, 195–212. https://doi.org/10.1016/j.enggeo.2009.08.007

Fan, X., Xu, Q., Liu, J., Subramanian, S.S., He, C., Zhu, X., Zhou, L., 2019. Successful early warning and emergency response of a disastrous rockslide in Guizhou province, China. Landslides 16, 2445–2457. https://doi.org/10.1007/s10346-019-01269-6

Fang, K., Tang, H., Li, C., Su, X., An, P., Sun, S., 2023. Centrifuge modelling of landslides and landslide hazard mitigation: A review. Geoscience Frontiers 14, 101493. https://doi.org/10.1016/j.gsf.2022.101493

Figi, D., Thöny, R., Breitenmoser, T., Brunold, F., Schwestermann, T., 2022. Rutschung Brienz/Brinzauls (GR): Geologisch-kinematisches und hydrogeologisches Modell.

Fort, M., 2011. Two large late Quaternary rock slope failures and their geomorphic significance, Annapurna Himalayas (Nepal). Geografia Fisica e Dinamica Quaternaria 34, 5–14.

Frattini, P., Crosta, G., Allievi, J., 2013. Damage to Buildings in Large Slope Rock Instabilities Monitored with the PSInSAR™ Technique. Remote Sensing 5, 4753–4773. https://doi.org/10.3390/rs5104753

Frisch, W., Meschede, M., Blakey, R.C., 2011. Plate Tectonics: Continental Drift and Mountain Building. Springer, Berlin, Heidelberg. https://doi.org/10.1007/978-3-540-76504-2

Froude, M.J., Petley, D.N., 2018. Global fatal landslide occurrence from 2004 to 2016. Natural Hazards and Earth System Sciences 18, 2161–2181. https://doi.org/10.5194/nhess-18-2161-2018

Gariano, S.L., Guzzetti, F., 2016. Landslides in a changing climate. Earth-Science Reviews 162, 227–252. https://doi.org/10.1016/j.earscirev.2016.08.011

Genevois, R., Ghirotti, M., 2005. The 1963 vaiont landslide. Giornale di Geologia Applicata 1, 41–52.

Gischig, V., Preisig, G., Eberhardt, E., 2016. Numerical Investigation of Seismically Induced Rock Mass Fatigue as a Mechanism Contributing to the Progressive Failure of Deep-Seated Landslides. Rock Mech Rock Eng 49, 2457–2478. https://doi.org/10.1007/s00603-015-0821-z

Glade, T., Anderson, M.G., Crozier, M.J., 2005. Landslide hazard and risk. Wiley Online Library.

Glade, T., Crozier, M.J., 2005. The Nature of Landslide Hazard Impact, in: Landslide Hazard and Risk. John Wiley & Sons, Ltd, pp. 41–74. https://doi.org/10.1002/9780470012659.ch2

Glastonbury, J., Fell, R., 2010. Geotechnical characteristics of large rapid rock slides. Can. Geotech. J. 47, 116–132. https://doi.org/10.1139/T09-080

Godone, D., Allasia, P., Notti, D., Baldo, M., Poggi, F., Faccini, F., 2023. Coexistence of a Marginal Mountain Community with Large-Scale and Low Kinematic Landslide: The Intensive Monitoring Approach. Remote Sensing 15, 3238. https://doi.org/10.3390/rs15133238

Gutiérrez, F., Ortuño, M., Lucha, P., Guerrero, J., Acosta, E., Coratza, P., Piacentini, D., Soldati, M., 2008. Late Quaternary episodic displacement on a sackung scarp in the central Spanish Pyrenees. Secondary paleoseismic evidence? Geodinamica Acta 21, 187–202. https://doi.org/10.3166/ga.21.187-202

Hagen, T., 1969. Report on the geological survey of Nepal. Denkschr. Schweiz. Naturf. Ges. 81, 185.

Handwerger, A.L., Rempel, A.W., Skarbek, R.M., Roering, J.J., Hilley, G.E., 2016. Rate-weakening friction characterizes both slow sliding and catastrophic failure of landslides. Proceedings of the National Academy of Sciences 113, 10281–10286. https://doi.org/10.1073/pnas.1607009113

Heim, A., 1932. Bergsturz und Menschenleben. Fretz & Wasmuth.

Helmstetter, A., Garambois, S., 2010. Seismic monitoring of Séchilienne rockslide (French Alps): Analysis of seismic signals and their correlation with rainfalls. Journal of Geophysical Research: Earth Surface 115. https://doi.org/10.1029/2009JF001532

Hermanns, R.L., Oppikofer, T., Dahle, H., Eiken, T., Ivy-Ochs, S., Blikra, L.H., Genevois, R., Prestininzi, A., 2013. Understanding long-term slope deformation for stability assessment of rock slopes: the case of the Oppstadhornet rockslide, Norway. Presented at the International Conference on Vajont–1963–2013, edited by: Genevois, R. and Prestininzi, A., Italian J. Eng. Geol. Environ., Book Ser, pp. 255–264.

Hewitt, K., 2002. Styles of rock-avalanche depositional complexes conditioned by very rugged terrain, Karakoram Himalaya, Pakistan, in: Reviews in Engineering Geology. Geological Society of America, pp. 345–377. https://doi.org/10.1130/REG15-p345

Hewitt, K., Clague, J.J., Orwin, J.F., 2008. Legacies of catastrophic rock slope failures in mountain landscapes. Earth-Science Reviews 87, 1–38. https://doi.org/10.1016/j.earscirev.2007.10.002

Hippolyte, J.-C., Bourlès, D., Braucher, R., Carcaillet, J., Léanni, L., Arnold, M., Aumaitre, G., 2009. Cosmogenic 10Be dating of a sackung and its faulted rock glaciers, in the Alps of Savoy (France). Geomorphology 108, 312–320. https://doi.org/10.1016/j.geomorph.2009.02.024

Hovius, N., Stark, C.P., Allen, P.A., 1997. Sediment flux from a mountain belt derived by landslide mapping. Geology 25, 231–234. https://doi.org/10.1130/0091-7613(1997)025<0231:SFFAMB>2.3.CO;2

Huggel, C., Clague, J.J., Korup, O., 2012. Is climate change responsible for changing landslide activity in high mountains? Earth Surface Processes and Landforms 37, 77–91. https://doi.org/10.1002/esp.2223

Hungr, O., Evans, S.G., 2004. Entrainment of debris in rock avalanches: An analysis of a long run-out mechanism. Geol Soc America Bull 116, 1240. https://doi.org/10.1130/B25362.1

Hungr, O., Leroueil, S., Picarelli, L., 2014. The Varnes classification of landslide types, an update. Landslides 11, 167–194. https://doi.org/10.1007/s10346-013-0436-y

IPCC, 2023. Climate Change 2023: Synthesis Report. Contribution of Working Groups I, II and III to the Sixth Assessment Report of the Intergovernmental Panel on Climate Change [Core Writing Team, H. Lee and J. Romero (eds.)]. IPCC, Geneva, Switzerland, pp. 35-115, doi: 10.59327/IPCC/AR6-9789291691647.

IRMA, 2023. Les Ruines de Séchilenne ou « la montagne qui s'écroule », Institut des Risques Majeurs (IRMA), Grenoble [WWW Document]. URL https://www.irma-grenoble.com/05documentation/04dossiers_articles.php?id_DTart=1&id_DT= (accessed 12.4.23).

Jaboyedoff, M., Michoud, C., Derron, M.H., Voumard, J., Leibundgut, G., Sudmeier-Rieux, K., Nadim, F., Leroi, E., 2018. Human-induced landslides: toward the analysis of anthropogenic changes of the slope environment. Landslides and Engineered Slopes. Experience, Theory and Practice; CRC Press: Boca Raton, FL, USA 217–232.

Jaboyedoff, M., Penna, I., Pedrazzini, A., Baroň, I., Crosta, G.B., 2013. An introductory review on gravitational-deformation induced structures, fabrics and modeling. Tectonophysics 605, 1–12. https://doi.org/10.1016/j.tecto.2013.06.027

Jaeger, J.C., Cook, N.G.W., Zimmerman, R.W., 2007. Fundamentals of rock mechanics, 4th ed. ed. Blackwell Pub, Malden, MA.

Jarman, D., Harrison, S., 2019. Rock slope failure in the British mountains. Geomorphology 340, 202–233. https://doi.org/10.1016/j.geomorph.2019.03.002

Jibson, R.W., Harp, E.L., Schulz, W., Keefer, D.K., 2004. Landslides Triggered by the 2002 Denali Fault, Alaska, Earthquake and the Inferred Nature of the Strong Shaking. Earthquake Spectra 20, 669–691. https://doi.org/10.1193/1.1778173

Katz, O., Morgan, J.K., Aharonov, E., Dugan, B., 2014. Controls on the size and geometry of landslides: Insights from discrete element numerical simulations. Geomorphology 220, 104–113. https://doi.org/10.1016/j.geomorph.2014.05.021

Kliche, C.A., 2018. Rock slope stability, 2nd edition. ed. Society for Mining, Metallurgy & Exploration, Englewood, Colo.

Klimeš, J., Rowberry, M.D., Blahůt, J., Briestenský, M., Hartvich, F., Košťák, B., Rybář, J., Stemberk, J., Štěpančíková, P., 2012. The monitoring of slow-moving landslides and assessment of stabilisation measures using an optical–mechanical crack gauge. Landslides 9, 407–415. https://doi.org/10.1007/s10346-011-0306-4

Korup, O., 2006. Rock-slope failure and the river long profile. Geol 34, 45. https://doi.org/10.1130/G21959.1

Korup, O., Clague, J.J., Hermanns, R.L., Hewitt, K., Strom, A.L., Weidinger, J.T., 2007. Giant landslides, topography, and erosion. Earth and Planetary Science Letters 12.

Korup, O., Densmore, A.L., Schlunegger, F., 2010. The role of landslides in mountain range evolution. Geomorphology 120, 77–90. https://doi.org/10.1016/j.geomorph.2009.09.017

Korup, O., McSaveney, M.J., Davies, T.R.H., 2004. Sediment generation and delivery from large historic landslides in the Southern Alps, New Zealand. Geomorphology, Hazards of Mass Movements 61, 189–207. https://doi.org/10.1016/j.geomorph.2004.01.001

Korup, O., Strom, A.L., Weidinger, J.T., 2006. Fluvial response to large rock-slope failures: Examples from the Himalayas, the Tien Shan, and the Southern Alps in New Zealand. Geomorphology, Mountain Rivers Part I: Watershed Scale Processes and Channel Morphology 78, 3–21. https://doi.org/10.1016/j.geomorph.2006.01.020

Kremer, K., Simpson, G., Girardclos, S., 2012. Giant Lake Geneva tsunami in AD 563. Nature Geosci 5, 756–757. https://doi.org/10.1038/ngeo1618

Lacroix, P., Amitrano, D., 2013. Long-term dynamics of rockslides and damage propagation inferred from mechanical modeling. J. Geophys. Res. Earth Surf. 118, 2292–2307. https://doi.org/10.1002/2013JF002766

Lacroix, P., Handwerger, A.L., Bièvre, G., 2020. Life and death of slow-moving landslides. Nat Rev Earth Environ 1, 404–419. https://doi.org/10.1038/s43017-020-0072-8

Le Breton, M., Bontemps, N., Guillemot, A., Baillet, L., Larose, É., 2021. Landslide monitoring using seismic ambient noise correlation: challenges and applications. Earth-Science Reviews 216, 103518. https://doi.org/10.1016/j.earscirev.2021.103518

Le Petit Journal, 2018. La montagne s'affaisse une nouvelle fois ! [WWW Document]. Le Petit Journal. URL https://www.lepetitjournal.net/65-hautes-pyrenees/2018/04/20/la-montagne-tombe-une-nouvelle-fois/ (accessed 12.5.23).

Le Roux, O., Schwartz, S., Gamond, J.F., Jongmans, D., Bourles, D., Braucher, R., Mahaney, W., Carcaillet, J., Leanni, L., 2009. CRE dating on the head scarp of a major landslide (Séchilienne, French Alps), age constraints on Holocene kinematics. Earth and Planetary Science Letters 280, 236–245. https://doi.org/10.1016/j.epsl.2009.01.034

Li, G.K., Moon, S., 2021. Topographic stress control on bedrock landslide size. Nat. Geosci. 14, 307–313. https://doi.org/10.1038/s41561-021-00739-8

List of landslides, 2023. . Wikipedia.

Livio, F.A., Zerboni, A., Ferrario, M.F., Mariani, G.S., Martinelli, E., Amit, R., 2022. Triggering processes of deep-seated gravitational slope deformation (DSGSD) in an un-glaciated area of the Cavargna Valley (Central Southern Alps) during the Middle Holocene. Landslides 19, 1825–1841. https://doi.org/10.1007/s10346-022-01892-w

Lucas, A., Mangeney, A., Ampuero, J.P., 2014. Frictional velocity-weakening in landslides on Earth and on other planetary bodies. Nat Commun 5, 3417. https://doi.org/10.1038/ncomms4417

Lucchitta, B.K., 1979. Landslides in Valles Marineris, Mars. Journal of Geophysical Research: Solid Earth 84, 8097–8113. https://doi.org/10.1029/JB084iB14p08097

Mahr, T., Nemčok, A., 1977. Deep-seated creep deformations in the crystalline cores of the tatry Mts. Bulletin of the International Association of Engineering Geology 16, 104–106. https://doi.org/10.1007/BF02591461

Mansour, M.F., Morgenstern, N.R., Martin, C.D., 2011. Expected damage from displacement of slow-moving slides. Landslides 8, 117–131. https://doi.org/10.1007/s10346-010-0227-7

Marc, O., Behling, R., Andermann, C., Turowski, J.M., Illien, L., Roessner, S., Hovius, N., 2019. Long-term erosion of the Nepal Himalayas by bedrock landsliding: the role of monsoons, earthquakes and giant landslides. Earth Surface Dynamics 7, 107–128. https://doi.org/10.5194/esurf-7-107-2019

Marinos, Vassilis., Carter, Trevor.G., 2018. Maintaining geological reality in application of GSI for design of engineering structures in rock. Engineering Geology 239, 282–297. https://doi.org/10.1016/j.enggeo.2018.03.022

Marmoni, G.M., Martino, S., Censi, M., Menichetti, M., Piacentini, D., Scarascia Mugnozza, G., Torre, D., Troiani, F., 2023. Transition from rock mass creep to progressive failure for rockslide initiation at Mt. Conero (Italy). Geomorphology 437, 108750. https://doi.org/10.1016/j.geomorph.2023.108750

Masch, L., Wenk, H.R., Preuss, E., 1985. Electron microscopy study of hyalomylonites—evidence for frictional melting in landslides. Tectonophysics 115, 131–160. https://doi.org/10.1016/0040-1951(85)90103-9

Massiver Felssturz am südlichen Fluchthorn (Ganzes Video) [Video], 2023.

McCalpin, J.P., Irvine, J.R., 1995. Sackungen at the Aspen Highlands Ski Area, Pitkin County, Colorado. Environmental & Engineering Geoscience I, 277–290. https://doi.org/10.2113/gseegeosci.I.3.277

McColl, S.T., 2015. Landslide Causes and Triggers, in: Landslide Hazards, Risks, and Disasters. Elsevier, pp. 17–42. https://doi.org/10.1016/B978-0-12-396452-6.00002-1

Moon, S., Perron, J.T., Martel, S.J., Holbrook, W.S., St. Clair, J., 2017. A model of three-dimensional topographic stresses with implications for bedrock fractures, surface processes, and landscape evolution: Three-Dimensional Topographic Stress. J. Geophys. Res. Earth Surf. 122, 823–846. https://doi.org/10.1002/2016JF004155

Moro, M., Saroli, M., Gori, S., Falcucci, E., Galadini, F., Messina, P., 2012. The interaction between active normal faulting and large scale gravitational mass movements revealed by paleoseismological techniques: A case study from central Italy. Geomorphology 151–152, 164–174. https://doi.org/10.1016/j.geomorph.2012.01.026

Moro, M., Saroli, M., Salvi, S., Stramondo, S., Doumaz, F., 2007. The relationship between seismic deformation and deep-seated gravitational movements during the 1997 Umbria–Marche (Central Italy) earthquakes. Geomorphology 89, 297–307. https://doi.org/10.1016/j.geomorph.2006.12.013

Mreyen, A.-S., Donati, D., Elmo, D., Donze, F.V., Havenith, H.-B., 2022. Dynamic numerical modelling of co-seismic landslides using the 3D distinct element method: Insights from the Balta rockslide (Romania). Engineering Geology 307, 106774. https://doi.org/10.1016/j.enggeo.2022.106774

Munjiza, A.A., 2004. The combined finite-discrete element method. John Wiley & Sons.

Nappo, N., Peduto, D., Mavrouli, O., van Westen, C.J., Gullà, G., 2019. Slow-moving landslides interacting with the road network: Analysis of damage using ancillary data, in situ surveys and multi-source monitoring data. Engineering Geology 260, 105244. https://doi.org/10.1016/j.enggeo.2019.105244

Nicolussi, K., Spötl, C., Thurner, A., Reimer, P.J., 2015. Precise radiocarbon dating of the giant Köfels landslide (Eastern Alps, Austria). Geomorphology 243, 87–91. https://doi.org/10.1016/j.geomorph.2015.05.001

Normandeau, A., Campbell, D.C., Piper, D.J.W., Jenner, K.A., 2019. Are submarine landslides an underestimated hazard on the western North Atlantic passive margin? Geology 47, 848–852. https://doi.org/10.1130/G46201.1

Ostermann, M., Sanders, D., 2017. The Benner pass rock avalanche cluster suggests a close relation between long-term slope deformation (DSGSDs and translational rock slides) and catastrophic failure. Geomorphology, Slope tectonics: inherited structures, morphology of deformation and catastrophic failure 289, 44–59. https://doi.org/10.1016/j.geomorph.2016.12.018

Pachoud, A., 1991. Une catastrophe naturelle majeure : l'écroulement du Mont Granier dans le massif de la Chartreuse au XIII e siècle. La Houille Blanche 77, 327–332. https://doi.org/10.1051/lhb/1991030

Palis, E., Lebourg, T., Tric, E., Malet, J.-P., Vidal, M., 2017. Long-term monitoring of a large deep-seated landslide (La Clapiere, South-East French Alps): initial study. Landslides 14, 155–170. https://doi.org/10.1007/s10346-016-0705-7

Pánek, T., 2021. Landslides and Related Sediments, in: Encyclopedia of Geology. Elsevier, pp. 708–728. https://doi.org/10.1016/B978-0-12-409548-9.12529-1

Pánek, T., 2019. Landslides and Quaternary climate changes—The state of the art. Earth-Science Reviews 196, 102871. https://doi.org/10.1016/j.earscirev.2019.05.015

Pánek, T., 2015. Recent progress in landslide dating: A global overview. Progress in Physical Geography 32.

Pánek, T., Klimeš, J., 2016. Temporal behavior of deep-seated gravitational slope deformations: A review. Earth-Science Reviews 156, 14–38. https://doi.org/10.1016/j.earscirev.2016.02.007

Pánek, T., Mentlík, P., Engel, Z., Braucher, R., Zondervan, A., 2017. Late Quaternary sackungen in the highest mountains of the Carpathians. Quaternary Science Reviews 159, 47–62. https://doi.org/10.1016/j.quascirev.2017.01.008

Patton, A.I., Rathburn, S.L., Capps, D.M., 2019. Landslide response to climate change in permafrost regions. Geomorphology 340, 116–128. https://doi.org/10.1016/j.geomorph.2019.04.029

Peng, M., Zhang, L.M., 2012. Breaching parameters of landslide dams. Landslides 9, 13–31. https://doi.org/10.1007/s10346-011-0271-y

Petley, D., 2012. 14 Remote sensing techniques and landslides, in: Landslides: Types, Mechanisms and Modeling. Cambridge University Press, p. 159.

Petley, D., 2009. The biggest landslide of them all - Saidmareh, Iran. The Landslide Blog. URL https://blogs.agu.org/landslideblog/2009/07/03/the-biggest-landslide-of-them-all-saidmareh-iran/ (accessed 8.27.23).

Petley, D.N., Allison, R.J., 1997. The mechanics of deep-seated landslides. Earth Surface Processes and Landforms 22, 747–758. https://doi.org/10.1002/(SICI)1096-9837(199708)22:8<747::AID-ESP767>3.0.CO;2-#

Popescu, M.E., 1994. A suggested method for reporting landslide causes. Bulletin of the International Association of Engineering Geology 50, 71–74. https://doi.org/10.1007/BF02594958

Pratt-Sitaula, B., Burbank, D.W., Heimsath, A.M., Humphrey, N.F., Oskin, M., Putkonen, J., 2011. Topographic control of asynchronous glacial advances: A case study from Annapurna, Nepal: ASYNCHRONOUS GLACIAL ADVANCES. Geophys. Res. Lett. 38, n/a-n/a. https://doi.org/10.1029/2011GL049940

Preisig, G., Eberhardt, E., Smithyman, M., Preh, A., Bonzanigo, L., 2016. Hydromechanical Rock Mass Fatigue in Deep-Seated Landslides Accompanying Seasonal Variations in Pore Pressures. Rock Mech Rock Eng 49, 2333–2351. https://doi.org/10.1007/s00603-016-0912-5

Read, J., Stacey, P. (Eds.), 2009. Guidelines for open pit slope design, Reprint. with corr. ed. CSIRO Publ. [u.a.], Collingwood, Vic.

Reynolds, N.D., O'Connor, J.E., Pringle, P.T., Bourdeau, A.C., Schuster, R.L., 2022. Age of the late Holocene Bonneville landslide and submerged forest of the Columbia River Gorge, Oregon and Washington, USA, by radiocarbon dating. Quaternary Research 109, 65–82. https://doi.org/10.1017/qua.2022.7

Riva, F., Agliardi, F., Amitrano, D., Crosta, G.B., 2018. Damage-Based Time-Dependent Modeling of Paraglacial to Postglacial Progressive Failure of Large Rock Slopes. J. Geophys. Res. Earth Surf. 123, 124–141. https://doi.org/10.1002/2017JF004423

Roering, J.J., Kirchner, J.W., Dietrich, W.E., 2005. Characterizing structural and lithologic controls on deep-seated landsliding: Implications for topographic relief and landscape evolution in the Oregon Coast Range, USA. GSA Bulletin 117, 654–668. https://doi.org/10.1130/B25567.1

Scholtès, L., Donzé, F.V., 2015. A DEM analysis of step-path failure in jointed rock slopes. Comptes Rendus Mécanique 343, 155–165. https://doi.org/10.1016/j.crme.2014.11.002

Schuster, R.L., Alford, D., 2004. Usoi Landslide Dam and Lake Sarez, Pamir Mountains, Tajikistan. Environmental and Engineering Geoscience 10, 151–168. https://doi.org/10.2113/10.2.151

Schuster, R.L., Highland, L.M., 2001. Socioeconomic and environmental impacts of landslides in the Western Hemisphere. Open-File Report. https://doi.org/10.3133/ofr01276

Schuster, R.L., Salcedo, D.A., Valenzuela, L., 2002. Overview of catastrophic landslides of South America in the twentieth century, in: Evans, S.G., Degraff, J.V. (Eds.), Catastrophic Landslides. Geological Society of America, p. 0. https://doi.org/10.1130/REG15-p1

Segall, P., Rubin, A.M., Bradley, A.M., Rice, J.R., 2010. Dilatant strengthening as a mechanism for slow slip events. Journal of Geophysical Research: Solid Earth 115. https://doi.org/10.1029/2010JB007449

Sewell, R.J., Parry, S., Millis, S.W., Wang, N., Rieser, U., DeWitt, R., 2015. Dating of debris flow fan complexes from Lantau Island, Hong Kong, China: The potential relationship between landslide activity and climate change. Geomorphology 248, 205–227. https://doi.org/10.1016/j.geomorph.2015.07.041

Shugar, D.H., Jacquemart, M., Shean, D., Bhushan, S., Upadhyay, K., Sattar, A., Schwanghart, W., McBride, S., de Vries, M.V.W., Mergili, M., Emmer, A., Deschamps-Berger, C., McDonnell, M., Bhambri, R., Allen, S., Berthier, E., Carrivick, J.L., Clague, J.J., Dokukin, M., Dunning, S.A., Frey, H., Gascoin, S., Haritashya, U.K., Huggel, C., Kääb, A., Kargel, J.S., Kavanaugh, J.L., Lacroix, P., Petley, D., Rupper, S., Azam, M.F., Cook, S.J., Dimri, A.P., Eriksson, M., Farinotti, D., Fiddes, J., Gnyawali, K.R., Harrison, S., Jha, M., Koppes, M., Kumar, A., Leinss, S., Majeed, U., Mal, S., Muhuri, A., Noetzli, J., Paul, F., Rashid, I., Sain, K., Steiner, J., Ugalde, F., Watson, C.S., Westoby, M.J., 2021. A massive rock and ice avalanche caused the 2021 disaster at Chamoli, Indian Himalaya. Science 373, 300–306. https://doi.org/10.1126/science.abh4455

Sorriso-Valvo, M., Gullà, G., Antronico, L., Tansi, C., Amelio, M., 1999. Mass-movement, geologic structure and morphologic evolution of the Pizzotto–Greci slope (Calabria, Italy). Geomorphology 30, 147–163. https://doi.org/10.1016/S0169-555X(99)00051-3

Spreafico, M.C., Sternai, P., Agliardi, F., 2021. Paraglacial rock-slope deformations: sudden or delayed response? Insights from an integrated numerical modelling approach. Landslides 18, 1311–1326. https://doi.org/10.1007/s10346-020-01560-x

Stead, D., Eberhardt, E., 2013. Understanding the mechanics of large landslides. Ital. J. Eng. Geol. Environ. Book Ser 6, 85–112.

Stead, D., Eberhardt, E., Coggan, J.S., 2006. Developments in the characterization of complex rock slope deformation and failure using numerical modelling techniques. Engineering Geology 83, 217–235. https://doi.org/10.1016/j.enggeo.2005.06.033

Stead, D., Wolter, A., 2015. A critical review of rock slope failure mechanisms: The importance of structural geology. Journal of Structural Geology 74, 1–23. https://doi.org/10.1016/j.jsg.2015.02.002

Strauhal, T., Zangerl, C., Fellin, W., Holzmann, M., Engl, D.A., Brandner, R., Tropper, P., Tessadri, R., 2017. Structure, Mineralogy and Geomechanical Properties of Shear Zones of Deep-Seated Rockslides in Metamorphic Rocks (Tyrol, Austria). Rock Mech Rock Eng 50, 419–438. https://doi.org/10.1007/s00603-016-1113-y

Sun, L., Grasselli, G., Liu, Q., Tang, X., Abdelaziz, A., 2022. The role of discontinuities in rock slope stability: Insights from a combined finite-discrete element simulation. Computers and Geotechnics 147, 104788. https://doi.org/10.1016/j.compgeo.2022.104788

Tarolli, P., Mudd, S.M., 2020. Remote Sensing of Geomorphology. Elsevier.

Terzaghi, K., 1950. Mechanism of Landslides, in: Paige, S. (Ed.), Application of Geology to Engineering Practice. Geological Society of America, p. 0. https://doi.org/10.1130/Berkey.1950.83

Thompson, S.C., Clague, J.J., Evans, S.G., 1997. Holocene Activity of the Mt. Currie Scarp, Coast Mountains, British Columbia, and Implications for its Origin. Environmental & Engineering Geoscience III, 329–348. https://doi.org/10.2113/gseegeosci.III.3.329

Tibaldi, A., Pasquarè, F.A., 2008. Quaternary deformations along the 'Engadine–Gruf tectonic system', Swiss–Italian Alps. Journal of Quaternary Science 23, 475–487. https://doi.org/10.1002/jqs.1150

Tolomei, C., Taramelli, A., Moro, M., Saroli, M., Aringoli, D., Salvi, S., 2013. Analysis of the deep-seated gravitational slope deformations over Mt. Frascare (Central Italy) with geomorphological assessment and DInSAR approaches. Geomorphology 201, 281–292. https://doi.org/10.1016/j.geomorph.2013.07.002

Turner, A.K., 2018. Social and environmental impacts of landslides. Innov. Infrastruct. Solut. 3, 70. https://doi.org/10.1007/s41062-018-0175-y

Utili, S., Crosta, G.B., 2011. Modeling the evolution of natural cliffs subject to weathering: 2. Discrete element approach. J. Geophys. Res. 116, n/a-n/a. https://doi.org/10.1029/2009JF001559

Varnes, D.J., 1978. Slope movement types and processes. Special report 176, 11–33.

Viles, H.A., 2013. Linking weathering and rock slope instability: non-linear perspectives: Linking weathering and rock slope instability. Earth Surf. Process. Landforms 38, 62–70. https://doi.org/10.1002/esp.3294

Voigtländer, A., Leith, K., Krautblatter, M., 2018. Subcritical Crack Growth and Progressive Failure in Carrara Marble Under Wet and Dry Conditions. Journal of Geophysical Research: Solid Earth 123, 3780–3798. https://doi.org/10.1029/2017JB014956

von Poschinger, A., 2011. The Flims rockslide dam, in: Natural and Artificial Rockslide Dams. Springer, pp. 407–421.

Walter, F., Amann, F., Kos, A., Kenner, R., Phillips, M., de Preux, A., Huss, M., Tognacca, C., Clinton, J., Diehl, T., Bonanomi, Y., 2020. Direct observations of a three million cubic meter rock-slope collapse with almost immediate initiation of ensuing debris flows. Geomorphology 351, 106933. https://doi.org/10.1016/j.geomorph.2019.106933

Weidinger, J.T., 2006. Predesign, failure and displacement mechanisms of large rockslides in the Annapurna Himalayas, Nepal. Engineering Geology 83, 201–216. https://doi.org/10.1016/j.enggeo.2005.06.032

Weidinger, J.T., Korup, O., 2009. Frictionite as evidence for a large Late Quaternary rockslide near Kanchenjunga, Sikkim Himalayas, India — Implications for extreme events in mountain relief destruction. Geomorphology, Dating, triggering, modelling, and hazard assessment of large landslides 103, 57–65. https://doi.org/10.1016/j.geomorph.2007.10.021

Weidinger, J.T., Korup, O., Munack, H., Altenberger, U., Dunning, S.A., Tippelt, G., Lottermoser, W., 2014. Giant rockslides from the inside. Earth and Planetary Science Letters 389, 62–73. https://doi.org/10.1016/j.epsl.2013.12.017

Wen, B., Wang, S., Wang, E., Zhang, J., 2004. Characteristics of rapid giant landslides in China. Landslides 1, 247–261. https://doi.org/10.1007/s10346-004-0022-4

Wolter, A., Roques, C., Gröble, J., Ivy-Ochs, S., Christl, M., Loew, S., 2020. Integrated multi-temporal analysis of the displacement behaviour and morphology of a deep-seated compound landslide (Cerentino, Switzerland). Engineering Geology 270, 105577. https://doi.org/10.1016/j.enggeo.2020.105577

Zangerl, C., Eberhardt, E., Perzlmaier, S., 2010. Kinematic behaviour and velocity characteristics of a complex deep-seated crystalline rockslide system in relation to its interaction with a dam reservoir. Engineering Geology 112, 53–67. https://doi.org/10.1016/j.enggeo.2010.01.001

Zangerl, C., Schneeberger, A., Steiner, G., Mergili, M., 2021. Geographic-information-system-based topographic reconstruction and geomechanical modelling of the Köfels rockslide. Natural Hazards and Earth System Sciences 21, 2461–2483. https://doi.org/10.5194/nhess-21-2461-2021

Zaruba, Q., Mencl, V., 1982. Landslides and their control. Elsevier.

Zerathe, S., Lebourg, T., Braucher, R., Bourlès, D., 2014. Mid-Holocene cluster of large-scale landslides revealed in the Southwestern Alps by 36Cl dating. Insight on an Alpine-scale landslide activity. Quaternary Science Reviews 90, 106–127. https://doi.org/10.1016/j.quascirev.2014.02.015

Zheng, Y., Wang, R., Chen, C., Meng, F., 2021. Analysis of Flexural Toppling Failure in Rock Slopes Using Discrete Element Method. Front. Earth Sci. 9, 773088. https://doi.org/10.3389/feart.2021.773088

Zischinsky, U., 1968. Über Bergzerreißung und Talzuschub. Geol Rundsch 58, 974–983. https://doi.org/10.1007/BF01820741

# CHAPTER 2 – BEDROCK LANDSLIDES IN THE ANNAPURNA MASSIF

## 2.1 Introduction

The Himalayas are one of the world's youngest and most active mountain ranges. The Himalayan range extends over more than 2 500 km along a WNW-ENE axis, between the Western and Eastern Himalayan syntaxes. Along with the Karakorum and Tibet, it constitutes the largest relief on Earth. With a width of around 200 km, the Himalayas are home to the highest peaks on Earth. This spectacular topography results from the collision between India and Eurasia, and ongoing convergence that foster crustal thickening and uplift of the range.

The central Himalayan mountains are subject to very intensive erosion due to their topography and high relief as well as the abundant monsoon precipitation (e.g., Burbank et al., 2012). This is reflected in the large number of landslides that occur along the Himalayan slopes (Roback et al., 2018; Marc et al., 2019; Jones et al., 2020, 2021). These landslides have a major human and economic cost on the Himalayan region (e.g., Petley et al., 2007; KC et al., 2024).

Despite their importance and societal impact, compared with active regions such as Japan, Taiwan or the European Alps, studies on Himalayan landslides are more limited, and many open questions remain (e.g., Pánek, 2015, 2019). In this thesis chapter (Figure 2.1), before presenting our new results on bedrock landslides in the Annapurna Massif, in particular giant catastrophic rock avalanches (in Section 2.5 and 2.6) and non-catastrophic rock slope failures, i.e. DSGSDs (in Section 2.7 and 2.8), we first present the geological and climatic contexts of the central Himalayas (Section 2.2), discuss the state of research on bedrock landslides in this region (Section 2.3), and describe the methods used in this study (Section 2.4).

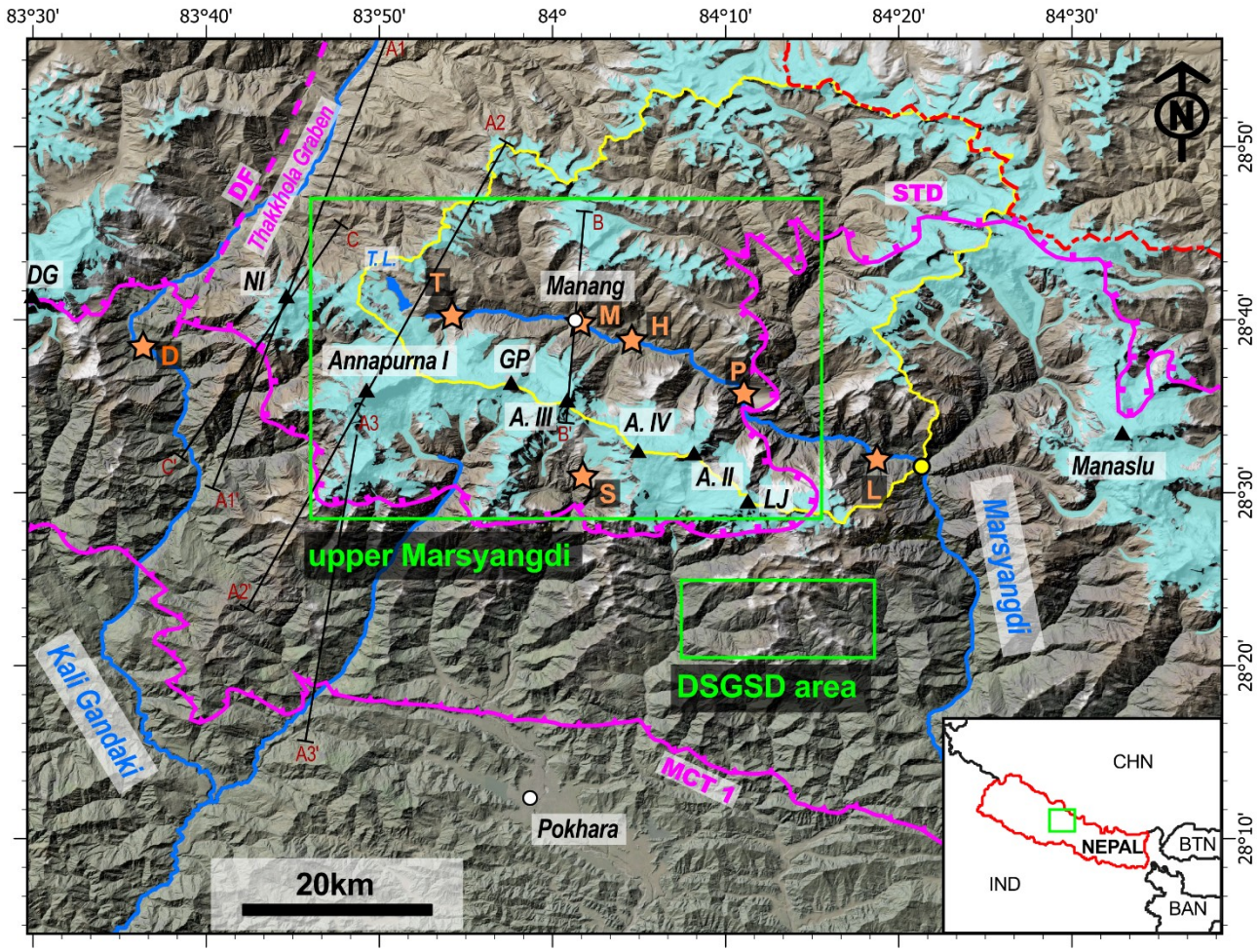


*Figure 2.1: Map showing study region of the Annapurna Massif including the two sub-areas for investigation of bedrock landslides: the upper Marsyangdi Valley, and the Annapurna south-face area with DSGSD-morphology present ("DSGSD area"). Orange stars: giant catastrophic rock slope failures which are referred to in this study: L = Latamrang, P = Pisang Bowl, H = Humde, M = Manang, T = Tilicho Lake , D = Dhampu-Chhoyo, S = Sabche. Prominent mountain peaks are show in black triangles: A. = Annapurna, GP = Gangapurna, NI = Nilgiri (North Peak), LJ = Lamjung Himal. Upper Marsyangdi drainage basin is indicated with yellow line. Major tectonic boundaries after Parsons et al. (2014) are shown in magenta: STD = South Tibetan Detachment, MCT1 = Main Central Thrust 1, DF = Dangardzong Fault of Thakkhola Graben (Hurtado et al., 2001). Glaciated areas are highlighted with light "icy" blue, GLIMS global glacial dataset (Raup et al., 2007). T. L. is Tilicho Lake.*

## 2.2 Study area

Physiographically, the central Himalayan range is made up of four main sub-sets, arranged in parallel from north to south:

- The Tibetan plateau, in the north, at a high average altitude (5 000 to 5 500 m) but with a moderate relief.

- The High Himalayas, or High Range, characterized by its glaciated peaks of major altitude (some of which are over 8 000 m), a very marked relief (local relief of up to 5 000 m between valley bottoms and summits), and generally very steep slopes.

- The Lower or Lesser Himalayas, at lower altitudes between 300 and 3 000 m, with less relief and gentler slopes.

- Finally, the Siwaliks foothills, which form a series of fairly dissected narrow ranges, but at an altitude of less than 1 000 m and bordered to the south by the Terai or Ganga plain.

### 2.2.1 Geologic and tectonic setting of the central Himalayas

The Himalayan range and Tibetan plateau result from the collision between the Indian and Eurasian continental plates that began between the Palaeocene and the Eocene (Patriat and Achache, 1984; Rowley 1996) and which is currently continuing at a rate of 35 to 40 mm/year with a general increase of this rate from West to East (Wang et al, 2001).

Tectonic activity in the Himalayas features thrusting within the upper Indian plate towards the south along major faults, which displace individual thrust sheets and merge at depth towards a main overthrust plane, the MHT (Main Himalayan Thrust) that presents in central Nepal a flat-ramp-flat geometry (e.g., Schelling and Arita, 1991; Pandey et al., 1995; Figure 2.2). Ruptures along these faults are the source of strong earthquakes on the Himalayan range front that sometimes rupture towards the surface (Lavé et al., 2005; Sapkota et al., 2013). Apart from the recent 2015 earthquake (see, e.g., Avouac et al., 2015), other major (Mw 7,0 – 8,0) and great earthquakes (Mw ≥ 8,0) that have significantly impacted central Nepal are known from the historic record (Arora and Malik, 2017; Bollinger et al., 2016; Wesnousky et al. 2017). Hypocentres are expected at a depth of about 10 – 20 km at the middle of the ramp geometry of the MHT (Figure 2.2). The present return time for great earthquakes in the central Himalayas is estimated in the order of a few hundred years (e.g., Bollinger et al., 2014; Bungum et al., 2017).

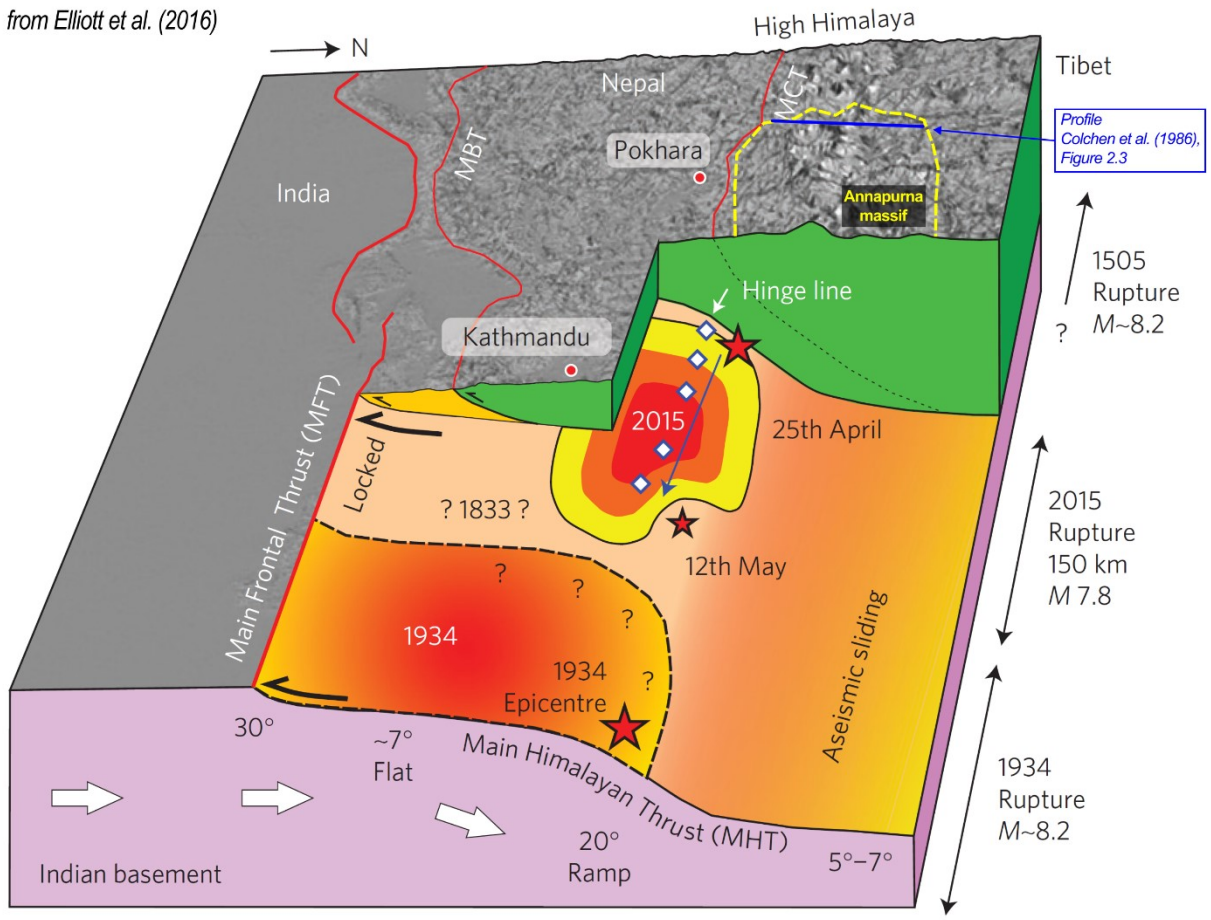


*Figure 2.2: Schematic cartoon of the 2015 Gorkha earthquake rupture on the MHT, after Elliott et al. (2016). Geometry of the MHT got resolved by application of a geometrical inversion strategy. Poorly constrained previous ruptures are indicated as well: 1934 (M ~8.2), 1833 (M ~7.6) and 1505 (M ~8.2). White diamonds are high-frequency seismic sources. For this PhD manuscript, indications showing the location of the Annapurna Massif and the position of the profile in Figure 2.3 were added.*

The geology in the Annapurna Massif is studied and mapped, with the most synoptic contributions by Colchen et al. (1986) and Parsons et al. (2016) (see also source references listed therein). However, in some specific areas which are not easily accessible, field verifications are missing and mapping is based largely on interpolations or observations on satellite imagery. The geology outcropping in the Annapurna Massif can be divided into three sub-domains bounded by major tectonic faults: The Lesser Himalayan (LH) metasediments units are overthrusted by the Higher Himalayan (HH) gneisses along a main ductile thrust, the Main Central Thrust 1 (MCT1, after Searle et al. (2008), see Figure 2.1), located at the foothill of the High Range. This Higher Himalayan Sequence (HHS) is made up, from bottom to top, of biotitic paragneiss and quartzite, followed by calc-silicate gneisses and meta-carbonates (including marbles), and finally by orthogneisses. These units are of Neoproterozoic to Early Palaeozoic age (Colchen et al., 1986; Parsons et al., 2016). Their foliation is on average gently dipping towards the north with some secondary folds (Figure 2.3). The summit of the HHS sequence is deformed and intersected by a major detachment fault system, the South Tibetan Detachment (STD), which is roughly coinciding in the Annapurna Massif with the Annapurna Detachment Fault (ADF in Figure 2.3). The STD brings the Tethyan Himalayan Sequence (THS) into contact with the HHS gneisses. The THS units consist of slightly metamorphosed Phanerozoic sediment units that become younger in age towards the north, and include marbles, limestones, marly schists, shales, quartzites or sandstones. These units are folded on a large scale (Figure 2.3).

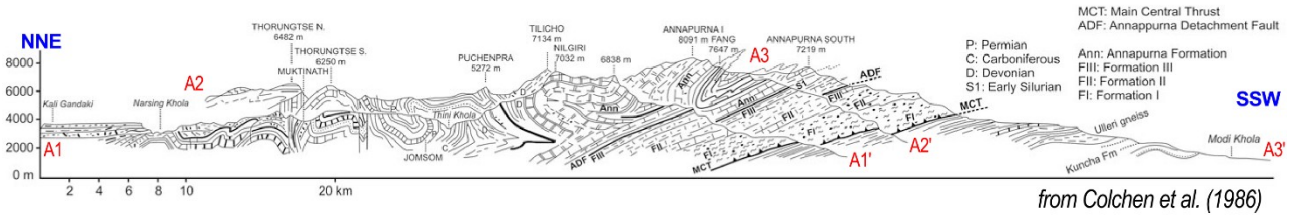


*Figure 2.3: Geologic cross-section through the western Annapurna Massif after Colchen et al. (1986) (with slight modifications by Dhital (2015). See location cross sections in Figure 2.1). The thrust referred to as MCT is not identical to MCT1 in Figure 2.1, as the designation and location of a thrust named MCT is disputed in the literature.*

### 2.2.2 Climate in the central Himalayas

The central Himalayas, located within the tropics, experience a climate primarily influenced by the annual shift of the Intertropical Convergence Zone (ITCZ). This shift results in a summer monsoon (Indian summer monsoon) responsible for about 80% of annual precipitation amounts in Nepal falling from June to September, with monsoon intensity peaking between June and August (Shrestha, 2000; Gadgil, 2003; Sharma et al., 2020). During the winter months, the High Range and the southern Tibetan Plateau in central Nepal are under the influence of the westerlies which bring limited snow precipitation above 3 000 m from January to March (Dawadi et al., 2023), and result in dry conditions along the southern flank of the range.

The climate in central Nepal is significantly impacted by the dramatic rise in elevation from south to north. Altitudes change dramatically from the Terai (<200 m.a.s.l) to the highest peaks on Earth (>8 000 m.a.s.l) within approximately 100-120 km, and then another 100 km to the Tibetan Plateau (~5 000 m.a.s.l.). This extreme relief leads to orographic precipitation, creating a sharp contrast in precipitation (and to a lesser extent, temperature) between the humid south-facing Himalayan foothills and the Midlands, and the arid and colder zone beyond the main ridge line (e.g., Bookhagen and Burbank, 2006; Andermann et al., 2012; and see Figure 2.4). Regarding directly measured precipitation levels, Burbank et al. (2003) highlight a striking contrast: annual precipitation exceeds 3 m on the Annapurna/Lamjung south-face compared to 0,5 – 1 m in the upper Marsyangdi Valley (see Figure 2.1), north of the orographic barrier of the High peaks of the Annapurna Massif.

Due to the significant relief and resulting differences in altitude, the atmospheric thermal gradient plays a crucial role in determining temperatures at specific locations. While areas at 2 000 m of elevation on the southern side barely experience frost during winter months (modelled climate by Meteoblue, 2024 for Sikles, Annapurna south face, ~1900 m.a.s.l.), permafrost is present in the high mountains above approximately 4 500 m (Chauhan and Thakuri, 2017; see also Permafrost Zonation Index (PZI), Gruber, 2012). The high mountain regions are covered in ice and glaciers flow down their slopes (Lovell et al., 2019). The present day equilibrium line altitude (ELA) for glaciers in the Annapurna Massif is situated around 5 000 – 5 500 m (Burbank et al., 2003).

The glacier extent in the Annapurna Massif has varied in the past, as we know from glacial landforms such as moraine ridges and a U-shaped valley topography below the termini of modern glaciers (see Figure 2.4C; and Nagaoka, 1990; Owen et al., 1998). Unfortunately, there is significant variability between the reconstructed glacier chronologies based on absolute dating methods (14C carbon burial dating and cosmogenic nuclides) between individual study localities in the central Himalayas, making it difficult to derive consistent trends of past glacial phases across the entire area. A review by Owen and Dortch (2014) recalculated cosmogenic

nuclide ages (mostly 10Be-samples) for the whole Himalayan range and Tibet uniformly and combined them with other dating techniques applied on glacial features in the area to obtain an overall view on the glacial record. They found consistent evidence for Late glacial and early Holocene glacial advances with some minor advances during the mid Holocene. Alternatively, in a modelling study for the monsoon-influenced southern part of the Himalaya, Yan et al. (2020) suggested a continuous decline in glacier cover from the Last Glacial Maximum (LGM; ~20 ka BP) to the EHCO, but slightly greater ice cover in the second half of the Holocene. Glacial chronologies in the Annapurna Massif and the whole central Himalayas lack understanding to the present day as there are only isolated studies and no summarized analysis has yet been undertaken. Influences of local climate factors can also be expected and can further complicate comprehension (Pratt-Sitaula et al., 2011; Salerno et al., 2023). The whole Himalayan region is lacking a calibration site for 10Be cosmogenic nuclide dating which adds additional uncertainty on age constraints derived from this method (see the online calculator CREP, Martin et al. (2017)).

Several studies on glacial landforms in the Annapurna Massif have gone beyond descriptive analysis and relative chronological classification by applying absolute dating methods to gain a deeper understanding of the region's paleo-glaciology. Pratt-Sitaula et al. (2011) used 10Be exposure dating on moraine boulders across five valleys to reconstruct glacial stages, identifying periods of larger glacier extents in the late-Glacial (~13-15 ka BP) and early Holocene (~8 ka BP) (see also Pratt-Sitaula, 2005). Heimsath and McGlynn (2008) quantified paraglacial erosion by a glacier in the upper Marsyangdi Valley and found evidence of a recent glacial advance a few hundred years ago. Other studies that have employed absolute dating techniques on glacial landforms also suggest variability in past glacier extents but have not yet provided a comprehensive understanding of paleo-glacier dynamics in the Annapurna Massif (Röthlisberger and Geyh, 1986; Zech et al., 2009).

*Figure 2.4 (on next page): (A) Averaged rainfall amounts between Jan. 1998 and Dec. 2005. Space-borne data, Tropical Rainfall Measurement Mission (TRMM) satellite, Kummerow et al. (1998). From Bookhagen and Burbank (2006). (B) Swath profile across the Annapurna Massif (location indicated in map above by black rectangle) showing topography and precipitation data. APHRODITE database, see Yatagai et al. (2009) and Andermann et al. (2011)).Topography extracted from SRTM3. Mean, maximum and minimum values along each swath profile are shown by grey shading. From Andermann et al. (2012). The rise of elevation at the southern front of the central Himalayan mountains form a clear orographic barrier to the north (Tibetan Plateau). This is reflected by a strong and sharp contrast in precipitation. (C) Reconstructions of past glacial limits by Owen et al. (1998) provide an outline of the maximum glacial extend that occupied the upper Marsyangdi Valley during the recent Pleistocene glaciations. The area covered by the map is roughly the green rectangle marked "upper Marsyangdi" in Figure 2.1.*

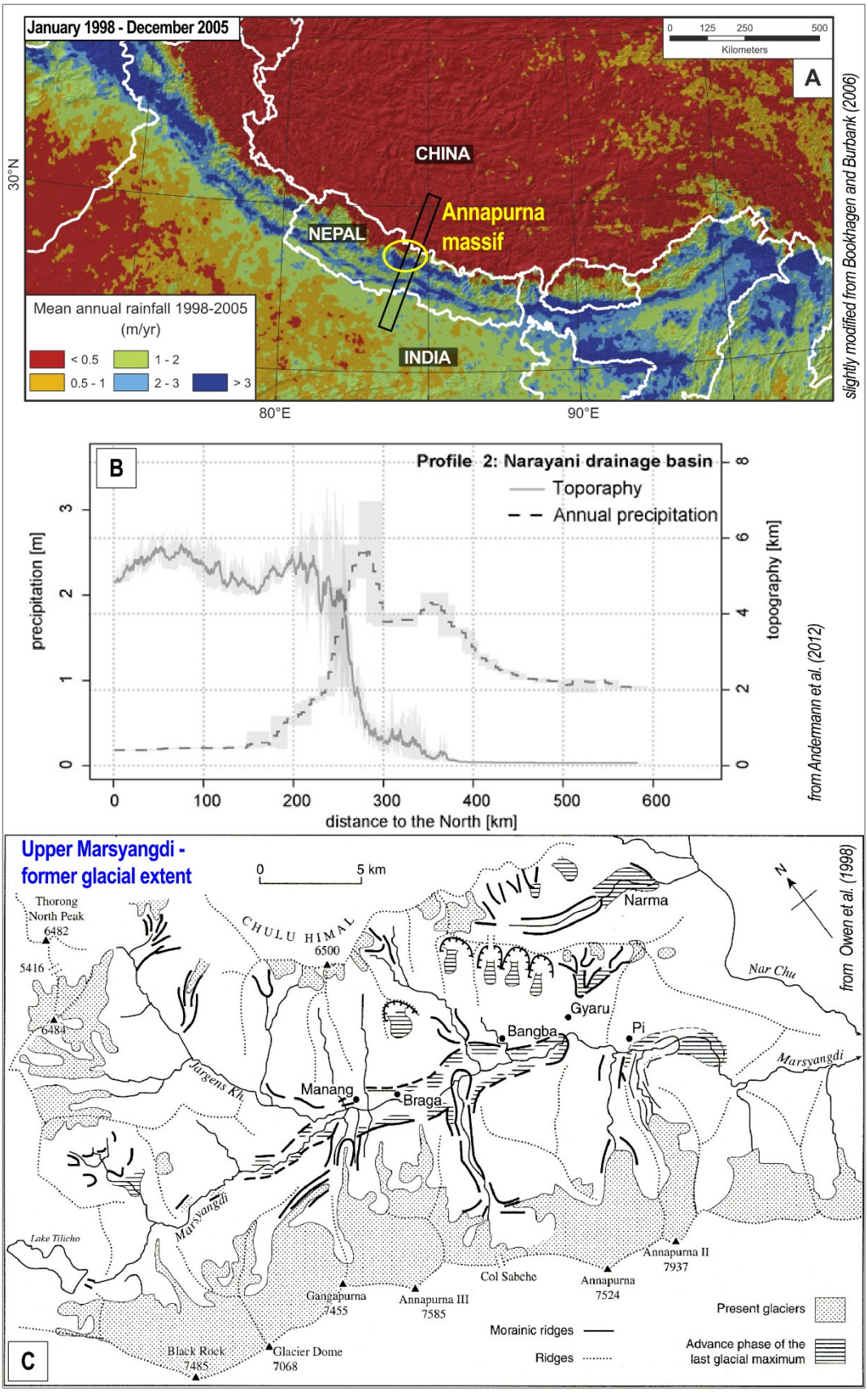
January 1998 - December 2005
0 125 250 500
Kilometers
A
CHINA
NEPAL
Annapurna massif
INDIA
Mean annual rainfall 1998-2005 (m/yr)
< 0.5
0.5 - 1
1 - 2
2 - 3
> 3
30°N
80°E
90°E
slightly modified from Bookhagen and Burbank (2006)
B
Profile 2: Narayani drainage basin
Toporaphy
Annual precipitation
precipitation [m]
topography [km]
distance to the North [km]
from Andermann et al. (2012)
Upper Marsyangdi - former glacial extent
0 5 km
Thorong North Peak 6482
5416
6484
CHULU HIMAL 6500
Narma
Nar Chu
Gyaru
Bangba
Pi
Marsyangdi
Jargens Kh.
Manang
Braga
Lake Tilicho
Gangapurna 7455
Annapurna III 7585
Col Sabche
Annapurna 7524
Annapurna II 7937
Black Rock 7485
Glacier Dome 7068
Present glaciers
Morainic ridges
Ridges
Advance phase of the last glacial maximum
C
from Owen et al. (1998)

## 2.3 Landslides in the central Himalayas and in the Annapurna Massif

Landslides in the central Himalayas are a manifold phenomenon. They come in many forms, from superficial to deep-seated slides and topples, to flows, and non-catastrophic slope deformations, i.e. DSGSDs ( e.g., Marc et al. 2023). The main concerns for studying landslides in the central Himalayas can be broadly divided into two sub-domains:

- **The hazards and risks concern:** It is of particular interest for the people living in the central Himalayas that substantial knowledge exists about the occurrence, abundance, frequency, and characteristics of landslides in the region and the processes involved causing them. Research progress on landslide dynamics in the central Himalayas helps to better anticipate, mitigate, or avoid landslides in the region. The knowledge gained can also be transferred to other regions of the world. This is particularly important at a time when we are facing significant climate change, both in the central Himalayan region and globally.

- **The mountain evolution concern:** A general understanding of how orogens form and erode over time is not only in the interest of a better understanding of our Earth's history in general. Landslides are also considered to be the most important erosion process in active mountain regions. Therefore, better knowledge of landslides is needed to better interpret erosion processes and flows and to understand how erosion shapes mountains.

Fundamental to these topics is the question of why landslides do form? What are the Causes and Triggers of landslides in the central Himalayas and in mountainous regions around the world?

Factors that influence the stability of a slope can be differentiated according to the role they play in slope destabilisation (Glade and Crozier, 2005; McColl, 2015; see Section 1.2.2, and Figure 1.2): Precondition Factors are static, inherent characteristics of the rock mass like rock mechanical properties or structures inherited from its genetic past, including layering or foliation. In theory they do not change over time and can either favour or impede slope failure by influencing how the Preparatory Factors act. Preparatory Factors actively reduce the stability of a slope before failure. They can either act “internal” from the inside (for example: deep-seated weathering) or “external” from the outside (for example: erosion at the base of the slope) on the stability of the slope. Triggers are events that immediately bring a slope to failure from a state in which it is already marginally stable (FoS drops below 1, see Figure 1.2).

In this chapter of the thesis we will focus on the Causes and Triggers of bedrock landslides in the central Himalayas. Bedrock landslides are failures of slopes consisting of solid, coherent rock and excludes the failure of loose sediment or soil (see Section 1.1.2). They are often deep-seated and are particularly important for

the above-mentioned issues, as they can contain large volumes, which is of great importance for erosion fluxes from the mountains. They also have a high hazard and risk potential. The lithology and the structures within the slope can control whether a slope failure will occur or not (Precondition factors). But what influence do climatic conditions, topography and seismicity have as Preparatory factors in the central Himalayas? And finally, what are the possible Triggers that lead slopes to failure?

Amongst the deep-seated rock slope failures in the Annapurna Massif, we will further narrow down to two particular phenomena, which we examine further in this chapter:

- **Giant rock avalanches in the upper Marsyangdi Valley** (Sections 2.5 and 2.6)
- **Large-scale non-catastrophic rock slope failures (i.e. DSGSDs)** (Sections 2.7 and 2.8)

We will work on the reconnaissance and investigation of giant rock avalanche deposits and DSGSD morphology, and will build on existing studies if available. We will temporally constrain slope failure events using absolute dating techniques and eventually inquire into their Causes, the relative importance of the various factors involved and hypothesise possible Triggers.

But first, we will provide an overview on the study of hazards and risks in the central Himalayas (Section 2.3.1), the role of bedrock landslides in mountain-scale erosion (Section 2.3.2), existing knowledge about Causes and Triggers of landslides in the central Himalayas (Section 2.3.3), and finally a short summary of relevant studies of giant landslides and DSGSDs in our study region (Sections 2.3.4 and 2.3.5). Which is then followed by explaining our methods (Section 2.4).

### 2.3.1 Hazards and risks from central Himalayan bedrock landslides

In Nepal, there is a large body of literature available on the contemporary phenomenon of landslides and the hazards and risks involved for society (e.g., Petley et al., 2007; KC et al., 2024). Landslides cause a considerable amount of fatalities and economic loss every year which has increased over the past few years. Particularly, in light of intensified initiatives aimed at enhancing and extending Nepal's road infrastructure in recent years, there has been a growing focus among researchers on assessing the vulnerability of roads to landslides (e.g., Hasegawa et al., 2009; Devkota et al., 2013; McAdoo et al., 2018; Gnyawali et al., 2020; Gurung et al., 2020). The objective of these studies is to mitigate the effects of landslides on both road construction and maintenance, thereby fostering the development of more financially sustainable roads for the future.

Deep-seated bedrock slope failures have been found especially relevant posing a potential secondary hazard

from Landslide Lake Outburst Floods (LLOFs) in the central Himalayan region (Weidinger, 1998; Shrestha and Nakagawa, 2016; Ruiz-Villanueva et al., 2017, sets focus on events in the western Himalayas, but gives overview to the phenomenon for the whole Himalayas). LLOFs can alter the affected river channel morphology substantially.

Albeit the non-catastrophic landslide activity induce lower hazards and risks in the central Himalayas than catastrophic bedrock failures, they have the potential of causing inconvenient difficulties, delays, and cost overruns for engineering projects located in affected areas (e.g., Thuro et al., 2004, example from the western Himalaya). Furthermore, non-catastrophic bedrock landslides can provoke catastrophic rapid-moving landslide phenomena within their deformed bodies and so they can be indirectly responsible for more hazardous events (e.g., Pánek and Klimeš, 2016; see also Intro).

### 2.3.2 The role of bedrock landslides in mountain-scale erosion

Due to its steep topography, active tectonics and wet climate, the Himalayan range is affected by intense erosive activity. In the central Himalayas, mean erosion rates reach ~1,6 mm/yr (Lupker et al., 2012; Morin et al., 2018) but can peak at 3 – 4 mm/yr in the High range (e.g., Burbank et al., 2003; Herman et al., 2010; Godard et al., 2012). Intense erosion of the landscape is driven by active river incision (Lavé and Avouac, 2001) and then transmitted to the hillslopes. Of the various slope erosion processes, bedrock landslides are considered to be the dominant process in active mountains. In the central Himalaya, this view has been confirmed by the large volume of sediments produced by landslides during past decades (Marc et al., 2019; Jones et al., 2021) and by the signature of unweathered bedrock in the sediment exported out of the range (Morin et al., 2018). Landslides are therefore one of the key processes governing the evolution of Himalayan landscapes.

Giant rock avalanches certainly play a decisive role with respect to erosion fluxes in the central Himalayas and likely have a significant impact on the evolution of the topography (Marc et al. 2019). For the understanding of mountain scale erosion in the area, it is essential to know the frequency of their occurrence and to have reliable volume estimates for individual events. An exhaustive record of these giant failures, including volume estimates and age constraints, is an important component for the study of erosion fluxes in the central Himalayas, which does not exist so far. As part of this PhD, we are working towards completion of these records, which will help researchers studying erosion budgets in the future.

Although the movement rates of non-catastrophic bedrock landslides are generally very low, they can potentially have a significant impact on erosion fluxes (Agliardi et al., 2013). By progressively damaging

slopes, they prepare slopes for secondary landslides that occur from their moving body (see Section 1.4.1). DSGSDs in the Himalaya are poorly studied, and there are hardly any studies on their present-day movement characteristics, let alone reconstructions of their paleo-movement behaviour over longer time scales (ka time-scales). This blank spot does not allow for any assessment of their quantitative contribution to erosional fluxes at the moment. Within this chapter we are presenting the first study in the central Himalayas investigating the paleo-movement behaviour of non-catastrophic landslides.

### 2.3.3 Causes and Triggers of central Himalayan rock slope failures

Contemporary small-scale (< $10^6$ $m^3$) and mostly shallow landslides are widespread in the central Himalayas, they occur predominantly during the monsoon season and are to a great extent controlled by precipitation (e.g., Marc et al., 2019; Jones et al. 2021). Threshold behaviour for shallow landslides triggered by rainfall was determined in the central Himalayas (Dahal and Hasegawa, 2008) and a minimum of monsoon precipitation is necessary to render slopes susceptible to failure (Gabet et al., 2004). Total landslide volume increases exponentially with the total amount of monsoon precipitation in an area and cloudburst events are a very important Trigger of contemporary landsliding in the region (Dimri et al., 2017; Jones et al. 2021; Bell et al. 2021). All studies on contemporary small-scale landslides in the central Himalayas show that precipitation and pore pressures in slopes are of great importance both as Preparatory factor and as Trigger for slope failures.

In general, landslides, also voluminous ones, are known to be triggered by earthquakes (Keefer, 1994). After the 2015 Gorkha earthquake (Mw 7,9), a five- to ten-fold increase in monsoon-related landslides was observed in some landslide-affected catchments (compared to 2010-2014), and in the following two years, landslide occurrence returned to pre-earthquake levels (Kargel et al., 2016; Roback et al., 2018; Marc et al., 2019; Jones et al, 2021). Outburst flood is another contemporarily observed mechanism that can trigger landslides in the central Himalayas (e.g., Cook et al. 2018).

Causes and Triggers of giant rock avalanches remain largely unexplored for the central Himalayas. This is due to the incomplete record of such events in the region and the often missing absolute age constraint for the individual events. At this stage, Causes and Triggers of the giant rock avalanches in the Annapurna Massif are mostly based only on speculation. The comprehensive studies on giant rock avalanches in the region by Fort (2011) and Weidinger (2006) propose structural preconditioning and glacial retreat as slope destabilising factors, and earthquakes or heavy rainfalls as possible Triggers. Lavé et al. (2023), based on a very precise reconstructed age for the Sabche cirque failure, assumed permafrost retreat as a result of a climatic warm phase as the most likely cause of the rock avalanche, but we will discuss this further below. For rock

avalanches in the northwestern Himalaya and Karakorum, previous studies have established a link between the prevailing climatic conditions in the past and the occurrence of giant bedrock landslides: Bookhagen et al. (2005) and Dortch et al. (2009) correlate dated catastrophic rock slope failures (depositional volumes of more than 0,5 $km^3$ and more than 0,1 $km^3$, respectively) with intensified phases of the Indian monsoon in the early Holocene and late Pleistocene. They argue that higher amounts of precipitation and consequently higher discharge during these periods led to increased pore water pressure in the slopes and increased erosion of adjacent river channels at their bases. This ultimately led to voluminous slope failures during these times.

### 2.3.4 Giant catastrophic bedrock landslides in the central Himalayas and the Annapurna Massif

The term “giant landslides” refers to rock slope failure events of considerable volume that are assumed to be the largest of their kind. In literature, there is no consensus on the lower limit of volume at which a rock collapse can be described as "giant" (e.g., Wen et al., 2004; Korup et al., 2007). In this PhD thesis bedrock failures bigger than 0,1 $km^3$ are considered as giant, as defined by Korup et al. (2007).

There are only a few giant pre-historic catastrophic bedrock landslide events, or rock avalanches, studied in the central Himalayas which have revealed themselves through the deposits they left behind (see for example lists by Fort (2011) and Korup et al. (2006)). Two better known examples of giant catastrophic rock slope failures further away from the Annapurna Massif are the Tsergo Ri rock slope failure in the Langtang area (e.g., Heuberger, 1986) or the Phoksumdo - Ringmo deposit, which dams a beautiful lake in the Dolpo region (Yagi, 1997).

In the Annapurna Massif and its close proximity, a few of such giant events are recognised and were already studied by researchers in the past (see also Figure 2.1).

In the upper Marsyangdi Valley, the following giant catastrophic bedrock failures are known:

- **Latamrang**: A > 1 $km^3$ sediment body clearly identified as a rock avalanche deposit (see Figure 2.5A). The giant bedrock failure detached from the slopes, south of the valley, consisting of calc-silicate and ortho-gneisses and quartzitic marble (Weidinger, 2006). The rock avalanche occurred ~5,4 ka BP and dammed the Marsyangdi River forming a lake that lasted ~200 hundred years and, which is testified by lacustrine sediments (Pratt-Sitaula et al., 2007).

- **Pisang Bowl** (a.k.a. Dhukur Pokhari, the locality just upstream of the rockslide deposit, the name translates to “small pigeon’s pond” from Nepali): A spectacular translational rockslide detached along bedding planes/schistosity of Tibetan limestone and schists on the left valley flank of the upper Marsyangdi River. This deposit has so far no absolute age constrain, but is considered as post-glacial and at least 1 $km^3$ in size (Weidinger, 2006). Bowl-shaped from folded strata, the failure surface of the Pisang Bowl rockslide presents itself spectacularly at the entrance to the highest, glacially shaped part of the upper Marsyangdi Valley (see, e.g., Nagaoka, 1990; Owen et al., 1998). A "shallow relict lake" exists upstream of the rockfall deposit, which resulted from the damming of the Marsyangdi River by the rockfall deposit and may have had a larger extent in the past (Fort, 2011).

- **Braga**: First recognised by Hagen (1969) as a rock avalanche deposit by comparing the characteristics of the sediments around Braga to the Flims rockslide deposit of the Swiss Alps (Heim, 1932). For a reach of about 10 km along the upper Marsyangdi River, the deposit material is outcropping and shows characteristic erosion structures (pinnacles) on both flanks of the valley (see Figure 2, B and C). Weidinger (2006) and Fort (2011) have investigated the locality, but their studies contradict each other with regard to the estimated original deposit volume (respectively 5 and 15 $km^3$) and the interpretation of the source area. No absolute age constraints exist for this rock avalanche deposits so far, but previous authors concluded an interstadial age of the deposit going back to before the last glacial advance, at the end of the last ice age. Such a chronology is supported by a dated Moraine sequence at Manang by Röthlisberger and Geyh (1986) which reaches back to the Mid-Holocene. Fort (2011) also mentions lacustrine deposits upstream of Manang.

To the south of the main ridge crest:

- **Sabche cirque**: The recent study by Lavé et al. (2023) recognizes the extensive breccia deposit south of the main Annapurna ridge line located in proximity to the Annapurna III and Annapurna peaks as the remnants of a gigantic rock avalanche deposit (Figure 2.1 and 2.5D). Further, they not only provide absolute dating for the timing of the rock avalanche event (~1,190 AD), but also estimate the failure volume (~23 $km^3$, the largest slope failure known to date in the Himalayas), convincingly determine a source area for this gigantic slope failure, and even explore pre-failure topographies. They are able to link the Sabche cirque as the origin of the Pokhara conglomerates, a huge sedimentary fill, one hundred metres thick that has buried the Seti valley downstream of the ridge collapse (see, Fort, 2010; Schwanghart et al., 2016; Stolle et al., 2017).

In the Kali Gandaki Valley, which borders the Annapurna Massif directly to the west (Figure 2.1):

> **Dhampu-Chhoyo**: Another giant rock avalanche deposit is found in the Kali Gandaki valley originating from HHS gneisses. The rockslide detached on a dip-slope on the southern flank of the valley about 4-5,5 ka BP and the deposit volume was estimated to ~3 $km^3$ (Fort, 2000; Zech et al., 2009). Deciphering the geomorphological evolution of the area is complicated. There is evidence for a large lake of older age that occupied the valley upstream of the rock avalanche deposit (see Fort, 2000). Damming of the Kali Gandaki by glaciers during the Ice Age seems plausible, or another older slope failure. The presence of other voluminous, younger, sedimentary deposits is also described.

Although the record for the central Himalayas and the Annapurna Massif is not complete, the deposits of giant catastrophic bedrock landslides seem to be especially abundant in and around the Annapurna Massif. 5 out of 9 giant and giant catastrophic rock slope failures in the central Himalayas are found there. Nevertheless, a bias from the already existing literature cannot be fully excluded. So far, the giant catastrophic rock slope failures in this exceptional place remain only partially explored by scientific research. Key important investigations, like absolute timing, a more systematic and careful mapping, volume reconstructions, or source area determination are missing so far for the upper Marsyangdi Valley deposits of Pisang Bowl and Braga. Also, there is the possibility of further additional deposits not recognised so far further upstream from Braga, which could have led to the conflicting views of the researchers working there before.

### 2.3.5 Non-catastrophic bedrock landslides in the central Himalayas and the Annapurna Massif

Studies on slow-moving bedrock failures, including DSGSDs, are very scarce throughout the whole Himalayas, especially in comparison to places where research on such phenomena is much more established like the European Alps or North America (e.g., Pánek and Klimeš, 2016; Lacroix et al., 2020).

When looking at remote sensing-based studies of deep-seated, non-catastrophic slope failures in the central Himalayas, it is not always clear whether the landslides under investigation are actually bedrock landslides or whether the failing material consists of soil or sediment. Lacroix et al. (2022) examined “slow-moving landslides” composed of fractured rock and/or weakened regolith in central Nepal, to the north-east of Kathmandu on the humid south-flank of the orogen (see Section 2.2.2), using space-borne optical and SAR imagery. Their studied landslides composed of monogenetic landslide material can be considered as non-catastrophic bedrock slope failures in a late stage of their evolution. The study captured co- and post-seismic

landslide movements after the 2015 Gorkha earthquake, revealing that landslide activity increased particularly after such a strong seismic event, with elevated activity sustained for about a month. In some cases, this activity was preceded by a lag-time of a few days. The authors suggest that elevated post-seismic landslide movements are provoked either by pore-pressure increases due to material compaction and the opening of vertical fractures, or by internal reconfiguration within the landslide body.

Bekaert et al. (2020) identified six "slow-moving landslides" in central Nepal in a setting very similar to the one studied by Lacroix et al. (2022), to the north-west of Kathmandu. They used InSAR analysis from satellite imagery to determine average deformation rates, finding consistent movement during two dry seasons (September to May) in the years 2014-2015 and 2016-2017. Despite the proximity of the 2015 Gorkha earthquake, which occurred between these observation periods, the long-term average dry season deformation rates (2.1 to 8.8 cm/year) were not significantly affected. The authors suggest that the slightly higher rates detected in the 2014-2015 period may be attributed to a greater amount of cumulative rainfall during the preceding monsoon season compared to the 2016-2017 period. Unfortunately, high-quality InSAR data to track landslide evolution immediately following the Gorkha earthquake was not available.

The study by Ambrosi et al. (2018) mapped hazard of landslides, including DSGSDs in two areas located in the High Himalayas in western Nepal and north-western Bhutan (altitudes between 1 800 – 7 000 m.a.s.l.; western Bhutan may strictly not be considered as central Himalayas, but the setting is very similar). Through photointerpretation of satellite data and interferometry technics (incl. InSAR), they found that not only 6-11 percent of the total area are affected by landsliding, but that DSGSDs occupy more than two-thirds of the surface area mapped as the landslide area. Often rapid-moving catastrophic, more hazardous landslides are nested within them. Most of the DSGSDs are identified as active, only 27% or 11% are considered as dormant/relict. So, active slope deformation strongly involving DSGSD phenomena is therefore not uncommon in their research areas.

Yagi et al. (2018) investigated a vast area in central Nepal (upper Sunkosi watershed) looking for deep-seated landslides through aerial photo interpretation. They found a similar percentage of total area affected by landsliding: up to 32 %, largely varying by the underlying lithology. The deep-seated landslides are described as dormant, occupy large areas (up to 10 $km^2$, or even more), and are more prone to develop on dip slopes (oriented along bedding, foliation planes) than on anti-dip slopes within identical lithological bedrock conditions. These dormant deep-seated landslides, i.e. DSGSDs, were not activated during the 2015 Gorkha earthquake, only shallow landsliding on lower parts of hillslopes occurred due to seismic loading.

Other studies from the High Himalayas of north-western Bhutan are at least partially concerned with slow-moving non-catastrophic bedrock landslides: Dini et al. (2019) chose a study area of ~7 550 $km^2$ with average elevations between 2 800 and 4 400 m.a.s.l. to identify and quantify displacements on slopes with InSAR

techniques, optical satellite images and a high-resolution digital surface model. Areas of displacements were classified and 77,5 % of these slope failures were assigned to rock slope failures, certainly including many DSGSDs. The abundance of slope failures is influenced by lithologies and structures in the bedrock, i.e. bedding, foliation, and tectonic faults, control failure mode and landslide frequency (structural control in most parts of the study region; see Dini et al., 2020).

Large-scale non-catastrophic rock slope failures, i.e. DSGSDs, in close proximity to the Annapurna Massif are described in the recent investigations by Chigira et al. (2022). Along the Kali Gandaki river (see Figure 2.1), occurrence of catastrophic rapid-moving rock slope failures and DSGSDs were studied in the field and with Digital Elevation Models derived from satellite data (see Figure 2.5E). The authors mentioned the constant and uniform dip of the gneissic lithologies in the area (strike NW - SE, dip at 30° - 50° to the NE) and conclude its strong control on the prevailing failure mode of the slope failures present: Dip-slopes, i.e. cataclinal slopes, are deformed by DSGSDs and brittle folding of the foliation planes develops in the lower sections of the slopes, i.e. buckling. DSGSD deformation on cataclinal slopes has characteristically altered the topography of the right valley flank of the Kali Gandaki. This is in contrast to the other side of the river, were anti-dip slopes, i.e. anaclinal slopes (see terminology by Cruden and Hu, 1996), are present. Here the valley flanks failed rapidly at four locations. Towards the north, the gneisses have a higher calcite content. Chigira et al. (2022) argue that the more competent lithology is responsible for the Dhampu-Chhoyo avalanche transitioning from a non-catastrophic to a rapid catastrophic slope failure (see Figure 2.1 and Section 2.2.3.2). Buckling deformation of the gneisses can be observed in the detachment area of the Dhampu-Chhoyo rock avalanche.

On the south-face of the Annapurna Massif, well below the permafrost zone, Gallo and Lavé (2014) analysed retrogressive erosion scars with satellite-based remote sensing data. These prominent features propagate upslope through fractured and deformed bedrock characterised by periods of increased activity and dominate erosional flows in smaller tributary catchments for at least several decades (see Figure 2.5E). The bedrock appears to be significantly affected by DSGSD activity on these slopes. This is supported by the presence of DSGSD features that are easily recognisable from satellite imagery on the south-facing Annapurna slopes.

Albeit the relevance of non-catastrophic landslide activity for hazards and risks in mountain areas is certainly much lower compared to catastrophic bedrock failures due to the slow- movement rates involved, non-catastrophic slope failures have the potential of causing inconvenient difficulties, delays, and cost overruns for engineering projects located in affected areas (e.g., Thuro et al., 2004, example from the western Himalaya). Furthermore, non-catastrophic bedrock landslides can provoke rapid-moving catastrophic landslide phenomena within their deformed bodies and so they can be indirectly responsible for more hazardous events (e.g., Pánek and Klimeš, 2016; see also Intro).

*Figure 2.5 (on next page): (A) Outcrop of Latamrang rock-avalanche deposit studied by Weidinger (2006); gn = gneissic base, db = pre-existing debris; dl = deformed layer, ld = cemented cataclastic rockslide material, md = direction of movement. (B) View towards east in the upper Masyangdi valley. Village in the foreground (right) is Braga, white mountain in the back is Tilicho Peak; rock slope failure deposits evolve into characteristic pinnacles by erosion. From Fort (2011). (C) Small-scale outcrop of Manang rock-avalanche deposit in Fort (2011): dark clasts with jigsaw-facies within whitish clastic matrix. (D) View of Sabche cirque towards NW (taken from an ultra-light airplane, with summit of Annapurna III in background). From Lavé et al. (2023). (E) DSGSD-type slope failure on a dip slope at Dana, right flank of Kali Gandaki valley. Scarp at the top indicated with yellow dotted line. View towards SW. From Chigira et al (2022). (F) Midhi Khola landslide on the south-facing Annapurna slope. View towards north-west, peak of Machhapuchhare in the back. From Gallo and Lavé (2014).*

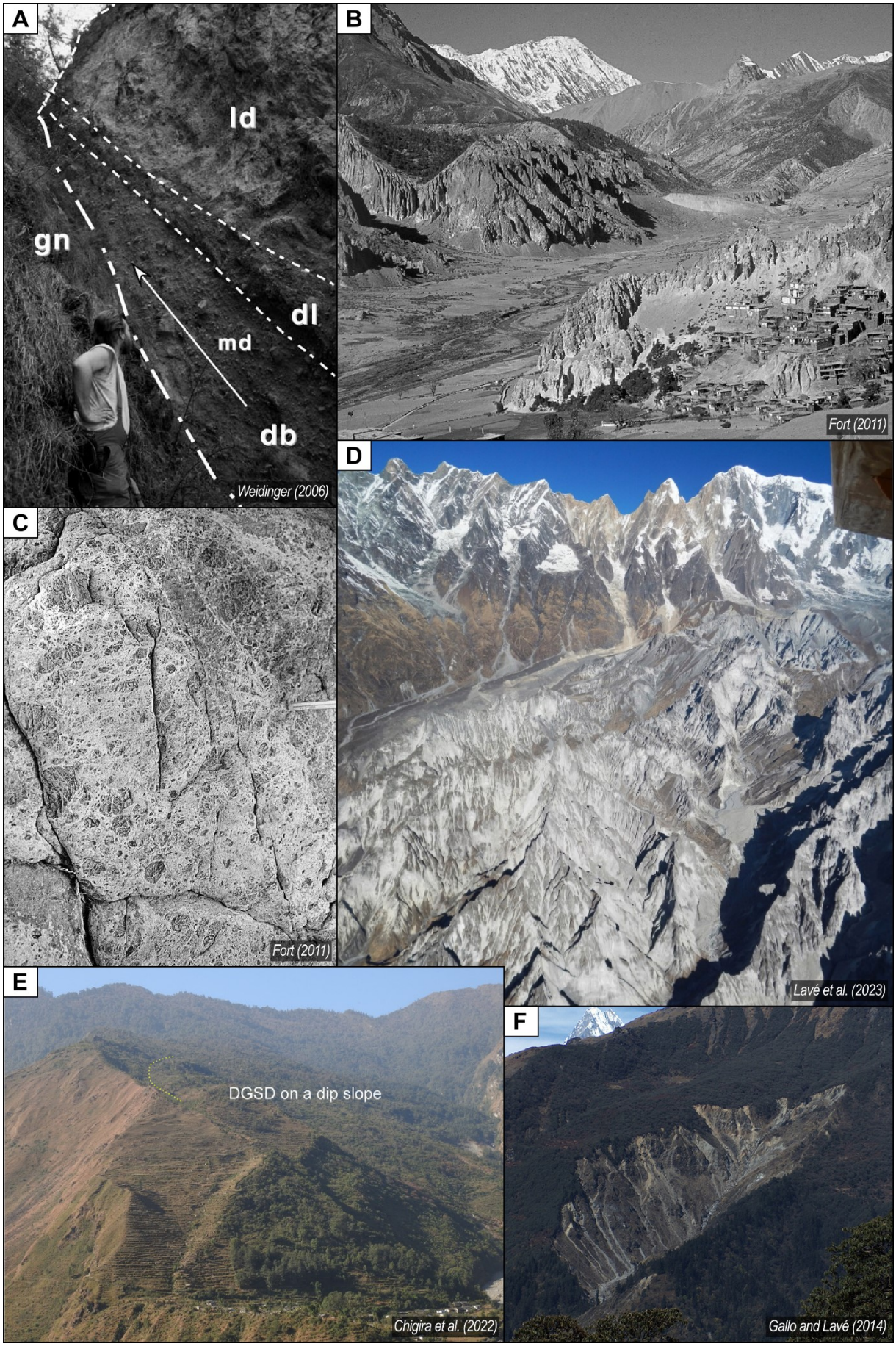
A
ld
gn
dl
md
db
Weidinger (2006)
B
Fort (2011)
C
Fort (2011)
D
Lavé et al. (2023)
E
DGSD on a dip slope
Chigira et al. (2022)
F
Gallo and Lavé (2014)

## 2.4 Methods

In the framework of this PhD-thesis we explore two sub-areas featuring catastrophic and non-catastrophic bedrock failures, respectively (two squares in Figure 2.1). Our research methods are outlined below for each one of the two targeted objects:

**Catastrophic giant rock avalanches of the upper Marsyangdi Valley:**

- General observations of deposits in the field (deposit and outcrop scale) – Section 2.4.1.1
- Reconnaissance and mapping with satellite data, including deposit volume reconstructions – Sections 2.4.1.2 and 2.4.4
- Cosmogenic nuclide dating (10Be and 36Cl) of boulders and failure scarps, additional 14C radiogenic carbon dating at one location (Pisang Bowl) – Sections 2.4.1.3, 2.4.2, 2.4.3.1, 2.4.3.2 and 2.4.3.3

**Non-catastrophic rock slope failures on the south facing slopes of the Annapurna Massif:**

- General observations of morphological features in the field – Section 2.4.1.1
- Reconnaissance and mapping with satellite data – Section 2.4.1.2
- Scarp paleo-movement reconstruction with help of 10Be cosmogenic nuclide dating – Sections 2.4.1.4, 2.4.3.1, 2.4.3.3 and 2.4.3.4
- Trench at scarp for additional movement reconstruction with the help of 14C radiogenic carbon dating – Sections 2.4.1.4, 2.4.2, 2.4.3.1 and 2.4.3.3
- Additional dating of surfaces and boulders in the area with 10Be – Sections2.4.3.1 and 2.4.3.3

## 2.4.1 Field study and mapping

### *2.4.1.1 Field surveys*

Prior to a field study dedicated to this PhD project in autumn 2021 that was attended by the PhD-student, the upper Marsyangdi area had already been visited, for partially separate purposes, by J. Lavé and M. Lupker, in 2014, 2017, 2018 and 2020. During these previous field excursions and in 2021, general observations about the geomorphological features and geology were made, and the giant catastrophic rock slope failure deposits were studied on outcrops located throughout the valley (Figure 2.6A). Sampling for cosmogenic nuclide exposure dating (10Be and 36Cl, see below) was conducted on m-scale boulders located on deposit surfaces and a failure scarp at Pisang Bowl (Figure 2.6 B-E). Sampled surfaces were chosen in consideration of avoiding post-depositional erosion or other relocation processes that could have possibly affected the sampled objects after the giant catastrophic bedrock landslide event. The selection of the sampling sites followed the recommendations given in the literature (e.g. Ivy-Ochs and Kober, 2008).

The field survey dedicated for investigating the non-catastrophic bedrock landslide at the Phalo Danda site was conducted in autumn 2021, following initial reconnaissance work by J. Lavé in 2013. These visits were preceded by previous field surveys conducted in the sector further east in the Khudi Khola valley (and on the ridge that separates the Midhi and Khudi Khola valleys; Khola means stream, small tributary river in Nepali) between 2009 and 2014 by J. Lavé and colleagues. Samples for cosmogenic nuclide dating of m-scale boulders and scarps dislocated or exposed by bedrock landsliding of these earlier field campaigns from the years 2010 and 2013 were treated as part of this PhD-thesis (see, e.g., Figure 2.7A). During the 2021 field survey, morphological structures were studied in an area between Khudi Khola valley to the east and Phalo Danda to the west. Surveying included taking photographs in the field and measuring orientation and dip of the bedrock's foliation at various places. At the Phalo Danda site, profiles of 10Be cosmogenic nuclide samples for scarp movement reconstruction were collected (Figure 2.7B, and see paragraph 2.3.2.3 below for further explanations) on the main and a secondary scarp of the Phalo Danda DSGSD. The same sampling procedures were used for the profile samples as for the cosmogenic exposure samples in the upper Marsyangdi Valley (see paragraph 2.3.1.1 above). In addition, a trench for scarp movement reconstruction was dug across an offset step of the main carp nearby one of the 10Be-profiles (see Figure 2.7C and section 2.4.1.3 below).




*Figure 2.6: (A) Looking at an outcrop of the Tilicho rock avalanche deposit, autumn 2021. (B) Boulder sampled for 36Cl exposure dating on rock avalanche deposit north of Humde, near the village of Ngawal, view towards NE, photo by M. Lupker, autumn 2020. (C) Boulder sampled for 36Cl exposure dating on rock avalanche deposit WSW of Humde, view towards SW, autumn 2021. (D) Boulder sampled for 36Cl exposure dating on rock avalanche deposit near Tilicho Lake, view towards ESE, photo by J. Lavé, autumn 2021. (E) Sampling of failure scarp at Pisang Bowl for 36Cl exposure dating, view towards SW, photo by M. Lupker, autumn 2020. (F) Sampling of wood fragments at base of Pisang Bowl rockslide deposit for 14C carbon burial dating, view towards SE, photo by J. Lavé, autumn 2018.*




*Figure 2.7: (A) Boulder sampled for 10Cl exposure dating on Khudi Ridge that toppled due to DSGSD activity, view towards NNW, photo by J. Lavé, 2010. (B) Profile of cosmogenic nuclide samples taken on secondary scarp for movement reconstruction, Phalo Danda DSGSD, view towards SW, photo by J. Lavé, autumn 2021. (C) Offset step of the main scarp at Phalo Danda DSGSD before a trench was dug, view towards NW, autumn 2021.*

*2.4.1.2 Spatial data sets used*

The following publicly available spatial satellite data sets were used for observations and mapping, alongside field observations and photographs taken in the field:

- ALOS Global Digital Surface Model "**ALOS World 3D** (AW3D30)", 30 meter resolution, version 3.1 (Takaku et al., 2020),
- **FABDEM** (Forest And Buildings removed Digital Elevation Model), based on Copernicus GLO 30 Digital Elevation Model, 30 meter resolution, version 1-2 (Copernicus, 2019; Neal and Hawker, 2023),
- High Mountain Asia (**HMA**) Digital Elevation Model derived from Optical Imagery, 8 meter resolution, version 1 (Shean, 2017),
- various **Google Earth Pro imagery**, including historical imagery (Google Earth Pro),
- **ArcGIS Pro 2D basemap "Imagery"** (Esri, 2023).

For further analysis of the morphology on the Annapurna south-face study area, high-resolution optical imagery was additionally used to produce the following data set:

- Digital terrain model derived from **Pléiades** optical imagery in "**Tristereo** acquisition" applying the NASA Ames Stereo Pipeline (ASP) software, 2 m resolution (Coeurdevey and Fernandez, 2012; Beyer et al., 2018).

The Pléiades Tristereo digital terrain model for the Annapurna south face was first produced and then further refined in-house by the PhD-student and collaborators (S. Daout, F. Leder, S. Breton).

The creation of maps was carried out on the geographic information system (GIS) software ArcGIS Pro (Esri, 2023).

*2.4.1.3. Dating giant rock slope failures*

Several strategies have been implemented to date giant rock slope failures (see the reviews on rock avalanches and landslides in general by Hewitt et al. (2008) and Pánek (2015, 2019):

- Dating of **the deposit surface**, mainly by cosmogenic exposure ages of blocks sitting on a surface that remained mostly undisturbed since the time of deposition.
- Dating **the failure surface**, i.e. detachment plane, of the slope failure, again using exposure dating.
- Dating **frictionite**, i.e. pseudotachylite glassy material from melting of the deposit material during deposition by OSL or fission track dating on zircon grains (Wagner, 1995; Takagi et al., 2007; see also Section 1.3.5 in Introduction Chapter).
- Dating **buried soils or entrained fragments of vegetation using 14C carbon burial dating**

In the northern Marsyandi Valley, we did not find any frictionite in the outcrops we observed. But we were able to find suitable objects to apply most of the dating strategies mentioned above. In one case, the Pisang Bowl rockslide, we were able to compare the results of different strategies.

*2.4.1.4 Reconstructing paleo-movement of non-catastrophic rock slope failures*

Two main strategies are commonly implemented to document the past activity of non-catastrophic bedrock landslides, i.e. DSGSDs: the excavation of 'palaeoseismic' trenches and cosmogenic exposure dating of scarps.

- **Trenching:**

  Excavating trenches over sedimentary bodies or soils displaced by large-scale non-catastrophic rock slope failures, i.e. DSGSDs, is a method rooted in paleo-seismology (e.g., McCalpin, 2009). This approach has gained prominence in recent decades and offers valuable insights into the long-term displacement behaviour along DSGSD-scarps (e.g., Pánek and Klimeš, 2016, and references therein). Trenches are usually dug perpendicular to the failure scarps were digging is feasible (substratum not too hard to dig). Offset or deformed strata in soils or sediments provide evidence for movement along the scarp. Sometimes cracks formed within the material of the hanging wall side that were later filled by material from above. These movement induced structures can be targeted by Quaternary dating methods, which allow the respective scarp activity to be temporally constrained (mostly luminescence or 14C carbon burial dating; see, e.g., Pánek and Klimeš, 2016 and citations

therein).

- **Cosmogenic exposure dating:**

  Paleo-movement reconstruction on scarps using cosmogenic nuclide dating can be found in literature for more than two decades now. At first such approach was applied on tectonic faults using the 36Cl-method in search of paleo-earthquakes and reconstruction of cumulative slip or paleo-slip rates (Zreda and Noller, 1998; Schlagenhauf et al., 2010; Benedetti et al., 2013). Later cosmogenic nuclides were also utilized for movement reconstructions on scarps related to non-catastrophic bedrock landslides, e.g. DSGSDs, by applying both 10Be (e.g., Hippolyte et al., 2009; Le Roux et al., 2009; Hermanns et al., 2013) and 36Cl cosmogenic dating methods (e.g., Zerathe et al., 2014).

### 2.4.2 Carbon burial dating (14C)

Organic material suitable for radiogenic 14C carbon dating has been prepared and measured at two different laboratories:

- The samples collected in 2018 by J. Lavé and M. Lupker in the upper Marsyangdi (samples of Sabche deposit in this manuscript, Figure 2.5F) were processed and measured at ETH Zurich. M. Lupker prepared the samples following classical ABA cleaning procedure and $CO_2$ ampoules were later sent for $^{14}C$ content measurement at the Ion Beam Physics Laboratory at ETH Zurich, Switzerland (Wacker et al., 2010).

- The samples collected in 2021 along the southern front of the High Range (trench across DSGSD fracture) were prepared (see, Dumoulin et al., 2017) and analysed at the LMC14 AMS facility 'ARTEMIS' (Moreau et al., 2013 ; Mook and van der Plicht, 1999).

For both data sets, final 14C-ages were converted into calendar years with the OxCal online calculator (Bronk Ramsey, 2021; version OxCal 4.4) using the Intcal20 calibration curve (Reimer et al., 2020). The ages are given in Anno Domini (AD) or in Before Present (BP), i.e. before 1950 AD, whichever is more convenient.

## 2.4.3 Cosmogenic nuclide dating

### *2.4.3.1 Beryllium exposure dating (10Be)*

The target mineral for 10Be surface exposure dating is quartz. 10Be exposure dating was mainly applied on the gneissic sample lithologies of the Annapurna south face. The samples were crushed and sieved at CRPG. For further purification of quartz the 250-1 000 µm grain fractions of the samples originating from gneissic lithologies underwent two passes of magnetic separation (Frantz). Afterwards, gneissic samples went through heavy liquid density separation (mostly with sodium polytungstate, some with diiodomethane) in order to remove mineral grains with higher density than quartz. This step is necessary for samples originating from Higher Himalayan gneisses from the Annapurna south face due to the varying but overall very high kyanite abundance in these rocks. The kyanite in these samples has proven to be very acid-resistant and has the potential to survive several acid treatments alongside the quartz in significant amounts. Kyanite crystals surviving quartz purification procedures would eventually alter the measured beryllium ratios in our samples and falsify the final results. The few samples consisting of marly schists and marbles that were treated for 10Be surface exposure dating (total of three) first underwent a de-carbonisation step with highly concentrated hydrochloric acid (HCl). This was done in an open beaker until calcite grains were consumed to a great extent under strong $CO_2$ outgassing.

In the following, all 10-Be samples were cleaned in multiple steps in Nalgene bottles with a mixture of highly concentrated 1/3 HCl and 2/3 hexafluorosilicic acid (H2SiF6) or a mixture of low-concentrated hydrofluoric (HF) and nitric acid (HNO3) (1%/1%). Some samples were treated with additional hot ultrasonic baths. Afterwards, samples were further treated for atmospheric beryllium removal. The atmospheric $^{10}$Be absorbed by the edges of the quartz crystals was removed with a three-step partial dissolution procedure with HF. Then, samples were weighed, diluted with a $^{9}$Be bearing solution (i.e. spike solution, with known $^{9}$Be concentration) and then underwent column chemistry and PH-precipitation steps for further beryllium isolation. Refer to Kohl and Nishiizumi (1992), Ditchburn and Whitehead (1994), and Stone (2004) for more details on the cleaning of 10Be exposure dating samples and chemical isolation of beryllium from quartz grains. After chemical isolation, samples were oxidised from solution to solid beryllium-oxide (BeO), pressed to AMS targets at CRPG, and finally sent to CEREGE were they were subsequently measured at the ASTER platform (calibrated with in-house standards: see, Arnold et al., 2010; Braucher et al., 2015; external AMS error of 0,5%).

Two 10Be exposure samples, UM-18-9 and NEQ-17-5-59, were handled by our collaborator M. Lupker: They underwent similar procedures of mineral separation, acid cleaning, and chemical isolation treatment than

the other samples processed at CRPG, but in the laboratories of the Geological Institute at ETH Zurich, Switzerland. These two samples were subsequently measured at the Laboratory of Ion Beam Physics at ETH Zurich using the 0.5 MV TANDY AMS facility (Christl et al., 2013).

After receiving the results back from CEREGE (and ETH Zurich, in case of UM-18-9 and NEQ-17-5-59) concentrations were corrected with analytical blanks (for both, chemical isolation and AMS measurements) and then exposure ages were calculated with a development version of the online calculator CREP (Martin et al., 2017; Schimmelpfennig, 2022). We used the Lal/Stone time dependent scaling scheme (Lal, 1991; Stone, 2000; Balco et al., 2008), the ERA-40 atmosphere database (Uppala et al., 2005) and the RPI-calibrated VDM geomagnetic database (Pavón-Carrasco et al., 2014; Lifton, 2016) for calculating exposure ages. As 10Be production rate a weighted mean of all existing production rate calibration sites was chosen (4,04 ± 0,19 at/g/yr). Exposure ages were calculated on 29 January 2024 with an assumed rock density of 2,65 g/cm$^3$ for all samples. All ages are given in Before Present (BP), i.e. before 1950 AD.

*2.4.3.2 Chlorine exposure dating (36Cl)*

36Cl exposure dating was preferred over 10Be for samples originating north of the STD in the upper Marsyangdi Valley. Here, sample lithologies range from meta-carbonatitic marly schists and marbles, to limestones, shales, and quartzites. These rock-types not necessarily lack a substantial content of quartz (needed for 10Be exposure dating, see above), but quartz grains in these lithologies have sometimes very small grain sizes and appear to be intergrown with other crystals. If not targeting quartz veins, it can be extremely difficult to perform the mineral separations and quartz purifications required for 10Be sample preparation in these lithologies.

The samples were crushed at CRPG and aliquots (by use of riffle splitter) were taken for later analyses of major and trace elements at the French National Facility for geochemical analysis (SARM) at CRPG (Supplementary Table A2.2). The sample material was then sieved to 250-1 000 µm grain fractions and then sent to the Centre Européen de Recherche et d'Enseignement des Géosciences de l'Environnement (CEREGE, Aix-en-Provence, France). There, samples were further processed by V. Guillou following standard procedures (Stone et al., 1996; Schlagenhauf et al., 2010). $^{35}Cl/^{37}Cl$ and $^{36}Cl/^{37}Cl$ ratios of samples were measured after isotope dilution by accelerator mass spectrometry (AMS) at the ASTER platform at CEREGE.

36Cl surface exposure ages were calculated considering chemical compositions (SARM analysis) using a development version of the online calculator CREP (Cosmic Ray Exposure Program) which recently enables the calculation of 36Cl samples (Martin et al., 2017; Schimmelpfennig, 2022). Like for the 10Be-samples (see above), the Lal/Stone time dependent scaling scheme (Lal, 1991; Stone, 2000; Balco et al., 2008), the ERA-40

atmosphere database (Uppala et al., 2005), and the RPI-calibrated VDM geomagnetic database (Pavón-Carrasco et al., 2014; Lifton et al., 2016) were used for the calculation. We adopted values for $^{36}Cl$ spallation production rates from Schimmelpfennig et al. (2011) for Ca (42,2 ± 4,8 at/$g_{Ca}$/yr), from Schimmelpfennig et al. (2014) for K (145,5 ± 7,7 at/$g_{K}$/yr), from Moore and Granger (2019) for Fe (1,628 ± 0,04 at/$g_{Fe}$/yr), and from Masarik (2002), Stone et al. (2005), and Marrero et al. (2016) for Ti (3,8 ± 0,4 at/$g_{Ti}$/yr). Further, a neutron production rate from Cl of Marrero et al. (2016) was adopted (691 ± 186 at/$g_{Cl}$/yr). Exposure ages were calculated on 29 January 2024 with an assumed rock density of 2,65 g/cm$^3$ for all samples. All ages are given in Before Present (BP), i.e. before 1950 AD.

*2.4.3.3 Corrections and exposure age calculation*

In order to calculate exposure ages from Terrestrial Cosmogenic Nuclide (TCN) concentrations, a few corrections are required: topographic shielding, snow or soil shielding, and surface erosion corrections.

- ***Topographic shielding***

  If applicable, individual close-range shielding masks for later topographic shielding calculations were measured with a hand-held compass and recorded. For inclined sampled surfaces, the inclination and orientation of the sampled surfaces were also noted also for later topographic shielding calculations. Otherwise, for all the samples, the far field topographic shielding was computed later in the lab using a Matlab code, using the FABDEM digital elevation model with a resolution of 30 m (see Section 2.4.1.2 above). Far field and close-range shielding masks were incorporated into the final calculation, along with the sample surface dip and orientation, where applicable.

- ***Shielding by snow and soil***

  Snow shielding needs to be considered as especially relevant for the samples located at high elevation (> 3500m) due to snow cover mostly during the winter months. Especially for the Tilicho Lake samples, the shielding effect of a persistent layer of snow lasting over several months of the year should not be neglected. In the absence of any datasets that exist for snow cover in the upper Marsyangdi Valley, we based our estimates of snow cover thickness and durations on a meteorological dataset from Putkonen (2004). This dataset includes snow thickness records from the eastern Annapurna Massif lasting from the years 1999 to 2003, and enables to derive a relationship between snow cover thickness and duration as function of the elevation. Because of potential variations of snowfall amount between the southern slopes of the Annapurna Massif, were most of Putkonen (2004)'s data was collected, and the upper Marsyangdi Valley, and because of potential variations of snowfall amount during the time period between present day and the initial exposure

of a given sample, the snow cover shielding present large uncertainties. In addition, snow cover on a boulder highly depends on boulder height, or exposure to wind and sun light. To simplify our snow cover estimates, we assumed, however, uniform snow cover for all samples within a particular sampling area. Snow shielding was calculated following Dunai (2010), with an attenuation coefficient of 160 g/cm$^2$, and with an estimated average density of snow cover of 0,5 g/cm$^3$ (Supplementary Table A2.1). Despite the large uncertainties, the limited amplitude of the snow shielding correction (maximum of 10%) means that this correction has a minimal impact on our age calculation, even for the most elevated samples.

The 10Be-samples were treated identically to the 36Cl-samples when calculating snow shielding. Two samples for 10Be surface exposure dating were covered with soil or loose sediment before sampling. Cosmogenic rays are shielded from the rock surface by these coverings, similar to snow. We assumed that the thickness and density of the soil/sediment cover remained constant during the entire exposure and soil/sediment shielding was calculated following Dunai (2010), with an attenuation coefficient of 160 g/cm$^2$, and with an estimated average density of the soil/sediment layer (see Supplementary Table A2.1).

- ***Surface erosion***

  An assessment of the erosion of the rock surface was carried out before sampling and the thickness of the cosmogenic exposure sample was noted after sampling.

  For biotitic, gneissic samples, surface weathering is commonly observed and is manifested by quartz-rich veins or pegmatites in slight relief from the average surface of the rock. This weathering-controlled erosion of the surface is estimated to reach a few millimetres to a few centimetres. Such a priori limited erosion does not require correction for surface erosion (related error lower than the analytic uncertainty).

  By contrast, the TSS marly schistosed rocks, sampled at high altitudes, are subject to frost-cracking induced by frequent freeze-thaw cycles. Their foliated structure is conducive to weathering along foliation planes, and in many cases, the surface of the blocks shows significant signs of erosion by chipping or spalling. The conditions that control erosion on exposed rock surfaces can vary greatly from site to site and are highly dependent on the individual rock fabric, and its lithologic nature (chipping increases with the marly nature). The value of the erosion rates that affect sampled rock surfaces are therefore hard to quantify in our study. Furthermore, in the case of chipping, the assumption of a constant rate of erosion over the entire period of exposure, as is commonly assumed, may be called into question. Therefore, incorporating erosion in exposure age considerations and calculations remains a challenging task. Targeting surfaces in the field that are as pristine as possible showing minimal evidence of erosion is the best that can be done. In our study

we decided to deliver a quantitative comment on the matter of surface erosion rather than calculating our samples with any assumed exposure-time-averaged erosion rate. So, input erosion rates are zero in all our calculations. This consequently means that, strictly speaking, all our calculated exposure ages need to be considered as minimum ages.

Finally, after corrections applied and individual age calculation, we calculated weighted means of the most trustworthy exposure ages with the online calculator IsoplotR (version 6.0, see Vermeesch, 2018). While excluding outliers from these calculations, we provide singular ages for individual formation events of rock slope failure deposits. In general, to enhance the robustness and reliability of cosmogenic exposure dating results for geomorphic features originating from momentary events in the past, which includes catastrophic rock slope failures, it is best to process as many samples representing the individual formation event as possible. More individual exposure ages will eventually make outliers from unconstrained analytical errors or samples with problematic exposure histories recognizable.

*2.4.3.4 Scarp movement reconstruction*

Concentrations measured from the samples are expected to increase towards the top of the exposed scarp. However, deriving a history of movement cannot be achieved simply by applying only the usual corrections as we know them from simple, classical object dating, like boulders, and using CREP (far range topo-shielding, scaling scheme, atmospheric and geomagnetic corrections; see Sections 2.4.3.1 and 2.4.3.3 above). To understand the past movements on a DSGSD scarp accurately, it is crucial to consider the potential complex shielding history of each measured sample located on the scarp. The shielding to which the samples were subjected is dependent on both the movement history and the specific geometry of the scarp (see Schlagenhauf et al., 2010; and Figure 2.8).

The concentration profile expected on the scarp can be modified by the following movement characteristics:

- **Type of movement**: Discrete offset events on the scarp at certain moments in the past (step-like movement) or continuous creep, or alternation of both

If we assume step-like movement (see Figure 2.8B for periodic rupture of constant offset and Figure 2.8C for one step instead of three with two different timings):

- **Number of discrete steps**: one offset event or multiple offset events on the scarp

- **Timing of discrete steps**: chronological succession of individual offset events, clustering of offset events or constant intervals

- **Created offset by each individual step**: The displacement of the hanging wall can be variable, large or small steps

With only a few measurement points, a measured profile can be used to reconstruct movement, but this is by no means unambiguous, even if the geometrical conditions of the scarp are well constrained. There may be different displacement histories fitting the same concentration profile. This ambiguity is further exacerbated by measurement inaccuracies and other sources of error. Additionally, the exhumation history of the site, i.e. surface erosion on and off the scarp, affects the cosmogenic nuclide concentrations further (Figure 2.8C). Finally, a colluvium wedge at the bottom of the scarp has an impact on the concentration on the scarp, too.

Reconstructing the movement history of a scarp from a profile of cosmogenic nuclide measurements necessitates an advanced calculation technique involving an iterative scheme that can simulate numerous individual movement histories. Eventually, the most likely fits are found by assigning a weighting parameter

to each fit (see Schlagenhauf et al., 2010).

To reconstruct the movement history of the scarps sampled with 10Be exposure dating profiles at the Phalo Danda site, a Matlab code was developed by J. Lavé. The code randomly generates different discrete slip scenarios on the fracture plane and calculates the predicted TCN concentrations for each sample. Scenarios with minimum Root Mean Square (RMS) between measured and calculated concentrations are then considered as possible solutions. In the code, the variables that can be varied randomly are: the number of slip events (or alternatively the offset value of the discrete events),the timing of the discrete, and the initial concentration of the samples at surface and at depth.

As the scarp develops, the code calculates the instantaneous TCN production for each sample, due to the spallation and muogenic components, as a function of the geometric configuration of the escarpment at that moment. For example, a sample not yet exhumed along the fault mirror (Figure 2.8) will accumulate TCN as a result of exposure to cosmic rays passing through both the footwall of the fracture plane and the rays passing through its hanging wall.

With regard to the initial concentration of the samples, for two sampled profiles we observe a scarp that offsets an initial smooth surface. Because the scarp activity seems to be older than this smooth surface (see discussion further), we presume that the smooth surface was created during a phase of active erosion, either by sub-glacial erosion, or by intense frost-cracking processes (e.g. Tucker et al., 2011).

These two distinct initial surface erosion options can be considered in the code: either applying a constant erosion rate to the site or assuming from the removal of several meters of rock by glacier erosion. In both cases, the surface erosion is supposed to drop to nearly zero after this phase of accelerated denudation, i.e. during the later development of the topographic expression of the scarp. To well constrain this pre-ruptures concentration, we collected one sample on the smooth surface at a few meters from the scarp along the footwall. This sample is considered as representative of the concentration at the top of the profile. This requires to know with precision the exact position of the scarp edge, or in case of uncertainty to account for it in the calculation. Snow and far-field topographic shielding was addressed using the same procedure employed for the other cosmogenic nuclide samples presented in this thesis, and assumed uniform for all samples within a given scarp. The calculation can also take into account the presence of a colluvial wedge at the base of the escarpment, which develops correlatively with the height of the escarpment.

Finally, to visualize the slip scenarios that are compatible with the TCN concentrations measured along the profile, a probability density map is shown.

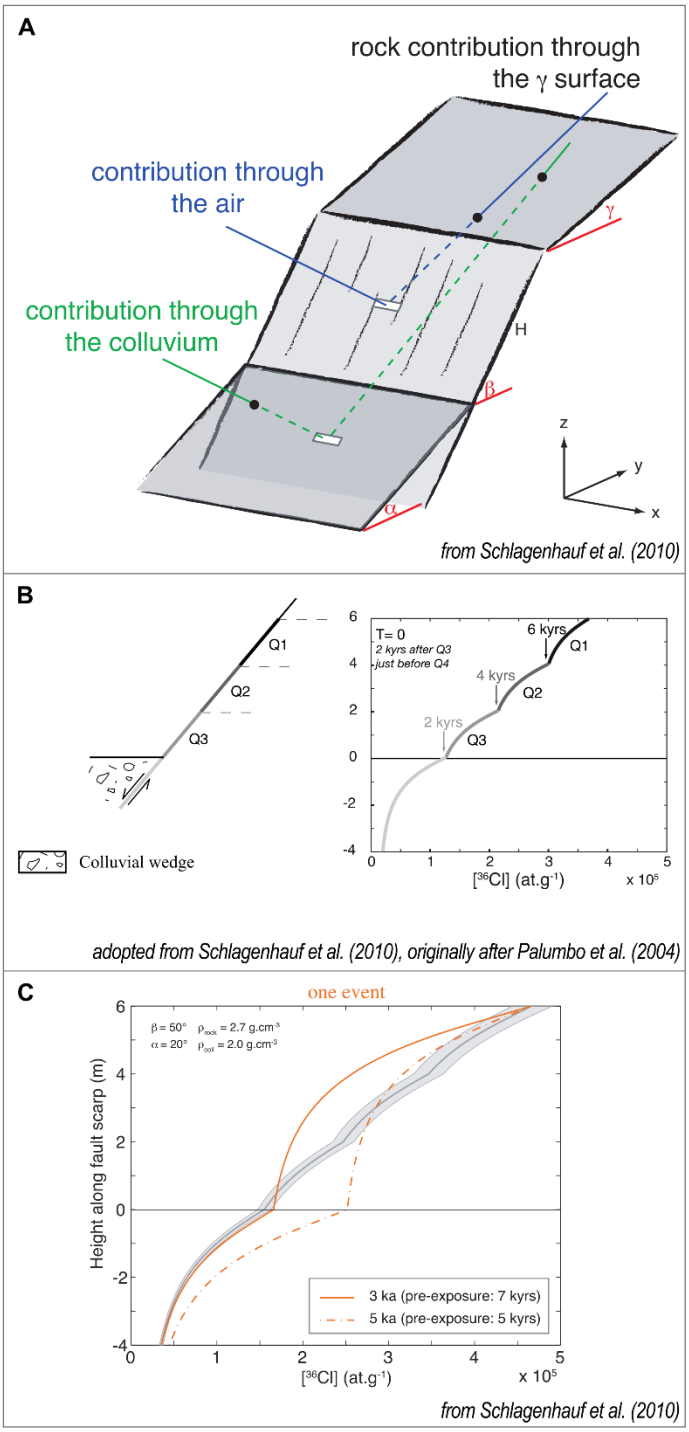


*Figure 2.8: (A) The sketch shows the different paths that cosmogenic radiation can take when it reaches a sample on the scarp plane. In order to take the shielding of the sample into account, the geometry of the scarp must be considered. From Schlagenhauf et al. (2010). (B) Schematic plot showing the theoretical cosmogenic nuclide concentration curves (here $^{36}$Cl) on the scarp. Earthquakes occurred regularly every 2 kyr and the offset was constant at 2 m for each event. Adopted from Schlagenhauf et al. (2010), originally after Palumbo et al. (2004). (C) Impact of the number of discrete steps (one and three) and exhumation history (for one step) on the cosmogenic nuclide concentration curve (here $^{36}$Cl). The grey band represents a ±5 per cent analytical uncertainty. From Schlagenhauf et al. (2010).*

2.4.4 Volume reconstruction of valley deposits

In literature, little is said about the approaches or strategies researchers applied for volume estimates of rock avalanche deposits. We guess this estimates are done fitting easy geometries, likely different kinds of prisms in the valley and the deposit extend. Possibly this is done with a good amount of confidence and negligence of second-order topographic features, like sediment bodies related to glacial or fluvial deposition before or after failure, or rock ledges on the valley slope. Such simplifications may well be justified with regard to the large uncertainties that can be involved.

In this PhD work, we try to go a bit further, also motivated by the size and complexity of some of the deposits in the upper Marsyangdi Valley and their advanced erosion state. As the reader will notice below, Braga and Tilicho deposits spread over multiple valleys and are highly eroded. Probably other good examples of volume reconstructions of rock avalanches can be found in literature, or of other topographic features comparable in size and shape. However, we are familiar with the elaborate deposit and pre-failure topography reconstructions by Lavé et al. (2023) of the Sabche cirque rock avalanche (see section 2.2.3.2 above), and with the thorough approach of Zangerl et al. (2021). It needs to be noted here that Zangerl et al. (2021)'s approach can consult and rely on drilling and seismic data, as well as extensive field observations from an overall comprehensive history of investigations. This is certainly not the case in a remote field area like the Annapurna Massif when working on deposits with limited scientific investigations so far. For processing spatial data for the volume reconstructions, we used the GIS-software ArcGIS Pro (Esri, 2023). The mapping results, additional spatial data, and satellite images (also with Google Earth Pro) were consulted (see Section 2.4.1.2 for more details on the mapping and datasets used).

Inspired by the methods of the research contributions mentioned above, we developed an approach for this PhD thesis and list the most important steps below:

- **Creation of a base digital surface model without holes and cleaned from significant artefacts**: We down-sampled the ALOS World 3D 30 m resolution global digital surface model to the 8 m resolution of the High Mountain Asia (HMA) digital elevation model in order to fill holes in the HMA model. A unified surface model with the most detailed possible representation of the topography was created. Smaller holes and artefacts were removed from the raster dataset using dedicated tools available within ArcGIS Pro (Esri, 2023). At the three ridges leading to the peak named Roc Noir (one of them comes down from Annapurna I summit), the HMA model has holes and the ALOS one has serious artefacts. Here we used digitised contour lines of a topographic map of these ridge lines (TopoMap – "TILICHO", 2001) for creation of an alternative digital surface model. This was done only for the purpose of visualisation of our results. However the volume reconstruction was not affected by these artefacts.

The following steps were performed for each deposit individually:

1. **Reconstruction of pre-failure topography**
    - Creation of 3D points on valley flank surfaces that are assumed to have remained unchanged since the time of deposition (i.e. preferably bedrock surfaces with no signs of post-depositional erosion).
    - Creation of a TIN from these points and addition of more surface points. The pre-depositional topography was modelled by use of interpolations, assumptions, and sometimes best guesses.

      Challenges and possible sources of errors:

      It is sometimes difficult to identify areas of post-depositional erosion (e.g. epigenetic gorges) on the valley flanks, or make assumptions about sediments that were already present in the valley before or were deposited after the rock-avalanche. This is especially challenging where only limited or no field observations were conducted (Figure 2.9).

2. **Reconstruction of post-failure topography**
    - Definition of an assumed outline of the deposit

      Challenges and possible sources of errors:

      The outline may be overestimated or underestimated due to onlap on other older sediments (including other rock-avalanche deposits), erosion of the deposits, or newer sedimentation (alluvial fills or glacial moraines).
    - Creation of 3D points on deposit top surfaces that were not or not substantially altered after the deposition of the rock avalanche deposit. The pre-depositional topography of the deposit was modelled by use of interpolations, assumptions, and sometimes best guesses.

      Challenges and possible sources of errors:

      If erosion has removed significant portions of the deposit, interpolations between points separated by considerable distances (e.g., across the valley) may be required, and second-order topography such as ridges or depressions cannot be reconstructed (see Figure 2.9).
3. **Raster calculations**
    - Once the two reconstructed TIN surfaces are finalized, they can be converted into raster datasets, enabling further calculations. These raster datasets have a consistent pixel size of 8 m, matching that of the base digital surface model.
    - Where the raster data sets representing pre-failure topography and post-failure topography overlap, the **initial deposit volume ($V_{D,init}$)** can be calculated:

$$V_{D,init} = \sum_{i=1}^{i=m} A(z_{i,postDepo} - z_{i,preDepo}) \cdot [z_{i,postDepo} - z_{i,preDepo} > 0] \quad (2.1),$$

with $z_{i,postDepo}$ and $z_{i,preDepo}$ representing the pixel elevation of pixel i of the reconstructed post-depositional and pre-depositional surfaces, respectively, A is the area of one pixel (64 $m^2$), and m is the number of pixels considered for the calculation. Differences in pixel height are only considered for the summation if they are greater than zero. This renders a smaller impact on the sum by areas the post-deposition surface is erroneously below the pre-deposition surface.

- By subtracting the reconstructed pre-depositional topography from the present day topography (represented by the base digital surface model), we get the **remnant deposit volume ($V_{D,remn}$):**

$$V_{D,remn} = \sum_{i=1}^{i=m} A(z_{i,postDepo} - z_{i,presentTopo}) \cdot [z_{i,postDepo} - z_{i,presentTopo} > 0] \quad (2.2),$$

with $z_{i,presentTopo}$ representing the pixel elevation of pixel i of the present day topography. Again, differences in pixel height are only considered for the summation if they are greater than zero.

- Finally the **deposit volume that got eroded since deposition ($V_{D,erod}$)** is simply calculated as:

$$V_{D,erod} = V_{D,init} - V_{D,remn} \quad (2.3).$$

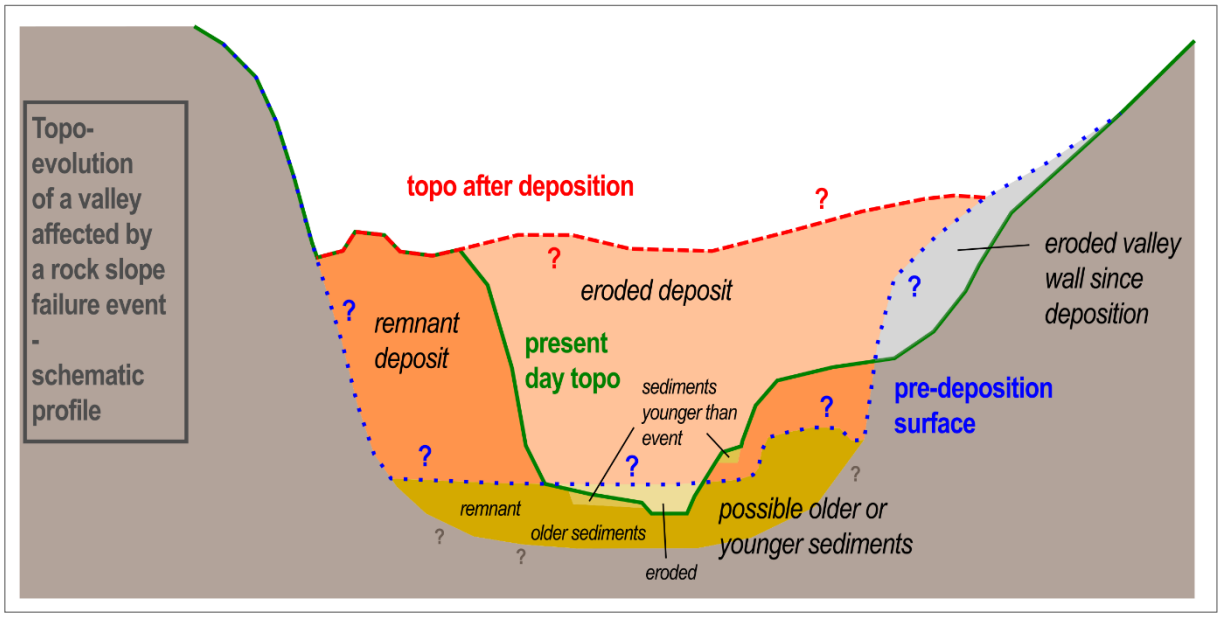


*Figure 2.9: Schematic cross-section of a valley showing altered topography resulting from a rock slope failure event occurring in the past. Apart from the present day topography, contacts still buried by the deposit and contacts already eroded in the time after deposition remain unknown and must be estimated as best as possible through assumptions and interpolations. This causes uncertainty in the volume reconstruction. The presence of other sediments in the valley (fluvial, glacial, or other landslides), both older or younger than the rock slope failure, can further complicate the situation.*

## 2.5 Results – Upper Marsyangdi

### 2.5.1 Pisang Bowl

#### *2.5.1.1 Field observations and mapping – Pisang Bowl*

The location of the Pisang Bowl or Dukhur Pokhari rock avalanche within the upper Marsyangdi Valley is peculiar: it is situated at the transition between an incised V-shaped valley to the east and a wider U-shaped valley bottom to the west (See Figure 2.10). The rock avalanche deposit is sitting mostly on the right river bank vis-à-vis a spectacular bowl-shaped hillslope. This steeply dipping slope (~30° in its central part) of the Pisang Bowl corresponds to the periclinal termination of a wide syncline affecting the THS series. It was identified as the source area of the rock avalanche deposit that resulted from a planar translational detachment (Weidinger, 2006) (Figure 2.11). The lithology of the outcropping rocks at the base of the Pisang Bowl, which can be observed on the failure surface and in a small epigenetic gorge at the upstream end of the deposit (see Figure 2.6F and mapping below), consists of competent, rather massive to schistose, meta-carbonate, micaceous marbles (see Figures 2.6, E+F; 2.12, C+D; and A2.1, C+D). The boulders sampled along the various ridges of the rockslide deposit show lithologies alike (Figures 2.12B; and A2.1, E-H; see also chemical compositions of 36Cl-samples, Figure A2.2). This lithological correspondence, together with the absence of vegetation in the bowl surface, is the main argument in favour of the relationship between the Pisang Bowl and the rockslide deposit. The strong asymmetry of the rockslide deposit in the valley, with a majority of the material on the valley side opposite to the rockslide scar, is attributed to the high initial elevation of the rockslide source and subsequent elevated kinetic energy of the falling mass when it reached the valley floor.

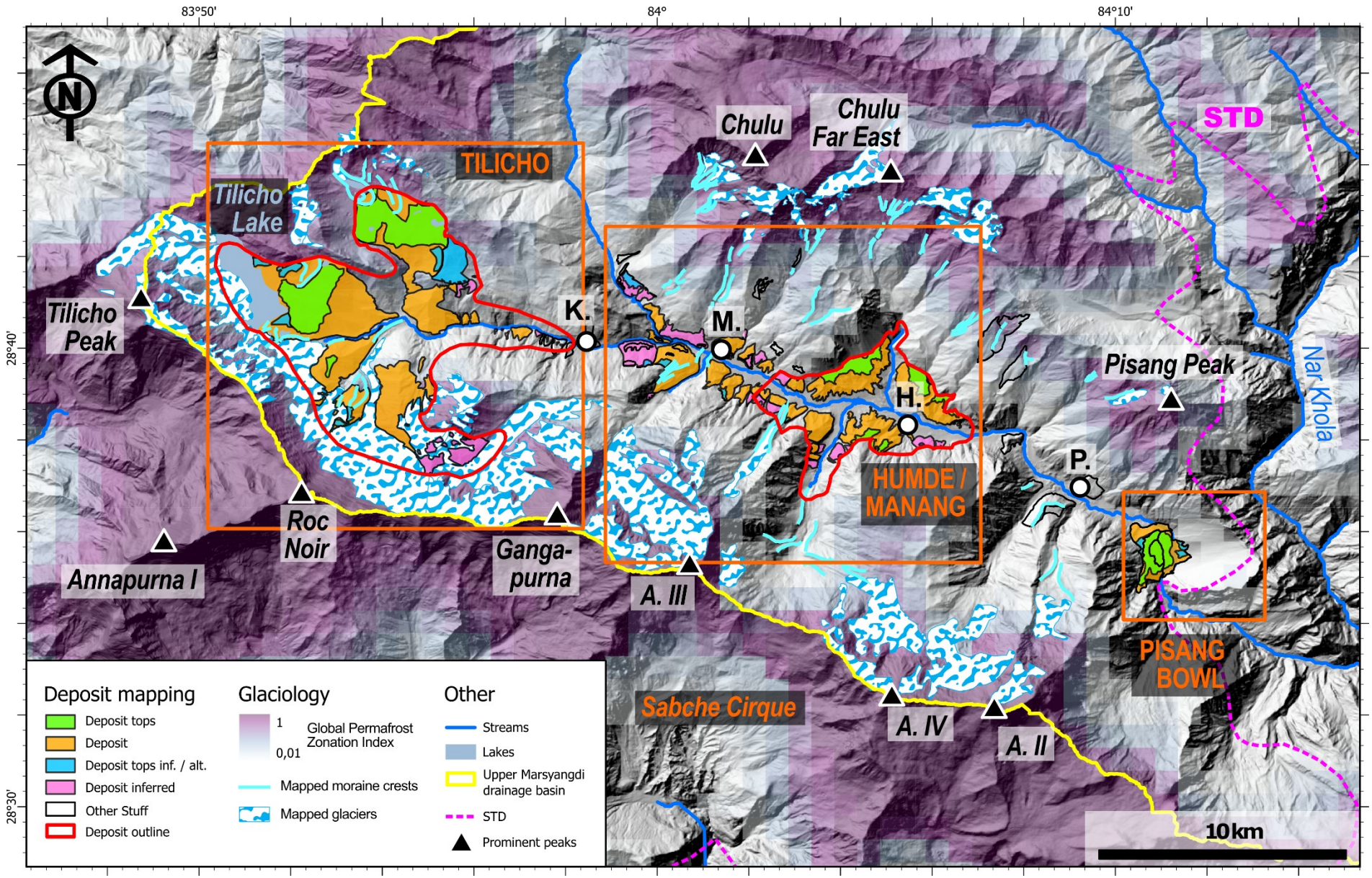


*Figure 2.10: Overview of mapping performed on rock avalanche deposits and other geomorphological features in the upper Marsyangdi Valley. See Figure 2.1 for the map location in the Annapurna massif. Additionally, in this map, the glaciological characteristics of the valley are shown: the Permafrost Zonation Index (PZI) (Gruber, 2012) and mapped moraines and glacier ice. K. = Khangsar, M. = Manang, H. = Humde, P. = Pisang. STD from Parsons et al. (2014).*

The downstream and southern part of the rockslide deposit has been deeply eroded by the Marsyangdi River, exposing the rockslide material along a steep, high slope, i.e. escarpment (Figure 2.12 A, E, and F). Large-scale structures or unconformities were not clearly spotted within this large outcrop and the material appears overall very massive. In some places, the erosion of the steep slope is forming pinnacles in a similar way than observed further upstream among the rock avalanche deposits described by Fort (2011) around Braga (Figure 2.5B). From distance, the diamictic sediment consists of poorly sorted, angular to sub-angular blocks with a high matrix content (Figure 2.12 A, E, and F). Its characteristics do match an intensely fractured version of the typical "main body facies" in rock avalanche deposits (see Section 1.3.5; Figure 1.5; and Hewitt et al., 2008; Weidinger et al., 2014).

While mapping the Pisang Bowl deposit with satellite imagery and a high resolution digital surface model (HMA, 8 m resolution; see Section 2.4.1.2 for more details) the deposit surface was divided into three categories: preserved surface of the original deposit top, slightly modified or altered deposit tops, and highly modified surfaces (original deposit tops are eroded away) (Figure 2.13). The topography of the rockslide deposit is characterized by three individual ridges, separated by topographic depressions (Figure 2.13). The First and the Third Ridge are interpreted as preserved surfaces of rockslide deposits. In contrast, the second ridge was interpreted as a gravitational failure of the highest Third Ridge. It is suggested by the transition between ridges two and three, as well as by the failure head scar that dissects the Third Ridge, which has an arcuate shape typical of rotational slides (see white arrows in Figure 2.13). Although this hypothesis requires further fieldwork to be fully confirmed, we have therefore chosen not to study and sample this second ridge.

The three ridges are covered in pine trees and relatively dense shrubbery. However, at the northern transition between the First and the Third Ridge, and as well as at the west of the Third Ridge along a relatively flat depression, non-vegetated fields of chaotic boulders (m-scale boulders) can be found. These boulder fields resemble a typical top most unit in rock avalanche deposits, and referred to as "carapace" in literature (see Section 1.3.5; Figure 1.5; Figure 2.12B; and Hewitt et al., 2008; Weidinger et al., 2014). The area from which the material of the Pisang Bowl rock avalanche deposit once detached was estimated. Based on transitions in the surface structure and presence of vegetation that can be seen at the edge of the bowl, a maximum possible detachment area was mapped (see Figure 2.12D; and Figure 2.13).

The volume of the rockslide deposit was estimated to range between 0,3 and 0,5 $km^3$ depending on the chosen initial geometry of the valley, V-shaped or U-shaped respectively (M. Groult and A. Diarra, Mémoire of second year students at ENSG, under the supervision of J. Lavé). Despite the erosion of the southern edge of the deposit by the Marsyandi River (see escarpment in Figures 2.11B; 2.12, A+E+F; and 2.13), most of the initial volume has remained preserved: this is partly due to the pinning of the Marsyandi River into a bedrock epigenetic gorge along most of the rockslide deposit.




*Figure 2.11: (A) Pisang Bowl with its spectacular failure scarp and deposit from the distance, the village Pisang in front. View towards south-east. Photo by M. Lupker, autumn 2020. (A) Panoramic view of Pisang Bowl rock avalanche deposit from approximate location of sample UM-20-05. Ridge lines on top of the deposit are traced on the photograph. Cosmogenic nuclide sample locations (10Be and 36Cl, orange arrows), and the location at the river were the 14C carbon burial samples were collected (red arrow) are indicated. Compare with Figure 2.13 and Tables 2.1 and 2.2 below. Photo by M. Lupker, autumn 2020.*

*2.5.1.2 Dating results – Pisang Bowl*

**14C carbon burial dating:**

At Pisang Bowl, organic material suitable for radiogenic 14C carbon burial dating was found along the present day Marsyandi River banks close to the small epigenetic canyon that exposes the contact between the marble bedrock and the breccia of the rockslide deposit. Here, organic material (wood pieces) was collected in two distinct units: within the basal part of the rockslide breccia deposit that includes vegetation debris entrained by the avalanche (UM-18-5) (see Figure A2.1 A and B, and compare with Section 1.3.5; Figure 1.5;); and preserved palaeosol buried by the rockslide deposit (UM-18-6). Calculated burial ages (68,3% probability, see Section 2.4.2) fall in a range between 729 to 1174 a (Table 2.2, Figure A2.7). The five measurements subdivide into three sub-groups: UM-18-5B & C fall in an age range from 729 to 783 a, UM-18-5D & 6 fall within 800 to 928 a, and the single sample UM-18-5A fall within 977 to 1174 a (Figure 2.14). The two older 14C age sub-groups might derive from dead wood that could have persisted for one to three centuries within soil or regolith overridden by the rock avalanche, facilitated by the local climatic conditions (dry and cold). We therefore consider the youngest sub-group as most representative of the timing of a rock-avalanche event that would have occurred between 730 and 780 a.

**Cosmogenic nuclide dating:**

At the Pisang Bowl site, a total of 16 samples were processed for cosmogenic nuclide exposure dating (see Table 2.1): three 10Be-samples and thirteen 36Cl-samples were processed, two sampling spots were treated with both methods (NEQ-17-5-59 and UM-18-10), one 10Be sample derives from a quartz vein instead of bulk rock (UM-18-9), and six samples were taken on the failure surface compared to ten from boulders sitting on top of the deposit (see also Figure 2.13). Sampled boulders are located at different locations: Four exposure ages come from the surface previously mapped as the First Ridge, three ages were measured from boulders sitting on the Third Ridge, and three measurements were processed from two boulders sampled within the chaotic boulder field to the west of the Third Ridge (see Figure 2.13). Photographs of the sampled surfaces are shown in Figure A2.1 (unfortunately, boulders UM-21-01, 02, & 03 were sampled in advanced twilight and no photographs can be presented for them).Most cosmogenic nuclide ages from the Pisang Bowl site (except NEQ-17-5-59 & 60) were plotted together with their 1σ-errors and their probability density functions (PDFs) (output from CREP, see Section 2.4.3 above) in Figure 2.14. Two distinct groups of ages can be identified in the clustering of cosmogenic nuclide measurement at Pisang Bowl: The boulders from the First Ridge and the failure scarp yield clearly younger ages than two samples from the Third Ridge. Weighted means of exposure ages were calculated with the online calculator IsoplotR (version 6.0, see Vermeesch, 2018). The weighted mean of the First Ridge and failure scarp samples is 0,50 ± 0,05 ka, the weighted mean for the two coinciding Third Ridge samples is 0,73 ± 0,13 ka, thus they are significantly older despite much

larger analytical error. In addition to the weighted means, the PDF sum of all First Ridge and scarp ages was plotted (see Figure 2.14).

Two samples are considered as outliers. The 10Be-sample from bulk rock (UM-18-10) shows a significantly older age than its 36Cl counterpart. We presume that this could arise from an analytical problem. The quartz crystals for this sample were very small (silt size) compared to the grain size usually analysed: the usual protocol for cleaning the atmospheric 10Be component could be partially unsuited for very small grain sizes (see also Section 2.4.3.1 above). The other sample considered as an outlier is one of the samples located on the Third Ridge (UM-21-43). Here, inheritance from previous exposure of the boulder's rock surface could be a possible explanation.




*Figure 2.12: (A) Panoramic view of the escarpment exposed by active erosion of the rock avalanche deposit by the Marsyangdi River (see also Figure 2.13 below). Photo by J. Lavé, autumn 2018. (B) Boulder field situated west of, or behind, the Third Ridge. Two boulders were sampled here for cosmogenic exposure dating (NEQ-17-5-59 & 60). View towards north-north-east. Photo by M. Lupker, autumn 2017. (C) Pisang Bowl failure scarp from the road. Eroded deposit on the other side of the river below (see also Figure 2.13 below). View towards north-north-east. Photo taken in autumn 2021. (D) The northern part of the Pisang Bowl failure scarp as seen from the Third Ridge (approximately at location of sample UM-21-45). A transition towards more vegetation in the upper part of the slope may indicate a tear-off edge of a rockslide (yellow dotted line). View towards east-north-east. Photo taken in autumn 2021. (E+F) Close-up view on diamictic, matrix ridge "main body facies" exposed at two locations within the escarpment (red and blue arrows in A). Photos taken in autumn 2021.*

From these results and from 14C dating results, we consider that two distinct failure events are represented by the clustering of cosmogenic nuclide measurements at Pisang Bowl. The oldest group found along the Third Ridge matches well the 14C ages: this corresponds to a rock-avalanche event (Event 1) that would have occurred between 730 and 780 a (in consideration of the youngest age group of the 14C samples, see above). The second and most recent rock avalanche event (Event 2) dated by exposure ages on the First Ridge and on the lower part of the rockslide failure surface would have occurred between 450 and 550 a, i.e. around 200 to 300 years after the first event (Event 1). This second rockslide involves a lower rock volume and represents a minor fraction of the total volume of 0,3-0,5 km$^3$.

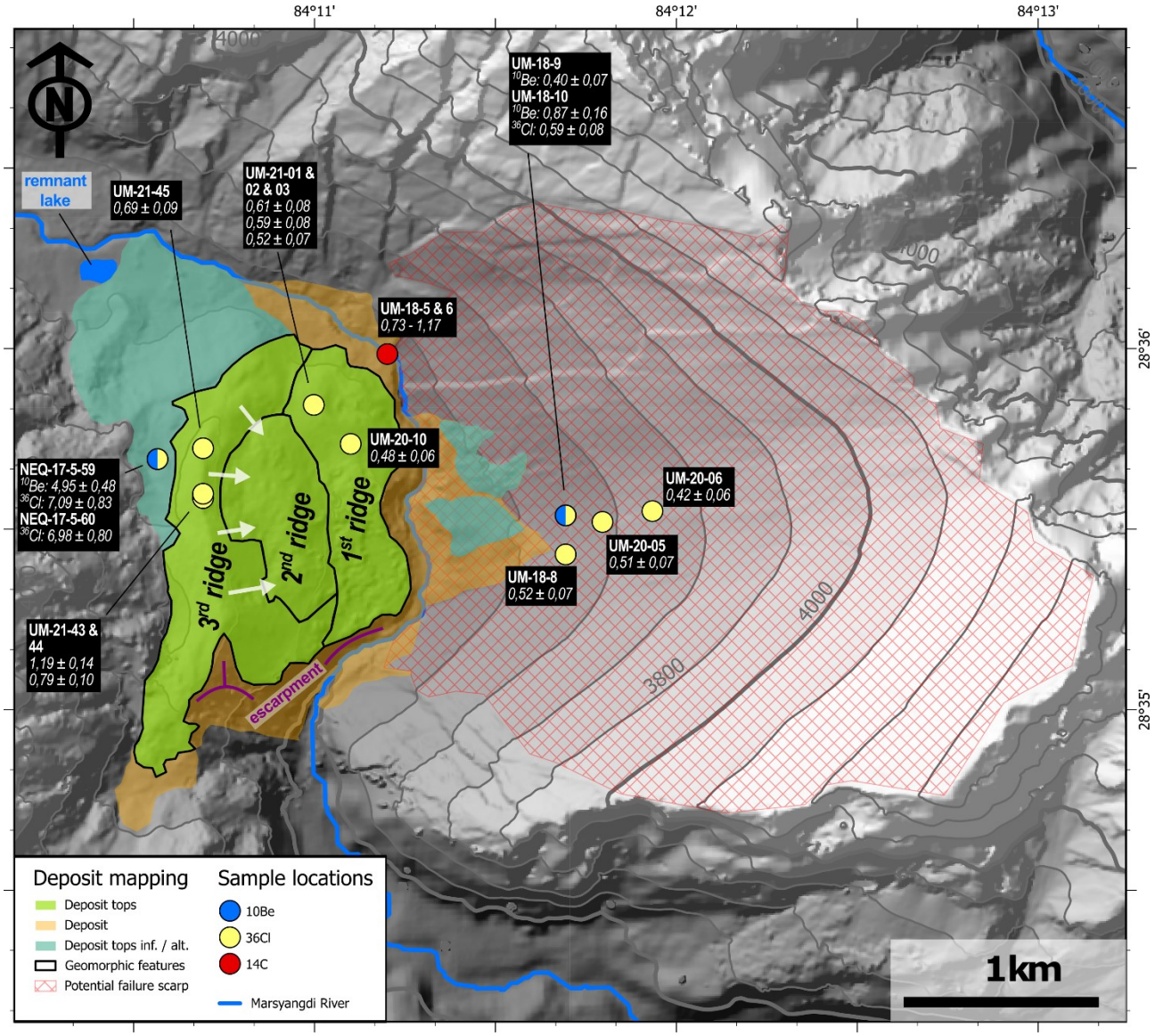


*Figure 2.13: Mapping and dating results (cosmogenic nuclides and 14C carbon burial) at Pisang Bowl. See Figure 2.10 for the location of this map area in the Marsyangdi Valley. The three ridges that were identified from the topography of the deposit's top surface are shown. White arrows indicate the hypothetical gravitational collapse of the Third Ridge, which forms the second ridge. The topography is represented by a combination of grey-scale altitude colouring and a transparent hillshade. The digital surface model is a combination of ALOS and HMA datasets (see Section 2.4.1.2 for more details on the datasets).*

Finally, it has to be noted that two exposure ages from individual boulders sampled from the chaotic boulder field (NEQ-17-5-59 & 60, as shown in Figure 2.12B), which is behind the Third Ridge and seem a priori to belong to its aprons, yield significantly older ages than the boulders sampled on top of the Third Ridge (they are not plotted in Figure 2.14, refer to Table 2.1). The $^{36}Cl$ measurements on these two boulders provide similar exposure ages (Table 2.1), and a weighted mean value of 7.0 ± 1.1 ka BP. So far, we did not find a solid explanation for these older samples. We can only propose conjectures. Boulders were possibly pre-exposed to cosmic rays while situated at the surface of the pre-failure topography, i.e. they have an inherited concentration. If the boulder fields at Pisang Bowl are the product of blocks that remained at the top of the rock avalanche mass during its collapse ("carapace", see above; Section 1.3.5; and Figure 1.5), this explanation seems plausible. However, in such a scenario, similar ages as measured for the two blocks are somewhat unexpected, since this requires the two blocks transported by the rock-avalanche to be orientated identically, i.e. presenting the same pre-exposed face upwards despite probable independent shaking and rolling. Another hypothesis is that the boulder field behind the Third Ridge could be from an even earlier rock slope failure at the Pisang Bowl site, preceding the events responsible for the emplacement of both the First and Third Ridge (see Figure 2.13). If we regard these older ages at ~7 ka as indicative of an independent rock avalanche event, it suggests that multiple translational rockslide occurrences shaped the present-day appearance of Pisang Bowl, with the oldest event dating back to the early Holocene period.

In any case, we found strong evidence for at least two rock slope failure events which are responsible for most of the deposit present at the Pisang Bowl site.

**Table 2.1: Pisang Bowl cosmogenic nuclide samples - Exposure dating results**

**10Be exposure samples**

| Sample name | Lat. [°] | Lon. [°] | Alt. [m a.s.l.] | Object sampled | *Erosion comment* | Sample thickness [cm] | Shielding: topo / snow / total [-] | $^{10}Be/^{9}Be$ ratio [$10^{-14}$] ± 1σ | Amount of carrier [µg] (1) | Dissolved quartz [g] | $^{10}Be$ conc. [$10^{3}$ at/g] ± 1σ (2) | Exposure age [ka before 1950 AD] ± 1σ (3) |
|---|---|---|---|---|---|---|---|---|---|---|---|---|
| **NEQ-17-5-59** | 28,5949 | 84,1761 | 3364 | boulder | *hard, resistant rock, no signs of erosion* | 4,0 | 0,949 / 0.995 / 0,944 | 20,273 ± 1,886 | 308,1 | 29,58 | 131,65 ± 13,23 | **4,95 ± 0,48** |
| **UM-18-9** | 28,5923 | 84,1949 | 3275 | quartz vein on failure scarp | *looks prestine, spalling of 3-10 cm sheets possible* | 1,0 | 0,921(4) / 0,995 / 0,917 | 3,746 ± 0,361 | 253 | 43,23 | 11,61 ± 1,52 | **0,40 ± 0,07** |
| **UM-18-10** | 28,5923 | 84,1949 | 3275 | failure scarp | *looks prestine, spalling of 3-10 cm sheets possible* | 3,0 | 0,921(4) / 0,995 / 0,917 | 2,442 ± 0,343 | 251,1 | 35,36 | 21,87 ± 3,42 | **0,87 ± 0,16** |

*(1) NEQ-17-5-59 & UM-18-9: carrier solution of 990 µg/g $^{9}Be$ atoms; UM-18-10: carrier solution "Phena 1" of 2020 ± 83 µg/g $^{9}Be$ atoms*

*(2) after Blank correction: NEQ-17-5-59 & UM-18-9 corrected with 1,25038 · $10^{5}$ ± 2,6061 · $10^{4}$ and 2,38265 · $10^{5}$ ± 7,2542 · $10^{4}$ $^{10}Be$ atoms, derived from 5 and 2 blank measurements in preceding months from same laboratory, respectively; UM-18-10 corrected with one blank from same sample run with a $^{10}Be/^{9}Be$ ratio [$10^{-15}$] of 1,60802 ± 0,27647*

*(3) calculated with CREP developement version on 30 January 2024 with an assumed rock density of 2,65 g/cm $^{3}$ and zero erosion rate (see Section 2.4.3.1 for more details and references)*

**36Cl exposure samples**

| Sample name | Lat. [°] | Lon. [°] | Alt. [m a.s.l.] | Object sampled | *Erosion comment* | Sample thickness [cm] | Shielding: topo / snow / total [-] | Dissolved rock mass [g] (% of total) | Cl in target [ppm] ± 1σ (1) | CaO in target [%] ± 1σ (1) | $K_2O$ in target [%] ± 1σ (1) | $^{35}Cl/^{37}Cl$ ratio [-] ± 1σ | $^{36}Cl/^{37}Cl$ ratio [$10^{-13}$] ± 1σ | $^{36}Cl$ conc. [$10^{3}$ at/g] ± 1σ (2) | Exposure age [ka before 1950 AD] ± 1σ (3) |
|---|---|---|---|---|---|---|---|---|---|---|---|---|---|---|---|
| **NEQ-17-5-59** | 28,5949 | 84,1761 | 3364 | boulder | *hard, resistant rock, no signs of erosion* | 4,0 | 0,949 / 0.995 / 0,944 | 10,53 (90%) | 3,80 ± 0,11 | 53,42 ± 1,34 | 0,00 ± 0,00 | 66,90 ± 1,09 | 6,58 ± 0,26 | 938,38 ± 38,14 | **7,09 ± 0,83** |
| **NEQ-17-5-60** | 28,5949 | 84,1761 | 3364 | boulder | *hard, resistant rock, no signs of erosion* | 3,5 | 0,949 / 0.995 / 0,944 | 24,41 (75%) | 9,56 ± 0,23 | 64,60 ± 1,62 | 0,00 ± 0,00 | 18,83 ± 0,31 | 14,30 ± 0,54 | 1132,75 ± 43,70 | **6,98 ± 0,80** |
| **UM-18-8** | 28,5905 | 84,1949 | 3289 | failure scarp | *looks prestine, spalling of 3-10 cm sheets possible* | 3,0 | 0,923(4) / 0,995 / 0,918 | 40,60 (59%) | 10,73 ± 0,38 | 56,49 ± 1,41 | 0,00 ± 0,00 | 18,57 ± 0,48 | 0,85 ± 0,04 | 74,39 ± 3,72 | **0,52 ± 0,07** |
| **UM-18-10** | 28,5923 | 84,1949 | 3275 | failure scarp | *looks prestine, spalling of 3-10 cm sheets possible* | 3,0 | 0,921(4) / 0,995 / 0,917 | 45,26 (55%) | 8,11 ± 0,20 | 57,16 ± 1,45 | 0,00 ± 0,00 | 24,05 ± 0,40 | 0,93 ± 0,05 | 81,70 ± 4,52 | **0,59 ± 0,08** |
| **UM-20-05** | 28,5920 | 84,1966 | 3366 | failure scarp | *weathered, spalling of 3-10 cm sheets possible* | 1,5 | 0,925(4) / 0,995 / 0,920 | 60,26 (40%) | 13,42 ± 0,34 | 59,58 ± 1,50 | 0,00 ± 0,00 | 19,82 ± 0,34 | 0,71 ± 0,04 | 82,47 ± 4,61 | **0,51 ± 0,07** |
| **UM-20-06** | 28,5925 | 84,1989 | 3478 | failure scarp | *weathered, spalling of 3-10 cm sheets possible* | 2,0 | 0,929(4) / 0,995 / 0,924 | 37,04 (63%) | 6,44 ± 0,16 | 55,06 ± 1,38 | 0,00 ± 0,00 | 24,96 ± 0,41 | 0,94± 0,05 | 68,30 ± 3,74 | **0,42 ± 0,06** |
| **UM-20-10** | 28,5956 | 84,1850 | 3221 | boulder | *hard resistant rock, some weathering* | 3,0 | 0,937 / 0,995 / 0,932 | 14,91 (85%) | 14,44 ± 0,39 | 54,33 ± 1,36 | 0,00 ± 0,00 | 10,73 ± 0,18 | 1,16 ± 0,06 | 75,93 ± 3,76 | **0,48 ± 0,06** |
| **UM-21-01** | 28,5976 | 84,1833 | 3262 | boulder | *few signs of erosion apart from a bit of scaling* | 2,0 | 0,945 / 0,995 / 0,940 | 39,86 (60%) | 8,50 ± 0,36 | 51,10 ± 1,28 | 0,22 ± 0,01 | 19,00 ± 0,60 | 1,14 ± 0,06 | 79,91 ± 4,54 | **0,61 ± 0,08** |
| **UM-21-02** | 28,5974 | 84,1833 | 3265 | boulder | *few signs of erosion apart from a bit of scaling* | 2,0 | 0,946 / 0,995 / 0,941 | 41,60 (58%) | 8,23 ± 0,36 | 51,54 ± 1,29 | 0,00 ± 0,00 | 19,46 ± 0,63 | 1,04 ± 0,06 | 72,10 ± 4,36 | **0,59 ± 0,08** |
| **UM-21-03** | 28,5974 | 84,1832 | 3261 | boulder | *few signs of erosion apart from a bit of scaling* | 1,0 | 0,946 / 0,995 / 0,941 | 37,12 (62%) | 9,59 ± 0,42 | 52,03 ± 1,30 | 0,20 ± 0,00 | 16,31 ± 0,53 | 1,12 ± 0,07 | 74,62 ± 4,53 | **0,52 ± 0,07** |
| **UM-21-43** | 28,5931 | 84,1782 | 3428 | boulder | *weathered, easy to split* | 2,5 | 0,962 /0,995 / 0,958 | 48,60 (51%) | 4,49 ± 0,20 | 52,17 ± 1,30 | 0,00 ± 0,00 | 36,31 ± 1,22 | 2,06 ± 0,10 | 158,78 ± 8,26 | **1,19 ± 0,14** |
| **UM-21-44** | 28,5933 | 84,1782 | 3431 | boulder | *surface of very competent rock* | 1,5 | 0,963 / 0,995 / 0,958 | 11,78 (88%) | 2,07 ± 0,10 | 52,59 ± 1,31 | 0,00 ± 0,00 | 43,27 ± 1,44 | 2,46 ± 0,11 | 108,28 ± 5,05 | **0,79 ± 0,10** |
| **UM-21-45** | 28,5954 | 84,1782 | 3414 | boulder | *resistant, but could have been chipped 2-3 cm laterally* | 2,5 | 0,963 / 0,995 / 0,958 | 24,41 (76%) | 3,11 ± 0,14 | 52,67 ± 1,32 | 0,17 ± 0,00 | 34,42 ± 1,18 | 1,95 ± 0,09 | 97,85 ± 4,84 | **0,69 ± 0,09** |

*(1) target chemical concentrations measured with ICP-AES (inductively coupled plasma atomic emission spectrometry) at CEREGE*

*(2) after Blank correction: NEQ-17-5-59 & 60, UM-18-8 & 10, and UM-20-05 & 06 & 10 corrected with one blank from same sample run with a $^{35}Cl/^{37}Cl$ ratio [-] of 242,35940 ± 4,82909 and a $^{36}Cl/^{37}Cl$ ratio [$10^{-16}$] of 5,28551 ± 1,39018; UM-21-01 & 02 & 03, and UM-21-43 & 44 & 45 corrected with one blank from same sample run with a $^{35}Cl/^{37}Cl$ ratio [-] of 240,82170 ± 9,60827 and a $^{36}Cl/^{37}Cl$ ratio [$10^{-16}$] of 25,65117 ± 7,84054*

*(3) calculated with CREP developement version on 30 January 2024 with an assumed rock density of 2,65 g/cm³, zero erosion rate and a formation age of 10 Ma (see Section 2.4.3.2 for more details and references)*

*(4) when calculating the topographical shielding of these sample surfaces, the strike and dip measurements of the failure scarp were taken into account: UM-18-8, UM-20-05 & 06: 185/29; UM-18-9 & 10: 160/26*

*for chemical composition of target and bulk rock of 36Cl-samples refer to Table A2.2 in Annexe*

**Table 2.2: Pisang Bowl radiogenic 14C carbon dating - Results and calibration**

| 14C carbon burial samples | | | | | | |
|---|---|---|---|---|---|---|
| Sample name | Lat. [°] | Lon. [°] | Alt. [m a.s.l.] | *Object sampled* | Radiocarbon age [y BP] | Burial age (68,3% probability) [a before 1950 AD] (1) |
| UM-18-5A | 28,5997 | 84,1867 | 3129 | *small branch* | 1149 ± 22 | **977 - 1174** |
| UM-18-5B | 28,5997 | 84,1867 | 3129 | *wood fibers of branch or trunck* | 856 ± 22 | **729 - 775** |
| UM-18-5C | 28,5997 | 84,1867 | 3129 | *wood fibers of branch or trunck* | 874 ± 22 | **737 - 783** |
| UM-18-5D | 28,5997 | 84,1867 | 3129 | *fragment like charcoal + fragment of branch* | 958 ± 22 | **800 - 915** |
| UM-18-6 | 28,5998 | 84,1867 | 3129 | *wood fragment in the dark gray breccia near the contact* | 986 ± 22 | **805 - 928** |

*(1) calculated with the OxCal online calculator using the Intcal20 calibration curve; full range of output ages, gaps omitted*

*see Section 2.4.2 and Figure A2.7 for more details and references*

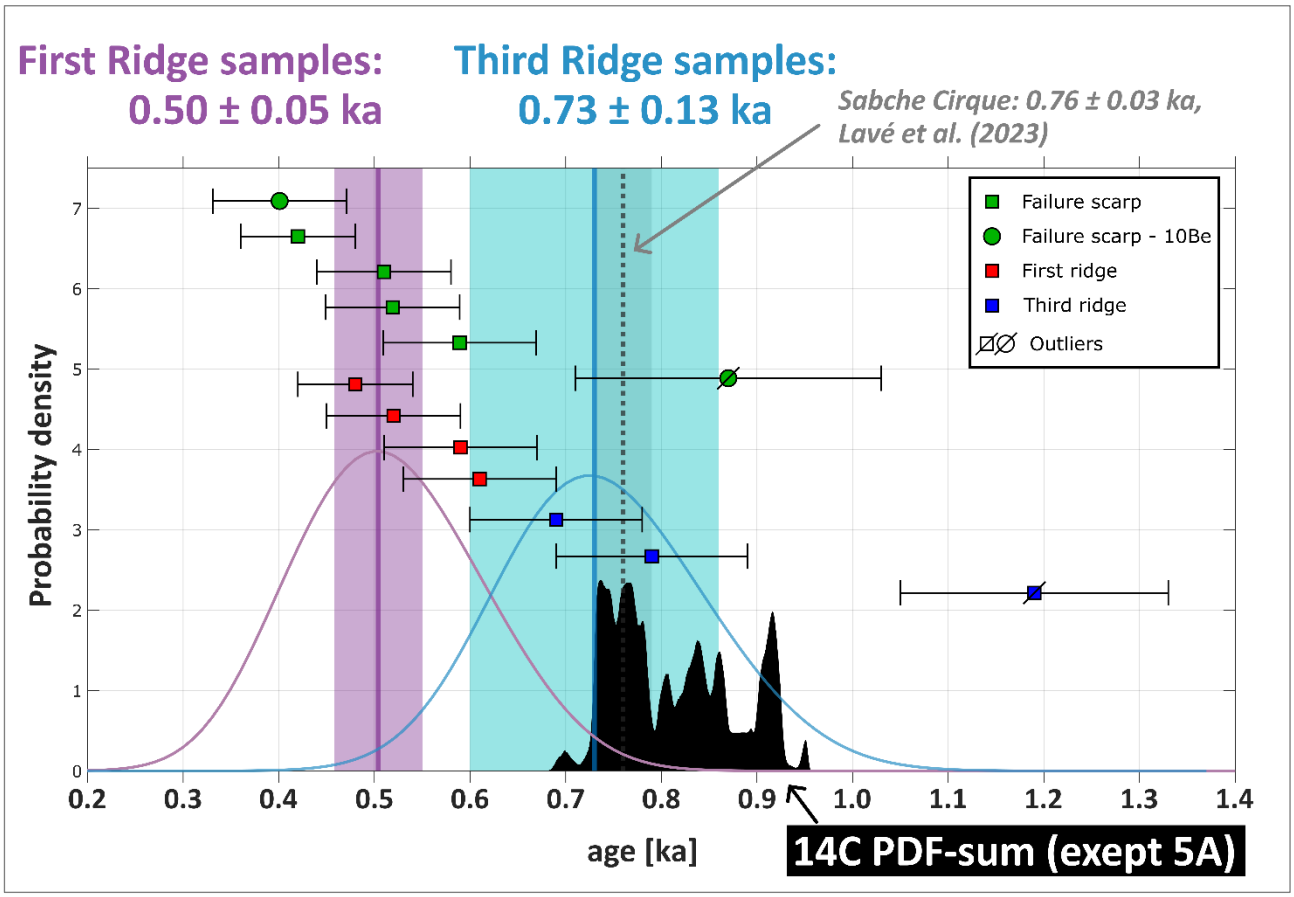


*Figure 2.14: Cosmogenic nuclide samples measured from the Pisang Bowl rock avalanche site (36Cl and 10Be) plotted with 1σ-errors (see Table 2.1). Weighted mean with 1σ-error of First Ridge and Failure Scarp ages combined (in magenta), and weighted mean with 1σ-error of two Third Ridge boulders (in blue) are shown. Cumulative PDFs of First Ridge / Failure Scarp and Third Ridge samples are shown in magenta and blue, respectively. Sum of PDFs from all 14C carbon burial samples taken at the Pisang Bowl site except UM-18-5A (see Table 2.2) is shown in black. The proposed timing of the Sabche cirque rock avalanche, 760 ± 30 a, after Lavé et al. (2023) is indicated with a grey dotted line and a grey bar.*

## 2.5.2 Deposits around Humde / Manang

### *2.5.2.1 Field observations and outcrops – Humde/Manang*

About 3 km upstream of Pisang village, the Marsyangdi Valley is widening due to the presence of two large tributaries, the Julu Khola draining the Chulu massif and Chulu Far East Peak to the north, and the Sabche Khola entering the valley from the south and draining the Annapurna main ridge between Annapurna III and IV (see Figure 2.10 and Section 2.5.2.2 below). Here, sedimentary fills cover both valley flanks for a stretch of more than 10 km, in some places up to several hundred meters above the present day valley floor, and are sometimes topped off by flat surfaces (see Figure 2.15A-D). These deposits are in the process of ongoing severe erosion and show spectacular shapes, featuring steep escarpments (Figure 2.15A-D) and pinnacles (Figure 2.15C+D). Some earlier scholars identified these deposits solely as remnants of an extended valley glaciation, i.e. glacial origin, from a Pleistocene past, see Bordet et al. (1975) and Nagaoka (1990). Others have attributed these sedimentary bodies, at least in part, to the remains of a gigantic rock slope failure, see Hagen (1968), Weidinger (2006), and Fort (2011). The valley morphology is U-shaped and an extensive glacier in the past may have caused overdeepening, i.e. erosion of the bedrock to a trough below the present day fluvial profile (see, e.g., Cook and Swift, 2012), in the section of the valley around Humde (see Figure 2.10 and Section 2.5.2.2 below). Glacial sediments are likely to be found in this area and we did find them. The Marsyangdi River erodes into basal till at about 4.5 km downstream of Humde (outcrop along the right bank), and possibly further upstream (see Figure 2.16E and Section 2.5.2.2 below).

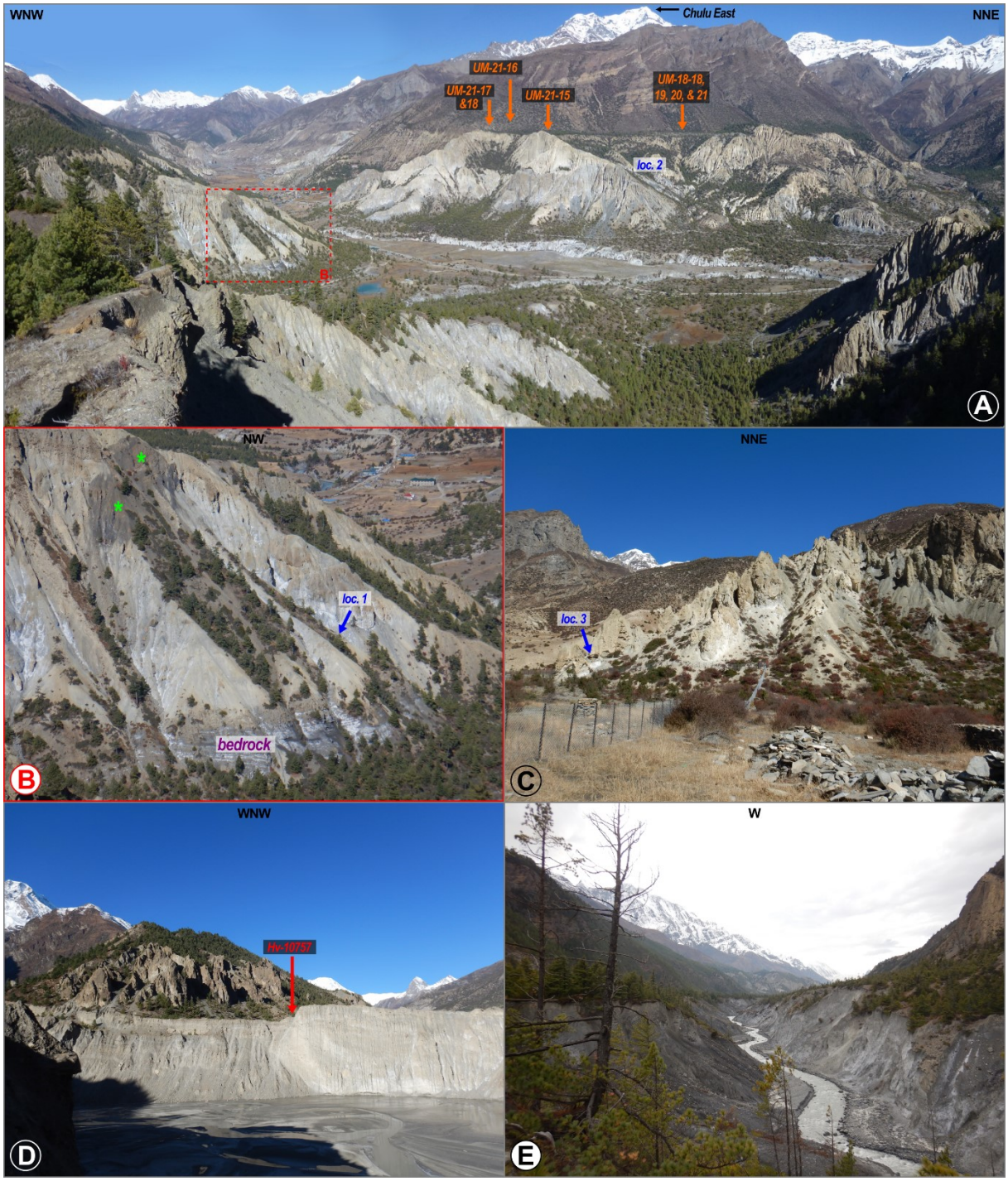


*Figure 2.15: (A) Panoramic view over the upper Marsyangdi Valley. Rock avalanche deposits flanking the valley around the Sabche Khola confluence in the foreground and more deposits upstream towards Manang. Viewpoint is shown in Figure 2.17. Cosmogenic nuclide sample locations on the other valley side are indicated with orange arrows. Photo by J. Lavé, autumn 2021. (B) Zoomed in view to one of the deposits in A. Patches of coherent darker source rock are visible as large-scale structure within the deposit (green stars). Bedrock is outcropping below the deposit. Photo taken in autumn 2021. (C) Erosion forms pinnacles west of Braga. Photo taken in autumn 2021. (D) Lateral moraine of Gangapurna glacier, west of Manang. Pinnacles formed within rock-avalanche deposit in the background. Sample location of Röthlisberger and Geyh (1985) indicated with red arrow. Photo taken in autumn 2021. (E) The Marsyangdi River incising into glacial basal tills downstream of Humde. Viewpoint is shown in Figure 2.17. Photo taken in autumn 2021.*

During the field surveys, we looked at outcrops of the voluminous sedimentary fills around Humde and Manang and were able to identify all of them, with the exception of the basal till directly at the Marsyangdi River, as rock avalanche deposits, which we will present in the following:

The outcrop of rock avalanche deposit displaying the most coherent sections of source rock was encountered near the Sabche Khola confluence (refer to location 1 (loc. 1) in Figures 2.15, A&B; 2.16A; and 2.17). Here, highly deformed calcite veins were observed within the dark source rock, likely pre-existing before the rock avalanche. Moving further upslope at this site, darker portions within the rock avalanche material were discernible from a distance, potentially corresponding to the same coherent block of source rock (Figure 2.15B).

About halfway between the deposit surface and the valley floor north-west of Humde, a significant internal contact was observed (see loc. 2 in Figures 2.15A; 2.16B; and 2.17). On both sides of the sharp contact the fabrics of the sediments are similar but the colour is clearly darker in the upper section. We argue this contact is a shear zone within the rock avalanche deposit, as described, for example, by Weidinger et al. (2014). The colour contrast could result from different source rock lithologies, which could originate from different stratigraphic positions within the failed rock wall. Close to this internal contact we spotted a typical feature known from rock avalanche deposits that could be described as a phantom clast (see Weidinger et al., 2014): This refers to a block whose original outline remains visible within the deposit, yet its interior appears thoroughly fragmented, easily crumbling upon contact at the outcrop (Figure 2.16C).

An important outcrop that needs to be discussed here is the one located west of Braga (see loc. 3 in Figures 2.15C; 2.16, D&E; and 2.17). Here, two breccias, which clearly show the characteristics of rock avalanche deposition, more precisely a highly fractured facies (see Figure 2.16, F&G; Section 1.3.5; and Figure 1.5), are separated by a layer of gravel a few metres thick. This layer, mostly consisting of well sorted pebbles with some cobbles and small boulders is horizontally layered and shows imbrication. It features therefore a typical fluvial sediment. Explaining the presence of these gravels from entrainment by a rock avalanche can be excluded, because otherwise the layering should be deformed. These gravels must have been deposited in-situ in between two individual rock avalanche events, separated by a least a couple of hundred years: the lower rockslide deposit was probably several tens or hundreds of meters thick and rivers need a minimum time to erode this breccia layer and then deposit fluvial sediments at the top of the unconformity. This contact between the two events must continue in the deposits around Braga. It probably manifests itself primarily as a direct contact between the two rock avalanche deposits. We were unfortunately unable to track this contact any further, but we reckon it is the same contact described earlier by Hagen (1968) and interpreted as a contact between glacial deposits at the base and a rock avalanche deposit at the top.

Additionally at loc. 3, we found good exposures of typical jigsaw facies (Figure 2.16E) and whitish patches within the rock avalanche deposit consisting of almost completely pulverised rock (Figure 2.16G).

In some places, we observed rounded pebbles and cobbles that are embedded into the breccia material, either isolated and scattered, or in the form of small pockets. Some of these pebbles show striations and we interpret them as fluvial or glacial sediments entrained by the rock avalanche. The example shown in Figure 2.16H, at loc. 4, is near the top of the deposit, but not far from the bedrock wall (Figure 2.17). In any case, this is a peculiar location for sediment-rock avalanche interactions normally expected closer to the valley floor (see Section 1.3.5; Figure 1.5; and Hewitt et al., 2008; Weidinger et al., 2014).

During our limited field investigations, we did not encounter the lacustrine beds mentioned by Fort (2011) upstream of Manang Village, nor did we encounter lacustrine sediments elsewhere in the upper Marsyangdi Valley. Whether due to the glacier that enters the main valley at Manang, as suggested by Fort (2011), or caused by a rock avalanche deposit, a dam that impounded a lake cannot have persisted long enough to leave significant lacustrine sediments behind. Moreover, no morphological evidence or sedimentary remains of a catastrophic lake drainage have been found or are known to us further downstream in the Marsyangdi Valley.

We did not observe any frictionite, i.e., partial melting of rock avalanche material during deposition, within all the rock avalanche outcrops in the upper Marsyangdi Valley (see Section 1.3.5; Figure 1.5; Masch et al., 1985; Weidinger et al., 2014). We assume that the calcareous source lithologies are unfavourable for the formation of partial melts despite the size of the deposits and the expected high energies involved.

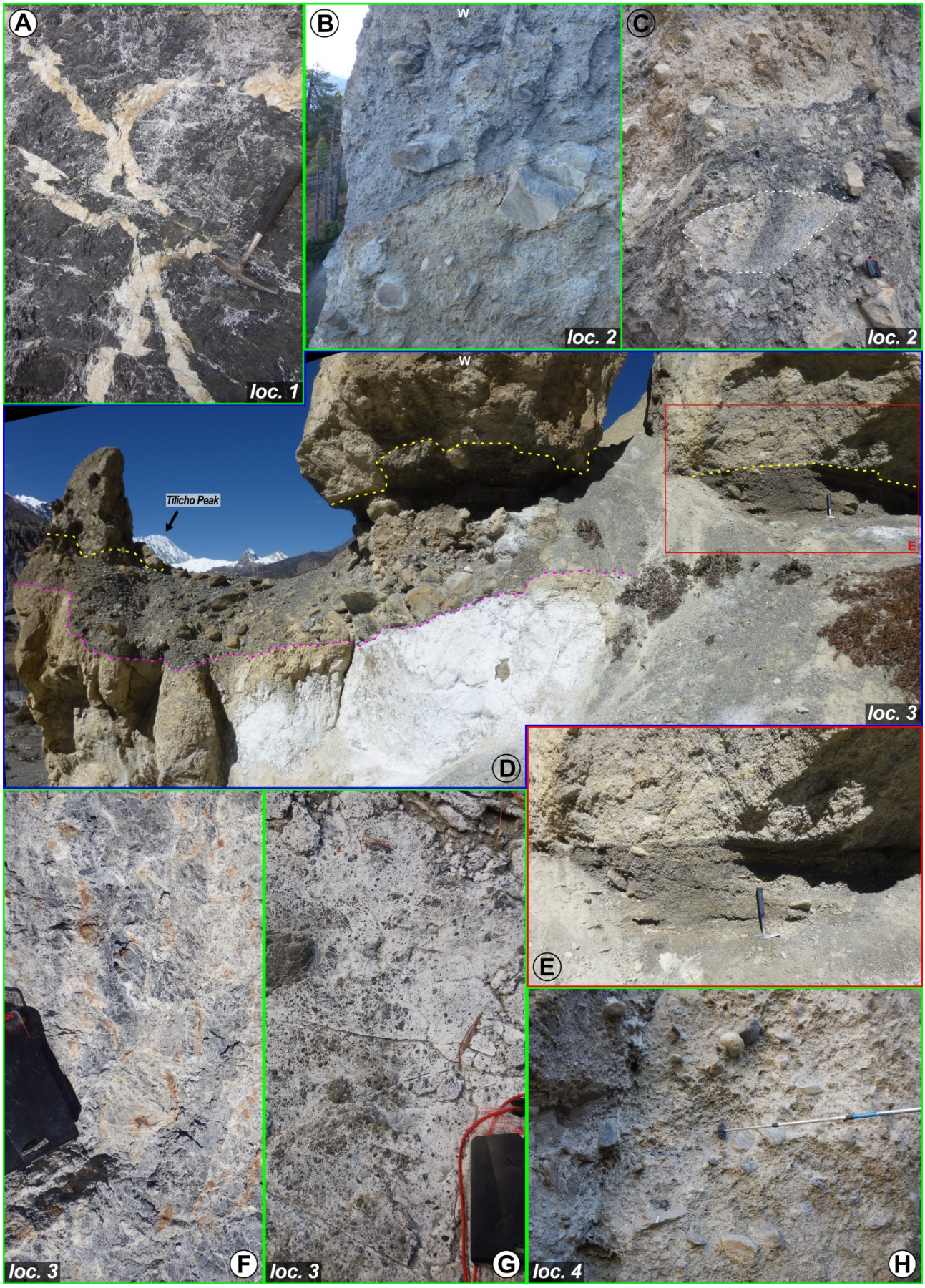
A
loc. 1
B
W
loc. 2
C
loc. 2
W
Tilicho Peak
loc. 3
D
E
F
loc. 3
G
loc. 3
H
loc. 4

*Figure 2.16 (on previous page): Outcrop locations are indicated in Figure 2.17. (A) Highly deformed calcite veins within dark source rock at outcrop location 1 (loc. 1). Photo taken in autumn 2021. (B) Internal contact interpreted as a small shear zone that juxtaposes 2 distinct fragmented bedrock units within the rock avalanche deposit north-west of Humde. The transition is sharp and clearly recognisable by the different colours. Photo by J. Lavé, autumn 2021. (C) Phantom clast within rock avalanche deposit (white dashed line). Photo taken in autumn 2021. (D) Gravel layer in between two breccias identified as rock avalanche deposits. Lower contact (pink dashed line) and upper contact (yellow dashed line) mark a significant hiatus between two individual rock avalanche events during which fluvial deposition took place. Photo by J. Lavé, autumn 2021. (E) Zoomed in view to the gravel layer in D. Pebbles show clearly imbrication. Photo by J. Lavé, autumn 2021. (F) Jigsaw facies within rock avalanche deposit (see Section 1.3.5). Photo taken in autumn 2021. (G) Whitish spot within rock avalanche deposit of almost completely pulverised rock at location 1. Photo taken in autumn 2021. (H) Rounded pebbles chaotically dispersed in sticky matrix, possible a pocket of fluvial sediments entrained into the rock avalanche during emplacement. Photo taken in autumn 2021.*

#### *2.5.2.2 Mapping and volume reconstruction – Humde/Manang*

A mapping of the rock avalanche deposits in the Humde/Manang area was initiated in order to shed light into their formation and as a basis for the reconstruction of deposit volume (see below). Mapping was performed by use of digital surface models and satellite imagery (see Section 2.4.1.2 for more details on datasets used), and supported by photographs taken in the field. Particular attention was paid to the flat surfaces on the valley flanks and their heights above the valley bottom. Attempts were made to recognise which of these surfaces could be the top surface of a rock avalanche deposit and whether there could be either rock avalanche material or bedrock beneath this surface. It can be quite challenging to differentiate rock avalanche deposits from outcropping bedrock, or from other sediments like colluvial wedges or glacial diamictons by using digital surface models and satellite imagery alone. Some distinctions can only be made on the basis of "best guesses". Whenever available, photographs from the field were consulted to make a judgement. In addition to hillshades, slope maps were created from the digital surface models (ALOS World 3D, HMA) in order to support the mapping.

Rock avalanche deposits in the Humde/Manang area were mapped into four groups:

- **Deposit certain**: supported by field observations and/or field photography, correlation along coherent morphological features;
- **Deposit inferred**: Strong evidence from Google Earth Pro or ArcGIS Pro basemap imagery (e.g., from characteristic pillar erosion structure), correlation along coherent morphological features;
- **Deposit Tops certain**: supported by field observations and field photography, no or only minor

alteration by erosion or coverage by younger sediments, no relocation of surface by tilting or slumping, correlation from other remaining deposit tops;

- **Deposit Tops inferred**: Strong evidence from Google Earth Pro or ArcGIS Pro basemap imagery that the surface is possibly related to the original surface of the deposit, even if altered by erosion or displaced by tilting or slumping, correlation from other remaining deposit tops.

Additionally, glaciers, moraine crests, lakes, and other landslide related geomorphological features were mapped.

After the mapping was completed, an attempt was made to determine an outline for a rock avalanche event around Humde (see Figure 2.17). From both the mapping and the attempt to outline a single event, it became evident that we are likely dealing with two major individual rock avalanche deposits within the valley section from downstream Humde to upstream Manang. These deposits should overlap approximately at the place where the village of Braga is located (see Figure 2.17).

A closer look at the heights of the deposit tops suggests two separate deposits aroung Humde and Manang:

The flat deposit top surface opposite to Manang (at ~3 910 m.a.s.l., the area not encroached by moraines) is at about the same elevation as the highest surface around Humde, the one on the left bank of the Sabche Khola confluence to the main valley (~3 930 m.a.s.l.) (see Figure 2.17). These surfaces lie 360 respectively 490 m above the valley floor and are separated by a 5,8 km long valley section. Rock avalanches can involve enormous volumes and spread over several kilometres (see, e.g., Hewitt et al., 2008). A single rock avalanche that filled this entire valley section with several hundred metres of sediment must have been extremely large, which is certainly not impossible in terms of sheer volume. However, this seems unlikely because, firstly, there is no obvious large-scale detachment area on the directly neighbouring valley flanks and, secondly, no larger tributary valley can enters this valley section from which a gigantic rock avalanche, originating from higher detachment zones, could have filled the valley towards two sides. It therefore seems much more logical that two individual giant rock avalanches from two separate tributary valleys filled up the valley stretch from two separate directions.

For the "overlap area", mapping was sometimes difficult to conduct due to the ambiguity of the remaining flat surfaces preserved in the area and the highly eroded state of the deposits (including Milarepa glacier, see Figure 2.17).

The field evidence from outcrop location 3 supports our interpretation that these are indeed deposits from two individual rock avalanches, and we accordingly draw an outline for a single deposit around Humde (see Section 2.5.2.1 above).

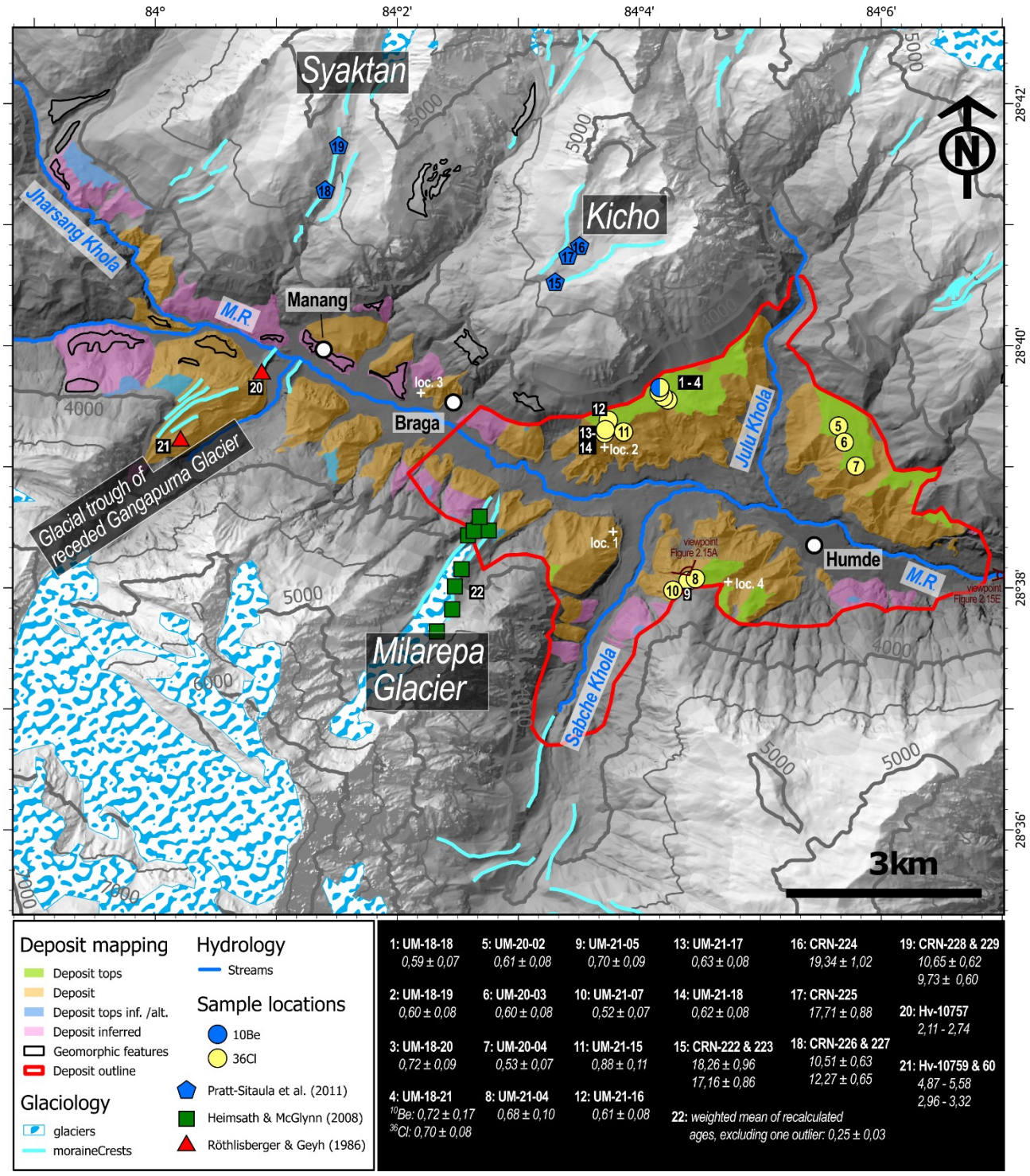


*Figure 2.17: Mapping and dating results (cosmogenic nuclides) for the rock avalanche deposits around Humde and Manang. See Figure 2.10 for the location of this map area in the Marsyangdi Valley. In addition, the absolute dating results of other studies in this valley reach are added to the map (Röthlisberger and Geyh, 1986; Heimsath and McGlynn, 2008; Pratt-Sitaula et al., 2011). Outcrop locations are indicated (loc. 1-4, see Section 2.5.2.1). The topography is represented by a combination of grey-scale altitude colouring overlaid with a transparent hillshade. The digital surface model is a combination of ALOS and HMA datasets (see Section 2.4.1.2 for more details on the datasets). M.R. = Marsyangdi River.*

To reconstruct the volume of the deposit around Humde (refer to Section 2.4.4 for technical specifics), we draw an outline that features a straight line just downstream of Braga, spanning from one valley flank to the other (refer to Figure 2.17). This approach aimed to exclude areas from the volume calculation where significant overlap with another rock avalanche deposit around Manang was anticipated.

Various assumptions made for the reconstruction of the volume of the deposit are responsible for considerable, but not quantitatively constrained, uncertainty on our final estimate (see also Section 2.4.4). Especially, the pre-failure topography at Humde is concerned. We make no estimates of the sediments that were present in the valley prior to deposition, except for the flat valley floor, which we assume was filled by basal till as it is today (Figure 2.18). The presence of other glacial deposits in the form of terminal or lateral moraines, sediments from other landslides, or the presence of colluvial aprons (or pediments) is very likely. For the shape of the pre-deposition valley flanks, we adopted a conservative approach: we assumed that their slope was close to that of the valley's current topography (just above the deposit tops or where no landslide deposits remain), rather than imagining an overdeepened U-shape valley with steep lateral slopes (Figure 2.18). This strategy may lead to underestimate the volume if steep bedrock valley flanks were present at that time.

The uneroded remnants of the Humde deposit show small secondary topographies, such as small ridges and depressions, particularly to the north-west of Humde, but their amplitude remains limited and less than 50 m high. (Figure 2.18). For our volume estimate, we modelled a simple, smooth topography by interpolating between remnant top surfaces. This does not take into account a more complex morphology of the deposit top, which formed during deposition.

Another aspect that adds uncertainty to our estimate is tied to the fact that the Humde deposit extends into a total of four valley openings: the two sides of the main valley as well as the two tributary valleys of the Sabche Khola and the Julu Khola (see Figure 2.17). The original extent of the rock avalanche deposit in the opening of the Marsyangdi Valley downstream of Humde and in the tributary valley openings can only be estimated with difficulty as deposits are not well preserved in these areas due to the evident erosive force of the river there.

With all the possible challenges mentioned above, we are aware that the unconstrained uncertainty within our volume estimate is considerable.

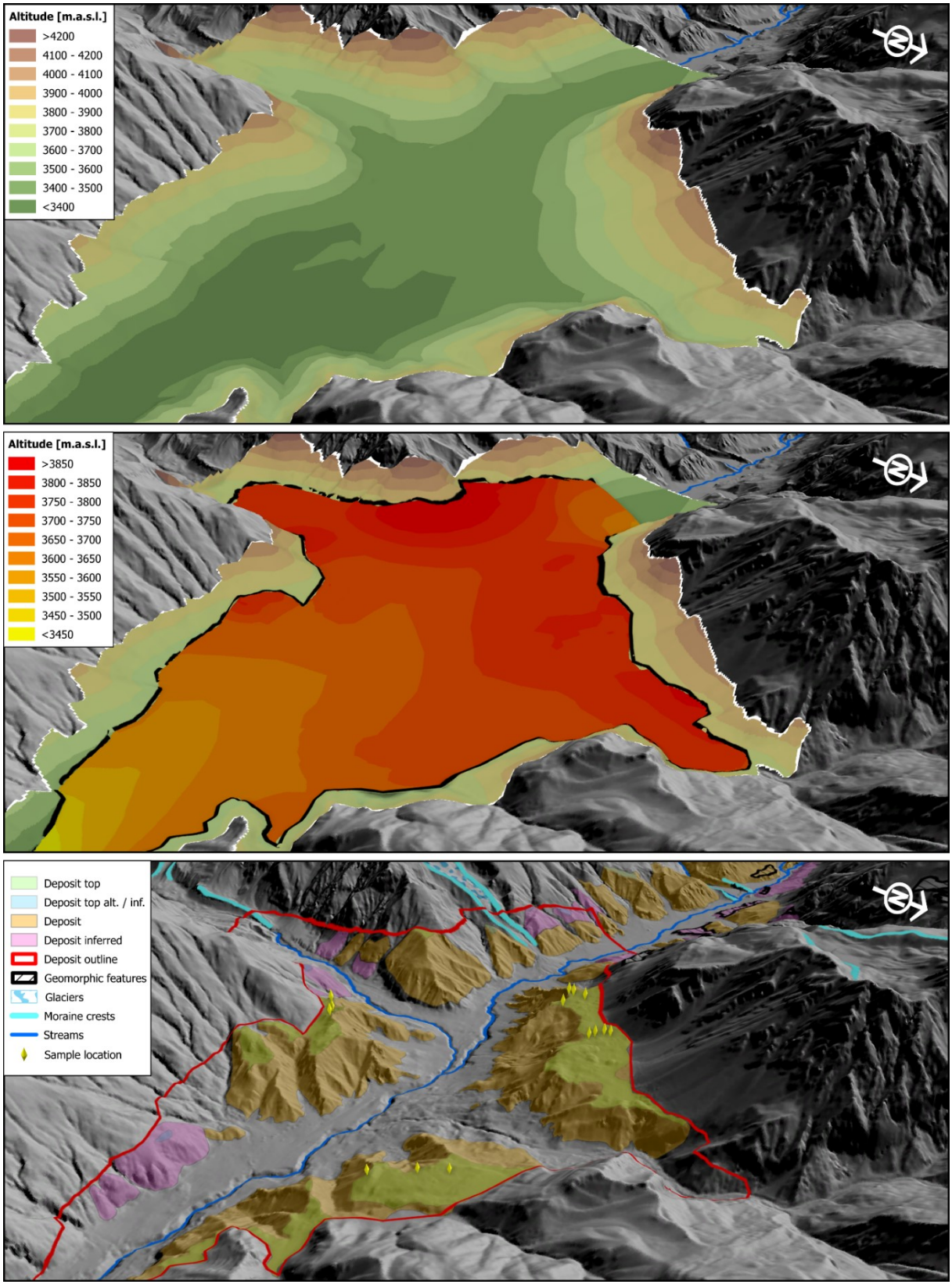


*Figure 2.18:Volume reconstruction for the rock avalanche event responsible for the deposits around Humde: Pre-failure topography (top) and surface of deposit just after emplacement (middle) were reconstructed for the volume estimate. Mapping results for the rock avalanche deposits in 3D-view in the bottom (see also Figure 2.17. The digital surface model is a combination of ALOS and HMA datasets (see Section 2.4.1.2 for more details on the datasets).*

Finally, our volume estimate for a contiguous deposit at Humde is 4,8 $km^3$ with about 75% of the original deposit already eroded at the present day.

The outline of the Humde deposit and the volume estimate based on it can certainly be improved by further investigations in the field. In particular, the delineation of the Braga and Manang deposits, and of the overall extent of the Manang rockslide deposit, require further field studies. Considering the large dimensions of remnant sediment bodies on both sides of the river at Manang and under the assumption that they once filled the valley in between, we can assume that the Manang rock avalanche deposit definitely had a volume of >1 $km^3$ after the rock avalanche event took place.

*2.5.2.3 Dating results – Humde/Manang*

We dated the exposure of a total of 14 individual boulders sampled on the deposit tops west, north west and north of Humde with 36Cl cosmogenic nuclide dating (refer to Sections 2.4.3.2 and 2.4.3.3; Figures 2.6, B+C; 2.17; 2.18; A2.2; and A2.3). One boulder sample (UM-18-21) was additionally processed and measured for 10Be cosmogenic nuclide dating (refer to Sections 2.4.3.1 and 2.4.3.3; and Figure A2.2D). Results of the cosmogenic nuclide dating effort around Humde are presented in Table 2.3 and Figures 2.17 and 2.19.

All the exposure ages fall into a conjoined time range between 500 and 900 a. Each 1σ-error range of a measurement overlaps with at least four others. We assume that the exposure of the boulders and thus the deposit tops represent the same formation event of a rock avalanche. The three samples we consider in the following as outliers (UM-20-04, UM-21-07, and UM-21-15) are located on three different sampled surfaces on opposite valley flanks. The one 10Be-measurement matches very well with its 36Cl counterpart, unlike the “double-sampling” results from Pisang Bowl. However the analytical error of this sample is quite large compared to the other 36Cl ages, due to the small amount of quartz that we were able to extract and process from the sample consisting of marly schist rock (see Table 2.3).

A weighted mean of 0,64 ± 0,05 ka was calculated with the online calculator IsoplotR (version 6.0, see Vermeesch, 2018), excluding the three outliers mentioned above (see also Figure 2.19).

Both surface erosion and inheritance appear to be conceivable for the outlier samples: For the two slightly younger samples (UM-20-04 and UM-21-07), our field notes indicate possible erosion of the sampled surfaces (see erosion comments in Table 2.3). The other samples considered for the weighted mean also cluster in two groups since four of them are slightly older than the others (UM-18-20, UM-18-21, UM-21-04, and UM-21-05) (see Figure 2.19 and Table 2.3). Here we cannot recognise any systematics from the erosion

comments, and therefore think that this is a usual variance that can occur in cosmogenic nuclide dating (normally distributed age population; see e.g., Dunai, 2010).

Our dating results can be compared with other absolute age constraints in the area, the ones which are directly associated with the deposits around Braga and Manang.

South-east of Braga, on the southern flank of the valley the Humde rockslide deposit is indeed dissected by an old and elongated glacial valley that almost reaches the Marsyandi valley floor and which displays an active glacier, Milarepa Glacier, and prominent lateral moraines (see Figure 2.17). Heimsath and McGlynn (2008) performed 10Be cosmogenic nuclide dating at Milarepa Glacier, on blocks carried by the glacier and also on blocks sitting on the moraine crests. They analysed both large individual boulders and aggregate samples of several smaller boulders. We recalculated the ages from the moraine crests only with the intention of obtaining an age for the deposition of these morphological features. The same procedure was used as for the 10Be samples analysed in this thesis (using a global mean production rate of 4,04 ± 0,19 at/g/yr, see 2.4.3.1). Out of eight samples from the moraine crests three yield young ages (100 – 390 a, 1σ-error range), four yield intermediate ages (510 – 840 a, 1σ-error range), and one an older age (1,21 ± 0,20 ka). For the young and intermediate ages, we calculated a weighted mean of 0,25 ± 0,03 ka (using the online calculator IsoplotR, version 6.0, see Vermeesch, 2018), considering that the older age is considerably affected by inheritance. These moraines therefore probably stem from a glacial advance during the Little Ice Age (LIA), a climatic phase of slightly colder and drier conditions known from the global and regional paleo-climate record (~1350 - ~1850 AD for the central Himalayas; see Section 2.6.2.4 below for more information). The Milarepa moraines were formed after the Humde event, when the glacier tongue encroached on what was probably already a heavily eroded rock avalanche deposit (Figure 2.17). This glacial advance was likely quite recent, assuming that some of the samples already carried significant inheritance prior to deposition on the moraine crests. Heimsath and McGlynn (2008) found several hundred years of inheritance in cosmogenic nuclide samples (their supraglacial samples) for glacial debris sitting and being transported on top of Milarepa Glacier.

Röthlisberger and Geyh (1986) found horizons of weak soil formation in the lateral moraine walls of the Gangapurna Glacier opposite to Manang (Figure 2.17). Here, the glacier eroded a deep trough into rock avalanche deposit, leaving steep walls on the sides. The glacial tongue still entered the main valley in the early 1950s (see Hagen, 1968). These paleo-soil horizons from the lowest lateral moraine adjacent to the eroded glacial gully were sampled for 14C carbon burial dating (see Figures 2.15D, and 2.17). We recalibrated these 14C-ages from the 1980s using the modern Intcal20 calibration curve (see Section 2.4.2; Reimer et al., 2020). Ages are mid to late Holocene, therefore clearly older than the boulder exposure on top of the

deposits around Humde. A separate rock avalanche deposit around Manang, however, needs to be older than these ages, because the moraines must have formed after a deposition event around Manang. Therefore, the 14C samples of Röthlisberger and Geyh (1986) provide a minimum age of 4,9 – 5,6 ka (oldest sample Hv-10759) for the Manang rock avalanche deposit, providing further evidence for a separate Manang deposit.

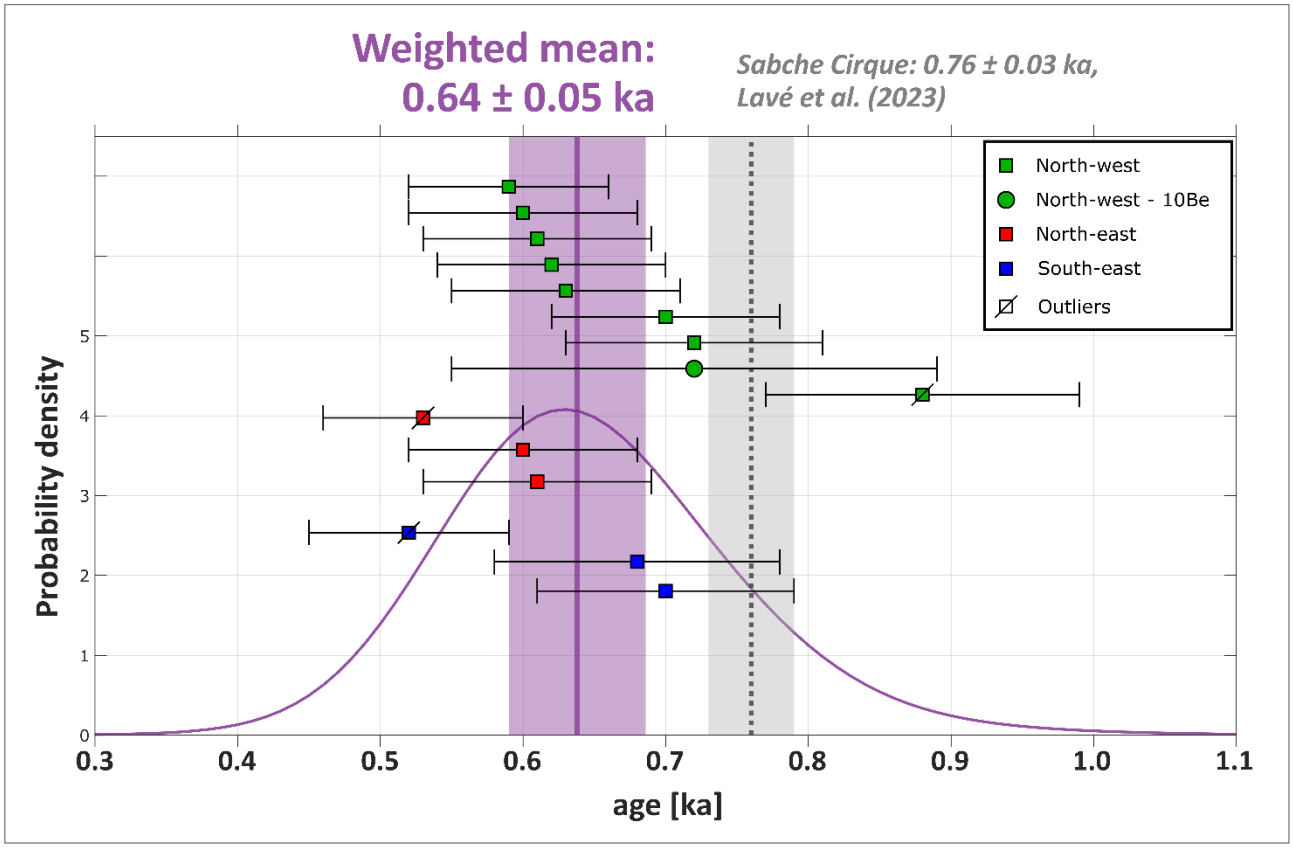


*Figure 2.19: Cosmogenic nuclide samples measured from the Humde rock avalanche site (36Cl and 10Be) plotted with 1σ-errors (see Table 2.3). Weighted mean with 1σ-error of boulder exposure ages (outliers excluded, in magenta), and cumulative PDF of all measurements considered for the weighted mean (in magenta) are shown. The proposed timing of the Sabche cirque rock avalanche, 760 ± 30 a, after Lavé et al. (2023) is indicated with a grey dotted line and a grey bar.*

## Table 2.3: Humde cosmogenic nuclide samples - Exposure dating results

**10Be exposure samples**

| Sample name | Lat. [°] | Lon. [°] | Alt. [m a.s.l.] | Object sampled | *Erosion comment* | Sample thickness [cm] | Shielding: topo / snow / total [-] | $^{10}Be/^{9}Be$ ratio [$10^{-14}$] ± 1σ | Amount of carrier [µg] (1) | Dissolved quartz [g] | $^{10}Be$ conc. [$10^{3}$ at/g] ± 1σ (2) | Exposure age [ka before 1950 AD] ± 1σ (3) |
|---|---|---|---|---|---|---|---|---|---|---|---|---|
| **UM-18-21** | 28,6609 | 84,0695 | 3797 | boulder | *hardly weathered surface, less foliated, spalling unlikely* | 4,0 | 0,955 / 0.989 / 0,944 | 0,742 ± 0,104 | 255,8 | 8,04 | 24,96 ± 4,75 | **0,72 ± 0,17** |

*(1) UM-18-21: carrier solution "Phena 1" of 2020 ± 83 µg/g $^{9}Be$ atoms*

*(2) after Blank correction: UM-18-21 corrected with one blank from same sample run with a $^{10}Be/^{9}Be$ ratio [$10^{-15}$] of 1,60802 ± 0,27647*

*(3) calculated with CREP developement version on 30 January 2024 with an assumed rock density of 2,65 g/cm $^{3}$ and zero erosion rate (see Section 2.4.3.1 for more details and references)*

**36Cl exposure samples**

| Sample name | Lat. [°] | Lon. [°] | Alt. [m a.s.l.] | Object sampled | *Erosion comment* | Sample thickness [cm] | Shielding: topo / snow / total [-] | Dissolved rock mass [g] (% of total) | Cl in target [ppm] ± 1σ (1) | CaO in target [%] ± 1σ (1) | $K_2O$ in target [%] ± 1σ (1) | $^{35}Cl/^{37}Cl$ ratio [-] ± 1σ | $^{36}Cl/^{37}Cl$ ratio [$10^{-13}$] ± 1σ | $^{36}Cl$ conc. [$10^{3}$ at/g] ± 1σ (2) | Exposure age [ka before 1950 AD] ± 1σ (3) |
|---|---|---|---|---|---|---|---|---|---|---|---|---|---|---|---|
| **UM-18-18** | 28,6596 | 84,0700 | 3796 | boulder | *hardly weathered, spalling of a cm-scale sheet possible* | 4,0 | 0,971 / 0.989 / 0,960 | 59,32 (76%) | 2,74 ± 0,07 | 56,05 ± 1,42 | 0,00 ± 0,00 | 45,58 ± 0,76 | 1,73 ± 0,08 | 107,96 ± 4,78 | **0,59 ± 0,07** |
| **UM-18-19** | 28,6592 | 84,0706 | 3795 | boulder | *hardly weathered , less foliated than UM-18-18, spalling unlikely* | 1,0 | 0,975 / 0.989 / 0,960 | 57,54 (71%) | 3,95 ± 0,10 | 55,23 ± 1,40 | 0,00 ± 0,00 | 34,99 ± 0,58 | 1,70 ± 0,10 | 111,34 ± 6,78 | **0,60 ± 0,08** |
| **UM-18-20** | 28,6603 | 84,0694 | 3798 | boulder | *less competent than UM 18-18+19 & 21, erosion by crumbling possible* | 2,5 | 0,962 / 0,989 / 0,951 | 56,40 (73%) | 2,93 ± 0,08 | 55,41 ± 1,39 | 0,00 ± 0,00 | 44,79 ± 0,82 | 2,02 ± 0,08 | 131,85 ± 5,65 | **0,72 ± 0,09** |
| **UM-18-21** | 28,6609 | 84,0695 | 3797 | boulder | *hardly weathered , less foliated than UM-18-18, spalling unlikely* | 4,0 | 0,955 / 0,989 / 0,944 | 34,20 (44%) | 3,21 ± 0,09 | 51,59 ± 1,29 | 0,76 ± 0,00 | 60,89 ± 0,99 | 1,13 ± 0,05 | 119,36 ± 5,59 | **0,70 ± 0,08** |
| **UM-20-02** | 28,6556 | 84,0941 | 3728 | boulder | *massive competent rock, looks pristine, area of active pasturing* | 2,0 | 0,989 / 0,989 / 0,978 | 61,40 (72%) | 4,21 ± 0,11 | 51,42 ± 1,29 | 0,37 ± 0,01 | 31,69 ± 0,54 | 1,71 ± 0,08 | 106,21 ± 4,99 | **0,61 ± 0,08** |
| **UM-20-03** | 28,6534 | 84,0949 | 3728 | boulder | *competent rock, hardly weathered, stone build structure nearby* | 4,0 | 0,991 / 0,989 / 0,979 | 27,22 (32%) | 6,61 ± 0,17 | 54,6 ± 1,39 | 0,00 ± 0,00 | 41,93 ± 0,71 | 0,79 ± 0,04 | 106,41 ± 5,66 | **0,60 ± 0,08** |
| **UM-20-04** | 28,6501 | 84,0965 | 3733 | boulder | *weathering grooves along foliation, erosion by chipping possible* | 3,0 | 0,991 / 0,989 / 0,980 | 83,03 (90%) | 4,32 ± 0,18 | 51,70 ± 1,29 | 0,19 ± 0,00 | 24,40 ± 0,76 | 2,03 ± 0,10 | 95,77 ± 4,83 | **0,53 ± 0,07** |
| **UM-21-04** | 28,6343 | 84,0734 | 3743 | boulder | *competent rock, looks pristine, spalling of sheet unlikely* | 1,5 | 0,985 / 0,989 / 0,974 | 22,15 (23%) | 23,46 ± 1,01 | 51,55 ± 1,29 | 0,00 ± 0,00 | 18,27 ± 0,58 | 0,63 ± 0,05 | 113,64 ± 9.29 | **0,68 ± 0,10** |
| **UM-21-05** | 28,6330 | 84,0713 | 3733 | boulder | *little alteration, little chipping* | 2,0 | 0,981 / 0,989 / 0,970 | 48,70 (52%) | 2,87 ± 0,13 | 52,43 ± 1,31 | 0,00 ± 0,00 | 51,15 ± 1,67 | 1,50 ± 0,08 | 111,45 ± 5,88 | **0,70 ± 0,09** |
| **UM-21-07** | 28,6346 | 84,0744 | 3755 | boulder | *block easily disintegrates into cm-thick slabs, spalling possible* | 3,0 | 0,986 / 0,989 / 0,974 | 70,90 (74%) | 4,05 ± 0,18 | 52,87 ± 1,32 | 0,00 ± 0,00 | 29,16 ± 0,96 | 1,76 ± 0,09 | 94,83 ± 5,18 | **0,52 ± 0,07** |
| **UM-21-15** | 28,6548 | 84,0645 | 3770 | boulder | *rugged surface, vertical foliation , breakout of slabs possible* | 4,0 | 0,984 / 0,989 / 0,973 | 65,87 (68%) | 3,32 ± 0,14 | 54,18 ± 1,36 | 0,00 ± 0,00 | 36,14 ± 1,16 | 2,54 ± 0,11 | 144,09 ± 6,63 | **0,88 ± 0,11** |
| **UM-21-16** | 28,6564 | 84,0624 | 3785 | boulder | *breaks loose along foliation planes, chipping of mm-cm sheets possible* | 1,5 | 0,976 / 0,989 / 0,965 | 48,65 (49%) | 4,17 ± 0,18 | 50,68 ± 1,27 | 0,00 ± 0,00 | 38,27 ± 1,18 | 1,35 ± 0,07 | 102,00 ± 5,77 | **0,61 ± 0,08** |
| **UM-21-17** | 28,6546 | 84,0619 | 3788 | boulder | *foliated rock,block is removed easily, no chipping, in forested area* | 3,0 | 0,985 / 0,989 / 0,973 | 73,22 (77%) | 4,51 ± 0,22 | 50,83 ± 1,27 | 0,17 ± 0,00 | 26,29 ± 0,96 | 2,08 ± 0,11 | 111,26 ± 6,27 | **0,63 ± 0,08** |
| **UM-21-18** | 28,6551 | 84,0620 | 3787 | boulder | *compact block of competent rock, no chipping, overgrown by tree* | 3,5 | 0,983 / 0,989 / 0,972 | 56,95 (61%) | 3,88 ± 0,17 | 50,38 ± 1,26 | 0,37 ± 0,01 | 35,73 ± 1,15 | 1,65 ± 0,09 | 107,86 ± 5,73 | **0,62 ± 0,08** |

*(1) target chemical concentrations measured with ICP-AES (inductively coupled plasma atomic emission spectrometry) at CEREGE*

*(2) after Blank correction: UM-18-18 & 19 & 20 & 21, and UM-20-02 & 03 corrected with one blank from same sample run with a $^{35}Cl/^{37}Cl$ ratio [-] of 242,35940 ± 4,82909 and a $^{36}Cl/^{37}Cl$ ratio [$10^{-16}$] of 5,28551 ± 1,39018; UM-20-04, and UM-21-04 & 05 & 07 & 15 & 16 & 17 & 18 corrected with one blank from same sample run with a $^{35}Cl/^{37}Cl$ ratio [-] of 240,82170 ± 9,60827 and a $^{36}Cl/^{37}Cl$ ratio [$10^{-16}$] of 25,65117 ± 7,84054*

*(3) calculated with CREP developement version on 30 January 2024 with an assumed rock density of 2,65 g/cm³, zero erosion rate and a formation age of 10 Ma (see Section 2.4.3.2 for more details and references)*

*for chemical composition of target and bulk rock of 36Cl-samples refer to Table A2.2 in Annexe*

## 2.5.3 Rock avalanche at Tilicho Lake

### *2.5.3.1 Field observations and outcrops – Tilicho Lake*

Upstream from Manang and the village of Khangsar, in the highest reaches of the upper Marsyangdi catchment area, there is a valley that is often visited by trekkers as an alternative route or as a detour from the original Annapurna Circuit (Figures 2.1 and 2.10). We are not aware of any geomorphological explorations so far in this area. On the way to Tilicho Base Camp (TBC), large parts of both valley flanks are covered with sedimentary bodies (Figure 2.10 and 2.20A). The ongoing erosion of these sediments created spectacular erosion structures, which includes pinnacles, escarpments, and steep hillslopes devoid of vegetation but covered with scree (Figure 2.20, B, C, and D).

The valley branches out at TBC and the confluence of Phache Khola from the north, and opens up spectacularly towards the south, giving view to glacial chutes, morainic material forming ridges, and the spectacular rock faces of the Annapurna massifs main crest to the south (Figure 2.20, E and F). The peak of Roc Noir (7 485 m.a.s.l., aka Khangsar Kang) appears strikingly dark. Behind it another ridge line continues up to the peak of Annapurna I (8 091 m.a.s.l.).

A bit less than a 900 m climb in altitude to the west of TBC leads to Tilicho Lake which is surrounded by a high plateau (Figure 2.20G). Tilicho Lake, with a surface elevation of 4 919 m.a.s.l. one of the highest lakes that holds considerable water volume on Earth, is dammed by a huge sedimentary fill to the west of Tilicho Peak (7 134 m.a.s.l.). Glaciers are encroaching on the lake on the south shore. The lake has no subaerial outflow, but drains through springs, located 140-180 m below the lake level and 1.7 km from its eastern shore. The spring appears in the valley carved out in the past by the glacier that was coming from the eastern Tilicho massif and flowing towards TBC.


A
W
Tilicho Peak
Tilicho Lake
loc. 1
B
W
Tilicho Peak
Tilicho Lake
bedrock
epigenetic gorge
C
ENE
D
ENE
E
SW
Roc Noir
F
SSE
Roc Noir
Gangapurna
SW
Tilicho Peak
NW
G

*Figure 2.20 (on previous page): Viewpoints of photographs are shown in Figure 2.22. (A) View towards the highest reaches of the upper Marsyangdi Valley from Khangsar towards Tilicho Peak. Eroding rock avalanche deposits stand out in grey against the vegetation. Photo taken in autumn 2021. (B) Closer look towards the area around TBC. The river cut an epigenetic gorge towards the south. Photo by J. Lavé, autumn 2021. (C) Rock avalanche deposits close to the Marsyangdi River featuring pinnacle erosion structures. Photo taken in autumn 2021. (D) More pinnacle erosion on steep slope covered with scree, close to TBC. Photo by J. Lavé, autumn 2021. (E) View towards Roc Noir from close to TBC. A detachment of rock from this rock face forming the rock avalanche seems likely. Glaciers and streams erode into the rock avalanche deposit. Photo taken in autumn 2021. (F) View from the high plateau at Tilicho Lake towards Gangapurna and Roc Noir peaks. Remnant rock avalanche material partially covered by glaciers. Photo taken in autumn 2021. (G) Panoramic view of Tilicho Lake (foreground) and Tilicho Peak (background) at sample location UM-21-22. Photo taken in autumn 2021.*

During our field survey of the area, we were able to examine outcrops of the voluminous sedimentary fills on the way up to the TBC and to Lake Tilicho. Not only are the observed erosion forms of these deposits typical for rock avalanche deposits in this region (in comparison with the Pisang Bowl and Humde/Manang localities, refer to Lavé et al. (2023), and see Sections 2.5.1.1 and 2.5.2.2), but a closer look quickly confirms the assumption of a giant rock avalanche as origin for the vast deposits present between Khangsar and Tilicho Lake (Figure 2.21). Along the right bank of the Marsyangdi Valley, one kilometre upstream of the village of Khansar, the base of the rock avalanche deposit can be observed at loc. 1 in sharp contact on top of glacial sediments, most likely basal till (Figures 2.21, A-B; and 2.22, loc. 1). Further upstream, highly deformed calcite veins within an intensely fractured rock mass can be spotted (Figures 2.21C; and 2.22, see loc. 2). Here, the rock avalanche deposit shows characteristics of a typical main body facies with larger blocks and larger structures of the source rock that remained preserved (see Section 1.3.5; Figure 1.5; and Hewitt et al., 2008; Weidinger et al., 2014). At loc. 3, west of TBC, closer inspection reveals angular, shattered rock fragments in a whitish, sandy matrix displaying jigsaw facies (Figures 2.21D; and 2.22, see loc. 3). At an outcrop at the same location, a brownish coloured band was spotted within a blocky mass of rock avalanche deposit (Figure 21E; and 2.22, see loc. 3). Possibly a shear zone of highly crushed material, and a preferential pathway of groundwater seeping through the slope. However, major shear zones with obvious schistosity or frictionite were not found within the rock avalanche deposits at Tilicho Lake and the valley towards Khansar.

Locally, similarly indurated deposits may lie unconformably on the rockslide breccia facies. Close to TBC, the rock avalanche deposit is overlain by horizontally layered sediments (Figure 2.21F; and 2.22, see loc. 4). Clasts are quite angular and grading can be observed between individual beds, suggesting a deposition by debris flows.




*Figure 2.21: Outcrop locations are indicated in Figure 2.22. (A) Sharp basal contact of rock avalanche deposit on glacial sediments (see Figure 2.20 for location, too). Yellow dots indicate contact. Photo taken in autumn 2021. (B) Closer look on glacial sediments of A. Photo taken in autumn 2021. (C) The rock avalanche deposit features highly deformed calcite veins. Large-scale structures within failed rock mass are preserved. Photo by J. Lavé, autumn 2018. (D) Shattered rock avalanche material with jigsaw facies. (E) Brown band, possibly shear zone within blocky rock avalanche deposit. Photo taken in autumn 2021. (F) Clast-supported, bedded sediments outcrop on top of the rock avalanche deposit. Angular clasts and grading indicate deposition by debris flows. Photo taken in autumn 2021.*

*2.5.3.2 Mapping and volume reconstruction – Tilicho Lake*

Mapping and volume reconstruction of the rock avalanche deposits at Tilicho Lake from satellite imagery, digital surface models, slope maps, and field photographs were performed in a very similar way than it was done for the area around Humde and Manang (see Sections 2.4.1.2, 2.4.4, and 2.5.2.2). Identical feature groups were used and moraine crests, lakes, and other landslide related geomorphological features were mapped.

The rock avalanche deposit apparently altered the course of rivers and the drainage of the area: Just downstream of TBC, towards the south, i.e. right bank, the river carved an epigenetic gorge into the bedrock (Figure 2.20B and 2.22). Further, a small tributary stream entering the Marsyangdi River from the north was shifted eastward in its lower reaches (see "re-directed drainage" in Figure 2.22). Nowadays, this stream erodes a steep gully into the valley flank and gained some drainage area by the filling of the Phache Khola valley (a little lake drains now to the east, Figure 2.22).

Particular challenges were encountered in preparing the map and a possible outline of the rock avalanche deposit at Tilicho Lake: Due to the large extent of the deposits, many assumptions or suppositions were made that we could not corroborate with field observations or photographs. For example, the sedimentary fills in the Phache Khola valley were assigned to originate from the same rock avalanche event responsible for the deposits around TBC and further down the Marsyangdi Valley, although we did not explore the valley and therefore did not study any outcrops there (Figures 2.22 and 2.23). Rock avalanche deposits at high altitudes are covered by glaciers and Tilicho Lake, and often the base of the deposit is not exposed, making it difficult to estimate its thickness. As with the reconstruction of the Humde rock avalanche volume, the presence of glaciers and fluvial or glacial sediments deposited prior to the slope failure brings further uncertainty for the volume reconstruction. The amount of glacial ice entrained in or buried by the rock avalanche depends on the glacial extent at the time of failure. The volumes of glaciers could have been significantly larger than today. In any case, interaction between the rock avalanche deposit and glaciers is certainly much more likely at Tilicho Lake compared to the Humde deposit. Glacier volumes are not included in our estimates but, given the size of the deposit here, the uncertainty coming from glaciers and sediments is limited (see also Lavé et al., 2023). In addition, the epigenetic canyon was removed during the pre-failure topography reconstruction. Negative volumes are not considered when estimating the volume of the remaining deposits. No adjustments to the calculation are therefore required for the estimate to take into account the erosion of the valley flanks after deposition (see Section 2.4.4).

In view of the above limitations, we estimate the volume of the deposit to have reached approximately 20,8 $km^3$, with some significant unconstrained error involved. According to our calculations, around 52% of the rock avalanche deposit have already been eroded to date (see Figure 2.23).

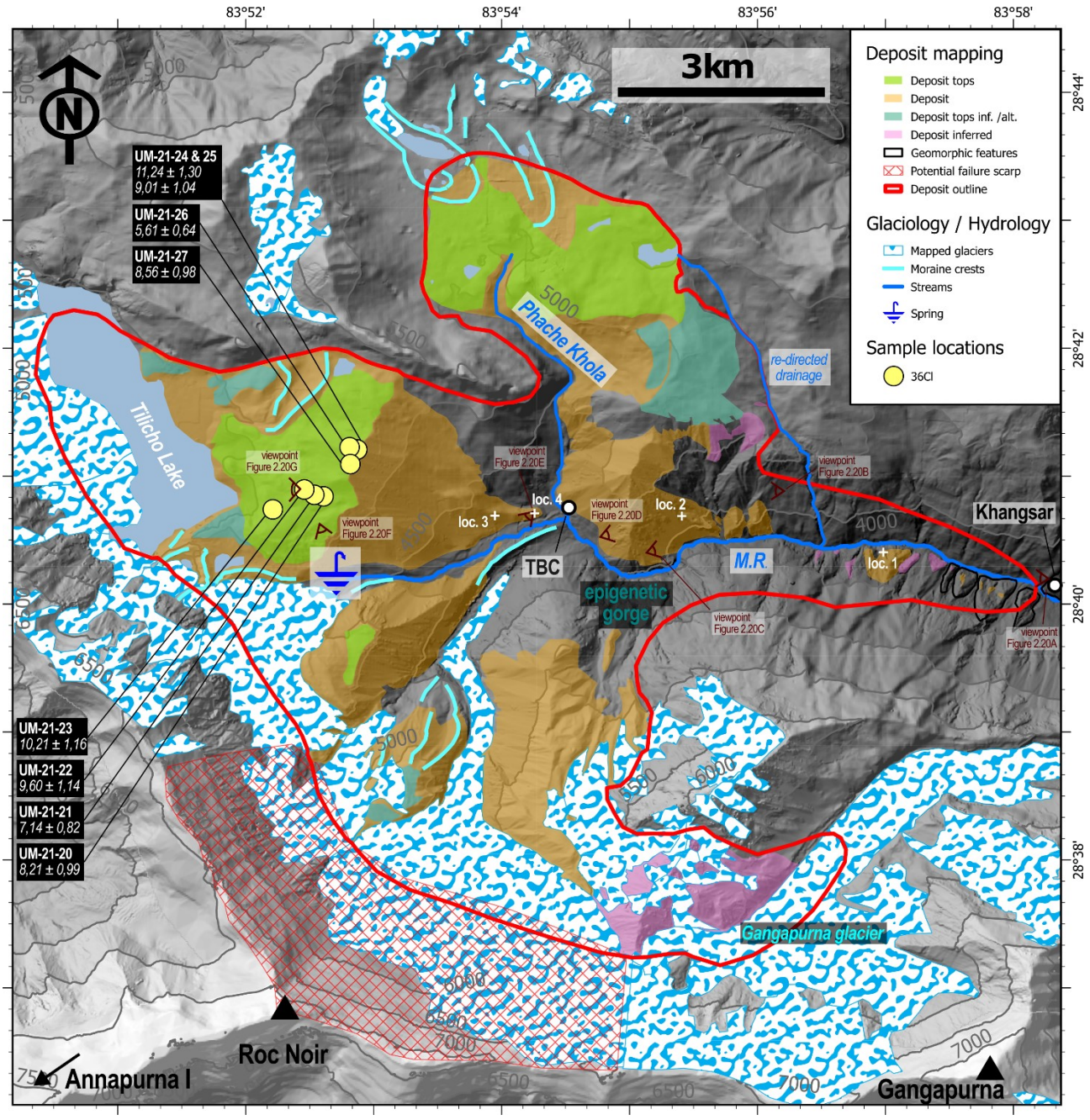


*Figure 2.22: Mapping and dating results (cosmogenic nuclides) for the rock avalanche deposit at Tilicho Lake. See Figure 2.10 for the location of this map area in the Marsyangdi Valley. Outcrop locations are indicated (loc. 1-4, see Section 2.5.3.1). The topography is represented by a combination of grey-scale altitude colouring overlaid with a transparent hillshade. The digital surface model is a combination of ALOS and HMA datasets (see Section 2.4.1.2 for more details on the datasets). TBC = Tilicho Base Camp, M.R. = Marsyangdi River.*

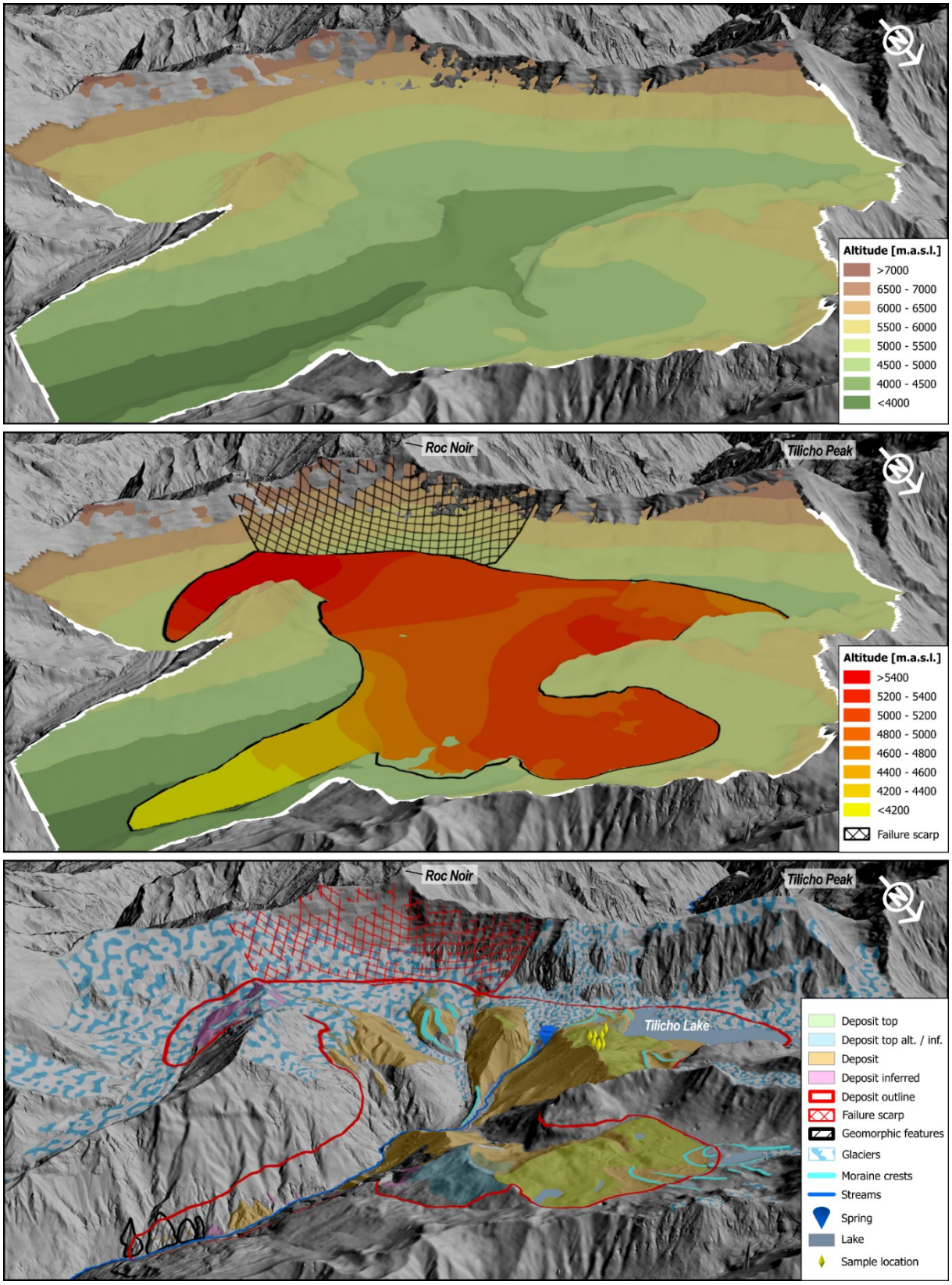


*Figure 2.23: Volume reconstruction for the rock avalanche event responsible for the deposits around Tilicho Lake: Pre-failure topography (top) and surface of deposit just after emplacement (middle) were reconstructed for the volume estimate. Mapping results for the rock avalanche deposits in 3D-view in the bottom (see also Figure 2.22. The digital surface model is a combination of ALOS and HMA datasets (see Section 2.4.1.2 for more details on the datasets).*

*2.5.3.3 Dating results – Tilicho Lake*

We utilized 36Cl cosmogenic nuclide dating to determine the exposure ages of eight individual boulders collected from the elevated surface that represents the top of the large mass of rockslide deposit damming the Tilicho Lake (refer to Sections 2.4.3.2 and 2.4.3.3; Figure 2.6D; Figure A2.4, and Figures 2.22 and 2.23). The results from our cosmogenic nuclide dating are summarized in Table 2.4 and exposure ages are presented in Figures 2.22 and 2.24.

Exposure ages spread out over a time period of 5,0 to 12,5 ka (including 1σ-error ranges; see Figure 2.24), which is somewhat unexpected for boulders that were all supposed to come from a surface created by a single formation process, namely the Tilicho Lake rock avalanche. In search for an explanation of this variance, the effect of erosion on the sampled surfaces seems to be the most obvious. The boulders are exposed to harsh conditions at high altitudes, i.e. strong winds and frost cracking, and they have been in place for long periods of several thousand years. The dating results correlate to some extent with the erosion comments made in the field or from photographs of the sampled surfaces (see Table 2.4). The surfaces with older exposure ages are noted as weathered and for some of them the possibility of erosion is mentioned, while the younger samples in most cases showed clear signs of erosion when sampled, or at least some indication of possible erosion.

The oldest three samples have largely overlapping 1σ-error ranges (see Figure 2.24). We consider them to be the least affected by surface erosion and therefore argue that they best represent the actual time of deposition of the rock avalanche deposit at Tilicho Lake. The other five younger depositional ages are considered outliers. This assessment is by no means unequivocal, partly due to the possibility that the samples with the highest concentrations of cosmogenic nuclides are affected by inheritance. Although improbable considering the size of the rock avalanche, this possibility cannot be entirely ruled out. A weighted mean of 10,3 ± 1,4 ka was calculated with the online calculator IsoplotR (version 6.0, see Vermeesch, 2018) with the oldest three samples (see also Figure 2.24). For the following discussions in this thesis, we will use this age as the event age of the Tilicho Lake giant rock avalanche.

The selection of the five youngest samples as outliers is a highly subjective decision, not based on any statistical analysis (similar approach already taken for the Pisang Bowl and Humde samples, Figures 2.14 and 2.19). One could consider applying a statistical criterion to identify outliers, such as Chauvenet's or Peirce's criterion (for details, see Dunai, 2010; Taylor, 1997). These methods assume that the probability distribution of individual measurement points around an expected true value follows a normal (Gaussian) distribution.

In general, the application of statistical criteria for outlier selection in cosmogenic nuclide dating is particularly challenging. It is erroneous to assume that the uncertainties produced by natural processes

affecting exposure ages are always normally distributed. In fact, inheritance leads only to older dating results, while erosion or shielding leads only to younger results. The importance of these individual processes can vary depending on the specific setting in which the samples were collected.

Therefore, it is worth questioning whether the application of statistical criteria is appropriate for the spread of exposure ages we observe at Tilicho Lake: The geological process most likely to be responsible for the uncertainty (or error) in our dating measurements is surface erosion, with snow shielding possibly also playing a role to a lesser extent. These processes are expected to be of greater significance than analytical and methodological uncertainties (Dunai, 2010). By assuming a unique deposition event, it can be expected that both processes skew the dating results mostly towards younger ages, thereby rendering the distribution of dates unlikely to follow a normal distribution.

As an alternative to the weighted mean calculated above, in case we entirely dismiss the possibility of inheritance due to the scale of the deposit and the improbability of inherited blocks being exposed, we could argue that the oldest age in the distribution is the most representative of the true timing of the rock avalanche. The age of the oldest sample, 11,2 ± 1,3 ka, would then be considered a minimum age, acknowledging that surface erosion cannot be excluded.

**Table 2.4: Tilicho cosmogenic nuclide samples - Exposure dating results**

**36Cl exposure samples**

| Sample name | Lat. [°] | Lon. [°] | Alt. [m a.s.l.] | Object sampled | *Erosion comment* | Sample thickness [cm] | Shielding: topo / snow / total [-] | Dissolved rock mass [g] (% of total) | Cl in target [ppm] ± 1σ (1) | CaO in target [%] ± 1σ (1) | $K_2O$ in target [%] ± 1σ (1) | $^{35}Cl/^{37}Cl$ ratio [-] ± 1σ | $^{36}Cl/^{37}Cl$ ratio [$10^{-13}$] ± 1σ | $^{36}Cl$ conc. [$10^3$ at/g] ± 1σ (2) | Exposure age [ka before 1950 AD] ± 1σ (3) |
|---|---|---|---|---|---|---|---|---|---|---|---|---|---|---|---|
| **UM-21-20** | 28,6807 | 83,8768 | 5170 | boulder | *very hard rock, rugged, strongly weathered, abraded, exposed loc.* | 1,0 | 0,981 / 0.944 / 0,926 | 57,33 (60%) | 2,42 ± 0,11 | 53,38 ± 1,35 | 0,21 ± 0,01 | 51,63 ± 1,60 | 39,61 ± 1,98 | 2556,22 ± 129,62 | **8,21 ± 0,99** |
| **UM-21-21** | 28,6809 | 83,8756 | 5160 | boulder | *very foliated rock , thin, cm-scale sheets peel off easily, spalling likely* | 2,0 | 0,992 / 0.944 / 0,936 | 40,38 (40%) | 1,83 ± 0,10 | 51,95 ± 1,30 | 0,26 ± 0,01 | 80,11 ± 2,53 | 24,24 ± 0,94 | 2159,12 ± 85,85 | **7,14 ± 0,82** |
| **UM-21-22** | 28,6816 | 83,8743 | 5144 | boulder | *strong vertical foliation, highly weatheres, lichen, breakouts possible* | 4,0 | 0,992 / 0.944 / 0,936 | 31,71 (32%) | 2,07 ± 0,12 | 52,89 ± 1,32 | 0,00 ± 0,00 | 86,61 ± 2,68 | 24,27 ± 0,96 | 2756,89 ± 111,98 | **9,60 ± 1,14** |
| **UM-21-23** | 28,6790 | 83,8702 | 5057 | boulder | *very hard rock, looks pristine, lichen, sampled at edge* | 2,5 | 0,988 / 0.944 / 0,932 | 28,27 (28%) | 3,23 ± 0,16 | 46,18 ± 1,15 | 0,62 ± 0,02 | 69,64 ± 2,18 | 20,33 ± 0,82 | 2609,18 ± 107,19 | **10,21 ± 1,16** |
| **UM-21-24** | 28,6868 | 83,8811 | 5363 | boulder | *foliated rock looks strongly weathered, chipping* | 4,0 | 0,998 / 0.944 / 0,942 | 70,08 (74%) | 2,50 ± 0,11 | 54,10 ± 1,35 | 0,00 ± 0,00 | 43,22 ± 1,36 | 69,40 ± 2,53 | 3704,79 ± 138,40 | **11,24 ± 1,30** |
| **UM-21-25** | 28,6868 | 83,8812 | 5363 | boulder | *foliated rock disintegrates strongly by chipping, less promissing* | 2,5 | 0,998 / 0.944 / 0,942 | 59,72 (77%) | 2,48 ± 0,11 | 57,87 ± 1,45 | 0,19 ± 0,00 | 48,76 ± 1,54 | 53,62 ± 1,97 | 3307,06 ± 124,63 | **9,01 ± 1,04** |
| **UM-21-26** | 28,6871 | 83,8802 | 5349 | boulder | *less weathered and less chipping than 24 & 25, refreshed surface?* | 2,0 | 0,997 / 0.944 / 0,941 | 63,01 (72%) | 2,07 ± 0,09 | 54,02 ± 1,35 | 0,30 ± 0,01 | 53,76 ± 1,68 | 32,22 ± 1,26 | 1873,82 ± 75,00 | **5,61 ± 0,64** |
| **UM-21-27** | 28,6849 | 83,8803 | 5329 | boulder | *snow may cover fallen off pieces, not so much chipping* | 3,0 | 0,997 / 0.944 / 0,941 | 72,43 (72%) | 5,01 ± 0,21 | 54,19 ± 1,35 | 0,20 ± 0,01 | 24,37 ± 0,76 | 53,04 ± 1,97 | 2926,70 ± 111,73 | **8,56 ± 0,98** |

*(1) target chemical concentrations measured with ICP-AES (inductively coupled plasma atomic emission spectrometry) at CEREGE*

*(2) after Blank correction: UM-21-20 & 21 & 22 & 23 & 24 & 25 & 26 & 27 corrected with one blank from same sample run with a $^{35}Cl/^{37}Cl$ ratio [-] of 240,82170 ± 9,60827 and a $^{36}Cl/^{37}Cl$ ratio [$10^{-16}$] of 25,65117 ± 7,84054*

*(3) calculated with CREP developement version on 30 January 2024 with an assumed rock density of 2,65 g/cm³, zero erosion rate and a formation age of 10 Ma (see Section 2.4.3.2 for more details and references)*

*for chemical composition of target and bulk rock of 36Cl-samples refer to Table A2.2 in Annexe*

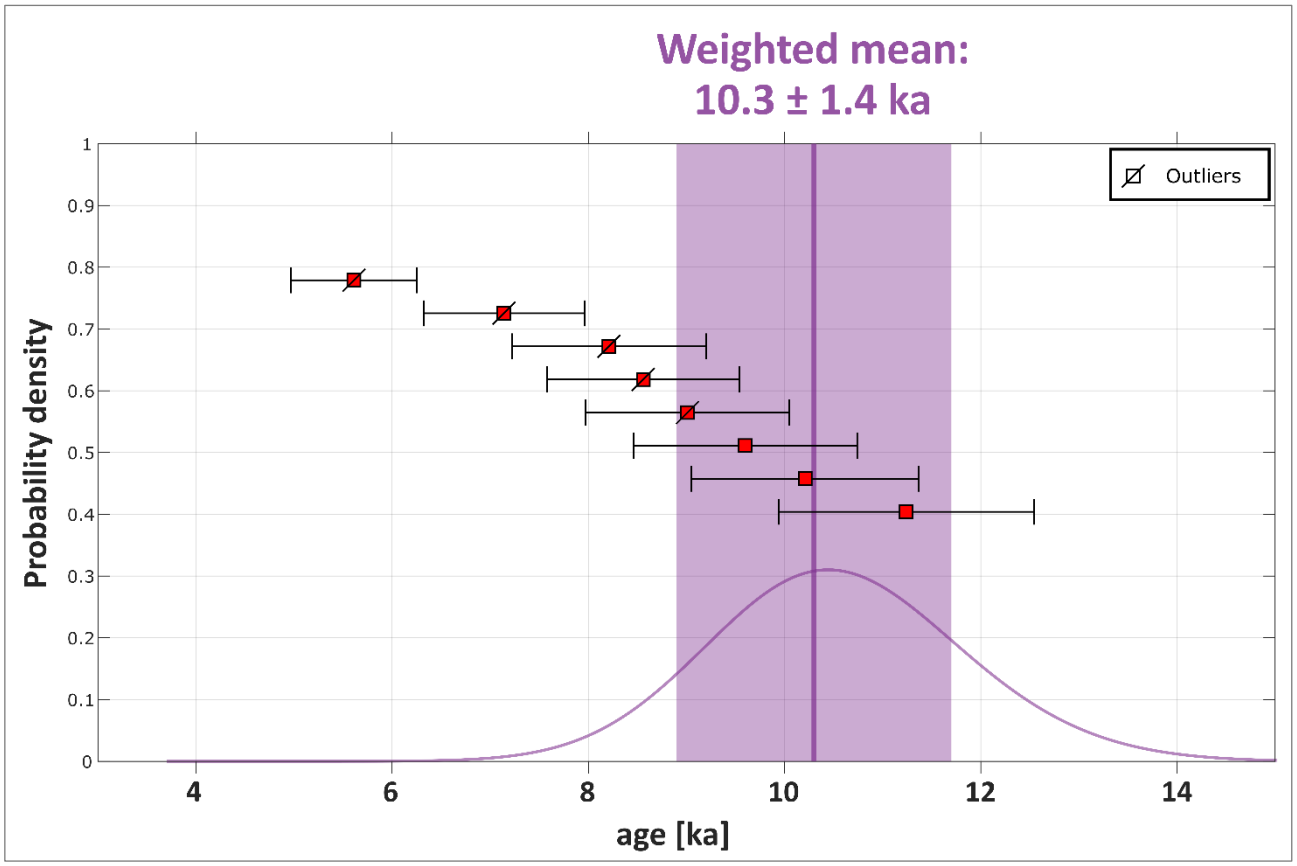


*Figure 2.24: Cosmogenic nuclide samples measured from boulders sampled on the high plateau at Tilicho Lake (36Cl exposure dating only) plotted with 1σ-errors (see Table 2.4). Weighted mean with 1σ-error of boulder exposure ages (outliers excluded, in magenta), and cumulative PDF of all measurements considered for the weighted mean (in magenta) are shown.*

## 2.6 Discussion – Upper Marsyangdi

### 2.6.1 Integration of our results into the central Himalayan giant rock avalanche record

Our new quantitative estimates for deposition ages and volumes of the giant rock avalanche deposits in upper Marsyangdi Valley can now be compared with already existing estimates published in earlier studies (Weidinger, 2006; Fort, 2011). Additionally, our results can now be integrated in the existing record of rock avalanche deposits in the Annapurna massif and the central Himalayan region. All known ages and volume estimates of giant rock avalanche deposits in the central Himalayan region are summarized in Table 2.5.

The Pisang Bowl rock avalanche deposit is the smallest of the deposits in the upper Marsyangdi Valley investigated as part of this PhD. Two Master's students, M. Groult and A. Diarra, conducted a volume reconstruction of the Pisang Bowl rock avalanche deposit as part of a laboratory project supported by J. Lavé and the PhD student. They assumed either a V- or U-shaped valley topography beneath the deposit and used a methodology similar to that outlined in this thesis (see Section 2.4.4). Using digital surface models and raster calculations, they estimated the total volume of the Pisang Bowl deposit to be either 0,3 or 0,5 $km^3$ for a V- or U-shaped valley, respectively, with only about 4% of the deposit having been eroded to date (Table 2.5 and Figure A2.5). This estimate is in contrast to the higher volume proposed by Weidinger (2006) and Korup et al. (2006) of "at least 1 $km^3$". We attribute this discrepancy to differing assumptions regarding the underlying bedrock surface of the valley and subsequently the topography prior to the deposit emplacement. Determining the pre-failure topography proves challenging, as the transition from a U-shaped to a V-shaped valley occurs precisely at the location of the deposit. Future investigations of the Pisang Bowl rockslide should work towards resolving these conflicting views on the total volume of the deposit. Based on the different age groups we have obtained in the absolute dating of the deposit, a multi-event history can be assumed (Events 0-2 in Table 2.5). Researchers working on the Pisang Bowl in the future should try to better decipher the individual events and the associated volumes.

The Humde deposit is considerably bigger in volume than the deposit at Pisang Bowl: nearly ten times greater if we refer to our estimates (0,5 vs. 4,8 $km^3$). Previous estimates vary widely (5 – 15 $km^3$, see Table 2.5), but the existence of another separate deposit around Manang was not considered in these studies. Therefore, they cannot be directly compared with our new estimate. We estimated the proportion of the volume eroded to date to be around 75%, which corresponds to a volume of 3,6 $km^3$. In view of the "young" age of the

deposit of only 640 ±50 a, this is remarkable, if not an issue hard to explain. How was it possible to erode so much sediments from that valley stretch in such a short time? The example of the Sabche cirque (Lavé et al., 2023) demonstrates that very rapid removal of thick debris accumulation is possible in Himalayan setting, even if the two contexts are quite distinct. We can indeed see that the river gradient of the upper Seti river in the Sabche cirque is much higher than that of the upper Marsyandi river. However, we presume that this difference is compensated for by the much greater discharge of the Marsyandi river, which allows it to maintain a high fluvial transport capacity.

Whatever the response to this question, several other questions also remain unanswered: If the debris have been rapidly eroded, where did it go and where could we find these sediments today? Was there a catastrophic Landslide Lake Outburst Flood (LLOF) created by overtopping of the deposit by the Marsyangdi River? Why are there no signs of a lake that formed upstream? Why do we find no sign of a catastrophic outburst flood further down in the valley, either? The absence of lacustrine deposits and the lack of evidence for a LLOF is somewhat contradicting. These questions should be further investigated through additional research supported by further field investigations in the area. In addition to the erosion issue, which should be a primary goal for further research into the rock avalanche deposits around Humde and Manang, future investigations should find further evidence of a separate and older deposit at Manang. Subsequently, work should be done on deciphering age and volume constraint of the Manang event.

Possible detachment areas of rock avalanches in the Humde/Manang valley stretch must also be explored. Whereas source areas are quite evident for both Pisang Bowl and Tilicho Lake deposits (see Sections 2.5.1.1 and 2.5.3.2; and Figures 2.11; 2.12D; 2.13; 2.20, E+F; and 2.22), a possible origin of the rock avalanche deposits around Humde and Manang is debated in the existing literature. It must be mentioned that a second, chronologically older deposit at Manang has not yet been considered in previous studies.

Based on the lithology of the rock avalanche material, Fort (2011) proposes that the detachment area was located to the south of the Marsyangdi Valley and that the rock avalanche originated from a fold hinge collapse on the northern slopes of the Annapurna main ridge crest (see Figure 2.10). Nonetheless, a specific area is not mentioned. On the contrary, Weidinger (2006) suggests a detachment area to the north-west of Humde on the slopes facing to the south-west towards the Julu Khola confluence (see Figure 2.17). He based his assessment on the lithologies of clasts he found in the avalanche deposit by comparing them with geological maps that exist for the area (Hagen, 1968; Bordet et al., 1971; Colchen et al., 1986).

We did not find during our field investigation any strong evidence to support or discard one of the two scenarios. We can only speculate based on the overall geometry of the rockslide deposit.

From our mapping and volume reconstruction results, an emplacement direction for the Humde deposit can be anticipated considering the heights of the surface of the deposit immediately after emplacement (see Figures 2.17 and 2.18). The deposit tops show their highest elevations south-west of the confluence of the Sabche Khola and the Marsyangdi River, within the deposit body where our outcrop 1 (loc. 1) is located. The deposit tops west and east of Julu Khola are considerably lower in elevation, about 130 and 190 m, respectively (see Figures 2.17 and 2.18). When a rock avalanche falls from great heights, involves very large volumes, is likely to have been laterally confined while travelling through a tributary valley, and is finally deposited in a confined valley, a build-up of rock avalanche material may occur by impact on the slope opposite the direction of origin (see, e.g. Hewitt, 2002). In other words, the highest deposition heights should occur on the opposite slope if the emplacement was very energetic, which can be fairly possible for the Humde rock avalanche due to the enormous size of the deposit, the high degree of fractionation generally observed (see Section 2.5.2.1 above), and the high relief of the surrounding slopes in general. Nonetheless, a proper analysis of potential detachment areas and runout characteristics must first be carried out to make informed predictions about the expected form of deposition and the possibility of build-up on the opposite slope. Such an analysis could be carried out, for example, by applying empirical equations from natural examples (Nicoletti and Sorriso-Valvo, 1991; Strom et al., 2019) or by using a runout model (e.g., Aaron et al., 2022). However, this only makes sense once possible detachment areas have been explored through additional fieldwork and a selection of possible detachment areas exists for analysis.

However, I speculate that the rock avalanche likely entered the Marsyangdi Valley from the north, from the Julu Khola valley. The detachment area could be south of the Chulu Far East Peak (Figure 2.10). According to this hypothesis, the material of the rock avalanche had to be slightly deflected by a ridge (north of the deposits north-west of Humde) during the collapse to follow the course of the Julu Khola valley (see also Figure 2.17). It was then thrown back into the main valley from the slopes to the east of the Julu Khola.

The detachment area proposed here for the Humde rock avalanche matches with the one proposed by Hagen (1968), who identified the same area on the eastern flank of the Chulu massif as the detachment area of a massive rock avalanche and inferred glacial undercutting of dip-slope beds as a Preparatory factor of the rock avalanche.

The slopes north of Braga and Manang, where boulders on glacial moraines were dated by Pratt-Sitaula et al. (2011) to the late Pleistocene and early Holocene (see Figure 2.17), can be excluded as potential detachment zones of rock avalanches in this valley section, at least for the time since glaciers were active there. If these moraines had been hit by an energetic rock avalanche after their formation, this would have made such dating impossible.

Both valley flanks, north and south of the Humde and Manang deposits, generally show large-scale structures that favour extremely voluminous rock slope failures (see Section 2.6.2 below). Unfortunately, the lithologies in the deposit were not studied in detail and compared with the existing geological maps. The proposed independent Manang rock avalanche east of the Humde deposit could originate from either the north or south side of the valley. Further research is required to clarify this.

The rock avalanche deposit at Tilicho Lake is a completely new entry in the list of rock avalanches in the central Himalayas (see Table 2.5). With an estimated deposit volume of 20,8 $km^3$, this rock slope failure represents the second largest event to date in the central Himalayas after the rock avalanche in the Sabche cirque (volume of 27 +4/-3 $km^3$ ) (Lavé et al., 2023). Given the age of 10,3 ± 1,4 ka, it is not surprising that large parts of the deposit are already eroded (estimated 52%). According to the rock avalanche deposit geometry, the debris lithology (relatively similar to Ordovician and Silurian rocks found in the Sabche valley) and the regular shape of the steep cliff at this location, we hypothesize that the potential detachment area of the Tilicho Lake rock avalanche was the steep E-W ridge of the Roc Noir and Eastern Nilgiri massif (called the Great Barrier) (see Figure 2.22).

The Annapurna massif shows a particular abundance of very voluminous giant rock avalanche deposits. Within a stretch of about 30 km along the main crest of the massif, three extremely giant deposits (~5 $km^3$ or larger) are found (see Figures 2.1, 2.10), from west-to east: Tilicho Lake, Humde, and Sabche cirque. Presumably, a fourth one with considerable volume is situated at Manang. Apart from the Annapurna massif, only one other rock avalanche deposit of comparable size is known for the central Himalayan record: The much older Tsergo Ri rock avalanche deposit with an estimated volume of ~10 $km^3$ and an age of ~50 ka (see citations in Table 2.5). This accumulation of giant rock avalanches in the Annapurna massif is astonishing. Is it based simply on an observational bias and many more deposits wait for recognition in the other massifs of the central Himalayas? Is it simply a coincidence or could there be some explanation to that? We will inquire possible Precondition and Preparatory factors of the giant rock avalanche events in the Annapurna massif in Section 2.6.2 below.

It can certainly be expected that unmapped deposits of giant rock avalanches in the central Himalayas have not yet appeared in the scientific literature and/or are completely unknown.

**Table 2.5: Volume and ages of upper Marsyangdi giant rock avalanche deposits and comparison with other giant rock avalanches in the central Himalayas**

| UPPER MARSYANGDI GIANT ROCK AVALANCHES | | | | | | |
|---|---|---|---|---|---|---|
| | | New estimates | | Previous estimates | | |
| **Locality** | | **Deposit volume [km³] (eroded thereof)** | **Absolute dating of event [ka BP (before 1950 AD)]** | **Deposit volume [km³] (eroded thereof)** | **Absolute dating of event [ka BP (before 1950 AD)]** | *References* |
| **Latamrang** | | min. 1,5 (44%) (1) | *no new estimate* | 5,5 (18%) | 5,44 +0,04/-0,05 | *Pratt-Sitaula et al. (2007); Korup et al. (2006)* |
| **Pisang Bowl (Dhukur Pokhari)** | total | 0,5 (4%) (1) | | min. 1 ("largely intact") | none ("postglacial"), "at least one huge rockslide" | *Weidinger (2006); Korup et al. (2006)* |
| | event 0 ? | ? | 7,0 ± 1,1 | | | |
| | event 1 | ? | 0,73 - 0,78 | | | |
| | event 2 | ? | 0,50 ± 0,05 | | | |
| **Humde** | | ~4,8 (75%) | 0,64 ± 0,05 | ~15 (Humde and Manang together) | none ("interstadial ?, pre- last glacial advance") | *Fort (1993, 2011)* |
| | | | | 5 (20-40%) (Humde and Manang together) | none ("interglacial") | *Weidinger (2006)* |
| **Manang** | | unconstrained, but considerable | none, but min. several 100 years older than Humde | *not recognised so far, considered as part of Humde* | | |
| **Tillicho** | | ~21 (52%) | 10,3 ± 1,4 | *not recognised as rock slope failure before* | | |

| OTHER GIANT ROCK AVALANCHES STUDIED IN THE CENTRAL HIMALAYAS | | | | |
|---|---|---|---|---|
| **Locality** | **Deposit volume [km³] (eroded thereof)** | **Absolute dating of event [ka BP (before 1950 AD)]** | *References* | **Comments** |
| **Sabche** | 27 +4/−3 (~90%) | 0,76 ± 0,03 | *Lavé et al. (2023)* | |
| **Dhampu-Chhoyo** | ~3 | 4,7 ± 0,8 (2) | *Fort (2000); Zech et al. (2009)* | possibly another older rockslope failure (~30 ka), complexity by damming and glaciation |
| **Phoksumdo - Ringmo rockslide** | 1,5 | 20,9 ± 1,7 | *Yagi (1997); Ibetsberger and Weidinger (2000); Fort et al. (2014)* | stable lake formed upstream of deposit |
| **Tsergo Ri** | ~10 | 10Be: 50,4 ± 3,7; FT: 51 ± 13 (3) | *Heuberger et al. (1984); Weidinger et al. (1996); Barnard et al (2006); Takagi et al. (2007)* | |
| **Khumjung** | 2,1 | none ("pre- last glacial advance") | *Heuberger (1986)* | |
| **Dzongri (Kangchenjunga massif)** | ~2,5 (84%) | none (estimated min. 20-21) | *Weidinger and Korup (2009)* | |

*(1) analyses performed by student project of A. Diarra and M. Groult, see Figures A2.5 and A2.6*

*(2) recalculated from Zech et al. (2009)'s 10Be-samples LE41 and LE51 in the same way as the samples of this PhD-thesis, the development version of the online calculator CREP was used applying an identical scaling scheme and databases (global mean production rate of 4,04 ± 0,19 at/g/yr); see Section 2.4.3.1 for more information and references*

*(3) recalculated from Barnard et al (2006)'s landslide sample with highest 10Be-concentration KTM10 in the same way as the samples of this PhD-thesis, the development version of the online calculator CREP was used applying an identical scaling scheme and databases (global mean production rate of 4,04 ± 0,19 at/g/yr); see Section 2.4.3.1 for more information and references; FT stands for fission-track, dating of pseudotachylyte by Takagi et al. (2007)*

## 2.6.2 Causes and Triggers of giant rock avalanches in the upper Marsyangdi Valley

### *2.6.2.1 Precondition Factors*

Possible Precondition factors for giant rock avalanches are suggested by the characteristics of the bedrock and tectonic structures in the area.

Our study area lies in the upper Marsyangdi Valley, situated north of the South Tibetan Detachment (STD) (please refer to Section 2.2.1 for details). The metasediments found there consist of hard and competent marbles, schists, and quartzites. These rocks tend to fracture along bedding or schistosity planes and form joint sets that cut across them. Additionally, they exhibit large-scale folding, with a predominant structure located north to the Annapurna main ridge crest, extending from the Nilgiri peaks in the west to Annapurna II in the east (see Figures 2.1 and 2.10). This structure is an overturned anticline leaning towards the north, meaning the fold's axial plane inclines southward (see Figure 2.3 and profiles in Figure 2.25). The location of this anticlinal structure aligns with the detachment zone we identified for the Tilicho Lake rock avalanche (compare profiles' location in Figure 2.1 with the detachment zone in Figure 2.22). Large-scale catastrophic rock slope failures are known to be associated with anticlinal folding (see Stead and Wolter, 2015; Fossen, 2010). Damage to the rock mass due to the folding and jointing perpendicular to the bedding creates preferential failure planes. We consider anticlinal folding to be a significant precondition for the Tilicho Lake rock avalanche.

The fracture surface of the Pisang Bowl largely follows a single bedding plane within a syncline whose hinge line is inclined by about 30° to the west and forms a spectacular bowl-shaped fold in the metamorphosed sedimentary layers there (see Figures 2.11 and 2.13). This rock slide features a good example of a typical dip-slope failure and detachment along schistosity planes that also serve as sliding surfaces, a very common failure mechanism among catastrophic rock slope failures (see Section 1.3.3, Stead and Wolter, 2015, and inventory by Glastonbury and Fell, 2010). Another giant rock avalanche featuring a dip-slope failure within the central Himalayan record is the Dhampu-Chhoyo rock avalanche in the Kali Gandaki valley (see Table 2.5; and, e.g., Fort, 2000).

A more detailed study of lithological and structural controls on the failure behaviour of the rock avalanches studied in this PhD are limited by the field observations undertaken. In future surveys of the detachment zones, a better assessment of rock mechanical conditions in the headwalls, including fracturing, could help to link lithological characteristics to the occurrence of the slope failures (see, e.g., Brideau et al., 2009). This is certainly not feasible for the Roc Noir headwall at Tilicho Lake, which is difficultly accessible due to its high

altitude (~5 700 – ~7 450 m.a.s.l.), steep slopes, and to the thick ice cover (see Figures 2.20, E+F; and 2.22).

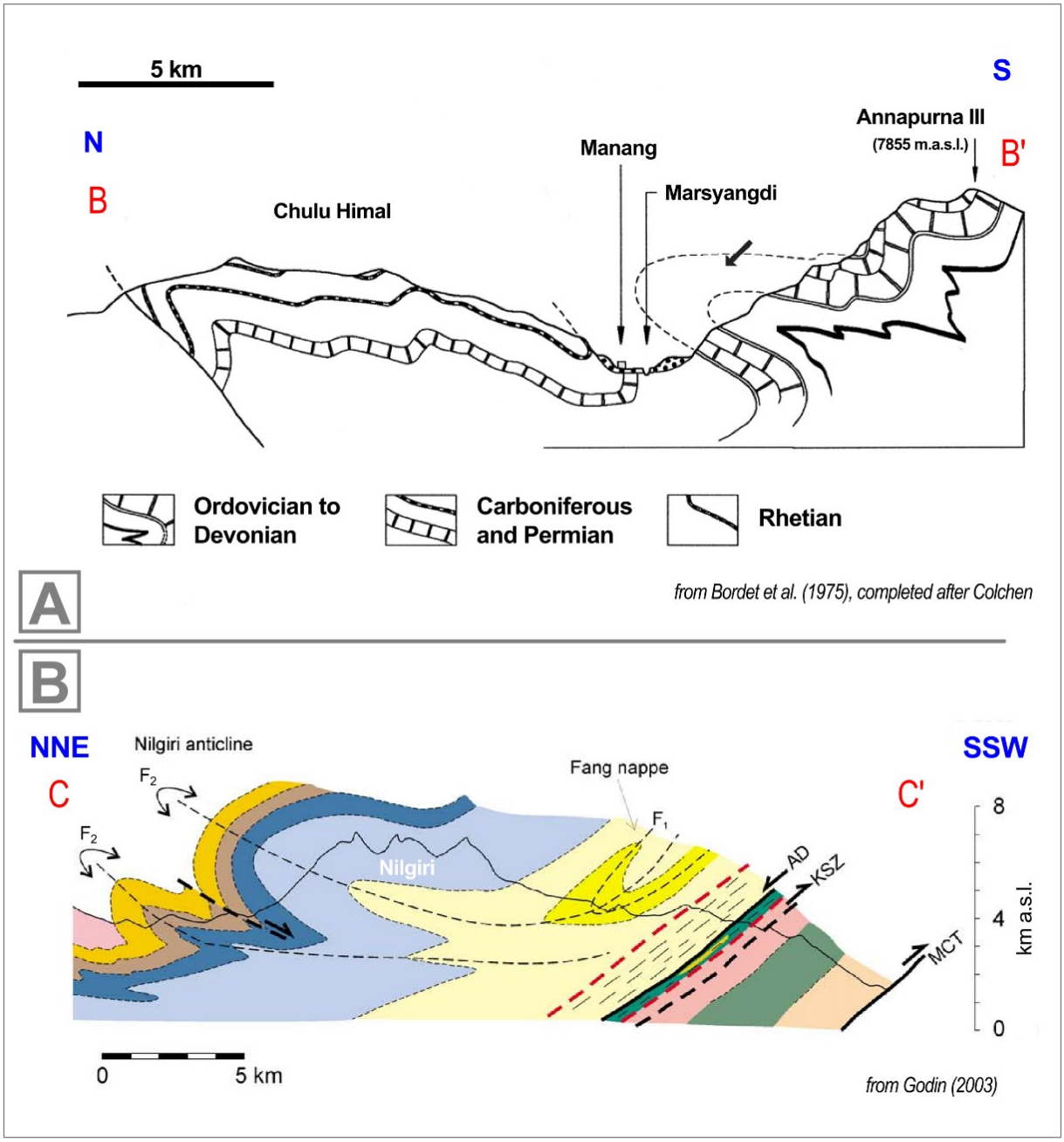


Figure 2.25: See location of profiles in Figure 2.1. The large-scale anticlinal structure to the north of the Annapurna ridge crest and within the THS is evident. (A) Profile after Bordet et al. (1975) showing tectonic folding and the orientation of bedding planes at Manang. (B)Profile over the Nilgiri peaks by Godin (2003) to the west of Tilicho Lake. AD means Annapurna Detachment which roughly coincides with the STD in the Annapurna massif.

*2.6.2.2 Internal Preparatory Factors*

Preparatory Factors can be considered acting on a slope internally or externally, reducing the stability of a slope up to a point it reaches a marginally stable state (see, McColl, 2015; see also Section 1.2.1 and Figure 1.2). Internal Preparatory Factors are processes that destabilise the slope from within the slope. Because we are investigating large-scale deep-seated slope failures, we are concerned with processes that act deep into the subsurface and thus have the potential to actively reduce the stability of rock slopes at greater depth. The following processes are considered as relevant, or potentially relevant, for our study area:

- **Groundwater** presence introduces pore pressure into the rock material and thus reduces the stability of slopes by altering the mechanical properties of the rock (e.g., Jaeger et al., 2007). Slopes with higher water tables are generally less stable because pore water is reducing the effective stresses within the rock. In addition, pore pressure enhances subcritical crack growth (progressive rock damage, see Section 1.2.3; Brantut et al., 2013; Voigtländer et al., 2018) and repeated changes in pore pressure due to a fluctuating groundwater table can additionally weaken rock masses over time (e.g., Preisig et al., 2016). Groundwater within rock masses is strongly controlled by water percolating into the slope and therefore by external factors, most notably precipitation, i.e. rain or snow. Groundwater, i.e. pore pressure, can be considered as an internal Preparatory Factor with a strong link to external forcing. Due to the rapid response time of groundwater, or alternatively pore pressure, to forcing by precipitation, it can sometimes act as a Trigger as well (see below).

- **Deep-seated weathering processes** (chemical and bacteria) (see, e.g., Ollier 2010; Viles, 2013) are probably limited in the upper Marsyangdi Valley due to the low temperatures and a constant permafrost cover at high altitudes. Also, the Marsyangdi Valley experiences much less precipitation than the slopes south of the Annapurna main ridge crest (see Section 2.2.2), which probably further limits deep weathering processes. However, if there is sufficient groundwater flow, chemical solution and reaction processes, potentially supported by microorganisms, increase sub-critical crack growth (see Brantut et al., 2013). Particularly, calcite dissolution could occur due to the high lime content of the rocks and subsequently such groundwater pathways could develop into particular weak zones within the slopes (refer to Table A2.2 for the chemical composition of our measured boulder samples from the upper Marsyangdi Valley).

- **Repeated seismic loading by reoccurring earthquakes** is certainly conceivable for our Annapurna study region. The Annapurna region is probably affected by strong seismic events at intervals of a century or more (see Section 2.2.1; Bollinger et al., 2014; Bungum et al., 2017).

It is difficult to assess the impact of the internal Preparatory factors on the slopes in our study region and to determine the extent to which they could contribute to the occurrence of giant rock avalanches. However, it would be interesting to investigate in subsequent field studies whether there are signs of their action in the rock faces exposed by the giant rock avalanches.

#### *2.6.2.3 High relief*

By far the most important external Preparatory factor responsible for the presence of giant rock avalanches is relief. High and steep slopes are the basic prerequisite for having giant deep-seated rock slope failures in the upper Marsyangdi Valley and the large failure volumes mobilized constituting the deposits found. High relief in the area (up to 8 091 m for Annapurna I) is the product of high exhumation rates and steepening of hillslopes by strong glacial and fluvial erosion (see e.g., Lavé and Avouac, 2001; Burbank et al. 2003).

Lavé et al. (2023) offered an explanation for the towering peaks of the Annapurna massif (and potentially elsewhere), shedding light on why the immense Sabche rock avalanche might have originated south of the Annapurna main ridge crest (refer to Figures 2.1, 2.5D, and 2.10). As a ridge ascends due to significant tectonic uplift, it enters a zone where glaciers sculpt the mountain's slopes (see Figure 2.26, a). Despite glaciers continuing to erode with increasing altitude, there comes a point where cold-based glacier flow cannot further erode the steep slopes (Figure 2.26, b). Concurrently, ongoing uplift and limited erosional effects from snow avalanches and other periglacial processes on steepening slopes (Figure 2.26, c) contribute to the ridge's elevation into the realm of permanent freezing, characterized by continuous permafrost conditions. This inhibits water percolation into the rock mass, preventing mechanical destabilization or deep-seated weathering processes (as discussed in Section 2.6.2.2). As the ridge height continues to increase, the steep slopes experience high deviatoric stresses, leading eventually to instability and the occurrence of a massive rock avalanche that shears off the ridge crest (Figure 26, d+e).

Such a scenario proposed by Lavé et al. (2023) offer a convincing explanation for the Tilicho Lake rock avalanche, which once occurred on a high and steep mountain where the present steep headwall of Roc Noir is located, situated in the permanently frozen zone (refer to PZI in Figure 2.10 (Gruber, 2012); and Figures 2.20, E+F, and 2.22). If we assume that the Humde rock avalanche originated from high altitudes as well, which is quite plausible given its size, similar conclusions can be drawn. A speculative source area south of Chulu Far East Peak also lies within the permanent permafrost zone (Figure 2.10). In contrast, the detachment zone of the Pisang Bowl rockslide lies beneath the permafrost zone, and a distinct explanation has be found.

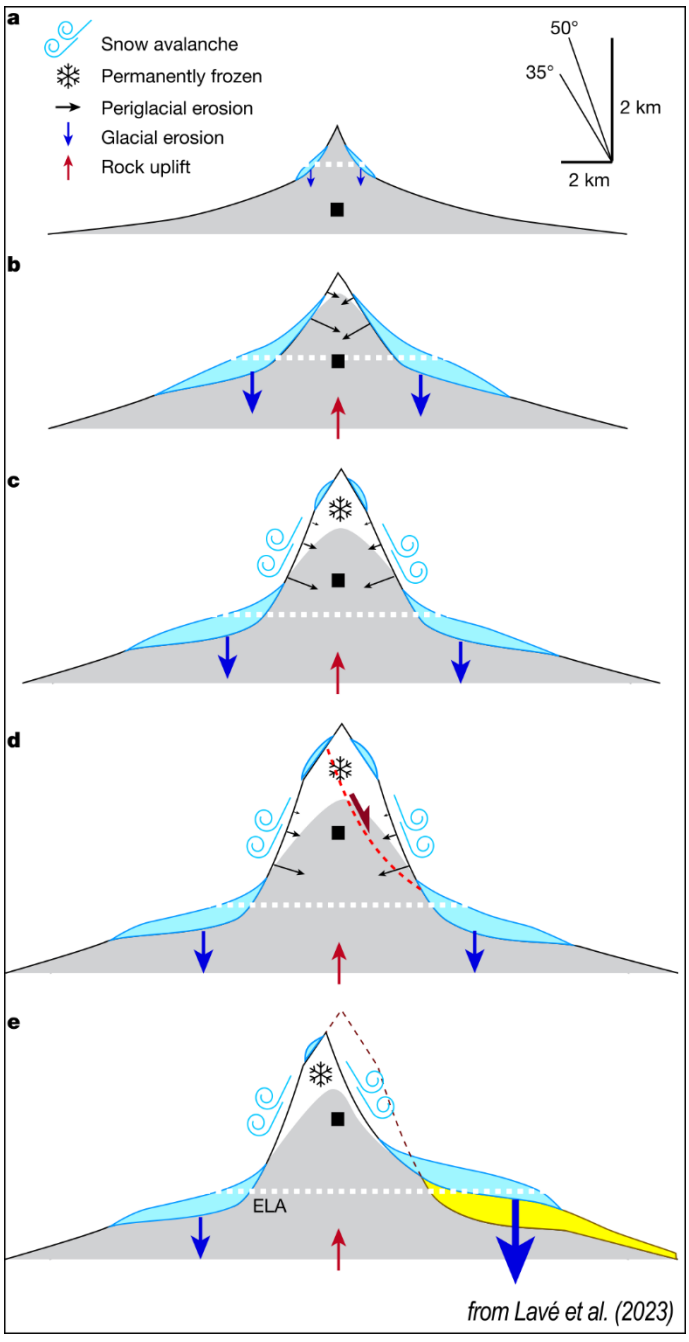


*Figure 2.26: Sketch describing the evolution of a ridge "growing" into the permanent permafrost realm by continuous rock uplift and erosion characteristics on its slopes. Eventually a deep-seated failure occurs resulting in a rock avalanche. From Lavé et al. (2023).*

*2.6.2.4 Climatic forcing*

Our dating results for the upper Marsyangdi rock avalanches yield ages that span the Holocene period. Given the long timescales involved, it is conceivable that Preparatory Factors of the bedrock slope failures are climatically controlled (see Section 1.2.2; Glade and Grozier, 2005; McColl, 2015), encompassing both internal and external Preparatory Factors. Internal factors actively weaken slopes over time from the inside (see Section 2.6.2.2), while external factors destabilize slopes from the outside.

The following external Preparatory Factors are considered to be relevant for causing rock slope failures in our upper Marsyangdi study region:

- **Precipitation**: The amount of precipitation over a given area is crucial in determining how much water percolates into the subsurface, affecting groundwater levels and pore pressures within slopes (see Section 2.6.2.2). Additionally, precipitation influences surface runoff and glacier nourishment, which contributes to stream and river discharge as well as to the extent of glaciation, directly linking it to erosion processes.
- **Erosion processes, fluvial or glacial**: Modifications to a slope's shape through erosion can significantly impact its stability, particularly at the base. Slope destabilisation can occur through river incision, glacial or fluvial scouring, or glacial debuttressing due to glacier retreat.
- **Permafrost retreat:** The presence of permafrost affects hydrological connectivity in the subsurface and its response to atmospheric conditions (see Section 1.3.3; Patton et al., 2019 and citations therein). By altering hydrological conditions, changes in permafrost cover therefore have the potential to destabilise slopes deep underground, not only associated with superficial failures and rock falls.

Our new age constrains on the upper Marsyangdi rock avalanches all fall within the Holocene period. The Pleistocene to Holocene transition was a time of global warming (e.g., Shakun and Carlson, 2010) and of the strengthening of the Indian monsoon, which is recorded particularly in $\delta^{18}O$-measurements from speleothems (e.g., Dutt et al., 2015) and the Guliya ice cap from the northwestern Tibetan Plateau (Thompson et al., 2022), and lake sediments from the Tibetan plateau (e.g., Gasse et al., 1996; Hou et al., 2017). Due to a stronger monsoon, the climate in the Himalayas was warmer and wetter in the first half of the Holocene than it is today. This period is called Early Holocene Climatic Optimum (EHCO) (e.g., Herzschuh, 2006; Yadav et al., 2022). Around 5,5 ka BP conditions started to become gradually dryer and colder as the monsoon weakened, which is reflected among other climate proxies by the decline of Tibetan lake extends

at that time (e.g., Liu et al. 2013; Chen et al., 2013). This weak interglacial monsoon phase broadly lasts on up to the present day.

It is known from global climate reconstructions, however, that there have been two excursions from this trend that are relevant for our study (e.g., Mann et al., 2009): the Medieval Warm Period (MWP), a phase of slightly warmer conditions in some regions of the northern hemisphere lasting approximately from 950 to 1250 AD (global signal), and the Little Ice Age (LIA), a phase of colder and dryer conditions globally from a about 1450 to 1850 AD (global signal). In the central Himalayan region a slight warming and wetting during the MWP is expected due to a slight strengthening of the Indian monsoon, which is recorded in climate proxies on the Indian subcontinent (e.g., Yadav et al., 2022) and predicted by climate modelling (Zhou et al., 2011; about 1°C increase in temperature at high elevation). Specific paleoclimate reconstructions from the central Himalayan region show similar trends, although the exact timing of the transition of MWP to LIA conditions is not well resolved and reconstructions at the specific localities may differ for this transition (Shukla et al., 2020; Roy et al., 2022; Mehrotra et al., 2023). The MWP in the central Himalayan region could have lasted a century or two longer than the global record predicts (see above).

Holocene climate trends can be summarized as follows for our central Himalayan study region with respect to today's climate:

| | |
|---|---|
| **~11,0 – ~5,5 ka BP** | **EHCO: warmer and significantly wetter conditions** |
| **~950 – ~1450 (?) AD** | **MWP: slightly warmer and wetter conditions** |
| **~1350 (?) – ~1850 AD** | **LIA: slightly colder and dryer conditions** |

The record of glacial extends and dynamics in the past can be an important asset for deciphering the climatic forcing of the giant rock avalanches in the Annapurna Massif. For the upper Marsyangdi Valley, we recalculated existing 10Be-exposure dating measurements from Pratt -Sitaula et al. (2011) with a global mean production rate (4,04 ± 0,19 at/g/yr; development version of the online calculator CREP (Martin et al., 2017; Schimmelpfennig, 2022)). These ages represent the formation of two morainic assemblies north of Manang and north-west of Braga, respectively (see Figure 2.17), and date back to the Pleistocene – Holocene transition (10,74 ± 0.61 ka; weighted mean calculated using the online calculator IsoplotR, version 6.0, see Vermeesch, 2018) and to the Lateglacial (18,01 ± 0.91 ka; weighted mean). They can be interpreted as the timing of glacial retreat. These glacial stages presumably find expression elsewhere in Nepal. Such glacial chronology could be compared to the glacial chronology in the Annapurna Massif and the central Himalayan region as a whole (see also Section 2.2.2). This includes recalculating the existing cosmogenic nuclide exposure ages from several previous studies in a consistent and reliable manner, including the use of the

same production rate, optimally cross-calibrated with other dating methods. This should be followed by a comparative analysis of the timing of the glacial landforms. However, this is beyond the scope of this PhD study.

We can analyse the timing of the upper Marsyangdi rock avalanches alongside the established age constraints for rock avalanches in the central Himalayas, in conjunction with the reconstructed Holocene paleoclimate trends (see Figure 2.27A, and refer to Table 2.5). The rock avalanche at Tilicho Lake (10.3 ± 1.4 ka) dates to the beginning of the Holocene and the EHCO in the Indian monsoon influenced region, a time of climatic transition to much warmer and wetter conditions. The speculative Event 0 at Pisang Bowl (7.0 ± 1.1 ka) (Section 2.5.1.2), the Latamrang (~5.4 ka), and the Dhampu-Chhoyo (4.7 ± 0.8 ka) rock avalanches all date precisely to the middle, end and shortly after the EHCO. Thus, these slope failures occurred after a considerable time span of warmer and wetter conditions. We found relatively young ages for the other events at Pisang Bowl (Event 1: 1170 – 1220, and Event 2: 1400 – 1500 AD (1σ-error range)) and the Humde deposit (1260 – 1360 AD) (see Sections 2.5.1.2, and 2.5.2.3 and Table 2.5). The older rockslide at Pisang Bowl (Event 1), the Humde rock avalanche and the Sabche cirque rock avalanche (1160 – 1220 AD; Lavé et al., 2023) fit right into or at the end of the MWP. The younger event at Pisang Bowl (event 2 in Table 2.5) may date after the MWP.All the Holocene giant rock avalanches in the central Himalayan region appeared within or shortly after more humid and warm climatic periods (EHCO and MWP) (see Figure 2.27A).

We can speculate on how climatic forcing destabilised the slopes during this period by reasoning about possible Preparatory Factors of slope failure (see internal and external factors stated above and Section 2.6.2.2):

The higher precipitation amounts during these periods must have directly led to more water percolating into the slopes and thus to a generally more groundwater and higher pore pressures in the underlying rock masses. This resulted subsequently in widespread decrease in the stability of all slopes. Some slopes have reached a state where they could be triggered to fail, which would not have been possible under drier climatic conditions. Also, higher precipitation presumably led to greater fluvial erosion at the base of slopes, i.e. to undercutting of slopes, which could have significantly impaired their stability. Warmer climate eventually led to a rise of the isotherms in the region further decreasing the stability of the slopes by glacier retreat and diminishing permafrost cover. Once the glacier ice melted away, it could no more serve as a buttress at the foot of slopes, i.e. glacial debuttressing. Under warmer conditions, water could percolate into rock masses that had been sealed off from surface water infiltration by permafrost during colder times before (see above and Section 1.3.3). A process argued as possible destabilisation mechanism by Lavé et al. (2023) for the Sabche cirque failure.

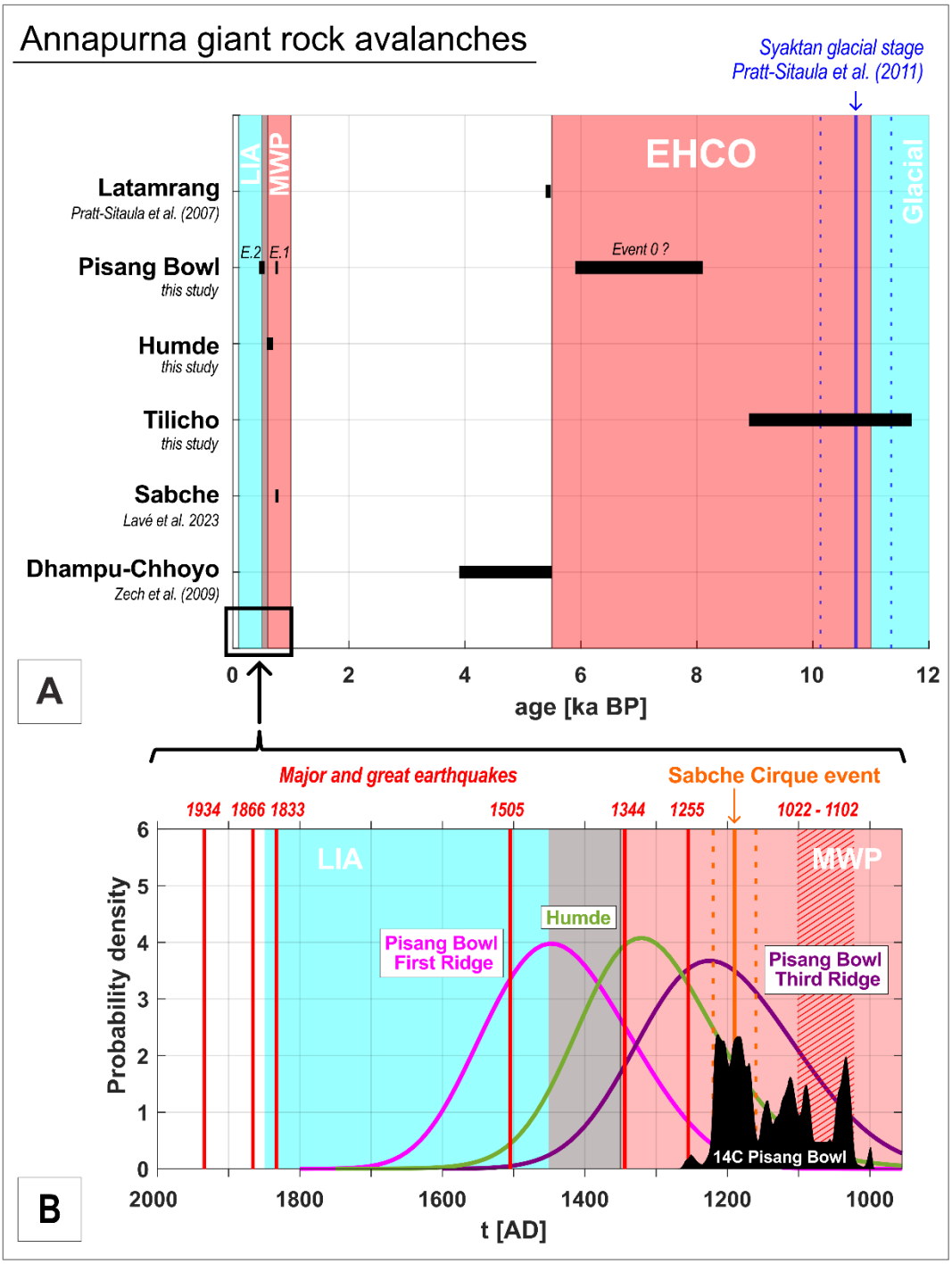


*Figure 2.27: (A) Timing of the giant rock avalanches in the Annapurna Massif, compared to the main climatic periods during the Holocene. Age of glacial stage north of Manang (Syaktan, see Figure 2.17) from Pratt-Sitaula (2011) added to the plot (weighted mean including 1σ errors from cosmogenic nuclide samples). (B) Zoom on medieval giant rock avalanche events: Event ages from this study derived from cosmogenic nuclide samples are shown with cumulative PDF curves (together with 14C PDF sum from the Third Ridge of the Pisang Bowl), the proposed timing of the Sabche Cirque event by Lavé et al. (2013) is additionally indicated, and recorded major (Mw ≥ 7.0) or giant (Mw ≥ 8.0) earthquakes are plotted for comparison (earthquake record according to Sapkota et al. (2013) and Bilham (2019) and citations therein).*

The fact that all Holocene giant rock avalanches in the central Himalayan region, with the exception of Tilicho Lake, occurred in the middle, at the end, or shortly after the warm and humid climatic periods could just be a coincidence related to the individual Triggers at work. Alternatively, a sub-critical progressive weakening of the rock slopes can be hypothesised to have been significantly enhanced during the warm and humid phases (see Section 1.2.3). Increased progressive weakening presumably provoked by climatically controlled internal and external Preparatory Factors. Higher pore pressures in combination with altered hydrological conditions and/or intensified weathering processes resulted in a higher degree of progressive rock damage, especially in weak zones. The slopes needed some time to substantially destabilise by these progressive sub-critical weakening processes which could have led to the observed lag times since the start of the EHCO and the MWP. Assuming an enhanced progressive reduction of slope stability during the warm and wet phases, it can be hypothesised that the Humde, Sabche and MWP slope failures at Pisang Bowl may have been largely primed for their failure as early as the EHCO. In the cold and dry phase after the EHCO, the already weakened slopes were temporarily stabilised, which then, with the slight return to warmer and wetter conditions and again increased progressive weakening, brought the slopes into a marginally stable state that was eventually susceptible to a trigger.

The Tilicho Lake rock avalanche stands out as the only giant rock slope failure in the Annapurna Massif that occurred around the Pleistocene-Holocene transition, during a period of significant climate change from the colder conditions of the previous Ice Age to the much wetter and warmer conditions of the EHCO. Given that the area of the Tilicho Lake failure was likely heavily glaciated during the Lateglacial period, it's reasonable to assume that a retreat of glaciers at the beginning of the EHCO contributed to slope destabilization at Tilicho Lake. This hypothesis is supported by the presence of the moraine stage north of Manang dating to the same period (referred to as Syaktan, see Figure 2.17). However, the extend of glaciation was less significant in the high-relief, high-altitude areas of the tropical Himalayas compared to high-latitude mountain ranges like the European Alps (see Section 2.2.2 and Figure 2.4C). In the Alps, glacial ice filled pronounced flow channels for extended periods and covered high-altitude areas with a thick ice sheet (e.g., Seguinot et al., 2018). At the Tilicho Lake rock avalanche site, it is probable that only a limited section at the base of the slope was glacially eroded during glacial times. This section was simultaneously supported by a large glacier tongue that occupied the U-shaped valley trough during the last ice age (see Figure 2.23, top). With the onset of warming at the beginning of the Holocene, which led to the melting of these supporting ice masses, glacial retreat resulted in debuttressing. This process likely left the mountain slope in a marginally stable state, prone to failure. Additionally, the significant temperature increase during this period could have caused permafrost retreat, further impacting slope stability (see above and Section 1.3.3). The Tilicho Lake rock avalanche may exemplify how high-altitude glaciers in the Himalayas contribute to landscape shaping, a role that fluviatile processes assume in lower-altitude regions. Regardless of the relative importance of the

factors that led to the Tilicho Lake failure, our study provides an explanation for the formation of Lake Tilicho, one of the highest lakes on Earth that holds a considerable volume of water.

After discussing all the climate-related Preparatory factors, it can be assumed that slopes in the central Himalayas are generally less stable during humid and warm climatic periods, and therefore also more susceptible to a Trigger. From the occurrence of most of the giant rock avalanches in the central Himalayan region towards the end of and shortly after warmer and wetter climatic periods, a progressive weakening of the slopes can be inferred. Climatic forcing most probably plays an important role in causing giant rock avalanches in the central Himalayan region. However, the exact nature and involvement of climate-related Preparatory factors may depend on the specific site localities.

*2.6.2.5 Potential Triggers*

The most significant Triggers of rock avalanches documented in historical records are earthquakes and extreme weather events (see, review by Hewitt et al., 2008). In our study area in the central Himalayas, the documentation of extreme climatic events only extends back a few decades. Similarly, the earthquake records for the region become sparse quickly as we look further into the past, with only the strongest events, such as major earthquakes (Mw ≥ 8,0), being listed for the past few hundred years (see, Bilham, 2019). The old ages and the large analytical uncertainties associated with the age constraints for the giant rock avalanches treated in our study make correlation with any kind of record anyway difficult. However, we can make a few speculations.

Throughout history, it has been well-documented that earthquakes have triggered numerous rock slope failures, including very voluminous ones (Keefer, 1994). Among the rock avalanches in our study, only one could potentially be correlated with a historically recorded earthquake (see Table 2.5 and Figure 2.27B; Bilham, 2019): a seismic event in 1344 AD falls within the determined time range for the Humde failure (1260-1360 AD). This 1344 event is mentioned in a chronicle from the Kathmandu Valley, where it caused devastating destruction and fatally injured a king (Bollinger et al., 2016). This major or great earthquake likely originated from a rupture on the Main Himalayan Thrust (MHT), but the exact location of the epicentre remains unknown. The 1344 AD earthquake could have significantly affected the Annapurna Massif, potentially serving as a seismic trigger for the Humde failure.

The older landslide at Pisang Bowl aligns with the Sabche cirque rock avalanche (1160 - 1220 AD; see Figure 2.27B; Lavé et al., 2023). The 50-year overlap within the analytical uncertainties hypothetically suggests a shared trigger which may not be a seismic one according to the historical earthquake record and Lavé et al. (2023).

However, it must be emphasised that despite the absence of paleo-seismic evidence, earthquakes cannot be discounted as potential Triggers for the giant rock avalanches in the central Himalayas. An unrecorded strong seismic event is certainly conceivable, also in view of the active Thakkola graben, which comprises a major normal fault system only about 20 km northwest of Tilicho Lake (see Figure 2.1; Hurtado et al., 2001).

Alternatively, we can hypothesise about potential atmospheric Triggers (i.e. changes within the atmosphere above the slope, including precipitation) for the giant rock avalanches in the central Himalayas. Extreme weather events can be responsible for high amounts of precipitation falling in a particular area or leading to instant permafrost retreat. These can be long periods of continuous rain or cloudbursts combined with heavy snowmelt (e.g. Shrestha et al., 2012; Dimri et al., 2017). Intensive water percolation into the subsurface can elevate pore pressures in already existing weak zones, ultimately leading the slope to failure (here, an increase in pore pressure leads instantly to slope failure and therefore can be considered a Trigger and not a Preparatory factor; see Section 2.6.2.2). Additionally, extreme floods or debris flow events could erode the base of a slope, while the gravitational loading by ice-fall on high altitude slopes is another conceivable Trigger.

## 2.7 Results – Annapurna south-face

### 2.7.1 Khudi Ridge and Phalo Danda site

The southern slopes of the Annapurna-Lamjung Himal range show numerous traces of gravitational movements, which can take a wide variety of forms, from rapid-moving catastrophic landslides (Marc et al., 2019) to non-catastrophic and deep-seated deformations of the sackung or DSGSD type. Among the large-scale non-catastrophic failures, satellite images show large failed masses, or failed hillslopes, on the one hand, and long ridges fractured by DSGSDs on the other hand (see Figure 2.28).

In the Khudi Ridge/Phalo Danda area, failed hillslopes , the failed hillslopes are characterised by large masses of highly fractured rock displaced several hundred metres downslope and an upper topography with gentle topography (see orange dashed lines in Figure 2.28). In two locations, two large failed masses are affected by retrogressive erosion and secondary landsliding that extend from the valley bottom up to hillslope midsection (yellow shading on Figure 2.28; Section 2.2.3.2; see also Figures 2.5F; 2.29B; 2.30, a+c; refer also to Gallo and Lavé (2014)). These failed hillslopes were, however, only partially studied in this thesis work and only preliminary dating of these features is presented in Section 2.7.4. Most of this chapter focuses in fact on DSGSDs. However, the relation between these two hillslope deformation phenomena will be discussed later.

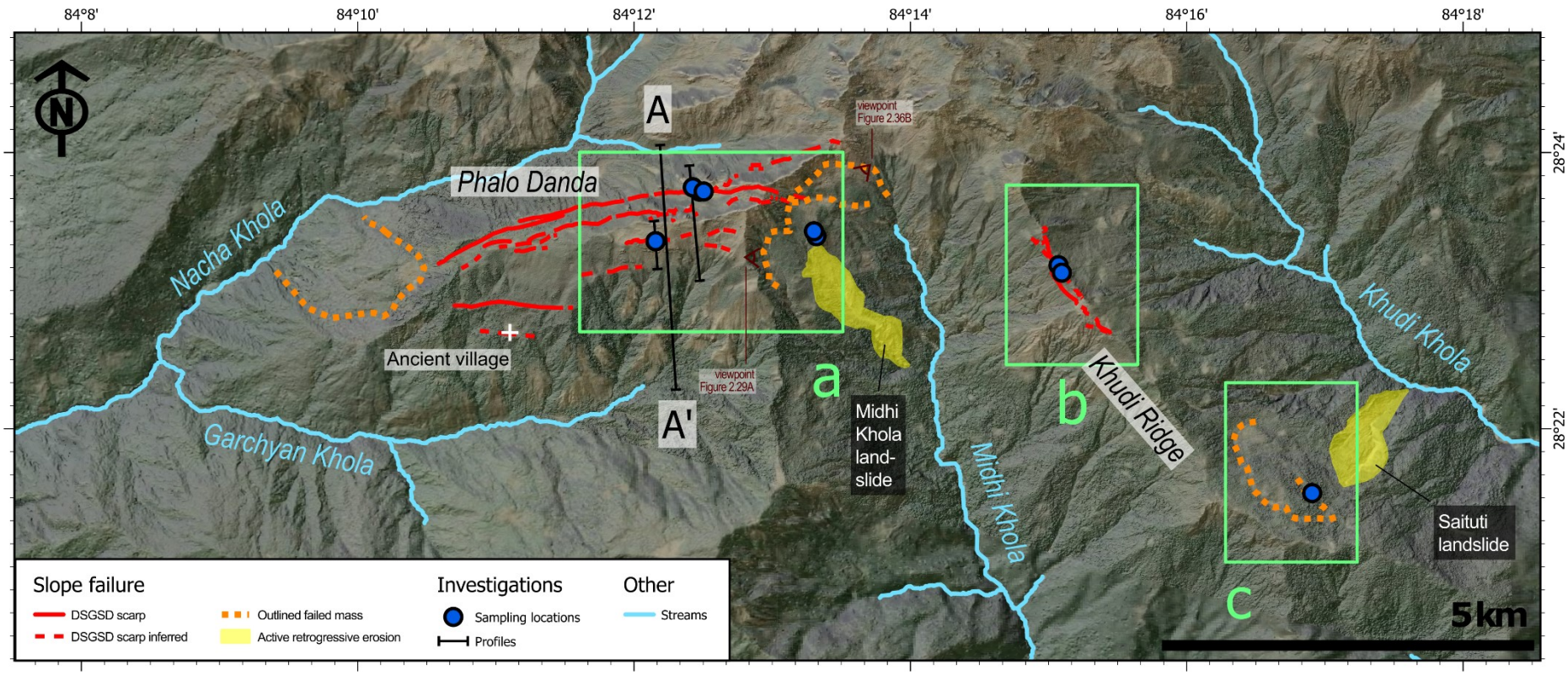


*Figure 2.28: Map of the Khudi Ridge and Phalo Danda areas using a hillshade derived from a digital surface model with a resolution of 2 metres. The surface model was created from Pléiades optical imagery (refer to Section 2.4.1.2 for more information). See Figure 2.1 for the map location in the Annapurna massif. Structures of slope failure were mapped and further investigations are indicated. See Figure 2.30 for the zoom-in views.*

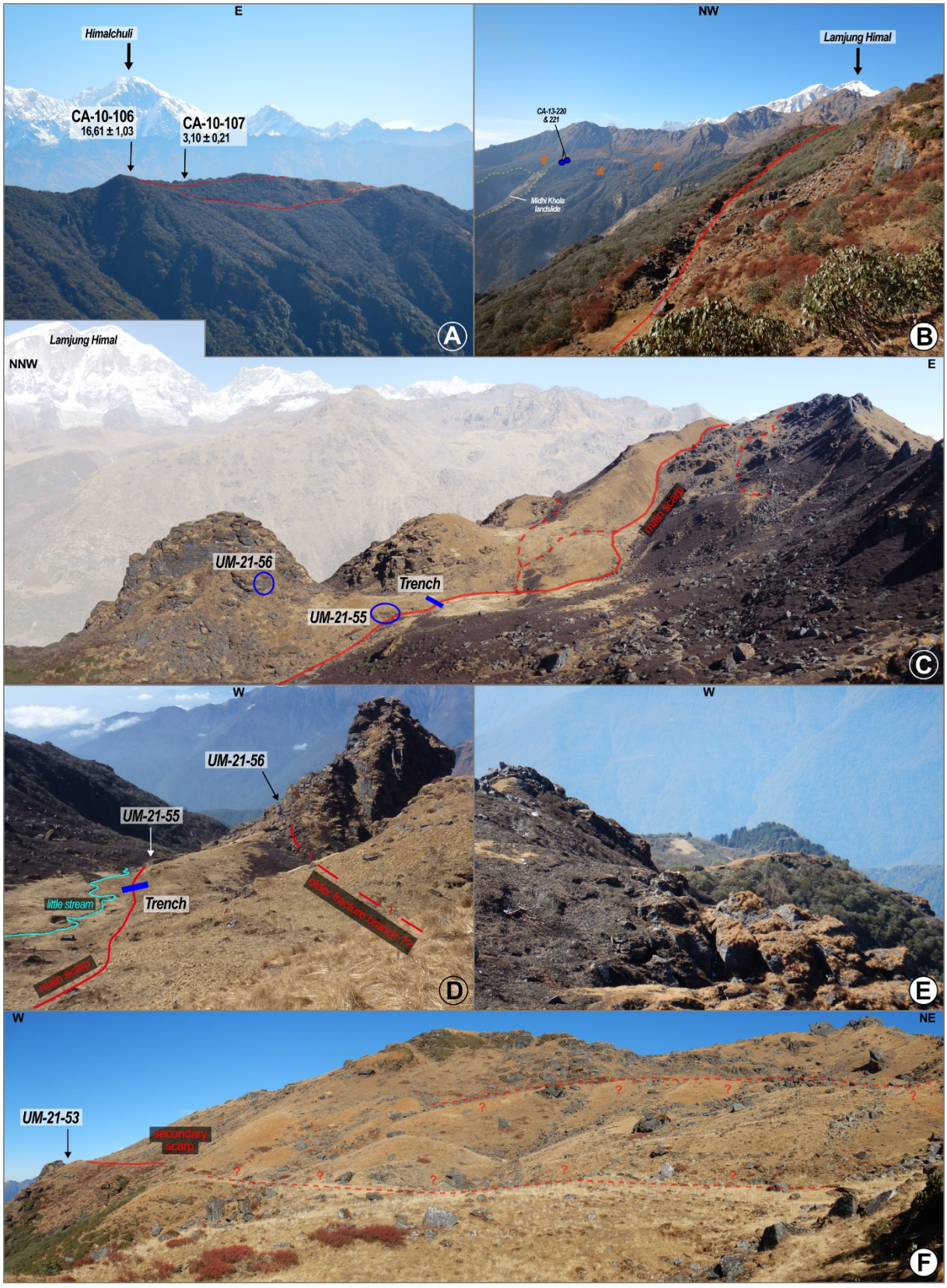
E
Himalchuli
CA-10-106
16,61 ± 1,03
CA-10-107
3,10 ± 0,21
A
NW
Lamjung Himal
CA-13-220
& 221
Midhi Khola
landslide
B
Lamjung Himal
NNW
E
UM-21-56
Trench
UM-21-55
main scarp
C
W
UM-21-56
UM-21-55
little stream
Trench
older fracture branch ??
main scarp
D
W
E
W
NE
UM-21-53
secondary
scarp
F

*Figure 2.29 (on previous page): DSGSD morphology present on ridges south of Lamjung Himal, Annapurna massif's south-face. Refer additionally to Figures 2.1, 2.28, and 2.30 for orientation and viewpoints of the photographs. (A) Khudi ridge from the west with DSGSD scarps dissecting the ridge crest. Photo taken in autumn 2021. (B) DSGSD-scarp at Khudi Ridge. Midhi Khola landslide and Phalo Danda locality behind the ridge in the background. Photo taken in autumn 2021. (C) Panoramic view of Phalo Danda main scarp. The landscape behind the Phalo Danda ridge is shown with a transparent white shading for better visibility. Photo by J. Lavé, autumn 2021. (D) Another angle on Phalo Danda main scarp. Photo by J. Lavé, autumn 2021. (E) View over Phalo Danda ridge crest towards the west. Fractured rock masses and tilted blocks in the foreground, DSGSD Main scarp in the background. Photo taken in autumn 2021. (F) Panoramic view of deformed rock masses and secondary conjugate scarp at Phalo Danda site. Photo taken in autumn 2021.*

*Figure 2.30 (on next page): Zoom-in views of Figure 2.28. Map was made using a hillshade derived from a digital surface model with a resolution of 2 metres. The surface model was created from Pléiades optical imagery (refer to Section 2.4.1.2 for more information). Structures of slope failure were mapped and further investigations are indicated.*

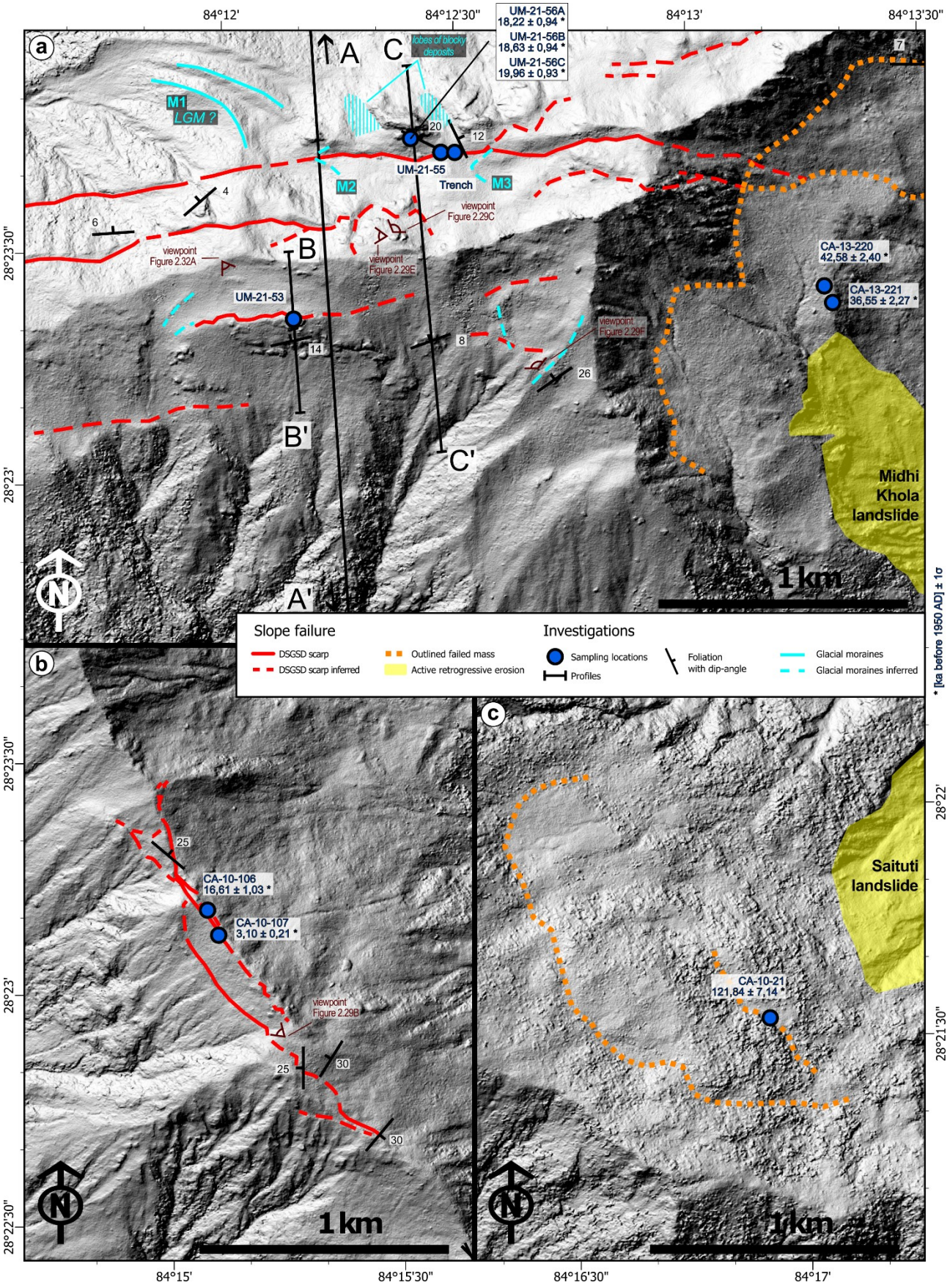
a
b
c
84°12'
84°12'30"
84°13'
84°13'30"
28°23'30"
28°23'
28°22'30"
84°15'
84°15'30"
84°16'30"
84°17'
28°22'
28°21'30"
A
A'
B
B'
C
C'
M1
LGM ?
M2
M3
Lobes of blocky deposits
UM-21-56A
18,22 ± 0,94 *
UM-21-56B
18,63 ± 0,94 *
UM-21-56C
19,96 ± 0,93 *
UM-21-55
Trench
UM-21-53
CA-13-220
42,58 ± 2,40 *
CA-13-221
36,55 ± 2,27 *
CA-10-106
16,61 ± 1,03 *
CA-10-107
3,10 ± 0,21 *
CA-10-21
121,84 ± 7,14 *
viewpoint Figure 2.32A
viewpoint Figure 2.29C
viewpoint Figure 2.29E
viewpoint Figure 2.29F
viewpoint Figure 2.29B
Midhi Khola landslide
Saituti landslide
1 km
N
Slope failure
DSGSD scarp
DSGSD scarp inferred
Outlined failed mass
Active retrogressive erosion
Investigations
Sampling locations
Profiles
Foliation with dip-angle
Glacial moraines
Glacial moraines inferred
* [ka before 1950 AD] ± 1σ

On the hillslopes to the south of the Annapurna massif's main crest, structures that indicate DSGSD activity can be spotted easily on satellite imagery, more specifically double-crested ridge lines and scarps parallel to the ridges (see Section 1.4.1; and see, e.g., reviews by Agliardi et al. (2012) and Pánek and Klimeš (2016)). These structures are particularly abundant along the Khudi Ridge and in the Phalo Danda area, south of the Lamjung Himal (see Figures 2.1; and 29, A+C). Here we mapped DSGSD scarps, distinguishing between two categories: those that could be clearly identified and inferred ones (Figures 2.28; and 30, a+b). This mapping was performed using satellite imagery and digital surface models (including a 2 m resolution model derived from Pléiades tri-stereo acquisition, see Section 2.4.1.2), as well as photographs taken in the field. The underlying bedrock of these ridges is made of gneisses of the HHS Formation I (quartz and aluminosilicate rich metasediments, see Section 2.21, and Colchen et al. (1986), and Parsons et al. (2016)), mostly gently dipping northwest to northeast (see foliation measurements in Figure 30). Our study region is located at an altitude ranging between about 4 200 m.a.s.l., from the highest ridge crests, to about 2 000 m.a.s.l. at the base of the slopes where streams flow continuously throughout the year. We are just below the zone where permafrost can occur (refer to Permafrost Zonation Index, Gruber (2012)), but the Phalo Danda area displays remnants of glacial landforms like glacial moraines, relatively well expressed on the northern flank of the ridge, and much more subtle on the southern flank (Figure 2.30a). Mean annual precipitation is high on the south-facing Annapurna slopes, mostly falling during the monsoon season (<3 m, see Section 2.2.2 and Burbank et al., 2003). In general, there is dense vegetation, except on the highest exposed ridge lines, which include the Phalo Danda site (Figure 27).

The locality named Phalo Danda (adopted from a topographic map of the area, see TopoMap – "LAMJUṄ HIMĀL", 2001) is a ridge oriented west-north-west to east-north-east bordered by two streams: Nacha Khola to the north and Garchyan Khola to the south (see Figure 2.28). The ridge is intensively deformed with extensive DSGSD structures present, especially at its crest with many scarps visible in the field and on remote sensing data (Figures 27, C – F; 28, and 29). The main failure plane cuts the topography along the northern slope of the ridge and has created a prominent escarpment, referred to in the following as the main scarp, (Figure 28; 29, C+E; and 30a). On the opposite and south-facing slope, secondary scarps, conjugate of the main failure plane, are also well expressed (Figure 28, 29F,and 30). The area in between is dissected by one secondary scarp that is oriented parallel to the main scarp (Figure 28 and 30a). In addition, along the ridge top, the bedrock, if not concealed by scree or boulders, appears heavily fractured and features tilted blocks (Figure 29, C-F). The DSGSD activity obviously caused substantial deformation in the sub-surface. To illustrate the situation schematically, we draw a profile in Figure 2.31, which reflects our interpretation of the main fracture zones in the subsurface, derived from studying the morphology at the surface. The base of the south-facing slope is cleared of forest cover. Here, we interpret that fractured rock masses are subject to bulging deformation as a consequence of the DSGSD-movement (see, e.g., Jaboyedoff et al., 2013), despite the lack

of field observations conducted in the area.

In the following, we present an analysis of the temporal evolution of DSGSD motion on the main and one conjugate secondary scarp based on cosmogenic nuclide profiles and a trench (see Sections 2.4.1.1, 2.4.1.4, 2.4.2, 2.4.3.1, 2.4.3.3 and 2.4.3.4).

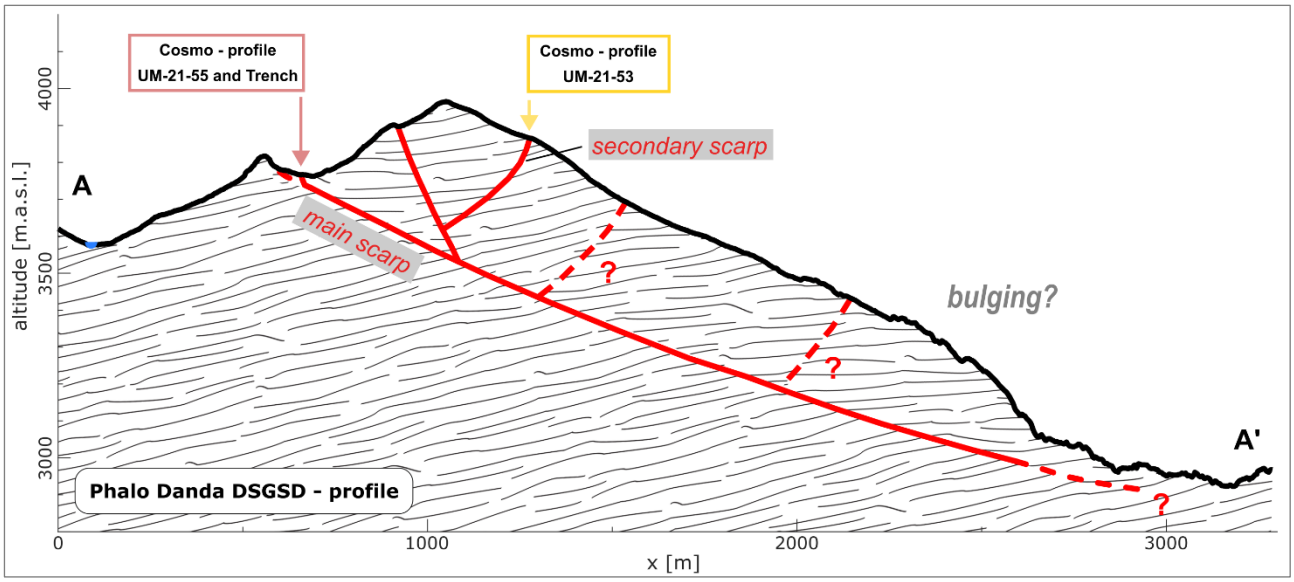


*Figure 2.31: Schematic profile of the Phalo Danda DSGSD with main fracture zones interpreted from the surface morphology. Profile location is shown in Figures 2.28 and 2.29.*

2.7.2 Movement reconstruction on conjugate scarp at Phalo Danda

The most expressed conjugate secondary scarp of the Phalo Danda DSGSD was sampled for cosmogenic nuclide dating (Figure 2.7B; and 2.32, A+B). We collected four samples along a vertical profile on the scarp-face at approximately regular intervals. Suitable spots for sampling showed no signs of major spalling or chipping, i.e. erosion of the rock surface, though no evidence of striation was found. We sampled on surfaces that were as plane as possible and, if possible, in a similar orientation to the overall orientation of the scarp. The locations of the profile samples in relation to the base of the scarp face were measured in the field with a measuring tape, so there is a certain degree of measurement uncertainty involved (we assumed 5 cm as a reasonable estimate, see Table 2.6). Sample location A is a few meters away from the profile, i.e. off scarp, it represents exposure not interfered by scarp movement (see Figures 2.32A, and A2.8A). Taking such a sample is necessary for movement reconstruction after measuring $^{10}$Be cosmogenic nuclide concentrations (see Section 2.4.3.4). It is meant to provide the exposure age of the flat surface above the edge of the scarp and therefore theoretically transposed exactly on the edge. For the location of Sample A the measurement uncertainty was estimated to be a bit higher than for the samples located on the scarp (± 10 cm).

After the samples were processed, measured, and necessary corrections were applied (see Sections 2.4.3.1, 2.4.3.3; and Table 2.7), results showed that $^{10}$Be nuclide concentrations are increasing with sample height above the base of the scarp, and the concentration is maximal for the top sample A (Figure 2.32C). This is in accordance with the expected trend due to progressive exhumation of a DSGSD scarp. It suggests that the scarp face was not subject to a substantial disturbance, for instance by block falls, or that there are no analytical issues with the samples. Movement on the scarp was reconstructed with the Matlab code presented in Section 2.4.3.4. For the cosmogenic input parameters, please refer to Table 2.8. The regional slope of the area dissected by the scarp at the sampling location is estimated from field photographs and from the high resolution digital surface model (see Figure 2.32A). The scarp angle and the small colluvial wedge at the base of the scarp were assessed from both field measurements and photographs of the sampled profile (see Figure 2.7B, and 2.32B). The colluvial wedge is also included into the scarp movement reconstruction (see Section 2.4.3.4 and Tables 2.6, and 2.8). The number of ruptures explored ranged from 6 to 15 which gives enough freedom to investigate many different failure scenarios. With the code, rupture events separated only by very short time intervals can be simulated, which in reality can be equivalent to a single offset event. Accordingly, the minimum number of rupture events is not a limitation for finding slope movement scenarios with fewer individual ruptures, but allows the calculation enough leeway to explore multiple possible slip scenarios.

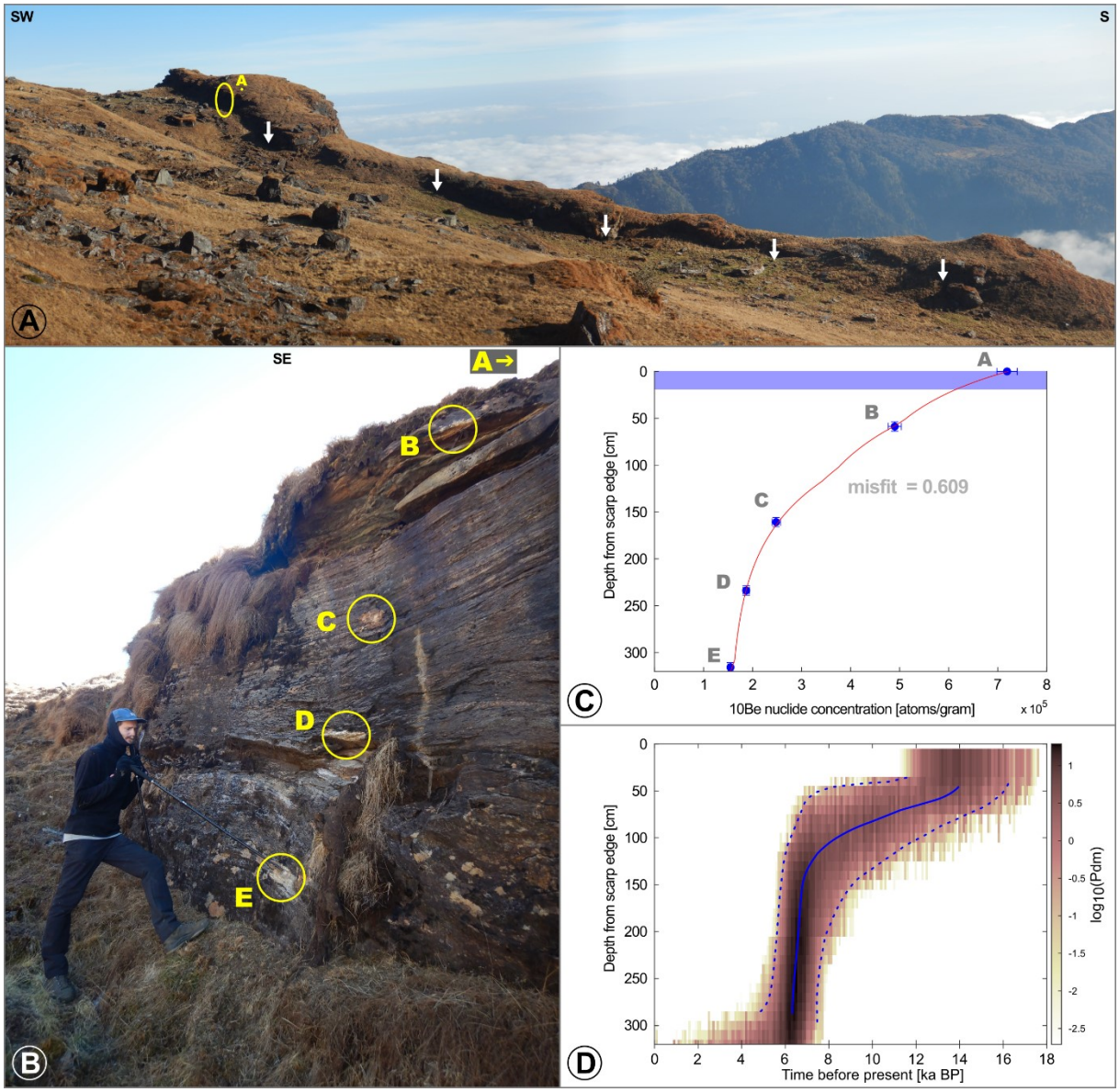


*Figure 2.32: (A) Panoramic view of Phalo Danda conjugate scarp. Location on the scarp sampled for a cosmogenic nuclide profile is indicated with a yellow circle. A closer look at the sampling spot of sample A can be found in Figure A2.8A. White arrows indicate downthrow of the conjugate scarp. Photos taken in autumn 2021. (B) Rock face sampled for 10Be cosmogenic nuclide dating after sampling, individual sampling locations indicated. Photo taken in autumn 2021. (C) $^{10}$Be nuclide concentrations after sample processing plotted versus depth from scarp edge. The best fit simulated nuclide concentration curve from the movement reconstruction calculation is added to the plot. (D) Probability density plot of movement reconstruction calculation. An outline of the domain with visualised probability and a line showing the path of the highest probability was drawn on top in blue.*

The Phalo Danda ridge shows some evidence for glacial erosion in the past, probably late-Pleistocene according to moraine dating in nearby glacial landforms (Pratt-Sitaula et al., 2011; see also our recalculated moraine ages in Section 2.6.2.4). For this reason, we presumed several meters of late Pleistocene erosion of the surface surrounding the scarp area (see Section 2.4.3.4), which follows a former phase of low erosion rate (0.1 mm/yr) during the previous unglaciated period. The thickness of the rock eroded by the glacier before the first rupture occurred was arbitrarily chosen equal to two metres (Table 2.8).

**Table 2.6: Cosmogenic nuclide scarp movement reconstruction, sample position**

| | *Conjugate scarp* | | | *Main scarp* | | | |
|---|---|---|---|---|---|---|---|
| | UM-21-53 | height above scarp base [cm] | uncertainty [cm] | UM-21-55 | height above scarp base [cm] * | uncertainty [cm] | |
| top | A | 350 | ± 10 | F | 460 | ± 20 | scarp edge |
| movement ↓ | B | 300 | ± 5 | E | 362 | ± 10 | |
| | C | 198 | ± 5 | D | 265 | ± 10 | |
| | D | 125 | ± 5 | C | 144 | ± 10 | |
| | E | 43 | ± 5 | B | 52 | ± 10 | |
| bottom | | | | A | 24 | ± 10 | |
| wedge height [cm] | 50 | | | 30 | | | |
| wedge inclination [°] | 25 | | | 30 | | | |

**for UM-21-55 we considered an 8° lateral scarp face inclination, see Figure 2.33B*

The $^{10}$Be concentration curve of the simulated rupture scenario that best fits the measured $^{10}$Be cosmogenic nuclide concentrations has a RMS-misfit of ~0.609 and is plotted in Figure 2.32C. The probability density map of all simulated scenarios is shown in Figure 2.32D. The visualised probability range has been outlined roughly and a path leading along the maximum probability has been drawn (in blue; see Figure A2.9a for other probable slip scenarios in this model run, which are plotted on top of each other and coloured according to their probability). The code incorporates two specific parameter explorations for the glacial erosion option, which means a range of a certain input parameter is explored through random exploration by the simulated rupture scenarios: On the one hand, different positions of the slope edge were explored within the calculation and subsequently a probability density function showing which values yielded the most probable results was calculated (see also Section 2.4.3.4). Within the uncertainty range of 20 cm entered for the exploration (see Table 2.6), the output shows similarly high probabilities, except for very high and low positions of the scarp edge within this range (Figure A2.9b). Another parameter exploration is performed for the assumed exposure of the scarp after deglaciation, before the first rupture occurred on the scarp (see Section 2.4.3.4): The most likely scenarios for the scarp movement are obtained at a scarp exposure of about 5 000 years after deglaciation (see Figure A2.9c).

Inversion of the profile shows a well resolved central part and the two basal and summit parts poorly resolved (Figure 32D). The summit section is largely constrained by sample A taken from the surface. This sample has remained constantly exposed since the retreat of the glacier and is therefore insensitive to the age of the first scarp break following this retreat. Despite the constraints provided by the samples along the escarpment (B and more), the age of the first break is poorly constrained between 12 and 17 ka (see Figure 32D). Nevertheless, we can state that between this uncertain date and 8 ka BP, slip on the fracture plane was limited to 1 or 1.5 m, and that DSGSD activity was not very intense. This was followed by a phase of accelerated activity, which was well constrained, leading to a slip of at least 2 m between 8 and 6 ka (Figure 32D). However, the density of samples is insufficient to distinguish between a scenario in which the entire scarp slip occurred as a single major event, and a scenario associated with a succession of smaller slip events over a short period of time. Finally, for the basal part, the absence of samples taken at the very base of the scarp, underneath the colluvial wedge, precludes knowing whether a more recent rupture of less than 1 m amplitude has occurred since 6-7 ka. In any case, this basal portion indicates a clear reduction, or even cessation, in the activity of the conjugate scarp since that date.

**Table 2.7: Annapurna south face cosmogenic nuclide samples - Exposure dating results**

| 10Be exposure samples | | | | | | | | | | | | | |
|---|---|---|---|---|---|---|---|---|---|---|---|---|---|
| Sample name | | Lat. [°] | Lon. [°] | Alt. [m a.s.l.] | Object sampled | *Erosion comment* | Sample thickness [cm] | Shielding: topo / snow / total [-] | $^{10}Be/^{9}Be$ ratio [$10^{-14}$] ± 1σ | Amount of carrier [µg] (1) | Dissolved quartz [g] | $^{10}Be$ conc. [$10^{3}$ at/g] ± 1σ (2) | Exposure age [ka before 1950 AD] ± 1σ |
| **CA-10-21** | | 28,3573 | 84,2841 | 2957 | displaced block | *quartz vein that protrudes 5cm above the surface was sampled* | 5,0 | 0,991 / 0.995 / 0,986 | 179,732 ± 2,991 | 256,1 | 20,65 | 3005,49 ± 133,26 | **121,84 ± 7,14** |
| **CA-10-106** | | 28,3864 | 84,2512 | 3839 | displaced slab | *protruding quartz veins form relief >3 cm, surface erosion* | 3,0 | 0,956(4) / 0.975 / 0,932 | 60,247 ± 1,287 | 248,1 | 33,62 | 598,61 ± 27,74 | **16,61 ± 1,03** |
| **CA-10-107** | | 28,3855 | 84,2516 | 3836 | displaced block | - | 3,0 | 0,980 / 0.975 / 0,923(5) | 5,758 ± 0,181 | 256,1 | 20,05 | 96,48 ± 5,07 | **3,10 ± 0,21** |
| **CA-13-220** | | 28,3899 | 84,222 | 3715 | displaced block | - | 2,0 | 0,984 / 0.985 / 0,969 | 63,467 ± 1,223 | 260,2 | 13,38 | 1662,26 ± 75,48 | **42,58 ± 2,40** |
| **CA-13-221** | | 28,3905 | 84,2217 | 3728 | displaced block | - | 2,0 | 0,982 / 0.985 / 0,908(5) | 40,257 ± 0,907 | 257,7 | 10,76 | 1295,74 ± 60,79 | **36,55 ± 2,27** |
| **UM-21-53** | **A** | 28,3893 | 84,2026 | 3895 | **DSGSD conjugate scarp** | *moos and lichen* | 1,5 | 0,992(6)/ 0.968 / 0,960 | 23,562 ± 0,619 | 424,1 | 19,79 | 718,73 ± 20,727 | **no exposure age, separate calculation for DSGSD movement reconstruction, see Section 2.4.3.4 and Figure 2.8** |
| | **B** | | | | | *darkened weathered surface* | 5,0 | | 32,577 ± 0,802 | 210,2 | 19,89 | 490,24 ± 13,394 | |
| | **C** | | | | | *darkened weathered surface* | 1,0 | | 17,444 ± 0,590 | 196,1 | 19,61 | 248,14 ± 8,91 | |
| | **D** | | | | | *darkened weathered surface, moss* | 3,0 | | 11,223 ± 0,357 | 208,9 | 17,84 | 186,52 ± 6,37 | |
| | **E** | | | | | *moss & lichen* | 2,5 | | 10,195 ± 0,331 | 212,4 | 19,82 | 155,12 ± 5,38 | |
| **UM-21-55** | **A** | 28,3953 | 84,2079 | 3917 | **DSGSD main scarp** | *moss* | 2,5 | 0,992(6)/ 0.962 / 0,954 | 2,029 ± 0,117 | 206,2 | 19,81 | 29,38 ± 1,80 | |
| | **B** | | | | | *moss* | 3,0 | | 3,814 ± 0,139 | 218,7 | 19,70 | 59,47 ± 2,33 | |
| | **C** | | | | | - | 6,0 | | 7,273 ± 0,231 | 201,0 | 19,75 | 104,84 ± 3,58 | |
| | **D** | | | | | *darkened weathered surface, moss* | 2,5 | | 10,563 ± 0,356 | 207,1 | 19,83 | 156,54 ± 5,62 | |
| | **E** | | | | | *grooves along foliation, due to weathering?* | 1,5 | | 17,910 ± 0,571 | 217,1 | 19,76 | 280,00 ± 9,55 | |
| | **F** | | | | | *very weathered surface* | 2,5 | | 34,294 ± 0,791 | 214,3 | 19,64 | 533,04 ± 13,82 | |
| **UM-21-56-A** | | 28,3958 | 84,2071 | 3931 | rocky scarp | *darkened weathered surface, moss* | 1,5 | 0,556(4)/ 1.000 / 0,556 | 27,548 ± 0,767 | 210,9 | 19,77 | 418,42 ± 12,66 | **18,22 ± 0,94** |
| **UM-21-56-B** | | 28,3958 | 84,2071 | 3931 | rocky scarp | *darkened weathered surface, moss* | 3,0 | 0,722(4)/ 1.000 / 0,722 | 36,897 ± 0,981 | 206,2 | 19,70 | 550,08 ± 16,01 | **18,63 ± 0,94** |
| **UM-21-56-C** | | 28,3958 | 84,2071 | 3931 | rocky scarp | *darkened weathered surface, moss* | 3,0 | 0,798(4)/ 1.000 / 0,798 | 41,407 ± 0,899 | 218,9 | 19,66 | 656,80 ± 16,23 | **19,96 ± 0,93** |
| **PT-2** | | 28,3953 | 84,2084 | 3919 | sediment covered rock surface | *gneiss surface without much relief* | 1,0 | 0,991 / 0.962 / 0,321(5) | 10,932 ± 0,337 | 211,6 | 19,73 | 166,54 ± 5,52 | **12,87 ± 0,73** |

*(1) CA-10-21 & 106 & 107, CA-13-220 & 221: carrier solution "Phena 1" of 2020 ± 83 µg/g $^{9}Be$ atoms; UM-21-53(A-E) & 55(A-F) & 56(A-C) and PT-2: carrier solution "S2" of 2135 ± 25 µg/g $^{9}Be$ atoms*

*(2) after Blank correction: CA-10-21 & 106 & 107, CA-13-220 & 221 corrected with one blank from same sample run with a $^{10}Be/^{9}Be$ ratio [$10^{-15}$] of 1,60802 ± 0,27647; UM-21-53A & 53C & 53E, UM-21-55A & 55C & 55E and PT-2 corrected with one blank from same sample run with a $^{10}Be/^{9}Be$ ratio [$10^{-16}$] of 5,05996 ± 1,98541; UM-21-53B & 53D, UM-21-55B & 55D and UM-21-56A & 56B & 56C corrected with one blank from same sample run with a $^{10}Be/^{9}Be$ ratio [$10^{-16}$] of 5,83413 ± 2,10306*

*(3) calculated with CREP developement version on 8 February 2024 with an assumed rock density of 2,65 g/cm³ and zero erosion rate (see Sections 2.4.3.1 and 2.4.3.3 for more details and references)*

*(4) when calculating the topographical shielding of these sample surfaces, the strike and dip measurements of the failure scarp were taken into account: CA-10-106: 100/37; UM-21-56-A: 90/85; UM-21-56-B: 100/70; UM-21-56-C: 85/62*

*(5) shielding by soil/sediment cover included: equation 4.20 of Dunai (2010) with attenuation coefficient 160 g/cm² was used; CA-10-107: 10 cm cover with 0,5 g/cm³material density, CA-10-221: 20 cm cover with 0,5 g/cm³ material density, PT-2: 83 cm cover with 2,1 g/cm³ material density*

*(6) strike and dip of sampled surface omitted for topo-shielding*

The effect of some input parameters on the output probability density plots was investigated by performing some additional model runs to check the sensitivity of the model output: No significant changes to the model output are obtained by changing the regional slope angle to 0°, removing the wedge at the base of the failure scarp completely, or changing the glacial erosion of the rock surface (before rupture initiates) to one metre instead of two metres (Figures A2.10, a-c).

We arbitrarily changed the angle of inclination of the scarp from by 10° in order to test the sensitivity of our movement reconstruction to this parameter (Figure A2.10d). The timing of our reconstructed scarp movement shifts to older ages (~1 kyrs). This parameter is therefore very important for determining the exact timing of the active displacement phases of the scarp and should therefore be selected as accurately as possible in order to avoid unrestricted uncertainties in the scarp movement reconstruction.

Finally, we also tested an alternative simulation with regard to the initial exposure history of the regional surface: i.e. the absence of a glacier and glacial erosion, and instead a steady erosion of the surface by periglacial processes at rates potentially between 0,05 and 0,3 mm/a, followed by a sharp drop in erosion efficiency at the end of the Glacial time (see Section 2.4.3.4 for more information). Considering constant steady-state erosion shows no significant change for the reconstructed offsets in the lower section of the scarp (Figure A2.10e). However, the offsets reconstructed for the upper section show a higher probability of younger ruptures. For this alternative simulation, the inversion procedure indicates furthermore that an initial erosion rate of 0,1 mm was found to be the most probable value (Figure A2.10f).

## Table 2.8: Parameter input table for scarp movement reconstruction Matlab code

| Input Parameters | Conjugate scarp UM-21-53 | Main scarp UM-21-55 |
|---|---|---|
| **Cosmogenic input parameters** | | |
| SLHL $^{10}$Be production rate [atoms/g/yr] (1) | 4,09 | |
| Attenuation length for neutrons [g/cm$^2$] | 160 | |
| $^{10}$Be production rate for slow muons [atoms/g/yr] (2) | 0,052 | |
| $^{10}$Be production rate for fast muons [atoms/g/yr] (2) | 0,0075 | |
| Attenuation length for slow muons [g/cm$^2$] (2) | 700 | |
| Attenuation length for fast muons [g/cm$^2$] (2) | 6300 | |
| Local nucleons production factor [-] (3) | 10,68 | |
| Local muons production factor [-] (3) | 4 | |
| **Material parameters** | | |
| Rock material density [g/cm$^3$] | 2,65 | |
| Colluvium wedge density [g/cm$^3$] | 1,5 | |
| **Scarp geometry** | | |
| Regional slope [°] (4) | 10 | 15 |
| Scarp slope [°] | 75 | 85 |
| **Number of ruptures explored** | | |
| Minimum number of ruptures [-] | 6 | |
| Maximum number of ruptures [-] | 15 | |
| **Erosion parameters** | | |
| Erosion rate before glacial erosion [mm/yr] | 0,1 | |
| Thickness of rock eroded by glacier before rupture [m] | 2 | |
| Minimum lag time between glacial retreat and first rupture [yrs] | 1000 | |
| Maximum lag time between glacial retreat and first rupture [yrs] | 6500 | |

*(1) calculated by a weighted mean of all existing calibration sites globally with the CREP developement version (time-corrected Lal-Stone, ERA40, and atmospheric 10Be-based VDM, please refer to Sections 2.4.3.1 for more details and references*

*(2) based on a 2nd degree polynomial fitting on the production rate curves of Heisinger (2002a&b)*

*(3) at 3900 m altitude and a latitude of 28° N, after Stone (2000)*

*(4) positive is same sense than inclination of the scarp slope*

## 2.7.3 Main scarp movement reconstruction at Phalo Danda

### *2.7.3.1 Exposure dating profiles*

For the Phalo Danda main scarp, two profiles were sampled for scarp movement reconstruction using cosmogenic nuclides.

**Site 1:**

A suitable scarp face was found not far from a small ephemeral stream (Figure 2.29, C+D; Figure 2.33, A+B). Sample F was sampled a few meters away from the scarp face to represent off-scarp exposition (see also Figure A2.8B for a close-up view of that sampling spot). Sample locations on the rock face in relation to the scarp base were measured with a measuring tape (Table 2.6). Our sampled profile here is not vertical but follows an oblique line (Figure 2.33, A+B). Along this oblique profile, the upper edge and the base of the scarp follow two more or less regular lines, parallel to each other and sloping towards the west. This sloping line (pink dashed line on Figure 2.33B) was therefore used as a reference to reconstruct the displacement distance of each sample (see Table 2.6). As the samples are further apart and not positioned vertically on top of each other, we have assumed a higher measurement uncertainty (± 10 cm) for the sample positions compared to the conjugate scarp (Table 2.6). The results of the cosmogenic nuclide measurements on the Phalo Danda main scarp are presented in Table 2.7 after all necessary corrections and calculations were applied (see also Sections 2.4.3.1 and 2.4.3.3).

We expect the area where we have sampled the scarp to be affected by glacial erosion during the LGM. As usually observed for the north-facing sides of mountains (in the Northern hemisphere), signs of glaciation and of glacial erosion are much more obvious here than in the area where we sampled the conjugate scarp along the south-facing side of the Phalo Danda ridge (see Section 2.7.2). In the field, we observed a small frontal morainic arc about a hundred metres upstream of the sampled scarp. On satellite imagery, two prominent lateral moraines are also observed at the exit of the small perched valley at the centre of which the cosmogenic nuclide profile was sampled (E-W oriented valley confined between the main ridge to the south and the main scarp to the north; see Figures 29, C+D; 2.30a; and 2.22A). Finally, in the footwall of the trench (see Section 2.7.3.2), the contact between the bedrock and the sediments presents a smooth, horizontal surface such as those produced by subglacial erosion.

As for the previous profile sampled on the conjugate scarp, the six samples display $^{10}$Be nuclide concentrations that are increasing from the scarp base to its top, which again makes us confident about the scenario of the progressive scarp exhumation.

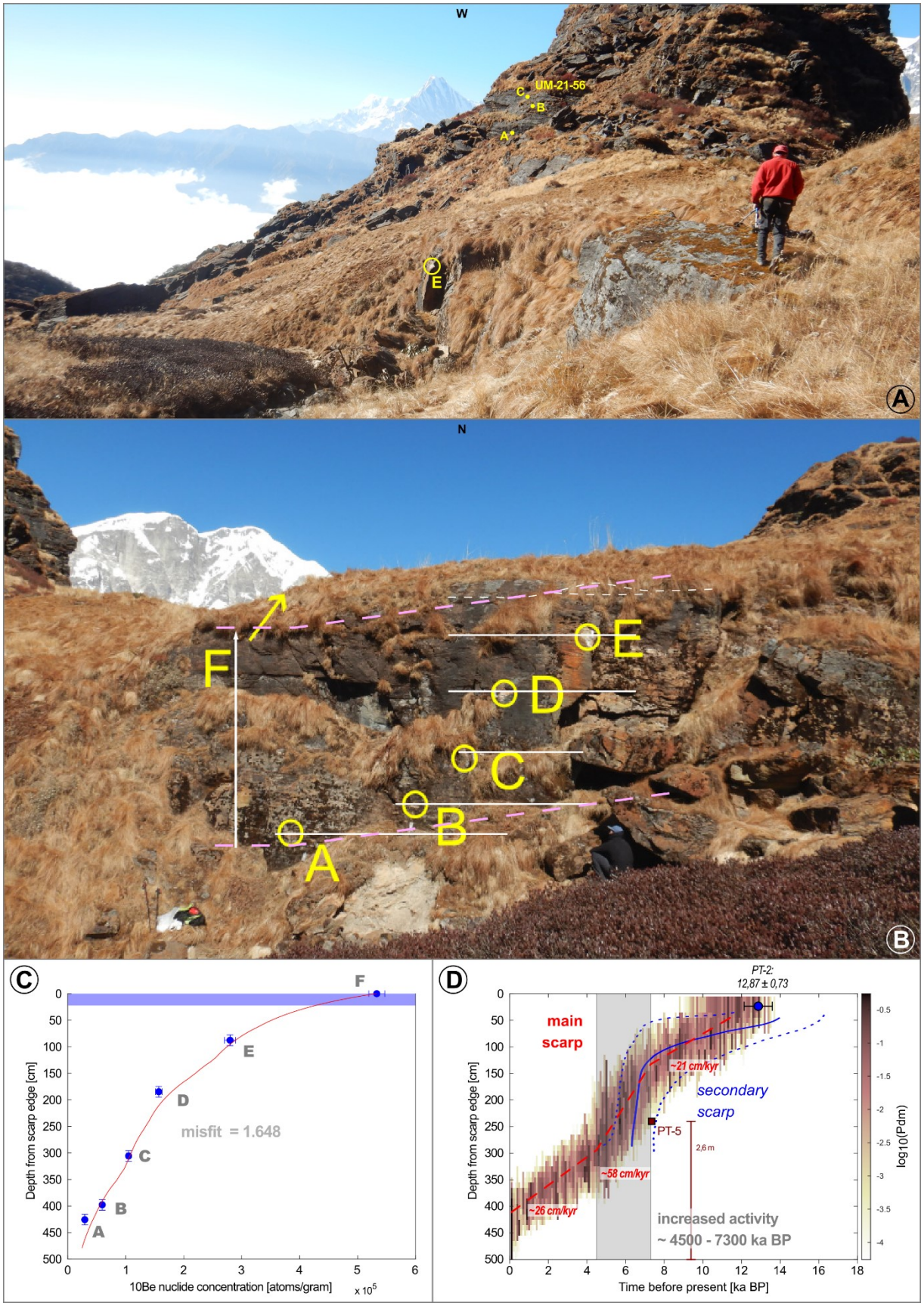
W
UM-21-56
C
B
A
E
A
N
F
E
D
C
B
A
B
C
F
E
D
misfit = 1.648
C
B
A
Depth from scarp edge [cm]
10Be nuclide concentration [atoms/gram]
x 10^5
D
PT-2:
12,87 ± 0,73
main
scarp
~21 cm/kyr
secondary
scarp
PT-5
2,6 m
~58 cm/kyr
~26 cm/kyr
increased activity
~ 4500 - 7300 ka BP
Depth from scarp edge [cm]
Time before present [ka BP]
log10(Pdm)

*Figure 2.33 (on previous page): Scarp movement reconstruction from a cosmogenic nuclide profile for the main scarp of Phalo Danda DSGSD. (A) Side view of the sampled scarp face. UM-21-56 samples in the background. Photo taken in autumn 2021. (B) Frontal view of the sampled scarp face. Sample locations and the lateral scarp face inclination considered for the calculation are indicated (see Table 2.6) .For the sampled surface of sample F refer to Figure A2.8B. Photo taken in autumn 2021. (C) $^{10}$Be nuclide concentrations after sample processing plotted versus depth from scarp edge. The best fit modelled nuclide concentration curve from the movement reconstruction calculation is added to the plot. (D) Probability density plot of movement reconstruction calculation. Shape of density plot from the conjugate scarp indicated in blue, averaged movement rate estimates in red. Exposure age of PT-2 in ka BP (before 1950 AD).*

To invert the slip reconstruction on this scarp, the input parameters were adjusted to the specificity of the scarp geometry (see Section 2.4.3.4). This includes the regional angle and scarp face inclination, and the colluvial wedge at the base of the scarp (see Tables 2.6 and 2.8). Most probable rupture scenarios show higher RMS-misfits compared to the scenarios reconstructed for the conjugate scarp (Figure 2.33C, and Figure A2.9d for paths of individual rupture scenarios). This difficulty to fit the measured nuclide concentrations could arise from the obliquity of our profile, as well as from potential disturbance induced by the small ephemeral stream running close to the scarp base.

No signals for individual movement steps can be identified or discussed here, the reconstructed failure scenarios are too ambiguous. However, averaged movement rates drawn from the probability density plot can be extracted and clearly show that movement rates vary over time (Figure 2.33D): The scarp movement reconstruction reveals a time period of lower averaged movement rate of about 21 cm/kyrs in the early Holocene compared to a subsequent period between 4,5 to 7,3 ka BP, where the activity of the scarp appears to be elevated to ~58 cm/kyrs. The early phase of this increased activity coincides with the big offset on the lower section of the conjugate scarp face (Figure 2.33D). We infer from our scarp movement reconstruction a present day movement rate of about 26 cm/kyrs, lasting since about 4 500 years.

The parameter exploration conducted within our final model run for the main scarp showed no clear trend for different scarp edge positions, i.e. high and low probabilities throughout a 40 cm uncertainty range (see Figure A2.9e), but more likely scenarios are obtained for short exposures after deglaciation of about 0-3 000 years than beyond (Figure A2.9f). Given our output density plot (Figure 2.33D), this corresponds to glacial exhumation between about 12 and 15 ka BP for the location of the cosmogenic profile (UM-21-55).

The possibility of stream erosion at the base of the scarp is not considered by the scarp movement reconstruction calculation. However, due to the proximity of the scarp face to the neighbouring little stream, this cannot be completely ruled out, although we spotted no signs of fluvial erosion on the sampled scarp

face (see Figure 2.33, A+B). Another possible source of unconstrained uncertainty that needs to be considered in relation to the nearby stream is a possible change in wedge characteristics during the time of exposure, i.e. dimensions or density. More specifically, the stream could have eroded colluvium or deposited sediment. However, in view of our input variation analysis performed for the conjugate scarp (see Section 2.7.2), where complete removal of the colluvial wedge had little effect on the resulting density curve (see again Figure A2.10b), we expect that some evolution of the wedge at the base has only limited impact on our movement reconstruction results.

Nevertheless, an unconstrained uncertainty inflicting our results originating from the neighbouring stream must be acknowledged, especially for the reconstruction of the movement at the base of the scarp and thus for our estimate of the average movement rate for the last 4 500 years.

**Site 2:**

The second sampled profile (UM-21-56) presents a more ambiguous nature (see Figures 2.29, C+D; 2.30a; 2.33A; and 2.34). The morphologic object consists of a flat and smooth surface sloping at about 60° located at about 90 m north-west of profile UM-21-55. It was originally considered as a possible DSGSD failure scarp. However, after looking at the main scarp orientation on the field, on satellite images, and the high-resolution DSM of the area, this sampled surface does not appear to be aligned with the trace of the main scarp, and is instead located slightly further north.

We therefore envisage two possibilities: 1) this rocky face actually corresponds to an older fracture branch of the Phalo Danda main scarp (Figures 29, C+D; Figure 2.33A; and 2.34), and in that case, it could be used to complement scarp activity; 2) the surface corresponds to a glacially smoothed bedrock surface left exposed after LGM glacier recession. The azimuth of this surface is just as compatible with the orientation of the main scarp as with that of the perched, previously glaciated, valley.

The three samples collected on that rock face (Table 2.7, and see Sections 2.4.3.1 and 2.4.3.3) all yield Late Pleistocene exposure ages ranging between 18 and 20 ka . The ages are getting older towards the top-most sample, which is compatible with progressive exhumation along a scarp. However, the ages of the samples are fairly close to each other, despite the fact that the lower and upper samples are about 7,5 m apart (see Figure 2.34), which implies a vertical slip rate definitely greater than 200 cm/kyr (1σ-error included), i.e. much faster than those recorded during the Holocene on the main scarp. Alternatively, the relative similarity of the exposure ages is consistent with a glacially eroded surface. In addition, the ages correlate with the presumed last glacial maximum extent in the monsoon-influenced Greater Himalaya (Owen and Dortch et al., 2014; Yan

et al., 2020; see also the recalculated moraine ages of Pratt-Sitaula et al., 2011 in Section 2.6.2.4 and Figure 2.17). Though we cannot fully exclude a DSGSD fracture scarp, we rather conclude that the UM-21-56 $^{10}$Be concentrations express bedrock resetting by glacial erosion and then surface exposure since the retreat of the LGM glacier tongue.

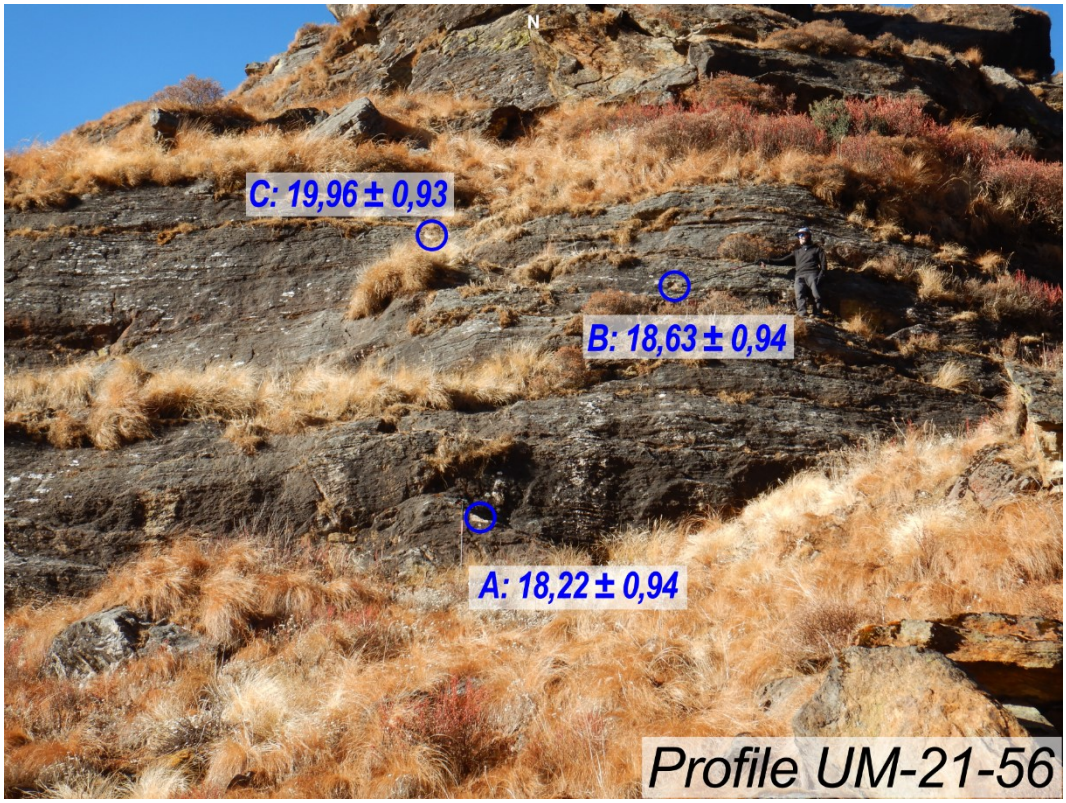


*Figure 2.34: Cosmogenic nuclide profile UM-21-56 which was eventually not processed for scarp movement reconstruction. See also Figures 2.29, A+D; 2.30a; and 2.33A for additional views and location. Person in picture for scale.*

*2.7.3.2 Trench*

About 50 m eastward of the cosmogenic nuclide sampling profile (UM-21-55), a small topographic step, bordering a flat, boggy depression, was identified as the surface expression of the Phalo Danda DSGSD main scarp (see Figure 2.7C). A trench for paleo-movement reconstruction was dug perpendicular across this step (see Section 2.4.1.4; and Figures 29, C+D; 30a; and 2.35A).

The two walls of the trench were described in detail in the field by J. Lavé: this included existing layering and fabric of sediment and soil, and fractures offsetting them. Additionally, the walls were photographed and samples were collected for radiogenic 14C carbon burial and 10Be exposure dating (Figure 2.35). The footwall presents a flat, smoothed surface covered by less than 1 m of sediment cover, made of matrix supported material with angular clasts. We interpret the bedrock surface as abraded by subglacial erosion, and the sediment as a glacial diamicton, original or remobilized by slope processes.. The hanging wall, i.e. downthrow side to the south, reveals a succession of sediments: At the base, a grey, brownish unsorted diamictic sediment with angular clasts (layer A in Figure 2.35C). This sediment is followed by sand and gravel layers towards the top (layers B-G in Figure 2.35C) featuring interfingering of colluvial wedge (layer C in Figure 2.35C) and fluvial deposition (layers B, D-F in Figure 2.35C) by the nearby little stream (see Figure 29, C+D). Over time colluvium and alluvium have filled the space freed up by the episodic scarp movements. Bedrock on the downthrow side was not reached at the bottom of the trench.

The sedimentation observed in the trench was not warped, which would be the case with a constant creep movement (see, e.g., review by Pánek and Klimeš, 2016). Instead, the sediments of the downthrow side are dissected by fractures clearly offsetting the lower sedimentary layers, more precisely units A, B and the basal part of unit C (F1-F3 in Figure 2.35C). Their mode of failure is extensional. It can be assumed that a rupture on the main scarp pulled the sediments apart, which deformed subsequently by settling in connection with further sedimentation at the top. The exception is the family of fractures 4 (F4) which cuts through all the sedimentary layers from the bottom up to layer E, and affected those layers by a vertical offset of ~30 cm (Figure 2.35C). It was not possible to establish a connection between the footwall and the hanging wall units. The sediments on top of the foot wall are close to the soil, i.e. affected by slope processes and bioturbation. Directly on the bedrock scarp, a thin wedge that thickens along the scarp shows a brecciated shear zone with many bedrock fragments broken off the scarp (Figure 2.35C). We suspect that during each DSGSD sliding event a significant component of the slip occurs on F0 (Figure 2.35C) and breaks the surface.

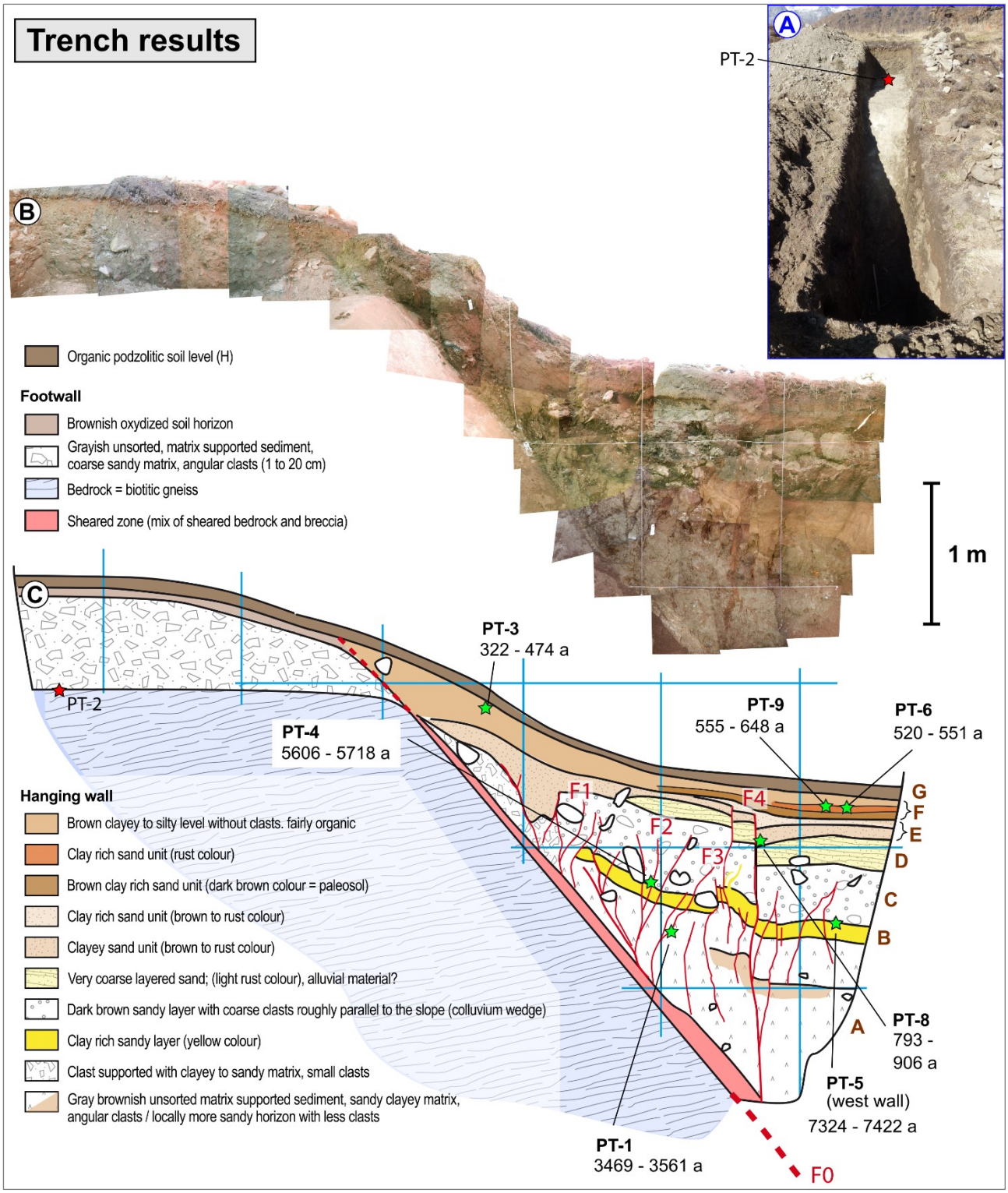


*Figure 2.35: (A) Trench dug across an offset step at Phalo Danda main scarp (see also Figure 2.7C). Photo by J. Lavé, autumn 2021. (B) Photographs of the east wall stitched together. (C) Recording of trench: detailed description of sediments and fractures by J. Lavé on the east wall of the trench.*

The 14C carbon burial samples, aimed at obtaining a better timing for the sedimentation and fracture processes, can be divided into two groups (see Table 2.9 and Figure 2.35C, refer to Figure A2.11 for more details on the calibrated ages):

- **Samples dating sedimentary units:**

  They consist of charcoal or of individual pieces of oxidized organic material embedded in a given sedimentary unit. As such, they provide a temporal constrain for the sedimentation of this unit (from top to bottom):

  Unit F, top section (PT-3): *322 – 474 a (before 1950 AD)*

  Unit F, midsection (PT-6 & 9): *520 – 551 a (PT-6 is younger)*

  Base of unit E (PT-8): *793 – 906 a*

  Layer B, top (PT-5): *7324 – 7422 a*

- **Samples taken from fracture fillings:**

  Dark organic-rich formless material was found filling some of the extensional fractures and is interpreted as material that presumably fell down or percolated from the topsoil after the opening of the fracture. It therefore dates the opening of the fracture.

  PT-1 from F3: *3469 – 3561 a*

  PT-4 from F2: *5606 – 5718 a*

**Table 2.9: Radiogenic 14C carbon dating from trench at Phalo Danda - Results and calibration**

| 14C carbon burial samples | | | | | | |
|---|---|---|---|---|---|---|
| Sample name | Lat. [°] | Lon. [°] | Alt. [m a.s.l.] | *Object sampled* | Radiocarbon age [y BP] | Burial age (68,3% probability) [a before 1950 AD] (1) |
| **PT-1** | 28,3953 | 84,2084 | 3919 | ***fracture filling*** *- black material in sediment* | 3300 ± 30 | **3469 - 3561** |
| **PT-3** | 28,3953 | 84,2084 | 3919 | *charcoal within* ***sediment layer*** | 355 ± 30 | **322 - 474** |
| **PT-4** | 28,3953 | 84,2084 | 3919 | ***fracture filling*** *- dark, rich in organic matter ?* | 4960 ± 30 | **5606 - 5718** |
| **PT-5** | 28,3953 | 84,2084 | 3919 | *organic particles (?) scattered in* ***sediment layer*** | 6440 ± 35 | **7324 - 7422** |
| **PT-6** | 28,3953 | 84,2084 | 3919 | *charcoal within* ***sediment layer*** | 530 ± 30 | **520 - 551** |
| **PT-8** | 28,3953 | 84,2084 | 3919 | *charcoal within* ***sediment layer*** | 935 ± 30 | **793 - 906** |
| **PT-9** | 28,3953 | 84,2084 | 3919 | *charcoal within* ***sediment layer*** | 620 ± 30 | **555 - 648** |

*(1) calculated with the OxCal online calculator using the Intcal20 calibration curve; full range of output ages, gaps omitted*

*see Section 2.4.2 and Figure A2.11 for more details and references*

Units A, B and the basal part of C are affected by fractures F2 and F3. Therefore they must be older than 5,6 – 5,7 ka (age of PT-4) (see Figure 2.35C and Table 2.9). The timing of the F4 rupture can be constrained between the sedimentation ages of layers E and F (midsection) because the rupture extended into the basal part of layer E, but not into F (see Figure 2.35C). Derived from the sedimentation ages mentioned above, the time span for the rupture event responsible for the opening of F4 is between 520 and 906 a, which corresponds to a period between 1044 and 1430 AD. The last recognisable rupture on the main scarp appeared at that time (except for a rupture that would affect only F0 without being accompanied by other ruptures in the hanging wall).

The vertical offset on F4 measured from the base of layer D is about 30 cm (see Figure 2.35C). The vertical offset inhered by the fracturing restricted to the layers A to C, which includes fractures F2 and F3, is also 30 to 40 cm, measured from the top of layer B. However, this represents a minimum vertical offset for this sliding event since some unconstrained displacement could have also occurred on the main rupture zone F0.

The maximum possible total displacement along the scarp can be estimated by analysing the layering of the overlying sediment under the following assumption: The layers of the hanging wall were always deposited spatially below or at the same level as the sediment top of the footwall. Following this assumption, a maximum offset of 2,6 m is recorded by unit B, since 7,3 to 7,4 ka (see Figure 2.35C). This comes about one metre short to the cumulative offset determined by the cosmogenic nuclide profile for this time period (see density plot in Figure 2.35D). This discrepancy may be due to variability in offsets along the scarp: Sediments on the downslope side may behave differently depending on the characteristics of the sediments when affected by fractures on the scarp and subsequent recompaction. However, this discrepancy could also indicate a larger offset that occurred just before the deposition of unit B and the subsequent wash in of clayey sediments into the resulting depression by surface water. Before this time, the depression was probably not so pronounced that this type of sediment, which indicates the presence of stagnant water, could be deposited. Such consideration would be consistent with the scarp movement reconstructions of the two cosmogenic profiles, which indicate a phase of higher activity, more specifically a large offset for the conjugate scarp or an increase in offset rate for the main scarp, around that time (see age of PT-5 plotted in Figure 2.35D)

Summarising the evaluation of the trench, the following can be said: We have found that the DSGSD main scarp ruptures in discrete events and we have identified at least 3 of these events at ~520 - 906 a, at ~3.5 ka and at ~5.7 ka. This result is consistent with the cosmogenic nuclide profile, which shows continuous activity between 5.7 ka and the present.

Finally, the cosmogenic nuclide concentration measured in the sample taken from the smooth bedrock surface at the trench footwall (PT-2) was corrected for shielding by the present sediment cover (see Section 2.4.3.3 and Table 2.7 for details). This sample is supposed to date the glacier retreat at this location. More precisely, the glacier retreat between the most distal glacier position (westernmost moraine M1 in Figure 2.30a), presumably representing an LGM stage, and the most proximal retreat position (small morainic arc M3 ~100 m east of the trench). The glacier at the location of the trench must have disappeared around 13 ka BP, which is slightly older than the last glacial stage documented by Pratt-Sitaula et al. (2011) north of Manang, dated at ~10.5 ka (see Section 2.6.2.4 and "Syaktan" in Figure 2.17). The representation of a corresponding glacial stage at Phalo Danda may be the small moraine arc to the east of the trench (M3 in Figure 2.30a). The exposure age of PT-2 is also consistent with the timing of glacial retreat as calculated from the nearby cosmogenic nuclide profile from the top sample UM-21-55-F (see PT-2 in Figure 2.33D), and agrees well with the older age of UM-21-56, A-C further west, which represent a larger glacial extent at that time (see Section 2.7.3.1 above; and Figures 2.29, C+D; 2.30a; 2.33A; and 2.34).

### 2.7.4 DSGSD activity of the western Khudi ridge

Although less spectacular than the summit fractures that run along the Phalo Danda ridge, the N-S ridge that limits the Kudhi and Midhi Khola basins is also affected by large fractures (see Figures 2.28, 2.29A, and 2.30b). The associated topographic offsets are limited to a few metres, and the fault mirrors are less well preserved than at Phalo Danda. At the level of a double-crested M-shaped ridge, a sample (CA-10-106) was taken from the upper part of what could be a remnant of a fracture mirror (see Figure A2.8C), and 100 m to the south another sample (CA-10-107) was taken from the surface of a large block that had fallen and tilted during DSGSD activity (see Figure 2.7A).

The first sample on the Khudi ridge crest yields an exposure age of 16,61 ± 1,03 ka (CA-10-106), whereas the dislocated and fallen block presents an age of 3,10 ± 0,21 ka (CA-10-107) (see Table 2.7). These two ages are insufficient to draw any firm conclusions. Nevertheless, they indicate probable activity of the DSGSD during the Holocene, similar to what is observed on the Phalo Danda ridge, with displacements of several metres (particularly evident at CA-10-106). The western Khudi ridge was not glaciated at the LGM (it is located at a lower altitude of 3800 m.a.s.l.) and its topography has not been remodelled by glacial erosion. To explain the absence of large topographic offset at the fracture levels, it is proposed that the onset of DSGSD activity on the western crest of the Khudi is more recent than at Phalo Danda.

### 2.7.5 Dating failed masses in Midhi and Khudi valleys

The failed hillslopes present in the Midhi and Khudi valleys are characterized by an upper surface topography featuring gentle slopes (Figures 2.28; and 2.30, a+c). A few massive multi-metric to decametric boulders lie at the top of these surfaces. Following the example of the massive deposits of giant landslides studied in the upper Marsyangdi Valley, it is assumed that these surface blocks were exposed during the slope failure of these hillslopes, even though it is not clear if the hillslope failed progressively over thousands of years or much more rapidly.

The boulders on top of the Midhi Khola landslide mass are dated at 42,6 ± 2,4 ka (CA-13-220), and 36,6 ± 2,3 ka (CA-13-220) (Figures 2.29B; 2.36, A+B; and A2.8, D+E). Surprisingly, the boulder upslope of Saituti landslide (CA-10-21) (Figure 2.36, C+D) presents a much older age of 121,8 ± 7,1 ka BP. The possibility of pre-exposure of the block before their emplacement on top of the failed mass cannot be ruled out. However, our preliminary results suggest that major slope instabilities can leave long-term (> 100 ka) imprints in the

landscape. More generally, these additional dating results on boulders and bedrock scarps are evidence that the hillslopes on the Annapurna massif's south flank undergo active deformation both in glacial and interglacial times.

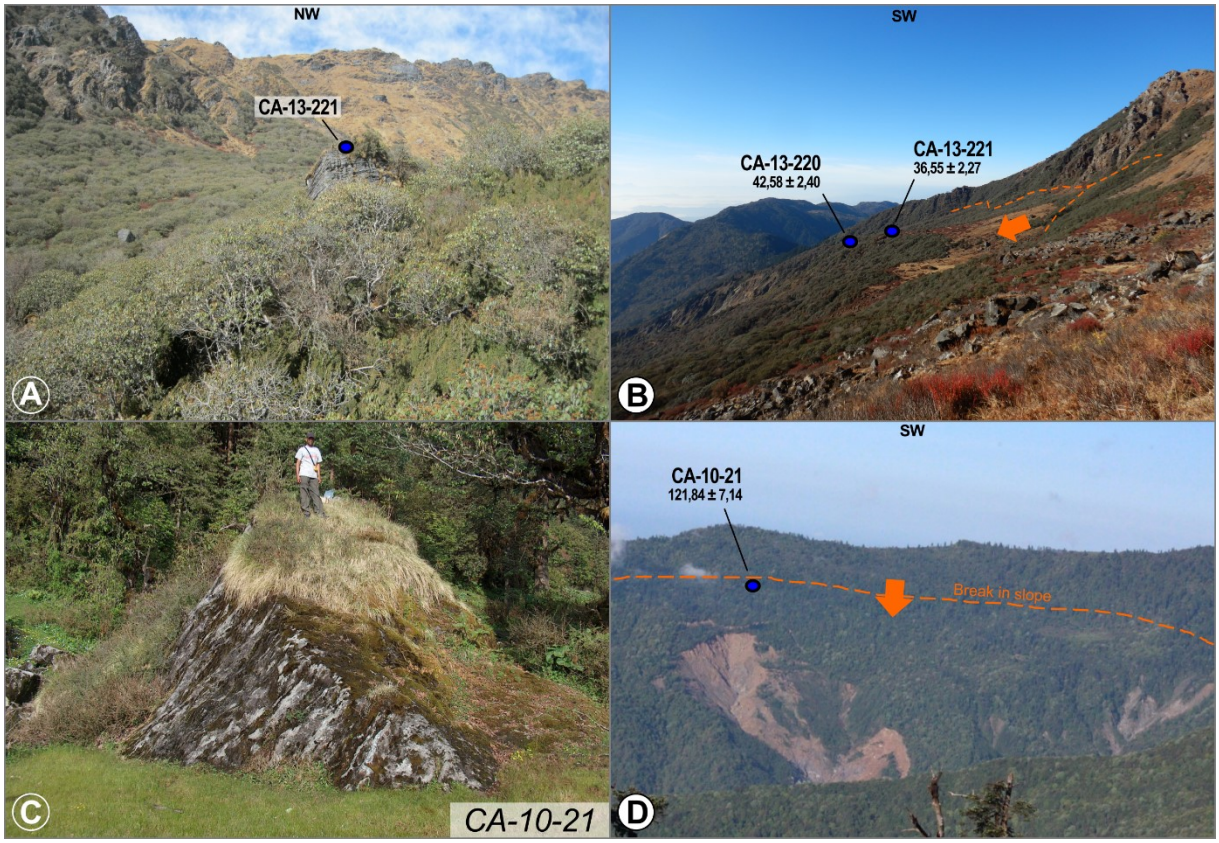


*Figure 2.36: Boulders sampled for 10Be nuclide exposure dating upslope of retrogressive erosion scars (refer to maps in Figures 2.28 and 2.29. All exposure ages in ka BP (before 1950 AD). (A) Boulder upslope of Midhi Khola landslide. Photo by J. Lavé, autumn 2013. (B) View of sampled boulders upslope of Midhi Khola landslide from the distance. Photo taken in autumn 2021. (C) Boulder upslope of Saituti landslide. Photo by J. Lavé, 2010. (D) View on Saituti landslide from the distance. Photo by J. Lavé.*

## 2.8 Discussion – Annapurna south face

### 2.8.1 Causes of the Phalo Danda DSGSD movement

The lithologic and structural controls on the Phalo Danda DSGSD remain speculative, because the investigations in this direction do not go beyond some basic field observations. The biotitic gneisses (Formation I) of the Phalo Danda site are foliated. In general DSGSDs are more commonly observed in layered and foliated rocks (see Section 1.4.2 and, e.g. Agliardi et al., 2012). In neighbouring study areas in the central Himalayan region, the upper Sunkosi catchment and the Kali Gandaki valley (see Section 2.2.4.1; and Yagi et al., 2018; Chigira et al., 2022), DSGSDs appear to develop predominantly on dip-slopes, i.e. failures develop along bedding planes or foliation (also termed cataclinal slopes, see Cruden and Hu (1996)). In northwestern Bhutan, Dini et al. (2020) found strong structural control on DSGSD-type failures, with slope failures generally more abundant on dip-slopes.

For the Phalo Danda DSGSD, the principal failure plane /zone, i.e. main scarp, dips in the opposite direction to the gneiss foliation (refer to the foliation measurements shown in Figure 2.30a and the profile in Figure 2.31). The DSGSD thus intersects the foliation planes and we can designate this slope failure as the failure of an anti-dip slope, i.e. anaclinal slope (see terminology by Cruden and Hu, 1996). This seems atypical for DSGSDs studied so far in the Himalayas. DSGSD formation could be linked to the presence of a tectonic fault in the area (see Section 1.4.2 and see, e.g., review by Jaboyedoff et al., 2013), but we are not aware of any structures that could have some genetic connection with the formation of the DSGSD at this location.

With our investigations on the Phalo Danda DSGSD, we were able to reconstruct the following history of movement for the main scarp and the one major conjugate secondary scarp:

- The conjugate scarp shows a primary phase of activity in between 6 to 7,5 ka BP with a vertical offset on the scarp face of 2 m minimum. Since then the conjugate scarp appears dormant.
- The main scarp moved in steps throughout the Holocene. Dm-scale vertical displacements resulted from discrete fracture events.
- The main scarp experienced a more active phase of movement between 4,5 and 7,3 ka BP.
- Compared to the main scarp, the conjugate scarp ruptures only occasionally. During most rupture events on the main scarp, the conjugate scarp remains dormant.

It is important to remember that the resolution of our paleo-movement reconstruction, with only a few samples taken on a failure scarp, does not allow us to distinguish whether the higher activity on the scarps is

due to a higher number of individual offset events, or whether larger offsets for a temporally consistent rupture frequency are responsible for the higher activity (see Sections 2.7.2 and 2.7.3.1). However, with this new insights into the dynamics of the Phalo Danda DSGSD, we can argue about possible factors that maintain its activity over time (Movement Sustaining Factors) (see Section 1.2.2). The continuous occurrence of fractures on the main scarp during the Holocene suggests that the variability in activity is not simply due to random variation in the intensity and distribution of triggering events strong enough to cause rupture, but that the Movement Sustaining Factors (composition or importance) change over time.

A climatic forcing during the active phases determined for the scarps, which roughly overlap at 7 ka BP, can certainly be assumed (see Figure 2.33D): The active phases coincide with the EHCO, a phase spanning from about 11,0 – 5,5 ka (see Section 2.6.2.4. for more information). During this period the central Himalayas were affected by warmer and significantly wetter climatic conditions, due to a stronger Indian monsoon.

It is known from monitoring studies of actively creeping DSGSDs that groundwater pressure is the most important factor controlling the movement of these types of slope failures (see Section 1.4.2 and reviews by Pánek and Klimeš, 2016; Lacroix et al., 2020). During the wetter climate of the late EHCO, the Phalo Danda DSGSD was in a state of higher activity than during the drier conditions of the second half of the Holocene. Increased precipitation leads to increased percolation of water into the subsurface, i.e. higher groundwater tables, possibly contributing to generally elevated pore pressure conditions in the weak zones. Either this resulted in a greater offset for individual ruptures, or the slope was more susceptible to triggering events, eventually leading to more frequent discrete ruptures and ultimately increased slip activity on the Phalo Danda DSGSD scarps.

This hypothesis suggests a dynamic relationship between climate conditions and the movement dynamics of the Phalo Danda DSGSD over time. But why was the Phalo Danda DSGSD not already more active during the first half of the EHCO? Reconstructed movement rates for the main scarp are similar for the early Holocene and the last 4 500 years despite the fact that the climatic conditions were very different (see Figure 2.33D). We could apply the same reasoning used to explain the delayed timing of the giant catastrophic failures in the upper Marsyangdi Valley to the delayed onset of higher DSGSD activity: higher rates of progressive damage (see Section 1.2.3) gradually destabilized the fracture zones of the DSGSD (see Figure 2.31) before reaching a state in which higher rates of movement could eventually set in. The processes responsible for this progressive damage in the weak zones are the same as those identified for the giant rock avalanches: higher and fluctuating groundwater levels and enhanced deep weathering processes as a consequence of increased temperature (as compared to pre-Holocene times) and increased precipitation in the area (see Sections 2.6.2.2 and 2.6.2.4). For the DSGSD, this would represent a delayed hydromechanical response to increased precipitation, occurring approximately 4,000 years after the onset of the EHCO.

Alternatively, could there be another climatic factor that led to the increased activity at the end of the EHCO? Perhaps the enhanced activity was due to more frequent occurrences of sufficiently potent atmospheric triggers during this period. Another possibility is that the increased activity is related to erosion in the stream channel at the foot of the DSGSD (see Figure 2.31). Increased erosion at the slope base during the EHCO could have altered the stress conditions within the failure and rendered the slope more unstable.

Looking at the failure processes in Phalo Danda from a mechanical point of view offers an alternative perspective. The correlation between the significant offset of the conjugate scarp and the period of heightened intensity on the main scarp may stem from the site-specific mechanical condition of the DSGSD, more precisely a mechanical connection between the two scarps which has influence on the movement pattern of the DSGSD as a whole: When a fracture occurs on a conjugate scarp, the internal stresses between the individual fracture blocks may adjust to a post-fracture state, i.e. a modulation of the stresses within the fracture zones. As a consequence such readjustment could allow for a larger offset on the main scarp. This effect could last both during the event that triggered the conjugate scarp to rupture and could have presumably persisted during subsequent ruptures on the main scarp. This aspect could be further investigated using a mechanical model. Climatically induced rock damage would have most likely provoked the failure of the conjugate scarp in the first place (see above).

The connection between Phalo Danda's deglaciation and DSGSD ruptures remains unclear. The simulated rupture scenarios of the movement reconstruction with the cosmogenic nuclide profile on the main slope resulted in relatively short lag times between deglaciation and the first post-glacial rupture on the scarp (<3 000 years, see Section 2.7.3.1). Considering the analytical uncertainties associated with our reconstruction, it must therefore be concluded that no significant lag time can be observed. Given the small size of glaciers that the ridge at Phalo Danda held, it is unlikely that the limited glaciation had a major impact on the movement dynamics of the Phalo Danda DSGSD.

The Triggers for the individual ruptures remain elusive. Atmospheric triggers like intensive precipitation events (prolonged rain, or sudden cloudburst), intense snow melt, or a combination of those are conceivable (see Section 1.4.2 and ,e.g., reviews by Pánek and Klimeš, 2016). All this atmospheric triggering mechanisms result in a sudden high percolation of water into the subsurface and thus inevitably to an increase in pore pressure in the failure zone. Such rare extreme groundwater rises are probably sufficient to destabilise the slope to such an extent that they eventually trigger discrete ruptures on the Phalo Danda DSGSD scarps. Excess pore pressure in the failure zones could, however, also be directly linked to a seismic trigger as

hypothesised by Lacroix et al. (2022) for their study on non-catastrophic slow-moving landslide activity in the central Himalayas after the 2015 Gorkha earthquake. Seismic shaking can lead to increased groundwater flow, destabilising stagnant slope failures, which may explain the observed post-seismic movement of landslides after the strong earthquake. This could be due to co-seismic damage in rock masses opening vertical pathways into the subsurface and water release through material compaction. However, this conjecture still needs to be substantiated with further research that includes reliable groundwater measurements after earthquakes.

It is not possible to assign a rupture event with certainty to a specific earthquake in the past. The record of earthquakes in the central Himalayas, such as the list compiled by Bilham (2019), rapidly thins out for events further back in the past and does not even cover one thousand years. There may also have been a strong earthquake not recorded in the historical record. It could also have originated from the active Thakkhola Graben (see Section 2.6.2.5; Figure 2.1; and Hurtado et al., 2001). Nevertheless, one hypothetical conjecture that can be made concerns the F4 rupture, which was reconstructed from the trench and dated to a period between 1 044 and 1 430 AD. There is evidence of two major (Mw ≥ 7,0) or giant (Mw ≥ 8,0) earthquakes that must have caused considerable seismic shaking in central Nepal during this period: First, the earthquake of 1 255 AD, which caused great devastation to Kathmandu, killing about a third of the population including the king (see Sapkota et al., 2013). But, its rupture location on the MHT is disputed (see Wesnousky et al., 2017 and Bollinger et al., 2016). If located just underneath the Annapurna massif it could have been responsible for intensive seismic shaking in our field area. If rupture was further to the east (about 200 km as proposed by Bollinger et al., 2016), shacking could have attenuated considerably by this distance. The other possibility is an earthquake that happened somewhere between 1 022 to 1 102 AD, which was only reconstructed by paleo-seismicity trenching (Lavé et al., 2005; Wesnousky et al, 2017). This seismic event must have been of very high intensity. Here researchers agree that the associated rupture on the MHT occurred about 200 km to the east of the Annapurna Massif. For this earthquake, too, the impact on our study area may have been limited.

Surprisingly, an ancient village formerly inhabited by the Gurung/Tamu-mai, a Nepali ethnicity home to the south-facing slopes of the Annapurna massif, is located on the southern slope of the Phalo Danda ridge (see Figure 2.28). At its location we inferred the trace of a conjugate scarp. This archaeological site was investigated by Evans et al. (2009) and it's last occupation was estimated on the bases of 14C carbon burial samples between 790 – 1 300 AD (ages were recalibrated with the OxCal online calculator (Bronk Ramsey, 2021; version OxCal 4.4) using the Intcal20 calibration curve (Reimer et al., 2020)). Abandonment of the village and rupture of fracture F4 in our trench correlate (1 044 and 1 430 AD). The abandonment of this settlement may have been for socio-economic reasons, as discussed by Evans et al. (2009). But, an alternative

explanation could be a natural disaster. An alternative and highly speculative explanation, we admit, could be an earthquake that was responsible for the rupture of F4. The seismic event devastated the village and caused its inhabitants to migrate. Another reason for the abandonment of the settlement associated with the Phalo Danda DSGSD movement could have been the sealing of an important water spring at the village site, related to the activation of a DSGSD fracture nearby.

A recent reactivation of the Phalo Danda DSGSD during the 2015 Gorkha earthquake can be ruled out, since there were no signs of a recent rupture observed on both investigated scarps. This is consistent with the observations of Yagi et al. (2018), who did not observe reactivation of dormant deep-seated slope failures, i.e. DSGSDs, by the 2015 Gorkha earthquake. Above the eastern end of the Gorkha rupture, Lacroix et al. (2022) found that several non-catastrophic, slow-moving or dormant landslides were accelerated as a consequence of this earthquake. They were, however, mostly failed masses, so that we can conjecture that DSGSD either behave differently, or that the Phalo Danda ridge was too far away from the Gorkha rupture to be able to respond to the seismic shaking.

2.8.2 Long-term evolution of the Phalo Danda DSGSD

To investigate the total displacements that have occurred in the past on the two DSGSD scarps examined in this study, profiles were drawn approximately perpendicular to the scarps and parallel to the assumed principal movement direction of the Phalo Danda DSGSD (see profiles in Figure 2.37 and their locations on the map in Figures 2.28, and 2.30a). A two metres high resolution digital surface model derived from Pléiades optical imagery was used to extract the profiles (refer to Section 2.4.1.2 for more information). Crucial to this approach is how the evolution of the topography at the locations of the scarps is to be interpreted.

The topography prior to the rupture of the scarps was not necessarily flat and smooth. Some irregularities such as rock ledges could have been formed by previous erosion processes on the slopes. In addition, hillslope deformation induced by the DSGSD scarps could have changed the topography on the slopes over time. Due to rock fracturing, more exhumation may have taken place on the downthrow sides than on the respective foot walls. This certainly applies to the main ridge (see Figure 29, C+E). Glaciers may have played another important role for topography shaping, too. Particularly on the north side of the ridge, glacial erosion could have affected the small E-W oriented perched valley confined between the main ridge to the south and the eastern segment of the main scarp to the north (i.e. where we sampled and trenched the scarp, Figures 29 C+D; 30a; and 2.33A). Although glacial erosion must be considered limited due to the small size of the paleo-glacier, the superimposition of a lateral flank of a nascent U-shaped valley on the long-term escarpment of the DSGSD could have accentuated the significant topographic offset observed today. The slip offset values proposed below for the long term expression of the main scarp can therefore be considered as maximum values.

Based on the present-day topography displayed by the extracted profiles (see Figure 2.37), we have made two estimates, one minimum and one maximum, of total topographic offset measured from the extracted profiles that we attribute to long term displacement on the scarps over time (with all limitation underlined previously for the main scarp):

- **Conjugate secondary scarp**:
  Total offset on scarp: **35 – 60 m**
  Total vertical offset on scarp (scarp angle estimated to 60°): 30 – 52 m

- **Main scarp**:
  Total offset on scarp: **120 – 210 m**
  Total vertical offset on scarp (scarp angle estimated to 27°): 54 – 95 m

From these estimates we can infer subsequently the total lifespan of the Phalo Danda DSGSD. The Holocene averaged vertical displacement rate for the main scarp which was found by the cosmogenic nuclide profile is approx. 42 cm/kyr (roughly 5 m offset in about 12 000 years) (see Figure 2.33D). This converts into a ~93 cm/kyr rate on the failure plane (~27°). With the estimates of the total offset on the main scarp above, the Phalo Danda DSGSD could have been active for **130 to 225 thousand years**.

The Phalo Danda DSGSD appears to be active since a long time with certainly a pre-Holocene movement history. Movement on the main scarp may have initiated at the beginning of the last interglacial (assuming some uncertainty on our lower age estimate) or is much older. However, it is not certain at all that Holocene movement rates apply to glacial ones.

Paleo-movement reconstructions of DSGSDs in other regions on Earth where no extensive valley glaciers were present in the past repeatedly show very long lifespans. Their activity can extend far into the Last Glacial period, or beyond (see Pánek and Klimeš, 2016 and citations therein). The Phalo Danda DSGSD seems to be no exception.

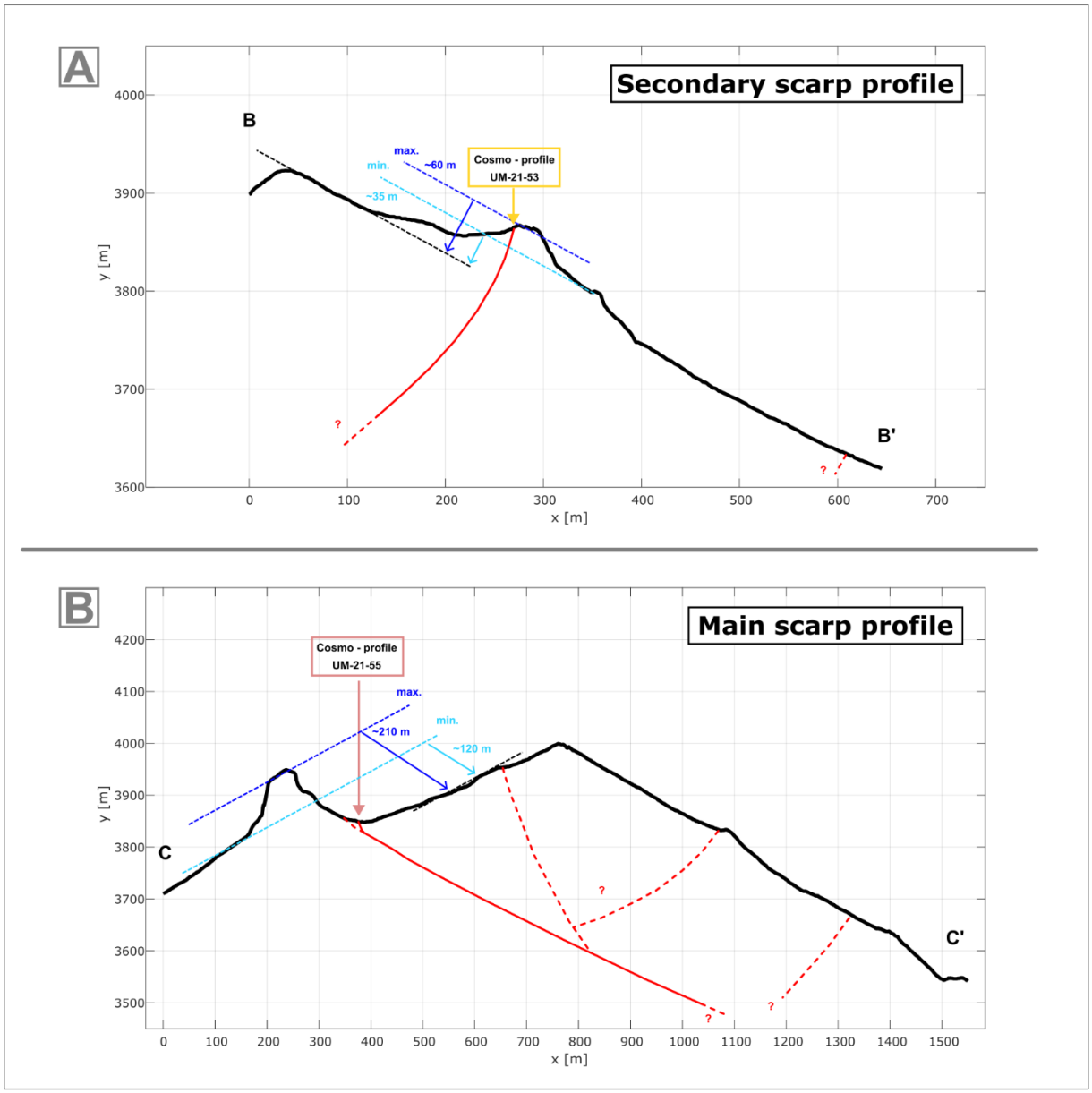


*Figure 2.37: Profiles of sampled conjugate (A) and main scarp (B), for the reconstruction of total displacement on these scarps. They were drawn parallel to the presumed movement direction of the Phalo Danda DSGSD. A digital surface model with a resolution of 2 metres was used. This surface model was created from Pléiades optical imagery (refer to Section 2.4.1.2 for more information).*

2.8.3 Landscape evolution on the southern Annapurna slopes

When looking at other slope processes in our south Annapurna study region, two areas with severe erosion immediately stand out because they have no vegetation cover (Figures 2,28; 2.29B; 2.30, a+c; and 2.36, B+D). Gallo and Lavé (2014) call these features Saituti and Midhi Khola landslides and describe the characteristics of their activity. These retrogressive erosion scars appear to erode into the highly fractured rock material of formerly failed masses following phases of variable activity and over periods of several decades (see Figure 2.38, A+B). During the time of their activity they highly dominate the erosional output of the Khudi and Midhi Khola valleys (Lavé et al., 2019).

In view of the presence of DSGSD features along the ridge crests in the area and our new findings from the Phalo Danda DSGSD, a hypothesis of cyclic erosion behaviour for hillslopes in the southern Annapurna region can be proposed (see the schematic sketch for hillslope erosion in the Khudi valley, Figure 2.38C, and schematic sketches of Figure 2.39):

1. **Long term DSGSD-type failure initiation on ridge crests** (see Figure 2.39A)

2. **Increase of the DSGSD displacement up to large mass sliding by several hundred meters along the hillslope accompanied by a reduction in hillslope relief and fracturing/disintegration of failed rock mass (partial or complete transition toward a catastrophic failure is conceivable)** (see Figure 2.39B)

   *Potential long period of dormancy*

3. **Pulse-like erosion into the lower and middle sections of the failed masses by retrogressive erosion scars, previously damaged rock having made the hillslope material easily erodible** (see Figure 2.39C)

   *Potential long period of dormancy*

The outlines of failed masses that were drawn while mapping our study area for DSGSD features (see Figures 2.28, and 2.30, a+c) and our dating of other features related to the deformation of the slopes in this area support this view (see Section 2.7.4;and Figures 2.29,A+B; and 2.36):

The boulder sitting upslope of Saituti landslide dated for 10Be cosmogenic exposure dating probably originates from a rockfall that detached close to the ridge crest upslope (CA-10-21: 121,84 ± 7,14 ka; see Figures 2.30c; and 2.36, C+D). Presumably, we are dealing with a block that was destabilised in connection with hillslope deformation, i.e. DSGSD activity. It could have travelled on an active DSGSD for a considerable

time during which the slope failure was still active. Eventually, the failed mass became dormant. The dated boulders upslope of Midhi Khola landslide could have experienced a similar scenario (CA-13-220 & 221) (see Figures 2.29B, and 2.36, A+B).

There are still many unresolved questions in the context of our investigations on the southern Annapurna slopes, our hypothesised slope evolution cycle and, in a broader context, the role of non-catastrophic rock failures, including DSGSDs, in the long-term denudation of active orogens:

- Are our observations and hypothesised slope evolution cycle only site-specific, i.e. do they only apply to our southern Annapurna study region? Or, is our hypothesis applicable only to slope settings on the Annapurna south face, or the monsoon-influenced southern flank of the central Himalayas? Or can similar observations be made in other tropical mountains with DSGSD activity? More specifically, can we observe regressive erosion scars associated with non-catastrophic slope failures elsewhere?

- What role does the bedrock lithology play in DSGSD formation in the central Himalayas? Do more competent gneisses tend to fail catastrophically, as suggested by Chigira et al. (2022) for the Kali Gandaki valley? What is the influence of the foliation and other mechanical properties of the rock?

- What influence does the annual amount of precipitation falling on slopes have on the development of DSGSD phenomena, also in comparison to other regions of the world? We did our investigations in an area of very high annual precipitation and observe a lot of DSGSD morphology. But, Agliardi et al. (2013) found a negative correlation between the frequency of DSGSD and annual precipitation in the European Alps.

- Our research area never experienced any major glacial shaping. The valleys were never occupied by glaciers. This is a particular difference to mountain ranges at higher latitudes where extensive glaciations occurred during glacial periods. DSGSDs in higher latitude mountain ranges have life spans limited to the last extensive glaciation, i.e. Last Glacial Maximum (LGM) (see Pánek and Klimeš, 2016). Glacial cycles in higher mountains do not allow the formation of older DSGSDs that could date further back into the Pleistocene. This is the case because glacial flows during glacial cycles presumably remove weakened rock masses that are the product of interglacial slope deformation, including DSGSDs and failed masses, from the valleys. DSGSDs in repeatedly glaciated mountains can probably never reach such an advanced stage, so that pulse-like erosion by retrogressive erosion scars can occur.

- Agliardi et al. (2013) observed for the European Alps that DSGSDs tend to appear more frequently in areas with intermediate exhumation rates. Our research area is subjected to very high exhumation rates (Lavé and Avouac, 2001; Burbank et al., 2003; Blythe et al., 2007). Obviously, the overall exhumation rates in the Himalayas are much higher than in the Alps. Does a correlation between the frequency of DSGSDs and exhumation rates also exist for the central Himalayas?

We suggest that long-term hillslope deformation, featuring DSGSDs and failed masses, are important drivers of hillslope denudation in non-glaciated mountain ranges that received little attention by researchers so far. They not only continuously reduce hillslope relief, but also weaken the bedrock to such an extent that associated erosion processes can only come into play.

Addressing these issues in more detail with a more dedicated discussion lies beyond the scope of this PhD-thesis and should be the subject of further research.

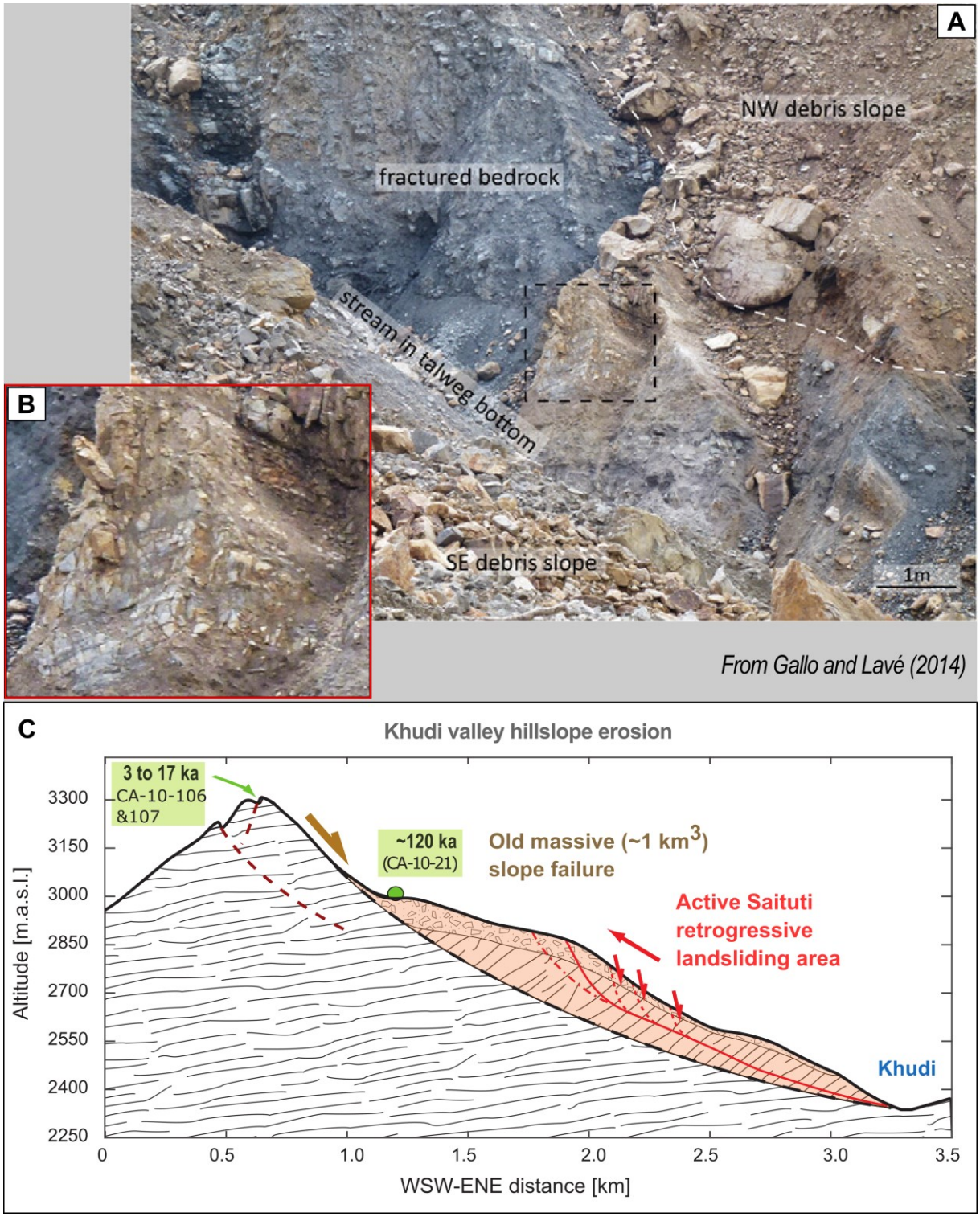


*Figure 2.38: (A) Intensely fractured and disintegrated gneisses at the bottom of the Saituti retrogressive erosion scarp (see Figures 2.28, 2.29c, and 2.34C+D for location a view from the distance). (B) closer look into the dashed rectangle in A: more coherent block of fractured bedrock where the where the foliation is still clearly visible. (C) Schematic sketch of hillslope deformation and erosion processes in the Khudi valley. Modified from J. Lavé.*

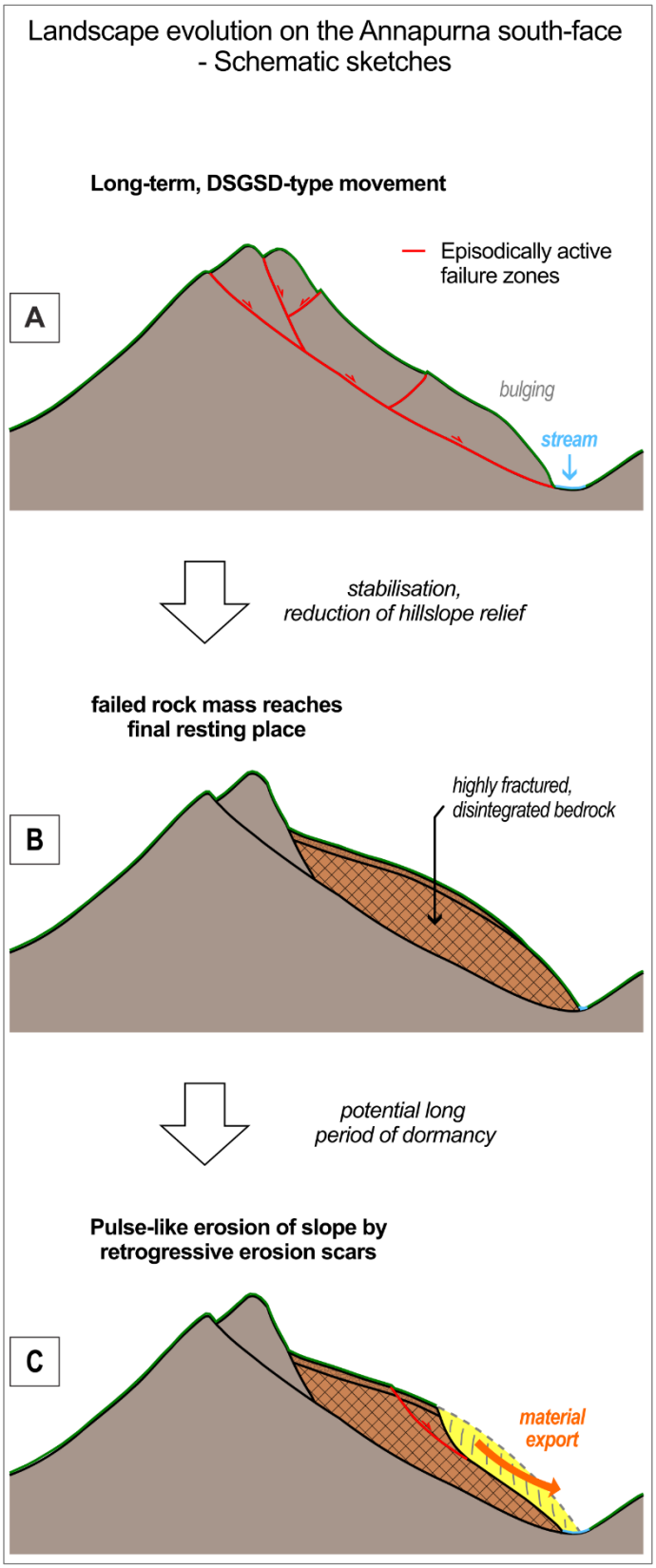


*Figure 2.39: Schematic sketches illustrating the long-term hillslope evolution on the Annapurna south-face, which did not experience valley glaciation during Glacial times: First there is DSGSD-type hillslope deformation (A), i.e. non-catastrophic rock slope failure, and in the following the hillslope deforms up to a point where the failed rock mass stabilises (B), Later there is retrogressive erosion into fractured, disintegrated bedrock (C).*

## 2.9 Discussion – Annapurna Massif

### 2.9.1 Causes of bedrock landslides in the central Himalayas

#### *2.9.1.1 Precondition Factors*

Our observations on bedrock landslides in the Annapurna Massif suggest preconditioning by structures and lithology. Studying the giant rock avalanches in the Annapurna Massif indicates preconditioning either by large-scale anticlinal folding or by failure along bedding planes, i.e., dip-slope failure. (see also Dhampu-Chhoyo event in Fort (2000); Section 2.6.2.1). The main failure plane of the Phalo Danda DSGSD dips in the opposite direction to the gneiss foliation which contradicts the qualitative assessment of other studies in this area, suggesting a favoured occurrence of DSGSDs on cataclinal slopes (Yagi et al., 2018; Chigira et al., 2022; see Section 2.8.1). For the Phalo Danda DSGSD, the orientation of the gneiss foliation relative to the slope may be less significant as a Precondition Factor for failure compared to other locations in the area. Instead, the topographical setting, i.e. a hillslope geometry, might have played a decisive role in the failure's localisation. Alternatively, apart from the foliation, other structural features (e.g., fractures, tectonic fault zones) could have influenced the formation of the DSGSD at Phalo Danda, though these factors remain unknown to us. For instance, structural features that are not ubiquitous and, for this reason, difficult to discover, particularly in inaccessible high-altitude areas or deep within the slope, could potentially affect the failure behaviour of the rock mass.

The lithological preconditioning of slopes for deep-seated failure in the Annapurna Massif can only be conjectured as, both in our study and in the existing literature, lithological descriptions of the relevant rocks are primarily limited to their stratigraphic context, without thorough investigation of their mechanical properties or state of weathering. The influence of lithological characteristics, such as porosity and strength anisotropy, on the effectiveness of internal Preparatory Factors for deep-seated failures, like progressive rock fatigue, deep-seated weathering, and damage from repeated seismic loading (see Section 2.6.2.2; Brantut et al., 2013; Viles, 2013), remains largely unexplored. The gneisses on the south-face likely exhibit different weathering characteristics compared to the meta-carbonates north of the STD (see Figure 2.1), including varying susceptibility to chemical dissolution (e.g., Elango and Kannan, 2007). The hydromechanical effects of groundwater also vary depending on the lithology type and the degree of fracturing within the rock mass (e.g., Rutqvist and Stephansson, 2003).

The localised field studies conducted in this doctoral thesis are too limited to fully decipher the role of structural and lithological preconditions in rock slope failures within the Annapurna Massif. However, the

existing literature highlights the significant impact of these factors on bedrock landslides in other regions, demonstrating their influence on failure geometry, on failure mode, and on their frequency (see Sections 1.3.3 and 1.4.2; e.g., Glastonbury and Fell, 2010; Crosta et al., 2013; Blondeau et al., 2021). For the Himalayas, a study by Dini et al. (2020) revealed substantial lithological and structural control over rock slope instabilities in a setting similar to the Annapurna Massif (see Section 2.3.5). Drawing from their findings and related research, we can reasonably expect that lithologic characteristics and structures play a crucial role in preconditioning rock slope failures in the Annapurna Massif.

To provide substantial evidence of lithological and structural preconditioning in the Annapurna Massif and to study it in more detail, large-scale analysis and mapping of bedrock landslide morpho-structures is required: both topographic features of non-catastrophic failures and catastrophic failureneed to be identified. Smaller catastrophic failures than giant ones, i.e. $<10^6$ km³, should also be considered in order to significantly increase the sample size and thus the statistical significance of the results. This could be done using a high resolution DSM, similar to studies carried out in other regions (for example, Blondeau et al. (2021) and Cui et al. (2022); see also the review by Guzzetti et al. (2012)). Spatially limited analyses that focus solely on giant rock avalanches or DSGSDs individually may lead to an oversimplified view, assuming a dichotomy where giant rock avalanches occur only along or north of the main ridge crest, and DSGSDs occur only on the south face. To avoid this, it is essential to check for evidence of non-catastrophic deep-seated rock slope failure and deposits of catastrophic failures, on both the north and south sides of the main ridge crest.

A dataset covering a large area of the Annapurna Massif, including both catastrophic and non-catastrophic rock slope failures, could be systematically compared with mapped structures or outcropping lithology (in combination with climatically controlled Preparatory Factors, see Section 2.9.1.2 below). This approach would facilitate a more comprehensive investigation into the role of structural and lithological preconditioning of bedrock landslides in the Annapurna Massif, particularly with regard to the influence of these factors on the occurrence of catastrophic or non-catastrophic failures, respectively. For example, Chigira et al. (2022) suspected that slopes underlain by more competent calcareous gneisses are more prone to catastrophic failures than those composed of mica-rich gneisses (see Section 2.3.5). Such hypotheses could be better assessed through a more exhaustive and systematic study.

Further investigations, both site-specific and broad-scale, could offer new insights into how lithology and structural features influence the frequency and characteristics of bedrock landslides in the Annapurna Massif. Nonetheless, this PhD-study has already laid a valuable foundation for future research in this area.

*2.9.1.2 Preparatory and Movement Sustaining Factor of bedrock slope failures*

The dating results obtained from this PhD-thesis and from other studies in the region allowed to draw inferences as to what may have led to a decrease in slope stability over time in the Annapurna Massif and eventually to the slope failures, both catastrophic and non-catastrophic, i.e. giant rock avalanches and DSGSD:

The new age constraints on timing of giant rock slope failures in the upper Marsyangdi Valley and the already existing event ages from and around the Annapurna Massif (Latamrang, Sabche cirque, and Dhampu-Chhoyo; see Figure 2.1 and Table 2.5; Pratt-Sitaula et al., 2007; Zech et al., 2009; Lavé et al, 2023) correlate with the EHCO and MWP warm and humid phases (see Figure 2.27 and Section 2.6.2.4). Additionally, our scarp movement reconstruction from the Phalo Danda DSGSD also shows an increase in movement rates at the end of the EHCO (approx. 4,5 – 7,3 BP; see also Section 2.8.1).

This study suggests the influence of climatic forcing by warmer and wetter conditions on the occurrence of giant rock avalanches in the Annapurna Massif (see Section 2.6.2.4). It is conjectured that slope destabilisation is intensified during warmer and wetter periods by processes acting either from within the slope, i.e. internal Preparatory Factors, or by external Preparatory Factors (see Section 2.6.2.2). Our inferred correlation of giant rock avalanche occurrence with warm and humid climatic periods is consistent with the conclusions drawn by Bookhagen et al. (2005) and Dortch et al. (2009), who found ages coincident with phases of increased monsoon climate for giant rock avalanches in the northwestern Himalayas and the Karakoram Mountains (warmer and wetter conditions). For comparison, “landslide” ages documented in the European Alps span the Holocene and late Pleistocene, without clear clustering during specific time periods (see reviews by Pánek (2019) and Ivy-Ochs et al. (2017)).

For the Himalayas, which might be representative of lower latitude tropical mountain ranges, it can be conjectured that climatic forcing of large rock avalanches is more pronounced than in the European Alps, which might be representative of higher latitude mountain ranges. This discrepancy could be explained by the fact that the European Alps were to a much higher degree shaped by Pleistocene glaciations (i.e. extensive valley glaciations; see Seguinot et al., 2018), which played a significant role in landscape evolution and consequently the occurrence of large catastrophic slope failures. Alternatively, or in addition, climatic shifts during the Holocene, particularly changes in mean annual precipitation, may have played a more significant role in forcing slope failures in the Himalayas than in the European Alps. Finally, it is important to note that the catalogue of events is much larger in the Alps and our conclusion in Himalaya might be partially biased by an insufficient number of dated events.

Assessing the relative importance of these Preparatory Factors for the giant rock avalanche failures described in this study is challenging, primarily because of the small sample size of giant rock slope failures available for study and the limited site-specific investigation performed so far for the failure events. However, if the area of origin is known, a sophisticated mechanical analysis of the failure might be feasible: for example, investigating the significance of fluvial gully incision at the foot of the slope at the Phalo Danda site (see Section 2.5.1.1 and Figures 2.11 and 2.13) or as done by Lavé et al. (2023) for the Sabche cirque failure.

The climate correlation for DSGSD activity at the Phalo Danda site is less explicit compared to the giant rock avalanches studied in this thesis. However, there is a temporal overlap between the end of the EHCO and the period of increased movement activity of the DSGSD scarps. For the conjugate scarp, any activity after the EHCO, i.e., after 5.5 ka BP, is quite unlikely (see Figure 2.32D). As for the main scarp, a higher level of activity is probable 1,000 years after the EHCO, up to around ~4.5 ka BP (see Figure 2.32D).

On the south side of the Annapurna Massif, in the setting of the Phalo Danda DSGSD, glacial erosion has minimally shaped the slopes, with no evidence of extensive valley glaciation (see Section 2.71 and Figure 2.30a). Instead, valley excavation is primarily driven by fluvial runoff, likely with significant contributions from erosion accomplished through catastrophic landslides triggered by infrequent extreme rainfall events (see Jones et al., 2021). The few paleo-movement reconstructions of DSGSDs in non-glaciated environments that exist in the literature indicate that DSGSD activity increases during wet climatic phases (Sewell et al., 2015, and references therein; Livio et al., 2022), consistent with our results. This contrasts with higher latitude topographies shaped by former valley glaciation, where the reconstructed paleo-movement behaviour is influenced by the last large glacial retreat of the Late Pleistocene. In these formerly glaciated areas, the chronologies of movement are inconsistent and do not show any kind of systematics (see Section 1.4.2 and the review by Pánek and Klimeš, 2016). It should be noted, however, that many paleo-movement reconstructions using cosmogenic nuclide exposure ages along DSGSD scarps in the existing literature need to be re-evaluated. Some studies do not take into account the initial inheritance related to the upper surface exposure before scarp initiation, nor the complexity that derives from the gradual exhumation of a scarp and the consequences for the shielding /exposure history of individual samples. To accurately interpret cosmogenic nuclide concentrations, they must be translated into potential scarp rupture scenarios using an advanced calculation scheme, as we applied for the cosmogenic nuclide profiles of the Phalo Danda DSGSD (see Sections 2.4.3.4, 2.7.2, 2.7.3.1, and Figures 2.8, 2.32 C+D, and 2.33 C+D; also refer to Schlagenhauf et al., 2010). Without such appropriate data treatment, the conclusions of paleo-movement reconstructions of DSGSD-scarps with cosmogenic nuclides should be approached with caution.

Although we successfully reconstructed the temporal development of a specific DSGSD body for the

Holocene period, it has to be acknowledged that this study cannot clearly identify the prevailing Movement Sustaining Factors of DSGSDs on the rainy south side of the central Himalayas, nor does it clearly determine their relative importance. However, based on our new research findings and existing literature on paleo-movement reconstructions of DSGSDs in non-glaciated settings, we can hypothesize that long-term DSGSD movement is generally more uniform in non-glaciated areas compared to glaciated ones. It also appears that DSGSD activity tends to follow, at least to some extent, the long-term trend of precipitation. Future studies should consider exploring the site-specific mechanical evolution of the Phalo Danda failure body in greater detail, an aspect that has not been thoroughly analysed so far, but is likely to superimpose long-term trends driven by precipitation.

The Annapurna Massif forms a strong orographic rainfall barrier, resulting in high precipitation on the south face and much drier conditions along and north of the main ridge crest (see Section 2.2.2; Figure 2.4, A+B). Could precipitation influence the occurrence and characteristics of large-scale bedrock landslides? More specifically, it could be hypothesized that the humid south face of the Annapurna Massif is more prone to non-catastrophic DSGSDs, while catastrophic giant rock avalanches are more likely to occur along or north of the main ridge crest, where less precipitation is falling. However, this dichotomy remains speculative without systematic exploration of bedrock landslide morpho-structures across the Annapurna Massif. Whether or not DSGSD features are present in the high, arid areas to the north of the main ridge crest has not been investigated to date. Additionally, the small sample size of the extremely large catastrophic rock slope failures analysed in this PhD study is insufficient to establish significant relationships. To better understand the relationship between precipitation and bedrock landslide abundance and type, an inventory that includes smaller-than-giant catastrophic failures ($<10^6$ km³) would be necessary in order to significantly increase the sample size and thus the statistical significance of the results (as already proposed for the study of Precondition Factors in Section 2.9.1.1 above). Furthermore, it is important to consider that the modern precipitation distribution may not exactly reflect past precipitation patterns.

Studies using landslide inventories from the European Alps have shown that there is no correlation between modern precipitation patterns and the arial density of bedrock landslides (Blondeau et al., 2021, for the western Alps). In fact, for DSGSDs, a negative correlation between abundance and modern annual precipitation has been observed (Agliardi et al., 2013). However, it is important to consider that the evolution and morphology of valleys in the Alps differ significantly from those in the central Himalayas, where valley glaciation during the Pleistocene was much less extensive. This difference could influence the contemporary relationship between precipitation and DSGSDs observed in these regions.

The relationship between permafrost presence and the occurrence and characteristics of deep-seated slope failures in the Annapurna Massif requires further attention. In the European Alps, no clear correlation has been identified between permafrost and the occurrence or type of deep-seated slope failures, as both rock avalanches and DSGSDs extend into present-day permafrost zones (Blondeau et al., 2021). Could reduced hydrological connectivity due to permafrost ("hydro-sealing" of slopes) affect rock slope failure by impeding brittle creep in the subsurface of slopes (see Patton et al., 2019 and citations therein; Lavé et al., 2023; and see also Sections 1.3.3 and 2.6.2.4)? A more detailed assessment of the role of permafrost on deep-seated rock slope failures in the Annapurna Massif would be desirable.

An ongoing concern in the study of large-scale bedrock landslides is whether there is a genetic link between catastrophic and non-catastrophic failures. More explicitly, whether non-catastrophic slope deformation acts as a precursor or Preparatory Factor for catastrophic failure (see Section 1.4.3; reviews by Hewitt et al., 2008; Pánek and Klimeš, 2016; Lacroix et al., 2020; Discenza and Esposito, 2021). Do large-scale non-catastrophic failures have the potential to evolve into catastrophic collapses? In the Annapurna Massif, DSGSD deformation may have preceded the giant catastrophic rock avalanches. This possibility seems quite likely, since non-catastrophic deformation has been identified in the presumed detachment zone of the Dhampu-Chhoyo giant rock avalanche (see Section 2.3.4 and Table 2.5 with references). At this locality recent field studies have found evidence of non-catastrophic slope deformation, including linear depressions and buckling of the foliated gneiss (Chigira et al., 2022), as well as active deformation detected by remote sensing data (InSAR analysis by Sato et al., 2020).

To our knowledge, DSGSD structures have not been thoroughly investigated at the other giant rock avalanche sites in the Annapurna Massif where the source areas are known. Using the remote sensing data exploited for this thesis (see Section 2.4.1.2), brief investigations of the proposed detachment scars at Tilicho Lake, Sabche Cirque, Pisang Bowl and Latamrang do not reveal clear evidence of DSGSD structures. However, investigations using higher resolution DSMs may yield different results.

In contrast to the other detachment areas, the Dhampu-Chhoyo giant rock avalanche detached well below the present day permafrost zone (approx. 3300 m.a.s.l.; see Permafrost Zonation Index (PZI), Gruber, 2012). The presence of permafrost likely has an influence on the development of non-catastrophic hillslope deformation, i.e. DSGSDs (see above).

*2.9.1.3 Triggers*

Reconstructing the prehistoric Triggers of large-scale bedrock landslides, such as giant rock avalanches and discrete individual movement events of DSGSDs, is a challenging task, and conclusions are often highly speculative. Without historical records, it is nearly impossible to determine what exactly happened during a short moment in time far back in the past. However, findings from contemporary bedrock landslides, including DSGSD monitoring studies, can offer insights into possible Triggers of the distant past. Literature shows that for both catastrophic and non-catastrophic failures, the most significant Triggering mechanism is a rise in groundwater levels (due to increased water percolation caused by intense precipitation or snowmelt) followed by seismic shaking (e.g., Wen et al., 2004; Glastonbury and Fell, 2010; Pánek and Klimeš, 2016; Lacroix et al., 2020).

For the Annapurna Massif, it is plausible that periods like the EHCO and MWP, with their warmer and wetter climates, also saw an increase in the frequency and intensity of atmospheric Triggering events (i.e. more extreme weather), particularly extreme precipitation (either short-term cloudbursts or prolonged rains; see Sections 2.6.2.4 and 2.6.2.5). Alternatively, a few days or weeks of significantly warmer temperatures than usual may be regarded as a potential Trigger for rock slope failures as well. Probably more relevant for the high altitude detachment areas of the giant rock avalanches than for the DSGSDs could these short-term warm phases lead to instantaneous permafrost melting, maybe intensified by additional weather effects. Melting permafrost has the potential to create new pathways for surface water percolation, altering subsurface hydromechanical conditions and triggering deep-seated failures (increased groundwater levels and higher pore pressure in weak zones) (see Sections 1.3.3 and 2.6.2.4; and, e.g., Patton et al., 2019).

Not much can be done about the uncertainty of past atmospheric Triggers of large-scale bedrock landslides, as weather phenomena are difficult to reconstruct without historical records, which only extend back a few decades.

Possible seismic Triggers for the bedrock landslides analysed in this study can neither be significantly substantiated nor rejected. However, there is only limited overlap between the more recently dated giant rock avalanches in the Annapurna Massif and the existing earthquake record (see Section 2.6.2.5 and Figure 2.27B). Lacroix et al. (2022) found evidence of post-seismic movement in non-catastrophic, slow-moving landslides in central Nepal following the 2015 Gorkha earthquake. They proposed a mechanism where seismic activity triggers movement by local pore pressure increase following new pathways opening for water percolation within bedrock due to the seismically induced opening of cracks. This mechanism could potentially apply to the Phalo Danda DSGSD, even though the landslides in Lacroix et al. (2022)'s study are significantly smaller in scale (see also Section 2.8.1).

Similar to reconstructing past heavy rainfall Triggers, exploring potential seismic triggers is also highly challenging due to the limited paleo-earthquake record in the central Himalayan region and the time resolution of applied absolute dating techniques (see also Sections 2.6.2.5 and 2.8.1; Bilham, 2019). However, further studies that focus on investigating paleo-seismicity, such as excavating trenches across surface-rupturing fault zones, have the potential to expand the paleo-earthquake record in the region to some extent (e.g., Lavé et al., 2005; Bollinger et al., 2014). Such investigations would be particularly valuable not only for earthquakes directly linked to the north-south thrusting of the orogen, but also for nearby secondary structures, such as the Dangardzong Fault in the Thakkhola Graben (see also Sections 2.6.2.5, 2.8.1; Figure 2.1; Hurtado et al., 2001).

Another approach to reconstructing prehistoric earthquakes is to find evidence of these events in lake sediments by correlating dated mass movements, as has been done in other regions like the European Alps (e.g., Petersen et al., 2014; Kremer et al., 2017). Additional research is needed to try establishing a comprehensive paleo-seismic record from lake sediments in the central Himalayan region. Currently, the existing records are quite limited. Aside from Rara Lake (about 200 km WNW of the Annapurna Massif), which was studied by Ghazoui et al. (2019), other lakes such as Phoksundo Lake (around 100 km WNW of the Annapurna Massif) or Tilicho Lake could be explored. However, it is likely that only lake sediments dating back a few hundred to a few thousand years can be recovered, given the technical limitations of the coring techniques.

More site-specific investigations could offer valuable insights into the triggering mechanisms of catastrophic rock slope failures in the Annapurna Massif. Detailed reconstructions of the pre-failure state of slopes could potentially reveal clues about the Triggers of specific slope failures.

As our study reveals, large-scale bedrock landslides deform slopes infrequently. Failure events, whether catastrophic rock avalanches in a given area or discrete movement phases of individual DSGSDs, are separated by long periods of dormancy, occurring only every few hundred years. The most promising approach to investigating potential Trigger mechanisms behind these rare landslides is to study contemporary slope failures of smaller scale using remote sensing monitoring techniques such as optical image correlation or InSAR (see Sections 1.4.2 and 2.3.5). These modern slope failures can be examined using satellite data, which spans roughly over the last two to three decades, depending on the availability, coverage, quality, and resolution of the data. Detected catastrophic or non-catastrophic slope failures can be compared with existing meteorological and seismic data. Or vice versa: If a potential triggering event, such as an earthquake or cloudburst, happened, slope failures can be detected and analysed.

For example, it could be investigated whether the 2015 Gorkha earthquake triggered discrete DSGSD ruptures in the region, similar to the analyses of Lacroix et al. (2022) for smaller-scale, slow-moving slope deformation in the upper Bhote Koshi area (about 170 km east-southeast of the Annapurna Massif; see Section 2.3.5). There is still significant potential in the central Himalayan region to explore the effects of earthquakes and meteorological events on recent bedrock slope failures using available data. Large parts of the central Himalayas available remote sensing data has not yet been systematically analysed for large-scale bedrock slope failures. Because satellite data acquisition is ongoing, data can be analysed also if a strong earthquake occurs in the central Himalayan region in the near future. Observing a contemporary large-scale bedrock landslides in this region has the potential to provide far more valuable insights into the Triggering mechanisms of such slope failures than relying only on speculative interpretations of past events.

It is also possible that catastrophic giant rock avalanches do not always require an atmospheric or seismic Trigger. Instead, progressive non-catastrophic slope deformation (brittle creep) could reach a critical state where tertiary creep or runaway failure occurs, ultimately leading to a collapse (see Sections 1.2.3 and 1.4.3). This possibility is corroborated by observations from optical imagery of the Ronti Peak rock slope failure in the Indian Garhwal Himalayas (about 450 km WNW of the Annapurna Massif), where progressive deformation was detected five years prior to the catastrophic collapse, without the presence of a seismic or extraordinary meteorological event on the day of failure (Shugar et al., 2021). In such cases, advanced progressive non-catastrophic slope deformation can be considered a triggering mechanism. Such a process is also conceivable for the giant rock avalanches in the Annapurna Massif.

### 2.9.2 Implications for natural hazards

Exploring Precondition and Preparatory Factors of bedrock landslides, more precisely giant rock avalanches and DSGSD phenomena, has some important implications for the assessment of natural hazards and risks in the area.

In order to assess potential natural hazards from slope failures, researchers need to know the factors that influence slope stability; this is the basis of multi-parameter input for hazard and risk mapping (see, e.g., landslide susceptibility mapping of Nepal by Gnyawali et al. (2023)). However, huge rock avalanches occur much less frequently in the central Himalayas than smaller-scale bedrock landslides (Marc et al., 2019) and therefore have only limited relevance for hazard and risk assessment in the area. Nevertheless, as we can draw from the reconstructed past infill of the Pokhara valley (Lavé et al., 2023; Stolle et al., 2017; Schwanghart et al., 2016), the downstream consequences of a giant rock slope failure, here the Sabche cirque rock avalanche, have a high potential to be disastrous for the people living in affected areas. In a present-day scenario, the economic impact and threat to human life in a densely populated area is potentially tremendous. Secondary hazards from a giant rock slope failure deposit are particularly menacing: extreme channel avulsion or, even worse, catastrophic floods or debris flows either from outburst flooding (e.g., Evans et al., 2011), or in the aftermath by rain events and sediment remobilisation are conceivable. The discrete movement type DSGSD, as observed in our study at Phalo Danda (see Section 1.4.2), has limited hazard and risk potential due to its low activity rates and low-mass displacement over time. More active, non-catastrophic rock slope failures could be more hazardous, for example, for villages directly affected by the movement or secondary landsliding, i.e. landslides that occur within the deformed DSGSD mass (see Section 1.4.1), or for road construction (Thuro, 2004 (for the Himalayas)).

The evidence of climate forcing on bedrock landslides presented in this doctoral thesis may have significant implications, especially in today's context. We are currently experiencing rapid, human-induced global climate change, which is only just beginning to unfold. The anticipated climatic changes in the Himalayas are expected to vary spatially, with scenarios predicting a 2° to 6° increase in temperature, alongside increased monsoonal precipitation and intensified precipitation extremes (see Rangwala et al., 2020; Shrestha et al., 2015; Dimri et al., 2020). It is thus reasonable to assume that we are entering another warm and humid phase in the central Himalayas.

Hypothetically, other giant rock avalanches in the central Himalayas can occur anytime, there just has to be a sufficiently effective Trigger. Assuming our interpretation of progressive slope destabilisation by progressive rock damage within the deep substrate of the hillslopes throughout the Holocene, there may be hillslopes that are already underlain by substantially weakened zones and are already within a marginal state of stability. However, we can assume that the progressive weakening of rock slopes by groundwater and

deep weathering processes was slowed down during the LIA. Additionally, an increased decline in slope stability as a result of newly intensified progressive damage in weak zones as a consequence of climate change will probably take some time to become effective (as argued for the timing of our giant rock avalanches and DSGSD movement; see Sections 2.6.2.4 and 2.8.1). Following this reasoning, we would not expect an immediate increase in deep-seated catastrophic rock slope failures or non-catastrophic rock landslide activity in response to an increased rate of progressive damage of rock slopes. Thus, bedrock landslide activity might not rise immediately after an increase in precipitation.

Another Preparatory Factor expected to become more important due to climate change, with an immediate impact on slope stability, is erosion at the base of slopes. It can occur either through extreme flood events or debris flows, both of which are predicted to become more frequent and intense in the central Himalayas as extreme precipitation events increase due to climate change (Sigdel and Ma, 2017; Karki et al., 2017), or through glacial retreat. Glacial retreat can lead to glacial debuttressing of slopes, where the loss of glacier mass at the foot of the slope alters its geometry and thus its stability. However, this slope destabilisation by glacial retreat is relevant only in high-altitude regions where glaciers are present. Another immediate consequence of warming temperatures due to climate change is the retreat of permafrost, which affects as well only high-altitude terrain. Permafrost retreat impacts slope stability both through the direct mechanical loss of stability as ground ice melts and through its hydromechanical consequences for the deeper slope by more and varied water percolation to the subsurface (see Patton et al., 2019 and citations therein). Therefore, as the effects of climate change are likely to have the most immediate impact on slope stability in glaciated, high altitude areas, it can be hypothesised that climatically forced rock slope failures will be more likely to occur in these areas in the near future.

For large -scale non-catastrophic rock slope deformations, i.e. DSGSDs, an increased activity in the central Himalayas due to climate change is likely to have a limited impact on natural hazards and risks in the region. However, an increase in secondary landsliding is expected as a result of higher activity rates due to increased precipitation in the future (see Section 1.4.1).

2.9.3 Implications for erosion fluxes

The new findings from this PhD-thesis, in particular the extension of the existing record of giant rock avalanches for the central Himalayas, which includes volume estimates, could be of interest to researchers concerned with erosional fluxes. The new volume estimates for the upper Marsyangdi rock avalanche deposits include large amounts of sediment, some of which has already been significantly removed by erosion. By far the largest volumes among the giant rock avalanches recorded in the central Himalayas were produced by the Sabche cirque failure (27 +4/-3 $km^3$) and the Tilicho Lake (~21 $km^3$) failure. They are thus among the largest rock avalanche deposits in the Himalayas and worldwide and represent extraordinary sediment production (see study with inventory by Korup et al. (2007)). For the upper Marsyangdi Valley alone, we estimate that in the last ~700 years 3,6 $km^3$ of rock avalanche-derived sediment has been exported from the valley stretch at Humde alone. Since the Tilicho Lake failure, i.e. in the Holocene, and including the eroded sediments of this event, a sediment volume of at least 14,5 $km^3$ has been exported from the whole stretch of the upper Marsyangdi Valley. We have no age constraint or volume estimate for the Manang deposit yet, but it is likely that this event also happened within the Holocene period adding further significant sediment volume to the estimate above. This is a lot of sediment going down the Marsyangdi River and our new estimates need to be taken into account for estimates of erosion fluxes in future studies, especially the Tilicho Lake rock avalanche, which was not recognised by previous estimates of landslide erosion (Marc et al., 2019).

The volume of sediment eroded from the giant rock avalanche deposits can be translated into catchment-averaged erosion rates imposed by these events. For the upper Marsyangdi Valley, these rates are calculated using the catchment area upstream of the Dudh Khola confluence (outlined in yellow in Figures 2.1 and 2.10). The sediment export from the Humde giant rock avalanche alone translates into a catchment-averaged erosion rate of approximately 3 mm/yr over the last ~700 years. When this is combined with the exported volume from the Tilicho Lake deposit and an additional 0,7 $km^3$ of sediment exported from the Pisang Bowl and Latamrang deposits (see Table 2.5), the erosion rate from giant rock avalanches over the Holocene can be calculated. This results in a Holocene catchment-averaged contribution to the erosion by giant rock avalanches of approximately 0,7 mm/yr for the upper Marsyangdi Valley (see yellow outline in Figures 2.1 and 2.10). It is important to note that these catchment-averaged erosion rates are minimum estimates, as the sediment export from the giant rock avalanche deposits at Manang and other potential deposits within the catchment have not been accounted for.

Estimates of long-term denudation rates from low-temperature thermochronometry (specifically apatite fission-track dating) for the High Himalayas or High Range of the Annapurna Massif (see Section 2.2) suggest values of ≥2-5 mm/yr (Burbank et al., 2003). A study by Gabet et al. (2008) used suspended sediment

concentrations in river water discharge over a three-year period in the early 2000s (2000-2005 AD) to estimate a catchment-averaged erosion rate of ~0.4 mm/yr for the upper Marsyangdi Valley (see yellow outline in Figures 2.1 and 2.10). An independent estimate based on 10Be cosmogenic nuclide concentrations in fluvial sediments indicates an erosion rate of ~4,5 mm/yr (Godard et al. , 2012), but the non-uniform distribution of quartz in the carbonate rich TSS units makes this estimate poorly reliable. Nevertheless, comparing rates derived from our sediment export estimates from the giant rock avalanches with existing estimates for the same area suggests that sediment from these deposits significantly contributed to, if not dominated, the erosion fluxes in the upper Marsyangdi Valley during the last few hundred years and the Holocene.

These large volumes of eroded sediment have implications for studies addressing orogen evolution and denudation in a broader context, globally (see, e.g., Korup et al., 2007) and in the central Himalayan region (see, e.g., Burbank et al., 2003). First, the catchment-averaged giant rock avalanche erosion rates derived from this PhD-thesis (see Section 2.9.3), need to be properly integrated into the erosion budget of the central Himalayas. How can our results be interpreted together with basin-averaged erosion rates for larger basins across the orogen (see e.g., Lupker et al., 2012)?

From a process perspective, it must be investigated how so much sediment at Humde could have been eroded so rapidly without evidence of an outburst flood downstream (see Section 2.6.1). This question needs to be looked into, also by the help of additional field surveys building on our existing observations.

Non-catastrophic slope failures with very slow rates of movement have much less potential to release significant amounts of sediment into the river system in a short period of time, as is the case with deposits from catastrophic failures. However, DSGSD-type hillslope deformation processes are expected to have a significant impact on the long-term denudation and evolution of mountain ranges through the reduction of relief and the gradual weakening of the affected rock masses (see, Agliardi et al., 2013). This is a topic that has hardly been studied worldwide and has been overlooked so far for the partially non-glacially shaped Himalayas. In our study, we found evidence that progressive hillslope weakening processes, including DSGSDs, are at work over long time-scales, impacting sediment fluxes from hillslopes (see Section 2.8.3). Further research into these processes is therefore important to better understand the evolution of landscapes in the Himalayas, and globally. This research focus should therefore receive more attention from researchers in the future.

## 2.10 Conclusion

We investigated both giant rock avalanches in the upper Marsyangdi Valley and DSGSDs on the south-facing Annapurna slopes.

For the giant rock avalanches, we provide new age constraints on their timing using cosmogenic nuclides (10Be and 36Cl) and 14C carbon dating, as well as new volume estimates that significantly extend the existing record in the region. We found evidence for multi-failure history at Pisang Bowl and a not yet recognised deposit at Manang, which has to be explored further. The Tilicho Lake rock avalanche deposit is a completely new entry to the record with a very large deposit volume and Early Holocene age. Large-scale tectonic structures and bedding planes serve as Precondition Factors of the giant rock avalanches. From the distribution of ages obtained we argue that warm and wet phases of intensified monsoon (EHCO and MWP) enhance climatically forced Preparatory Factors. Higher precipitation amounts and warmer climate result in progressive destabilisation of slopes, most likely due to an increase in pore pressure and an intensification of deep-weathering processes. Possible reasons for the delayed response of slope failure to onset of climatic warm and wet phases needs to be explored further. The rock avalanche at Tilicho Lake dates back to the beginning of the Holocene, supposedly a time of glacial retreat in the area. Therefore deglaciation can be considered as another important Preparatory Factor of giant rock avalanches responsive to climate forcing in the Annapurna Massif.

Paleo-movement reconstructions on DSGSD scars on the Annapurna south-face, by two cosmogenic nuclide profiles and a trench, revealed that discrete fractures occurred throughout the Holocene. Further, an increased phase of DSGSD activity (4.5 – 7.3 BP) on the main ridge and a secondary ridge can best be explained by warmer and wetter climatic conditions during the EHCO. It is possible that a progressive weakening of the slope since the beginning of the EHCO, similar to the giant rock avalanches, may have led to the greater DSGSD activity at the end of that climatic phase. Alternatively, a mechanical explanation for the variable movement rates observed would also be conceivable. The Phalo Danda DSGSD has been presumably active for a long time (130 - 225 ka BP) and the progressive failure of slope instabilities of this type may eventually lead to the failed rock masses observed on adjacent hillslopes.

Our research on two phenomena of slope failure, which either occur with very low frequency or involve very low-mass displacement over time, have only marginal significance for hazards and risks in the central Himalayas. However, these may increase due to climate change. Our extension of the giant rock avalanche record means that higher sediment fluxes from the upper Marsyangdi Valley must be expected than previously assumed. The extreme effective erosion of the Humde deposits raises questions about the erosion processes at work, which should be investigated. Our new findings on the Annapurna south-face provide new insights but also raise questions about DSGSD contribution to mountain denudation.

# References:


Aaron, J., McDougall, S., Kowalski, J., Mitchell, A., Nolde, N., 2022. Probabilistic prediction of rock avalanche runout using a numerical model. Landslides 19, 2853–2869. https://doi.org/10.1007/s10346-022-01939-y

Agliardi, F., Crosta, G.B., Frattini, P., 2012. Slow rock-slope deformation, in: Clague, J.J., Stead, D. (Eds.), Landslides. Cambridge University Press, Cambridge, pp. 207–221. https://doi.org/10.1017/CBO9780511740367.019

Agliardi, F., Crosta, G.B., Frattini, P., Malusà, M.G., 2013. Giant non-catastrophic landslides and the long-term exhumation of the European Alps. Earth and Planetary Science Letters 365, 263–274. https://doi.org/10.1016/j.epsl.2013.01.030

Ambrosi, C., Strozzi, T., Scapozza, C., Wegmüller, U., 2018. Landslide hazard assessment in the Himalayas (Nepal and Bhutan) based on Earth-Observation data. Engineering Geology 237, 217–228. https://doi.org/10.1016/j.enggeo.2018.02.020

Andermann, C., Bonnet, S., Crave, A., Davy, P., Longuevergne, L., Gloaguen, R., 2012. Sediment transfer and the hydrological cycle of Himalayan rivers in Nepal. Comptes Rendus Geoscience, Erosion–Alteration: from fundamental mechanisms to geodynamic consequences (Ebelmen's Symposium) 344, 627–635. https://doi.org/10.1016/j.crte.2012.10.009

Andermann, C., Bonnet, S., Gloaguen, R., 2011. Evaluation of precipitation data sets along the Himalayan front. Geochemistry, Geophysics, Geosystems 12. https://doi.org/10.1029/2011GC003513

Arnold, M., Merchel, S., Bourlès, D.L., Braucher, R., Benedetti, L., Finkel, R.C., Aumaître, G., Gottdang, A., Klein, M., 2010. The French accelerator mass spectrometry facility ASTER: Improved performance and developments. Nuclear Instruments and Methods in Physics Research Section B: Beam Interactions with Materials and Atoms 268, 1954–1959. https://doi.org/10.1016/j.nimb.2010.02.107

Arora, S., Malik, J.N., 2017. Overestimation of the earthquake hazard along the Himalaya: constraints in bracketing of medieval earthquakes from paleoseismic studies. Geosci. Lett. 4, 19. https://doi.org/10.1186/s40562-017-0083-6

Avouac, J.-P., Meng, L., Wei, S., Wang, T., Ampuero, J.-P., 2015. Lower edge of locked Main Himalayan Thrust unzipped by the 2015 Gorkha earthquake. Nature Geosci 8, 708–711. https://doi.org/10.1038/ngeo2518

Balco, G., Stone, J.O., Lifton, N.A., Dunai, T.J., 2008. A complete and easily accessible means of calculating surface exposure ages or erosion rates from 10Be and 26Al measurements. Quaternary Geochronology, Prospects for the New Frontiers of earth and Environmental Sciences 3, 174–195. https://doi.org/10.1016/j.quageo.2007.12.001

Barnard, P.L., Owen, L.A., Finkel, R.C., Asahi, K., 2006. Landscape response to deglaciation in a high relief, monsoon-influenced alpine environment, Langtang Himal, Nepal. Quaternary Science Reviews 25, 2162–2176. https://doi.org/10.1016/j.quascirev.2006.02.002

Bekaert, D.P.S., Handwerger, A.L., Agram, P., Kirschbaum, D.B., 2020. InSAR-based detection method for mapping and monitoring slow-moving landslides in remote regions with steep and mountainous terrain: An application to Nepal. Remote Sensing of Environment 249, 111983. https://doi.org/10.1016/j.rse.2020.111983

Bell, R., Fort, M., Götz, J., Bernsteiner, H., Andermann, C., Etzlstorfer, J., Posch, E., Gurung, N., Gurung, S., 2021. Major geomorphic events and natural hazards during monsoonal precipitation 2018 in the Kali Gandaki Valley, Nepal Himalaya. Geomorphology 372, 107451. https://doi.org/10.1016/j.geomorph.2020.107451

Benedetti, L., Manighetti, I., Gaudemer, Y., Finkel, R., Malavieille, J., Pou, K., Arnold, M., Aumaître, G., Bourlès, D., Keddadouche, K., 2013. Earthquake synchrony and clustering on Fucino faults (Central Italy) as revealed from in situ 36Cl exposure dating. Journal of Geophysical Research: Solid Earth 118, 4948–4974. https://doi.org/10.1002/jgrb.50299

Beyer, R.A., Alexandrov, O., McMichael, S., 2018. The Ames Stereo Pipeline: NASA's Open Source Software for Deriving and Processing Terrain Data. Earth and Space Science 5, 537–548. https://doi.org/10.1029/2018EA000409

Bilham, R., 2019. Himalayan earthquakes: a review of historical seismicity and early 21st century slip potential. Geological Society, London, Special Publications 483, 423–482. https://doi.org/10.1144/SP483.16

Blondeau, S., Gunnell, Y., Jarman, D., 2021. Rock slope failure in the Western Alps: A first comprehensive inventory and spatial analysis. Geomorphology 380, 107622. https://doi.org/10.1016/j.geomorph.2021.107622

Blythe, A.E., Burbank, D.W., Carter, A., Schmidt, K., Putkonen, J., 2007. Plio-Quaternary exhumation history of the central Nepalese Himalaya: 1. Apatite and zircon fission track and apatite [U-Th]/He analyses. Tectonics 26. https://doi.org/10.1029/2006TC001990

Bollinger, L., Sapkota, S.N., Tapponnier, P., Klinger, Y., Rizza, M., Van der Woerd, J., Tiwari, D.R., Pandey, R., Bitri, A., Bes de Berc, S., 2014. Estimating the return times of great Himalayan earthquakes in eastern Nepal: Evidence from the Patu and Bardibas strands of the Main Frontal Thrust. Journal of Geophysical Research: Solid Earth 119, 7123–7163. https://doi.org/10.1002/2014JB010970

Bollinger, L., Tapponnier, P., Sapkota, S.N., Klinger, Y., 2016. Slip deficit in central Nepal: omen for a repeat of the 1344 AD earthquake? Earth Planets Space 68, 12. https://doi.org/10.1186/s40623-016-0389-1

Bookhagen, B., Burbank, D.W., 2006. Topography, relief, and TRMM-derived rainfall variations along the Himalaya. Geophysical Research Letters 33. https://doi.org/10.1029/2006GL026037

Bookhagen, B., Thiede, R.C., Strecker, M.R., 2005. Late Quaternary intensified monsoon phases control landscape evolution in the northwest Himalaya. Geology 33, 149–152. https://doi.org/10.1130/G20982.1

Bordet, P., Colchen, M., Le Fort, P., 1975. Recherches géologiques dans l'Himalaya du Népal, région du Nyi-Shang. Éditions du CNRS.

Bordet, P., Colchen, M., Le Fort, P., 1971. Esquisse géologique (geological sketch map) du Nyi-Shang (Népal central). Cent. Natl. Rech. Sci 1.

Brantut, N., Heap, M.J., Meredith, P.G., Baud, P., 2013. Time-dependent cracking and brittle creep in crustal rocks: A review. Journal of Structural Geology 52, 17–43. https://doi.org/10.1016/j.jsg.2013.03.007

Braucher, R., Guillou, V., Bourlès, D.L., Arnold, M., Aumaître, G., Keddadouche, K., Nottoli, E., 2015. Preparation of ASTER in-house 10Be/9Be standard solutions. Nuclear Instruments and Methods in Physics Research Section B: Beam Interactions with Materials and Atoms, The Thirteenth Accelerator Mass Spectrometry Conference 361, 335–340. https://doi.org/10.1016/j.nimb.2015.06.012

Brideau, M.-A., Yan, M., Stead, D., 2009. The role of tectonic damage and brittle rock fracture in the development of large rock slope failures. Geomorphology 103, 30–49. https://doi.org/10.1016/j.geomorph.2008.04.010

Bronk Ramsey, C., 2021. OxCal v. 4.4 https://c14. arch. ox. ac. uk/oxcal. OxCal. html.

Bungum, H., Lindholm, C.D., Mahajan, A.K., 2017. Earthquake recurrence in NW and central Himalaya. Journal of Asian Earth Sciences 138, 25–37. https://doi.org/10.1016/j.jseaes.2017.01.034

Burbank, D.W., Blythe, A.E., Putkonen, J., Pratt-Sitaula, B., Gabet, E., Oskin, M., Barros, A., Ojha, T.P., 2003. Decoupling of erosion and precipitation in the Himalayas. Nature 426, 652–655. https://doi.org/10.1038/nature02187

Burbank, D.W., Bookhagen, B., Gabet, E.J., Putkonen, J., 2012. Modern climate and erosion in the Himalaya. Comptes Rendus. Géoscience 344, 610–626. https://doi.org/10.1016/j.crte.2012.10.010

Chauhan, R., Thakuri, S., 2017. Periglacial environment in Nepal Himalaya: Present contexts and future prospects. Nep Jnl Environ Sci 5, 35–40. https://doi.org/10.3126/njes.v5i0.22713

Chen, Y., Zong, Y., Li, B., Li, S., Aitchison, J.C., 2013. Shrinking lakes in Tibet linked to the weakening Asian monsoon in the past 8.2 ka. Quat. res. 80, 189–198. https://doi.org/10.1016/j.yqres.2013.06.008

Chigira, M., Tsou, C.-Y., Higaki, D., Amatya, S.C., 2022. A series of rockslides and gravitational slope deformations aligned along the Kali Gandaki across the Nepal Himalaya. Geomorphology 400, 108098. https://doi.org/10.1016/j.geomorph.2021.108098

Christl, M., Vockenhuber, C., Kubik, P.W., Wacker, L., Lachner, J., Alfimov, V., Synal, H.-A., 2013. The ETH Zurich AMS facilities: Performance parameters and reference materials. Nuclear Instruments and Methods in Physics Research Section B: Beam Interactions with Materials and Atoms, Proceedings of the Twelfth International Conference on Accelerator Mass Spectrometry, Wellington, New Zealand, 20-25 March 2011 294, 29–38. https://doi.org/10.1016/j.nimb.2012.03.004

Coeurdevey, L., Fernandez, K., 2012. Pléiades Imagery – User Guide.

Colchen, M., Le Fort, P., Pêcher, A., 1986. Annapurna–Manaslu–Ganesh Himal. Centre National de la Recherche Scientifique, Paris 75–136.

Cook, K.L., Andermann, C., Gimbert, F., Adhikari, B.R., Hovius, N., 2018. Glacial lake outburst floods as drivers of fluvial erosion in the Himalaya. Science 362, 53–57. https://doi.org/10.1126/science.aat4981

Cook, S.J., Swift, D.A., 2012. Subglacial basins: Their origin and importance in glacial systems and landscapes. Earth-Science Reviews 115, 332–372. https://doi.org/10.1016/j.earscirev.2012.09.009

Copernicus, 2019. Copernicus Digital Elevation Model GLO-30.

Crosta, G.B., Frattini, P., Agliardi, F., 2013. Deep seated gravitational slope deformations in the European Alps. Tectonophysics 605, 13–33. https://doi.org/10.1016/j.tecto.2013.04.028

Cruden, D., Hu, X.Q., 1996. Hazardous Modes of Rock Slope Movement in the Canadian Rockies. Environmental and Engineering Geoscience 2, 507–516. https://doi.org/10.2113/gseegeosci.II.4.507

Cui, S., Wu, H., Pei, X., Yang, Q., Huang, R., Guo, B., 2022. Characterizing the spatial distribution, frequency, geomorphological and geological controls on landslides triggered by the 1933 Mw 7.3 Diexi Earthquake, Sichuan, China. Geomorphology 403, 108177. https://doi.org/10.1016/j.geomorph.2022.108177

Dahal, R.K., Hasegawa, S., 2008. Representative rainfall thresholds for landslides in the Nepal Himalaya. Geomorphology 100, 429–443. https://doi.org/10.1016/j.geomorph.2008.01.014

Dawadi, B., Sharma, S., Reynard, E., Shahi, K., 2023. Climatology, Variability, and Trend of the Winter Precipitation over Nepal. Earth Syst Environ 7, 381–391. https://doi.org/10.1007/s41748-023-00338-0

Devkota, K.C., Regmi, A.D., Pourghasemi, H.R., Yoshida, K., Pradhan, B., Ryu, I.C., Dhital, M.R., Althuwaynee, O.F., 2013. Landslide susceptibility mapping using certainty factor, index of entropy and logistic regression models in GIS and their comparison at Mugling–Narayanghat road section in Nepal Himalaya. Nat Hazards 65, 135–165. https://doi.org/10.1007/s11069-012-0347-6

Dimri, A.P., Bookhagen, B., Stoffel, M., Yasunari, T. (Eds.), 2020. Himalayan Weather and Climate and their Impact on the Environment. Springer International Publishing, Cham. https://doi.org/10.1007/978-3-030-29684-1

Dimri, A.P., Chevuturi, A., Niyogi, D., Thayyen, R.J., Ray, K., Tripathi, S.N., Pandey, A.K., Mohanty, U.C., 2017. Cloudbursts in Indian Himalayas: A review. Earth-Science Reviews 168, 1–23. https://doi.org/10.1016/j.earscirev.2017.03.006

Dini, B., Aaron, J., Manconi, A., De Palezieux, L., Leith, K., Loew, S., 2020. Regional-Scale Investigation of Preconditioning Factors of Rock Slope Instabilities in NW Bhutan. Journal of Geophysical Research: Earth Surface 125, e2019JF005404. https://doi.org/10.1029/2019JF005404

Dini, B., Manconi, A., Loew, S., 2019. Investigation of slope instabilities in NW Bhutan as derived from systematic DInSAR analyses. Engineering Geology 259, 105111. https://doi.org/10.1016/j.enggeo.2019.04.008

Discenza, M.E., Esposito, C., 2021. State-of-art and remarks on some open questions about dsgsds: hints from a review of the scientific literature on related topics. Italian journal of engineering geology and environment 31–59. https://doi.org/10.4408/IJEGE.2021-01.O-03

Ditchburn, R.G., Whitehead, N.E., 1994. The separation of 10Be from silicates. Presented at the Proceedings of the 3rd workshop of the South Pacific Environmental Radioactivity Association (SPERA) Extended abstracts, Australia, p. 103.

Dortch, J.M., Owen, L.A., Haneberg, W.C., Caffee, M.W., Dietsch, C., Kamp, U., 2009. Nature and timing of large landslides in the Himalaya and Transhimalaya of northern India. Quaternary Science Reviews 28, 1037–1054. https://doi.org/10.1016/j.quascirev.2008.05.002

Dumoulin, J.-P., Comby-Zerbino, C., Delqué-Količ, E., Moreau, C., Caffy, I., Hain, S., Perron, M., Thellier, B., Setti, V., Berthier, B., Beck, L., 2017. Status Report on Sample Preparation Protocols Developed at the LMC14 Laboratory, Saclay, France: From Sample Collection to 14C AMS Measurement. Radiocarbon 59, 713–726. https://doi.org/10.1017/RDC.2016.116

Dunai, T.J., 2010. Cosmogenic nuclides: principles, concepts and applications in the earth surface sciences. Cambridge University Press.

Dutt, S., Gupta, A.K., Clemens, S.C., Cheng, H., Singh, R.K., Kathayat, G., Edwards, R.L., 2015. Abrupt changes in Indian summer monsoon strength during 33,800 to 5500 years B.P. Geophysical Research Letters 42, 5526–5532. https://doi.org/10.1002/2015GL064015

Eberhardt, E., 2022. Influence of Transient Pore Pressures on the Progressive Failure of Rock Slopes. Presented at the PRF 2022, GSA Penrose Conference.

Elango, L., Kannan, R., 2007. Chapter 11 Rock–water interaction and its control on chemical composition of groundwater, in: Developments in Environmental Science. Elsevier, pp. 229–243. https://doi.org/10.1016/S1474-8177(07)05011-5

Elliott, J.R., Jolivet, R., González, P.J., Avouac, J.-P., Hollingsworth, J., Searle, M.P., Stevens, V.L., 2016. Himalayan megathrust geometry and relation to topography revealed by the Gorkha earthquake. Nature Geosci 9, 174–180. https://doi.org/10.1038/ngeo2623

ESRI, 2023. ArcGIS Pro, Version 3.2.1. Redlands, CA: Environmental Systems Research Institute.

Evans, C., Pettigrew, J., Tamu, Y.K., Turin, M., 2009. Grounded knowledge/walking land: Archeological research and ethno-historical identity in central Nepal.

Evans, S.G., Hermanns, R.L., Strom, A., Scarascia-Mugnozza, G. (Eds.), 2011. Natural and Artificial Rockslide Dams, Lecture Notes in Earth Sciences. Springer Berlin Heidelberg, Berlin, Heidelberg. https://doi.org/10.1007/978-3-642-04764-0

Fleitmann, D., Burns, S.J., Mudelsee, M., Neff, U., Kramers, J., Mangini, A., Matter, A., 2003. Holocene Forcing of the Indian Monsoon Recorded in a Stalagmite from Southern Oman. Science 300, 1737–1739. https://doi.org/10.1126/science.1083130

Fort, M., 2011. Two large late Quaternary rock slope failures and their geomorphic significance, Annapurna Himalayas (Nepal). Geografia Fisica e Dinamica Quaternaria 34, 5–14.

Fort, M., 2000. Glaciers and mass wasting processes: their in#uence on the shaping of the Kali Gandaki valley (higher Himalaya of Nepal). Quaternary International.

Fort, M., 1993. Etude géomorphologique d'une chaîne de collision intracontinentale: L'himalaya central, transversale des Annapurnas.

Fort, M., Braucher, R., Bourlès, D., Guillou, V., Rimal, L.N., Gribenski, N., Cossart, E., 2014. Geomorphic impacts, age and significance of two giant landslide dams in the Nepal Himalayas: Ringmo-Phoksundo (Dolpo District) and Dhampu-Chhoya (Mustang District). Presented at the EGU General Assembly Conference Abstracts, p. 5615.

Fossen, H., 2016. Structural geology. Cambridge university press.

Gabet, E.J., Burbank, D.W., Pratt-Sitaula, B., Putkonen, J., Bookhagen, B., 2008. Modern erosion rates in the High Himalayas of Nepal. Earth and Planetary Science Letters 267, 482–494. https://doi.org/10.1016/j.epsl.2007.11.059

Gabet, E.J., Pratt-Sitaula, B.A., Burbank, D.W., 2004. Climatic controls on hillslope angle and relief in the Himalayas. Geol 32, 629. https://doi.org/10.1130/G20641.1

Gadgil, S., 2003. The Indian monsoon and its variability. Annual Review of Earth and Planetary Sciences 31, 429–467.

Gallo, F., Lavé, J., 2014. Evolution of a large landslide in the High Himalaya of central Nepal during the last half-century. Geomorphology 223, 20–32. https://doi.org/10.1016/j.geomorph.2014.06.021

Gasse, F., Fontes, J.Ch., Van Campo, E., Wei, K., 1996. Holocene environmental changes in Bangong Co basin (Western Tibet). Part 4: Discussion and conclusions. Palaeogeography, Palaeoclimatology, Palaeoecology, Environmental Changes in the Tibetan Plateau and Surrounding Areas 120, 79–92. https://doi.org/10.1016/0031-0182(95)00035-6

Ghazoui, Z., Bertrand, S., Vanneste, K., Yokoyama, Y., Nomade, J., Gajurel, A.P., van der Beek, P.A., 2019. Potentially large post-1505 AD earthquakes in western Nepal revealed by a lake sediment record. Nat Commun 10, 2258. https://doi.org/10.1038/s41467-019-10093-4

Glade, T., Crozier, M.J., 2005. The Nature of Landslide Hazard Impact, in: Landslide Hazard and Risk. John Wiley & Sons, Ltd, pp. 41–74. https://doi.org/10.1002/9780470012659.ch2

Glastonbury, J., Fell, R., 2010. Geotechnical characteristics of large rapid rock slides. Can. Geotech. J. 47, 116–132. https://doi.org/10.1139/T09-080

Gnyawali, K., Dahal, K., Talchabhadel, R., Nirandjan, S., 2023. Framework for rainfall-triggered landslide-prone critical infrastructure zonation. Science of The Total Environment 872, 162242. https://doi.org/10.1016/j.scitotenv.2023.162242

Gnyawali, K.R., Zhang, Y., Wang, G., Miao, L., Pradhan, A.M.S., Adhikari, B.R., Xiao, L., 2020. Mapping the susceptibility of rainfall and earthquake triggered landslides along China–Nepal highways. Bull Eng Geol Environ 79, 587–601. https://doi.org/10.1007/s10064-019-01583-2

Godard, V., Burbank, D.W., Bourlès, D.L., Bookhagen, B., Braucher, R., Fisher, G.B., 2012. Impact of glacial erosion on 10Be concentrations in fluvial sediments of the Marsyandi catchment, central Nepal. Journal of Geophysical Research: Earth Surface 117. https://doi.org/10.1029/2011JF002230

Godin, L., 2003. Structural evolution of the Tethyan sedimentary sequence in the Annapurna area, central Nepal Himalaya. Journal of Asian Earth Sciences 22, 307–328. https://doi.org/10.1016/S1367-9120(03)00066-X

Google Earth, n.d. Satellite Imagery for central Nepal, from Google Earth Version 7.3.

Gruber, S., 2012. Derivation and analysis of a high-resolution estimate of global permafrost zonation. The Cryosphere 6, 221–233. https://doi.org/10.5194/tc-6-221-2012

Gurung, N., Haneberg, W.C., Ramana, G.V., Datta, M., 2011. Engineering Geology and Stability of the Laprak Landslide, Gorkha District, Western Nepal. Environmental and Engineering Geoscience 17, 23–38. https://doi.org/10.2113/gseegeosci.17.1.23

Guzzetti, F., Mondini, A.C., Cardinali, M., Fiorucci, F., Santangelo, M., Chang, K.-T., 2012. Landslide inventory maps: New tools for an old problem. Earth-Science Reviews 112, 42–66. https://doi.org/10.1016/j.earscirev.2012.02.001

Hagen, T., 1969. Report on the geological survey of Nepal. Denkschr. Schweiz. Naturf. Ges. 81, 185.

Hasegawa, S., Dahal, R.K., Yamanaka, M., Bhandary, N.P., Yatabe, R., Inagaki, H., 2009. Causes of large-scale landslides in the Lesser Himalaya of central Nepal. Environ Geol 57, 1423–1434. https://doi.org/10.1007/s00254-008-1420-z

Heim, A., 1932. Bergsturz und Menschenleben. Fretz & Wasmuth.

Heimsath, A.M., McGlynn, R., 2008. Quantifying periglacial erosion in the Nepal high Himalaya. Geomorphology 97, 5–23. https://doi.org/10.1016/j.geomorph.2007.02.046

Heisinger, B., Lal, D., Jull, A.J.T., Kubik, P., Ivy-Ochs, S., Knie, K., Nolte, E., 2002. Production of selected cosmogenic radionuclides by muons: 2. Capture of negative muons. Earth and Planetary Science Letters 200, 357–369. https://doi.org/10.1016/S0012-821X(02)00641-6

Heisinger, B, Lal, D., Jull, A.J.T., Kubik, P., Ivy-Ochs, S., Neumaier, S., Knie, K., Lazarev, V., Nolte, E., 2002. Production of selected cosmogenic radionuclides by muons: 1. Fast muons. Earth and Planetary Science Letters 200, 345–355. https://doi.org/10.1016/S0012-821X(02)00640-4

Herman, F., Copeland, P., Avouac, J.-P., Bollinger, L., Mahéo, G., Le Fort, P., Rai, S., Foster, D., Pêcher, A., Stüwe, K., Henry, P., 2010. Exhumation, crustal deformation, and thermal structure of the Nepal Himalaya derived from the inversion of thermochronological and thermobarometric data and modeling of the topography. Journal of Geophysical Research: Solid Earth 115. https://doi.org/10.1029/2008JB006126

Hermanns, R.L., Oppikofer, T., Dahle, H., Eiken, T., Ivy-Ochs, S., Blikra, L.H., Genevois, R., Prestininzi, A., 2013. Understanding long-term slope deformation for stability assessment of rock slopes: the case of the Oppstadhornet rockslide, Norway. Presented at the International Conference on Vajont–1963–2013, edited by: Genevois, R. and Prestininzi, A., Italian J. Eng. Geol. Environ., Book Ser, pp. 255–264.

Herzschuh, U., 2006. Palaeo-moisture evolution in monsoonal Central Asia during the last 50,000 years. Quaternary Science Reviews 25, 163–178. https://doi.org/10.1016/j.quascirev.2005.02.006

Heuberger, H., 1986. Der Bergsturz von Khumdschung, Mount-Everest-Gebiet, Nepal. Material und Technik 3, 175–181.

Heuberger, H., Masch, L., Preuss, E., Schrocker, A., 1984. Quaternary Landslides and Rock Fusion in Central Nepal and in the Tyrolean Alps. Mountain Research and Development 4, 345. https://doi.org/10.2307/3673238

Hewitt, K., 2002. Styles of rock-avalanche depositional complexes conditioned by very rugged terrain, Karakoram Himalaya, Pakistan, in: Reviews in Engineering Geology. Geological Society of America, pp. 345–377. https://doi.org/10.1130/REG15-p345

Hewitt, K., Clague, J.J., Orwin, J.F., 2008. Legacies of catastrophic rock slope failures in mountain landscapes. Earth-Science Reviews 87, 1–38. https://doi.org/10.1016/j.earscirev.2007.10.002

Hippolyte, J.-C., Bourlès, D., Braucher, R., Carcaillet, J., Léanni, L., Arnold, M., Aumaitre, G., 2009. Cosmogenic 10Be dating of a sackung and its faulted rock glaciers, in the Alps of Savoy (France). Geomorphology 108, 312–320. https://doi.org/10.1016/j.geomorph.2009.02.024

Hou, J., D'Andrea, W.J., Wang, M., He, Y., Liang, J., 2017. Influence of the Indian monsoon and the subtropical jet on climate change on the Tibetan Plateau since the late Pleistocene. Quaternary Science Reviews 163, 84–94. https://doi.org/10.1016/j.quascirev.2017.03.013

Hurtado, J.M., Jr, Hodges, K.V., Whipple, K.X., 2001. Neotectonics of the Thakkhola graben and implications for recent activity on the South Tibetan fault system in the central Nepal Himalaya. GSA Bulletin 113, 222–240. https://doi.org/10.1130/0016-7606(2001)113<0222:NOTTGA>2.0.CO;2

Ivy-Ochs, S., Kober, F., 2008. Surface exposure dating with cosmogenic nuclides. Quaternary Science Journal 57, 179–209.

Ivy-Ochs, S., Martin, S., Campedel, P., Hippe, K., Alfimov, V., Vockenhuber, C., Andreotti, E., Carugati, G., Pasqual, D., Rigo, M., Viganò, A., 2017. Geomorphology and age of the Marocche di Dro rock avalanches (Trentino, Italy). Quaternary Science Reviews 169, 188–205. https://doi.org/10.1016/j.quascirev.2017.05.014

Jaboyedoff, M., Penna, I., Pedrazzini, A., Baroň, I., Crosta, G.B., 2013. An introductory review on gravitational-deformation induced structures, fabrics and modeling. Tectonophysics 605, 1–12. https://doi.org/10.1016/j.tecto.2013.06.027

Jaeger, J.C., Cook, N.G.W., Zimmerman, R.W., 2007. Fundamentals of rock mechanics, 4th ed. ed. Blackwell Pub, Malden, MA.

Jones, J.N., Boulton, S.J., Stokes, M., Bennett, G.L., Whitworth, M.R.Z., 2021. 30-year record of Himalaya mass-wasting reveals landscape perturbations by extreme events. Nat Commun 12, 6701. https://doi.org/10.1038/s41467-021-26964-8

Jones, J.N., Stokes, M., Boulton, S.J., Bennett, G.L., Whitworth, M.R.Z., 2020. Coseismic and monsoon-triggered landslide impacts on remote trekking infrastructure, Langtang Valley, Nepal. QJEGH 53, 159–166. https://doi.org/10.1144/qjegh2019-048

Kargel, J.S., Leonard, G.J., Shugar, D.H., Haritashya, U.K., Bevington, A., Fielding, E.J., Fujita, K., Geertsema, M., Miles, E.S., Steiner, J., Anderson, E., Bajracharya, S., Bawden, G.W., Breashears, D.F., Byers, A., Collins, B., Dhital, M.R., Donnellan, A., Evans, T.L., Geai, M.L., Glasscoe, M.T., Green, D., Gurung, D.R., Heijenk, R., Hilborn, A., Hudnut, K., Huyck, C., Immerzeel, W.W., Liming, J., Jibson, R., Kääb, A., Khanal, N.R., Kirschbaum, D., Kraaijenbrink, P.D.A., Lamsal, D., Shiyin, L., Mingyang, L., McKinney, D., Nahirnick, N.K., Zhuotong, N., Ojha, S., Olsenholler, J., Painter, T.H., Pleasants, M., Pratima, K.C., Yuan, Q.I., Raup, B.H., Regmi, D., Rounce, D.R., Sakai, A., Donghui, S., Shea, J.M., Shrestha, A.B., Shukla, A., Stumm, D., van der Kooij, M., Voss, K., Xin, W., Weihs, B., Wolfe, D., Lizong, W., Xiaojun, Y., Yoder, M.R., Young, N., 2016. Geomorphic and geologic controls of geohazards induced by Nepal's 2015 Gorkha earthquake. Science 351, aac8353. https://doi.org/10.1126/science.aac8353

KC, R., Sharma, K., Dahal, B.K., Aryal, M., Subedi, M., 2024. Study of the spatial distribution and the temporal trend of landslide disasters that occurred in the Nepal Himalayas from 2011 to 2020. Environmental Earth Sciences 83, 42.

Keefer, D.K., 1994. The importance of earthquake-induced landslides to long-term slope erosion and slope-failure hazards in seismically active regions. Geomorphology 10, 265–284. https://doi.org/10.1016/0169-555X(94)90021-3

Kohl, C.P., Nishiizumi, K., 1992. Chemical isolation of quartz for measurement of in-situ -produced cosmogenic nuclides. Geochimica et Cosmochimica Acta 56, 3583–3587. https://doi.org/10.1016/0016-7037(92)90401-4

Korup, O., Clague, J.J., Hermanns, R.L., Hewitt, K., Strom, A.L., Weidinger, J.T., 2007. Giant landslides, topography, and erosion. Earth and Planetary Science Letters 12.

Korup, O., Strom, A.L., Weidinger, J.T., 2006. Fluvial response to large rock-slope failures: Examples from the Himalayas, the Tien Shan, and the Southern Alps in New Zealand. Geomorphology, Mountain Rivers Part I: Watershed Scale Processes and Channel Morphology 78, 3–21. https://doi.org/10.1016/j.geomorph.2006.01.020

Kremer, K., Simpson, G., Girardclos, S., 2012. Giant Lake Geneva tsunami in AD 563. Nature Geosci 5, 756–757. https://doi.org/10.1038/ngeo1618

Kummerow, C., Barnes, W., Kozu, T., Shiue, J., Simpson, J., 1998. The Tropical Rainfall Measuring Mission (TRMM) Sensor Package. Journal of Atmospheric and Oceanic Technology 15, 809–817. https://doi.org/10.1175/1520-0426(1998)015<0809:TTRMMT>2.0.CO;2

Lacroix, P., Gavillon, T., Bouchant, C., Lavé, J., Mugnier, J.-L., Dhungel, S., Vernier, F., 2022. SAR and optical images correlation illuminates post-seismic landslide motion after the Mw 7.8 Gorkha earthquake (Nepal). Sci Rep 12, 6266. https://doi.org/10.1038/s41598-022-10016-2

Lacroix, P., Handwerger, A.L., Bièvre, G., 2020. Life and death of slow-moving landslides. Nat Rev Earth Environ 1, 404–419. https://doi.org/10.1038/s43017-020-0072-8

Lal, D., 1991. The present scope of the field of terrestrial cosmogenic nuclides. Current Science 61, 744–751.

Lavé, J., Avouac, J.P., 2001. Fluvial incision and tectonic uplift across the Himalayas of central Nepal. Journal of Geophysical Research: Solid Earth 106, 26561–26591. https://doi.org/10.1029/2001JB000359

Lavé, J., Gallo, F., Lanord, C.F., Morin, G., Gajurel, A., 2019. Landslide dynamics and debris export in the central Himalaya, as documented by a multi-methods approach. Presented at the Geophysical Research Abstracts.

Lavé, J., Guérin, C., Valla, P.G., Guillou, V., Rigaudier, T., Benedetti, L., France-Lanord, C., Gajurel, A.P., Morin, G., Dumoulin, J.P., Moreau, C., Galy, V., 2023. Medieval demise of a Himalayan giant summit induced by mega-landslide. Nature 619, 94–101. https://doi.org/10.1038/s41586-023-06040-5

Lavé, J., Yule, D., Sapkota, S., Basant, K., Madden, C., Attal, M., Pandey, R., 2005. Evidence for a great medieval earthquake (~ 1100 AD) in the central Himalayas, Nepal. Science 307, 1302–1305.

Le Roux, O., Schwartz, S., Gamond, J.F., Jongmans, D., Bourles, D., Braucher, R., Mahaney, W., Carcaillet, J., Leanni, L., 2009. CRE dating on the head scarp of a major landslide (Séchilienne, French Alps), age constraints on Holocene kinematics. Earth and Planetary Science Letters 280, 236–245. https://doi.org/10.1016/j.epsl.2009.01.034

Lifton, N., 2016. Implications of two Holocene time-dependent geomagnetic models for cosmogenic nuclide production rate scaling. Earth and Planetary Science Letters 433, 257–268. https://doi.org/10.1016/j.epsl.2015.11.006

Liu, X.-J., Lai, Z.-P., Zeng, F.-M., Madsen, D.B., E, C.-Y., 2013. Holocene lake level variations on the Qinghai-Tibetan Plateau. Int J Earth Sci (Geol Rundsch) 102, 2007–2016. https://doi.org/10.1007/s00531-013-0896-2

Livio, F.A., Zerboni, A., Ferrario, M.F., Mariani, G.S., Martinelli, E., Amit, R., 2022. Triggering processes of deep-seated gravitational slope deformation (DSGSD) in an un-glaciated area of the Cavargna Valley (Central Southern Alps) during the Middle Holocene. Landslides 19, 1825–1841. https://doi.org/10.1007/s10346-022-01892-w

Lovell, A.M., Carr, J.R., Stokes, C.R., 2019. Spatially Variable Glacier Changes in the Annapurna Conservation Area, Nepal, 2000 to 2016. Remote Sensing 11, 1452. https://doi.org/10.3390/rs11121452

Lupker, M., Blard, P.-H., Lavé, J., France-Lanord, C., Leanni, L., Puchol, N., Charreau, J., Bourlès, D., 2012. 10Be-derived Himalayan denudation rates and sediment budgets in the Ganga basin. Earth and Planetary Science Letters 333–334, 146–156. https://doi.org/10.1016/j.epsl.2012.04.020

Mann, M.E., Zhang, Z., Rutherford, S., Bradley, R.S., Hughes, M.K., Shindell, D., Ammann, C., Faluvegi, G., Ni, F., 2009. Global Signatures and Dynamical Origins of the Little Ice Age and Medieval Climate Anomaly. Science 326, 1256–1260. https://doi.org/10.1126/science.1177303

Marc, O., Behling, R., Andermann, C., Turowski, J.M., Illien, L., Roessner, S., Hovius, N., 2019. Long-term erosion of the Nepal Himalayas by bedrock landsliding: the role of monsoons, earthquakes and giant landslides. Earth Surface Dynamics 7, 107–128. https://doi.org/10.5194/esurf-7-107-2019

Marc, O., Gnyawali, K., Schwanghart, W., Fort, M., 2023. Landsliding in the Himalaya, in: Himalaya, Dynamics of a Giant 3. pp. 95–129. https://doi.org/10.1002/9781394228683.ch4

Marrero, S.M., Phillips, F.M., Caffee, M.W., Gosse, J.C., 2016. CRONUS-Earth cosmogenic 36Cl calibration. Quaternary Geochronology 31, 199–219. https://doi.org/10.1016/j.quageo.2015.10.002

Martin, L.C.P., Blard, P.-H., Balco, G., Lavé, J., Delunel, R., Lifton, N., Laurent, V., 2017. The CREp program and the ICE-D production rate calibration database: A fully parameterizable and updated online tool to compute cosmic-ray exposure ages. Quaternary Geochronology 38, 25–49. https://doi.org/10.1016/j.quageo.2016.11.006

Masarik, J., 2002. Numerical simulation of in-situ production of cosmogenic nuclides. Geochim. Cosmochim. Acta 66, A491.

Masch, L., Wenk, H.R., Preuss, E., 1985. Electron microscopy study of hyalomylonites—evidence for frictional melting in landslides. Tectonophysics 115, 131–160. https://doi.org/10.1016/0040-1951(85)90103-9

MATLAB, 2023. The MathWorks Inc.

McAdoo, B.G., Quak, M., Gnyawali, K.R., Adhikari, B.R., Devkota, S., Rajbhandari, P.L., Sudmeier-Rieux, K., 2018. Roads and landslides in Nepal: how development affects environmental risk. Natural Hazards and Earth System Sciences 18, 3203–3210. https://doi.org/10.5194/nhess-18-3203-2018

McCalpin, J.P., 2009. Chapter 2A Field Techniques in Paleoseismology—Terrestrial Environments, in: International Geophysics, Paleoseismology. Academic Press, pp. 29–118. https://doi.org/10.1016/S0074-6142(09)95002-1

McColl, S.T., 2015. Landslide Causes and Triggers, in: Landslide Hazards, Risks, and Disasters. Elsevier, pp. 17–42. https://doi.org/10.1016/B978-0-12-396452-6.00002-1

Mehrotra, N., Basavaiah, N., Shah, S.K., 2023. Revisit the Medieval Warm Period and Little Ice Age in Proxy Records from Zemu Glacier Sediments, Eastern Himalaya: Vegetation and Climate Reconstruction. Quaternary 6, 32. https://doi.org/10.3390/quat6020032

Meteoblue, 2024. Simulated historical climate & weather data for Dhikur Pokhari, accessed Jan 26, 2024 [WWW Document]. meteoblue.com. URL https://www.meteoblue.com/en/weather/historyclimate/climatemodelled/dhikur-pokhari_nepal_7969496 (accessed 1.26.24).

Mook, W.G., van der Plicht, J., 1999. Reporting 14C Activities and Concentrations. Radiocarbon 41, 227–239. https://doi.org/10.1017/S0033822200057106

Moore, A.K., Granger, D.E., 2019. Calibration of the production rate of cosmogenic 36Cl from Fe. Quaternary Geochronology 51, 87–98. https://doi.org/10.1016/j.quageo.2019.02.002

Moreau, C., Caffy, I., Comby, C., Delqué-Količ, E., Dumoulin, J.-P., Hain, S., Quiles, A., Setti, V., Souprayen, C., Thellier, B., Vincent, J., 2013. Research and Development of the Artemis 14C AMS Facility: Status Report. Radiocarbon 55, 331–337. https://doi.org/10.1017/S0033822200057441

Morin, G.P., Lavé, J., France-Lanord, C., Rigaudier, T., Gajurel, A.P., Sinha, R., 2018. Annual Sediment Transport Dynamics in the Narayani Basin, Central Nepal: Assessing the Impacts of Erosion Processes in the Annual Sediment Budget. Journal of Geophysical Research: Earth Surface 123, 2341–2376. https://doi.org/10.1029/2017JF004460

Nagaoka, S., 1990. The glacial landforms in the Manang Valley, north of the great Himalayas, central Nepal. Geographical Reports of Tokyo Metropolitan University 109–123.

Neal, J., Hawker, L., 2023. FABDEM V1-2. https://doi.org/10.5523/bris.s5hqmjcdj8yo2ibzi9b4ew3sn

Nicoletti, P.G., Sorriso-Valvo, M., 1991. Geomorphic controls of the shape and mobility of rock avalanches. GSA Bulletin 103, 1365–1373. https://doi.org/10.1130/0016-7606(1991)103<1365:GCOTSA>2.3.CO;2

Ollier, C.D., 2010. Very deep weathering and related landslides. EGSP 23, 5–14. https://doi.org/10.1144/EGSP23.2

Owen, L.A., Derbyshire, E., Fort, M., 1998. The Quaternary glacial history of the Himalaya. Journal of Quaternary Science 13, 91–120.

Owen, L.A., Dortch, J.M., 2014. Nature and timing of Quaternary glaciation in the Himalayan–Tibetan orogen. Quaternary Science Reviews 88, 14–54. https://doi.org/10.1016/j.quascirev.2013.11.016

Palumbo, L., Benedetti, L., Bourlès, D., Cinque, A., Finkel, R., 2004. Slip history of the Magnola fault (Apennines, Central Italy) from 36Cl surface exposure dating: evidence for strong earthquakes over the Holocene. Earth and Planetary Science Letters 225, 163–176. https://doi.org/10.1016/j.epsl.2004.06.012

Pandey, M.R., Tandukar, R.P., Avouac, J.P., Lavé, J., Massot, J.P., 1995. Interseismic strain accumulation on the Himalayan crustal ramp (Nepal). Geophysical Research Letters 22, 751–754. https://doi.org/10.1029/94GL02971

Pánek, T., 2019. Landslides and Quaternary climate changes—The state of the art. Earth-Science Reviews 196, 102871. https://doi.org/10.1016/j.earscirev.2019.05.015

Pánek, T., 2015. Recent progress in landslide dating: A global overview. Progress in Physical Geography 32.

Pánek, T., Klimeš, J., 2016. Temporal behavior of deep-seated gravitational slope deformations: A review. Earth-Science Reviews 156, 14–38. https://doi.org/10.1016/j.earscirev.2016.02.007

Parsons, A.J., Law, R.D., Searle, M.P., Phillips, R.J., Lloyd, G.E., 2016. Geology of the Dhaulagiri-Annapurna-Manaslu Himalaya, Western Region, Nepal. 1:200,000. Journal of Maps 12, 100–110. https://doi.org/10.1080/17445647.2014.984784

Patriat, P., Achache, J., 1984. India–Eurasia collision chronology has implications for crustal shortening and driving mechanism of plates. Nature 311, 615–621. https://doi.org/10.1038/311615a0

Patton, A.I., Rathburn, S.L., Capps, D.M., 2019. Landslide response to climate change in permafrost regions. Geomorphology 340, 116–128. https://doi.org/10.1016/j.geomorph.2019.04.029

Pavón-Carrasco, F.J., Osete, M.L., Torta, J.M., De Santis, A., 2014. A geomagnetic field model for the Holocene based on archaeomagnetic and lava flow data. Earth and Planetary Science Letters 388, 98–109. https://doi.org/10.1016/j.epsl.2013.11.046

Petersen, J., Wilhelm, B., Revel, M., Rolland, Y., Crouzet, C., Arnaud, F., Brisset, E., Chaumillon, E., Magand, O., 2014. Sediments of Lake Vens (SW European Alps, France) record large-magnitude earthquake events. J Paleolimnol 51, 343–355. https://doi.org/10.1007/s10933-013-9759-x

Petley, D.N., Hearn, G.J., Hart, A., Rosser, N.J., Dunning, S.A., Oven, K., Mitchell, W.A., 2007. Trends in landslide occurrence in Nepal. Nat Hazards 43, 23–44. https://doi.org/10.1007/s11069-006-9100-3

Pratt-Sitaula, B., Burbank, D.W., Heimsath, A.M., Humphrey, N.F., Oskin, M., Putkonen, J., 2011. Topographic control of asynchronous glacial advances: A case study from Annapurna, Nepal: ASYNCHRONOUS GLACIAL ADVANCES. Geophys. Res. Lett. 38, n/a-n/a. https://doi.org/10.1029/2011GL049940

Pratt-Sitaula, B., Garde, M., Burbank, D.W., Oskin, M., Heimsath, A., Gabet, E., 2007. Bedload-to-suspended load ratio and rapid bedrock incision from Himalayan landslide-dam lake record. Quaternary Research 68, 111–120. https://doi.org/10.1016/j.yqres.2007.03.005

Pratt-Sitaula, B.A., 2005. Glaciers, climate, and topography in the Nepalese Himalaya - PhD thesis. University of California, Santa Barbara.

Preisig, G., Eberhardt, E., Smithyman, M., Preh, A., Bonzanigo, L., 2016. Hydromechanical Rock Mass Fatigue in Deep-Seated Landslides Accompanying Seasonal Variations in Pore Pressures. Rock Mech Rock Eng 49, 2333–2351. https://doi.org/10.1007/s00603-016-0912-5

Putkonen, J.K., 2004. Continuous Snow and Rain Data at 500 to 4400 m Altitude near Annapurna, Nepal, 1999–2001. Arctic, Antarctic, and Alpine Research 36, 244–248. https://doi.org/10.1657/1523-0430(2004)036[0244:CSARDA]2.0.CO;2

Rangwala, I., Palazzi, E., Miller, J.R., 2020. Projected climate change in the Himalayas during the twenty-first century, in: Himalayan Weather and Climate and Their Impact on the Environment. Springer, pp. 51–71.

Raup, B., Racoviteanu, A., Khalsa, S.J.S., Helm, C., Armstrong, R., Arnaud, Y., 2007. The GLIMS geospatial glacier database: A new tool for studying glacier change. Global and Planetary Change, Climate Change Impacts on Mountain Glaciers and Permafrost 56, 101–110. https://doi.org/10.1016/j.gloplacha.2006.07.018

Reimer, P.J., Austin, W.E.N., Bard, E., Bayliss, A., Blackwell, P.G., Ramsey, C.B., Butzin, M., Cheng, H., Edwards, R.L., Friedrich, M., Grootes, P.M., Guilderson, T.P., Hajdas, I., Heaton, T.J., Hogg, A.G., Hughen, K.A., Kromer, B., Manning, S.W., Muscheler, R., Palmer, J.G., Pearson, C., Plicht, J. van der, Reimer, R.W., Richards, D.A., Scott, E.M., Southon, J.R., Turney, C.S.M., Wacker, L., Adolphi, F., Büntgen, U., Capano, M., Fahrni, S.M., Fogtmann-Schulz, A., Friedrich, R., Köhler, P., Kudsk, S., Miyake, F., Olsen, J., Reinig, F., Sakamoto, M., Sookdeo, A., Talamo, S., 2020. The IntCal20 Northern Hemisphere Radiocarbon Age Calibration Curve (0–55 cal kBP). Radiocarbon 62, 725–757. https://doi.org/10.1017/RDC.2020.41

Roback, K., Clark, M.K., West, A.J., Zekkos, D., Li, G., Gallen, S.F., Chamlagain, D., Godt, J.W., 2018. The size, distribution, and mobility of landslides caused by the 2015 Mw7.8 Gorkha earthquake, Nepal. Geomorphology 301, 121–138. https://doi.org/10.1016/j.geomorph.2017.01.030

Röthlisberger, F., Geyh, M.A., 1986. 10000 Jahre Gletschergeschichte der Erde. Sauerländer, Aarau.

Rowley, D.B., 1996. Age of initiation of collision between India and Asia: A review of stratigraphic data. Earth and Planetary Science Letters 145, 1–13. https://doi.org/10.1016/S0012-821X(96)00201-4

Roy, I., Ranhotra, P.S., Tomar, N., Shekhar, M., Agrawal, S., Bhattacharyya, A., Kumar, P., Patil, S.K., Sharma, R., 2022. Reconstruction of the late Holocene climate variability from the summer monsoon dominated Bhagirathi valley, western Himalaya. Journal of Asian Earth Sciences 227, 105080. https://doi.org/10.1016/j.jseaes.2022.105080

Ruiz-Villanueva, V., Allen, S., Arora, M., Goel, N.K., Stoffel, M., 2017. Recent catastrophic landslide lake outburst floods in the Himalayan mountain range. Progress in Physical

Geography: Earth and Environment 41, 3–28. https://doi.org/10.1177/0309133316658614

Rutqvist, J., Stephansson, O., 2003. The role of hydromechanical coupling in fractured rock engineering. Hydrogeology Journal 11, 7–40. https://doi.org/10.1007/s10040-002-0241-5

Saha, S., Owen, L.A., Orr, E.N., Caffee, M.W., 2019. High-frequency Holocene glacier fluctuations in the Himalayan-Tibetan orogen. Quaternary Science Reviews 220, 372–400. https://doi.org/10.1016/j.quascirev.2019.07.021

Salerno, F., Guyennon, N., Yang, K., Shaw, T.E., Lin, C., Colombo, N., Romano, E., Gruber, S., Bolch, T., Alessandri, A., Cristofanelli, P., Putero, D., Diolaiuti, G., Tartari, G., Verza, G., Thakuri, S., Balsamo, G., Miles, E.S., Pellicciotti, F., 2023. Local cooling and drying induced by Himalayan glaciers under global warming. Nat. Geosci. 16, 1120–1127. https://doi.org/10.1038/s41561-023-01331-y

Sapkota, S.N., Bollinger, L., Klinger, Y., Tapponnier, P., Gaudemer, Y., Tiwari, D., 2013. Primary surface ruptures of the great Himalayan earthquakes in 1934 and 1255. Nature Geosci 6, 71–76. https://doi.org/10.1038/ngeo1669

Sarkar, S., Prasad, S., Wilkes, H., Riedel, N., Stebich, M., Basavaiah, N., Sachse, D., 2015. Monsoon source shifts during the drying mid-Holocene: Biomarker isotope based evidence from the core 'monsoon zone' (CMZ) of India. Quaternary Science Reviews 123, 144–157. https://doi.org/10.1016/j.quascirev.2015.06.020

Sato, H.P., Chigira, M., Tsou, C.-Y., 2020. Measurement of landslide surface deformation along Kali Gandaki River, Nepal using time-series Sentinel-1 InSAR images. Presented at the Japan Geoscience Union.

Schelling, D., Arita, K., 1991. Thrust tectonics, crustal shortening, and the structure of the far-eastern Nepal Himalaya. Tectonics 10, 851–862. https://doi.org/10.1029/91TC01011

Schimmelpfennig, I., Benedetti, L., Garreta, V., Pik, R., Blard, P.-H., Burnard, P., Bourlès, D., Finkel, R., Ammon, K., Dunai, T., 2011. Calibration of cosmogenic 36Cl production rates from Ca and K spallation in lava flows from Mt. Etna (38°N, Italy) and Payun Matru (36°S, Argentina). Geochimica et Cosmochimica Acta 75, 2611–2632. https://doi.org/10.1016/j.gca.2011.02.013

Schimmelpfennig, I., Blard, P., Tesson, J., Zakari, M., Benedetti, L., Balco, G., Martin, L., Simon, Q., Lavé, J., 2022. The CREp 36Cl exposure age calculator: development version "dev." https://doi.org/10.31223/X5QH03

Schimmelpfennig, I., Schaefer, J.M., Putnam, A.E., Koffman, T., Benedetti, L., Ivy-Ochs, S., Team, A., Schlüchter, C., 2014. 36Cl production rate from K-spallation in the European Alps (Chironico landslide, Switzerland). Journal of Quaternary Science 29, 407–413. https://doi.org/10.1002/jqs.2720

Schlagenhauf, A., Gaudemer, Y., Benedetti, L., Manighetti, I., Palumbo, L., Schimmelpfennig, I., Finkel, R., Pou, K., 2010. Using in situ Chlorine-36 cosmonuclide to recover past earthquake histories on limestone normal fault scarps: a reappraisal of methodology and interpretations. Geophysical Journal International 182, 36–72. https://doi.org/10.1111/j.1365-246X.2010.04622.x

Schwanghart, W., Bernhardt, A., Stolle, A., Hoelzmann, P., Adhikari, B.R., Andermann, C., Tofelde, S., Merchel, S., Rugel, G., Fort, M., Korup, O., 2016. Repeated catastrophic valley infill following medieval earthquakes in the Nepal Himalaya. Science 351, 147–150. https://doi.org/10.1126/science.aac9865

Searle, M.P., Law, R.D., Godin, L., Larson, K.P., Streule, M.J., Cottle, J.M., Jessup, M.J., 2008. Defining the Himalayan Main Central Thrust in Nepal. JGS 165, 523–534. https://doi.org/10.1144/0016-76492007-081

Seguinot, J., Ivy-Ochs, S., Jouvet, G., Huss, M., Funk, M., Preusser, F., 2018. Modelling last glacial cycle ice dynamics in the Alps. The Cryosphere 12, 3265–3285. https://doi.org/10.5194/tc-12-3265-2018

Sewell, R.J., Parry, S., Millis, S.W., Wang, N., Rieser, U., DeWitt, R., 2015. Dating of debris flow fan complexes from Lantau Island, Hong Kong, China: The potential relationship between landslide activity and climate change. Geomorphology 248, 205–227. https://doi.org/10.1016/j.geomorph.2015.07.041

Shakun, J.D., Carlson, A.E., 2010. A global perspective on Last Glacial Maximum to Holocene climate change. Quaternary Science Reviews, Special Theme: Arctic Palaeoclimate Synthesis (PP. 1674-1790) 29, 1801–1816. https://doi.org/10.1016/j.quascirev.2010.03.016

Sharma, S., Hamal, K., Khadka, N., Joshi, B.B., 2020. Dominant pattern of year-to-year variability of summer precipitation in Nepal during 1987–2015. Theor Appl Climatol 142, 1071–1084. https://doi.org/10.1007/s00704-020-03359-1

Shean, D., 2017. High Mountain Asia 8-meter DEM Mosaics Derived from Optical Imagery, Version 1. [tiles 641, 642, 674, and 675]. Accessed February 2021 & March 2023. https://doi.org/10.5067/KXOVQ9L172S2

Shrestha, A.B., Agrawal, N.K., Alfthan, B., Bajracharya, S.R., Maréchal, J., Oort, B. van, 2015. The Himalayan Climate and Water Atlas: impact of climate change on water resources in five of Asia's major river basins.

Shrestha, B.B., Nakagawa, H., 2016. Hazard assessment of the formation and failure of the Sunkoshi landslide dam in Nepal. Nat Hazards 82, 2029–2049. https://doi.org/10.1007/s11069-016-2283-3

Shrestha, D., Singh, P., Nakamura, K., 2012. Spatiotemporal variation of rainfall over the central Himalayan region revealed by TRMM Precipitation Radar. Journal of Geophysical Research: Atmospheres 117. https://doi.org/10.1029/2012JD018140

Shrestha, M.L., 2000. Interannual variation of summer monsoon rainfall over Nepal and its relation to Southern Oscillation Index. Meteorology and Atmospheric Physics 75, 21–28. https://doi.org/10.1007/s007030070012

Shugar, D.H., Jacquemart, M., Shean, D., Bhushan, S., Upadhyay, K., Sattar, A., Schwanghart, W., McBride, S., de Vries, M.V.W., Mergili, M., Emmer, A., Deschamps-Berger, C., McDonnell, M., Bhambri, R., Allen, S., Berthier, E., Carrivick, J.L., Clague, J.J., Dokukin, M., Dunning, S.A., Frey, H., Gascoin, S., Haritashya, U.K., Huggel, C., Kääb, A., Kargel, J.S., Kavanaugh, J.L., Lacroix, P., Petley, D., Rupper, S., Azam, M.F., Cook, S.J., Dimri, A.P., Eriksson, M., Farinotti, D., Fiddes, J., Gnyawali, K.R., Harrison, S., Jha, M., Koppes, M., Kumar, A., Leinss, S., Majeed, U., Mal, S., Muhuri, A., Noetzli, J., Paul, F., Rashid, I., Sain, K., Steiner, J., Ugalde, F., Watson, C.S., Westoby, M.J., 2021. A massive rock and ice avalanche caused the 2021 disaster at Chamoli, Indian Himalaya. Science 373, 300–306. https://doi.org/10.1126/science.abh4455

Shukla, T., Mehta, M., Dobhal, D., Bohra, A., Pratap, B., Kumar, A., 2020. Late-Holocene climate response and glacial fluctuations revealed by the sediment record of the monsoon-dominated Chorabari Lake, Central Himalaya. The Holocene 30, 953–965. https://doi.org/10.1177/0959683620908654

Sigdel, M., Ma, Y., 2017. Variability and trends in daily precipitation extremes on the northern and southern slopes of the central Himalaya. Theor Appl Climatol 130, 571–581. https://doi.org/10.1007/s00704-016-1916-5

Stead, D., Wolter, A., 2015. A critical review of rock slope failure mechanisms: The importance of structural geology. Journal of Structural Geology 74, 1–23. https://doi.org/10.1016/j.jsg.2015.02.002

Stolle, A., Bernhardt, A., Schwanghart, W., Hoelzmann, P., Adhikari, B.R., Fort, M., Korup, O., 2017. Catastrophic valley fills record large Himalayan earthquakes, Pokhara, Nepal. Quaternary Science Reviews 177, 88–103. https://doi.org/10.1016/j.quascirev.2017.10.015

Stone, J., 2004. Extraction of Al and Be from quartz for isotopic analysis. UW Cosmogenic Nuclide Lab Methods and Procedures 1025.

Stone, J.O., 2000. Air pressure and cosmogenic isotope production. Journal of Geophysical Research: Solid Earth 105, 23753–23759. https://doi.org/10.1029/2000JB900181

Stone, J.O., Allan, G.L., Fifield, L.K., Cresswell, R.G., 1996. Cosmogenic chlorine-36 from calcium spallation. Geochimica et Cosmochimica Acta 60, 679–692. https://doi.org/10.1016/0016-7037(95)00429-7

Stone, J.O., Fifield, K., Vasconcelos, P., 2005. Terrestrial chlorine-36 production from spallation of iron. Presented at the Abstract of 10th International Conference on Accelerator Mass Spectrometry, Berkeley California.

Strom, A., Li, L., Lan, H., 2019. Rock avalanche mobility: optimal characterization and the effects of confinement. Landslides 16, 1437–1452. https://doi.org/10.1007/s10346-019-01181-z

Takagi, H., Arita, K., Danhara, T., Iwano, H., 2007. Timing of the Tsergo Ri landslide, Langtang Himal, determined by fission-track dating of pseudotachylyte. Journal of Asian Earth Sciences, The 19th Himalaya-Karakoram-Tibet Workshop (HKT19) held at Niseko, Hokkaido, Japan, 10–13 July 2004 29, 466–472. https://doi.org/10.1016/j.jseaes.2005.12.002

Takaku, J., Tadono, T., Doutsu, M., Ohgushi, F., Kai, H., 2020. Updates of 'AW3D30' ALOS Global Digital Surface Model with other Open Access Datasets. Int. Arch. Photogramm. Remote Sens. Spatial Inf. Sci. XLIII-B4-2020, 183–189. https://doi.org/10.5194/isprs-archives-XLIII-B4-2020-183-2020

Taylor, J., 1997. Introduction to error analysis, the study of uncertainties in physical measurements.

Thompson, L.G., Severinghaus, J.P., Yao, T., Davis, M.E., Mosley-Thompson, E., Beaudon, E., Sierra-Hernández, M.R., Porter, S.E., 2022. Use of δ18Oatm in dating a Tibetan ice core record of Holocene/Late Glacial climate. Proceedings of the National Academy of Sciences 119, e2205545119. https://doi.org/10.1073/pnas.2205545119

Thuro, K., Eberhardt, E., Gasparini, M., 2004. Deep Seated Creep and it's Influence on a 1.5 GW Hydroelectric Power Plant in the Himalayas.

TopoMap, 2001a. Map produced by the Survey Department of His Majesty's Government of Nepal in co-operation with the Government of Finland - Sheet No. 2883 08, TILICHO.

TopoMap, 2001b. Map produced by the Survey Department of His Majesty's Government of Nepal in co-operation with the Government of Finland - Sheet No. 2884 09, LAMJUŃ HIMĀL.

Tucker, G.E., McCoy, S.W., Whittaker, A.C., Roberts, G.P., Lancaster, S.T., Phillips, R., 2011. Geomorphic significance of postglacial bedrock scarps on normal-fault footwalls. Journal of Geophysical Research: Earth Surface 116. https://doi.org/10.1029/2010JF001861

Uppala, S.M., KÅllberg, P.W., Simmons, A.J., Andrae, U., Bechtold, V.D.C., Fiorino, M., Gibson, J.K., Haseler, J., Hernandez, A., Kelly, G.A., Li, X., Onogi, K., Saarinen, S., Sokka, N., Allan, R.P., Andersson, E., Arpe, K., Balmaseda, M.A., Beljaars, A.C.M., Berg, L.V.D., Bidlot, J., Bormann, N., Caires, S., Chevallier, F., Dethof, A., Dragosavac, M., Fisher,

M., Fuentes, M., Hagemann, S., Hólm, E., Hoskins, B.J., Isaksen, L., Janssen, P. a. E.M., Jenne, R., Mcnally, A.P., Mahfouf, J.-F., Morcrette, J.-J., Rayner, N.A., Saunders, R.W., Simon, P., Sterl, A., Trenberth, K.E., Untch, A., Vasiljevic, D., Viterbo, P., Woollen, J., 2005. The ERA-40 re-analysis. Quarterly Journal of the Royal Meteorological Society 131, 2961–3012. https://doi.org/10.1256/qj.04.176

Vermeesch, P., 2018. IsoplotR: A free and open toolbox for geochronology. Geoscience Frontiers 9, 1479–1493. https://doi.org/10.1016/j.gsf.2018.04.001

Viles, H.A., 2013. Linking weathering and rock slope instability: non-linear perspectives: Linking weathering and rock slope instability. Earth Surf. Process. Landforms 38, 62–70. https://doi.org/10.1002/esp.3294

Voigtländer, A., Leith, K., Krautblatter, M., 2018. Subcritical Crack Growth and Progressive Failure in Carrara Marble Under Wet and Dry Conditions. Journal of Geophysical Research: Solid Earth 123, 3780–3798. https://doi.org/10.1029/2017JB014956

Wacker, L., Bonani, G., Friedrich, M., Hajdas, I., Kromer, B., Němec, M., Ruff, M., Suter, M., Synal, H.-A., Vockenhuber, C., 2010. MICADAS: Routine and High-Precision Radiocarbon Dating. Radiocarbon 52, 252–262. https://doi.org/10.1017/S0033822200045288

Wagner, G.A., 1995. Altersbestimmung von jungen Gesteinen und Artefakten: physikalische und chemische Uhren in Quartärgeologie und Archäologie. F. Enke.

Wang, Q., Zhang, P.-Z., Freymueller, J.T., Bilham, R., Larson, K.M., Lai, X., You, X., Niu, Z., Wu, J., Li, Y., Liu, J., Yang, Z., Chen, Q., 2001. Present-Day Crustal Deformation in China Constrained by Global Positioning System Measurements. Science 294, 574–577. https://doi.org/10.1126/science.1063647

Weidinger, J.T., 2006. Predesign, failure and displacement mechanisms of large rockslides in the Annapurna Himalayas, Nepal. Engineering Geology 83, 201–216. https://doi.org/10.1016/j.enggeo.2005.06.032

Weidinger, J.T., 1998. Case history and hazard analysis of two lake-damming landslides in the Himalayas. Journal of Asian Earth Sciences 16, 323–331. https://doi.org/10.1016/S0743-9547(98)00026-9

Weidinger, J.T., Ibetsberger, H.J., 2000. Landslide dams of Tal, Latamrang, Ghatta Khola, Ringmo, and Darbang in the Nepal Himalayas and related hazards. Journal of Nepal Geological Society 22, 371–380.

Weidinger, J.T., Korup, O., 2009. Frictionite as evidence for a large Late Quaternary rockslide near Kanchenjunga, Sikkim Himalayas, India — Implications for extreme events in mountain relief destruction. Geomorphology, Dating, triggering, modelling, and hazard assessment of large landslides 103, 57–65. https://doi.org/10.1016/j.geomorph.2007.10.021

Weidinger, J.T., Korup, O., Munack, H., Altenberger, U., Dunning, S.A., Tippelt, G., Lottermoser, W., 2014. Giant rockslides from the inside. Earth and Planetary Science Letters 389, 62–73. https://doi.org/10.1016/j.epsl.2013.12.017

Weidinger, J.T., Schramm, J.-M., Surenian, R., 1996. On preparatory causal factors, initiating the prehistoric Tsergo Ri landslide (Langthang Himal, Nepal). Tectonophysics 260, 95–107. https://doi.org/10.1016/0040-1951(96)00078-9

Wen, B., Wang, S., Wang, E., Zhang, J., 2004. Characteristics of rapid giant landslides in China. Landslides 1, 247–261. https://doi.org/10.1007/s10346-004-0022-4

Wesnousky, S.G., Kumahara, Y., Chamlagain, D., Pierce, I.K., Karki, A., Gautam, D., 2017. Geological observations on large earthquakes along the Himalayan frontal fault near Kathmandu, Nepal. Earth and Planetary Science Letters 457, 366–375. https://doi.org/10.1016/j.epsl.2016.10.006

Yadav, A., Mehta, B., Anoop, A., Mishra, P.K., 2022. Monsoon variability in the Indian subcontinent—A review based on proxy and observational datasets, in: Holocene Climate Change and Environment. Elsevier, pp. 369–390. https://doi.org/10.1016/B978-0-323-90085-0.00001-2

Yagi, H., 1997. Origin of the Phoksundo Tal (lake), Dolpa district, western Nepal. Journal of Nepal Geological Society 15, 1–7.

Yagi, H., Hayashi, K., Higaki, D., Tsou, C.-Y., Sato, G., 2018. Dormant landslides distributed in upper course of Sun Kosi Watershed and landslides induced by Nepal Gorkha Earthquake 2015. Journal of Nepal Geological Society 55, 61–67. https://doi.org/10.3126/jngs.v55i1.22790

Yan, Q., Owen, L.A., Zhang, Z., Jiang, N., Zhang, R., 2020. Deciphering the evolution and forcing mechanisms of glaciation over the Himalayan-Tibetan orogen during the past 20,000 years. Earth and Planetary Science Letters 541, 116295. https://doi.org/10.1016/j.epsl.2020.116295

Zangerl, C., Schneeberger, A., Steiner, G., Mergili, M., 2021. Geographic-information-system-based topographic reconstruction and geomechanical modelling of the Köfels rockslide. Natural Hazards and Earth System Sciences 21, 2461–2483. https://doi.org/10.5194/nhess-21-2461-2021

Zech, R., Zech, M., Kubik, P.W., Kharki, K., Zech, W., 2009. Deglaciation and landscape history around Annapurna, Nepal, based on 10Be surface exposure dating. Quaternary Science Reviews, Natural Hazards, Extreme Events and Mountain Topography 28, 1106–1118. https://doi.org/10.1016/j.quascirev.2008.11.013

Zerathe, S., Lebourg, T., Braucher, R., Bourlès, D., 2014. Mid-Holocene cluster of large-scale landslides revealed in the Southwestern Alps by 36Cl dating. Insight on an Alpine-scale landslide activity. Quaternary Science Reviews 90, 106–127. https://doi.org/10.1016/j.quascirev.2014.02.015

Zhou, T., Li, B., Man, W., Zhang, L., Zhang, J., 2011. A comparison of the Medieval Warm Period, Little Ice Age and 20th century warming simulated by the FGOALS climate system model. Chin. Sci. Bull. 56, 3028. https://doi.org/10.1007/s11434-011-4641-6

Zreda, M., Noller, J.S., 1998. Ages of Prehistoric Earthquakes Revealed by Cosmogenic Chlorine-36 in a Bedrock Fault Scarp at Hebgen Lake. Science 282, 1097–1099. https://doi.org/10.1126/science.282.5391.1097

# CHAPTER 3 – NUMERICAL MODELLING EXPERIMENT

## 3.0 Motivation

Layering and foliation are universally present in the metamorphic and sedimentary bedrock lithologies of the Annapurna Massif, as detailed in Section 2.2.1 (see also profiles in Figures 2.3 and 2.25). During our field investigations (see Section 2.4.1.1), we observed that the outcropping rocks prominently display anisotropic fabrics. This was evident both to the north of the main ridge crest of the Annapurna Massif, where the rocks are primarily within the Tethyan Himalayan Sequence (THS), and along the Annapurna south-face, which consists of various types of gneisses (Figure 2.1).

- In the upper Marsyangdi Valley, bedding and/or schistosity within the bedrock have a significant impact on the location and geometry of the giant rock avalanches that occurred there (see Section 2.6.2.1). At the Pisang Bowl site, these planes are responsible for forming the spectacular bowl-shaped failure scarp (Figures 2.6E; 2.11; 2.12, B-D; A2.1, C+D). Similarly, bedding and schistosity are also present at the Humde/Manang and Tilicho Lake localities and are thought to play an important role in controlling location and geometry of the giant rock avalanches at these sites (Figures 2.15A, 2.20G, A2.2F, A2.4).
- On the Annapurna south-face, the consistently dipping gneisses may significantly influence slope stability and the failure characteristics and evolution of the DSGSD at the Phalo Danda site, even though the main scarp cuts across the foliation (Figures 2.29 C-F; 2.31; 2.32B; 2.33 A+B; 2.34; see also Section 2.8.1). This influence likely extends to slope failures on the south-face in general (see Figures 2.5E and 2.38).

Layering and foliation introduce a transverse isotropy to the rock's resistance to failure, i.e. rock strength anisotropy, which strongly controls the stability and failure mode of rock slopes. This significant Precondition Factor of bedrock landslides (see Section 1.2.2) has not yet been systematically explored in terms of different orientations relative to the slope (see Section 1.5.2). In this chapter, we will address this issue using numerical models based upon the Discrete Element Method (DEM). The study begins with an introduction to the research objectives, followed by an explanation of the method and a presentation and discussion of the results for the full 180° variation of anisotropy orientation toward the slope. This study aims to improve our understanding of the influence of rock strength anisotropy on slope failure processes in the Annapurna Massif and other mountain ranges.

The following content of this chapter was published as a **Research paper** in the journal **Geomorphology** under the following title:

# Stability and failure modes of slopes with anisotropic strength: Insights from discrete element models

It can be accessed via this citation:

*Huber, M., Scholtès, L., Lavé, J., 2024. Stability and failure modes of slopes with anisotropic strength: Insights from discrete element models. Geomorphology 444, 108946. https://doi.org/10.1016/j.geomorph.2023.108946*

Publication steps:

- Received 13 July 2023
- Received in revised form 18 October 2023
- **Accepted 19 October 2023**
- Available online 29 October 2023

Reviewers:

- Dr Sam McColl, Massey University, Palmerston North, New Zealand
- One anonymous reviewer

The research paper was reformatted for the purpose of integration into this PhD-thesis mémoire. The content of this chapter is identical to the published research paper (word by word), except that declarations and Acknowledgements were omitted.

**Abstract**

**This paper investigates the relationships between hillslope stability and fabric anisotropy of brittle rock materials and the implications for landscape shaping. We use discrete element models to study the stability and failure modes of slopes made of transverse isotropic rock materials, focusing more particularly on the influence of the material orientation relative to the topographic slope. After validating the numerical approach with a limit equilibrium analytical solution in the case of an isotropic material, we modify our numerical slope models to simulate the rheological features of anisotropic gneissic rocks. Systematic exploration of the transverse isotropy plane's orientation in two dimensions (dip angle) reveals that slope collapse requires strength values that are highly dependent on the orientation of the material relative to the slope. For a 1000 m high escarpment, the stability of a slope with a fixed gradient requires strength that is one order of magnitude greater in a configuration where the isotropy plane is slightly less inclined than the topographic slope (i.e., cataclinal overdip configuration) than in a configuration where the isotropy plane is perpendicular to the slope (i.e., anaclinal configuration). Mirroring this highly variable stability according to the relative orientation of the material, four modes of deformation or gravitational instability are observed: in order of appearance, when the transverse isotropy plane orientation goes from 0 to 180° with respect to the horizontal (going from cataclinal to anaclinal configurations), the slope collapses respectively by sliding, buckling, toppling and crumbling. The crumbling mode corresponds to a very stable configuration for which the preferred ground movements will be rock falls from the cliff compared to the structurally controlled, deep-seated deformation modes leading to sliding and toppling. Despite the simplifications inherent to the numerical approach, our study highlights the essential characteristics of landslides occurring along slopes cut in transverse isotropic materials and reproduces the various instability modes observed in natural slopes. It also enables assessing their respective kinetics as well as the volumes of material they mobilize. Finally, by comparing our findings on the azimuthal variations in hillslope gradients observed along the central Himalaya (Nepal), in an area characterized by the relatively uniform orientation of the anisotropy in gneissic and mica-schist formations, we show that, even though multiple environmental factors come into play, landscape shaping is indeed strongly controlled by material anisotropy.**

## 3.1 Introduction

Landslides are known to play a key role in shaping landscapes (Densmore and Hovius, 2000; Korup et al., 2010) and are a major hazard for millions of people and infrastructure globally (Glade et al., 2005; Davies, 2022), especially evident nowadays in mountainous regions in times of global warming (e.g., Huggel et al., 2012). The study of their dynamics and the control by factors like climate, lithology, and tectonics on predisposing and triggering slope failures is fundamental for improving of natural disaster preparedness and better understanding of the Earth's surface evolution over time.

Among the factors governing slope deformation, geological structures, with their different forms related to nature and scale, are probably the most critical (Jaboyedoff et al., 2011; Stead and Wolter, 2015). Apart from large discrete structures such as folds, faults, and unconformities, intrinsic textural anisotropy is commonly present in many rocks near Earth's surface through the lithology itself in the form of layering and/or foliation. This homogeneously distributed matrix anisotropy, that predominantly corresponds to transverse isotropy (TI), is not necessarily localized by bedding planes or joints, and usually concerns the entire rock mass. The ability of TI rock materials to deform and withstand stresses varies according to the orientation of stresses relative to their isotropy plane (Hoek, 1964; Barton and Quadros, 2015). Therefore, the orientation of a slope with respect to the plane of isotropy significantly affects its overall stability, particularly the rupture localization and the associated failure mode. Slope failures related to bedding planes, schistosity, or joint sets have been described and studied for either natural (e.g., Stead and Wolter, 2015) or engineered slopes (e.g., Read and Stacey, 2009; Cheng and Lau, 2014). For natural slopes, such failure characteristics should play a key role in shaping the landscape.

Indeed, topography associated with underlying inclined bedrock of layered or foliated rocks commonly features landforms described by geomorphologists as dip slopes, escarpments or homoclinal ridges (e.g., Cotton, 1949). Cruden and Hu (1999) and Cruden (2000), based on a theory that links bedding orientations to slope angles in sedimentary sequences of the Canadian Rocky Mountains, identified two major failure modes, sliding and toppling, respectively, and observed that slope angles decrease when the bedding is oriented parallel to the slope. Chigira (1992) identified different deformation patterns governed by the preferential orientation of structures relative to the slope morphology from analyses of slow-moving landslides in Japan. Chigira (2000) built upon these observations to define four distinct failure modes controlled by the relative orientation of the slope with respect to the bedding (or foliation), i.e., sliding, toppling, buckling, and a dragging mode for slopes that are principally stable but nonetheless subjected to a deep-seated deformation process with a rupture zone cross-cutting the bedding planes at depth. Grelle et al.

(2011) also identified in southern Italy certain conditions strongly related to the bedding orientation with respect to the slope, susceptible to promoting landslides in a bedrock composed of an interlayering of clayey and stony sediments. Besides, studying landslides triggered by the 1933 Diexi earthquake in China, Cui et al. (2022) found variability in failure mode, frequency, and landslide-affected area as a function of lithology and bedding orientation relative to the slope. All these studies show that the mode of failure and the susceptibility of a slope to failure is strongly dependent on the orientation of material anisotropy, i.e., bedding, schistosity, or regular jointing.

Many rock-mechanical lab-scale tests have been performed on a variety of TI rocks worldwide to assess their direction-dependent properties (see e.g., Donath, 1961; Hoek, 1964; McLamore and Gray, 1967; Niandou et al., 1997; Nasseri et al., 2003; Bonnelye et al., 2017). All these tests show that strength properties and failure modes are highly direction-dependent in such rock materials. For instance, Tien et al. (2006) used compression tests on an analog rock material to illustrate how the failure mode and strength change depending on the isotropy plane inclination with respect to the principal stress. Transferring results from laboratory tests to the slope-scale requires scaling considerations (e.g., Brideau et al., 2009; Marinos and Carter, 2018) which makes assessing and characterizing the mechanical failure behavior of anisotropic rock media at the slope scale difficult. Existing studies with analog models can provide valuable insight into the behavior of slopes made up of regular pervasive joints: see, for instance, the centrifuge experiments that replicate flexural toppling (Adhikary et al., 1997) and sliding (Li et al., 2014), or the experiments with rigid blocks by Aydan et al. (1989). However, these studies remain descriptive, are performed only for a few joint orientations, lack scaling considerations for larger slope dimensions, and are technically challenging. It is, therefore, a logical step for scientists to resort to numerical methods to study anisotropic rock slopes, given their capacity to reproduce results systematically and to conduct comprehensive parametric studies, as well as the possibility they offer to set up geometries and loading procedures that could not otherwise be realized by analog experiments.

Numerical studies of slope stability considering transverse isotropy are not so common in the literature. Some studies based on continuum approaches, included anisotropic rock strength in their model formulation for specific case studies (Agliardi et al., 2012; Roy et al., 2015; Wang et al., 2018) because it is unavoidable to take into account the direction-dependent strength of layered or foliated rock slopes. Azami et al. (2012) used the finite element method (FEM) to investigate the stability of a simple step-like geometry considering the full 180° range of angles possible in a slope made up of a TI material in two dimensional plane strain configuration. They determined the factor of safety for 22 different angular configurations and found two stability minima and two stability maxima when plotting their results against the full angle range. However, they did not use their methodology to track the temporal evolution or mode of failure in their simulations. Discontinuum approaches, thanks to their capability to explicitly describe discrete structures in materials,

have been widely used for slope stability analysis and landslide research (see, e.g., the review by Stead and Wolter, 2015). These approaches, which apply either the discrete element method (DEM) (Cundall and Strack, 1979) or a hybrid method that combines the latter with the FEM (FDEM, Munjiza, 2004) can describe large deformation typical of rock slope failures as well as their progressive failure (Wang et al., 2003; Utili and Crosta, 2011; Scholtès and Donzé, 2012; Katz et al., 2014). They have been successfully used to investigate and reproduce complex failure mechanisms of historic landslides in anisotropic rock formations (see, e.g., case studies from Benko and Stead, 1998 and Zou et al., 2017), or to mimic and theoretically study step path failures of mono- or multi-modal pervasive joint sets inside rock slopes (Scholtès and Donzé, 2015; Zheng et al., 2018; Zheng et al., 2021; Sun et al., 2022). Nonetheless, despite their intrinsic capabilities and strengths over continuum methods, discontinuum methods have not yet been used to perform a valuable, comprehensive study covering the full range of possible rock strength anisotropy to slope face angles within rock slopes.

Here, we propose such an investigation to gain better insight into how anisotropy quantitatively affects slope stability and governs deformation characteristics and failure modes, aiming to shed light on how the TI rock orientation potentially modulates the Earth's surface topography and hazards in mountainous regions. First, we present our modeling approach and justify its relevance for simulating rock slopes and TI materials. Then, after comparing our model's predictions to an analytical limit equilibrium solution that describes failure in isotropic slopes, we present a comprehensive study of TI rock slope stability that covers the full range of isotropy plane vs. slope orientation in two dimensions for two different slope gradients. The stability and failure modes observed over the entire range of orientations are then discussed, and a comparison is finally made with a satellite data extraction of the Annapurna Massif of Nepal to compare our findings in a natural setting.

## 3.2 Methods

### 3.2.1 The DEM model

To study rock slope stability, we used the discrete element method (DEM) implemented in the open-source software Yade Open DEM (Šmilauer et al., 2021). The rock material was simulated by spherical discrete elements (DE) bonded to one another through elastic-cohesive-frictional interaction laws governed by a modified Mohr-Coulomb criterion, as defined in the bonded particle model (BPM) of Scholtès and Donzé (2013) (see also Fig. A3.1). In the present study, we built upon previous works dedicated to investigating slope stability using the same BPM (Scholtès and Donzé, 2012, 2015; Bonilla-Sierra et al., 2015, 2017). The mechanical properties of the interparticle bonds dictate the overall emergent behavior of the DE assembly. The bonds can break to give place to purely frictional inter-particle interactions. Every time a bond breaks, a "crack" is defined at the former bond location. Cracks can be either of tensile nature (mode I) or of shear nature (mode II), depending on the local stress field. As classically done in the DEM, the simulations were calculated in iteration steps where the positions of the particles are updated based on an explicit time integration of Newton's second law of motion. In addition, a non-viscous type damping was introduced to dissipate kinetic energy and favor the quasi-static nature of the simulated behavior. We used a damping coefficient of 0.5 for all the models presented hereafter (for details of the implementation, please refer to previously cited works and to Šmilauer et al., 2021).

### 3.2.2 Modeling anisotropic rock materials

The BPM implemented in Yade has been recently enhanced to simulate TI rocks thanks to the introduction of isotropy planes at the scale of particle contacts (Dinç and Scholtès, 2018). Here, we make use of the same methodology to account for TI in our slope models (Fig. 3.1a). Using the smooth contact logic proposed by Scholtès and Donzé (2012), preferentially oriented discrete weak bonds are introduced homogeneously within the particle assembly so that the overall emergent behavior presents the typical features of transverse isotropic materials, i.e., direction-dependent properties or anisotropic strength. As shown in Dinç and Scholtès (2018), the amount of these weak bonds and their mechanical properties have to be chosen carefully to ensure the simulated behavior is representative of the target rock material. In this study, we chose to simulate slopes made of a metamorphic rock. Following the procedure proposed by Dinç and Scholtès (2018), we thus calibrated our BPM to mimic the laboratory scale behavior of a gneissic rock presented in Saroglou et al. (2004). To do so, we performed a series of uniaxial test simulations (Fig. 3.1b) and adjusted the BPM parameters to match the experimental behaviors described by Saroglou et al. (2004) with emphasis put on

the direction-dependent strength properties characteristic of such rock type. As shown in Fig. 3.1c, the calibrated BPM can reproduce the experimental observations: the uniaxial compressive strength evolves as a function of the angle θ between the principal stress direction and the isotropy plane with a typical asymmetric U-shape, the maximum strength corresponding to θ = 90° (loading perpendicular to the foliation), and the minimum strengths corresponding to θ ∈ [30°, 60°] (see the model properties in Table A3.1). Similarly, the Young modulus $E_{lab}$ of the simulated material varies with θ, $E_{lab}$being minimum for θ = 90°, and maximum for θ = 0° such as $E_{lab}^{0°}/E_{lab}^{90°} \approx 1.5$, with $E_{lab}^{0°} \approx 55$ GPa. Of course, given our objective to simulate large rock slopes, we used a specific strategy to upscale these properties for our slope models (see Section 2.3.2).

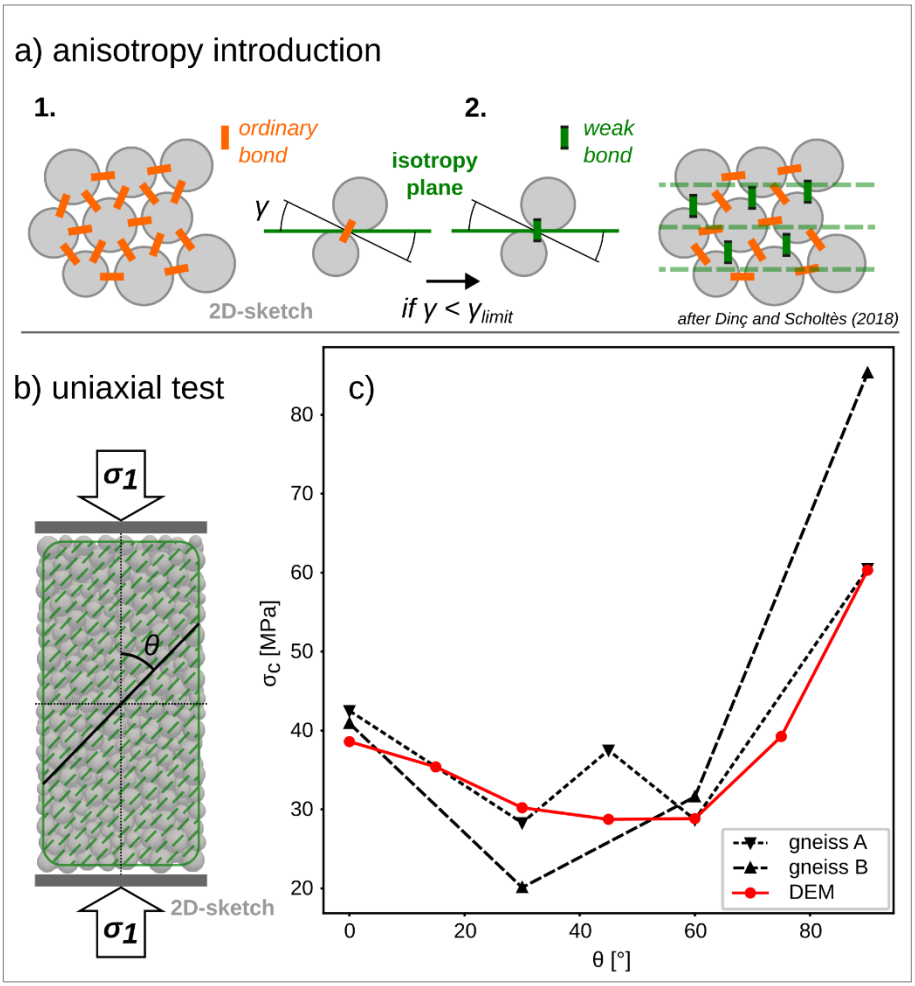


*Fig. 3.1. a) Selection (1) and reorientation (2) of ordinary bonds to preferentially oriented weak bonds in a DEM assembly to produce an emergent transverse isotropic behavior (after Dinç and Scholtès, 2018). γ is the angle used to detect contacts subparallel to the isotropy plane and to change the corresponding ordinary bonds to weak bonds. b) Uniaxial testing simulation used to calibrate the DEM model. θ is the angle between the isotropy plane and the major principal stress direction (axis of compression here). c) Comparison of the model prediction with the experimental observations by Saroglou et al. (2004): change in the uniaxial compressive strength as a function of θ.*

### 3.2.3 *Model set-up*

#### *3.2.3.1 Geometry, boundary conditions and preconditioning*

Our slope failure experiments are performed on slope slices with a height of 1000 m and a slope angle β that can be varied (Fig. 3.2a-b). To avoid numerical artifacts caused by regular packings, the slope models were made up of particles presenting a polydisperse size distribution (with variation up to 1/3 of the predefined mean particle radius). The packings were generated through the progressive growth of particles initially randomly placed within a predefined closed volume (i.e., as a cloud of polydisperse particles). The growth was stopped when the porosity of the packing reached 30 %, and the packing was mechanically stable. The mean particle radius was set to 20 m. The thicknesses of our slope slices are designed so that approximately 10 particles were present in the out-of-plane direction, a resolution that proved to give mesh objective results (see Section 3). Lateral boundary conditions were defined by blocking the translation in the direction normal to the boundary for the outermost particles (those whose centers are located within a zone of 3 times the mean particle radius from the boundary). At the bottom of the model, translations and rotations were blocked in all three directions for an equally defined layer of particles (Fig. 3.2b).

To initialize stresses within our slope models, we adapted the loading procedure proposed by Katz et al. (2014), as illustrated in Fig. A3.2. First, we applied gravity to a square packing of particles whose density $\rho_p$ was adjusted to ensure that the gravity-induced stress within the model corresponds to the stress found in a slope made up of a material with density $\rho = 2500$ kg/m$^3$ (i.e., $\rho_p = \rho \cdot V/V_p$, with $V$ the volume of the model and $V_p$ the volume occupied by the particles). This gravity loading was performed considering 200 m of overburden above the final height of the slope. Then, after cutting of the overburden by eliminating particles from the simulation, the slope geometry was defined in a similar way by removing particles located above the final topography (Fig. A3.2). This process was chosen to mimic the natural genesis of mountains where the subsurface is under the influence of the overlaying rock mass, and the topography only develops later through erosion, as observed for valleys forming through fluvial or glacial erosion in mountainous environments. The strength of all the interparticle bonds was set to a very high value during this preconditioning stage to ensure an elastic response of the model (i.e., no internal damage was induced up to the end of the preconditioning stage) (step 4 in Fig. A3.2; Table 3.1).

Table 3.1: Inter-particle bond properties of the slope models before SR is applied

| Parameter | ordinary bonds | anisotropy bonds |
|---|---|---|
| Interaction radius intR [-] | 1.0 | - |
| Elastic modulus Y [GPa] | 10 | 1 |
| Stiffness ratio P [-] | 0.1 | 0.1 |
| Tensile strength $T_p$ [MPa] | 100 | 0 |
| Cohesion $C_p$ [MPa] | 100 | 0 |
| Friction angle $\varphi_p$ [°] | 10 | 0 |
| Dilation angle ψ [°] | - | 0 |
| Angle range $\gamma_{limit}$ [°] | - | 55 |

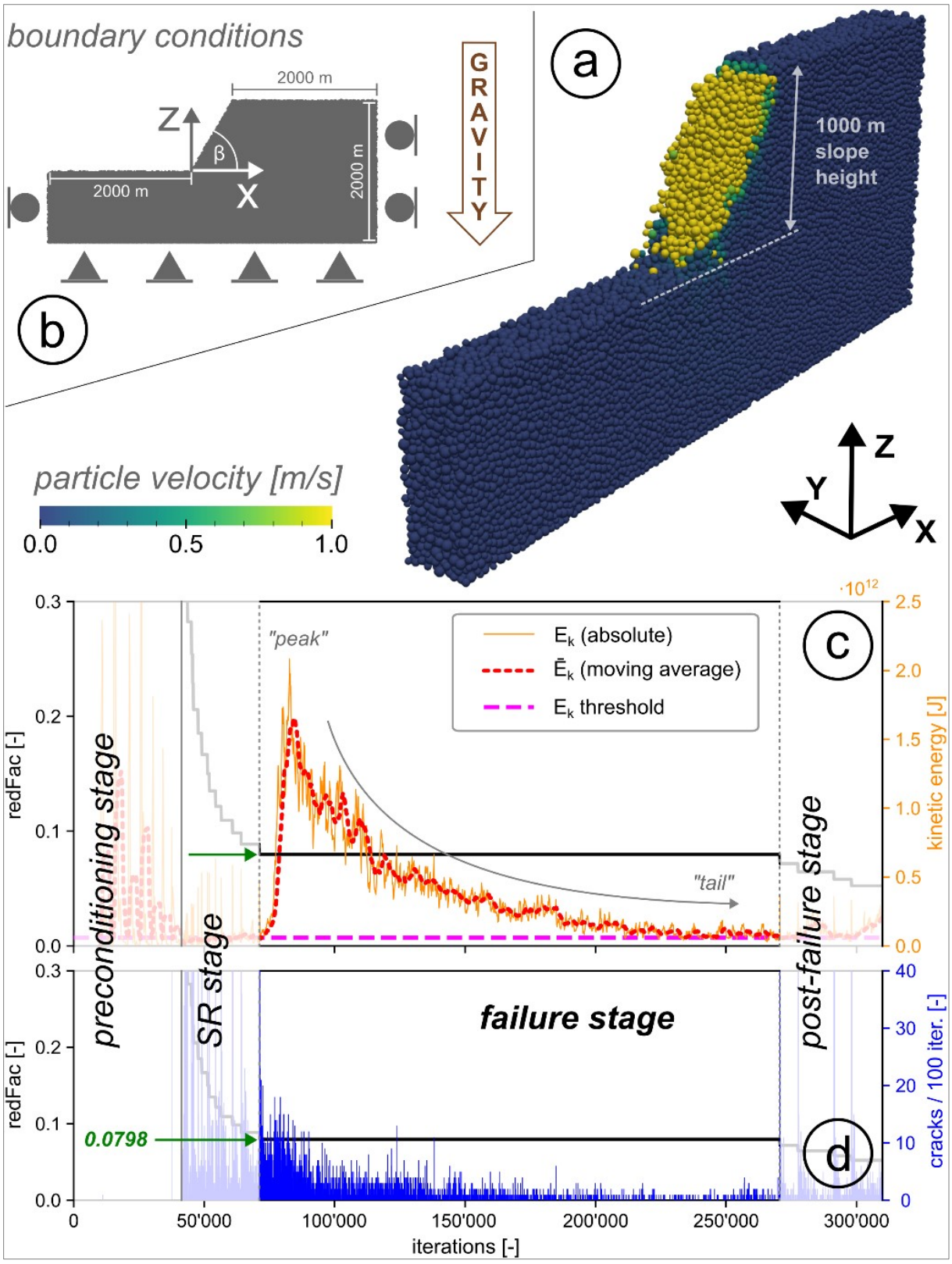


*Fig. 3.2. a) 3D view of a slope model at failure; b) boundary conditions; recordings from a simulation (anisotropy angle α = 70° and slope angle β = 60°) that has been brought to failure by strength reduction (SR): c) reduction factor (redFac) and kinetic energy indices (absolute value $E_k$ and moving average $\bar{E}_k$), and d) crack frequency plotted over iterations.*

*3.2.3.2 Upscaled mechanical behavior*

To define the properties of our slope models, we followed a procedure classically used in rock engineering where lab-scale properties are upscaled based on rock mass classification and associated empirical scaling indexes. For instance, the elastic properties of the slope models were defined following the approach by Hoek and Diederichs (2006), who proposed an empirical relation that relates the lab-scale Young's modulus of the rock material Elab to the rock mass deformation modulus *E* as a function of the Geological Strength Index (GSI):

$$E = E_{lab} \times \left(0.02 + \frac{1-D/2}{1+e^{((60+15D-GSI)/11)}}\right) \quad (3.1)$$

where D is a disturbance factor related to the excavation method (we considered D = 0 here). The GSI is a rock mass classification index that relies on the description of rock structures and block surface condition, which can vary between 0 and 100 depending on the quality of the rock mass (Hoek et al., 2002). Originally built upon a large data set of field measurements, the GSI approach has been used successfully by geotechnical engineers for decades to upscale the mechanical properties of rock masses from lab-scale measurements. We used Eq. 3.1 to define the elastic bond properties of our slope models based on the lab-scale values measured by Saroglou et al. (2004) and a GSI value ranging between 15 and 30 (see Table 3.1 for values). This GSI value would correspond to a moderately to severely damaged rock and could be assumed realistic for natural slopes affected by weathering and tectonism (Marinos and Hoek, 2000; Marinos and Carter, 2018).

In addition, we also altered the intrinsic strength of our slope models by adjusting the intR parameter of the BPM which is an explicit representation of the degree of particle interlocking (Scholtès and Donzé, 2013). At the lab scale, intR can be adjusted to simulate the behavior of more or less porous rocks, which would respectively present typical linear Mohr-Coulomb failure envelopes for intR = 1 or non-linear Hoek and Brown failure envelopes for intR >1. Considering the scale of our slope models, the degree of particle interlocking can be seen as an indicator of the fracturing degree of the rock mass, and we thus made the choice to define intR = 1 in our simulations in order to take into account the role of defects of all sorts coexisting within the medium (faults, fractures, joints, etc.). Given the method that we used in our simulations, we don't have to define upscaled values for the strength parameters (see the following section).

*3.2.3.3 Strength reduction method*

Once the slope model is stabilized under gravity and the slope topography is cut, all bond strengths are initialized at the predefined values (see Table 3.1) and the actual simulation starts (Fig. A3.2, step 4). The intrinsic model time is set to zero at this exact moment. The simulation consists of a strength reduction (SR) method that involves the progressive decrease of the interparticle bond strength, as proposed by Bonilla-Sierra et al. (2015). The tensile strength $T_p$ and the cohesion $C_p$ of the bonds (ordinary bonds only, since the weak bonds do not have any strength, as shown in Table 3.1) are reduced simultaneously to promote failure of the slope. The SR method enables to reach failure without having to predefine an upscaled strength for the rock material. Also, it provides critical strength reduction values at failure, which are case-dependent and thus enables assessing the proneness of different slope models to fail by comparing the amount of strength reduction needed to reach failure.

Practically, $T_p$ and $C_p$ decreased stepwise by 10 % up to failure, the strength reduction factor (redFac) defining the cumulative reduction applied (see Fig. A3.1 and Table 3.1). In this study, we combined different criteria to check if the slope models were stable and if further SR was needed (see Fig. 3.2c-d). Practically, SR is applied if the three following conditions are met:

- the overall kinetic energy ($E_k$) remains below a threshold,
- a moving average of $E_k$, namely $\bar{E}_k$, remains below a threshold,
- no cracks were generated since the previous checkpoint.

The redFac plotted over the iterations of a simulation allows us to determine the critical inter-particle strength needed for stability for each simulation (Fig. 3.2c). For more information on the SR method, please refer to the Annexe A3.1.

### 3.3 Relevance of the discrete element approach for investigating slope stability

Assessing the capability of numerical models to simulate slope failure in anisotropic materials is not straightforward. A recent study (Stockton et al., 2019) explores, using a semi-analytical procedure, the stability of slopes in the presence of frictional or cohesive anisotropy. However, the proposed definition of anisotropic cohesion as a sin2() function of the angle between the isotropy plane and the principal stress direction is not consistent with our emergent TI behavior nor with uniaxial laboratory results for gneisses (Fig. 3.1), so a direct comparison was not possible. We, therefore, preferred to assess the relevance of our numerical models by comparing their predictions with an analytical solution derived from stability analysis in the case of an isotropic material. We performed such a comparison considering the same geometry, loading procedure, SR method, and inter-particle bond properties as the ones presented in Table 3.1, except that no weak bonds were introduced into the model (see Section 2.2 and Figs. 3.2 and A3.2). We compared our model results to the analytical solution derived by Leshchinsky et al. (1985) based on the limit equilibrium theory and a variational calculation scheme. The solution consists of a log-spiral failure geometry associated with a factor of safety (FoS) obtained for a slope step with a certain slope angle (β), made of a homogeneous Mohr-Coulomb (MC) type material with given cohesion (C) and friction angle ($\varphi$). It is thus possible to determine the critical MC strength properties (C, $\varphi$) of a slope and its rupture surface by considering FoS = 1.

The comparison exercise was also an opportunity to test the objectivity of the numerical model when varying some of its parameters, such as the number and size of its constitutive elements, their spatial arrangement, or the criteria used for the SR method. To this end, we carried out a total of 48 slope simulations on eight different packings built up with two different mean particle radii (R = 20 m and R = 15 m) and cut at two different slope angles β (40° and 60°). This parametric study showed that the results obtained are generally insensitive to the choice of particle radius or spatial arrangement, indicating that they are overall robust (see Annexe A3.2 for further details).

$C_p$ and $T_p$) and the corresponding emergent MC parameters at failure ($C_e$ and $\varphi_e$) obtained for the 48 slope simulations (see in Annexes A3.2 and A3.3 how these properties were obtained based on results of dedicated bi-axial tests, Fig. A3.3). They are compared to the MC parameters predicted by the 2D solution of Leshchinsky et al. (1985). For both slope angles tested here, $\varphi_e$ ranges around 32°. For such a value of the friction angle $\varphi$, the analytical 2D solution predicts critical cohesion values C that are slightly different from the Ce of the numerical material. Agreement on the cohesion values can be reached, however, by considering a slightly lower (around -2° offset) or higher (around 3° offset) friction angles for the 40° and 60° slopes, respectively. These minor deviations are nonetheless acceptable, taking into account the dispersion of the original $T_p$ and $C_p$ values (see Table A3.2) and the procedure used to obtain the emergent MC parameters (fitting a Mohr- Coulomb criterion to discrete values). Regarding the geometry of the failure plane, the

numerical and analytical rupture surfaces are in close agreement for the β = 60° slope simulations (Fig. 3.3). For β = 40°, the analytical solution shows a slightly more pronounced curvature than the numerical solution (Fig. A3.5). Overall, our numerical results compare relatively well with the analytical solution for both the MC strength parameters at failure and the geometry of the failure surface.

We did not increment the slope height in our simulations because, according to limit-equilibrium description of slope stability problems (e. g., Leshchinsky et al., 1985), changing the slope height (e.g. to 100 m or 500 m) does not significantly change the geometry of the failure plane, but only changes the strength at failure by a proportionally inverse amount. For instance, for a slope height H = 100 m, we would simply get much higher $C_p$ and $T_p$ values at failure (see Fig. 3.4) than for H = 1000 m with a similar rupture plane geometry, as predicted by the non-dimensional parameter N = C/ρgH (Leshchinsky et al., 1985), with material density ρ and gravitational acceleration g.

*Table 3.2: Comparison of DEM results and analytical solution after Leshchinsky et al. (1985). The DEM interparticle properties at failure correspond to means calculated over 4 different slope models run with different packings (see Table A3.2 in the Annexe). The emergent MC parameters were obtained from back analyses of biaxial test simulations (see Table A3.2 in the Annexe). The MC parameters at failure were obtained based on the 2D analytic solution (Leshchinsky et al., 1985) (values of interest in bold).*

| | Topographic slope β = 40° | | Topographic slope β = 60° | |
|---|---|---|---|---|
| **DEM** | ***Interparticle strengths at failure*** | | | |
| | $\varphi_p$ [°] | $C_p$ & $T_p$ [MPa] | $\varphi_p$ [°] | $C_p$ & $T_p$ [MPa] |
| | 10 | 0.42 ± 0.13 | 10 | 2.86 ± 0.16 |
| | ***Emergent Mohr-Coulomb parameters*** | | | |
| | $\varphi_e$ [°] | $C_e$ [MPa] | $\varphi_e$ [°] | $C_e$ [MPa] |
| | 32 | 0.33 ± 0.03 | 32 | 1.14 ± 0.07 |
| **analytical solution** | ***Mohr-Coulomb parameters at failure*** | | | |
| | $\varphi$ [°] | C [MPa] | $\varphi$ [°] | C [MPa] |
| | 30 | **0.37** | 30 | 1.47 |
| | 31 | **0.31** | 31 | 1.40 |
| | **32** | 0.26 | **32** | 1.32 |
| | 33 | 0.21 | 33 | 1.25 |
| | 34 | 0.17 | 34 | **1.18** |
| | 35 | 0.13 | 35 | **1.11** |

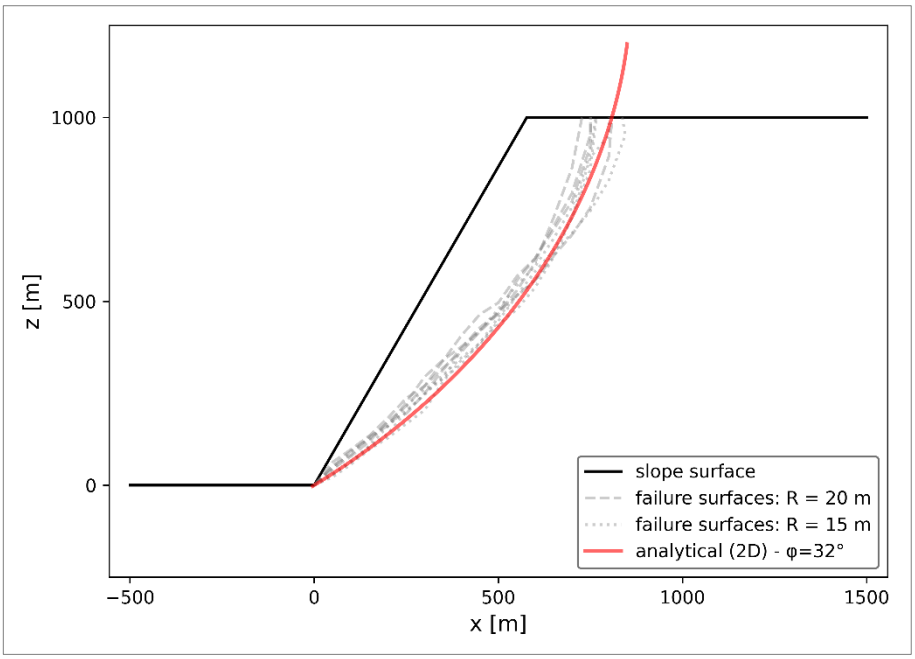


*Fig. 3.3. The β = 60° slope results obtained for 2 resolutions (mean particle radius R = 20 m and R = 15 m respectively) compared to Leshchinsky et al. (1985)'s 2D analytical slope stability solution for φ = 32° (red curve).*

### 3.4 Results

SR simulations were conducted on two different particle arrangements, referred to in the following as packings P1 and P2, each with an identical mean particle radius of 20 m and the same overall geometrical properties but created from two different initial clouds of particles (see Section 2.3). We explored slope stability in two dimensions considering the full range of possible orientations of the isotropy plane relative to the horizontal (dip both towards and away from the slope, hereafter designated as the anisotropy angle $\alpha \in [0°, 180°]$, Fig. 3.4) by running simulations every 10° increments considering two different slope angles ($\beta = 40°$ and 60°) for each packing.

#### 3.4.1 Slope stability over the 180° range

Overall, the $T_p$ and $C_p$ values at failure show similar trends for both the $\beta = 40°$ and 60° slopes, as well as strong variations depending on the angle $\alpha$ (Fig. 3.4). As expected, 40° slopes fail for considerably lower inter-particle strengths, whatever the configuration (40° slopes are intrinsically more stable than 60° slopes). Slope models with an isotropy plane that rises less than the slopes themselves ($\alpha \in [130°, 170°]$), classified as cataclinal overdip slopes by Cruden and Hu (1996), fail with the highest $T_p$ and $C_p$ values, meaning that they correspond to the least stable slopes. The stability minimum $S_{min}1$ corresponds to $\alpha \approx 160°$. Slope models with isotropy planes dipping sub-vertically towards the slope ($\alpha \in [60°, 90°]$), defined as anaclinal slopes with steepened escarpment by Cruden and Hu (1996), fail for lower $T_p$ and $C_p$ values than $S_{min}1$ and show another stability minimum, $S_{min}2$, at $\alpha = 80°$. Slopes with isotropy planes dipping at low angles into the slope ($\alpha \in [10°, 50°]$), classified as anaclinal slopes with subdued escarpment by Cruden and Hu (1996), fail for the lowest recorded inter-particle strengths, which means they correspond to the most stable slopes (for $\beta = 40°$, interparticle strength values drop down to zero for some cases). For $\beta = 60°$, the stability maximum $S_{max}1$ is at $\alpha = 20°$. Another stability maximum $S_{max}2$ can be identified around $\alpha = 100°$, a configuration that corresponds to cataclinal underdip slopes according to Cruden and Hu (1996).

By looking at the stability minima and maxima over the entire range of possible anisotropy angles, we observe an apparent symmetry over the $\alpha = 90°$ plane for both slope angles, with both minima and maxima lying 80° apart from each other.

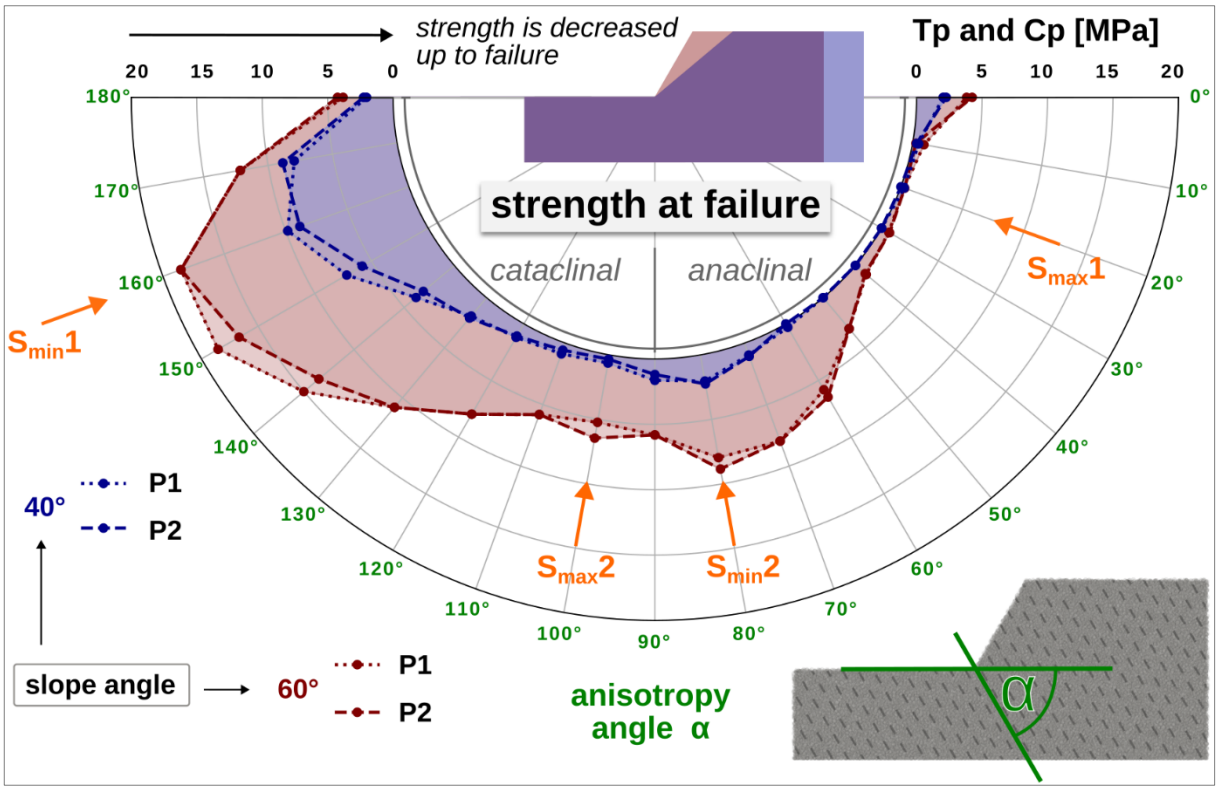


*Fig. 3.4. Stability curves over the full range of possible orientation (α) of the isotropy plane with respect to the horizontal: interparticle strength at failure ($T_p$ and $C_p$) obtained from DEM simulations performed on slopes with distinct angles (β = 40° and 60°). P1 and P2 are two different particle packings. Stability minima and maxima are indicated ($S_{min}$ and $S_{max}$).*

3.4.2 Stability extrema: overall kinetics

Our simulation results can be further explored by comparing failure index parameters evolving (like in Fig. 3.2, Section 2.3). Here, we only investigate the β = 60° slope angle simulations (packing P1) corresponding to the four stability extrema. In Fig. 3.5, we plot out their respective critical strength values, $T_p$ and $C_p$, their overall kinetic energy $E_k$, and their accumulated total number of cracks over the simulation time. Only cracks occurring near the slope surface are accounted for in the analysis (see Fig. A3.6). The plots reveal significant disparities in failure evolution for the four cases (the respective start and end of the failure stage are marked with vertical red lines in Fig. 3.5a-d).

First, the more stable configurations (α = 20° and 100°) need more time/iterations to fail since they need more SR. For α = 100°, a minor instability is responsible for a small pre-failure plateau in the SR-curve (Fig. 3.5b). $E_k$ does not rise high during this stage compared with the failure stage observed afterward, and we thus considered that this pre-failure stage was irrelevant when assessing the critical state parameters. This pre-failure stage resulted from the detachment of a few individual particles along the slope face that had to settle at the base of the slope before the SR could resume. For α = 20°, $E_k$ shows several peaks of low and similar magnitude, which were separated by periods of additional SR (see Fig. 3.5d). The principal slope failure was assigned over all three SR plateaus as a multi-step failure (in Fig. 3.4, $T_p$ and $C_p$ at failure were plotted for the lowest plateau in simulations where multi-stage failure occurred). The other three configurations display pronounced individual peaks of $E_k$ that differ in shape and magnitude (Fig. 3.5a-c). The α = 160° configuration shows the highest rise in magnitude, but the peak has a short tail. The failure duration correlates directly with the length of the $E_k$-peak's tail. The α = 100° and α = 80° configurations need more time to stabilize after failure initiates compared to the α = 160° configuration. The latter configuration exhibits the smallest amount of cracks accumulated before and at the end of failure among all simulations. The α = 20° case already has a very high number of total cracks before its first failure and a low gradient of the cracks-curve during the failure plateaus (see Fig. 3.5d). This can be explained similarly to the α = 100° pre-failure plateau by the detachment and subsequent fall-down of isolated particles. In contrast, the other simulations reveal much more intensified cracking during failure (Fig. 3.5: steeper gradient of cracks-curve reflects intensified cracking within the slope).

The slope failure evolution is additionally tracked by making use of marker particle recordings shown in Fig. 3.5e-h and Fig. A3.7. They indicate fundamental differences in the way deformation takes place within the slope. For α = 160° they show a coherent translation of the elements along the slope surface far into the failure process (Fig. 3.5e and Fig. A3.7a). In contrast to the lower marker particles, the upper two marker particles have already subsided by several meters before the main failure sets in (Fig. 3.5e). The marker particles of the α = 100° case (Fig. 3.5f and Fig. A3.7b) reveal that the mid-slope section (marker particles no.

2 and 3) drops down earlier than the lower part of the slope (marker particle no. 4). The lower two marker particles of the α = 80° case start to move a bit later but more suddenly and then faster than the upper two (Fig. 3.5g and Fig. A3.7c). For all simulations shown in Fig. 3.5e-g, marker particle no. 4 (red line), which is located at the base of the slope, does not fall down consistently like the other marker particles located further upslope. For simulations with sub-vertically dipping isotropy planes (α = 80° and α = 100°), the drop of marker particle no. 4 slows down significantly. Overall, the marker particles of α = 80° and α = 100° (Fig. 3.5e-f) move less uniformly than the ones of the α = 160° case (Fig. 3.5g; see also Fig. A3.7).

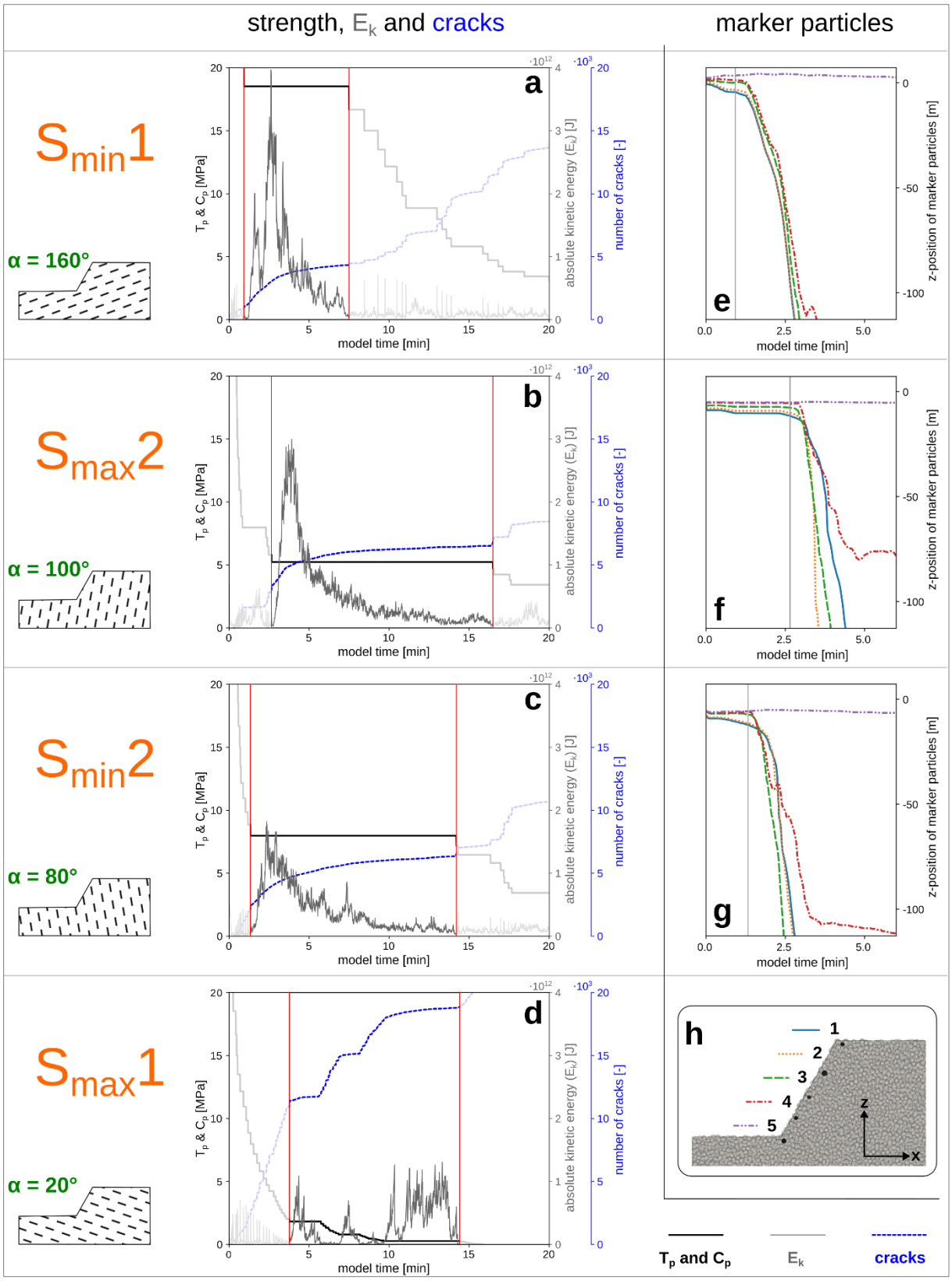


*Fig. 3.5. Failure characteristics of the four stability extrema observed for the β = 60° slope (packing P1). a - d: interparticle $T_p$ and $C_p$ reduced by SR method, absolute kinetic energy $E_k$, and cumulative number of cracks. Start and end of the main failure stage are indicated with red vertical lines. e - g: time records of the marker particles vertical position relative to their initial position; the vertical gray line indicates the start of failure; h: initial locations of marker particles on the slope.*

### 3.4.3 Stability extrema: failure behavior

The deformation processes of the four anisotropy angles that yield extreme $T_p$ and $C_p$ values at failure for $\beta = 60°$ are illustrated in Fig. 3.6. The deviatoric strain maps (Annexe A3.3; Catalano et al., 2014) are plotted for 2 states within the failure stage to examine the onset of failure and its progression throughout the slope. As an additional indicator of the deformation, the cracks (broken bonds) that have accumulated up until the respective deformation stages are also shown. In addition, we present so-called layer cake visualizations in which the particles are alternately colored according to the orientation of the isotropy plane to better illustrate the different failure behaviors at more advanced points of the simulation. Finally, we extracted videos using the layer cake visualizations of Fig. 3.6 from the beginning to the end of the failure stage for some configurations (for the Failure videos refer to the online version of this Research paper) and also displayed the final stage of the failure process, representing the displacement and the damage index of each particle (Fig. A3.8).

The failure of the stability minimum $S_{min}1$ ($\alpha = 160°$) initiates in the lower half of the slope and progresses further up along a rupture zone that eventually reaches the top of the slope (Fig. 3.6a-b). Cracks appear mostly in the zone of high deviatoric strain that predefines the post-failure rupture surface (thin white line). A quasi-translational failure is observed with a well-defined primary block that slides along the failure surface and a secondary block slightly tilted on the upper end of the mobilized volume (Fig. 3.6c). Cracks (i.e., damage) are mainly localized along the failure surface, corroborating the formation of a blocky structure that slides down the slope. The sliding mass retains most of its original shape, including a large undeformed chunk in its upper part (Fig. A3.8, a and e), and collapses with only a minimal rotation during failure. The dip of the rupture surface is slightly steeper than the dip of the isotropy plane; thus, the rupture cuts across the isotropy plane.

The mode of failure observed for $\alpha \in [130°, 170°]$ is sliding. The Failure videos show that the internal deformation at the early stages of failure is much higher for $\alpha = 130°$ and gets lower with the shallower dipping angle at $\alpha = 160°$ where big parts of the sliding mass remain coherent, and deformation localizes mostly on the rupture surfaces. For $\alpha \in [150°, 170°]$, failures involve high mobilized volumes and the lowest amount of cracks among all the cases (Fig. A3.9).

Fig. 3.6 reveals that failures observed for $\alpha = 80°$ and $\alpha = 100°$ develop clearly differently than for the sliding case ($\alpha = 160°$): both of these simulations with subvertical isotropy planes show similarities as shown in the strain deviator maps. However, deviatoric strains and cracks observed for $\alpha = 80°$ tend to initiate only at the base of the slope, while for $\alpha = 100°$ they appear on almost the entire slope from the beginning (Fig. 3.6c+e). For both cases, deformation is moving retrogressively towards the top and into the slope, soon affecting the entire slope and eventually defining the final rupture surfaces (Fig. 3.6d+f). Many more cracks in the deeper

subsurface formed for α = 80° and α = 100° compared to α = 160° since the SR at failure is more advanced (see Fig. 3.4). The layer cake visualization for α = 80° shows a clear bending or toppling of the material in the vicinity of the slope face (Fig. 3.6k), whereas the slope material appears to buckle with more particles detaching from the slope surface for α = 100° (Fig. 3.6j). For both configurations, the entirety of the slope is strongly affected by deformation, as corroborated by the high density of cracks within the slope. The fact that almost the entirety of the failed material is severely damaged after the main failure in these cases (Fig. A3.8f + g) indicates that failure occurs more diffusely compared to the blocky movement observed for α = 160° (sliding). However, the toe of the collapsed mass is located at a similar distance for the three configurations (Fig. A3.8, a-c and e-g), likely controlled by the residual friction angle of the loose elements (see also Katz et al., 2014).

All simulations with α ∈ [60°, 80°] fail in toppling or bending mode. At the onset of failure, a large portion of the slope tilts and rotates towards the toe of the slope before the material subsequently disintegrates. The failure mode obtained for α = 90° is not that clear, and it can be considered transitional between the toppling and buckling failure modes. Despite a slight buckling movement that can be spotted in the lower half of the failing slope, the rotational movement ultimately prevails, and we classified this failure as toppling (see Failure video α = 90°, accessible via the online version of this Research paper). Buckling is the mode of failure observed for all simulations with α ∈ [100°, 120°]. For all these cases, the material is bulging towards the surface in the lower half of the slope, followed by a rotational movement and severe break-up (hereafter referred to as buckling).

The shallow dipping, most stable configuration with α = 20° indicates a high amount of cracks even before the SR stops for the first time (see Fig. 3.6g and compare with Fig. 3.5d). The failure stage initiates with some superficial deformation detected in the upper part of the slope that likely corresponds to a few particles detaching. At a later point, the deviatoric strain is high along most parts of the slope surface, but, as shown in Fig. 3.6h, failure does not propagate further within the slope. The deviatoric strain at the surface of the slope (Fig. 3.6h) results from the detachment of a thin layer of particles which fall down the slope face, as illustrated in the layer cake visualization (Fig. 3.6l), and tend to accumulate at its toe (see also Fig. A3.8d + h). Interestingly, although no clear overall failure could be observed, extensive damage developed and spread over the entire slope, as evidenced by the high density of cracks within the medium. This extensive and deeply distributed damage was much more pronounced than in the other three extreme configurations, and the slope remains stable overall. Marker particles of the α = 20° case do not indicate relevant movements and were not presented.

The subdued anaclinal slopes with α ∈ [0°, 50°] fail in a mode that is best designated as “crumbling” (see Fig. 3.6l and Failure video for α = 20°, accessible via the online version of this Research paper). The transition

from crumbling to toppling mode is unambiguous (compare Failure videos α = 50° and 60°, accessible via the online version of this Research paper). This failure type observed in the most stable slope configurations is characterized by the detachment of individual particles on the slope face and, in the case of α = 50° and α ∈ [0°, 10°], by an advancing front of material disintegration from the slope face into the slope. Neither large-scale deformation before complete disintegration nor deformation acting deeper within the slope are visible for all the subdued anaclinal slopes. In Fig. A3.9, we observe that some of the crumbling failures produced for α = 20°, 30° and 40° involve very low mobilized volumes: basically, only the surface layer of particles crumbles down the slope. However, of all the simulations, the crumbling failures show the highest number of cracks in the vicinity of the slope face (Fig. A3.9).

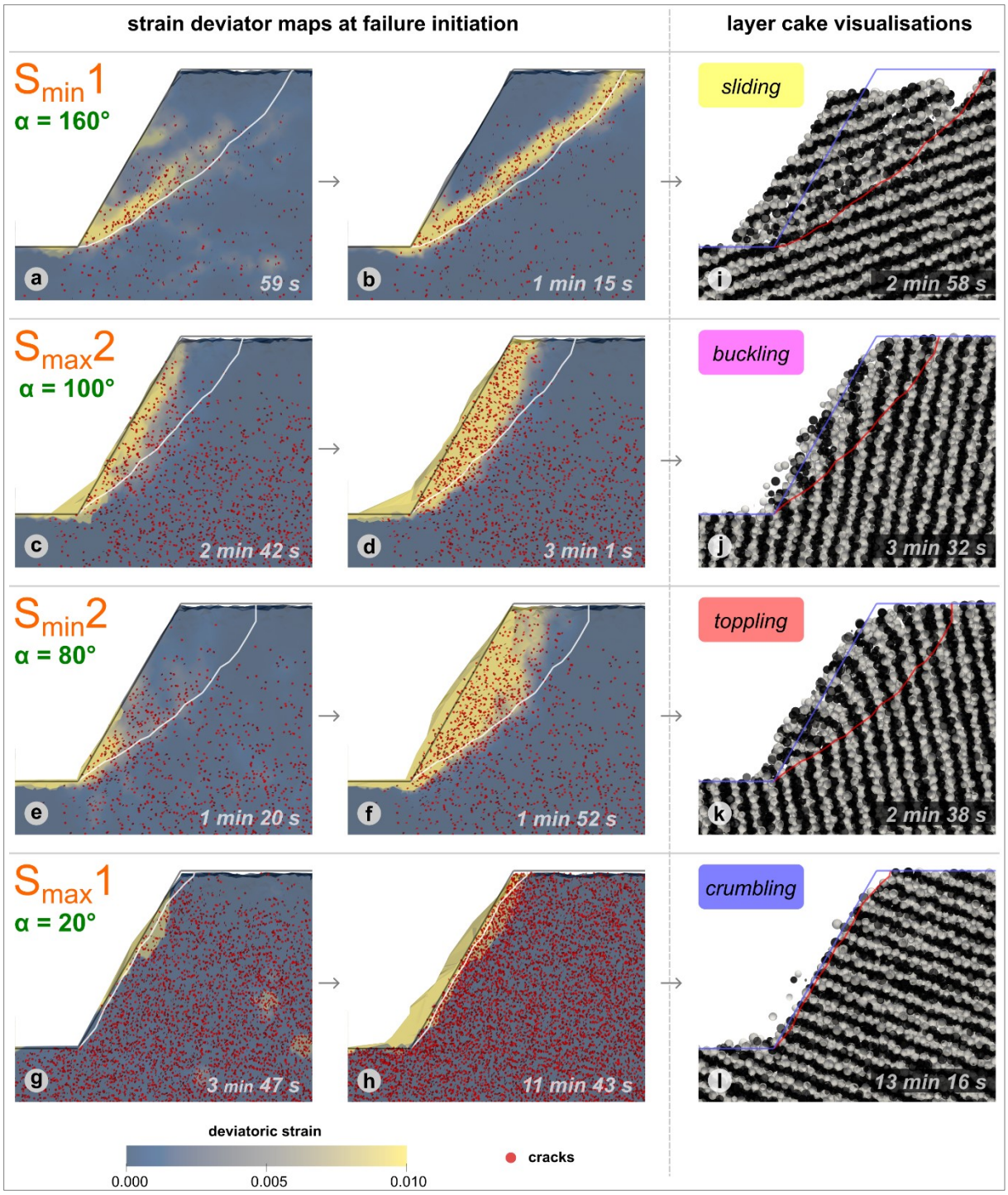


*Fig. 3.6. a - h: strain deviator maps (Annexe A3.3) with cracks at two early recording steps for the four stability extrema cases (β = 60°, packing P1). Black lines show original slope surface, white lines show rupture surfaces (Annexe A3.3). c - l: layer cake visualizations where layers are oriented according to the isotropy plane, final rupture surfaces here in red.*

## 3.5 Discussion

Our modeling results correlate relatively well with findings from former studies that have investigated a partial (Sun et al., 2022) or the full (Aydan et al., 1989; Azami et al., 2012) range of possible strength anisotropy orientations relative to the slope. In comparison to these studies also covering the full range of possible anisotropy angles, our DEM approach enables us to record the failure initiation and progression for the first time in great detail. We confirm the previous results of Azami et al. (2012) concerning stability variations according to the relative orientation of anisotropy, and go further by describing four distinct failure modes with respect to deformation characteristics, estimates of mobilized volumes and damage potential (number of cracks), as well as analyses of the kinetics of failure in both space and time (please refer to Figs. 3.4, 3.5, 3.6, A3.7, A3.8, A3.9). Overall, the configurations affected by sliding and toppling are the less stable ones, and the stability of each particular configuration is related to its failure mode (Aydan et al., 1989; Sun et al., 2022).

### 3.5.1 Modes of failure

The stability extrema generated by our numerical approach correspond to four different modes of failure that can be differentiated by initiation, localization, type, and progression of deformation within the slope (Figs. 3.5, 3.6, and A3.9): sliding (α = 160°), toppling (α = 80°), buckling (α = 100°) and a type of crumbling failure (α = 20°). Exploring the TI orientation for the entire 180° α-range (see also Failure videos, accessible via the online version of this Research paper), it further appears that the failure mode can always be described by one of these four end-members (Fig. 3.7). These anisotropy-induced failure modes are different from the circular failure mode observed in isotropic slopes (Fig. A3.10 and compared with Fig. 3.3).

The sliding and toppling modes observed for the least stable configurations are very well known and described in natural and engineered slopes with cataclinal overdip configuration or anaclinal slopes with steeply dipping layering, foliation or, joint sets (steepened escarpment), respectively (Hungr et al., 2014; Stead and Wolter, 2015). Buckling failure has been described in previous works for cataclinal slopes (e.g., Yang et al., 2020) but appears less frequently observed than the other two failure modes. Cruden (2000) also observed these three distinct failure processes (sliding, toppling, and buckling) on slopes in sedimentary rock masses in the Canadian Rockies, with buckling associated only with cataclinal dip slopes.

The crumbling mode, observed in our modeling for the highly stable shallow-dipping anaclinal configurations (subdued escarpment), has not been described as such in previous studies. However, Chigira (1992) described four modes of failure for slow-moving rock structures made up of different rock-types in Japan that are largely controlled by their host rock bedding or foliation angle. Besides the three modes of sliding,

buckling, and toppling that match very well with our findings, he observed that anaclinal slopes with shallow-dipping TI angles are either stable or fail in a “dragging” mode. This dragging mode of failure is a localized, deep-seated, ductile, and slow-moving deformation that cross-cuts the bedding or foliation at a wide angle. According to Cruden (2000), when the bedding plane angle is favorable for neither sliding nor toppling, which corresponds roughly to $\alpha \in [0°, 50°]$ (for $\beta = 60°$), failures tend to follow or be guided by structural joints or fractures oriented orthogonally to the bedding plane. This switch to a secondary preferential structural plane of failure cannot be reproduced by our current model set-up, where only one isotropy plane exists, and localized deep-seated failures with a discrete fracture plane or rupture zone that cross-cuts the isotropy plane at a wider angle do not form. Instead, the corresponding slope models remain stable, implying the possibility for such configurations to present very high slope angles. In certain mountainous regions, such as the Canadian Rockies (Cruden, 2003), the angle of slope can indeed reach 65° in low cohesion rock masses for gently dipping bedding and anaclinal slope configurations, i.e., slope values well above the values of 35–40° usually observed in mountain ranges (e.g., Schmidt and Montgomery, 1995). In addition, at the bottom of such steep cliffs, it is quite common to observe talus deposition, produced by the accumulation of numerous rock falls, similar to the accumulation of detached particles observed in our modeling for the crumbling mode.

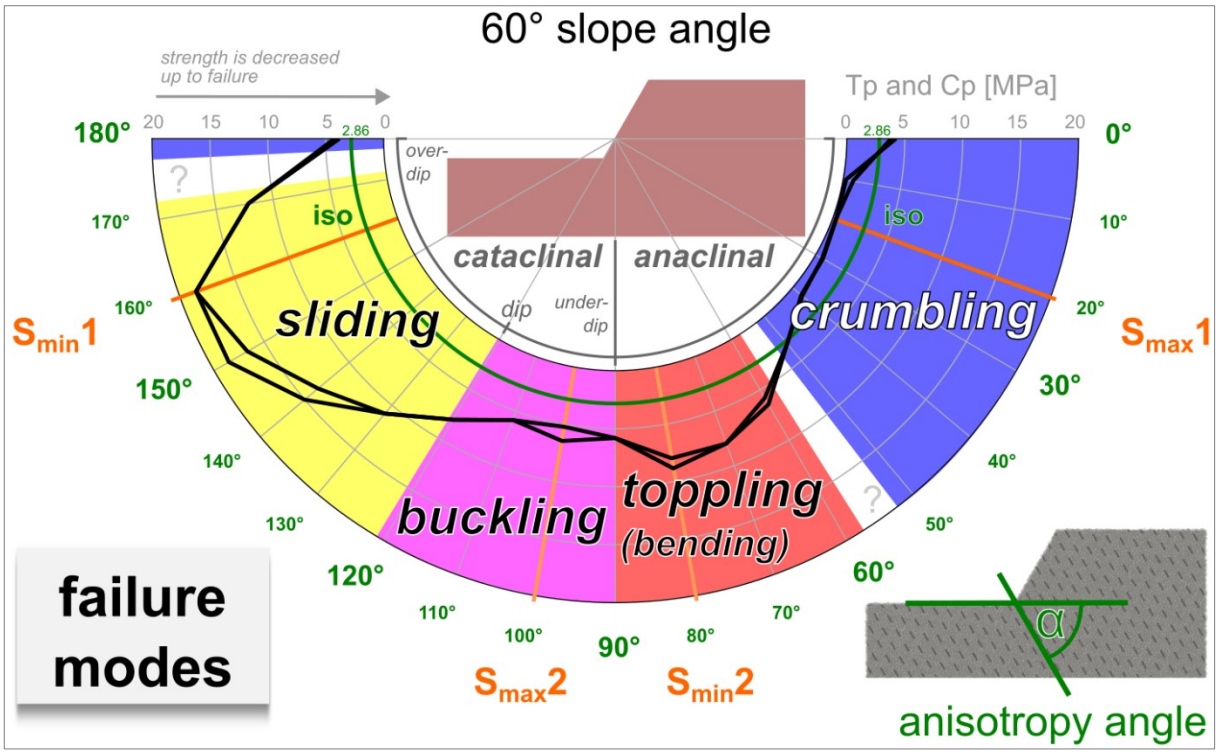


*Fig. 3.7. Failure modes observed for the β = 60° slope models depending on the orientation (α) of the isotropy plane with respect to the horizontal. See Fig. 3.6 for layer cake visualizations of extreme stability configurations ($S_{min}1$, $S_{min}2$, $S_{max}1$, $S_{max}2$) and the associated Failure video (see online version of this Research paper).*

### 3.5.2 Mechanical interpretation

The DEM set up enables us to extract the magnitudes and orientations of stresses acting on the particles that make up the slope (see Catalano et al. (2014) for details of the calculations). The magnitude of the differential stress ($\sigma_1$ - $\sigma_3$) and the orientation of the principal stress ($\sigma_1$) for all particles in the vicinity of the slope face are plotted together for both the stability extrema and the isotropic case in Fig. 3.8 just before their respective main failure initiates. They can be directly related to the dimensionless failure potential Φ, a measure of the potential for shear failure to occur adapted from Moon et al. (2017) and defined (Iverson and Reid, 1992):

$$\Phi = \left|\frac{(\sigma_1-\sigma_3)}{(\sigma_1+\sigma_3)}\right| \quad . \qquad (3.2)$$

Looking at the stresses within the isotropic slope model (Fig. 3.8), it is evident that failure occurs in the region where Φ > 1. This is much less evident for the anisotropic slopes because of the varying relation between stress orientation vs. isotropy plane orientation, and the direction-dependent shear strength (Fu and Dafalias, 2011).

In the overdip configuration failing in the sliding mode of $_{Smin}1$ (α = 160°), the isotropy plane is oriented favorably for the development of a shear zone oriented subparallel to it, as evidenced by the distribution of Φ within the slope (Fig. 3.8). Moreover, the principal stress tends to be slightly tilted towards the direction of the isotropy plane, thus favoring stress concentration along this direction.

When the isotropy plane dips deeper than the slope face, the material cannot fail anymore through sliding along the isotropy plane, and slope stability increases substantially (Figs. 3.4 and 3.7). For α = 100° ($S_{max}2$), Φ < 1 in most parts of the slope except along the slope face, and the principal stress is subparallel to the isotropy plane. This stress distribution favors transverse buckling, which initiates at the base of the slope, where the compressive stress is higher, and progresses upward as a result of the progressive material excavation (Fig. 3.6).

For toppling failures occurring in anaclinal slopes with steepened escarpments (α ∈ [60°, 90°]), our results tend to verify the criterion proposed by Goodman and Bray (1976), assuming an emergent friction angle of $\varphi \leq$ ~30°, which seems realistic in consideration of our analysis of the emergent mechanical properties of the DEM models (Section 2.3.2, Fig. 3.7). In these configurations, toppling initiates as a result of shearing/sliding along the isotropy planes at the bottom half of the slope, as illustrated in Fig. 3.8c for α = 80° ($S_{min}2$). There, contrasting Φ-values seem to be localized preferentially along the isotropy planes. As for the sliding mode, the mobilized volume is bigger than for the isotropic case and corresponds to the area where Φ > 1.

Unlike the sliding, buckling, and toppling failure modes, the crumbling failure mode corresponds to cases that are mostly more stable than the isotropic case (Fig. 3.7). Why are the anaclinal subdued slopes so stable despite reducing the inter-particle strength substantially up to zero? According to Goodman and Bray's (1976) criterion, shearing/ sliding cannot develop along the isotropy plane, and toppling cannot occur. Additionally, either circular or translational sliding failures would need shear zones to cross-cut the isotropy plane at a wide angle. Interestingly, the major principal stress ($\sigma_1$) of $S_{max}1$ ($\alpha = 20°$) does deviate more from the vertical than in the other extreme configurations, with $\sigma_1$ oriented almost orthogonally to the isotropy plane (Fig. 3.8d), a configuration that would correspond to the highest strength configuration for TI materials (Fig. 3.1). The slope finds itself in a "locking state" that promotes some sort of hardening of the material against failure (Fig. 3.8d). One can notice that bands of higher Φ values are localized along the isotropy plane: given the orientation of these bands with respect to the slope geometry and, given the boundary condition on the right side of the model, the overall slope failure towards the left is impeded and only superficial material disintegration occurs along the slope face (i.e., crumbling). Even if we might question the role of bond reorientation (intrinsically linked to the introduction of anisotropy into our model, Fig. 3.1a) in this hardening phenomenon, we note that this increase in shear resistance for certain isotropy plane orientations relative to the principal stress direction is known both from numerical and analog shear tests (Fu and Dafalias, 2011; Tong et al., 2014).

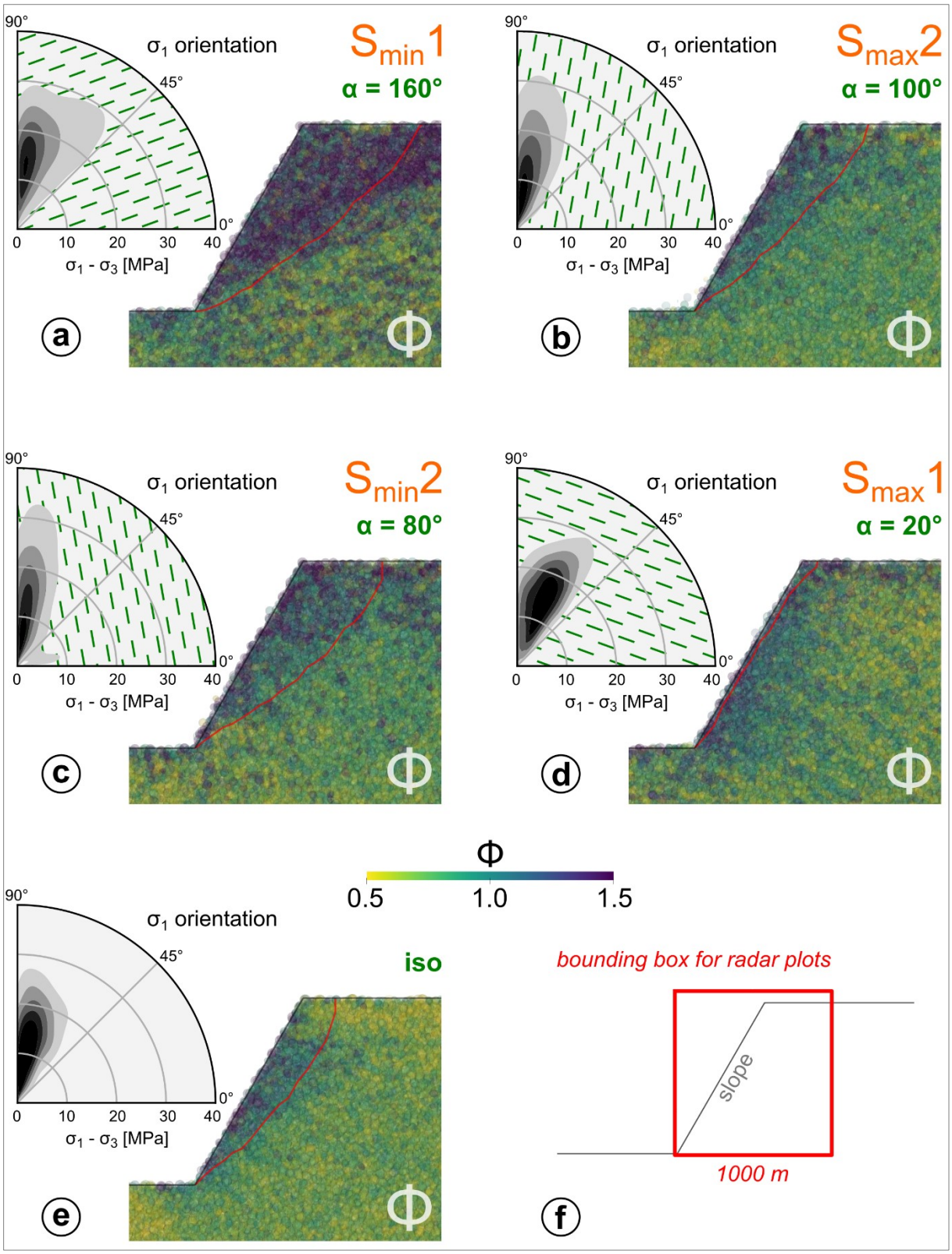


*Fig. 3.8. Stress distributions within the most representative slope models before failure: density plots show differential stress ($\sigma_1$-$\sigma_3$) plotted against principal stress orientation ($\sigma_1$) and slope visualizations show the dimensionless failure potential Φ. a-d: stability extrema with strength anisotropy, e: isotropic simulation, f: only particles in red box are used for the density plots.*

### 3.5.3 *Comparison with natural settings*

#### *3.5.3.1 How representative is our DEM approach?*

To remain practical, a model designed to represent real-world phenomena must adopt simplifications to reduce the complexity of a natural environment. Natural slopes do generally comprise a lot of heterogeneities in the form of different lithological layers and discrete structures like joints, faults, and folds. Additionally, rock texture and strength may vary towards the surface and along discontinuities due to progressive fatigue and weathering processes (e.g., Brantut et al., 2013; Viles, 2013), and natural slopes often present complex topography that evolves gradually over time. All these ingredients that make every natural slope unique have a great impact on their mechanical behavior and, subsequently, on their failure process and mode. Our slope models do not account for geometrical and mechanical complexity. They are based on a simple step like geometry to be as general as possible and consider a diffuse material anisotropy rather than discrete structures in order to ease the consideration of scale effect and to avoid the explicit influence of only a few critical structures on the overall behavior. Despite their simplicity, our numerical simulations are capable to reproduce fairly accurate failure modes observed in natural settings that are controlled by rock strength anisotropy as shown, for instance, in studies focusing on landslides in Japan (Chigira, 1992, 2000) or in the Canadian Rocky Mountains (Cruden and Hu, 1996, 1999; Cruden, 2000, 2003). Strikingly, in their analysis of landslides triggered by the 1933 Diexi earthquake in China, Cui et al. (2022) found no rock topples but mostly rock slides on cataclinal slopes, and no rock slides but mostly rock topples on anaclinal slopes, which coincides well with our modeling results.

Furthermore, the presence of groundwater is known to be one of the most influential driving and triggering factors of slope failure due to the effect of pore pressure on the effective stress (Jaeger et al., 2007; Glastonbury and Fell, 2010; Lacroix et al., 2020). We do not account for groundwater in our modeling, and thus only consider total stress analysis under dry conditions, although it is well known that slope deformations are often related to short-term variations of pore pressures (Agliardi et al., 2020).

The scaling we applied to derive realistic slope-scale mechanical properties based on the GSI approach was not initially designed for anisotropic rock masses (Marinos and Carter, 2018) and we are also aware that estimating GSI-values for large natural slopes is a complex undertaking (Brideau et al., 2009).

Another important aspect that distinguishes our simulations from natural slopes is the strength reduction method we applied. In our simulations, slopes are brought to failure by a homogeneous incremental decrease of strength up to a point where a small disturbance expands to a larger failure. Topography is already cut when SR sets in which does not correspond to the gradual evolution of slopes in natural settings. In nature,

strength degradation does happen over time due to progressive weathering of bedrock, deepening of the front of alteration (e.g., Anderson et al., 2019), or stress fatigue induced by repeated seismic shaking (Gischig et al., 2016) or/and pore pressure increase (Petley et al., 2005; Agliardi et al., 2020). However, strength reduction within slopes is certainly not homogeneously distributed -either in space or in time as it is prescribed in our models. For this reason, it is difficult to transfer the temporal evolution of our simulated slope failures to natural slopes. Nevertheless, we observe some relative differences for failure duration between different configurations over the full range of possible isotropy plane orientations (α-angle) which might be of interest for field studies (see Fig. A3.9c).

In our model results, the failure duration is minimal for the sliding mode, and double for the steeply dipping isotropy planes affected by buckling or toppling modes of deformation. It is difficult to assess the duration of failure of natural landslides. However, it may be asked whether anisotropic configurations and failure duration have an influence on the kinetic energy of the rock mass and on the mobility of the landslides. Similarly, could the differences observed between failure modes in the manner and speed at which failure propagates from bottom to top indicate differences in the type of instability? A reduced catalogue of DSGSDs in the Italian Alps (Ambrosi and Crosta, 2006) seems to indicate that these deep, progressive deformations develop more when the foliation of the rocks is relatively steep, i.e., when buckling or toppling are favored. At this stage, more exhaustive studies would be necessary, but the results of our study suggest a potential influence of the relative orientation of anisotropy on the overall dynamics of gravitational instabilities.

In concomitance with time scaling considerations, the transposition of our results to natural cases may require the addition of debris erosion in our modeling procedure. Indeed, as the collapse progresses, erosion of the debris base, particularly by a river, will modify the geometry of the debris apron and could promote the mobility of the collapsing slope. Future models dedicated to monitoring the temporal evolution of slope failure should consider erosion processes.

*3.5.3.2 Rock anisotropy and hillslope angle at erosional steady state*

In mountainous environments, as for any natural setting, strength reduction within slopes due to progressive weathering and fatigue of rock mass lead to a decrease of the resisting forces and therefore to hillslope instability. However, landslide triggering also is first of all driven by an increase of the tractive forces, i.e., the progressive increase of slope angle and relief. As tectonic processes uplift the land mass, rivers respond by incising their channel, thus lowering the local base level of the hillslopes: this leads to slope steepening and hillslope height increase until mechanical instability is reached. As denudation exhumes bedrock over time, the slope angles are therefore presumed to episodically adjust through landsliding, with an average angle that depends on the local bedrock strength (Townsend et al., 2020; Lavé et al., 2023). In the case of bedrock presenting TI characteristics (most sedimentary and metamorphic rocks), we expect the stability of slopes and average slope angles to vary significantly with slope orientations or slope aspects, as simulated by our study. In particular, anaclinal slopes should fail at higher slope angles than cataclinal slopes, as shown, for example, in Fig. 3.4 for $T_p = C_p = 5$ MPa: for these fixed inter-particle bond properties, 60° sloping scarps developed in an anaclinal configuration are still stable, whereas the 40° sloping scarps developed in the overdip cataclinal setting have already failed. This expected result was indeed observed in the Rocky Mountains (Cruden, 2000). Although various earlier studies have looked at the relationship between the direction of anisotropy and slope orientation, they have mainly focused on the modes of failure (Cruden and Hu, 1996, 1999; Cruden, 2000, 2003; Chigira, 1992, 2000; Teshebaeva et al., 2019; Cui et al., 2022) or on variations in landslide activity and frequency (Cruden and Eaton, 1987; Cui et al., 2022), but have paid, to our knowledge, little attention to the influence of this relative orientation on slope steepness.

To confirm that the anisotropy of the rock's resistance ultimately contributes to control the average slope angles in natural settings, we need to find a region where anisotropic structures are uniform at a scale larger than the typical hillslope length. Often, bedrock anisotropy is variable in an area due to folds, faults, and lithological changes, but in some places, the tectonic setting can result in large terrains of uniformly dipping unfolded rocks. Despite some minor secondary folding, this is the case for the south-facing slopes of the Annapurna Massif in central Nepal, where overthrusting due to continental collision is responsible for gneisses dipping consistently 10° - 40° towards NW - NE in between two major tectonic structures, the Main Central Thrust (MCT) and the South Tibetan Detachment (STD): see Fig. 3.9a-b and refer to geological maps of Colchen et al. (1986) and Parsons et al. (2016). There, we performed a simple raster data analysis on a 30 m digital terrain model (Hawker and Neal, 2021) for an area high 2000–4000 m a.s.l. (red polygon in Fig. 3.9a) actively eroding but devoid of any geomorphological evidence of hillslope glacial erosion and well below the permanently frozen areas where slope and rock mass cohesion are observed to be distinctively higher (Lavé et al., 2023). For the selected area, slope angle distributions appear to vary with slope orientation (Fig. 3.9c): south-facing slopes are, on average, up to 9° steeper than slopes facing east, north, and west. Anaclinal slopes

are, therefore, steeper than cataclinal slopes, as proven by our analysis (compare Figs. 3.4 and 3.9). This finding agrees well with the observations of Uhlir and Schramm (1997) for central Himalayan slopes in a near-identical geological setting: constant dip of bedrock schistosity towards the north coincides with south-facing-slopes significantly steeper than north-facing slopes. The slope-aspect diagram in Fig. 3.9c is qualitatively aligned with our modeling expectations if the variation in slope angle as a function of slope orientation is considered to be the cause of varying slope stability. However, a quantitative analysis of slope-scale mechanical conditions is difficult to perform at this stage, as it would be necessary to characterize the strength anisotropy of Himalayan gneisses, particularly at the scale of the hillslope (see Section 2.3). It would also be necessary to characterize slope stability when the azimuth of the isotropy plane is different from that of the topographic slope, i.e., we would need to numerically explore not only the dip angle of the isotropy plane in two dimensions but also its azimuth between 0 and 180° relative to the azimuth of the topographic slope in three dimensions. Additionally, the role of other factors, such as the distribution and orientation of fractures or the hydrology of groundwater, which is certainly influenced by stratified or foliated rocks (e.g., Dong et al., 2012), should be addressed.

As an additional corollary to this southern Annapurna slopes setting, we would expect, according to our modeling, differences in failure modes depending on the orientation of the slopes. Failures modes are difficult to assess by conventionally available satellite imagery due to rapid re-vegetation of landslide scars and the sparsity of large failures (>1 $km^2$ landslides only occur every ~500 years following Marc et al. (2019)). Capturing a statistically representative frequency of the different failure modes for different slope orientations would require an exceptional number of slope failure events due to, for example, a very large earthquake (as in Cui et al. (2022) for the eastern margin of the Tibetan plateau), and/or the availability of a high-resolution digital terrain model (e.g., airborne Lidar). Despite the absence of such a quantitative approach, observations along the southern flank of the Himalayas (see Fig. A3.11) are at least qualitatively in line with our model predictions. For instance, in the Ankhu Khola region (80 km to the east of the southern flank of the Annapurna Massif, in a near-identical setting), in conjunction with slope angle variability, slope failure modes are particularly contrasted between north-facing (cataclinal) and south-facing (anaclinal) slopes: low-volume rock falls, rock topples, and small rockslides appear to be more frequently observed on south-facing slopes, whereas numerous voluminous translational rockslides detach sub-parallel to the schistosity planes along north-facing slopes (Thouret, 1983; Uhlir and Schramm, 1997).

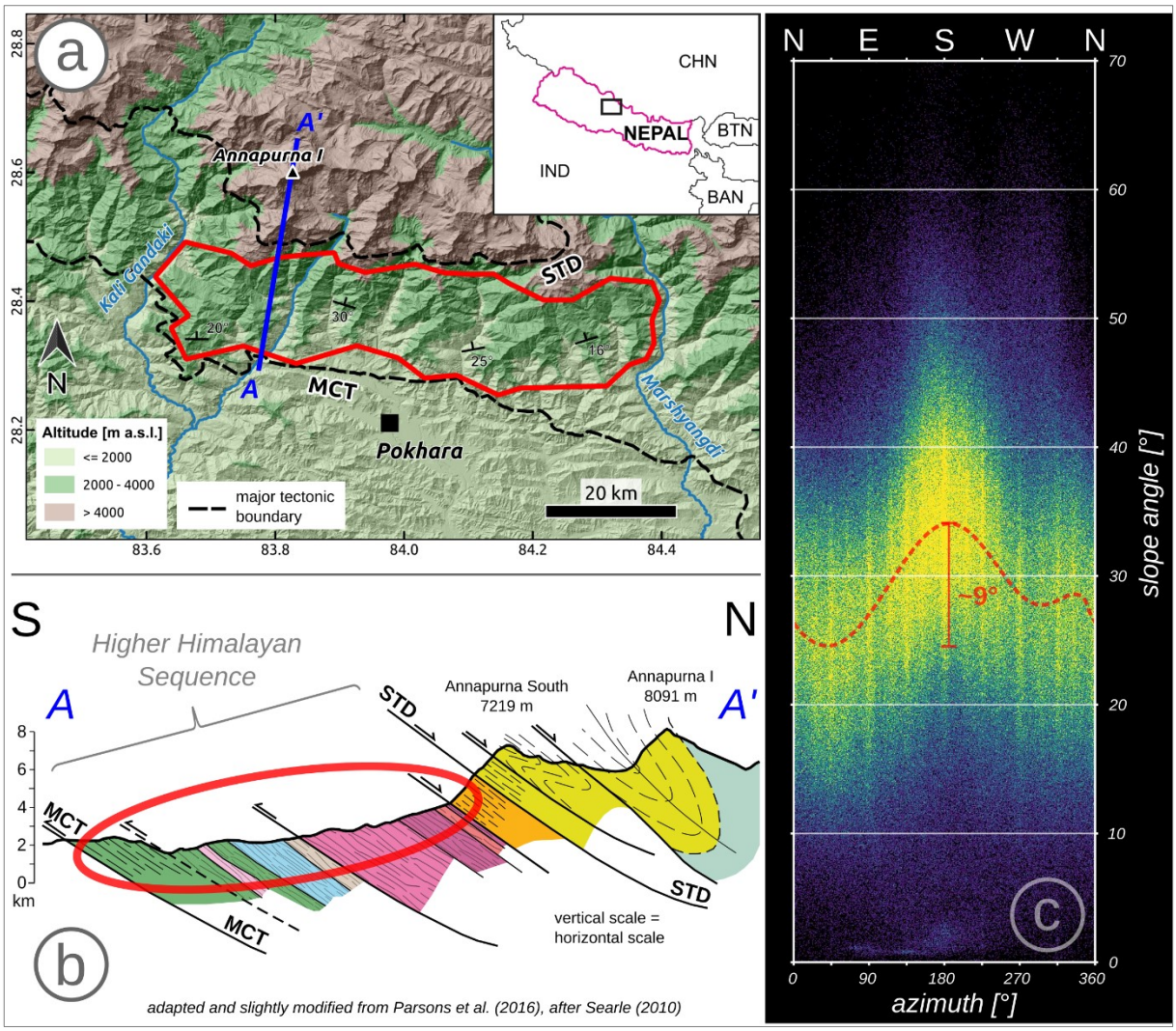


*Fig. 3.9. a: Topographic map of the Annapurna massif with location of area selected for raster data extraction (red polygon): country borders in white box (top left) serve as orientation, MCT and STD were extracted from the geological map of Parsons et al. (2016); b: tectonic profile modified after Searle (2010) (see location of blue line in a), red ellipse indicates terrain extracted for raster analysis; c) scatter plot showing azimuth - slope angle relationship colored by density (linear), red dashed line indicates the maximum density along azimuth.*

### 3.6 Conclusion

Understanding the factors influencing the deformation and failure of rock slopes is fundamental to assessing slope failure hazard better and understanding landscape evolution. Using parametric numerical modeling, we explored the influence of rock anisotropy on slope stability, focusing more specifically on slopes made of transverse isotropic materials and investigating their stability potential and deformation modes. Our study enables us to identify distinct failure behaviors caused by different orientations of the isotropy plane with respect to the slope face, as regularly observed on natural and artificial slopes: sliding in overdip cataclinal slopes, toppling (bending) in anaclinal slopes with steepened escarpment, and buckling in underdip cataclinal slopes. One can also note that the crumbling failure mode does resemble rockfalls on anaclinal subdued slopes. Moreover, our approach enables us to relate the stability of slopes to these deformation modes. It suggests, for instance, that anaclinal slopes are generally more stable than cataclinal ones, with subdued escarpments showing the highest stability potential and overdip cataclinal slopes showing the lowest stability potential. Obviously, natural slopes exceed the bounds suggested by our modeling exercise due to their inherent complexity. Nonetheless, our results comprehensively describe all the first-order mechanisms that govern landscape evolution in mountainous areas where stability potential drives the topography. To go further into the analysis, one would need to include the contribution of additional factors to slope deformation, like pore pressure built-up or seismic shaking, that could greatly impact the prevailing failure mode and other failure characteristics. Nevertheless, our study, like that of Chigira (2000) on natural objects, indicates a whole typology of deformation modes that seem to depend directly on the presence of anisotropic rocks and on the relative anisotropy orientation with respect to the topography. It is difficult to know whether other factors may also lead to the emergence of the four identified end-members or whether the orientation of the anisotropy is the sole source of this typology. In any case, slope stability analyses should consider this parameter more systematically so that the various possible deformation modes and associated hazards can be clearly identified.

# References:


Adhikary, D.P., Dyskin, A.V., Jewell, R.J., Stewart, D.P., 1997. A study of the mechanism of flexural toppling failure of rock slopes. Rock Mech Rock Engng 30, 75–93. https://doi.org/10.1007/BF01020126

Agliardi, F., Crosta, G.B., Frattini, P., 2012. Slow rock-slope deformation, in: Clague, J.J., Stead, D. (Eds.), Landslides. Cambridge University Press, Cambridge, pp. 207–221. https://doi.org/10.1017/CBO9780511740367.019

Agliardi, F., Scuderi, M.M., Fusi, N., Collettini, C., 2020. Slow-to-fast transition of giant creeping rockslides modulated by undrained loading in basal shear zones. Nat Commun 11, 1352. https://doi.org/10.1038/s41467-020-15093-3

Ambrosi, C., Crosta, G.B., 2006. Large sackung along major tectonic features in the Central Italian Alps. Engineering Geology 83, 183–200. https://doi.org/10.1016/j.enggeo.2005.06.031

Anderson, R.S., Rajaram, H., Anderson, S.P., 2019. Climate driven coevolution of weathering profiles and hillslope topography generates dramatic differences in critical zone architecture. Hydrological Processes 33, 4–19. https://doi.org/10.1002/hyp.13307

Aydan, Ö., Shimizu, Y., Ichikawa, Y., 1989. The effective failure modes and stability of slopes in rock mass with two discontinuity sets. Rock Mech Rock Engng 22, 163–188. https://doi.org/10.1007/BF01470985

Azami, A., Yacoub, T., Curran, J., 2012. Effects of strength anisotropy on the stability of slopes. Presented at the 65th Canadian Geotechnical Conference, CGS Geo-Manitoba.

Barton, N., Quadros, E., 2015. Anisotropy is Everywhere, to See, to Measure, and to Model. Rock Mech Rock Eng 48, 1323–1339. https://doi.org/10.1007/s00603-014-0632-7

Benko, B., Stead, D., 1998. The Frank slide: a reexamination of the failure mechanism. Canadian Geotechnical Journal 35, 299–311.

Bonilla-Sierra, V., Elmouttie, M., Donzé, F.-V., Scholtès, L., 2017. Composite wedge failure using photogrammetric measurements and DFN-DEM modelling. Journal of Rock Mechanics and Geotechnical Engineering 9, 41–53. https://doi.org/10.1016/j.jrmge.2016.08.005

Bonilla-Sierra, V., Scholtès, L., Donzé, F.V., Elmouttie, M.K., 2015. Rock slope stability analysis using photogrammetric data and DFN–DEM modelling. Acta Geotech. 10, 497–511. https://doi.org/10.1007/s11440-015-0374-z

Bonnelye, A., Schubnel, A., David, C., Henry, P., Guglielmi, Y., Gout, C., Fauchille, A.-L., Dick, P., 2017. Strength anisotropy of shales deformed under uppermost crustal conditions. Journal of Geophysical Research: Solid Earth 122, 110–129. https://doi.org/10.1002/2016JB013040

Brideau, M.-A., Yan, M., Stead, D., 2009. The role of tectonic damage and brittle rock fracture in the development of large rock slope failures. Geomorphology 103, 30–49. https://doi.org/10.1016/j.geomorph.2008.04.010

Catalano, E., Chareyre, B., Barthélémy, E., 2014. Pore-scale modeling of fluid-particles interaction and emerging poromechanical effects. International Journal for Numerical and Analytical Methods in Geomechanics 38, 51–71. https://doi.org/10.1002/nag.2198

Cheng, Y.M., Lau, C.K., 2014. Slope stability analysis and stabilization: new methods and insight, Second edition. ed. CRC Press, Taylor & Francis Group, Boca Raton.

Chigira, M., 2000. Geological structures of large landslides in Japan. Journal of Nepal Geological Society 22, 497–504. https://doi.org/10.3126/jngs.v22i0.32423

Chigira, M., 1992. Long-term gravitational deformation of rocks by mass rock creep. Engineering Geology 32, 157–184.

Colchen, M., Le Fort, P., Pêcher, A., 1986. Annapurna–Manaslu–Ganesh Himal. Centre National de la Recherche Scientifique, Paris 75–136.

Cotton, C.A., 1949. Geomorphology: an introduction to the study of landforms. John Wiley & sons, New York.

Cruden, D., Hu, X.Q., 1996. Hazardous Modes of Rock Slope Movement in the Canadian Rockies. Environmental and Engineering Geoscience 2, 507–516. https://doi.org/10.2113/gseegeosci.II.4.507

Cruden, D.M., 2003. The shapes of cold, high mountains in sedimentary rocks. Geomorphology 55, 249–261. https://doi.org/10.1016/S0169-555X(03)00143-0

Cruden, D.M., 2000. Some forms of mountain peaks in the Canadian Rockies controlled by their rock structure. Quaternary International 68–71, 59–65. https://doi.org/10.1016/S1040-6182(00)00032-X

Cruden, D.M., Eaton, T.M., 1987. Reconnaissance of rockslide hazards in Kananaskis Country, Alberta. Can. Geotech. J. 24, 414–429. https://doi.org/10.1139/t87-052

Cruden, D.M., Hu, X.-Q., 1999. The shapes of some mountain peaks in the Canadian Rockies. Earth Surface Processes and Landforms 24, 1229–1241. https://doi.org/10.1002/(SICI)1096-9837(199912)24:13<1229::AID-ESP42>3.0.CO;2-1

Cundall, P.A., Strack, O.D.L., 1979. A discrete numerical model for granular assemblies. Géotechnique 29, 47–65. https://doi.org/10.1680/geot.1979.29.1.47

Densmore, A.L., Hovius, N., 2000. Topographic fingerprints of bedrock landslides. Geology 28, 371–374.

Dinç, Ö., Scholtès, L., 2018. Discrete Analysis of Damage and Shear Banding in Argillaceous Rocks. Rock Mech Rock Eng 51, 1521–1538. https://doi.org/10.1007/s00603-017-1397-6

Donath, F.A., 1961. Experimental Study of Shear Failure in Anisotropic Rocks. Geol Soc America Bull 72, 985. https://doi.org/10.1130/0016-7606(1961)72[985:ESOSFI]2.0.CO;2

Dong, J.-J., Tu, C.-H., Lee, W.-R., Jheng, Y.-J., 2012. Effects of hydraulic conductivity/strength anisotropy on the stability of stratified, poorly cemented rock slopes. Computers and Geotechnics 40, 147–159. https://doi.org/10.1016/j.compgeo.2011.11.001

Fu, P., Dafalias, Y.F., 2011. Study of anisotropic shear strength of granular materials using DEM simulation. Int. J. Numer. Anal. Meth. Geomech. 35, 1098–1126. https://doi.org/10.1002/nag.945

Gischig, V., Preisig, G., Eberhardt, E., 2016. Numerical Investigation of Seismically Induced Rock Mass Fatigue as a Mechanism Contributing to the Progressive Failure of Deep-Seated Landslides. Rock Mech Rock Eng 49, 2457–2478. https://doi.org/10.1007/s00603-015-0821-z

Glastonbury, J., Fell, R., 2010. Geotechnical characteristics of large rapid rock slides. Can. Geotech. J. 47, 116–132. https://doi.org/10.1139/T09-080

Goodman, R.E., Bray, J.W., 1976. Toppling of rock slopes. Presented at the Proc. Specialty Conf. on Rock Engineering for Foundations and Slopes, Amer. Soc. Civil Eng., pp. 201–234.

Grelle, G., Revellino, P., Donnarumma, A., Guadagno, F.M., 2011. Bedding control on landslides: a methodological approach for computer-aided mapping analysis. Nat. Hazards Earth Syst. Sci. 11, 1395–1409. https://doi.org/10.5194/nhess-11-1395-2011

Hawker, L., Neal, J., 2021. FABDEM V1-0. https://doi.org/10.5523/bris.25wfy0f9ukoge2gs7a5mqpq2j7

Hoek, E., 1964. Fracture of anisotropic rock. Journal of the Southern African Institute of Mining and Metallurgy 64, 501–518.

Hoek, E., Carranza-Torres, C., Corkum, B., 2002. Hoek-Brown failure criterion-2002 edition. Proceedings of NARMS-Tac 1, 267–273.

Hoek, E., Diederichs, M.S., 2006. Empirical estimation of rock mass modulus. International Journal of Rock Mechanics and Mining Sciences 43, 203–215. https://doi.org/10.1016/j.ijrmms.2005.06.005

Huggel, C., Clague, J.J., Korup, O., 2012. Is climate change responsible for changing landslide activity in high mountains? Earth Surface Processes and Landforms 37, 77–91. https://doi.org/10.1002/esp.2223

Hungr, O., Leroueil, S., Picarelli, L., 2014. The Varnes classification of landslide types, an update. Landslides 11, 167–194. https://doi.org/10.1007/s10346-013-0436-y

Iverson, R.M., Reid, M.E., 1992. Gravity-driven groundwater flow and slope failure potential: 1. Elastic Effective-Stress Model. Water Resour. Res. 28, 925–938. https://doi.org/10.1029/91WR02694

Jaboyedoff, M., Crosta, G.B., Stead, D., 2011. Slope tectonics: a short introduction. SP 351, 1–10. https://doi.org/10.1144/SP351.1

Jaeger, J.C., Cook, N.G.W., Zimmerman, R.W., 2007. Fundamentals of rock mechanics, 4th ed. ed. Blackwell Pub, Malden, MA.

Katz, O., Morgan, J.K., Aharonov, E., Dugan, B., 2014. Controls on the size and geometry of landslides: Insights from discrete element numerical simulations. Geomorphology 220, 104–113. https://doi.org/10.1016/j.geomorph.2014.05.021

Korup, O., Densmore, A.L., Schlunegger, F., 2010. The role of landslides in mountain range evolution. Geomorphology 120, 77–90. https://doi.org/10.1016/j.geomorph.2009.09.017

Lacroix, P., Handwerger, A.L., Bièvre, G., 2020. Life and death of slow-moving landslides. Nat Rev Earth Environ 1, 404–419. https://doi.org/10.1038/s43017-020-0072-8

Lavé, J., Guérin, C., Valla, P.G., Guillou, V., Rigaudier, T., Benedetti, L., France-Lanord, C., Gajurel, A.P., Morin, G., Dumoulin, J.P., Moreau, C., Galy, V., 2023. Medieval demise of a Himalayan giant summit induced by mega-landslide. Nature 619, 94–101. https://doi.org/10.1038/s41586-023-06040-5

Leshchinsky, D., Baker, R., Silver, M.L., 1985. Three dimensional analysis of slope stability. Int. J. Numer. Anal. Methods Geomech. 9, 199–223. https://doi.org/10.1002/nag.1610090302

Li, X., Wartman, J., Tang, H., Yan, J., Luo, H., Hu, W., 2014. Dynamic Centrifuge Modelling Tests for Sliding Rock Slopes, in: Sassa, K., Canuti, P., Yin, Y. (Eds.), Landslide Science for a Safer Geoenvironment. Springer International Publishing, Cham, pp. 75–79. https://doi.org/10.1007/978-3-319-05050-8_13

Marinos, P., Hoek, E., 2000. GSI: a geologically friendly tool for rock mass strength estimation. Presented at the ISRM international symposium, ISRM, p. ISRM-IS.

Marinos, Vassilis., Carter, Trevor.G., 2018. Maintaining geological reality in application of GSI for design of engineering structures in rock. Engineering Geology 239, 282–297. https://doi.org/10.1016/j.enggeo.2018.03.022

McLamore, R., Gray, K.E., 1967. The Mechanical Behavior of Anisotropic Sedimentary Rocks. Journal of Engineering for Industry 89, 62–73. https://doi.org/10.1115/1.3610013

Moon, S., Perron, J.T., Martel, S.J., Holbrook, W.S., St. Clair, J., 2017. A model of three-dimensional topographic stresses with implications for bedrock fractures, surface processes, and landscape evolution: Three-Dimensional Topographic Stress. J. Geophys. Res. Earth Surf. 122, 823–846. https://doi.org/10.1002/2016JF004155

Munjiza, A.A., 2004. The combined finite-discrete element method. John Wiley & Sons.

Nasseri, M.H.B., Rao, K.S., Ramamurthy, T., 2003. Anisotropic strength and deformational behavior of Himalayan schists. International Journal of Rock Mechanics and Mining Sciences 40, 3–23. https://doi.org/10.1016/S1365-1609(02)00103-X

Niandou, H., Shaoi, J.F., HENRYf, J.P., Fourmaintraux, D., 1997. Laboratory Investigation of the Behaviour of Tournemire Shale. Int. J. Rock Mech. Min. Sci. 34, 3–16.

Parsons, A.J., Law, R.D., Searle, M.P., Phillips, R.J., Lloyd, G.E., 2016. Geology of the Dhaulagiri-Annapurna-Manaslu Himalaya, Western Region, Nepal. 1:200,000. Journal of Maps 12, 100–110. https://doi.org/10.1080/17445647.2014.984784

Petley, D.N., Higuchi, T., Petley, D.J., Bulmer, M.H., Carey, J., 2005. Development of progressive landslide failure in cohesive materials. Geol 33, 201. https://doi.org/10.1130/G21147.1

Read, J., Stacey, P. (Eds.), 2009. Guidelines for open pit slope design, Reprint. with corr. ed. CSIRO Publ. [u.a.], Collingwood, Vic.

Roy, S., Baruah, A., Misra, S., Mandal, N., 2015. Effects of bedrock anisotropy on hillslope failure in the Darjeeling-Sikkim Himalaya: an insight from physical and numerical models. Landslides 12, 927–941. https://doi.org/10.1007/s10346-014-0513-x

Saroglou, H., Marinos, P., Tsiambaos, G., 2004. The anisotropic nature of selected metamorphic rocks from Greece. Journal of the Southern African Institute of Mining and Metallurgy 104, 217–222. https://doi.org/10.10520/AJA0038223X_2825

Schmidt, K.M., Montgomery, D.R., 1995. Limits to Relief. Science 270, 617–620. https://doi.org/10.1126/science.270.5236.617

Scholtès, L., Donzé, F.V., 2015. A DEM analysis of step-path failure in jointed rock slopes. Comptes Rendus Mécanique 343, 155–165. https://doi.org/10.1016/j.crme.2014.11.002

Scholtès, L., Donzé, F.-V., 2013. A DEM model for soft and hard rocks: Role of grain interlocking on strength. Journal of the Mechanics and Physics of Solids 61, 352–369. https://doi.org/10.1016/j.jmps.2012.10.005

Scholtès, L., Donzé, F.-V., 2012. Modelling progressive failure in fractured rock masses using a 3D discrete element method. International Journal of Rock Mechanics and Mining Sciences 52, 18–30. https://doi.org/10.1016/j.ijrmms.2012.02.009

Searle, M.P., 2010. Low-angle normal faults in the compressional Himalayan orogen; Evidence from the Annapurna–Dhaulagiri Himalaya, Nepal. Geosphere 6, 296–315. https://doi.org/10.1130/GES00549.1

Šmilauer, V., Angelidakis, V., Catalano, E., Caulk, R., Chareyre, B., Chèvremont, W., Dorofeenko, S., Duriez, J., Dyck, N., Elias, J., Er, B., Eulitz, A., Gladky, A., Guo, N., Jakob, C., Kneib, F., Kozicki, J., Marzougui, D., Maurin, R., Modenese, C., Pekmezi, G., Scholtès, L., Sibille, L., Stransky, J., Sweijen, T., Thoeni, K., Yuan, C., 2021. Yade documentation. The Yade Project. https://doi.org/10.5281/zenodo.5705394

Stead, D., Wolter, A., 2015. A critical review of rock slope failure mechanisms: The importance of structural geology. Journal of Structural Geology 74, 1–23. https://doi.org/10.1016/j.jsg.2015.02.002

Stockton, E., Leshchinsky, B.A., Olsen, M.J., Evans, T.M., 2019. Influence of both anisotropic friction and cohesion on the formation of tension cracks and stability of slopes. Engineering Geology 249, 31–44. https://doi.org/10.1016/j.enggeo.2018.12.016

Sun, L., Grasselli, G., Liu, Q., Tang, X., Abdelaziz, A., 2022. The role of discontinuities in rock slope stability: Insights from a combined finite-discrete element simulation. Computers and Geotechnics 147, 104788. https://doi.org/10.1016/j.compgeo.2022.104788

Teshebaeva, K., Echtler, H., Bookhagen, B., Strecker, M., 2019. Deep-seated gravitational slope deformation (DSGSD) and slow-moving landslides in the southern Tien Shan Mountains: new insights from InSAR, tectonic and geomorphic analysis. Earth Surf. Process. Landforms 44, 2333–2348. https://doi.org/10.1002/esp.4648

Tien, Y.M., Kuo, M.C., Juang, C.H., 2006. An experimental investigation of the failure mechanism of simulated transversely isotropic rocks. International Journal of Rock Mechanics and Mining Sciences 43, 1163–1181. https://doi.org/10.1016/j.ijrmms.2006.03.011

Tong, Z., Fu, P., Zhou, S., Dafalias, Y.F., 2014. Experimental investigation of shear strength of sands with inherent fabric anisotropy. Acta Geotech. 9, 257–275. https://doi.org/10.1007/s11440-014-0303-6

Townsend, K.F., Gallen, S.F., Clark, M.K., 2020. Quantifying Near-Surface Rock Strength on a Regional Scale From Hillslope Stability Models. Journal of Geophysical Research: Earth Surface 125, e2020JF005665. https://doi.org/10.1029/2020JF005665

Utili, S., Crosta, G.B., 2011. Modeling the evolution of natural cliffs subject to weathering: 2. Discrete element approach. J. Geophys. Res. 116, n/a-n/a. https://doi.org/10.1029/2009JF001559

Wang, C., Tannant, D.D., Lilly, P.A., 2003. Numerical analysis of the stability of heavily jointed rock slopes using PFC2D. International Journal of Rock Mechanics and Mining Sciences 40, 415–424. https://doi.org/10.1016/S1365-1609(03)00004-2

Wang, P., Yang, T., Zhou, J., 2018. Slope failure analysis considering anisotropic characteristics of foliated rock masses. Arab J Geosci 11, 222. https://doi.org/10.1007/s12517-018-3583-6

Yang, C.-M., Kang, K.-H., Yang, S.-H., Li, K.-W., Wang, H.-J., Lee, Y.-T., Lin, K.-K., Pan, Y.-W., Liao, J.-J., 2020. Large paleo-rockslide induced by buckling failure at Jiasian inSouthern Taiwan. Landslides 17, 1319–1335. https://doi.org/10.1007/s10346-020-01360-3

Zheng, Y., Chen, C., Liu, T., Zhang, H., Xia, K., Liu, F., 2018. Study on the mechanisms of flexural toppling failure in anti-inclined rock slopes using numerical and limit equilibrium models. Engineering Geology 237, 116–128. https://doi.org/10.1016/j.enggeo.2018.02.006

Zheng, Y., Wang, R., Chen, C., Meng, F., 2021. Analysis of Flexural Toppling Failure in Rock Slopes Using Discrete Element Method. Front. Earth Sci. 9, 773088. https://doi.org/10.3389/feart.2021.773088

Zou, Z., Tang, H., Xiong, C., Su, A., Criss, R.E., 2017. Kinetic characteristics of debris flows as exemplified by field investigations and discrete element simulation of the catastrophic Jiweishan rockslide, China. Geomorphology 295, 1–15. https://doi.org/10.1016/j.geomorph.2017.06.012

# CHAPTER 4 – SYNTHESIS

## 4.1 Achievements of this PhD project

With our Annapurna case studies we investigated large-scale bedrock landslides, more specifically two types of slope instability: giant rock avalanches and DSGSDs. Giant rock avalanches are rare, low-frequency events (i.e. catastrophic failure), whereas DSGSDs involve slopes that undergo slow deformation over long time scales or, as in our case study site of Phalo Danda, deform stepwise with long periods of dormancy (i.e. non-catastrophic failure). Their dynamics are therefore difficult to observe directly. We investigated these large-scale slope failures by using absolute dating techniques, including cosmogenic nuclide dating. Additional investigations at the study sites, such as mapping, volume reconstructions for the giant rock avalanches, and a trench to gain further insight into the paleo-movement of a DSGSD scarp, complement our research efforts. With our results, we are able to shed more light on the Precondition and Preparatory Factors of these two types of rock slope failure, which were previously known only to a limited extent or were completely unexplored for this region. We found substantial evidences highlighting the role of climatic forcing on giant rock avalanche failures in the Annapurna Massif, in agreement with earlier observations made in other regions of the Himalayas (Bookhagen et al., 2005; Dortch et al., 2009).

Our investigations in the upper Marsyangdi Valley have greatly expanded the existing record of giant rock avalanches in the central Himalayan region, not only by providing reliable age constraints on previously known rock avalanche deposits, but also by providing a much more reliable estimate of the post-failure volume of an event responsible for the sedimentary fills around Humde (see Table 2.5). Evidence was found for another independent deposit around Manang (Sections 2.5.2 and 2.6.1). The Tilicho Lake rock avalanche was added as an entirely new entry to the record, again with reliable volume and age constraints (see Sections 2.5.3 and 2.6.1). At Pisang Bowl, we were able to distinguish at least two individual slope failures, i.e. a multi-event history, which occurred approximately 200-300 years apart and together formed the rock avalanche deposit at this site (see Sections 2.5.1 and 2.6.1).

Our documentation of the paleo-movement of a DSGSD is, to our knowledge, the first of its kind in the Himalayas (see review by Pánek and Klimeš (2016)). The scarps of the Phalo Danda DSGSD shows successive ruptures in discrete metric to decametric steps, which corresponds to an average slip rate on the main failure plane of ~1 m/kyr. This, extrapolated to the total observed displacement, gives an estimated rupture

initiation at 130 – 225 ka (see Section 2.8.2). Failed rock masses that have come to rest at the base and mid-sections of slopes in the vicinity of active DSGSD structures document that slope deformation acting on these highly fractured masses extends far back in time (at least ~120 ka) (see Section 2.7.5). We hypothesise that DSGSD activity on the south-facing Annapurna Massif, as it evolves, results in failed rock masses that are eventually eroded by retrogressive erosion scars (Gallo and Lavé, 2014) (see Section 2.8.3).

In a second part of this PhD project, we carried out a numerical modelling study to investigate a very important Precondition Factor that has not been systematically investigated so far: rock strength anisotropy (see Section 1.5.2). Our approach is based on the discrete element method and allows reproducing the behaviour of transverse isotropic rock materials (Dinç and Scholtès, 2018). We first worked on the construction of a slope model, ensuring that the rock mechanical properties of a gneissic material are well reproduced, and compared the predictions of our slope model with an analytical solution. Using our well-constructed model, we then analysed the full range of possible angles of anisotropy relative to the slope in two dimensions (2D; 0 - 180°) in an exhaustive parametric study. Despite the inherent limitations of our numerical model, we were able to draw some striking conclusions: 1. we have identified considerable variability in slope stability as a function of the orientation of the anisotropy; 2. we reproduce different failure modes that are commonly observed in natural slopes: sliding, buckling, toppling, and crumbling (i.e., rock falls). Furthermore, our systematic exploration provides an explanation for the azimuthally controlled slope angle distribution and failure modes observed on the southern flank of the Annapurna Massif.

Having studied natural examples in the Annapurna Massif and performed numerical simulations of slope failure, I have approached bedrock landslides from two fundamentally different perspectives but I nonetheless gained a deep understanding of the causes of landslides, especially deep-seated bedrock landslides. The outcome of this PhD project provides a renewed vision on deep-seated, large-scale bedrock landslides in the Annapurna Massif and on landslide process understanding, which can be useful for the assessment of natural hazards. It has also some important implications on the characterization of hillslope denudation and landscape evolution in the central Himalayas. The numerical modelling part, designed as a parametric approach to document the effect of rock strength anisotropy on slope stability, may be useful to slope stability analysts and helps to understand how rock strength anisotropy shapes landscapes at a larger scale. Based on our findings, and building on the existing scientific literature, further research could be undertaken to further improve our understanding of bedrock landslides (see Section 4.2 below).

## 4.2 Outlook and perspectives

### 4.2.1 Next steps for exploring Causes and Triggers of bedrock landslides in the central Himalayas

A logical first step in systematically investigating the Precondition and Preparatory Factors (also Movement Sustaining Factors for non-catastrophic failures) of bedrock landslides in the central Himalayas would be to compile an inventory of bedrock landslides for the Annapurna Massif, as already suggested in Sections 2.9.1.1 and 2.9.1.2. This inventory should include not only large-scale rock slope failures, such as the giant rock avalanches and DSGSDs discussed in Chapter 2, but also bedrock landslides of smaller volume (i.e., $<10^6$ km³; see Figure 1.3). Including medium-scale rock slope failures will enlarge the sample size for subsequent statistical analysis, while excluding superficial small-scale bedrock landslides will keep the mapping effort manageable. Catastrophic events of considerable size (affected area > ~0.08 km²) that occurred between 1972 and 2014 have already been mapped by Marc et al. (2019) for the south-face of the Annapurna Massif. Expanding this inventory to include older failures and those north of the Annapurna main ridge crest is possible, though it may be challenging, especially on the south-face, due to a thick vegetation cover and high erosion rates likely erasing traces of older, prehistoric events. Additionally, non-catastrophic rock slope failures must be systematically identified throughout the Annapurna Massif, on both the northern and southern sides of the main ridge crest. DSGSD structures and slow-moving hillslope failures could be mapped using advanced remote sensing techniques such as InSAR, and optical and radar image correlation (see e.g. reviews by Pánek and Klimeš, 2016; Lacroix et al., 2020). Therefore, a comprehensive inventory should categorize landslides by type, distinguishing between catastrophic bedrock landslides, and non-catastrophic rock slope failures like slow-moving landslides and DSGSDs. Similar inventories are found in the literature, for instance, Blondeau et al. (2021) and Cui et al. (2022) (see also Guzzetti et al., 2012).

With this inventory in hand, the relative importance of various Precondition and Preparatory Factors can be more effectively assessed by comparing the data with tectonic structures, the distribution of contemporary seismic activity, geological maps, the distribution of mean annual precipitation and permafrost, and the maximum glacial extent during the Late Pleistocene (many datasets appropriate for comparison are mentioned in Chapter 2). Statistical methods could be applied to analyse the distribution of landslides in relation to these factors. An especially valuable insight from such an extensive mapping effort would be determining whether DSGSD structures exist on the drier northern side of the main ridge crest of the Annapurna Massif (see Sections 2.2, 2.9.1.1, and 2.9.1.2; and Figure 2.1).

We are certainly aware that compiling an inventory of rock slope failures is a complex and time-intensive task, requiring high-resolution DSMs, and mapping is particularly challenging in vegetated and glaciated terrain. The presence of glacial landforms especially complicates the process, and ambiguities may only be resolved through additional fieldwork.

Using an inventory, the slopes of the Annapurna Massif could be more thoroughly examined from a geo-mechanical perspective to identify factors that may influence the occurrence and frequency of both catastrophic (including rock avalanches) and non-catastrophic rock slope failures (including DSGSDs). Among the structural and lithological Precondition Factors, the orientation of layering or foliation relative to the slope warrants special qualitative investigation. Rock slope failures are more frequently encountered in rock types with anisotropic strength, such as sedimentary and metamorphic rocks, where layering or foliation is present (e.g., Agliardi et al., 2013 for DSGSDs, Blondeau et al., 2021; see also Sections 1.3.3 and 1.4.2). Moreover, there is quantitative evidence from certain study areas that rock slope failures are more common on cataclinal slopes (see terminology by Cruden and Hu, 1996) than on anaclinal slopes (Cruden and Eaton, 1987; Cui et al., 2022). This suggests that the orientation of layering and foliation toward the slope plays a significant role in controlling landslide frequency, likely due to higher shear resistance in anaclinal configurations where weak planes introduced by lithology are hindered to be activated for stress and strain localisation (see Section 3.5.2; Fu and Dafalias, 2011; Tong et al., 2014). A higher frequency of landslides on cataclinal slopes could imply that the landscape is in a state of permanent disequilibrium, with the erosion of cataclinal slopes occurring at a faster rate than that of anaclinal slopes, thereby pushing the crests toward the anaclinal slopes.

Due to the impeded stress and strain localisation on anaclinal slopes, where potential failure zones crosscut the layering or foliation, it can be argued that deep-seated rock slope failures are more likely to develop into sub-critical, non-catastrophic events, such as DSGSDs, rather than catastrophic failures. These slopes may experience slow, long-term deformation before a critical failure occurs. Additionally, one could argue that due to the limited stress localisation, anaclinal slopes may require more advanced progressive rock damage or fracturing before catastrophic failure (e.g., rock avalanches) can occur, compared to cataclinal slopes. A bedrock landslide inventory could help quantitatively analyse the relationship between the likelihood of catastrophic or non-catastrophic failures and foliation orientation toward the slope (i.e., cataclinal vs. anaclinal slopes). No existing study to our knowledge has conducted such an analysis. It could be carried out for the Annapurna Massif alongside the evaluation of other Precondition and Preparatory Factors.

Besides an inventory of bedrock landslides in the Annapurna Massif, research could be undertaken to assess the condition of the subsurface rocks in the area with respect to deep weathering processes, which are

supposedly an important Preparatory and Movement Sustaining Factor for catastrophic and non-catastrophic rock slope failures in the area (see Sections 2.6.2.2, 2.8.1, 2.9.1.1, and 2.9.1.2; see also Ollier 2010; Viles, 2013). Spring locations could be identified and the chemical composition of the spring water analysed. Can anything be learnt from the dissolved chemical constituents? Is it possible to reconstruct which minerals decompose underground? Does the chemical content change seasonally or depending on the strength of the monsoon? And what are the expected mechanical effects on the failure zones in the subsurface? To begin with, it would be necessary to conduct a literature study on the existing knowledge about the processes of deep weathering and the chemistry of spring water. We can assume that clay minerals, as known from studied shear zones of DSGSDs from the Alps (e.g., Strauhal et al., 2017), are formed by the weathering of aluminosilicates, which are abundant in the gneisses outcropping on the Annapurna south-face (see Section 2.7.1).

To better understand the Triggers of bedrock landslides in the Annapurna Massif, research should focus on monitoring contemporary phenomena through the analysis of remote sensing data (such as optical and radar images correlation and InSAR techniques), as outlined in Section 2.9.1.3. Is there evidence of progressive slope deformation in high-relief areas that could indicate potential future giant rock avalanche failure zones? Or, for non-catastrophic DSGSD failures that move in discrete steps, did recent extreme meteorological events (like cloudbursts or prolonged rain) or strong seismic shaking (including the 2015 Gorkha earthquake) trigger movement at individual structures? Getting a more thorough perception of non-catastrophic slope deformation by detecting and monitoring it in the Annapurna Massif would also enhance our understanding of landscape evolution and would support natural hazard assessment in the region. Continuous slope failures, like those studied by Lacroix et al. (2022) in the upper Bhote Koshi area (about 170 km east-southeast of the Annapurna Massif; see Section 2.3.5), should also be considered. In these cases, Movement Sustaining Factors can be directly investigated (e.g., see reviews by Pánek and Klimeš, 2016; Lacroix et al., 2020).

### 4.2.2 Further site specific investigations

For the upper Marsyangdi Valley, there are still some questions with regard to the giant rock avalanches that need to be investigated. A better understanding of the rock avalanche deposit at Manang could be obtained by conducting further field studies with application of absolute dating methods. For both the Humde and the Manang deposits, the detachment areas still need to be identified by spending more time in the field looking, among other things, for motion indicators in the outcrops of the deposits, which could ultimately lead us to the direction of emplacement of the deposits. There are also other peculiar deposits in the valley, especially between Humde and Pisang Bowl (see Figure 2.10), that still need to be assigned more reliably to a formation process (rock-avalanche or glacial origin). Additional cosmogenic nuclide samples could be collected to date the Manang deposit for the first time and additionally date the surface to the north of Tilicho Base Camp, interpreted as deposit top of the Tilicho Lake failure (see Figures 2.17 and 2.22). The flat surface at Tilicho Lake, where samples were gathered in this study (Section 2.5.2.3), could be revisited to locate more suitable sampling targets, especially when snow cover is absent and doesn't impede the sampling effort.

In addition to conducting reconnaissance, delineating the extent, and determining the dates of individual events, the giant rock avalanches should also be more thoroughly analysed to understand the mechanical characteristics of the slope failures: Is it possible to estimate the pre-failure topography or the mechanical properties in the shear zones just before failure? Numerical modelling experiments tailored to individual sites could provide important insights to failure mechanisms. Such models could not only be used to simulate the runout distances of failed material but also help assess pre-failure rock mechanical conditions (i.e. slope stability) and the role of Precondition and Preparatory Factors that led to the failure (see Section 1.5 and related citations, and 2.9.1). A better understanding of the mechanics of an individual failure may even provide hints to the Trigger that could have been involved. The Yade open-source framework, which we used for the numerical modelling study in Chapter 3, could be applied to analyse a giant rock avalanche failure in the upper Marsyangdi Valley (see Sections 3.2 and 3.3 and relevant citations). Slope models built with Yade can incorporate discrete structural planes, individual structures or within fracture networks (Scholtès and Donzé 2012, 2015), and can represent 3D topography (e.g., Bonilla-Sierra et al., 2015). However, the computation times for individual simulation runs need to be reduced through improved parallelization, compared to those conducted in this PhD. This is particularly important for simulations involving a large number of discrete elements, such as 3D slope models. Moreover, any modelling study of a specific slope failure event would need to be supported by additional fieldwork and remote sensing analysis to gather structural and mechanical data to accurately reflect the rock mechanical conditions prior to failure (e.g., Brideau et al., 2009; review by Stead and Wolter, 2015).

If the research focus is specifically on the occurrence and frequency of extremely large-scale catastrophic rock slope failures, namely the giant rock avalanches, it can be assumed that the record of such events in the central Himalayas is certainly not complete. Some identified deposits, like the Kumjung and Dzongri failures, still lack absolute age constraints and reliable volume estimates (see Table 2.5; Heuberger, 1986; Weidinger and Korup, 2009), and it is very likely that there are several more rock avalanches that have not yet been identified as such. A systematic search for these giant slope failures using remote sensing data and subsequent field verification is essential to complete the record of these giant events as much as possible in the near future and make it accessible to the scientific community. In future field studies and analyses with DSMs, it is particularly interesting to investigate whether there are signs of non-catastrophic progressive slope deformation that preceded the catastrophic collapses (see Section 2.9.1.3).

The Phalo Danda DSGSD on the south-facing Annapurna Massif could be the subject of continuing research activities. Cosmogenic nuclide profiles and trenches could be especially interesting on scarps located lower in altitude, which were not affected by glaciers in the past and may reveal a movement history from Glacial times (see Figures 2.28 and 2.29E). Such an insight into pre-Holocene scarp movement characteristics has not been possible from our investigations at the Phalo Danda DSGSD in this study. We do not know whether the rates of movement on the Phalo Danda main scarp during the glacial period were similar to, higher than, or lower than those of the Holocene. Information on Glacial rates would potentially have a significant impact on the estimated period of activity for this DSGSD, because up to now we have simply transferred Holocene movement rates to the glacial period (see Section 2.8.2).

Despite its expected dormancy between individual rupture events it could be of interest to explore the Phalo Danda DSGSD with ground-based or remote sensing monitoring techniques (see, e.g., review by Pánek and Klimeš, 2016). Is it possible that some parts of the sliding mass move very slowly in the form of continuous creep? Or, what kind of secondary landsliding phenomena are active within the DSGSD affected area? However, as we know from our trench, it is unlikely that another discrete rupture on a scarp will be recorded in the next few years due to the low frequency of rupture events (see Section 2.7.3.2). Nevertheless, if a strong earthquake or a cloudburst, i.e. a potential trigger event, were to occur in the area in the future, the Phalo Danda site could be studied retrospectively using remote sensing techniques such as InSAR.

A better assessment of the state of rock weathering and rock damage in the Phalo Danda and Khudi Ridge areas, accompanied by an assessment of bedrock's mechanical condition, would be another avenue of investigation. This could be done by using outcrop descriptions known from engineering practice (see, e.g., Brideau et al. (2009) and GSI classification system by Hoek and Brown (2019)) or geophysical methods such as the measurement of shear wave velocities by setting up seismic acquisition lines (sledgehammer as a

source), as demonstrated by the study of Medwedeff et al. (2022) in the central Himalayas. They found enhanced weathering and reduced rock strength on the ridges they explored compared to hillslope sections further down slope and reached a maximum depth of investigation of about 20-30 meters. To reach deeper into the subsurface one or more boreholes would be required to investigate rock damage, groundwater conditions and the location and characteristics of shear zones. But in this remote area of the Nepalese Himalayas, such an undertaking is certainly difficult to conduct.

With a clearer understanding of the Phalo Danda subsurface, particularly the location and mechanical conditions of the shear zones, along with the hydrological conditions (such as the groundwater table), a site-specific investigation using a numerical model could be pursued. Combined with structural mapping of the area, numerical simulations would ultimately allow for the study of potential mechanical coupling between the main scarp and the studied conjugate scarp.

The mechanical conditions of the Phalo Danda DSGSD could be as well explored using the Yade DEM framework applied in our modelling study in Chapter 3 (see above where Yade modelling is proposed for the giant rock avalanches and the citations mentioned). To investigate the temporal evolution of the Phalo Danda DSGSD with a Yade numerical model, time-dependent laws that locally reduce strength and can represent progressive rock damage would need to be incorporated. This would enable the simulation of non-catastrophic failures over longer time scales (see also Section 4.2.5 below and Riva et al. (2018)). Currently, Yade slope models cannot reproduce this kind of progressive, time-dependent failure behaviour. However, implementing this type of failure behaviour in Yade slope models could be a potential avenue for future development.

As previously mentioned, having more paleo-movement reconstructions of DSGSDs across the central Himalayas would be valuable for the research community. Our current isolated study offers limited significance for drawing conclusions that apply to the region as a whole.

### 4.2.3 Modelling study

Regarding the modelling study, there are several things that could be done in continuation of this PhD-project:

As we have learned from the existing literature and our Himalayan case studies, the most important driver of rock slope failure is groundwater. Groundwater destabilises slopes most effectively by increasing the pore pressure and thus affecting the effective stress within the rock. It would therefore be of great interest to include in our slope models the representation of pore pressure, as it was done by other researchers before (see Section 1.5.2). As with our "dry" and homogeneous slope models, it should be systematically investigated how a groundwater table within a slope in combination with a variable orientation of the anisotropic rock strength influences slope stability and the failure modes. A methodological implementation would first have to be developed that is capable of representing a change in the mechanical conditions depending on the groundwater table and hence the pore pressure within the rock. The implementation of advanced hydromechanical failure laws would allow the study of differences in the temporal evolution of slope failures composed of anisotropic rocks as a function of the groundwater conditions in the slope. A systematic investigation of groundwater pore pressure using numerical modelling, independent of case study configurations and monitoring data, is so far missing in the literature. The effect of groundwater conditions should be investigated for different slope angles and geometries, and how the interaction of topography and hydrological conditions affects slope stability and failure behaviour.

The fundamental conceptual design of our simulations can be scrutinised in terms of how well it reflects the behaviour of natural slopes, particularly in terms of how anisotropic material strength is represented and how failure is initiated. In our approach, anisotropy is introduced uniformly throughout the slope material, and strength is also reduced evenly across the slope (see Section 3.2). Since our modelling does not directly account for stress or strain weakening effects in the discrete element formulation, it could be argued that the ability of our simulations to replicate stress and strain localization is somewhat limited compared to what may be the case for natural slopes. In other words, in many of our configurations, the material in our simulations is likely already too uniformly weakened before a failure surface can develop. And therefore, a localised failure zone only forms in our sliding mode configurations (see Section 3.4.3; and Figure 3.6). For the other configurations, material deterioration is already well advanced and complete particle disintegration occurs, as opposed to natural slopes where failure surfaces instead evolve more easily.

Without a fundamental change in the formulation and setup of our models, an alternative approach could involve introducing regularly spaced discrete weakness planes, with strength reduction applied specifically

to these planes rather than to the entire bulk mass. It would be interesting to see how the results of such a simulation series, likewise varying the orientation of weakness planes relative to the slope, would differ from the current simulation results in terms of stability and failure modes.

If the fundamental approach to inducing slope failure in the models were to be further scrutinised, failure could be simulated through evolution laws based on physical processes, rather than through uniform strength reduction. Incorporating time-dependent laws into a numerical model would allow for the introduction of stress and strain weakening (or even hardening) over time (see Section 1.4.3, and for example, the review by Lacroix et al., 2020, and Amitrano and Helmstetter, 2006). This would provide a much more realistic representation of progressive rock slope deformation as observed in natural settings (see Section 1.2.3 and related references), which exhibit subcritical failure, i.e. brittle creep. Following this path would eventually lead to more efficient stress and strain localisation, including the time-dependent initiation and evolution of basal shear zones and other fractures within the rock mass (see Riva et al., 2018).

Analyses of rock slope failure by means of numerical modelling should account for groundwater effects for the assessment of slope stability and failure mode and, additionally, progressive rock damage, in case a time-dependent failure evolution wants to be investigated. For the more distant future, several Precondition and Preparatory Factors could be systematically analysed together in a single simulation environment (dedicated multi-scale and multi-physics approaches) to better understand their different influences on slope stability and their interactions: besides pore pressure effects and progressive rock damage due to weathering, other processes like different lithological characteristics, the presence of structures, regional stress changes, dynamic loadings or basal erosional processes could be explored.

An advanced modelling framework could offer valuable insights into the factors that promote or inhibit critical versus sub-critical slope failure, or catastrophic versus non-catastrophic bedrock landsliding.

# References:


Agliardi, F., Crosta, G.B., Frattini, P., Malusà, M.G., 2013. Giant non-catastrophic landslides and the long-term exhumation of the European Alps. Earth and Planetary Science Letters 365, 263–274. https://doi.org/10.1016/j.epsl.2013.01.030

Amitrano, D., Helmstetter, A., 2006. Brittle creep, damage, and time to failure in rocks. Journal of Geophysical Research: Solid Earth 111. https://doi.org/10.1029/2005JB004252

Blondeau, S., Gunnell, Y., Jarman, D., 2021. Rock slope failure in the Western Alps: A first comprehensive inventory and spatial analysis. Geomorphology 380, 107622. https://doi.org/10.1016/j.geomorph.2021.107622

Bonilla-Sierra, V., Scholtès, L., Donzé, F.V., Elmouttie, M.K., 2015. Rock slope stability analysis using photogrammetric data and DFN–DEM modelling. Acta Geotech. 10, 497–511. https://doi.org/10.1007/s11440-015-0374-z

Bookhagen, B., Thiede, R.C., Strecker, M.R., 2005. Late Quaternary intensified monsoon phases control landscape evolution in the northwest Himalaya. Geology 33, 149–152. https://doi.org/10.1130/G20982.1

Brideau, M.-A., Yan, M., Stead, D., 2009. The role of tectonic damage and brittle rock fracture in the development of large rock slope failures. Geomorphology 103, 30–49. https://doi.org/10.1016/j.geomorph.2008.04.010

Cruden, D., Hu, X.Q., 1996. Hazardous Modes of Rock Slope Movement in the Canadian Rockies. Environmental and Engineering Geoscience 2, 507–516. https://doi.org/10.2113/gseegeosci.II.4.507

Cruden, D.M., Eaton, T.M., 1987. Reconnaissance of rockslide hazards in Kananaskis Country, Alberta. Can. Geotech. J. 24, 414–429. https://doi.org/10.1139/t87-052

Cui, S., Wu, H., Pei, X., Yang, Q., Huang, R., Guo, B., 2022. Characterizing the spatial distribution, frequency, geomorphological and geological controls on landslides triggered by the 1933 Mw 7.3 Diexi Earthquake, Sichuan, China. Geomorphology 403, 108177. https://doi.org/10.1016/j.geomorph.2022.108177

Dinç, Ö., Scholtès, L., 2018. Discrete Analysis of Damage and Shear Banding in Argillaceous Rocks. Rock Mech Rock Eng 51, 1521–1538. https://doi.org/10.1007/s00603-017-1397-6

Dortch, J.M., Owen, L.A., Haneberg, W.C., Caffee, M.W., Dietsch, C., Kamp, U., 2009. Nature and timing of large landslides in the Himalaya and Transhimalaya of northern India. Quaternary Science Reviews 28, 1037–1054. https://doi.org/10.1016/j.quascirev.2008.05.002

Gallo, F., Lavé, J., 2014. Evolution of a large landslide in the High Himalaya of central Nepal during the last half-century. Geomorphology 223, 20–32. https://doi.org/10.1016/j.geomorph.2014.06.021

Guzzetti, F., Mondini, A.C., Cardinali, M., Fiorucci, F., Santangelo, M., Chang, K.-T., 2012. Landslide inventory maps: New tools for an old problem. Earth-Science Reviews 112, 42–66. https://doi.org/10.1016/j.earscirev.2012.02.001

Heuberger, H., 1986. Der Bergsturz von Khumdschung, Mount-Everest-Gebiet, Nepal. Material und Technik 3, 175–181.

Hoek, E., Brown, E.T., 2019. The Hoek–Brown failure criterion and GSI – 2018 edition. Journal of Rock Mechanics and Geotechnical Engineering 11, 445–463. https://doi.org/10.1016/j.jrmge.2018.08.001

Karki, R., Hasson, S. ul, Schickhoff, U., Scholten, T., Böhner, J., 2017. Rising Precipitation Extremes across Nepal. Climate 5, 4. https://doi.org/10.3390/cli5010004

Lacroix, P., Gavillon, T., Bouchant, C., Lavé, J., Mugnier, J.-L., Dhungel, S., Vernier, F., 2022. SAR and optical images correlation illuminates post-seismic landslide motion after the Mw 7.8 Gorkha earthquake (Nepal). Sci Rep 12, 6266. https://doi.org/10.1038/s41598-022-10016-2

Lacroix, P., Handwerger, A.L., Bièvre, G., 2020. Life and death of slow-moving landslides. Nat Rev Earth Environ 1, 404–419. https://doi.org/10.1038/s43017-020-0072-8

Marc, O., Behling, R., Andermann, C., Turowski, J.M., Illien, L., Roessner, S., Hovius, N., 2019. Long-term erosion of the Nepal Himalayas by bedrock landsliding: the role of monsoons, earthquakes and giant landslides. Earth Surface Dynamics 7, 107–128. https://doi.org/10.5194/esurf-7-107-2019

Medwedeff, W.G., Clark, M.K., Zekkos, D., West, A.J., Chamlagain, D., 2022. Near-Surface Geomechanical Properties and Weathering Characteristics Across a Tectonic and Climatic Gradient in the Central Nepal Himalaya. Journal of Geophysical Research: Earth Surface 127, e2021JF006240. https://doi.org/10.1029/2021JF006240

Ollier, C.D., 2010. Very deep weathering and related landslides. EGSP 23, 5–14. https://doi.org/10.1144/EGSP23.2

Pánek, T., Klimeš, J., 2016. Temporal behavior of deep-seated gravitational slope deformations: A review. Earth-Science Reviews 156, 14–38. https://doi.org/10.1016/j.earscirev.2016.02.007

Riva, F., Agliardi, F., Amitrano, D., Crosta, G.B., 2018. Damage-Based Time-Dependent Modeling of Paraglacial to Postglacial Progressive Failure of Large Rock Slopes. J. Geophys. Res. Earth Surf. 123, 124–141. https://doi.org/10.1002/2017JF004423

Scholtès, L., Donzé, F.V., 2015. A DEM analysis of step-path failure in jointed rock slopes. Comptes Rendus Mécanique 343, 155–165. https://doi.org/10.1016/j.crme.2014.11.002

Scholtès, L., Donzé, F.-V., 2012. Modelling progressive failure in fractured rock masses using a 3D discrete element method. International Journal of Rock Mechanics and Mining Sciences 52, 18–30. https://doi.org/10.1016/j.ijrmms.2012.02.009

Stead, D., Wolter, A., 2015. A critical review of rock slope failure mechanisms: The importance of structural geology. Journal of Structural Geology 74, 1–23. https://doi.org/10.1016/j.jsg.2015.02.002

Strauhal, T., Zangerl, C., Fellin, W., Holzmann, M., Engl, D.A., Brandner, R., Tropper, P., Tessadri, R., 2017. Structure, Mineralogy and Geomechanical Properties of Shear Zones of Deep-Seated Rockslides in Metamorphic Rocks (Tyrol, Austria). Rock Mech Rock Eng 50, 419–438. https://doi.org/10.1007/s00603-016-1113-y

Viles, H.A., 2013. Linking weathering and rock slope instability: non-linear perspectives: Linking weathering and rock slope instability. Earth Surf. Process. Landforms 38, 62–70. https://doi.org/10.1002/esp.3294

Weidinger, J.T., Korup, O., 2009. Frictionite as evidence for a large Late Quaternary rockslide near Kanchenjunga, Sikkim Himalayas, India — Implications for extreme events in mountain relief destruction. Geomorphology, Dating, triggering, modelling, and hazard assessment of large landslides 103, 57–65. https://doi.org/10.1016/j.geomorph.2007.10.021

# ANNEXES

**A2: Annexes for Chapter 2 – Bedrock landslides in the Annapurna Massif**

A2 Supplementary Figures:

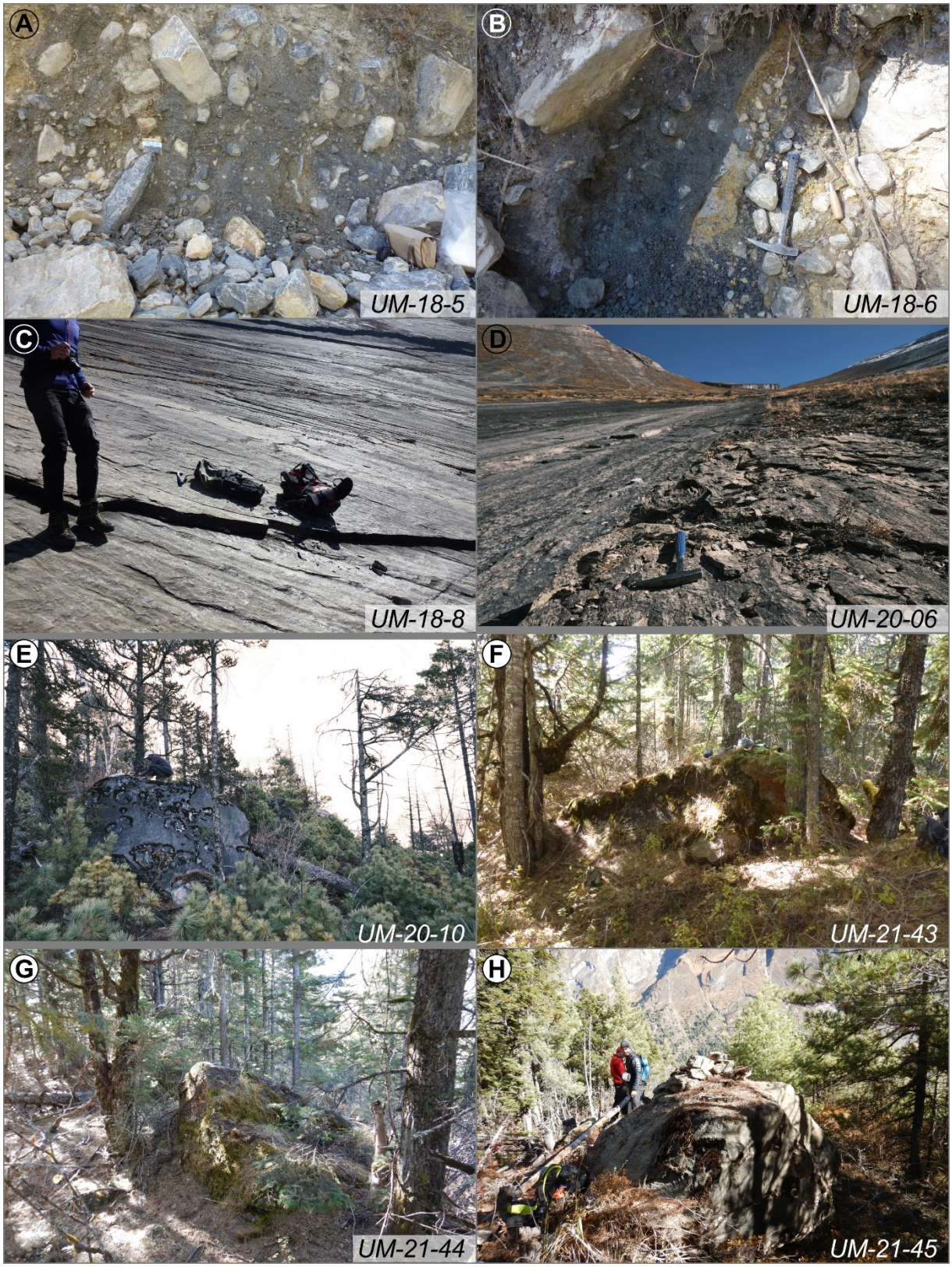


*Figure A2.1: Sampling spots / surfaces / objects at Pisang Bowl site. (A-C) photos by J. Lavé, autumn 2018; (D+E) photos by M., Lupker, autumn 2020; (F) photo by J. Lavé, autumn 2021; (G+H) photos taken in autumn 2021.*

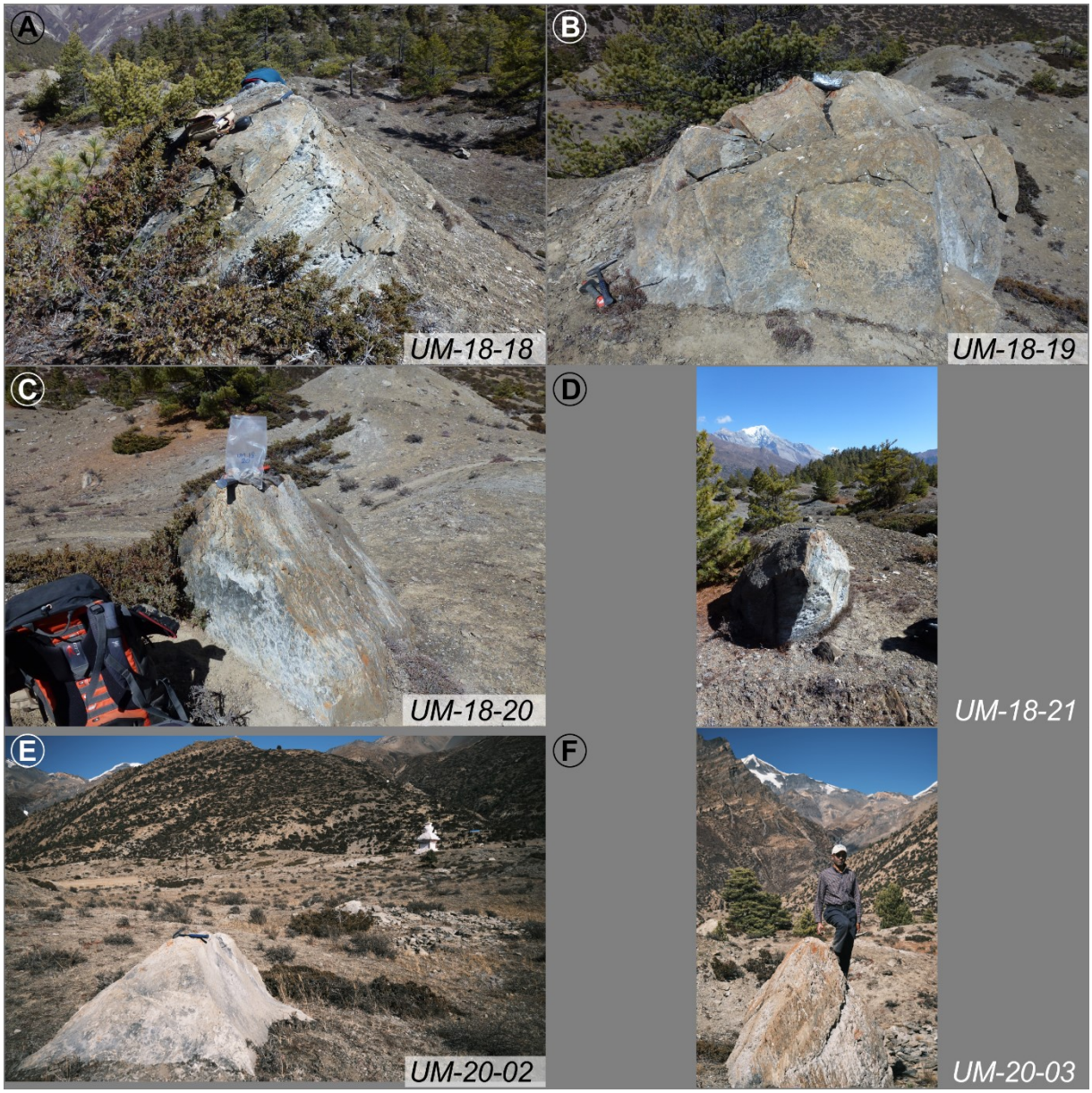


*Figure A2.2: Sampled boulders on top of Humde rock avalanche deposit from the years 2018 and 2020.* (A-C) *photos by J. Lavé, autumn 2018; (D-F) photos by M. Lupker, autumn 2020.*




*Figure A2.3: Sampled boulders on top of Humde rock avalanche deposit from the year 2021. (A-D) photos taken in autumn 2021; (E+F) photos by J. Lavé, autumn 2021.*




*Figure A2.4: Samples boulders on top surface of Tilicho rock avalanche deposit, near Tilicho Lake, from the year 2021. (A-D) photos taken in autumn 2021; (E-H) photos by J. Lavé, autumn 2021.*

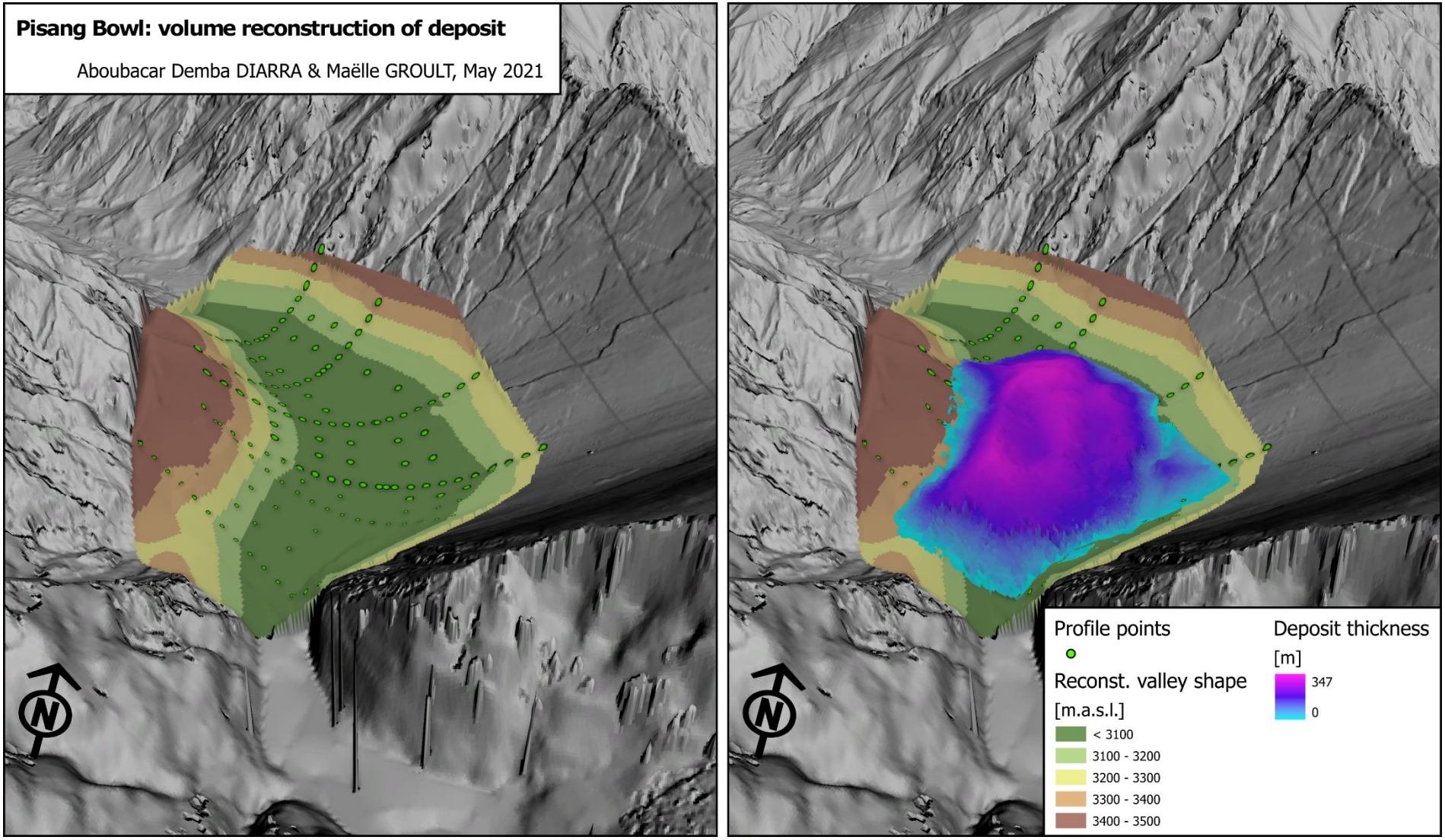
Pisang Bowl: volume reconstruction of deposit
Aboubacar Demba DIARRA & Maëlle GROULT, May 2021
N
N
Profile points
Reconst. valley shape
[m.a.s.l.]
< 3100
3100 - 3200
3200 - 3300
3300 - 3400
3400 - 3500
Deposit thickness
[m]
347
0

*Figure A2.5*

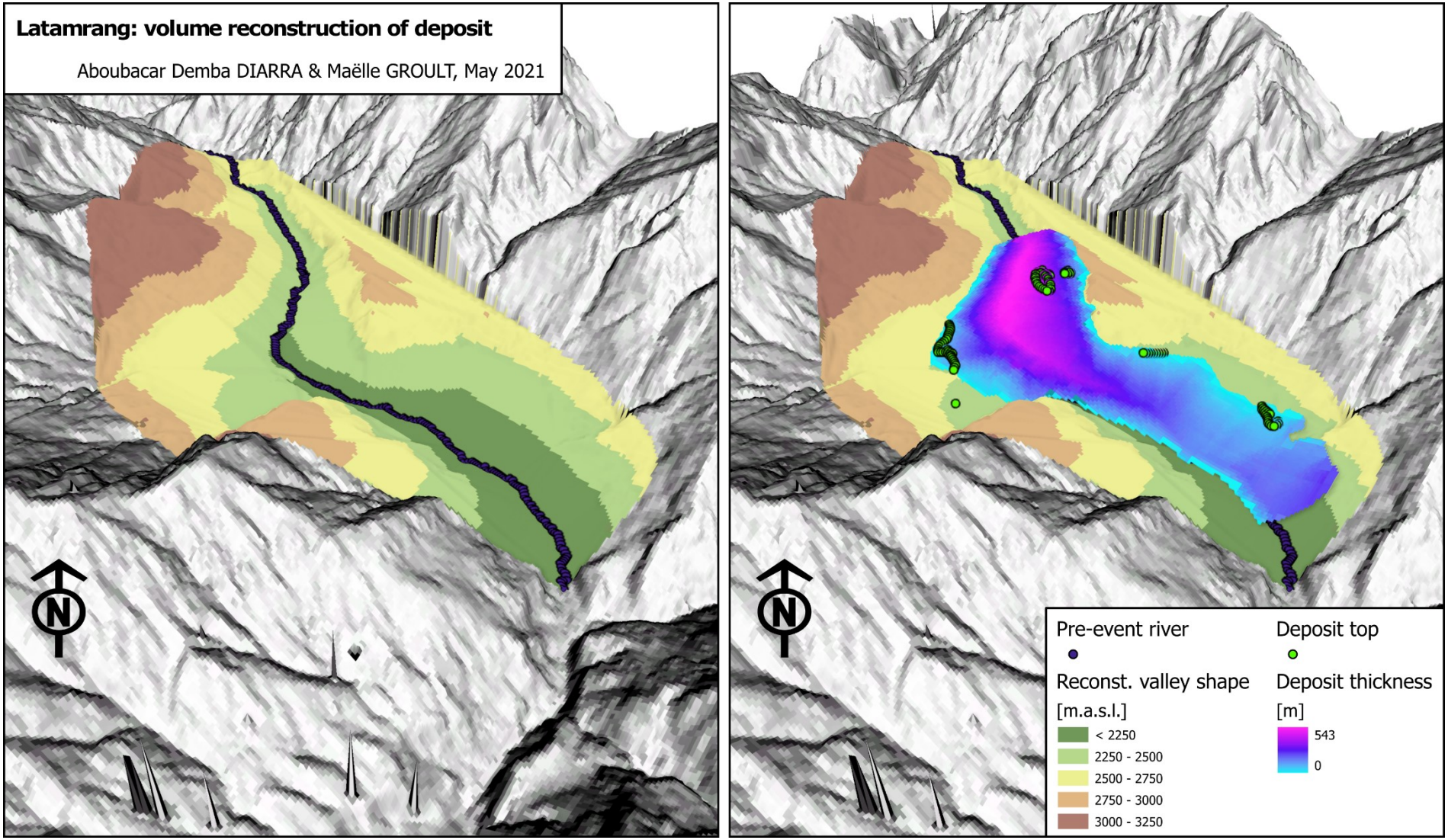
Latamrang: volume reconstruction of deposit
Aboubacar Demba DIARRA & Maëlle GROULT, May 2021
N
N
Pre-event river
Reconst. valley shape
[m.a.s.l.]
< 2250
2250 - 2500
2500 - 2750
2750 - 3000
3000 - 3250
Deposit top
Deposit thickness
[m]
543
0

*Figure A2.6*

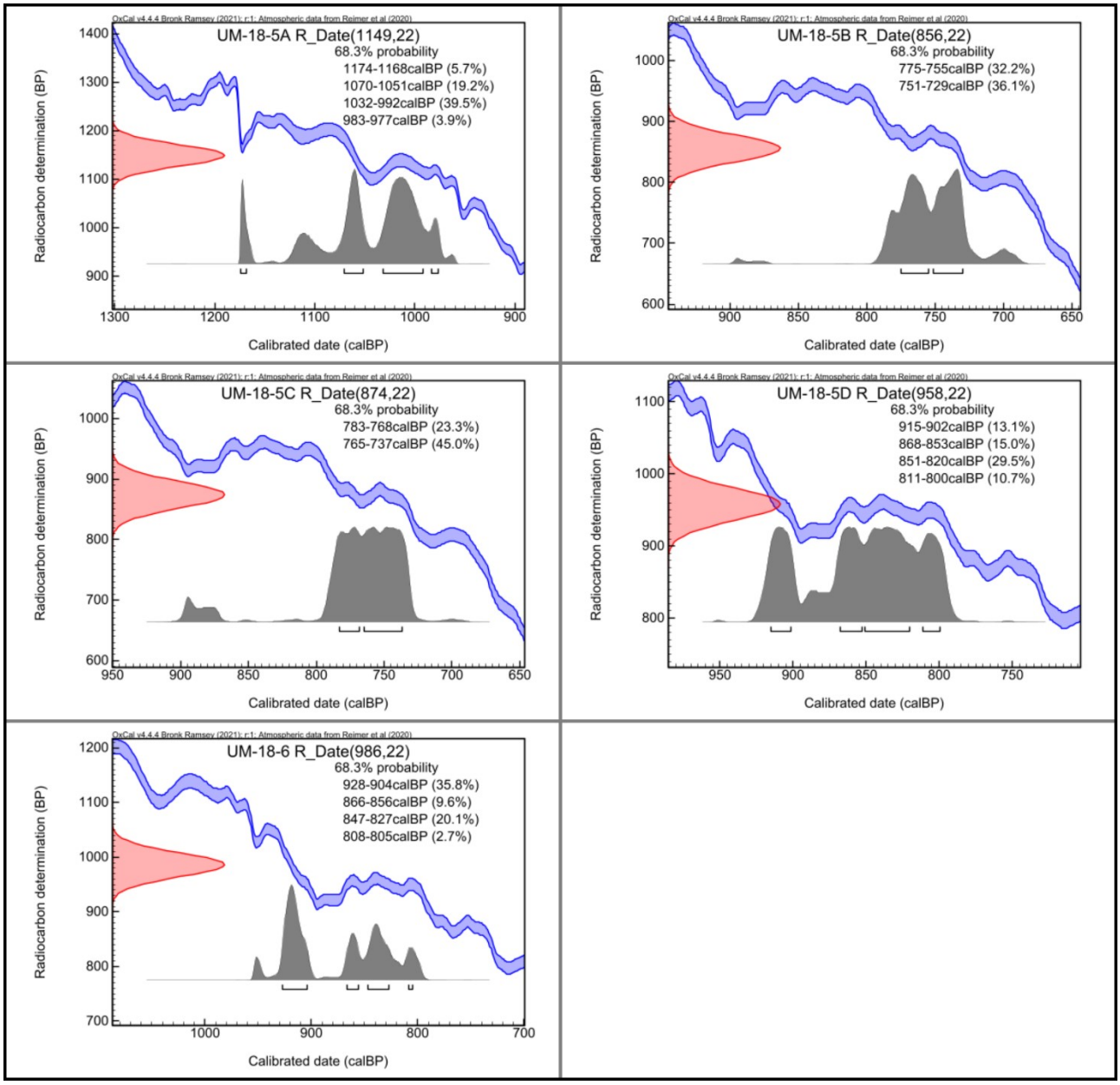


*Figure A2.7: Calculation of 14C carbon burial ages at the Pisang Bowl site: Output graphs created by the OxCal online calculator (Bronk Ramsey, 2021; version OxCal 4.4) using the Intcal20 calibration curve (Reimer et al., 2020). See main-text of Chapter 2 for references.*




*Figure A2.8: Additional sampling surfaces at Phalo Danda site and on Khudi Ridge: (A-C) photos taken in autumn 2021; (D+E) photos by J. Lavé, autumn 2013.*

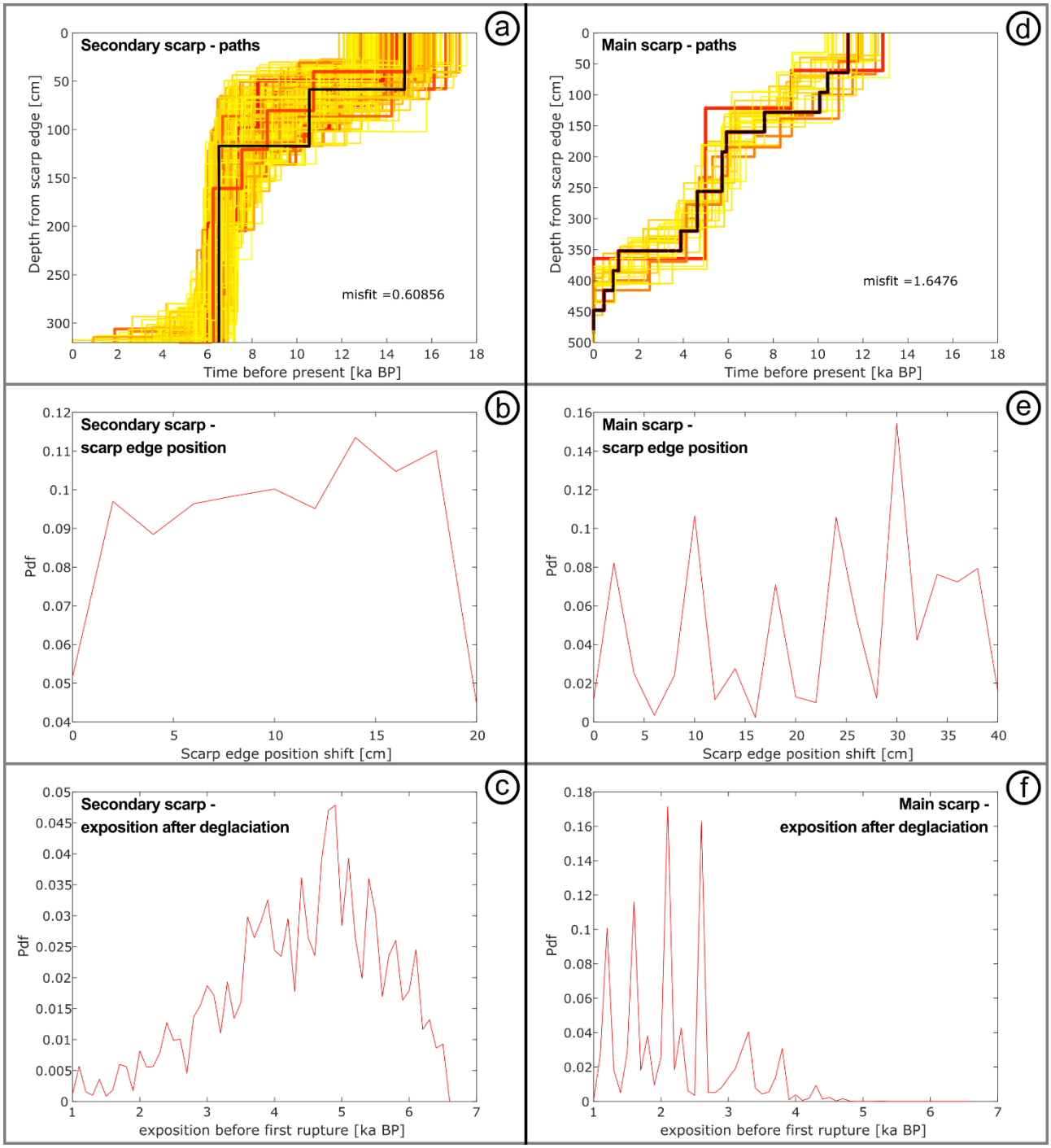


*Figure A2.9: Supplementary graphs showing the most probable rupture scenarios superimposed, coloured from low (yellow) to high (red) probability for the conjugate scarp (a) and the main scarp (d). The rupture scenarios with the lowest misfit of each calculation are shown in black. More additional plots for the variational analyses within the scarp movement reconstruction calculation: Scarp edge position within the estimated uncertainty range for the conjugate scarp (b) and the main scarp (e); exposure after deglaciation for the conjugate scarp (c) and the main scarp (f).*

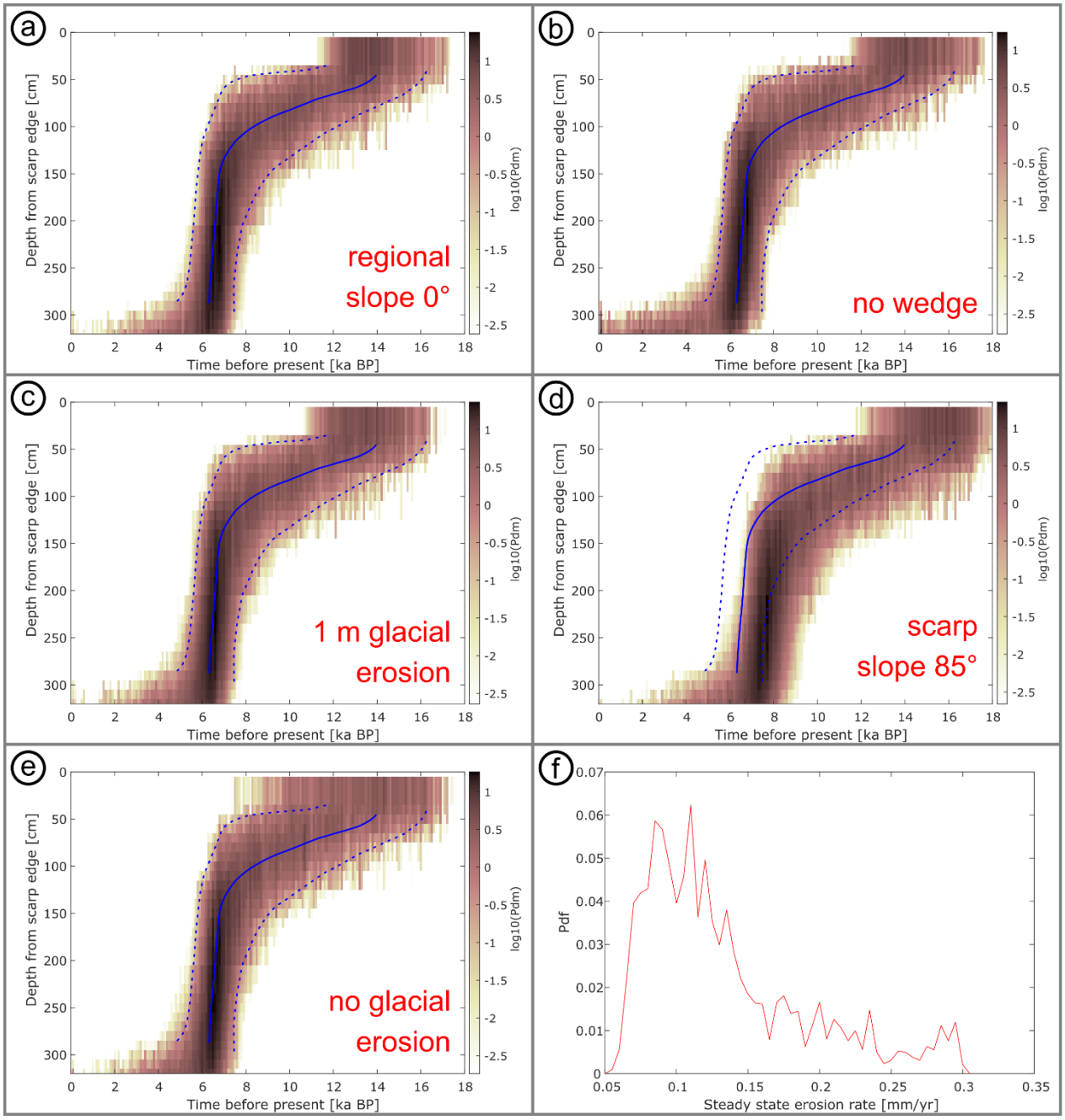


*Figure A2.10: Sensitivity analysis for some input parameters of the scarp movement reconstruction calculation. Output for the conjugate scarp at Phalo Danda was explored: (A) Regional slope changed from 10° to 0°; (B) colluvial wedge was removed; (C) glacial erosion before initial rupture was altered from two metres to one metre; (D) slope of scarp face was changed from 75° to 85°; (E) steady state erosion option applied to the calculation instead of glacial erosion; (F) variational analysis of different erosion rates within the calculation of (E), steady state erosion option applied, show different probabilities over the range explored by the rupture scenarios. The domain with significant probability and an orientation line of the highest probability from the original model run was placed on top in blue to facilitate comparison. See Table 2.8 for list of input parameters.*

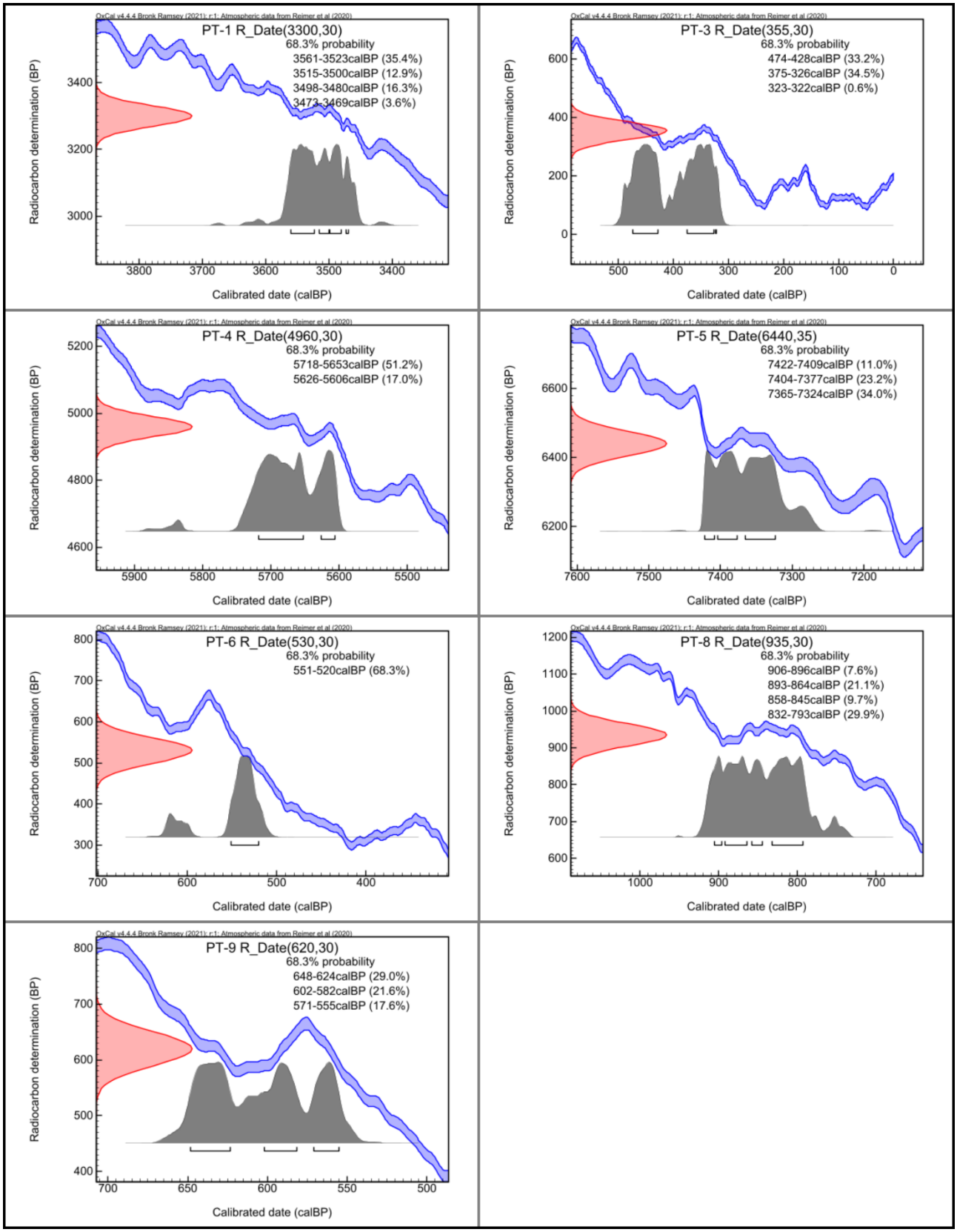


*Figure A2.11: Calculation of 14C carbon burial ages collected in the trench at Phalo Danda site: Output graphs created by the OxCal online calculator (Bronk Ramsey, 2021; version OxCal 4.4) using the Intcal20 calibration curve (Reimer et al., 2020). See main-text of Chapter 2 for references.*

# A2 Supplementary Tables:

**Table A2.1: Snow cover shielding calculation for cosmogenic exposure samples:**

Identical treatment was applied for 10Be and 36Cl-samples. Only spallation reactions are considered in this correction (see, Dunai, 2010, p. 89). Calculations follow equation 4.20 of Dunai (2010):

$$f_{\text{cover}} = e^{-z\rho/\Lambda}$$

A fixed estimated average density of ρ = 0,5 g/cm³ for the snow cover was assumed. The attenuation coefficient is Λ = 160 g/cm² in all calculations.

| | Sample name | *Location* | Alt. extracted from DEM (FABDEM) [m.a.s.l.] | Estimate of days of snow cover per year [d] | estimated average thickness of snow cover during these snow cover days [cm] | Snow shielding factor |
|---|---|---|---|---|---|---|
| 10Be | CA-10-21 | *A. south face* | 2957 | 30 | 20 | 0,995 |
| | CA-10-106 | *A. south face* | 3839 | 60 | 50 | 0,975 |
| | CA-10-107 | *A. south face* | 3836 | 60 | 50 | 0,975 |
| | CA-13-220 | *A. south face* | 3715 | 45 | 40 | 0,985 |
| | CA-13-221 | *A. south face* | 3728 | 45 | 40 | 0,985 |
| | NEQ-17-5-59 | *Pisang Bowl* | 3364 | 60 | 10 | 0,995 |
| | UM-18-9 | *Pisang Bowl* | 3275 | 60 | 10 | 0,995 |
| | UM-18-10 | *Pisang Bowl* | 3275 | 60 | 10 | 0,995 |
| | UM-18-21 | *Humde* | 3797 | 90 | 15 | 0,989 |
| | UM-21-53-A | *Phalo Danda* | 3895 | 75 | 50 | 0,968 |
| | UM-21-53-B | *Phalo Danda* | 3895 | 75 | 50 | 1,000 |
| | UM-21-53-C | *Phalo Danda* | 3895 | 75 | 50 | 1,000 |
| | UM-21-53-D | *Phalo Danda* | 3895 | 75 | 50 | 1,000 |
| | UM-21-53-E | *Phalo Danda* | 3895 | 75 | 50 | 0,994 |
| | UM-21-55-A | *Phalo Danda* | 3917 | 90 | 50 | 0,985 |
| | UM-21-55-B | *Phalo Danda* | 3917 | 90 | 50 | 1,000 |
| | UM-21-55-C | *Phalo Danda* | 3917 | 90 | 50 | 1,000 |
| | UM-21-55-D | *Phalo Danda* | 3917 | 90 | 50 | 1,000 |
| | UM-21-55-E | *Phalo Danda* | 3917 | 90 | 50 | 1,000 |
| | UM-21-55-F | *Phalo Danda* | 3917 | 90 | 50 | 0,962 |
| | UM-21-56-A | *Phalo Danda* | 3931 | 90 | 0 | 1,000 |
| | UM-21-56-B | *Phalo Danda* | 3931 | 90 | 0 | 1,000 |
| | UM-21-56-C | *Phalo Danda* | 3931 | 90 | 0 | 1,000 |
| | PT-2 | *Phalo Danda* | 3919 | 90 | 50 | 0,962 |
| 36Cl | NEQ-17-5-59 | *Pisang Bowl* | 3364 | 60 | 10 | 0,995 |
| | NEQ-17-5-60 | *Pisang Bowl* | 3364 | 60 | 10 | 0,995 |
| | UM-18-8 | *Pisang Bowl* | 3289 | 60 | 10 | 0,995 |
| | UM-18-10 | *Pisang Bowl* | 3275 | 60 | 10 | 0,995 |
| | UM-18-18 | *Humde* | 3796 | 90 | 15 | 0,989 |
| | UM-18-19 | *Humde* | 3795 | 90 | 15 | 0,989 |
| | UM-18-20 | *Humde* | 3798 | 90 | 15 | 0,989 |
| | UM-18-21 | *Humde* | 3797 | 90 | 15 | 0,989 |
| | UM-20-02 | *Humde* | 3728 | 90 | 15 | 0,989 |
| | UM-20-03 | *Humde* | 3728 | 90 | 15 | 0,989 |
| | UM-20-04 | *Humde* | 3733 | 90 | 15 | 0,989 |
| | UM-20-05 | *Pisang Bowl* | 3366 | 60 | 10 | 0,995 |
| | UM-20-06 | *Pisang Bowl* | 3478 | 60 | 10 | 0,995 |
| | UM-20-10 | *Pisang Bowl* | 3221 | 60 | 10 | 0,995 |
| | UM-21-01 | *Pisang Bowl* | 3262 | 60 | 10 | 0,995 |
| | UM-21-02 | *Pisang Bowl* | 3265 | 60 | 10 | 0,995 |
| | UM-21-03 | *Pisang Bowl* | 3261 | 60 | 10 | 0,995 |
| | UM-21-04 | *Humde* | 3743 | 90 | 15 | 0,989 |
| | UM-21-05 | *Humde* | 3733 | 90 | 15 | 0,989 |
| | UM-21-07 | *Humde* | 3755 | 90 | 15 | 0,989 |
| | UM-21-15 | *Humde* | 3770 | 90 | 15 | 0,989 |
| | UM-21-16 | *Humde* | 3785 | 90 | 15 | 0,989 |
| | UM-21-17 | *Humde* | 3788 | 90 | 15 | 0,989 |
| | UM-21-18 | *Humde* | 3787 | 90 | 15 | 0,989 |
| | UM-21-20 | *Tilicho* | 5170 | 150 | 45 | 0,944 |
| | UM-21-21 | *Tilicho* | 5160 | 150 | 45 | 0,944 |
| | UM-21-22 | *Tilicho* | 5144 | 150 | 45 | 0,944 |
| | UM-21-23 | *Tilicho* | 5057 | 150 | 45 | 0,944 |
| | UM-21-24 | *Tilicho* | 5363 | 150 | 45 | 0,944 |
| | UM-21-25 | *Tilicho* | 5363 | 150 | 45 | 0,944 |
| | UM-21-26 | *Tilicho* | 5349 | 150 | 45 | 0,944 |
| | UM-21-27 | *Tilicho* | 5329 | 150 | 45 | 0,944 |
| | UM-21-43 | *Pisang Bowl* | 3428 | 60 | 10 | 0,995 |
| | UM-21-44 | *Pisang Bowl* | 3431 | 60 | 10 | 0,995 |
| | UM-21-45 | *Pisang Bowl* | 3414 | 60 | 10 | 0,995 |

*A. = Annapurna*

**Table A2.2: Additional chemical compositions of 36Cl-samples:**

Target chemical compositions were measured with ICP-AES (inductively coupled plasma atomic emission spectrometry) at CEREGE, bulk rock chemical compositions (including major and trace element compositions) were measured with ICP-MS at SARM, CRPG.

**36Cl exposure samples - Additional chemical compositions**

| | target | | | | | | | | | | bulk | | | | | | | | | | | | | | | | | | | |
|---|---|---|---|---|---|---|---|---|---|---|---|---|---|---|---|---|---|---|---|---|---|---|---|---|---|---|---|---|---|---|
| Sample name | $SiO_2$ [%] | $Al_2O_3$ [%] | $Fe_2O_3$ [%] | MnO [%] | MgO [%] | $Na_2O$ [%] | $TiO_2$ [%] | $P_2O_5$ [%] | $H_2O$ [%] | $CO_2$ [%] | $SiO_2$ [%] | $Al_2O_3$ [%] | $Fe_2O_3$ [%] | MnO [%] | MgO [%] | CaO [%] | $Na_2O$ [%] | $K_2O$ [%] | $TiO_2$ [%] | $P_2O_5$ [%] | $H_2O$ [%] | $CO_2$ [%] | S [%] | Li [ppm] | B [ppm] | Cl [ppm] | Sm [ppm] | Gd [ppm] | Th [ppm] | U [ppm] |
| NEQ-17-5-59 | 0 | 0 | 0 | 0 | 1,83 | 0 | 0 | 0 | 0 | 44,75 | 6,15 | 1,62 | 0,96 | 0,02 | 2,04 | 48,30 | 0,02 | 0,57 | 0,08 | 0,00 | 0,46 | 0,00 | 0,00 | 3,50 | 14,90 | 20,00 | 0,90 | 0,70 | 1,71 | 0,54 |
| NEQ-17-5-60 | 0 | 0 | 0 | 0 | 2,28 | 0 | 0 | 0 | 0 | 33,13 | 6,64 | 2,08 | 0,97 | 0,02 | 2,24 | 47,49 | 0,03 | 0,71 | 0,09 | 0,00 | 0,51 | 0,00 | 0,00 | 4,60 | 19,60 | 23,00 | 0,90 | 0,70 | 2,53 | 0,79 |
| UM-18-8 | 0 | 0 | 0 | 0 | 1,83 | 0 | 0 | 0 | 0 | 41,68 | 20,68 | 8,00 | 2,68 | 0,03 | 2,54 | 35,07 | 0,32 | 2,53 | 0,31 | 0,00 | 0,82 | 0,00 | 0,00 | 8,90 | 66,50 | 21,00 | 3,50 | 2,90 | 8,30 | 1,47 |
| UM-18-10 | 0 | 0 | 0 | 0 | 2,03 | 0 | 0 | 0 | 0 | 40,81 | 30,14 | 4,21 | 1,53 | 0,03 | 1,79 | 33,51 | 0,09 | 1,29 | 0,20 | 0,00 | 0,51 | 0,00 | 0,00 | 4,40 | 39,70 | 20,00 | 2,50 | 2,10 | 5,92 | 1,22 |
| UM-18-18 | 0 | 0 | 0 | 0 | 0,98 | 0 | 0 | 0 | 0 | 42,97 | 13,00 | 2,76 | 1,19 | 0,03 | 1,42 | 44,18 | 0,43 | 0,73 | 0,14 | 0,00 | 0,73 | 0,00 | 0,00 | 7,20 | 16,50 | 20,00 | 1,60 | 1,50 | 3,50 | 0,64 |
| UM-18-19 | 0 | 0 | 0 | 0 | 1,65 | 0 | 0 | 0 | 0 | 43,12 | 15,96 | 4,29 | 1,53 | 0,03 | 2,09 | 40,49 | 0,44 | 1,23 | 0,18 | 0,00 | 0,96 | 0,00 | 0,00 | 12,80 | 22,40 | 20,00 | 2,60 | 2,10 | 4,56 | 0,85 |
| UM-18-20 | 0 | 0 | 0 | 0 | 2,19 | 0 | 0 | 0 | 0 | 42,4 | 15,06 | 3,81 | 1,85 | 0,03 | 2,40 | 40,54 | 0,42 | 1,03 | 0,16 | 0,00 | 0,96 | 0,00 | 0,00 | 11,00 | 22,60 | 20,00 | 2,20 | 1,90 | 4,00 | 0,58 |
| UM-18-21 | 0 | 0 | 0 | 0 | 6,05 | 0 | 0 | 0 | 0 | 42,36 | 23,15 | 6,96 | 2,50 | 0,03 | 4,21 | 31,10 | 0,52 | 1,83 | 0,29 | 0,00 | 1,75 | 0,00 | 0,00 | 23,00 | 31,40 | 20,00 | 2,50 | 2,20 | 8,07 | 1,14 |
| UM-20-02 | 0 | 0 | 0 | 0 | 5,21 | 0 | 0 | 0 | 0 | 43,37 | 13,94 | 3,02 | 1,04 | 0,00 | 3,07 | 40,71 | 0,57 | 0,92 | 0,15 | 0,00 | 0,58 | 0,00 | 0,00 | 9,20 | 15,40 | 20,00 | 1,10 | 0,90 | 3,63 | 0,63 |
| UM-20-03 | 0 | 0 | 0 | 0 | 7,25 | 0 | 0 | 0 | 0 | 37,4 | 40,50 | 7,95 | 1,91 | 0,02 | 3,69 | 21,14 | 1,11 | 2,35 | 0,44 | 0,00 | 1,41 | 0,00 | 0,00 | 23,50 | 36,60 | 20,00 | 3,80 | 3,10 | 11,32 | 1,52 |
| UM-20-04 | 0 | 0 | 0 | 0 | 3,36 | 0 | 0 | 0 | 0 | 44,75 | 5,81 | 1,36 | 0,58 | 0,00 | 2,46 | 48,03 | 0,23 | 0,42 | 0,07 | 0,00 | 0,47 | 0,00 | 0,00 | 5,00 | 8,60 | 20,00 | 0,90 | 0,70 | 2,07 | 0,42 |
| UM-20-05 | 0 | 0 | 0 | 0 | 2,04 | 0 | 0 | 0 | 0 | 38,02 | 31,28 | 8,46 | 2,68 | 0,03 | 3,16 | 27,31 | 0,35 | 2,41 | 0,38 | 0,00 | 1,03 | 0,00 | 0,00 | 13,00 | 78,80 | 39,00 | 3,00 | 2,50 | 10,59 | 1,77 |
| UM-20-06 | 0 | 0 | 0 | 0 | 1,69 | 0 | 0 | 0 | 0 | 43,24 | 23,14 | 5,01 | 1,59 | 0,03 | 1,99 | 36,01 | 0,28 | 1,45 | 0,22 | 0,00 | 0,64 | 0,00 | 0,00 | 7,00 | 47,00 | 20,00 | 2,90 | 2,40 | 5,65 | 0,93 |
| UM-20-10 | 0 | 0 | 0 | 0 | 1,89 | 0 | 0 | 0 | 0 | 43,78 | 7,86 | 2,35 | 0,95 | 0,00 | 2,21 | 45,94 | 0,09 | 0,79 | 0,11 | 0,00 | 0,58 | 0,00 | 0,00 | 6,00 | 12,10 | 23,00 | 1,10 | 0,90 | 2,57 | 0,80 |
| UM-21-01 | 0 | 0 | 0 | 0 | 1,65 | 0 | 0 | 0 | 0 | 47,03 | 24,79 | 7,97 | 2,58 | 0,03 | 3,10 | 31,61 | 0,27 | 2,34 | 0,33 | 0,00 | 1,32 | 0,00 | 0,00 | 13,30 | 84,70 | 48,00 | 3,60 | 2,80 | 10,44 | 1,80 |
| UM-21-02 | 0 | 0 | 0 | 0 | 1,41 | 0 | 0 | 0 | 0 | 47,05 | 27,18 | 7,24 | 2,21 | 0,03 | 2,47 | 31,57 | 0,31 | 2,05 | 0,33 | 0,00 | 1,34 | 0,00 | 0,00 | 11,60 | 95,60 | 29,00 | 3,10 | 2,70 | 7,22 | 1,67 |
| UM-21-03 | 0 | 0 | 0 | 0 | 2,15 | 0 | 0 | 0 | 0 | 45,62 | 20,28 | 8,81 | 3,00 | 0,03 | 3,57 | 32,49 | 1,97 | 1,56 | 0,45 | 0,00 | 1,30 | 0,00 | 0,00 | 16,30 | 10,80 | 29,00 | 3,70 | 3,10 | 13,52 | 2,66 |
| UM-21-04 | 0 | 0 | 0 | 0 | 0,59 | 0 | 0 | 0 | 0 | 47,86 | 47,58 | 13,83 | 4,87 | 0,04 | 2,04 | 12,37 | 0,52 | 4,23 | 0,59 | 0,00 | 3,17 | 0,00 | 0,00 | 40,20 | 145,00 | 20,00 | 5,80 | 4,70 | 17,48 | 2,33 |
| UM-21-05 | 0 | 0 | 0 | 0 | 1,95 | 0 | 0 | 0 | 0 | 45,62 | 28,76 | 8,00 | 2,37 | 0,02 | 3,40 | 28,49 | 0,62 | 2,06 | 0,41 | 0,00 | 1,98 | 0,00 | 0,00 | 28,00 | 74,20 | 20,00 | 2,60 | 2,20 | 11,07 | 1,64 |
| UM-21-07 | 0 | 0 | 0 | 0 | 1,62 | 0 | 0 | 0 | 0 | 45,51 | 15,31 | 4,55 | 1,99 | 0,03 | 2,02 | 39,67 | 0,26 | 1,30 | 0,17 | 0,00 | 1,15 | 0,00 | 0,00 | 15,20 | 48,20 | 20,00 | 1,60 | 1,30 | 4,43 | 0,71 |
| UM-21-15 | 0 | 0 | 0 | 0 | 0,97 | 0 | 0 | 0 | 0 | 44,85 | 19,69 | 5,22 | 1,61 | 0,02 | 1,85 | 37,80 | 0,51 | 1,46 | 0,23 | 0,00 | 1,25 | 0,00 | 0,00 | 16,80 | 45,80 | 20,00 | 2,90 | 2,50 | 6,20 | 0,99 |
| UM-21-16 | 0 | 0 | 0 | 0 | 3,59 | 0 | 0 | 0 | 0 | 45,73 | 28,55 | 6,99 | 1,35 | 0,02 | 2,64 | 30,11 | 0,85 | 2,15 | 0,39 | 0,00 | 1,24 | 0,00 | 0,00 | 19,20 | 47,60 | 20,00 | 2,90 | 2,20 | 10,42 | 1,67 |
| UM-21-17 | 0 | 0 | 0 | 0 | 3,60 | 0 | 0 | 0 | 0 | 45,39 | 13,19 | 3,26 | 1,03 | 0,02 | 2,69 | 41,71 | 0,50 | 1,02 | 0,17 | 0,00 | 0,73 | 0,00 | 0,00 | 9,60 | 19,60 | 20,00 | 1,80 | 1,40 | 4,32 | 0,61 |
| UM-21-18 | 0 | 0 | 0 | 0 | 3,57 | 0 | 0 | 0 | 0 | 45,68 | 23,75 | 5,47 | 1,50 | 0,02 | 2,89 | 33,52 | 0,78 | 1,67 | 0,27 | 0,00 | 1,14 | 0,00 | 0,00 | 15,30 | 31,70 | 28,00 | 2,60 | 2,10 | 6,95 | 1,09 |
| UM-21-20 | 0 | 0 | 0 | 0 | 1,56 | 0 | 0 | 0 | 0 | 44,86 | 28,35 | 5,33 | 1,21 | 0,02 | 1,48 | 32,47 | 1,00 | 1,79 | 0,29 | 0,00 | 1,16 | 0,00 | 0,00 | 14,90 | 33,50 | 26,00 | 2,90 | 2,20 | 8,65 | 1,08 |
| UM-21-21 | 0 | 0 | 0 | 0 | 1,38 | 0 | 0 | 0 | 0 | 46,41 | 48,01 | 6,41 | 1,28 | 0,03 | 1,13 | 20,52 | 1,48 | 2,14 | 0,32 | 0,00 | 1,09 | 0,00 | 0,00 | 11,60 | 31,50 | 20,00 | 3,70 | 3,00 | 10,92 | 1,50 |
| UM-21-22 | 0 | 0 | 0 | 0 | 0,65 | 0 | 0 | 0 | 0 | 46,46 | 53,07 | 7,26 | 0,65 | 0,00 | 1,03 | 17,94 | 0,43 | 3,06 | 0,11 | 0,00 | 1,50 | 0,00 | 0,00 | 32,90 | 14,80 | 20,00 | 4,50 | 3,30 | 18,26 | 3,30 |
| UM-21-23 | 0 | 0 | 0 | 0 | 5,02 | 0 | 0 | 0 | 0 | 48,17 | 53,17 | 8,38 | 1,87 | 0,03 | 2,78 | 14,15 | 1,63 | 2,75 | 0,43 | 0,00 | 1,31 | 0,00 | 0,00 | 27,60 | 38,30 | 20,00 | 4,50 | 3,60 | 12,72 | 1,71 |
| UM-21-24 | 0 | 0 | 0 | 0 | 1,27 | 0 | 0 | 0 | 0 | 44,63 | 16,88 | 3,97 | 1,25 | 0,02 | 1,53 | 40,06 | 0,56 | 1,22 | 0,21 | 0,00 | 1,01 | 0,00 | 0,00 | 13,60 | 21,30 | 20,00 | 2,70 | 2,20 | 5,73 | 0,95 |
| UM-21-25 | 0 | 0 | 0 | 0 | 0,74 | 0 | 0 | 0 | 0 | 41,2 | 20,21 | 2,91 | 0,85 | 0,02 | 0,78 | 40,16 | 0,85 | 0,57 | 0,14 | 0,00 | 0,81 | 0,00 | 0,00 | 6,00 | 13,20 | 20,00 | 3,30 | 2,80 | 4,08 | 0,87 |
| UM-21-26 | 0 | 0 | 0 | 0 | 1,36 | 0 | 0 | 0 | 0 | 44,31 | 15,99 | 4,75 | 1,93 | 0,03 | 1,90 | 39,24 | 0,54 | 1,53 | 0,27 | 0,00 | 1,27 | 0,00 | 0,00 | 18,60 | 20,60 | 20,00 | 3,60 | 3,00 | 6,82 | 1,04 |
| UM-21-27 | 0 | 0 | 0 | 0 | 1,14 | 0 | 0 | 0 | 0 | 44,47 | 19,05 | 3,76 | 0,99 | 0,02 | 1,16 | 39,32 | 0,59 | 1,32 | 0,19 | 0,00 | 0,76 | 0,00 | 0,00 | 12,50 | 25,50 | 20,00 | 1,90 | 1,50 | 5,44 | 0,85 |
| UM-21-43 | 0 | 0 | 0 | 0 | 1,43 | 0 | 0 | 0 | 0 | 46,41 | 29,57 | 7,29 | 2,54 | 0,04 | 2,36 | 29,90 | 0,28 | 2,36 | 0,32 | 0,00 | 1,00 | 0,00 | 0,00 | 9,80 | 68,90 | 23,00 | 3,70 | 3,00 | 8,26 | 1,49 |
| UM-21-44 | 0 | 0 | 0 | 0 | 2,19 | 0 | 0 | 0 | 0 | 45,21 | 7,80 | 2,30 | 1,26 | 0,02 | 2,45 | 45,60 | 0,03 | 0,81 | 0,11 | 0,00 | 0,56 | 0,00 | 0,00 | 4,10 | 21,20 | 20,00 | 1,10 | 0,90 | 2,59 | 0,64 |
| UM-21-45 | 0 | 0 | 0 | 0 | 1,47 | 0 | 0 | 0 | 0 | 45,69 | 15,54 | 4,74 | 1,80 | 0,04 | 1,92 | 39,78 | 0,10 | 1,63 | 0,22 | 0,00 | 0,90 | 0,00 | 0,00 | 6,00 | 37,00 | 20,00 | 2,40 | 1,90 | 5,12 | 0,98 |

**A3: Annexes for Chapter 3 – Numerical modelling experiment**

A3 Supplementary Text:

*A3.1 Strength reduction method: criteria*

As seen in Figure 3.2c, $E_k$ rises to a peak value at the beginning of the failure stage before it gradually decreases while the slope stabilises again to a new condition. From the initiation of failure, the combination of the three criteria presented is necessary to define stability since each criterion has proven insufficient when used independently. For instance, $E_k$ oscillates a lot and sometimes falls below the set threshold even though failure is still ongoing. The moving average of $E_k$, namely $\bar{E}_k$, is much more stable but is sometimes unable to detect a sudden failure initiation, whereas the absolute value $E_k$ jumps up instantly when failure begins. The crack criterion has proven to be critical for detecting faint deformation within the slope before failure occurs when the $E_k$ and $\bar{E}_k$ criteria are ineffective (Figure 3.3d). However, cracking does not occur in the late deformation stages of the slope failure when the particle assembly is already highly disintegrated.

After testing, we chose $6 \cdot 10^{10}$ J for both the $E_k$ and $\bar{E}_k$ threshold values for all our simulations. A bottom noise of $E_k$ exists and the thresholds should be set to be above that bottom noise for all configurations. The threshold should not be too high, otherwise it loses its effectiveness to detect failure. The recording interval of the moving average applied on $E_k$ ($\bar{E}_k$) was set to 3,000 iterations and was approved in tests discussed in Section 3. In all our simulations SR-criteria were checked every 100 iterations.

For the duration of the failure SR is halted and the inter-particle strength curve shows a horizontal line further referred to as the “failure plateau”. The plateau ends when the slope stabilises again after failure and further SR leads to more deformation on the already failed slope. In addition to the iterations, the Yade DEM formulation provides an intrinsic simulation time (iterations x timestep) during the execution of each simulation. For our results, we prefer this parameter over iterations to express the temporal dimension. This allows for a better comparison of the temporal evolution between different simulations, as the preconditioning stage duration can be quite different between configurations.

*A3.2 Parametrization sensitivity*

The averaged values of $T_p$ and $C_p$ at failure do not show major differences when varying parameterization, moving average interval (MAV-INT) for $\bar{E}_k$ and mean particle radius (R) or when using different particle arrangements (packings) (see Table A3.2). The tested moving average intervals yield values that do not differ greatly. However, we suspect that in some cases a moving average computed over a shorter interval (e.g., 1,000 iterations instead of 3,000) could lead to less SR by not giving the slope model sufficient time to respond. A moving average interval of 3,000 iterations seems to provide the best compromise for the extraction of inter-particle strength values. Even though the packings with higher particle number and lower particle radius (R = 15 m) tend to fail globally for slightly higher inter-particle strengths, this difference lies well within the range of values observed for packings with mean particle radius of R = 20 m (Table A3.2). For the lab-scale tests, we also examined the influence of the ratio between the thickness of the model and the diameter of the particles (ratio T/D). For a ratio T/D larger than 10 constriction effects become negligible (see also Calvetti et al. (1997), and Figure A3.4), and the results become insensitive to particle size. In our slope simulations, particles with a size of R = 20 m can therefore be used to reduce computational costs without significant loss of precision, while at a model resolution of T/D = 10, a model thickness of 400 m, ensures consistent results.

*A3.3 Results visualisations*

The failure surfaces of our slope simulations were all extracted at the last recorded state within the failure plateau (see Figure 3.2c+d). These surfaces are drawn from black and white displacement visualisations in side view of the model. The rupture surface lines are drawn using an intensity filter within the Engauge Digitizer software (Mitchell et al., 2023) where the averaged displacement exceeds the mean particle diameter.

The deviatoric strain maps were calculated with YADE: the values that represent the magnitude of shear strain are derived from the second invariant of the deviatoric part of the strain tensor (see details of the calculation in (Smilauer et al., 2021) and in (Catalano et al., 2013)). Deviatoric strain is calculated here over the previous 1,000 iterations which corresponds to one recording step.

For the visualisations of our DEM results, we used the open source software Paraview (Ahrens et al., 2005).

A3 Supplementary Figures:

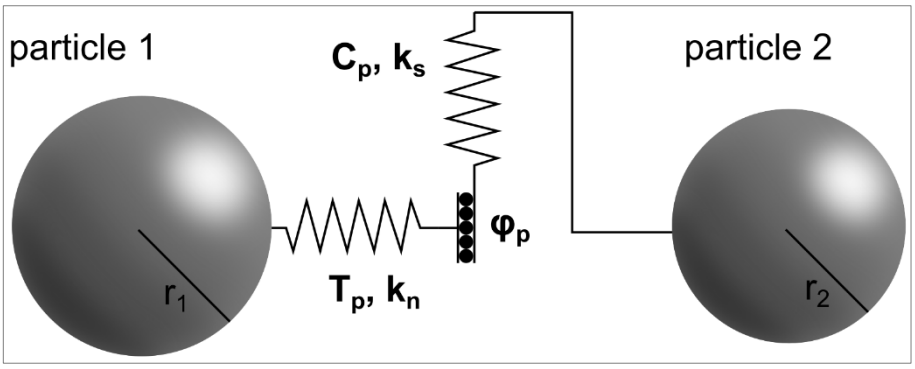


*Figure A3.1: Elastic-cohesive-frictional interparticle model used in this study: $k_n$ and $k_s$ are the normal and shear stiffnesses respectively, $T_p$ is the interparticle tensile strength, $C_p$ is the inter-particle cohesion, $\varphi_p$ is the inter-particle friction angle, and $r_1$ and $r_2$ are the particle radii.*

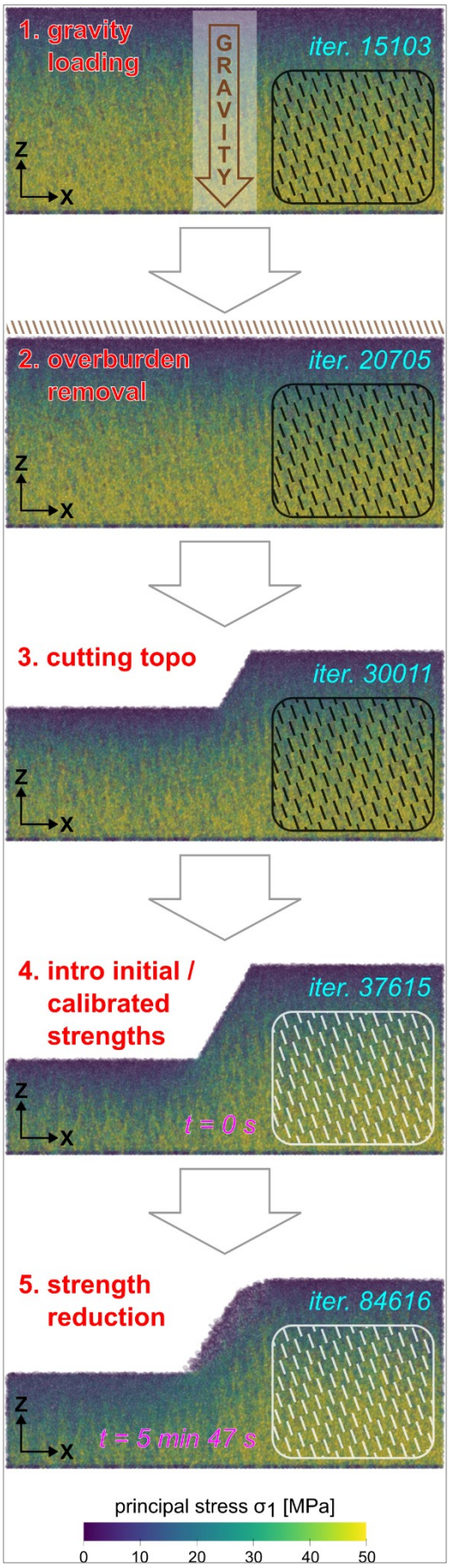


*Figure A3.2: the complete loading procedure illustrated for the configuration with anisotropy angle α = 70° and slope angle β = 60°: 1) gravity loading with overburden, 2,3) progressive cutting of the slope topography, 4) introduction of calibrated strengths, and 5) application of strength reduction up to failure. Note the difference between iterations and simulation time t which is set to 0 when the calibrated strengths are introduced.*

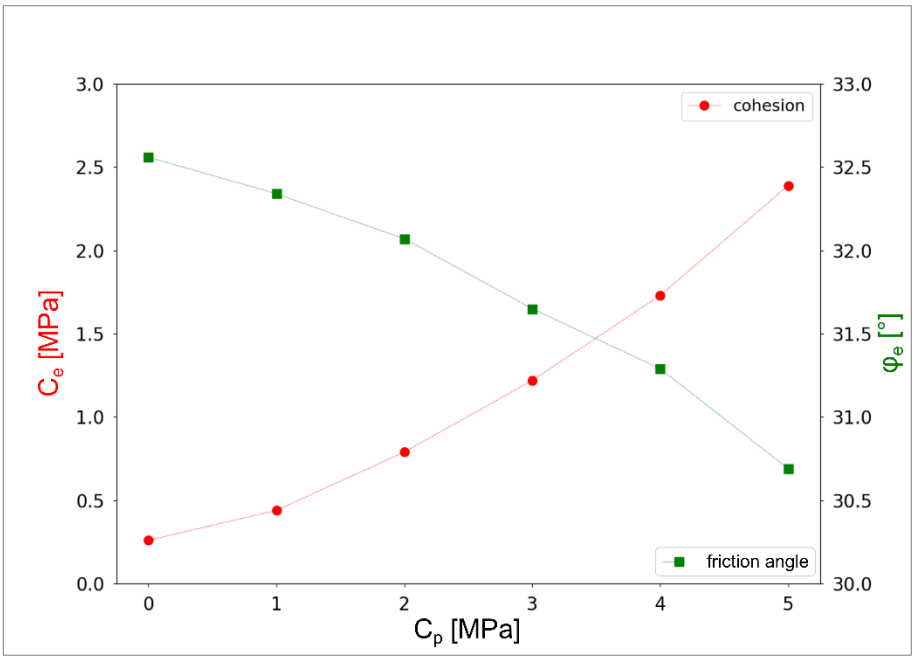


*Figure A3.3: Biaxial tests results (lab-scale) showing the evolution of the emergent Mohr-Coulomb properties, emergent cohesion $C_e$ and emergent friction angle $\varphi_e$, as functions of the interparticle cohesion values $C_p$.*

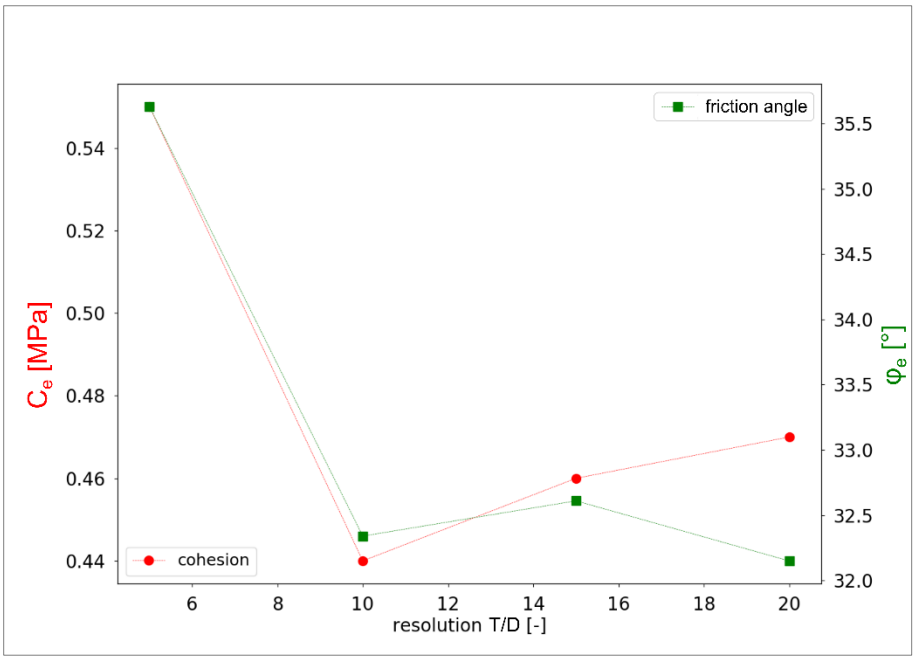


*Figure A3.4: Influence of the ratio between the thickness T of the model and the diameter D of the particles (T/D, also referred to as resolution) on the emergent properties ($C_e$ and $\varphi_e$) of the model explored by the use of biaxial test simulations (same as Figure A3.3).*

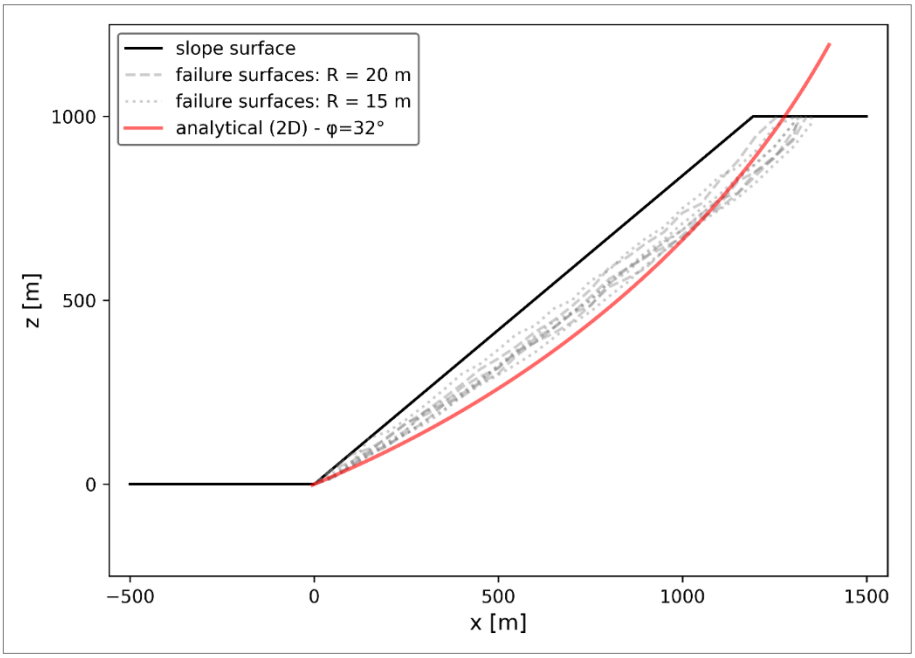


*Figure A3.5: The β = 40° slope results obtained for 2 resolutions (mean particle radius R = 20 m and R = 15 m respectively) compared to Leshchinsky et al. (1985)'s 2D analytical slope stability solution for φ = 32° (red curve).*

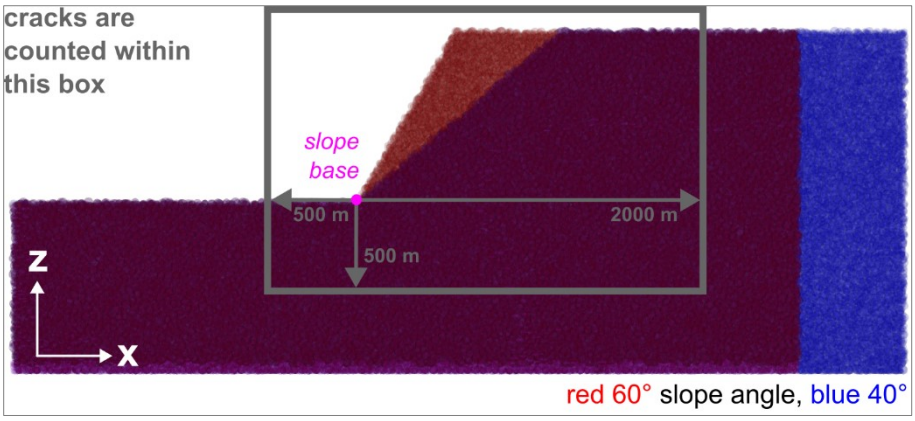


*Figure A3.6: For all simulations, cracks were only counted if they are located in the vicinity of the slope: 500 m before, 500 m below and 2000 m behind the slope base. The same bounds were used for the β = 40° and 60° slopes.*

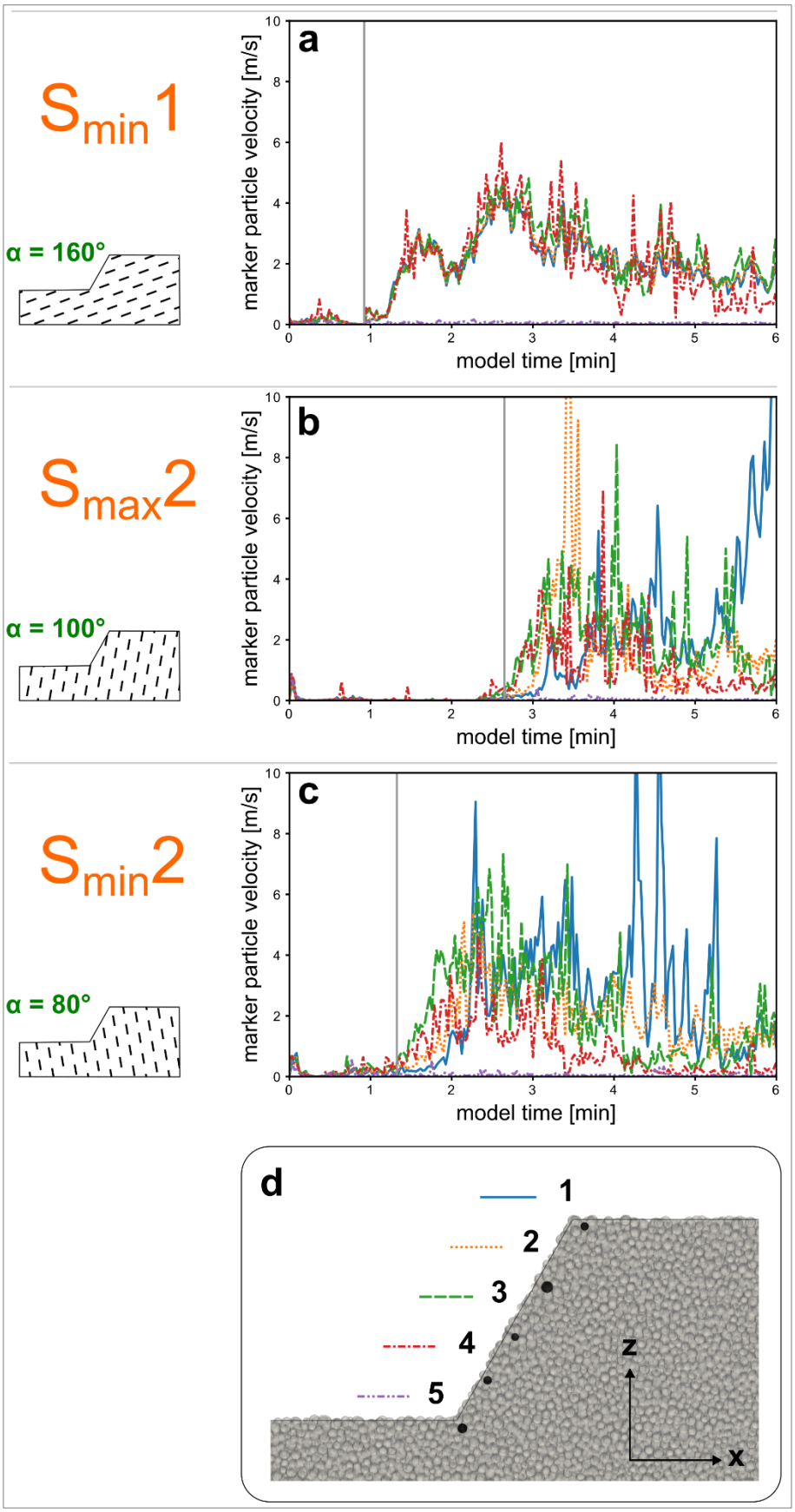


*Figure A3.7: Evolution of the velocity of the marker particles located on the β = 60° slope face for a) α = 160°, b) α = 100°, and c) α = 80°. Marker particles of α = 20° do not move considerably and there is therefore no need to present this case. The onset of the principal failure is marked with a grey vertical line. The initial position of the marker particles are indicated in d.*

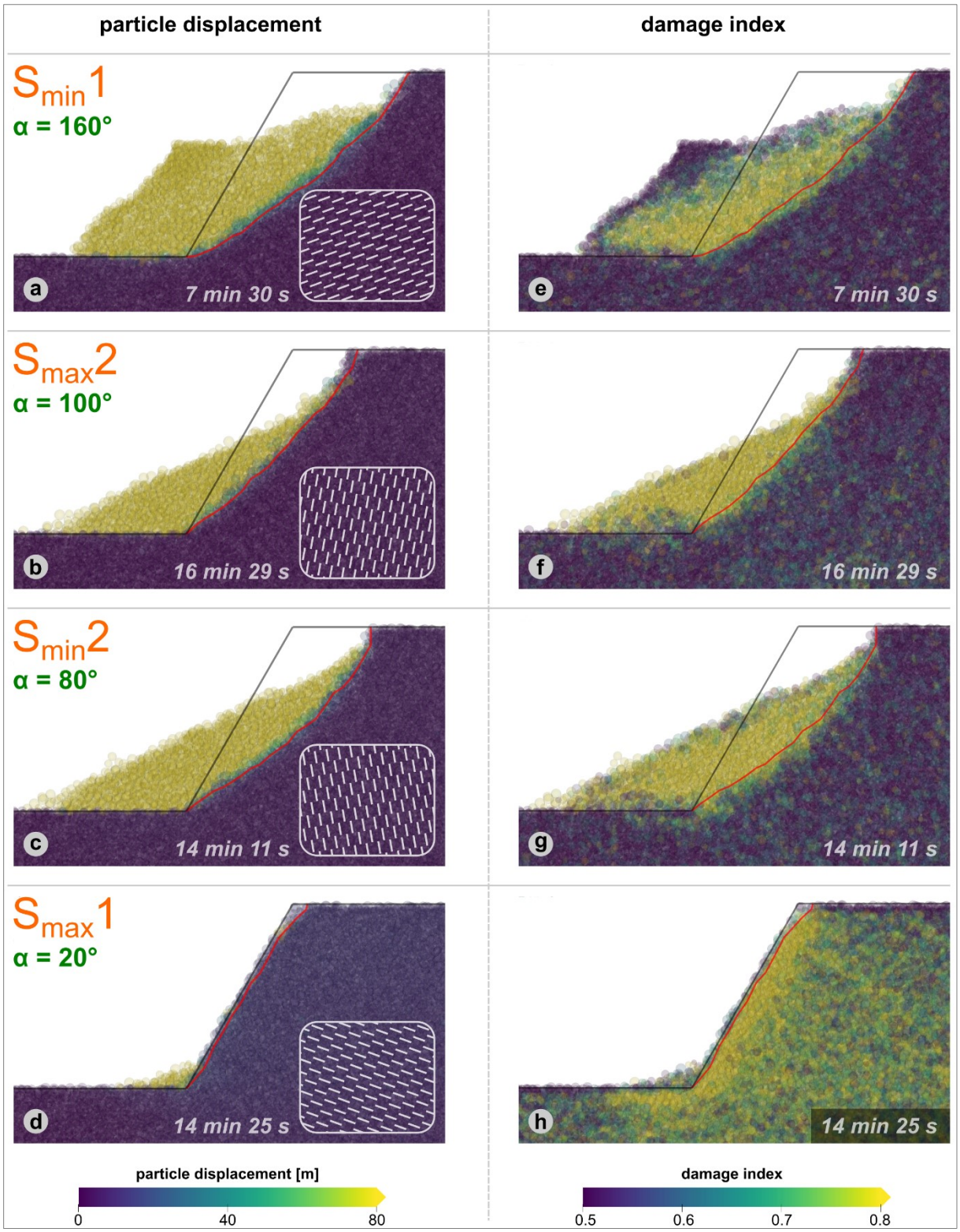


*Figure A3.8: Displacement of particles during failure (a - d) and damage index (ratio number of cracks per particle over initial number of cohesive bonds) at the end of failure (e - h) for the four stability extrema cases (packing P1). White boxes within displacement maps show the orientation of the isotropy plane. Black lines show original slope surface, red lines show rupture surfaces (see Section 2.3).*

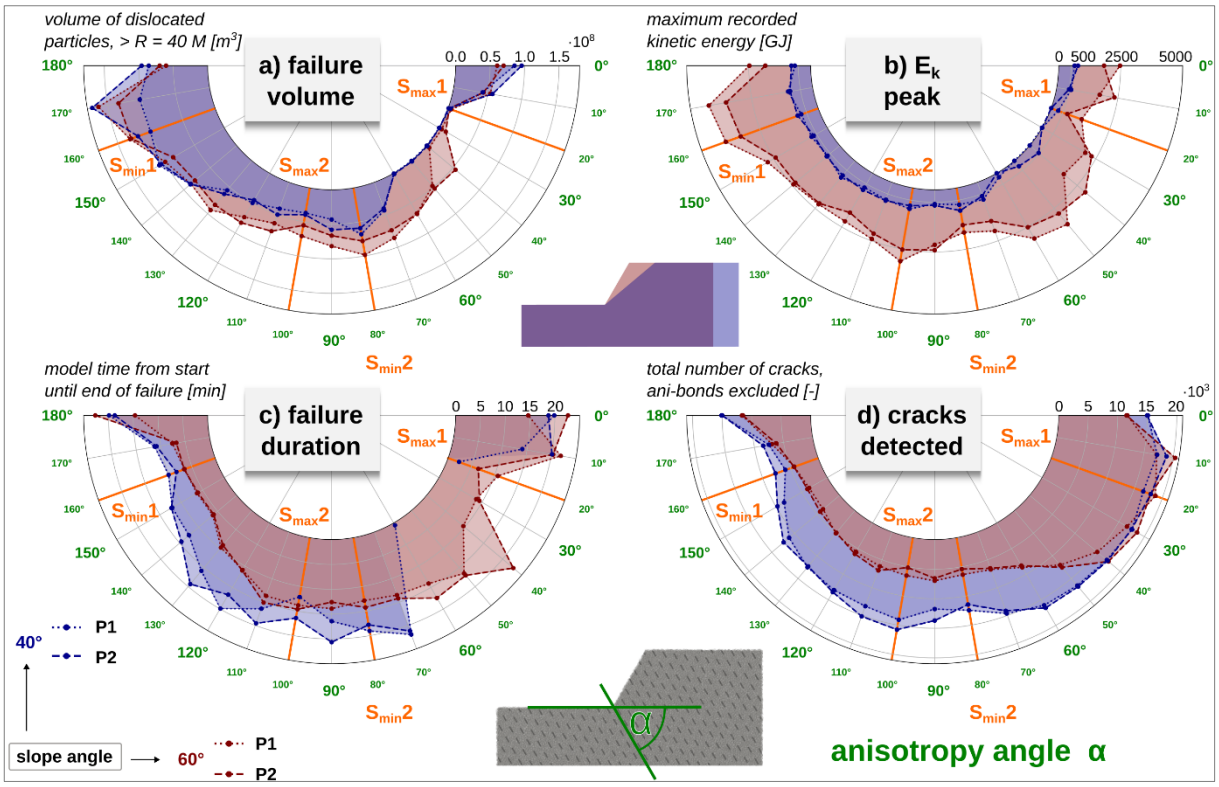


*Figure A3.9: Mobilized (failed) volume at failure, kinetic energy ($E_k$) peak at failure, failure duration and total number of cracks at the end of failure of all simulations in this study with anisotropic rock strength ($\alpha \in [0°, 180°]$ in 10° increments; $\beta = 40°$ and 60°; packings P1 and P2).*

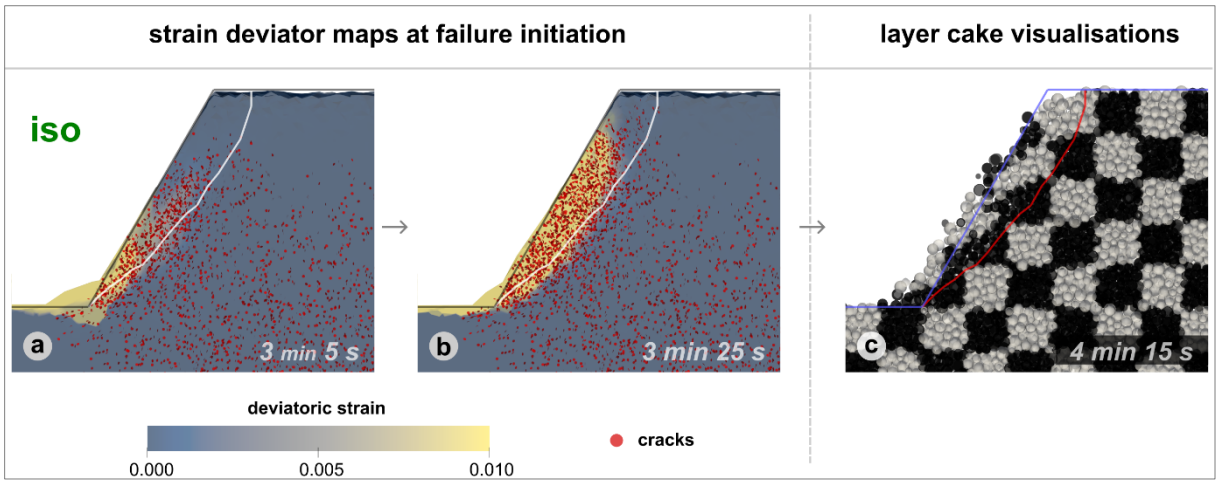


*Figure A3.10: a - b: strain deviator maps (Supplementary Text A3.3) with cracks at two early recording steps for the isotropic case (β = 60°, packing P1). Black lines show original slope surface, white lines show rupture surfaces (Supplementary Text A3.3). c: layer cake visualization for isotropic case, final rupture surface here in red.*

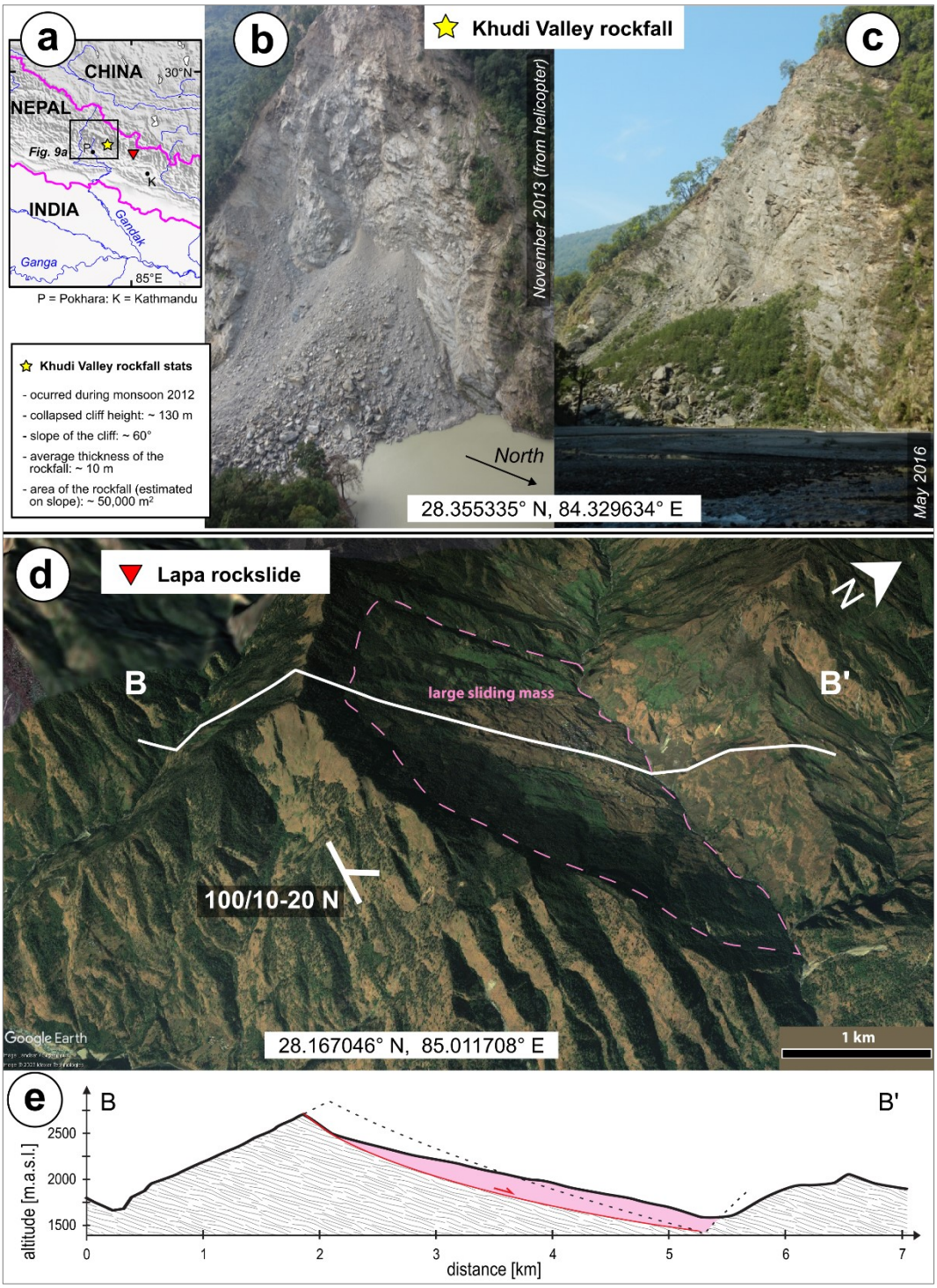


*Figure A3.11: a) Map showing locations and map dimensions from Figure 3.9a. b) Aerial photo of the Khudi Valley rockfall about one year after the event. c) Another photo of the same event after four years (note that vegetation quickly re-occupies the talus cone). d) Google Earth (2023) imagery of the Lapa rockslide in the Ankhu Khola region described by Thouret (1983). e) Profile of Lapa rockslide with estimated extent of event (failed rock material in pink).*

A3 Supplementary Tables:

Table A3.1: Inter-particle bond properties of the DEM material calibrated to a typical gneissic rock material (tested by Saroglou et al., 2004).

| Parameter | ordinary bonds | weakness plane bonds |
|---|---|---|
| Interaction radius intR [-] | 1.1 | - |
| Elastic modulus Y [GPa] | 300 | 1 |
| Stiffness ratio P [-] | 0.1 | 0.1 |
| Tensile strength $T_p$ [MPa] | 50 | 0 |
| Cohesion $C_p$ [MPa] | 50 | 0 |
| Friction angle $\varphi_p$ [°] | 10 | 0 |
| Dilation angle ψ [°] | - | 0 |
| Angle range $\gamma_{limit}$ [°] | - | 55 |

Table A3.2: Inter-particle $T_p$ and $C_p$ values (MPa) at failure for the isotropic slope models.

| nb of particles* | MAV-INT 1000 | | | | MAV-INT 3000 | | | | MAV-INT 5000 | | | |
|---|---|---|---|---|---|---|---|---|---|---|---|---|
| | β = 40° slope | | β = 60° slope | | β = 40° slope | | β = 60° slope | | β = 40° slope | | β = 60° slope | |
| **R = 20 m** | | | | | | | | | | | | |
| **86729** | 0.46 | | 2.78 | | 0.52 | | 2.78 | | 0.42 | | 3.09 | |
| **89212** | 0.34 | | 2.78 | | 0.25 | | 2.78 | | 0.27 | | 2.78 | |
| **89237** | 0.27 | **0.363** | 2.78 | **2.943** | 0.38 | **0.418** | 2.78 | **2.858** | 0.38 | **0.363** | 2.78 | **2.935** |
| **89544** | 0.38 | **± 0.079** | 3.43 | **± 0.325** | 0.52 | **± 0.130** | 3.09 | **± 0.155** | 0.38 | **± 0.064** | 3.09 | **± 0.179** |
| **R = 15 m** | | | | | | | | | | | | |
| **218967** | 0.25 | | 3.09 | | 0.38 | | 3.09 | | 0.38 | | 3.09 | |
| **219015** | 0.57 | | 3.09 | | 0.64 | | 3.09 | | 0.64 | | 3.09 | |
| **219052** | 0.52 | **0.420** | 3.43 | **3.175** | 0.52 | **0.480** | 3.09 | **3.090** | 0.46 | **0.445** | 3.43 | **3.175** |
| **219453** | 0.34 | **± 0.150** | 3.09 | **± 0.170** | 0.38 | **± 0.125** | 3.09 | **± 0.000** | 0.30 | **± 0.145** | 3.09 | **± 0.170** |

**represent individual packings used* *MAV-INT = moving average interval*

# References of Annexes:


Ahrens, J., Geveci, B., Law, C., 2005. ParaView: An End-User Tool for Large Data Visualization, Visualization Handbook.

Bronk Ramsey, C., 2021. OxCal v. 4.4 https://c14.arch.ox.ac.uk/oxcal.OxCal.html .

Calvetti, F., Combe, G., Lanier, J., 1997. Experimental micromechanical analysis of a 2D granular material: relation between structure evolution and loading path. Mech. Cohes.-Frict. Mater. 2, 121–163. https://doi.org/10.1002/(SICI)1099-1484(199704)2:2<121::AID-CFM27>3.0.CO;2-2

Dinç, Ö., Scholtès, L., 2018. Discrete Analysis of Damage and Shear Banding in Argillaceous Rocks. Rock Mech Rock Eng 51, 1521–1538. https://doi.org/10.1007/s00603-017-1397-6

Dunai, T.J., 2010. Cosmogenic nuclides: principles, concepts and applications in the earth surface sciences. Cambridge University Press.

Google Earth Pro V 7.3.6.9345, (December 2, 2010). Satellite Imagery for central Nepal. 28.167046° N, 85.011708° E. Landsat / Copernicus. Maxar Technologies 2023. https://earth.google.com retrieved: September, 2023.

Mitchell, M., Muftakhidinov, B., Winchen, T., 2023. Engauge Digitizer Software, https://doi.org/10.5281/zenodo.3941227.

Reimer, P.J., Austin, W.E.N., Bard, E., Bayliss, A., Blackwell, P.G., Ramsey, C.B., Butzin, M., Cheng, H., Edwards, R.L., Friedrich, M., Grootes, P.M., Guilderson, T.P., Hajdas, I., Heaton, T.J., Hogg, A.G., Hughen, K.A., Kromer, B., Manning, S.W., Muscheler, R., Palmer, J.G., Pearson, C., Plicht, J. van der, Reimer, R.W., Richards, D.A., Scott, E.M., Southon, J.R., Turney, C.S.M., Wacker, L., Adolphi, F., Büntgen, U., Capano, M., Fahrni, S.M., Fogtmann-Schulz, A., Friedrich, R., Köhler, P., Kudsk, S., Miyake, F., Olsen, J., Reinig, F., Sakamoto, M., Sookdeo, A., Talamo, S., 2020. The IntCal20 Northern Hemisphere Radiocarbon Age Calibration Curve (0–55 cal kBP). Radiocarbon 62, 725–757. https://doi.org/10.1017/RDC.2020.41

Saroglou, H., Marinos, P., Tsiambaos, G., 2004. The anisotropic nature of selected metamorphic rocks from Greece. Journal of the Southern African Institute of Mining and Metallurgy 104, 217–222. https://doi.org/10.10520/AJA0038223X_2825

Šmilauer, V., Angelidakis, V., Catalano, E., Caulk, R., Chareyre, B., Chèvremont, W., Dorofeenko, S., Duriez, J., Dyck, N., Elias, J., Er, B., Eulitz, A., Gladky, A., Guo, N., Jakob, C., Kneib, F., Kozicki, J., Marzougui, D., Maurin, R., Modenese, C., Pekmezi, G., Scholtès, L., Sibille, L., Stransky, J., Sweijen, T., Thoeni, K., Yuan, C., 2021. Yade documentation. The Yade Project. https://doi.org/10.5281/zenodo.5705394

Thouret, J.-C., 1983. Géodynamique des grands versants de l'Ankhu Khola, Népal central. Editions du Centre national de la recherche scientifique